Constraining cosmological models with the effective field theory of large-scale structures

Théo Simon

THÈSE POUR OBTENIR LE GRADE DE DOCTEUR DE L'UNIVERSITE DE MONTPELLIER

En Physique

École doctorale : Information, Structures, Systèmes

Unité de recherche : Laboratoire Univers et Particules de Montpellier

Constraining cosmological models with the effective field theory of large-scale structures

Présentée par Théo Simon

Le 27 février 2024

Sous la direction de Julien Lavalle et Vivian Poulin

Devant le jury composé de

Jean-Philippe Uzan, Directeur de recherche, Institut d'Astrophysique de Paris	Président
Guido D'Amico, Professore, Università degli studi di Parma	Rapporteur
Laura Lopez Honorez, Professeure associée, Université Libre de Bruxelles	Rapporteuse
Filippo Vernizzi, Directeur de recherche, Institut de Physique Théorique	Examinateur
Camille Bonvin, Professeure associée, Université de Genève	Invitée
Martina Gerbino, Ricercatrice, Istituto Nazionale di Fisica Nucleare (sezione di Ferrara)	Invitée
Julien Lavalle, Directeur de recherche, Laboratoire Univers et Particules de Montpellier	Directeur
Vivian Poulin, Chargé de recherche, Laboratoire Univers et Particules de Montpellier	Co-encadrant

UNIVERSITÉ DE MONTPELLIER

Remerciements

Les conditions initiales d'un système prédéterminent partiellement son évolution. L'Univers a son Big Bang, moi, j'ai Julien et Vivian. Et aujourd'hui, je vous le dis : du fond du coeur, merci. Vous m'avez transmis ce qu'il y a de plus beau et de plus authentique : la connaissance vraie, celle qui s'épanouit dans un travail qui n'en est plus un. Je ne saurais épuiser ici l'ensemble de vos qualités qui ont engendré mon épanouissement intellectuel au cours de ma thèse ; je retiendrai, dans ces lignes, votre indéfectible soutien à toute épreuve, votre bonne humeur quotidienne, ainsi que votre insatiable appétence pour la recherche que vous déléguez généreusement à chaque instant. Vivian, resteront gravées dans ma mémoire, à jamais, la totalité des bons moments que nous avons passés ensemble et toutes les choses que j'ai apprises à tes côtés[1]. Tes intempestives critiques sur la Bretagne n'ont pas (encore ?) réussi à ternir la reconnaissance infinie que je te porte. Julien, je ne saurais énumérer — bien que je sache m'en rappeler — l'ensemble des conversations fructueuses que nous avons eues. Je t'exprime ma plus sincère gratitude pour tout ce que tu as fait pour moi, pour ton investissement sans faille dans mon accompagnement, ainsi que pour ton soutien dans toutes les rudes épreuves administratives que nous avons parcourues ensemble. Je suis heureux de dire aujourd'hui, qu'à l'inverse de l'Univers, je sais d'où je viens. Et ça, c'est stylé !

Ma thèse aurait sans aucun doute eu beaucoup moins de saveur sans de précieuses rencontres professionnelles qui se sont rapidement muées en profondes amitiés : Pierre et Tristan[2], mes deux indéfectibles collaborateurs de la première heure. Je pense que vous n'imaginez pas tout ce que vous m'avez apporté. Sur le plan scientifique d'abord. Vous avez tous les deux participé activement à l'élaboration des savoirs que je possède aujourd'hui. Je remercie tout particulièrement Pierre de m'avoir initié et formé à l'EFTofLSS et, plus globalement, aux structures à grandes échelles. Puis, sur le plan humain ensuite. J'ai certes découvert que la recherche ne pouvait fonctionner sans la coopération de personnes qui partagent une exaltation commune, mais, avec vous, j'ai découvert quelque chose d'encore bien plus précieux : sans bienveillance et gentillesse, la recherche perd certainement la plus belle chose qu'elle a à gagner. Je souhaite à tous les thésards du monde entier d'avoir un Pierre et un Tristan pour les accompagner dans leur thèse !

J'exprime ensuite ma sincère gratitude à tous les membres de mon jury de thèse pour leur investissement le jour de ma soutenance et les palpitants échanges qui s'ensuivirent. Je tiens en particulier à remercier Guido d'Amico et Laura Lopez-Honorez, les deux rapporteur.euses de

[1] Je parle bien évidemment ici du football américain et de la recette de la pâte à pizza.

[2] Please allow me to write these lines in French, as this language is no longer a secret to you.

ma thèse, pour leur lecture attentive et leurs commentaires constructifs.

Il me semble également important de remercier ici Julien Bernard, mon encadrant de mémoire de philosophie, pour la confiance qu'il a placée dans mon projet, ainsi que pour ses multiples conseils avisés. Je le remercie de s'être adapté à ma situation particulière, et aux inhabituelles contraintes associées, dans la mesure où j'ai rédigé ce mémoire durant ma deuxième année de thèse. Je garderai un très bon souvenir de nos fructueux échanges qui m'ont permis d'avoir une première approche très réussie de la recherche en philosophie, et m'ont permis d'exploiter la complémentarité épistémique entre philosophie et physique. J'exprime également toute ma reconnaissance à Gauvin Leconte-Chevillard, pour ton absolue gentillesse ainsi que pour nos discussions très stimulantes. Parler de philosophie et de cosmologie avec toi est un immense plaisir, et j'espère que notre amitié ira au-delà de ce cadre.

Je profite de ces quelques lignes pour remercier le *Laboratoire Univers et Particules* pour tous les bons moments que j'y ai passés. Je remercie en particulier le personnel administratif pour sa patience et sa persévérance lors de toutes les difficultés administratives que j'ai rencontrées, ainsi que l'équipe de direction (notamment Denis Puy) pour la confiance et le soutien qu'elle m'a accordé à plusieurs reprises. Je remercie également tous les membres du laboratoire avec qui j'ai eu des échanges politiques enrichissants et qui ont participé activement à mon activité politique lors de ces trois dernières années, notamment Ana Palacios, Julien Larena, Julien Morin, Morgane Deal et Vincent Guillet.

Je souhaite également exprimer ma gratitude à Sergio Di Matteo et Aziz Ghoufi, mes deux enseignants de licence qui me suivent depuis le début de mon cursus universitaire et avec qui j'ai gardé aujourd'hui de très bons contacts. Vous avez été pour moi un exemple que je me suis efforcé de suivre durant toutes mes études. J'ai conscience que je vous dois énormément, et que sans votre rencontre, le physicien que je suis devenu aujourd'hui aurait été bien différent.

Je tiens à exprimer ma profonde gratitude à tous.tes mes ami.e.s qui m'ont directement accompagné lors de cette aventure montpellierenne. Tout d'abord, je remercie du fond du coeur mes compagnons de luxe de la toute première heure : Alice qui m'a appris mieux que quiconque à lire dans les étoiles, mais qui m'a surtout indéfectiblement soutenu à de nombreuses reprises ; Chadi pour ta douceur, ta bonne humeur et ton grand cœur qui font de toi un ami en or ; Hugo pour ta gentillesse infinie, pour m'avoir accompagné dans toutes les étapes de ma thèse (je ne pouvais espérer mieux), et pour tous les innombrables moments inoubliables que nous avons passés ensemble qui font de toi un ami absolument extraordinaire ; Kélian pour tes gaufres exceptionnelles et ta rayonnante joie de vivre capable de surmonter toutes les épreuves. Je remercie ensuite Giacomo pour toutes nos conversations passionnantes et pour toutes nos sorties sportives. Je remercie également Khalil pour toutes les luttes que nous avons menées ensemble et pour tous les moments forts que nous avons partagés (ainsi toutes les fois où tu as – volontairement ? – perdu au padel). Un grand merci à Justine pour nos innombrables discussions jusqu'au bout de la nuit et pour tes précieux conseils sur la vie. J'exprime ma profonde reconnaissance à Adèle, Arianna, Daniel, Elsa, Francesca, Jay, Michele, Natalie, Nathan x2, Pierre, Romain, Tais, Théo et Thomas pour tous les moments intenses que j'ai vécus avec vous au labo ou dans les rues de Montpellier. Je remercie sincèrement mes ami.e.s du L2C, Benjamin, Juliette et Tristan, pour nos indénombrables soirées mémorables et tous les délires que nous avons vécus ensemble. Je souhaite également remercier les anciens thésards

et postdocs qui ont croisé ma route et m'ont fortement inspiré : Gaétan, Marco, MJ, Riki et Rodrigo. J'adresse en particulier mes sincères remerciements à Guillermo pour ta patience et ton aide précieuse lors du démarrage de ma thèse : mille mercis ! Enfin, je remercie du fond du cœur Casey et Rebecca (sans oublier Jabba et Jasper !) pour tous les moments fantastiques que nous avons passés avec Tristan et Vivian.

Puis, une grande pensée me conduit naturellement vers mes ami.e.s d'avant. J'aimerais tous.tes vous énumérer ici, mais ça n'aurait pas beaucoup de sens : vous êtes dans mon cœur et vous le savez. Je souhaite cependant ici remercier chaleureusement mes ami.e.s du Master NPAC, notamment Antoine, Gilles, Lucas, Simon et Tyann, sans qui l'apprentissage de la physique aurait été bien triste. Je souhaite remercier Noémie, avec qui j'ai noué une amitié très profonde qui, j'en suis certain, traversera les décennies (et même les siècles) : merci, merci, merci, je te dois tellement ! Je souhaite remercier Alizé et Matilin pour leur intelligence de l'esprit, amis également leur intelligence du cœur : vous êtes des personnes extraordinaires. Une dernière pensée me conduit tout droit vers Adrien et JB, mes amis de toujours et pour toujours.

Je veux aujourd'hui témoigner toute ma reconnaissance à mes parents pour leurs multiples encouragements, et leur indéfectible soutien, que ce soit dans ce projet en particulier ou dans mes autres perspectives de vie. Sans vous, et sans la curiosité que vous m'avez transmise, je n'aurais jamais pu réaliser ce travail. Je vous remercie chaleureusement pour tout, et pour bien plus encore… Je remercie également tout le reste de ma famille, notamment Anaïs, Aurélie, Blandine, Corinne, Fabienne, Hervé et Sara, pour avoir suivi attentivement mon parcours. Je souhaite tout particulièrement remercier mon frère Alan et mes grands-parents, Geneviève, Jean-Pierre et Marinette (qui ont eu le courage d'assister à ma soutenance !), pour m'avoir supporté[3] ces longues années et pour avoir contribué à construire la personne qui a pu écrire cette thèse aujourd'hui.

Je terminerai en remerciant toutes les personnes (qui ont été) importantes dans ma vie, mais que ma pudeur m'empêche de mentionner explicitement ici.

[3] Dans tous les sens du terme.

Contents

I General introduction 1

1 The ΛCDM model in a nutshell 5
- 1.1 The ΛCDM ingredients . . . 6
  - 1.1.1 The cosmological principle . . . 6
  - 1.1.2 The two fundamental equations of modern cosmology . . . 7
  - 1.1.3 The components of the Universe . . . 11
  - 1.1.4 Initial conditions . . . 14
- 1.2 The smooth universe . . . 15
  - 1.2.1 The FLRW geometry . . . 15
  - 1.2.2 The stress-energy tensor of the smooth Universe and the continuity equation . . . 17
  - 1.2.3 The smooth Einstein equations . . . 18
  - 1.2.4 The smooth Boltzmann equations . . . 18
  - 1.2.5 Evolution of the smooth universe . . . 20
  - 1.2.6 Cosmological distances . . . 22
  - 1.2.7 Initial conditions: the inflationary paradigm . . . 24
- 1.3 Successes and challenges of the ΛCDM model . . . 26
  - 1.3.1 Successes of the ΛCDM model . . . 26
  - 1.3.2 Limits of the ΛCDM model . . . 27

2 The linearly perturbed universe and CMB physics 31
- 2.1 From the homogeneous universe to the perturbed universe . . . 33
  - 2.1.1 Perturbation of the metric . . . 33
  - 2.1.2 Perturbation of the stress-energy tensor . . . 34
  - 2.1.3 Perturbation of the phase-space distribution function . . . 36
- 2.2 The perturbed universe . . . 37
  - 2.2.1 Perturbed Einstein's equations . . . 37
  - 2.2.2 Conservation of the stress-energy tensor . . . 38
  - 2.2.3 Perturbed Boltzmann's equations . . . 41
  - 2.2.4 Partial summary . . . 45
- 2.3 Initial conditions . . . 47
  - 2.3.1 Adiabatic and isocurvature perturbations . . . 47
  - 2.3.2 Primordial power spectrum . . . 49
- 2.4 CMB physics . . . 52
  - 2.4.1 CMB power spectrum . . . 52
  - 2.4.2 The CMB anisotropies . . . 54
  - 2.4.3 A description of the CMB temperature power spectrum . . . 57
  - 2.4.4 Cosmological parameters. . . . 61

2.4.5 Other CMB power spectra 63

3 Beyond the linearly perturbed universe and large-scale structure physics 67
3.1 The linear matter power spectrum 68
3.1.1 The (relevant) perturbation equations 69
3.1.2 Solving the perturbation equations 70
3.1.3 The various analytical solutions 72
3.1.4 The transfer function 73
3.1.5 The shape of the matter power spectrum 74
3.1.6 The growth factor 74
3.1.7 Impact of the ΛCDM parameters on the matter power spectrum 75
3.2 Biased tracer statistics in linear perturbation theory 76
3.2.1 Biased tracers 76
3.2.2 Galaxy density field perturbation 82
3.2.3 The linear galaxy power spectrum 84
3.2.4 Alcock-Paczyński parameters and BAO 87
3.3 Beyond the linear theory 90
3.3.1 The Vlasov-Poisson system 91
3.3.2 The standard perturbation theory 93
3.3.3 Non-linear matter power spectrum 97
3.4 The effective field theory of large-scale structures 100
3.4.1 The basics of EFTofLSS 100
3.4.2 The EFTofLSS matter power spectrum 104
3.4.3 The EFTofLSS galaxy power spectrum 109
3.4.4 Additional effects 116

II The effective field theory of large-scale structures applied to (e)BOSS data and its consistency within the ΛCDM model 119

4 Cosmological inference from the EFTofLSS: the eBOSS QSO full-shape analysis 123
4.1 Analysis pipeline 124
4.1.1 Cosmological inference setup 124
4.1.2 Scale cut from governing scales 127
4.1.3 Assessing systematics beyond the EFT reach 129
4.1.4 Including redshift error in EFTofLSS 131
4.2 Constraints on flat ΛCDM 133
4.2.1 Flat ΛCDM from the EFT analysis of eBOSS 136
4.2.2 Comparison with several LSS probes 137
4.2.3 Comparison with Planck 140
4.3 Extensions to the flat ΛCDM model 141
4.3.1 $\Omega_k\Lambda$CDM 141
4.3.2 w_0CDM 144
4.3.3 $\nu\Lambda$CDM 146
4.3.4 $N_{\rm eff}\Lambda$CDM 147
4.4 Conclusions 148

5 Consistency of EFTofLSS analyses of the BOSS data **151**
5.1 The role of EFT priors . . . 153
5.1.1 The two EFT priors . . . 155
5.1.2 Prior weight and volume projection effects . . . 156
5.1.3 Pipeline validation check . . . 157
5.2 Impact of EFT priors in ΛCDM . . . 159
5.2.1 Highlighting the role of the priors . . . 159
5.2.2 How to beat the prior weights and volume effects . . . 162
5.3 Comparison of BOSS measurements . . . 165
5.3.1 Contenders . . . 166
5.3.2 The matchups . . . 166
5.3.3 Measurements comparison summary . . . 169
5.4 Comparison of Reconstructed BAO . . . 169
5.4.1 Inconsistency between post-reconstructed measurements . . . 169
5.4.2 Comparison of extraction methods of reconstructed BAO parameters . . . 171
5.5 Conclusions . . . 172

6 Frequentist investigation of EFTofLSS analyses of the BOSS and eBOSS data **177**
6.1 Analysis Methods . . . 178
6.1.1 Profile Likelihood and Markov Chain Monte Carlo . . . 179
6.1.2 Datasets and analysis choices . . . 181
6.2 The EFTofLSS parametrizations . . . 182
6.2.1 Different parametrizations . . . 183
6.2.2 Priors . . . 184
6.3 Consistency of EFTofLSS from profile likelihood analyses . . . 185
6.3.1 EC vs. WC parametrizations and comparison to MCMC . . . 185
6.3.2 Role of EFT "priors" in the frequentist setting . . . 187
6.3.3 Effect of more constraining data . . . 189
6.4 Profile likelihood results on cosmological parameters . . . 190
6.5 Conclusions . . . 194

III Constraining models beyond ΛCDM with the effective field theory of large-scale structures **197**

7 EFTofLSS' take on the Hubble tension and the early dark energy **205**
7.1 Early Dark Energy Model and Data . . . 207
7.1.1 Review of the EDE model . . . 207
7.1.2 Data and method . . . 210
7.1.3 Details on the BOSS measurements and EFT likelihoods . . . 212
7.2 Updated EFTBOSS constraints on EDE . . . 213
7.2.1 Preliminary study . . . 213
7.2.2 Constraints from various BOSS data . . . 214
7.2.3 Primary CMB-free constraints on EDE . . . 217
7.3 EFTBOSS combined with CMB data . . . 217
7.3.1 EFTBOSS+*Planck*TTTEEE . . . 217
7.3.2 EFTBOSS+*Planck*TT650TEE+ACT . . . 220

7.3.3 EFTBOSS+*Planck*TTTEE+ACT . . . 221
7.3.4 Impact of Pantheon+ data . . . 222
7.4 Conclusions . . . 225
7.4.1 EFTBOSS constraints on EDE alone . . . 225
7.4.2 *Planck*+EFTBOSS constraints on EDE . . . 226
7.4.3 ACT+EFTBOSS constraints on EDE . . . 226
7.4.4 Final comments . . . 227

8 EFTofLSS′ take on the Hubble tension and the acoustic dark energy 229
8.1 The model and the data . . . 230
8.1.1 Review of the ADE model . . . 230
8.1.2 Review of the axion-like EDE model . . . 232
8.1.3 Data and analysis methods . . . 233
8.2 Cosmological results . . . 235
8.2.1 Impact of the EFTofLSS analysis . . . 236
8.2.2 Impact of the Pantheon+ data . . . 238
8.3 Model variations . . . 241
8.3.1 Variation of c_s^2 . . . 241
8.3.2 The cADE model . . . 243
8.4 Conclusions . . . 243

9 EFTofLSS′ take on the S_8 tension and the decaying dark matter 245
9.1 Nonlinear power spectrum in DCDM cosmologies . . . 247
9.1.1 Dark radiation decay products (DCDM $\to$ DR model) . . . 247
9.1.2 Warm dark matter decay products (DCDM $\to$ WDM+DR model) . . . 251
9.2 A comprehensive MCMC analysis of the DCDM models . . . 256
9.2.1 Data and method . . . 256
9.2.2 Dark radiation decay products . . . 258
9.2.3 Warm dark matter decay products . . . 260
9.3 Conclusions . . . 265

10 Conclusion 267

A Cosmological inference from the EFTofLSS: the eBOSS QSO full-shape analysis 275
A.1 What happens if we vary n_s and ω_b in the LSS analyses? . . . 275

B Consistency of EFTofLSS analyses of the BOSS data 279
B.1 Impact of scale cut and multipoles . . . 279
B.2 PyBird vs CLASS-PT: direct comparison . . . 281

C Frequentist investigation of EFTofLSS analyses of the BOSS and eBOSS data 285
C.1 Impact of priors on EFT parameters . . . 285
C.2 Full profile and MCMC results . . . 286
C.3 Best-fit parameters . . . 288

D EFTofLSS′ take on the Hubble tension and the early dark energy 289
D.1 Window function normalization . . . 289

D.2 Additional comparison between the PyBird and CLASS-PT likelihood in EDE . 292
D.3 χ^2 per experiment 293

E EFTofLSS′ take on the Hubble tension and the acoustic dark energy 299
E.1 M_b prior 299
E.2 χ^2 table 299

F EFTofLSS′ take on the S_8 tension and the decaying dark matter 303
F.1 Comparison between the EFTofLSS and N-body methods for the DCDM $\to$ DR model 303
F.2 Assessing the validity of the EFTofLSS in the DCDM $\to$ WDM+DR model . . 305
F.3 The role of the S_8 prior 306
F.4 Supplementary tables of $\chi^2_{\rm min}$ values per experiment 306
F.5 ΛCDM parameters of the DCDM $\to$ WDM+DR model 307

G Résumé en français 313

Part I

General introduction

For many centuries, cosmology was regarded as a branch of metaphysics dealing with the ontological questions relating to the existence, genesis and constitution of the cosmos. Ever since the creation of philosophy and physics, which are considered to have been born together under the pen of the pre-Socratics, somewhere between the 6th and 5th centuries BC, cosmology has been a discipline in which all kinds of speculation were permitted about the supralunar world (which was originally the object of study of cosmology). This freedom in cosmological theories arose naturally from a lack of observational data, insofar as the only data available came from the observation of the motion of the bodies making up the solar system, giving rise to various cosmological theories, among which we can cite Plato's model of homocentric spheres, Hipparchus' model of epicycle circles and Ptolemy's theory of the equant point. For many years, cosmology was therefore considered to be a discipline that did not belong to the scientific circle, essentially due to (i) the absence of data that made it difficult to apply the falsification principle, and (ii) the absence of a complete theory that could describe the evolution and the behaviour of the Universe. However, since the middle of the 20th century, cosmological data has been accumulating, with the development of a large number of telescopes, both terrestrial and space-based, making it possible to collect a wealth of cosmological data going back to the origins of the Universe. In addition, at the beginning of the 20th century, physics underwent an unprecedented upheaval with the development of general relativity, providing a conceptual and theoretical framework for describing the history of the Universe. Insofar as the two points set out above are no longer adapted to the observational and theoretical discoveries of the 20th century, cosmology is now considered to be part of the broad spectrum of modern science, *i.e.*, a mathematical science that attaches particular importance to the empirical study of natural phenomena. However, it should be stressed that cosmology has a number of characteristics that distinguish it from other sciences. Among the many singularities inherent in cosmology, we can quickly mention two here. First, cosmology is unable to provide a substantial explanation of the origins of the initial conditions of the system under consideration, *i.e.*, the Universe, which is unique in physics. In addition, the main objective of cosmology is to derive and characterise the laws of nature that govern the behaviour and evolution of the Universe, but is it really adequate to talk about *laws of nature* when the physical system under study is unique?

Leaving aside these philosophical questions, in this thesis we will constrain models of modern cosmology mainly with data from the large-scale structures of the Universe using a theoretical formalism, *the effective field theory of large-scale structures*, which allows us to explain and describe these data. The work presented in this manuscript is based on several research projects that I carried out with various collaborators during my PhD: [4]

- **T. Simon**, P. Zhang and V. Poulin, *Cosmological inference from the EFTofLSS: the eBOSS QSO full-shape analysis*, **JCAP 07 (2023) 041**, arXiv:2210.14931.

- **T. Simon**, P. Zhang, V. Poulin and T. L. Smith, *Consistency of effective field theory analyses of the BOSS power spectrum*, **Phys. Rev. D 107 (2023) 123530**, arXiv:2208.05929.

- E. Brinch Holm, L. Herold, **T. Simon**, E. Ferreira, S. Hannestad, V. Poulin, and T. Tram, *Bayesian and frequentist investigation of prior effects in EFTofLSS analyses of full-shape BOSS and eBOSS data*, **Phys. Rev. D 108 (2023) 123514**, arXiv:2309.04468.

[4] The papers are listed in order of appearance in the manuscript.

- **T. Simon**, P. Zhang, V. Poulin and T. L. Smith, *Updated constraints from the effective field theory analysis of the BOSS power spectrum on early dark energy*, **Phys. Rev. D 107 (2023) 063505**, arXiv:2208.05930.

- **T. Simon**, *Can acoustic early dark energy still resolve the Hubble tension?*, **submitted to Phys. Rev. D**, arXiv:2310.16800.

- **T. Simon**, G. F. Abellán, P. Du, V. Poulin and Y. Tsai, *Constraining decaying dark matter with BOSS data and the effective field theory of large-scale structures*, **Phys. Rev. D 106 (2022) 023516**, arXiv:2203.07440.

Note that during my PhD I also had the opportunity to participate in other research projects which are not presented in this manuscript:

- R. Gsponer, R. Zhao, J. Donald-McCann, D. Bacon, K. Koyama, R. Crittenden, **T. Simon** and EM. Mueller, *Cosmological constraints on early dark energy from the full shape analysis of eBOSS DR16*, **MNRAS 530 (2024) 3, 3075-3099**, arXiv:2312.01977.

- N. Schöneberg, G. F. Abellán, **T. Simon**, A. Bartlett, Y. Patel and T. L. Smith, *Comparative analysis of interacting stepped dark radiation*, **Phys. Rev. D 108 (2023) 123513**, 2306.12469.

- T. L. Smith, V. Poulin and **T. Simon**, *Assessing the robustness of sound horizon-free determinations of the Hubble constant*, **Phys. Rev. D 108 (2023) 103525**, 2208.12992.

Before presenting my research work listed above, the first part of this thesis is devoted to explaining the theoretical and conceptual formalism of modern cosmology, on which all the work described here is based. In particular, in chapter 1 we describe the ingredients of the standard model of cosmology, the ΛCDM model, and we outline the behaviour of the Universe at very large scales (*i.e.*, in the regime where it is considered to be homogeneous and isotropic). In chapter 2, we focus on the evolution of cosmological perturbations in the purely linear regime, making it possible to describe the physics of the cosmic microwave background. Finally, in chapter 3, we describe the evolution of these perturbations in the mildly non-linear regime, providing an adequate characterisation of the formation and evolution of large-scale cosmological structures. This third chapter defines the conceptual framework and the theoretical formalism used in the work presented in this thesis.

I

The ΛCDM model in a nutshell

Contents

1.1 The ΛCDM ingredients **6**
1.1.1 The cosmological principle 6
1.1.2 The two fundamental equations of modern cosmology 7
1.1.3 The components of the Universe 11
1.1.4 Initial conditions 14
1.2 The smooth universe **15**
1.2.1 The FLRW geometry 15
1.2.2 The stress-energy tensor of the smooth Universe and the continuity equation 17
1.2.3 The smooth Einstein equations 18
1.2.4 The smooth Boltzmann equations 18
1.2.5 Evolution of the smooth universe 20
1.2.6 Cosmological distances 22
1.2.7 Initial conditions: the inflationary paradigm 24
1.3 Successes and challenges of the ΛCDM model **26**
1.3.1 Successes of the ΛCDM model 26
1.3.2 Limits of the ΛCDM model 27

The ΛCDM model, corresponding to the core model of the modern cosmology, is founded on four main ingredients:

1. two sets of fundamental equations, *i.e.*, the Boltzmann equations and the Einstein equations;

2. one philosophical principle that makes it possible to simplify these two sets of equations, *i.e.*, the cosmological principle;

3. five main constituents whose evolutions are governed by the Boltzmann equations and the Einstein equations;

4. initial conditions derived from the inflation paradigm.

With these four ingredients in hand, it turns out to be possible to explain with a very high degree of accuracy the wide variety of cosmological data from various probes. Nowadays, despite some discrepancies known as "cosmological tensions", the ΛCDM model constitutes an effective description of the Universe, corroborated by (most) observational data.

In this chapter, we first present in Sec. 1.1 the various theoretical ingredients of the ΛCDM model, while in Sec. 1.2 we provide an overview of the ΛCDM model in the context of a homogeneous and isotropic universe (*i.e.*, on very large scales). Finally, in Sec 1.3, we discuss the successes and challenges of this model.

1.1 The ΛCDM ingredients

In this section, we cover all the theoretical ingredients needed to describe the origin and evolution of the Universe within the ΛCDM paradigm.

1.1.1 The cosmological principle

The *cosmological principle* stipulates that the Universe can be considered as *homogeneous* and *isotropic* for very large distances, to the extent that the different components of the Universe have the statistical homogeneity of a fluid in stationary equilibrium at this scale. This postulate is based on a fundamental observation: from our location in the Universe, we observe that the geometry of the Universe as well as the energy distribution of the various components are isotropic on very large scales (from $\sim$ 100 Mpc), as evidenced by the cosmic microwave background (CMB) for example. However, this observation is only possible from our specific location in the Universe, and it is not possible to know whether the Universe is also isotropic for all other observers. The cosmological principle then corresponds to the fundamental hypothesis according to which the Universe on very large scales is isotropic for all observers at rest with respect to the CMB (and that the reference frame of each of the observers is identical). This is a sort of *Copernican principle* applied to the cosmological scale which could be formulated as follows: given that there is no privileged observer, this implies that all observers at rest with respect to the CMB must observe large-scale isotropy. In this regard, George F. R. Ellis asserts that [1]:

> If all observers see an isotropic universe, then spatial homogeneity follows; indeed homogeneity follows if only three spatially separated observers see isotropy. Now

> we cannot observe the universe from any other point, so we cannot observationally establish that far distant observers see an isotropic universe. Hence the standard argument is to assume a Copernican Principle: that we are not privileged observers. This is plausible in that all observable regions of the universe look alike: we see no major changes in conditions anywhere we look. Combined with the isotropy we see about ourselves, this implies that all observers see an isotropic universe.

From this cosmological principle follows the Ehlers–Geren–Sachs (EGC) theorem, stipulating that if all observers at rest relative to the CMB see an isotropic temperature, then the exact geometry of the Universe respects the Friedmann-Lemaître-Robertson-Walker (FLRW) solution [2, 3]. This solution makes it possible to describe a physical system that is expanding, homogeneous and isotropic, as is the case for the Universe at large scales. The Einstein and Boltzmann equations are then solved (and simplified) with respect to this particular geometry. In addition, it is thanks to the cosmological principle that we can define a cosmological time, as well as a cosmological reference frame, defined as the reference frame of all observers at rest relative to the CMB.

It is therefore important to understand that modern cosmology and the ΛCDM model depend on a philosophical principle, and that it has never yet been demonstrated that (i) the Universe is isotropic for all observers, and that (ii) the Universe is homogeneous and isotropic for scales larger than that of the CMB. For example, in a Bianchi Universe, which is homogeneous but not isotropic, one can show that the Universe can at some point reach an intermediate isotropy and thus mimic a FLRW geometry (despite a highly anisotropic state in the early and advanced stages) [4]. However, the cosmological principle can be falsified observationally and a number of research efforts are being made in this direction (see *e.g.*, Refs. [5, 6]). One of the most common ways of verifying this principle is to check whether the reference frame where the CMB is homogeneous is the same as the frame where the large-scale structure distribution is homogeneous, in particular by comparing the CMB dipole with that of large-scale structures (see *e.g.*, Refs. [7, 8]).

1.1.2 The two fundamental equations of modern cosmology

It is remarkable that the richness and complexity inherent in cosmology can be explained by two sets of fundamental equations. Einstein's equations and Boltzmann's equations, which are considered universally valid (insofar as no experiment has refuted them), are in fact capable of explaining and characterising the evolution of the various constituents of the Universe, as well as the dynamics of the Universe's geometry.

Einstein's equations

At the beginning of the 20th century, Newtonian mechanics was invalidated in favour of the theory of general relativity, when the latter was able to explain the anomaly of the advance of Mercury's perihelion. Since then, the theory of relativity has become the new consensus paradigm for explaining gravitational phenomena, to the detriment of Newtonian mechanics, insofar as it has since passed all the experimental and observational tests to which it has been subjected.

In order to understand the ontological structure of general relativity, it is necessary to introduce the three fundamental mathematical objects of this theory:

- **A four-dimensional differentiable manifold** M. This is a set of space-time points that make up a continuous four-dimensional grid, where each point is defined by its three spatial coordinates (x, y, z) and its time coordinate (t). All in all, *a differentiable variety of dimension 4 can be understood as a set of points with a topological structure and a differentiable structure, which allow the points to be related to each other and to be designated locally (and "smoothly") by 4 real numbers.* [1] It is important to understand that this manifold partially fixes the geometry of space-time, insofar as it can be used to link points of space-time together, but it cannot, on its own, be used to define distances.

- **The metric tensor** $g_{\mu\nu}$. It is a mathematical object that is defined at any point of the differentiable manifold of dimension 4 and encodes all gravitational and geometric effects. This object makes it possible to determine the causal structure of the physical system under consideration, *i.e.*, the way in which the points in space-time are interconnected, by introducing curves into the manifold. The $g_{\mu\nu}$ tensor is used to define whether or not an event is causally linked to another event. Moreover, it is only thanks to this object that it is possible to define distances within this manifold (explaining the name of metric tensor), and in particular to define the space-time interval s. It can therefore be used to calculate "four-dimensional lengths" in a space-time that is curved both by gravitational effects (*i.e.*, by the interactions between the various *massive objects*) and by geometric effects (*i.e.*, by the *intrinsic geometry* of the system under consideration). It is important to understand that this object has an ambivalent character in that it encodes both the properties of the gravitational field and those of the space-time geometry. In this way, gravitation and geometry become two aspects of a single physical entity, implying the annihilation of the differentiation between geometric effects and gravitational effects.

- **The stress-energy tensor** $T_{\mu\nu}$ This is a mathematical object, also defined at any point of the differentiable manifold of dimension 4, which encodes the distribution of mass and energy in space-time. It takes into account the energy distribution associated with massive objects as well as that associated with other sources of energy (for example, from electromagnetic radiation). This object makes it possible to assign to each point in space-time a set of dynamic properties associated with an energy entity in the Universe (such as energy density, pressure, impulsion, *etc.*).

General relativity reassesses our ordinary definition of matter and space-time. First of all, this theory calls into question the classical perception of the concept of matter, which is present in special relativity. In general relativity, matter (and energy in general) is described by two mathematical objects: the metric tensor and the stress-energy tensor. Consequently, it is not clear that the concept of matter exists within general relativity as a substantial entity, which is independent and indivisible, insofar as its properties are split into two different objects: the gravitational properties of matter are described by the $g_{\mu\nu}$ tensor, while the energetic properties of matter are described by the $T_{\mu\nu}$ tensor. Moreover, this loss of individuality of material objects is accentuated by the fact that the gravitational properties of matter tend to merge with the geometric properties of space-time within the metric tensor. With regard to the notion of

[1] Lam, Vincent, 'Aspects structuraux de l'espace-temps dans la théorie de la relativité générale", in Le Bihan, Soazig (ed.), *Précis de la philosophie de la physique*, Paris: Vuibert, 2013, p. 206.

space-time, the theory of relativity (whether general relativity or special relativity) also presents a number of metaphysical ambiguities. Like the concept of matter, space-time seems to be able to refer to two mathematical objects emerging from this theory: the differential variety M and the metric field $g_{\mu\nu}$. While the former makes it possible to establish a network of relationships between different points in space-time, the latter makes it possible to define space-time distances within M (insofar as the metric field generates the topological deformations of this variety). Thus, space-time is represented by a pair (M,g), where $g_{\mu\nu}$ is attached to M in order to define the properties of the network of relations instantiated by M. We can (very) schematically summarise the relativistic conception of matter and space-time as follows:

$$\begin{array}{c}\text{Space-time} = M + g_{\mu\nu};\\ \text{Matter} = T_{\mu\nu} + g_{\mu\nu}.\end{array}$$ [2]

We argued earlier that the metric tensor $g_{\mu\nu}$ has a dual role, in that it encodes both gravitational and geometric effects. Importantly, the $g_{\mu\nu}$ tensor respects differential equations that are directly linked to the $T_{\mu\nu}$ stress-energy field through Einstein's equations:

$$G_{\mu\nu} + \Lambda g_{\mu\nu} = 8\pi G \cdot T_{\mu\nu}, \tag{1.1}$$

where G is the *gravitational constant*, and where Λ is a (cosmological) constant representing the energy density of space-time in the absence of non-gravitational fields. We will see later that this parameter can parametrized dark energy. $T_{\mu\nu}$ corresponds to the *stress-energy tensor*, which implies that the right-hand side depends on the energy distribution in the Universe, whereas $G_{\mu\nu}$ corresponds to the *Einstein tensor* which depends solely on the metric field $g_{\mu\nu}$ and its derivatives, implying that the left-hand side fixes the geometry of space-time. These equations directly link the topology of space-time, encoded in the $g_{\mu\nu}$ field (and by the same occasion in the Einstein tensor), with the distribution of matter in the Universe, encoded in the $T_{\mu\nu}$ field. In other words, a change in the geometry of space-time will lead to a change in the distribution of matter, and inversely. Thus, to solve this equation one "only" needs to specify the stress-energy tensor $T_{\mu\nu}$ on the one hand, and the metric tensor $g_{\mu\nu}$ on the other hand.

Let us now clarify the mathematical nature of the Einstein tensor. The latter is related to the *Ricci tensor* $R_{\mu\nu}$:

$$G_{\mu\nu} \equiv R_{\mu\nu} - \frac{1}{2}\mathscr{R} g_{\mu\nu}\,, \tag{1.2}$$

where $\mathscr{R}$ is the Ricci scalar defined thanks to a contraction between the metric tensor and the Ricci tensor $\mathscr{R} = g^{\mu\nu}R_{\mu\nu}$. In addition, the Ricci tensor is defined as a contraction of the Riemann tensor ($R_{\mu\nu} = R^{\alpha}_{\ \mu\nu\alpha}$), and is used (schematically) to quantify the level of deviation of the local geometry of any metric from a Euclidean space. This tensor is entirely determined by the *metric tensor* $g_{\mu\nu}$, and its derivatives through the Christoffel symbol $\Gamma^{\mu}_{\ \alpha\beta}$:

$$R_{\mu\nu} = \Gamma^{\alpha}_{\ \mu\nu,\alpha} - \Gamma^{\alpha}_{\ \mu\alpha,\nu} + \Gamma^{\alpha}_{\ \beta\alpha}\Gamma^{\beta}_{\ \mu\nu} - \Gamma^{\alpha}_{\ \beta\nu}\Gamma^{\beta}_{\ \mu\alpha}\,, \tag{1.3}$$

where

$$\Gamma^{\mu}_{\ \alpha\beta} = \frac{g^{\mu\nu}}{2}\left(g_{\alpha\nu,\beta} + g_{\beta\nu,\alpha} - g_{\alpha\beta,\nu}\right). \tag{1.4}$$

[2] It should be noted that these "equations" are pedagogical and in no way fully encapsulate the ontological structure of general relativity

The Christoffel's symbol allows us to characterise the spatio-temporal dynamics of the basis vectors through their covariant derivative.

In general relativity, unlike Newtonian mechanics, it is the topology of space-time (and not the external forces) which determines the trajectory of the particles. A particle in a curved space-time follows a *geodesic*, corresponding to the smallest possible four-dimensional trajectory between two space-time coordinates. In other words, a geodesic is the generalization to any curved space-time of a straight line in Euclidean geometry. The trajectory of the particles in curved space-time then respects the so-called *geodesic equation*:

$$\frac{d^2x^\mu}{d\lambda^2} + \Gamma^\mu_{\alpha\beta}\frac{dx^\alpha}{d\lambda}\frac{dx^\beta}{d\lambda} = 0\,, \tag{1.5}$$

where the geodesic curve is parametrized by the scalar λ. Note that we can easily derive the geodesic equation thanks to the principle of least action, by minimizing the four-dimensional length of the trajectory:

$$\delta S = 0 \quad ; \quad S = \int ds\,, \tag{1.6}$$

where $ds = \sqrt{\pm g_{\mu\nu}(x)dx^\mu dx^\nu}$ corresponds to the line element.

Boltzmann's equations

The second fundamental equation that allows us to describe the evolution of our Universe is Boltzmann's equation, which describes the behaviour of the *phase-space distribution function* of a species a, $f_a(x,p,t)$. As in Ref. [9], one can define the distribution function as the number of particles of the species a, $N_a(x,p,t)$, in a small phase-space volume around (x,p):

$$N_a(x,p,t) = f_a(x,p,t)\cdot(\Delta x)^3\cdot\frac{(\Delta p)^3}{(2\pi)^3}\,. \tag{1.7}$$

If the number of particles in the phase-space volume defined by $(\Delta x\Delta p/2\pi)^3$ is conserved, then we obtain the Liouville's equation:

$$\frac{df}{dt} = \frac{\partial f}{\partial t} + \frac{\partial f}{\partial x^i}\cdot\frac{dx^i}{dt} + \frac{\partial f}{\partial p}\cdot\frac{dp}{dt} + \frac{\partial f}{\partial \hat{p}^i}\cdot\frac{d\hat{p}^i}{dt} = 0\,, \tag{1.8}$$

where one has decomposed the three-momentum p^i by the product of its amplitude p and its three-dimensional projection $\hat{p}^i$: $p^i = p\cdot\hat{p}^i$. However, in the general case, the number of particles in the phase-space volume is not conserved due to particle-particle interactions (scattering, pair creation, annihilation, particle decay, *etc.*), then quantified by the collision term $C[f]$. The Boltzmann equation then becomes:

$$\frac{\partial f}{\partial t} + \frac{\partial f}{\partial x^i}\cdot\frac{dx^i}{dt} + \frac{\partial f}{\partial p}\cdot\frac{dp}{dt} + \frac{\partial f}{\partial \hat{p}^i}\cdot\frac{\hat{p}^i}{dt} = C[f]\,. \tag{1.9}$$

If one wants to solve the Boltzmann equation, then one needs (i) to specify the collision terms of processes that modify the number of particles in the phase-space volume, and (ii) to determine the expressions of dx^i/dt, dp/dt and dp^i/dt thanks to the geodesic equation (and

must therefore specify a given metric $g_{\mu\nu}$).

To explain the collision term briefly (see Ref. [9] for more details), let us consider an interaction of the type

$$1_{[\mathrm{p},\mathrm{E}_1(\mathrm{p})]} + 2_{[\mathrm{q},\mathrm{E}_1(\mathrm{q})]} \leftrightarrow 3_{[\mathrm{p}',\mathrm{E}_3(\mathrm{p}')]} + 4_{[\mathrm{q}',\mathrm{E}_4(\mathrm{q}')]}\,. \tag{1.10}$$

Then the collision term for particle 1 takes the following form:

$$\begin{aligned} C[f_1(p)] = & \frac{1}{2E_1(p)} \int \frac{d^3q}{(2\pi)^3 2E_2(q)} \int \frac{d^3p'}{(2\pi)^3 2E_3(p')} \int \frac{d^3q'}{(2\pi)^3 2E_4(q')} \mid \mathscr{M} \mid \\ & \times (2\pi)^4 \delta_D^{(3)}[p+q-p'-q'] \delta^{(1)}[E_1(p)+E_2(q)-E_3(p')-E_4(q')] \\ & \times [f_3 f_4 (1 \pm f_1)(1 \pm f_2) - f_1 f_2 (1 \pm f_3)(1 \pm f_4)]\,, \end{aligned} \tag{1.11}$$

where δ_D is the delta Dirac's function which imposes the energy and momentum conservations, and where $\mathscr{M}$ is the scattering amplitude of the process. This equation subtracts to $f_1(p)$ the type 1 particles that had a momentum p before undergoing the process and adds back the type 1 particles that obtain a momentum p thanks to this process. Such an operation is performed via the sum of all the momentums q, p' and q' over the scattering amplitude squared multiplied by the term $(f_3 f_4 - f_1 f_2)$. In addition, the terms $(1 \pm f_1)(1 \pm f_2)$ and $(1 \pm f_3)(1 \pm f_4)$ allow us to encode the Pauli exclusion or the Bose-Einstein enhancement (with a $-$ for fermions and with a $+$ for bosons).

1.1.3 The components of the Universe

The dynamics and geometry of the Universe can be fully explained if we introduce five different energy components. Among these five species, three (baryons, neutrinos and photons) can be explained by the Standard Model of particle physics (or at least an extension of the Standard Model for neutrinos), while the other two (dark matter and dark energy) have an unknown intrinsic nature. These five constituents are postulated by the ΛCDM model, but we will see in part III that it is possible to build models beyond ΛCDM that involve other hypothetical constituents.

Photons

Today, the main radiation contribution of the Universe comes from *CMB photons*. The energy distribution of the CMB photons follows that of an almost perfect black body with a Bose-Einstein distribution function:

$$\rho_{\gamma,0} = g_\gamma \cdot \int \frac{d^3p}{(2\pi)^3} \frac{p}{e^{p/T}-1} = \frac{\pi^2}{15} T^4\,, \tag{1.12}$$

where $g_\gamma = 2$ corresponds to the two spin states of the photon. The FIRAS instrument on board the COBE satellite measured the temperature of the CMB photons with extremely high precision [10]:

$$\overline{T}_{\gamma,0} = 2.726 \pm 0.001 K\,. \tag{1.13}$$

Using Eq. (1.12), we can determine the current photon energy density in the Universe, and more specifically the fraction of radiation energy density relative to the total energy density in the Universe as

$$\Omega_{\gamma,0} = \frac{\rho_{\gamma,0}}{\rho_{\mathrm{crit},0}} = 2.47 \times 10^{-5} \cdot h^{-2}, \tag{1.14}$$

where $h = H_0/(100\,[\mathrm{km/s/Mpc}])$ is the dimensionless Hubble parameter today, and where $\rho_{\mathrm{crit},0}$ is the total energy density today for a flat universe (see below). This value is currently very low, but as we will see later, the Universe experienced a period in which radiation dominated its energy content. At that time, there were other sources contributing to the radiation energy density, in particular from relativistic particles that are no longer relativistic today. It should be noted that there are other sources of radiation today, notably from the reionization of the Universe (*i.e.*, the moment when the gas that made up the Universe after the CMB became re-ionised due to star formation), but these contributions are extremely negligible compared with the CMB photons.

Baryons

In cosmology, we call *baryons* everything that corresponds to ordinary matter that has a significant impact on the history of the Universe, *i.e.*, nuclei and electrons. Note that this is a misnomer, because electrons are leptons, but the main contribution to the energy density of this constituent does come from the baryons (via the nuclei). Within the framework of the standard model of cosmology, baryons represent only 5% of the energy content of the Universe. The most precise measures of this quantity come from the CMB anisotropies and the big bang nucleosynthesis (BBN). Concerning CMB, we will see that the temperature anisotropies are sensitive to the amount of baryon present at that time, making it possible to provide an accurate measure of the current energy density fraction of baryons. For instance, the *Planck* satellite measured [11]:

$$\Omega_b \cdot h^2 = 0.02237 \pm 0.00015\,. \tag{1.15}$$

Concerning BBN, the abundances of the light elements created during BBN depends on the quantity of baryons present in the Universe, which allows us to obtain a measurement independent of that of the CMB. This measurement is compatible with the *Planck* satellite measurement. For instance, Ref. [12] determined that

$$\Omega_b \cdot h^2 = 0.0222 \pm 0.0005\,. \tag{1.16}$$

This compatibility between these two probes is one of the many successes of the ΛCDM model.

Neutrinos

Neutrinos have also played an important role in the evolution of the Universe. However, cosmic neutrinos have never yet been observed, making their existence purely theoretical (despite very strong clues). Neutrinos are fermions, and we consider in this thesis (based on standard assumptions) that there are three species of neutrinos. The neutrino energy density in the relativistic regime ($m_\nu \ll p$) can be expressed as a function of the photon energy density as follows:

$$\rho_\nu = 3 \cdot \frac{7}{8} \left(\frac{T_\nu}{T}\right)^4 \rho_\gamma, \tag{1.17}$$

where the factor 3 indicates that there are three types of neutrino (with spin $1/2$), and the factor $7/8$ corresponds to the ratio between the the integration of the Fermi-Dirac distribution and the integration of the Bose-Einstein distribution [see Eq. (1.14)]. Importantly, the temperature of neutrinos is different from that of photons, because these two components decoupled very early in the Universe, implying that they evolve differently from a thermodynamic point of view. In the primordial plasma, neutrinos decouple before electron-positron annihilation, implying that the products do not thermalize with neutrinos. By imposing conservation of total entropy between the moment when electron-positron annihilation does not occur and the moment when it does, we can show that

$$\frac{T_\nu}{T} = \left(\frac{4}{11}\right)^{1/3} . \tag{1.18}$$

It is not possible to use Eq. (1.17) to directly infer the current energy density fraction of neutrinos, as we have known since the Super-Kamiokande experiments conducted in 1998 that neutrinos possess mass [13]. Thus, when the neutrino temperature drops below their mass ($T_\nu \sim m_{\nu_i}$, where m_{ν_i} is the mass a given neutrino generation), they are no longer relativistic and the previous equations are no longer valid. The energy density associated with a neutrino generation ν_i then becomes:

$$\rho_{\nu_i} = 2\int \frac{d^3p}{(2\pi)^2}\frac{1}{e^{p/T_\nu}+1}\sqrt{p^2+m_{\nu_i}^2}\,. \tag{1.19}$$

This allows us to numerically obtain that today

$$\Omega_\nu h^2 = \frac{\sum_i m_{\nu_i}}{94e\mathrm{V}}\,, \tag{1.20}$$

where $\sum_i m_{\nu_i}$ is not yet known. From the neutrino oscillation experiments, $\sum_i m_{\nu_i} > 0.06e\mathrm{V}$ for the normal hierarchy (see *e.g.*, Ref. [14]) and $\sum_i m_{\nu_i} > 0.10e\mathrm{V}$ for the inverse hierarchy (see *e.g.*, Ref. [15]).

Dark matter

Dark matter is not lacking in astrophysical evidence. The first evidence of a discrepancy between gravitational mass and observed mass was provided by Fritz Zwicky in 1933 when he observed the galaxy dynamics within the Coma cluster [16]. Fritz Zwicky then postulated the existence of invisible matter which could explain this discrepancy. The idea of dark matter was put aside for a while when, in 1970, Vera Rubin postulated the existence of a similar form of matter when she and her collaborators studied the rotation curves of galaxies [17]. Indeed, visible matter could not, on its own, explain why the rotation speed of the spiral galaxies did not decrease with distance to the center as predicted by the Newtonian equations carried out with the observed matter.

Cosmology also provides very strong evidence for dark matter, and at present no cosmological model can survive without dark matter. In particular, dark matter (as we shall see) explains the fluctuations of the CMB, and without this component it would not be possible to predict the existence of such fluctuations. The CMB fluctuations are therefore a good way of measuring the current dark matter fraction accurately, and, for instance, the *Planck* data determined that [11]:

$$\Omega_c h^2 = 0.1431 \pm 0.0025\,. \tag{1.21}$$

The amount of dark matter is around 25% of the current total budget of the Universe, which implies that it plays an important role in the expansion history of the Universe (which is also another evidence of its existence). All these pieces of evidence tell us that dark matter is non-relativistic, or "cold". Indeed, in order to explain the CMB fluctuations, dark matter must decouple very rapidly from the primordial plasma and acquire a thermodynamic autonomy in the first instants of the Universe. Furthermore, no evidence has yet been found for the existence of a non-gravitational interaction with the particles of the Standard Model or for an unstability of this constituent, which makes it possible to place constraints on its intrinsic nature.

Dark energy

In 1998, two groups (Riess *et al*. [18], and Perlmutter *et at*. [19]) have shown, by measuring the apparent magnitudes of dozens of Type Ia Supernovae, that the Universe is currently undergoing an acceleration of its expansion. We shall return briefly later to the physical principles of this discovery. The best explanation for the acceleration of the expansion of the Universe lies in the postulate of dark energy, a component of the Universe that has a constant energy density and that can be modelled with the cosmological constant Λ introduced in the Einstein equations. While the energy densities of all the other constituents of the Universe decrease with time, that of the dark energy remains constant, which implies that the dark energy dominates the Universe at some point, even though its initial contribution was negligible. In the ΛCDM model, this component is modelled as a cosmological constant with a constant potential $V_\Lambda = \overline{\rho}_\Lambda = 8\pi G \cdot \Lambda$, where Λ is the parameter representing the energy density of space-time in the absence of non-gravitational fields in the Einstein equation. It is estimated today that dark energy composed $\sim 70\%$ of the Universe content, while this value will continue to increase in the future of the Universe. In particular, the *Planck* satellite measured [11]:

$$\Omega_\Lambda = 0.6847 \pm 0.0073\,. \tag{1.22}$$

It should also be noted that dark energy, unlike all the other components of the Universe, does not seem to have any non-negligible fluctuations [11], and so we are going to treat it as a perfectly homogeneous and isotropic fluid.

1.1.4 Initial conditions

In order to fully describe the evolution of the Universe, it is necessary (as in any physical system) to know and characterise its initial conditions. These initial conditions, within the framework of the standard paradigm of cosmology, arise from inflation, a phase in the evolution of the Universe occurring before the radiation and matter areas (see below). The inflation model makes it possible to explain several problems that the ΛCDM model cannot explain on its own, and the combination of the inflation paradigm (which sets the initial conditions) with the ΛCDM model (which describes the evolution of these initial conditions) constitutes the standard model of cosmology. Note that adding inflation on top of the ΛCDM model does not alter any of its successes! Here we list very briefly the various problems (among others) that inflation can solve [20]:

- **Flatness problem.** The various cosmological data seem to show that the Universe is flat, *i.e.*, it has no curvature (see below for more details on curvature). This strong constraint on the curvature of the Universe necessitates a fine-tuning of Ω_K, the curvature energy

density fraction (*i.e.* the contribution of the curvature to the total energy density of the Universe), at early time. Current data seem to show that we need a value of $|\,\Omega_\kappa(t_{\rm pl}) - 1\,| \lesssim 10^{-60}$, where $t_{\rm pl}$ corresponds to the Planck scale. The inflationary paradigm avoids this fine-tuning insofar as the inflationary phase flatten space-time. Inflation thus makes it possible to explain why our Universe has been flat since the end of inflation, without requiring fine-tuned initial conditions.

- **Horizon problem.** Today, we observe that CMB photons have the same temperature in all directions of the sky. However, at the time of the last scattering surface (*i.e.*, when photons decoupled form the primordial plasma), some different regions of the sky were never in causal contact (if we assume no inflation), since the size of the CMB observed today is much greater than the particle horizon at the time of the CMB. This implies that no causal physical mechanism can explain, within the framework of the ΛCDM model, why all photons are emitted with the same temperature. Inflation overcomes this problem by asserting that photons were in causal contact before the inflationary phase of the Universe. In other words, the different scales of the Universe move from inside the horizon during inflation (where there has been a thermalization of these different scales) to outside the horizon (see below). Finally, to solve the Horizon issue, we need to postulate a phase where the (comoving) Hubble radius (or the particle horizon) decreases significantly in the early universe.

- **Density fluctuation problem.** *Where did the initial fluctuations observed in the CMB come from?* Inflation provides an elegant answer to this question. The basic idea can be briefly summarised as follows: the inflation field experiences quantum fluctuations before the inflationary phase, which are then stretched. During reheating (namely the period when the inflation field decays to give rise to all the particles of the Standard Model), the inflation field transmit its perturbations to the other species of the Universe.

We shall return to inflation in a little more detail later in this chapter (once we have specified the metric of the ΛCDM model), and we will briefly explain the initial conditions arising from inflation.

1.2 The smooth universe

In this section, we now apply the ingredients explained above to describe the behaviour of the homogeneous universe, *i.e.*, at very large scales ($\gtrsim 100$ Mpc). In particular, we derive here the cosmological equations, from the Einstein and Boltzmann equations coupled with the cosmological principle, for the different constituents of the Universe. The inhomogeneous universe will be studied in detail in the following chapters.

1.2.1 The FLRW geometry

As previously specified, if we want to solve the Einstein equations, then one needs to specify the metric tensor $g_{\mu\nu}$ and the stress-energy tensor $T_{\mu\nu}$ of the (homogeneous) Universe.

Let us start with the metric tensor for a homogeneous and isotropic expending universe. As specified above, the EGC theorem states that for an expanding universe that

respects the cosmological principle, the Universe has a geometry of type Friedmann-Lemaître-Robertson-Walker (FLRW):

$$ds^2 = g_{\mu\nu}dx^\mu dx^\nu = -dt^2 + a(t)^2\left[\frac{dr^2}{1-\kappa r^2} + r^2 d\theta^2 + r^2\sin^2\theta d\phi^2\right]. \tag{1.23}$$

This metric depends on just two parameters: the *scale factor* $a(t)$, which is time-dependent, and the constant κ, which corresponds to the Gaussian curvature of the Universe at time t such that $a(t) = 1$ (corresponding to today). This latter parameter corresponds to all the possible geometries of a homogeneous and isotropic 3-space, and can take the values $\kappa = -1, 0, 1$, where it respectively corresponds to an hyperbolic, Euclidean (or flat), and elliptical (locally isometric to a 3-sphere) geometry. It turns out that the current cosmological data favour a Euclidean Universe (see in particular chapter 4 for strong constraints on the curvature energy density fraction), *i.e.*, a Universe with $\kappa = 0$. The metric that will therefore be used in the rest of this thesis (unless otherwise specified) will be that of the flat ΛCDM model, namely

$$g_{\mu\nu} = \text{diag}\left[-1,\, a(t)^2,\, a(t)^2,\, a(t)^2\right]. \tag{1.24}$$

Note that this metric corresponds to a homogeneous and isotropic Universe since there is no privileged spatial direction (given that $g_{\mu\nu}$ is space-independent, has no extra-diagonal terms, and that $g_{xx} = g_{yy} = g_{zz}$). The expansion of the Universe is encoded in the *scale factor* $a(t)$, the parameter which allows to link the physical distance l_{phys} (*i.e*, the actual distance separating two objects in the Universe) with the comoving distance l_{com} (*i.e.*, the distance which follows the expansion of the Universe):

$$l_{\text{phys}} = a(t) l_{\text{com}}\,. \tag{1.25}$$

The scale factor is conventionally normalized such that $a(t_0) = 1$, where t_0 is the age of the Universe today. In particular, in the context of the comoving coordinates, the physical velocity of an object is given by the following relationship (known as the Hubble law):

$$v_{\text{phys}} = \frac{dl_{\text{phys}}}{dt} = v_{\text{pec}} + H(t)\cdot l_{\text{phys}}\,, \tag{1.26}$$

where $v_{\text{pec}} = a(t)\cdot dl_{\text{com}}/dt$ is the peculiar velocity of the object and where H is the Hubble parameter, defined as $H \equiv \dot{a}/a$. This parameter, which has the unit of Time^{-1}, quantifies the global expansion rate of the Universe. Its current value is around ~ 70 km/s/Mpc, which means that today a distance of 1 Mpc expands at a speed of ~ 70 km/s. In addition, the scale factor is related to the redshift z by the following formula:

$$\frac{a_0}{a(t)} = 1 + z \quad ; \quad 1 + z \equiv \frac{\lambda_{\text{obs}}}{\lambda_{\text{emit}}}\,, \tag{1.27}$$

where λ_{emit} is the wavelength of a photon when it was emitted, and λ_{obs} is the wavelength of the same photon when it is detected elsewhere in the Universe. The redshift is a direct consequence of the geometric expansion of the Universe undergone by a photon as it travels, implying that the inequality $\lambda_{\text{obs}} > \lambda_{\text{emit}}$ is always true.

Finally, note that using Eq. (1.4) with the metric defined in Eq. (1.24), we obtain only two non-zero Christoffel's symbols:

$$\Gamma^i{}_{j0} = \Gamma^i{}_{0j} = H\delta^i{}_j \quad ; \quad \Gamma^0{}_{ij} = a\dot{a}\delta_{ij}\,, \tag{1.28}$$

where $i, j = x, y, z$, and where δ stands for the Kronecker symbol.

1.2.2 The stress-energy tensor of the smooth Universe and the continuity equation

The stress-energy tensor of the species a, $T^a_{\mu\nu}$, can be written for a homogeneous and isotropic universe and under the assumption of perfect fluids as

$$\overline{T}^a_{\mu\nu} = [\overline{P}_a(t) + \overline{\rho}_a(t)]U_\mu U_\nu + \overline{P}_a(t) \cdot g_{\mu\nu}\,, \tag{1.29}$$

where $\overline{\rho}_a(t)$ and $\overline{P}_a(t)$ are respectively the mean energy density and the mean pressure of the species a (namely, the energy density and the pressure at large-scale), and where U_μ is the four-velocity of a given observer. Note that we cannot include any velocity or momentum in $T^a_{\mu\nu}$, otherwise we would break the isotropy of the Universe. Then, for an observer attached to the fluid, that is $U_\mu = (-1,0,0,0)$ and $g_{\mu\nu} = \eta_{\mu\nu}$ (where $\eta_{\mu\nu}$ is the Minkowski metric), one can rewrite the stress-energy tensor as

$$\overline{T}^a_{\mu\nu} = \mathrm{diag}\left[-\overline{\rho}_a(t),\, \overline{P}_a(t),\, \overline{P}_a(t),\, \overline{P}_a(t)\right]\,. \tag{1.30}$$

Let us note that $\overline{\rho}_a(t)$ is simply linked to $\overline{P}_a(t)$ through the *equation of state* $\overline{P}_a(t) = \omega_a \overline{\rho}_a(t)$, where ω_a is the equation of state parameter.

In addition, the stress-energy tensor has the fundamental property of being conserved under its *covariant derivative* for an expanding universe [3] (following Bianchi identities):

$$\nabla_\mu T^\mu_\nu \equiv \frac{\partial T^\mu_\nu}{\partial x^\mu} + \Gamma^\mu_{\alpha\mu} T^\alpha_\nu - \Gamma^\alpha_{\nu\mu} T^\mu_\alpha = 0\,. \tag{1.31}$$

This equation is the generalisation of the continuity (for $\nu = 0$) and Euler (for $\nu = i$) equations in a curved space-time.

The Euler's equation is trivially zero ($\partial P/\partial x^i = 0$) in the FLRW universe, because the spatial component of the metric is isotropic. This is a direct consequence from the fact that the peculiar velocity of each component is zero in the smooth universe. However, if we set $\nu = 0$ in Eq. (1.31), then one obtains:

$$-\frac{\partial \overline{\rho}_a}{\partial t} - \Gamma^\mu_{0\mu}\overline{\rho}_a - \Gamma^\alpha_{0\mu} T^\mu_\alpha = 0\,, \tag{1.32}$$

leading to the continuity equation of the smooth Universe:

$$\frac{\partial \overline{\rho}_a}{\partial t} + 3\frac{\dot{a}}{a}(\overline{\rho}_a + P_a) = 0. \tag{1.33}$$

By integrating this equation from a given $a(t)$ to a_0, and using the equation of state parameter w_a (under the assumption that the latter does not vary with time), one obtains:

$$\overline{\rho}_a(t) = \overline{\rho}_{a,0}\left(\frac{a(t)}{a_0}\right)^{-3(1+w_a)}\,, \tag{1.34}$$

where $\rho_{a,0}$ corresponds to the energy density of the constituent a today.

[3] This conservation is only true for species that do not interact with other species, otherwise a source term must be added (as in the Boltzmann equation). In reality, this is not the case for photons and baryons, which interact with each other before recombination. However, the number of photons and the number of baryons are conserved during their interaction. The continuity equation, which is the one we are interested in here, is directly linked to the conservation of the number of particles, and is therefore not modified by such an interaction term.

1.2.3 The smooth Einstein equations

We now have all the tools to determine the solutions to Einstein's equation. If one injects in the Einstein equations the FLRW metric tensor, and the stress-energy tensor as defined previously, one can obtain the Friedmann-Lemaître equations, which allow us to describe the evolution of the components in the homogeneous and isotropic universe. We can easily show that there are only two non-vanishing components of the Ricci tensor, namely

$$R_{00} = -3\frac{\ddot{a}}{a} \quad ; \quad R_{ij} = \delta_{ij}(2\dot{a}^2 + a\ddot{a} + 2\kappa)\,. \tag{1.35}$$

Therefore, the $\mu = \nu = 0$ component of the Einstein equations leads to the first Friedmann-Lemaître equation, while the $\mu = \nu = i$ component leads to the second Friedmann-Lemaître equation:

$$FLI : \left(\frac{\dot{a}}{a}\right)^2 \equiv H^2 = \frac{8\pi G}{3}\overline{\rho} - \frac{\kappa}{a^2} + \frac{\Lambda}{3}, \tag{1.36}$$

$$FLII : \frac{\ddot{a}}{a} = -\frac{4\pi G}{3}(\overline{\rho} + 3\overline{P}) + \frac{\Lambda}{3}, \tag{1.37}$$

where $\overline{\rho} = \sum_a \overline{\rho}_a$ and $\overline{P} = \sum_a \overline{P}_a$, with $a = \{c, \gamma, \nu, b\}$ respectively for cold dark matter, photons, neutrinos, and baryons. Let us note that we can define $\overline{\rho}_\Lambda = 8\pi G \cdot \Lambda$, together with $w_\Lambda = -1$, in order to absorb the $\Lambda/3$ terms in $\overline{\rho}$ and $\overline{P}$.

1.2.4 The smooth Boltzmann equations

For a homogeneous universe (using the cosmological principle), that is $\partial f/\partial \hat{p}^i = 0$, it is very straightforward to show that the Boltzmann equation becomes (see Ref. [9]):

$$\frac{\partial f}{\partial t} + \frac{p}{E}\frac{\hat{p}^i}{a}\frac{\partial f}{\partial x^i} - H(t)p\frac{\partial f}{\partial p} = C[f]\,, \tag{1.38}$$

where $E = \sqrt{p^2 + m^2}$ is the energy of the particle. To obtain this equation, we need to specify dx^i/dt and dp/dt in Eq. (1.8) thanks to the geodesic equation. Interestingly, this equation is valid for all particles, so all we need to do is specify the distribution function of the particle in question. For photons one uses the *Bose-Einstein* distribution function with zero chemical potential (if we are in equilibrium):

$$f_0(p) = [\exp(E/T) - 1]^{-1}\,, \tag{1.39}$$

where $E = p$ for photons. For fermions (like neutrinos) one uses the *Fermi-Dirac* distribution:

$$f_0(p) = [\exp(E/T) + 1]^{-1}\,, \tag{1.40}$$

where $E = \sqrt{m^2 + p^2}$.

We can now derive two specific cases of equation Eq. (1.38): the *relativistic limit*, when $p >> m$ for photons and relativistic neutrinos and the *non-relativistic limit*, when $p << m$ (for baryons and dark matter). For relativistic particles, we obtain:

$$\frac{\partial f}{\partial t} + \frac{\hat{p}^i}{a}\frac{\partial f}{\partial x^i} - H(t)p\frac{\partial f}{\partial p} = C[f]\,, \tag{1.41}$$

while for non-relativistic particle, one has:

$$\frac{\partial f}{\partial t}+\frac{p}{m}\frac{\hat{p}^i}{a}\frac{\partial f}{\partial x^i}-H(t)p\frac{\partial f}{\partial p}=C[f]\,. \tag{1.42}$$

Finally, by integrating over the 3-momentum, we can rewrite Eq. (1.38) in terms of the (mean) number density $\overline{n}(t)$ (see *e.g.*, Ref. [9]):

$$\frac{d\overline{n}(t)}{dt}+3H(t)\overline{n}(t)=\int\frac{d^3p}{(2\pi)^3}C[f]\,, \tag{1.43}$$

where

$$\overline{n}(t)=\int\frac{d^3p}{(2\pi)^3}f\,. \tag{1.44}$$

This equation is fundamental for deriving the (homogeneous) evolution of the energy density. We will see later that there is an analogous equation for the inhomogeneous Universe to describe the behaviour of density perturbations of the species under consideration. Note that this is the first moment of the Boltzmann equation, and that this equation is nothing other than the continuity equation. If we fix the interaction term at 0, then we find Eq. (1.33). The second moment leads to the Euler's equation which is 0 in the background universe (see above).

In the general case, one can define the particle current density and the stress-energy tensor from the phase-space distribution function as:

$$n^\mu(x^i,t)=g\int\frac{d^3P_j}{(2\pi)^3}\,\frac{1}{\sqrt{-\det(g_{\mu\nu})}}\,\frac{P^\mu}{P^0}f(x^i,P_j,t)\,, \tag{1.45}$$

$$T^\mu_{\ \nu}(x^i,t)=g\int\frac{d^3P_j}{(2\pi)^3}\,\frac{1}{\sqrt{-\det(g_{\mu\nu})}}\,\frac{P^\mu P_\nu}{P^0}f(x^i,P_j,t)\,, \tag{1.46}$$

where g corresponds to the internal degrees of freedom of the given particle, where $\det(g_{\mu\nu})=-a^6$ for the FLRW metric, and where $P^\mu=(P^0=E,P^i)$ is the covariant four-momentum of the particle. Note that the spatial part of P^μ depends on the physical 3-momenta p^i as $p^i\equiv aP^i$ (since $p^2=g_{ij}P^iP^j$). In addition, for a FLRW univers and according to the cosmological principle, we can simplify the phase-space distribution function as $f(x^i,P_j,t)=f(p,t)$, implying that we can define, in a homogeneous and isotropic universe, the number density $\overline{n}(t)$, the energy density $\overline{\rho}(t)$ and the pressure $\overline{P}(t)$ as:

$$\overline{n}(t)=n^0(t)=g\int\frac{dp\;p^2}{2\pi^2}f(p,t)\,, \tag{1.47}$$

$$\overline{\rho}(t)=-\overline{T}^0_{\ 0}=g\int\frac{dp\;p^2}{2\pi^2}Ef(p,t)\,, \tag{1.48}$$

$$\overline{P}(t)=\frac{1}{3}\sum_i\overline{T}^i_{\ i}=g\int\frac{dp\;p^2}{2\pi^2}\frac{p^2}{3E}f(p,t)\,. \tag{1.49}$$

It is easy to check that for a relativistic particle (*i.e.*, $E\sim p\gg m$), we have $w=\overline{P}/\overline{\rho}=1/3$, while for a non-relativistic particle (*i.e.*, $E\sim m\gg p$), we obtain $w\sim 1/3\cdot\langle p^2\rangle/m^2\sim 0$. Note

that we can also rewrite the comoving version of these equations in terms of the comoving momentum norm $q = ap$ and the comoving energy $\mathscr{E} = aE$ of the particle:

$$\overline{n}(t) = n^0(t) = \frac{g}{a^3}\int \frac{dq\cdot q^2}{2\pi^2} f(q,t)\,, \tag{1.50}$$

$$\overline{\rho}(t) = -T^0_0 = \frac{g}{a^4}\int \frac{dq\cdot q^2}{2\pi^2} \mathscr{E} f(q,t)\,, \tag{1.51}$$

$$\overline{P}(t) = \frac{1}{3}\sum_i T^i_i = \frac{g}{a^4}\int \frac{dq\cdot q^2}{2\pi^2}\frac{q^2}{3\mathscr{E}} f(q,t)\,. \tag{1.52}$$

1.2.5 Evolution of the smooth universe

First, we can apply the continuity equation (1.34) to non-relativistic matter (with $w_m = 0$), radiation (with $w_r = 1/3$) and dark energy (with $w_\Lambda = -1$) in order to obtain homogeneous energy density evolutions in terms of the scale factor a:

$$\overline{\rho}_m = \rho_{m,0}\left(\frac{a}{a_0}\right)^{-3} \text{ for matter,} \tag{1.53}$$

$$\overline{\rho}_r = \rho_{r,0}\left(\frac{a}{a_0}\right)^{-4} \text{ for radiation,} \tag{1.54}$$

$$\overline{\rho}_\Lambda = \rho_{\Lambda,0}\left(\frac{a}{a_0}\right)^{0} \text{ for dark energy.} \tag{1.55}$$

The origin of the a^{-3} dependence of the matter energy density is purely geometric. Let us rewrite $\overline{\rho}(t)$ as $\overline{\rho}(t) = \overline{E}(t)\cdot\overline{n}(t)$, where $\overline{E}(t)$ is the mean energy of one particle and $\overline{n}(t)$ is the mean number density. [4] With expansion, a volume $V(t_1)$ of the Universe at an instant t_1 is dilated by a factor $[a(t_2)/a(t_1)]^{-3}$ at an instant t_2, insofar as the dilatation is the same in the three dimensions of space. Thus, the mean energy density is modified by a factor $[a(t_1)/a(t_2)]^{-3}$, explaining the a^{-3} dependence of the matter energy density in Eq. (1.53) [by taking $a(t_1) = a$ and $a(t_2) = a_0$]. For photons (and radiation in general), the a^{-4} dependence is a combination of the dilation of the volume containing a given number of photons, *i.e.* the a^{-3} dependence of $\overline{n}(t)$, and the wavelength stretching. This last contribution adds a contribution in a^{-1} to the energy of a single photon: with the expansion, a travelling photon will see its wavelength change by $\lambda \to a\lambda$, and its energy to $1/\lambda \to 1/\lambda\cdot a^{-1}$. Finally, the radiation energy density will change according to the following transformation: $\overline{E}_\gamma(t)\cdot\overline{n}_\gamma(t) \to a^{-1}\overline{E}_\gamma(t)\cdot a^{-3}\overline{n}_\gamma(t)$, explaining the a^{-4} dependence in Eq. (1.54).

It is very common (and convenient) to define the *critical energy density* of the Universe, which is the total energy density today for a curvature-free universe (*i.e.*, $\kappa = 0$), obtained by inverting the first Friedmann-Lemaître equation at $a = a_0$:

$$\rho_{\text{crit},0} = \frac{3H_0^2}{8\pi G} = 1.9\times 10^{-29} h^2 \text{ g cm}^{-3}\,, \tag{1.56}$$

where $H_0 \sim 70$ km/s/Mpc is the Hubble parameter today, and where h is the dimensionless Hubble parameter today: $H_0 \equiv 100\cdot h$ km/s/Mpc. The $\rho_{\text{crit},0}$ parameter then

[4] Given that $\overline{\rho}(t) = \overline{E}(t)\cdot\overline{n}(t)$, we can very easily show that Eqs. (1.53) and (1.54) can be obtained from the Boltzmann equation (1.44) without collision term.

allows us to define the current energy density fraction of each of the constituents for a zero-curvature Universe (see above):

$$\Omega_r \equiv \frac{\overline{\rho}_r}{\rho_{\rm crit,0}} \quad ; \quad \Omega_m \equiv \frac{\overline{\rho}_m}{\rho_{\rm crit,0}} \quad ; \quad \Omega_\Lambda \equiv \frac{\overline{\rho}_\Lambda}{\rho_{\rm crit,0}} = \frac{\Lambda}{3H_0^2}\,. \tag{1.57}$$

In the general case (namely with a non-zero curvature), the following consistency relation holds:

$$\sum_a \Omega_a \equiv \Omega_r + \Omega_m + \Omega_\Lambda = 1 - \Omega_\kappa \quad ; \quad \Omega_\kappa = -\frac{\kappa}{H_0^2 a^2}\,, \tag{1.58}$$

where we recall that $\Omega_r = \Omega_\gamma + \Omega_\nu$ and $\Omega_m = \Omega_c + \Omega_b$. The Ω_a parameters allow us to rewrite the first Friedmann-Lemaître equation [see Eq. (1.36)] as follows:

$$H^2 = H_0^2 \left[\Omega_{m,0} \left(\frac{a}{a_0}\right)^{-3} + \Omega_{r,0} \left(\frac{a}{a_0}\right)^{-4} + \Omega_{\kappa,0} \left(\frac{a}{a_0}\right)^{-2} + \Omega_{\Lambda,0} \right]\,, \tag{1.59}$$

where $\Omega_{a,0} = \overline{\rho}_{a,0}/\rho_{\rm crit,0}$.

By isolating dt from Eq. (1.59), using the fact that $H^2 = (da/dt \cdot 1/a)^2$, one can obtain the exact equation of the age of the Universe $t_{\rm U}$:

$$t_{\rm U} = \int_0^{t_0} dt = \frac{1}{H_0} \int_0^1 \frac{dx}{[\Omega_{m,0} x^{-1} + \Omega_{r,0} x^{-2} + \Omega_{\Lambda,0} x^2 + \Omega_\kappa]^{1/2}}\,, \tag{1.60}$$

where $x = a/a_0$. Interestingly, if we assume that the present universe is entirely composed of matter, *i.e.*, $\Omega_{m,0} = 1$, then $t_{\rm U} = 2/3 \cdot H_0 \sim 9.3$ Gyr (for $H_0 = 70$ km/s/Mpc $= 7,15 \cdot 10^{-2}$ Gyr^{-1}). However, this value is lower than the age at which the first stars observed in the Universe appeared, namely ~ 13 Gyr ago. It is therefore obvious that the current universe cannot be composed of matter alone, and that it is necessary to find a mechanism that accelerates the expansion of the Universe. This is, in fact, the first evidence of dark energy! In addition, if we consider a empty Universe (*i.e.*, a *Milne Universe*), namely $\sum_a \Omega_a = 0 \Rightarrow \Omega_\kappa = 1$, then $t_{\rm U} = 1/H_0 \sim 14.0$ Gyr [see Eq. (1.60)], which is very close to the consensus value adopted in the ΛCDM model! This also highlights the fact that the inverse of the current Hubble parameter H_0 gives a relatively accurate estimate of the age of the Universe. The exact value provided by the ΛCDM model from Eq. (1.60), *i.e.*, with $\Omega_m = 0.31$ and $\Omega_\Lambda = 0.69$, gives: $t_{\rm U} = 13.7$ Gyr.

In Fig. 1.1, we plot the evolution of the various constituents of the Universe according to Eqs. (1.53)-(1.55). This figure highlights the fact that the Universe is first dominated by radiation, then by matter, and finally by the cosmological constant. In addition, it is easy to quickly identify the moment of transition between radiation and matter in this figure by equalising the radiation energy density and the matter energy density:

$$\Omega_{r,0} \left(\frac{a_{\rm eq}}{a_0}\right)^{-4} = \Omega_{m,0} \left(\frac{a_{\rm eq}}{a_0}\right)^{-3} \Rightarrow a_{\rm eq} = \frac{\Omega_{r,0}}{\Omega_{m,0}} \Rightarrow 1 + z_{\rm eq} \sim 3440\,. \tag{1.61}$$

Similarly, we can do the same for the transition between matter and dark energy:

$$\Omega_{m,0} \left(\frac{a_\Lambda}{a_0}\right)^{-3} = \Omega_{\Lambda,0} \Rightarrow a_\Lambda = \left(\frac{\Omega_{\Lambda,0}}{\Omega_{m,0}}\right)^{1/3} \Rightarrow 1 + z_\Lambda \sim 1.31\,. \tag{1.62}$$

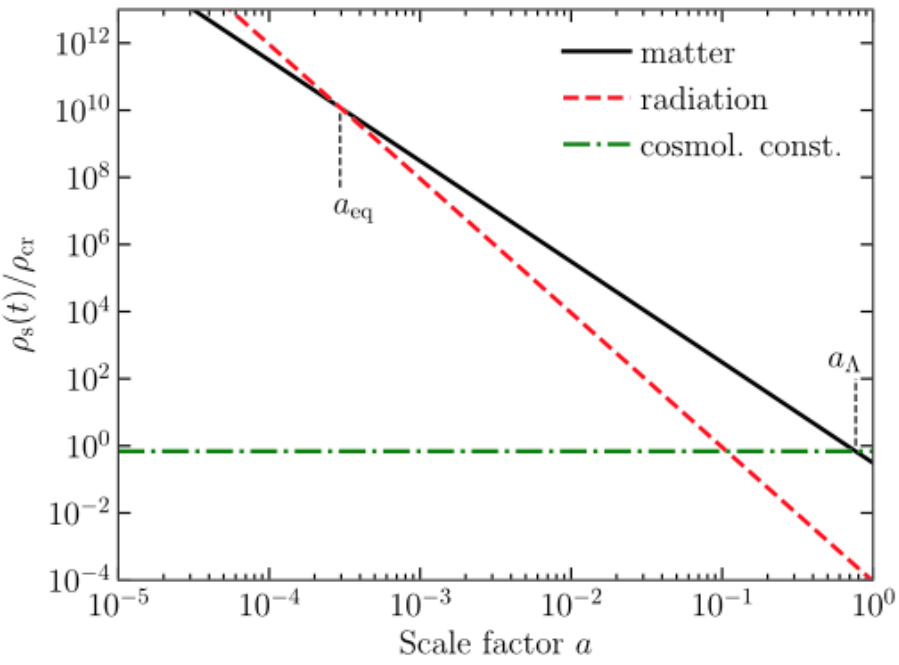

Figure 1.1: Evolution of the mean energy density of the constituents as a function of the scale factor. The universe is first dominated by radiation (dashed red line) which evolves as a^{-4}, then by matter (black line) which evolves as a^{-3} and finally by dark energy (dotted green line) which is constant with respect to a. Taken from Ref. [9].

Finally, in order to fully describe the evolution of the different constituents of the homogeneous universe, we still need to specify the time dependence of the scale factor for the different periods of the Universe. Therefore, for the different epochs, the temporal evolution of the Universe is determined by [see Eq. (1.60)]:

$$\text{Radiation era}: t = \frac{1}{H_0}\int_0^{a/a_0} \frac{x dx}{\sqrt{\Omega_{r,0}}} \Rightarrow \frac{a}{a_0} = (2H_0\sqrt{\Omega_r}t)^{1/2} \propto t^{1/2}, \tag{1.63}$$

$$\text{Matter era}: t = \frac{1}{H_0}\int_{a_eq/a_0\sim 0}^{a/a_0} \frac{\sqrt{x}dx}{\sqrt{\Omega_{m,0}}} \Rightarrow \frac{a}{a_0} \sim \left(\frac{3}{2}H_0\Omega_{m,0}t\right)^{2/3} \propto t^{2/3}, \tag{1.64}$$

$$\text{Dark energy era}: \int_{t_\Lambda}^{t} dt = \frac{1}{H_0}\int_{a_\Lambda/a_0}^{a/a_0} \frac{dx}{\sqrt{\Omega_{\Lambda,0}}x} \Rightarrow \frac{a_\Lambda}{a_0} = \exp\left\{H_0\sqrt{\Omega_{\Lambda,0}}(t-t_\Lambda)\right\} \propto \mathrm{e}^t. \tag{1.65}$$

1.2.6 Cosmological distances

In cosmology, there are several ways of measuring distances between different objects. These distance measurements are always dependent on the model under consideration (here ΛCDM) and only depend on the quantities coming from the homogeneous universe. First of all, let us rewrite the FLRW metric as:

$$ds^2 = g_{\mu\nu}dx^\mu dx^\nu = -dt^2 + a(t)^2\left[d\chi^2 + S_\kappa(\chi)(d\theta^2 + \sin^2\theta d\phi^2)\right], \tag{1.66}$$

where

$$S_\kappa(\chi) = \begin{cases} \sin^2\chi & \text{if} \quad \kappa = -1 \\ \chi^2 & \text{if} \quad \kappa = 0 \\ \sinh^2\chi & \text{if} \quad \kappa = 1\,. \end{cases} \tag{1.67}$$

Comoving distance. The first interesting and widely used distance in cosmology is the *comoving distance* for a photon (insofar as all cosmological information comes to us via electromagnetic radiation). Using the fact that $ds^2 = 0$ for a photon, we can define the comoving distance as:

$$\chi(a) = \int_{t_e}^{t_0} \frac{dt}{a(t)} = \int_{a(t_e)}^{a_0} \frac{da}{a(t)^2 H(a)} = \int_0^{z(t_e)} \frac{dz}{H(z)}\,, \tag{1.68}$$

where t_e is the time at which the photon is emitted. Let us note that if we take $a(t_e) = 0$ (or equivalently $z(t_e) = \infty$), then this quantity corresponds to the *comoving particle horizon*, namely the maximum distance a photon can have travelled since the end of inflation. This quantity then defines the size of the causal universe today!

The angular distance. The second important distance in cosmology is the *angular distance*. Let us imagine that we are looking at an object with a proper size $\delta l_{\rm object}$ seen from a small angle $\delta\theta$. Then the angular distance is define as:

$$d_A = \frac{\delta l_{\rm object}}{\delta\theta} = a \cdot S_\kappa(\chi) = \frac{1}{1+z} \cdot S_\kappa(\chi)\,, \tag{1.69}$$

where we have used the fact that $\delta l_{\rm object} = a \cdot S_\kappa(\chi)\delta\theta$ [see Eq. (1.66)]. This distance is important when we have a *standard ruler*, *i.e.*, an object with a known intrinsic distance $\delta l_{\rm object}$. This is for instance the case for the typical size of CMB fluctuations (in chapter 2, we use this quantity to define the angular acoustic scale at recombination θ_s, while in chapter 3 we use it in order to define the baryonic acoustic oscillation scale).

The luminosity distance. The last widely used distance in cosmology is the *luminosity distance*. This time, let us imagine we have a standard candle, *i.e.*, an object whose intrinsic luminosity L is known, at a comoving distance $\chi(a)$. This is for instance the case of the Supernovae Ia (SNIa). The flux received at a distance $d_L(a)$ from the source is then given by the following formula:

$$F = \frac{L}{4\pi d_L^2(a)}\,. \tag{1.70}$$

Now, it is also possible to derive an equivalent formula for the flux, which this time depends on the comoving distance $\chi(a)$:

$$F = \frac{1}{4\pi S_\kappa^2(a)} \times \frac{NE_0}{\delta t_0}\,, \tag{1.71}$$

where $4\pi S_\kappa^2(a)$ corresponds to the surface of the 3-sphere whose radius is determined by the physical distance between the source and the observer, and N the number of photons received

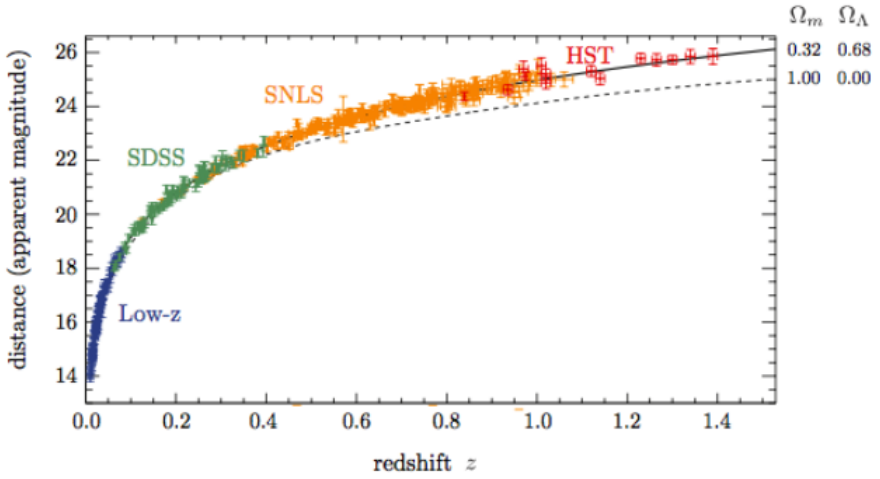

Figure 1.2: Evolution of the SNIa apparent magnitude as a function of the redshift z. The apparent magnitude, which depends on the luminosity distance d_L, is defined as $m = M + 5\log(d_L) + K$, where M is the absolute magnitude (which is known for a SNIa) and where K is a correction. Taken from Ref. [21].

with an energy E_0 during a fraction of time δt_0. Given that $L = NE_e/\delta t_e$, where E_e is the energy of the photons at emission, and that $E_0 = a \cdot E_e$ and $\delta t_0 = \delta t_e/a$, then

$$F = \frac{L \cdot a^2}{4\pi S_\kappa^2(a)}\,. \tag{1.72}$$

By equalizing this equation with Eq. (1.70), the luminosity distance is then defined as

$$d_L(a) = (1+z)S_\kappa(a)\,. \tag{1.73}$$

As shown in Fig. 1.2, it was thanks to this luminosity distance reconstructed from several SNIa that the Riess and Perlmutter groups were able to reveal the acceleration of the expansion of the Universe and, at the same time, the existence of dark energy.

Relationship between distances. In Fig 1.3, we plot these three distances as a function of the cosmological redshift z for an Euclidean expanding universe. Note that these three distances are linked by the following equations [with $S_\kappa(a) = \chi(a)$]:

$$d_A(a) = a\chi(a) = a^2 d_L(a) \Longleftrightarrow d_A(a) = \frac{\chi(z)}{1+z} = \frac{d_L(z)}{(1+z)^2}\,. \tag{1.74}$$

1.2.7 Initial conditions: the inflationary paradigm

As mentioned above, the ΛCDM model needs some initial conditions to work consistently, and it is necessary to bring in a complementary theory that not only explains these initial conditions but also solves some problems that the ΛCDM model cannot solve on its own. In the simplest models, inflation is caused by a single scalar field, called *inflaton* ϕ, which is minimally coupled to gravity in the following way:

$$\mathscr{L}_\phi = -\frac{1}{2}g^{\mu\nu}\partial_\mu\phi\partial_\nu\phi - V(\phi)\,, \tag{1.75}$$

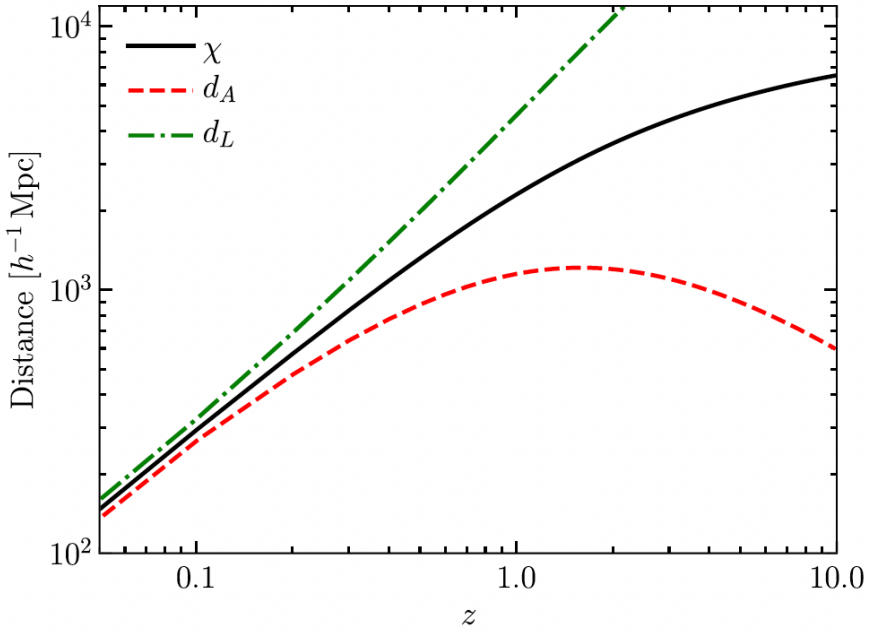

Figure 1.3: Evolution of the comoving distance $\chi(z)$, the angular distance $d_A(z)$ and the luminosity distance $d_L(z)$ in an Euclidean expanding universe as a function of the redshift z. Taken from Ref. [9].

where $V(\phi)$ is the inflation potential. One can then define the action of the inflation field as

$$S_\phi = \int d^4x\sqrt{-g}\mathscr{L}_\phi\,, \tag{1.76}$$

allowing us to determine the stress-energy tensor associated with the inflaton field thanks to the Noether's theorem:

$$T_{\mu\nu} \equiv \frac{2}{\sqrt{-g}}\frac{\delta S_\phi}{\delta g^{\mu\nu}} = \partial_\mu\phi\partial_\nu\phi - g_{\mu\nu}\left[\frac{1}{2}\partial^\alpha\phi\partial_\alpha\phi - V(\phi)\right], \tag{1.77}$$

where $g \equiv \det(g_{\mu\nu})$. Using this equation, we can determine the inflation energy density and the inflation pressure as

$$\overline{\rho}_\phi = -T^0_0 = \frac{1}{2}\dot{\phi} + V(\phi)\,, \tag{1.78}$$

$$\overline{P}_\phi = \frac{1}{3}\sum_i T^i_i = \frac{1}{2}\dot{\phi} - V(\phi)\,, \tag{1.79}$$

implying that the inflation equation of state parameter reads:

$$w_\phi = \frac{\overline{P}_\phi}{\overline{\rho}_\phi} = \frac{\frac{1}{2}\dot{\phi} - V(\phi)}{\frac{1}{2}\dot{\phi} + V(\phi)}\,. \tag{1.80}$$

In order to have an inflationary phase, *i.e.*, to have $\ddot{a} > 0$, inflation must satisfy the following condition [which derives directly from the second Freedman-Lemaître equation (1.37)]: $w_\phi < -1/3$.

In a FLRW metric, the equation of motion (known as the *Klein-Gordon equation*), derived from the principle of least action $\delta S_\phi/\delta_\phi = 0$, becomes:

$$\ddot{\phi} + 3H\dot{\phi} + \frac{dV(\phi)}{d\phi} = 0 \quad ; \quad H^2 = \frac{8\pi G}{3}\rho_\phi \,. \tag{1.81}$$

One of the main challenges of the inflation physics is to find a potential $V(\phi)$ which is compatible with several conditions, known as *slow-roll conditions*. This particular regime requires two conditions on the inflation scalar field ϕ:

$$\frac{\dot{\phi}}{2} \ll V(\phi) \quad ; \quad \ddot{\phi} \ll \frac{V(\phi)}{d\phi} = V'(\phi)\,, \tag{1.82}$$

where the first condition implies that $w \sim -1 < -1/3$. It is straightforward to show quickly that these two conditions can be expressed in the following way (allowing strong constraints to be placed on the type of inflation potential that can be used):

$$\varepsilon_V = \frac{M_{\rm pl}^2}{2}\left(\frac{V'_\phi}{V_\phi}\right)^2 \ll 1 \quad ; \quad |\,\eta_V\,| = M_{\rm pl}^2 |\frac{V''_\phi}{V_\phi}| \ll 1\,, \tag{1.83}$$

where $M_{\rm pl} = 1/\sqrt{8\pi G}$ is the reduced Planck mass. The first condition can be re-expressed as $\varepsilon = -\dot{H}/H \ll 1$, showing that this condition imposes a Hubble parameter that varies slowly during the slow-roll phase. In the limit where $\varepsilon \to 0$, we recover a de Sitter Universe, implying that inflation relies on a quasi de Sitter solution. In a de Sitter universe, we have

$$H^2 = \left(\frac{\dot{a}}{a}\right)^2 = \frac{\Lambda}{3} \quad ; \quad \dot{H} = 0\,, \tag{1.84}$$

giving a scale factor that evolves according to $a = e^{Ht}$. In this type of solution, the Universe is exponentially accelerated, while the Hubble radius remains constant, implying that the different modes become progressively bigger than the size of the particle horizon. These modes will then gradually re-enter the Hubble radius during the radiation, matter and dark energy domination eras. Finally, let us note that the slow-roll inflation ends when $\max(\varepsilon_V, \eta_V) = 1$.

1.3 Successes and challenges of the ΛCDM model

1.3.1 Successes of the ΛCDM model

In Fig 1.4, we summarise all the modern cosmology data as a function of the redshift $1+z$ and the scale $k = 2\pi/\lambda$ (where λ's are the typical distances observed by the experiment) under consideration. [5] It is remarkable that the ΛCDM model can provide an explanation and a rather good fit for all these data, even if some discrepancies seem to appear. The fact that this model is able to explain this wide variety of data from different tracers, and over a very wide range of scales and redshifts, is undeniably the greatest success of the ΛCDM model. In the rest of this thesis, we use data from experiments that have probed CMB anisotropies, CMB lensing, galaxy clustering and weak lensing for the inhomogeneous probes, as well as baryon acoustic

[5] Thank you so much Guillermo for this great figure, I know how much time you spent on it!

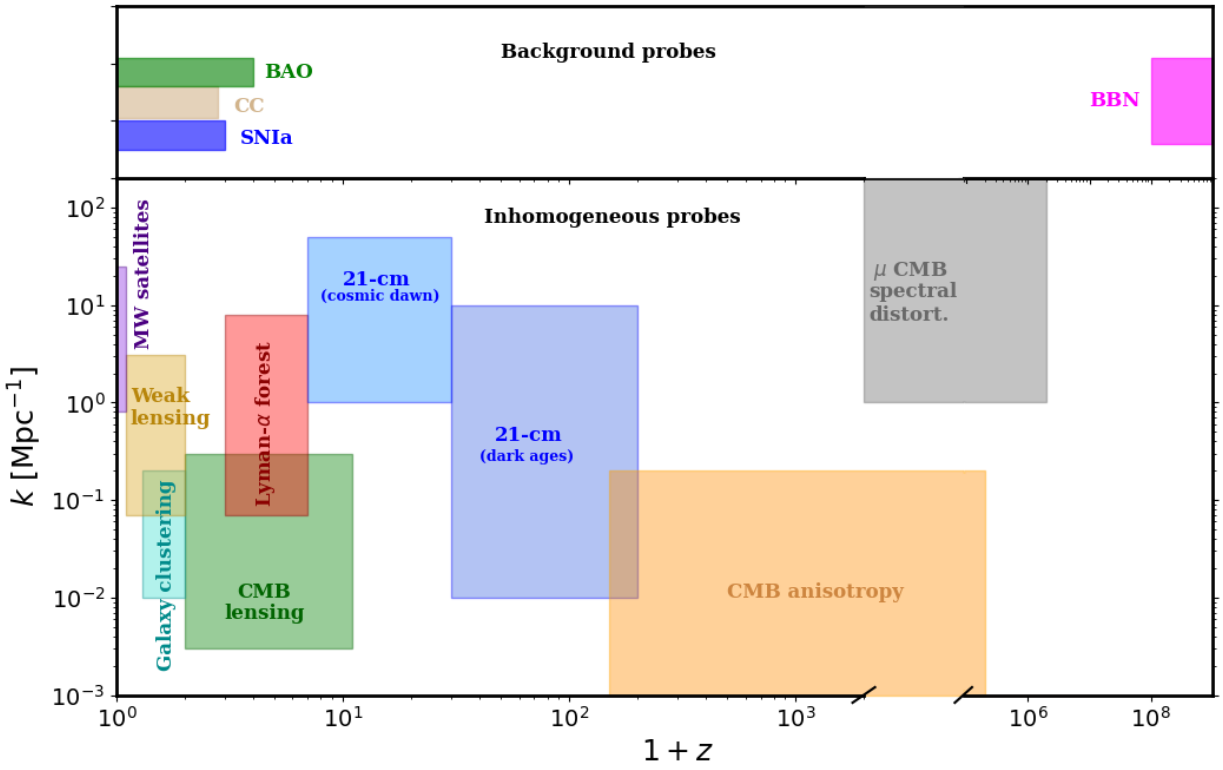

Figure 1.4: Redshift ranges as well as scale ranges covered by current and future cosmological probe. Taken from Ref. [22].

oscillations (BAO), supernovae of type Ia (SNIa) and big bang nucleosynthesis (BBN) for the background probes. We will see (especially in chapter 4) that the ΛCDM model is capable of explaining most of these data very accurately and that only six parameters (which we will describe at the end of chapter 2) are needed.

In particular, in chapter 2, we discuss in detail the theoretical framework used to describe CMB anisotropies and CMB lensing data, while in chapter 3, we describe the theoretical framework used to describe galaxy clustering and BAO data. In addition, we have already briefly described the SNIa physics, but we will not be talking about the BBN and weak lensing physics in this thesis. For a review on BBN see, *e.g.*, Ref. [23], and for a review on weak lensing see, *e.g.*, Refs. [24, 25].

1.3.2 Limits of the ΛCDM model

To close this chapter, we discuss the limitations of the ΛCDM model which will be of interest to us in the remainder of this thesis.

The intrinsic nature of the dark sector

The standard models of cosmology and particle physics have so far been unable to determine the intrinsic nature of the dark sector of the Universe, made up of dark matter and dark energy

(in the ΛCDM model). The framework of this thesis is in line with this axis of research, since we study models that make assumptions about the intrinsic nature of these two constituents and assess the extent to which these models can resolve cosmological tensions. There are several serious candidates to explain the origin and nature of these two dark components. Here we briefly list the candidates for dark matter:

- **WIMPs.** For a very long time, this hypothesis was very popular. Today, it remains a favoured option, even if its popularity has declined due to the absence of observations in particle colliders and direct detectors. These particles are assumed to be stable, neutral, to have a very weak interaction with Standard Model particles and to be very massive (of the order of G*e*V-T*e*V, which made them unobservable until now), hence the name *weakly interacting massive particles* (see Ref. [26] for a review). For instance, in the Supersymmetry framework the WIMP could be a *neutralino*.

- **Primordial black holes.** Primordial black holes is also a very popular model (see Ref. [27] for a review). These are black holes formed as a result of very large overdensities on small scales in the primordial Universe, causing a peak in the matter power spectrum. These black holes could today make up dark matter, or a fraction of it (which seems more likely).

- **Axions.** Axion is a hypothetical particle of low mass and neutral charge introduced in 1978 by Steven Weinberg [28] and Frank Wilczek [29] thanks to the work of Roberto Peccei and Helen Quinn in 1977 to solve the *strong CP problem* [30]. Quantum chromodynamics predicts that the strong interaction has no reason to preserve CP symmetry, while recent studies on the primordial asymmetry between baryons and antibaryons predict that the strong interaction must necessarily not preserve CP symmetry. However, experimentally one has never observed a CP violation by the strong interaction, which would be explained by the fact that the axion field symmetrizes the Langrangian of the strong interaction. Thus, quantum chromodynoamics with an axions field would then be able to explain this anomaly. The axion is also a very serious candidate for dark matter (see Refs. [31, 32] for reviews). The axion potential is usually written as

$$V(a) = m_a^2 f_a^2 \left(1 - \cos\frac{a}{f_a}\right), \tag{1.85}$$

  where m_a is the effective axion mass and f_a is the decay constant (note that QCD imposes a relation between m_a and f_a). The axion acquires its mass when the temperature falls below the QCD energy scale, and the axion then behaves like standard matter (namely $\rho_a \propto a^{-3}$) after rolling towards the minimum of its potential. There are currently axion models, called *axion-like particles*, inspired by the potential of the QCD axion, but which do not necessarily solve the strong CP problem.

- **Sterile neutrinos.** If one wants to explain neutrino oscillations and neutrino masses, then one needs to extend the Standard Model. One way of doing this postulates the existence of a right-handed neutrino called *sterile neutrino* (for instance with a *type-I seesaw mechanism*), that could make up dark matter (see Ref. [33] for a review).

For dark energy, a number of candidates are also receiving special attention, among which we can cite:

- **Cosmological constant.** This is the dark energy paradigm of the ΛCDM model, as explained above. It should be noted that this dark energy model faces a problem, known as the *cosmological constant problem* (or *vacuum catastrophe*). The latter arises from a mismatch between the measured energy density of dark energy determined from cosmology and the theoretical energy density of the vacuum (or, more precisely, the largest theoretical value of zero-point energy density) determined from quantum field theory. In principle, these two values should correspond within a coherent physical theory, but they disagree by 120 orders of magnitude!

- **Quintessence models.** This is a class of scenarios, first proposed by Bharat Ratra and Jim Peebles [34], where the dark energy equation of state is no longer necessarily equal to $w_\phi = -1$ and varies over time. In these scenarios, dark energy is then modelled by a dynamic scalar field that is minimally coupled to gravity. In order to have an accelerated expansion it is necessary to respect the condition (see the discussion above on inflation):

$$w_\phi = \frac{\frac{1}{2}\dot{\phi} - V(\phi)}{\frac{1}{2}\dot{\phi} + V(\phi)} < -1/3\,. \tag{1.86}$$

- **Modified gravity.** There are many modified gravity models that allow us to obtain a behaviour similar to dark energy. The idea of these models is to assert that the acceleration of the expansion of our Universe is not due to an additional component, but to an incompleteness in the general relativity equations. This is for example the case of the scalar-tensor theories described by the Horndeski action [35]. This theory encompasses all the possible ways of constructing a Lagrangian from a metric tensor and a scalar field. A fairly popular example is the $f(\mathscr{R})$ model, which modifies the Einstein-Hilbert action as follows:

$$S[g] = \int \frac{1}{16\pi G}\mathscr{R}\sqrt{-g}d^4x \;\rightarrow\; S[g] = \int \frac{1}{16\pi G} f(\mathscr{R})\sqrt{-g} \tag{1.87}$$

  where $\mathscr{R}$ is the Ricci scalar, and $f(\mathscr{R})$ a function of the Ricci scalar.

Cosmological tensions

Another current limitation of the ΛCDM model are the so-called cosmological tensions. As the accuracy of measurements has increased over the past few years, some intriguing discrepancies have emerged between the values of some cosmological parameters predicted by the ΛCDM model and their direct measurements in the local Universe. In particular, the "Hubble tension" is a significant discrepancy ($\sim 5\sigma$) between the value of the current expansion rate of the universe, *i.e.*, the Hubble parameter H_0, measured using SNIa data as a cosmic distance ladder (see above), and that inferred from CMB data using the ΛCDM model (see chapter 2). Additionally, a less significant ($\sim 2\sigma$), but older, tension exists which this time concerns the amplitude of the local matter fluctuations, typically parametrized as S_8. The S_8 tension is a mismatch of the value of this parameter between its prediction by the ΛCDM model from the CMB data on the one hand, and its direct and local determination from weak lensing (see Fig. 1.4) on the other hand. These tensions could be the first indication of new features in the dark components and give hope to access their fundamental properties. These two tensions are an important (though not the only) motivation for the third part of this thesis,

and we therefore deal with them in detail in the introduction to this part (see p. 199).

There are other interesting tensions that are not covered in this thesis, such as the $A_{\rm lens}$ *anomaly* [36], the *lithium problem* [37], the *small-scale crisis* [38] or the *cosmic dipole tension* [39]. A review of all the cosmological tensions can be found in Ref. [40].

II

The linearly perturbed universe and CMB physics

Contents

2.1 From the homogeneous universe to the perturbed universe **33**
2.1.1 Perturbation of the metric 33
2.1.2 Perturbation of the stress-energy tensor 34
2.1.3 Perturbation of the phase-space distribution function 36
2.2 The perturbed universe **37**
2.2.1 Perturbed Einstein's equations 37
2.2.2 Conservation of the stress-energy tensor 38
2.2.3 Perturbed Boltzmann's equations 41
2.2.4 Partial summary 45
2.3 Initial conditions **47**
2.3.1 Adiabatic and isocurvature perturbations 47
2.3.2 Primordial power spectrum 49
2.4 CMB physics **52**
2.4.1 CMB power spectrum 52
2.4.2 The CMB anisotropies 54
2.4.3 A description of the CMB temperature power spectrum 57
2.4.4 Cosmological parameters. 61
2.4.5 Other CMB power spectra 63

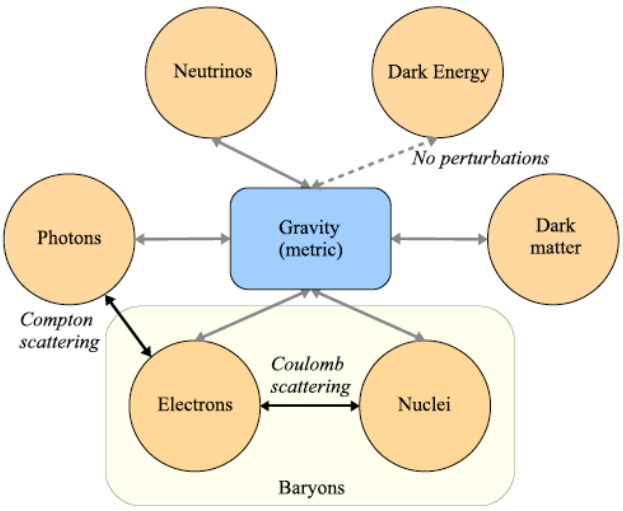

Figure 2.1: Summary of the various interactions of the perturbed universe. Taken from Ref. [9].

As we have seen in chapter 1, in order to describe temporal and spatial behaviour of the species in the Universe one needs to solve the Einstein and Boltzmann equations, that is Eqs. (1.1) and (2.58), and more specifically to specify the stress-energy tensor $T_{\mu\nu}$ and the metric tensor $g_{\mu\nu}$ for the former, and the distribution function $f(x,p,t)$ for the latter. In a flat, homogeneous, and isotropic universe, $T_{\mu\nu}$ is defined by Eq. (1.30), $g_{\mu\nu}$ by Eq. (1.24) and $f(x,p,t)$ by Eq. (1.39) for photons. These definitions allow us to obtain the equations governing the evolution of components in a homogeneous universe (*i.e.*, for characteristic distances larger than 100 Mpc), namely the Friedmann-Lemaître equations [Eqs. (1.36) and (1.37)] and the homogeneous and isotropic Boltzmann equations for an expanding universe [Eq. (1.38)]. Now, if one wants to understand the local evolution of the Universe, for example the evolution of the large-scale structures or the anisotropies of the CMB, one must release the homogeneity and isotropy constraints. This implies, as we shall see, a new solution of $T_{\mu\nu}$, $g_{\mu\nu}$ and $f(x,p,t)$. In each case, one starts from the homogeneous definition and then perturb it with small parameters depending on position and time, which makes it possible to obtain the perturbation equations of the various components describing the local inhomogeneities of our Universe. Actually, there are three types of metric perturbations: scalar, vector and tensor perturbations (relative to the group of spatial rotations). However, the scalar degrees of freedom (that interest us here) are decoupled from the other degrees of freedom at linear order (according to the *decomposition theorem*), which means that the other two types of perturbation are not mentioned in what follows. The main picture of the perturbed Universe is shown in Fig. 2.1. The aim of this section is to establish the general equations that couple the density perturbations of each of the constituents to the metric perturbations. In particular, we will establish that the scalar perturbations of the metric are coupled with the density perturbations of each of the constituents (except the cosmological, which influences the metric only at the level of the homogeneous solution through the scale factor), using the perturbed Boltzmann and Einstein equations.

In this chapter, we first introduce the formalism of the perturbed universe in Sec. 2.1, before perturbing the Boltzmann and Einstein equations in Sec. 2.2. Then, in Sec. 2.3, we discuss the initial conditions of the perturbed universe, and in Sec. 2.4 we deal with CMB physics. Let us note that Secs. 2.1 and 2.2 are based mainly on Ref. [41], while Sec. 2.4 is based mainly on Ref. [9].

2.1 From the homogeneous universe to the perturbed universe

To obtain the equations of the perturbed universe, the first step is to perturb (i) the metric, (ii) the stress-energy tensor, and (iii) the phase-space distribution function (for relativistic species). All calculations in this section are based on Ref. [41].

2.1.1 Perturbation of the metric

First of all, let us discuss the perturbations of the metric. Given that $g_{\mu\nu}$ is a symmetric tensor, one has ten independent degrees of freedom. However, the *decomposition theorem* states that of these ten degrees of freedom four are related to scalar perturbations and that at linear order they evolve independently from the other six degrees of freedom. In addition, in general relativity one has a gauge freedom due to the *diffeomorphism invariance* of this theory, which implies that, by a gauge choice, one can reduce these four degrees of freedom to two degrees of freedom, as does the *Newtonian gauge* (also known as the longitudinal gauge):

$$ds^2 = g_{\mu\nu}dx^\mu dx_\nu = [-1-2\psi(x,t)]\,dt^2 + a(t)^2\,[1-2\phi(x,t)]\,\delta_{ij}dx^i dx^j\,, \tag{2.1}$$

where $\psi(x,t)$ corresponds to the local Newtonian potential that governs the behaviour of slow-moving bodies and where $\phi(x,t)$ can be interpreted as the local scale factor perturbation, namely $a(t) \mapsto a(t)[1-\phi(x,t)]$. The parameters ϕ and ψ are very small compared to unity ($\phi, \psi \ll 1$), which allows us to consider them as perturbations of the homogeneous and isotropic FLRW solution. One can redefine this metric in a simpler way by using the conformal time τ, with the following transformation $t \mapsto \tau a(\tau)$:

$$g_{\mu\nu} = a(\tau)^2 \cdot \{[-1-2\psi(x,\tau)]\,dt^2 + [1-2\phi(x,\tau)]\,\delta_{ij}dx^i dx^j\}\,. \tag{2.2}$$

The main advantages of this gauge is that (i) the two scalar degrees of freedom have a very clear and well-defined physical meaning, and (ii) the equations take Newtonian forms on subhorizon scales within this gauge (hence the name).

We mention here another gauge which is sometimes simpler to use, because (as we shall see) it sometimes makes it possible to simplify the perturbation equations (see *e.g.*, the case of decaying cold dark matter models in chapter 9). This gauge, also widely used in cosmology, is called the *synchronous gauge*, where the scalar part of the perturbed metric is written as (using the conformal time)

$$ds^2 = g_{\mu\nu}dx^\mu dx^\nu = a^2(\tau)\cdot\left[-d\tau^2 + (\delta_{ij}+h_{ij}(x,t))dx^i dx^j\right]\,. \tag{2.3}$$

Here $h_{ij}(x,\tau)$ is defined as

$$h_{ij}(x,\tau) = \int d^3k e^{ik.x}[\hat{k}_i\hat{k}_j h(k,\tau) + \left(\hat{k}_i\hat{k}_j - \frac{1}{3}\delta_{ij}\right) 6\eta(k,\tau)], \tag{2.4}$$

where $h \equiv h_{ii}$ denotes the trace of h_{ij}, while η corresponds to the traceless scalar degree of freedom of the metric perturbation in Fourier space.[1] This gauge has a particular subtlety: we have to eliminate a residual gauge freedom due to the fact that this gauge does not set the initial hypersurface and its coordinate assignment. It is conventional to fix the synchronous coordinates to the dark matter rest frame in order to set this remaining gauge freedom. Therefore, in this gauge, we have $v_{i,\mathrm{CDM}} = \partial_i v_{i,\mathrm{CDM}} = 0$, which significantly simplifies the dark matter perturbation equations.

One can show (see *e.g.*, Ref. [41]) that the equivalence relations between these two arbitrary metrics can be written (in Fourier space) as follows

$$\psi(k,\tau) = \frac{1}{2k^2}\left[\ddot{h}(k,\tau) + 6\ddot{\eta}(k,\tau) + \frac{\dot{a}}{a}\dot{h}(k,\tau) + 6\frac{\dot{a}}{a}\dot{\eta}(k,\tau)\right], \tag{2.6}$$

$$\phi(k,\tau) = \eta(k,\tau) - \frac{1}{2k^2}\frac{\dot{a}}{a}\left[\dot{h}(k,\tau) + 6\dot{\eta}(k,\tau)\right]. \tag{2.7}$$

We warn the reader that in this chapter $\dot{X} = dX/d\tau$, unlike in the previous chapter where $\dot{X} = dX/dt$. The two metrics presented above now depend on x, unlike the unperturbed FLRW metric, which implies that the evolution of the Universe now depends on position: we are now in the framework of a non-homogeneous and non-isotropic universe.

2.1.2 Perturbation of the stress-energy tensor

Concerning $T_{\mu\nu}$, it will be affected by three modifications with respect to the homogeneous solution [see Eq. (1.30)]:

- one no longer considers fluids at rest, but they now have small local velocities, $v_i(\boldsymbol{x},\tau) = dx^i/d\tau$, leading to non-diagonal terms;
- we now perturb the homogeneous density field $\overline{\rho}(\tau)$ and the homogeneous pressure field $\overline{P}(\tau)$ with the overdensity and overpressure fields [$\delta\rho(x,\tau)$ and $\delta P(x,\tau)$], respectively defined as

$$\rho(x,\tau) \equiv \overline{\rho}(\tau) + \delta\rho(x,\tau), \tag{2.8}$$

$$P(x,\tau) \equiv \overline{P}(\tau) + \delta P(x,\tau), \tag{2.9}$$

  which will affect the diagonal terms of $T_{\mu\nu}$;

[1] In natural space, we thus have [if we take $\hat{k} = (0\ 0\ 1)$]:

$$ds^2 = a^2(\tau)\cdot\{-d\tau^2 + [1-2\eta(x,\tau)]dx^2 + [1-2\eta(x,\tau)]dy^2 + [1+h(x,\tau)+4\eta(x,\tau)]dz^2\}. \tag{2.5}$$

- one adds the anisotropic stress tensor $\Sigma_{ij}(\boldsymbol{x},\tau)$, which corresponds to the traceless component of T_{ij}. The main contribution to this tensor comes from neutrinos (or free streaming relativistic species in general).

These modifications allow us to write $\delta T^{\mu}_{\nu}(x,\tau) = T^{\mu}_{\nu}(x,\tau) - \overline{T}^{\mu}_{\nu}(\tau)$, which is valid for all components, as:

$$\delta T^{0}_{0}(x,\tau) = -\delta\rho(x,\tau)\,, \tag{2.10}$$

$$\delta T^{0}_{i}(x,\tau) = (\overline{\rho}(x,\tau)+\overline{P}(x,\tau))v_i\,, \tag{2.11}$$

$$\delta T^{i}_{j}(x,\tau) = \delta P(x,\tau)\delta^{i}_{j}+\Sigma^{i}_{j} \quad ; \quad \Sigma^{i}_{i}=0\,, \tag{2.12}$$

where $\delta\rho = \sum_a \delta\rho_a$ is the total overdensity field and $\delta P = \sum_a \delta P_a$ is the total overpressure field. Note that in the following, we sometimes use the total divergence of the fluid velocities, namely $\theta = \sum_a \partial_i v^i_a$, instead of the total velocity itself, since the perturbation equations only involve the derivative of the velocity. Finally, let us note that we can parametrize the anisotropic stress tensor as:

$$\Sigma_{ij} \equiv \left(\partial_i\partial_j - \frac{1}{3}\nabla^2\delta_{ij}\right)\Sigma + \frac{1}{2}(\partial_i\hat{\Sigma}_j + \partial_j\hat{\Sigma}_i) + \hat{\Sigma}_{ij}\,, \tag{2.13}$$

where Σ is the scalar degree of freedom of this tensor. Since we are only interested here in scalar modes, we consider only this degree of freedom in the remainder of this thesis. However, it is common to use the parameter σ instead, defined as

$$(\overline{\rho}+\overline{P})\nabla^2\sigma \equiv -\left(\partial_i\partial_j - \frac{1}{3}\nabla^2\delta_{ij}\right)\delta T^{i}_{j}\,. \tag{2.14}$$

This parameter is called the *shear* or *anisotropic* stress parameter, and like the other perturbation parameters, it is made up of the sum of the contribution of each of the components: $\sigma = \sum_a \sigma_a$.

Now, let us find the relationships that relate these four perturbations parameters ($\delta\rho$, δP, θ and σ) between these two gauges. T^{μ}_{ν} transforms like a tensor, which implies that the stress-energy tensor in synchronous gauge $T^{\mu}_{\nu}(\mathrm{Syn})$ is related to the stress-energy tensor in (conformal) Newtonian gauge $T^{\mu}_{\nu}(\mathrm{New})$ by:

$$T^{\mu}_{\nu}(\mathrm{Syn}) = \frac{\partial\hat{x}^{\mu}}{\partial x^{\alpha}}\frac{\partial x^{\beta}}{\partial\hat{x}^{\nu}}T^{\beta}_{\alpha}(\mathrm{New})\,, \tag{2.15}$$

where $\hat{x}^{\mu}$ denotes the coordinates of the synchronous gauge, while x^{μ} denotes the coordinates of the Newtonian gauge. From this equation, one can directly show that in Fourier space

$$T^{0}_{0}(\mathrm{Syn}) = T^{0}_{0}(\mathrm{New})\,, \tag{2.16}$$

$$T^{0}_{i}(\mathrm{Syn}) = T^{0}_{i}(\mathrm{New}) + ik_i\frac{\dot{h}+6\dot{\eta}}{2k^2}(\overline{\rho}+\overline{P})\,, \tag{2.17}$$

$$T^{i}_{j}(\mathrm{Syn}) = T^{i}_{j}(\mathrm{New})\,. \tag{2.18}$$

Using Eqs. (2.10)-(2.12), one can show that:

$$\delta(\text{Syn}) = \delta(\text{New}) - \frac{\dot{h}+6\dot{\eta}}{2k^2}\cdot\frac{\dot{\overline{\rho}}}{\overline{\rho}}, \tag{2.19}$$

$$\theta(\text{Syn}) = \theta(\text{New}) - \frac{\dot{h}+6\dot{\eta}}{2}, \tag{2.20}$$

$$\delta(\text{Syn})P = \delta P(\text{New}) - \frac{\dot{h}+6\dot{\eta}}{2k^2}\cdot\dot{\overline{P}}, \tag{2.21}$$

$$\sigma(\text{Syn}) = \sigma(\text{New}). \tag{2.22}$$

These equations work for the sum of the constituents as well as for each individual species.

2.1.3 Perturbation of the phase-space distribution function

Finally, the phase-space distribution function of photons (*i.e.*, the Bose-Einstein distribution) is perturbed in the following way thanks to the parameter $\Psi(x^i, p^j, \tau)$ defined as

$$f(x^i, P_j, \tau) = f_0(p,\tau)[1+\Psi(x^i, P_j, \tau)], \tag{2.23}$$

where $f_0(p,\tau)$ corresponds to the Bose-Einstein distribution of the homogeneous universe [see Eq. (1.39)]. P_j is the spatial part of the four-momentum, given by

$$P_i = a(1-\phi)\cdot p_i, \tag{2.24}$$

$$P_i = a(\delta_{ij}+\frac{1}{2}h_{ij})\cdot p^j, \tag{2.25}$$

in Newtonian gauge and synchronous gauge respectively, where p_i corresponds to the physical (proper) 3-momentum of the particle. In addition (and as in chapter 1), it is convenient to use the comoving quantity $q^j = a\cdot p^j$. It is also useful to decompose q^j as $q^j = q\cdot\hat{n}^j$, where q is the magnitude and $\hat{n}^j$ the direction of the momentum. Therefore, for practical reasons, we consider the following perturbed quantity: $\Psi(x^i, P_j, \tau) \to \Psi(x^i, q, \hat{n}_j, \tau)$.

This is equivalent to perturbing the photon temperature thanks to the parameter $\Theta(x^i, q, \hat{n}_j, \tau)$ as $\overline{T}(\tau) \mapsto \overline{T}(\tau)[1+\Theta(x^i, q, \hat{n}_j, \tau)]$, and to inject this new temperature into the homogeneous photon phase-space distribution function [see Eq. (1.39)]:

$$f(x^i, q, \hat{n}_j, \tau) = \left[\exp\left(\frac{q}{\overline{T}(\tau)[1+\Theta(x^i, q, \hat{n}_j, \tau)]}\right) - 1\right]^{-1} \tag{2.26}$$

$$\simeq f_0(q,\tau) - q\frac{\partial f_0(q,\tau)}{\partial q}\Theta(x^i, q, \hat{n}_j, \tau), \tag{2.27}$$

where the second line results from a first-order Taylor expansion in $\Theta(x^i, q, \hat{n}_j, \tau)$. $\Psi(x^i, q, \hat{n}_j, \tau)$ is therefore related to $\Theta(x^i, q, \hat{n}_j, \tau)$ by

$$\Psi(x^i, q, \hat{n}_j, \tau) = -\left(\frac{d\ln f_0(q)}{d\ln q}\right)\Theta(x^i, q, \hat{n}_j, \tau). \tag{2.28}$$

Note that in the case we are considering, $\Theta(x^i, q, \hat{n}_j, \tau) \to \Theta(x^i, \hat{n}_j, \tau)$ does not depend on q, the momentum magnitude, because we will consider that the photons interact with the

electrons solely by a Thomson interaction (since the electrons are at rest when $T \ll m_e$, which is the relevant regime for studying the CMB). This implies that the photon momentum is (approximately) conserved over the cosmological eras considered.

The same can be done for neutrinos by considering the Fermi-Dirac equation:

$$f_\nu(x^i, q, \hat{n}_j, \tau) = \left[\exp\left(\frac{q}{T_\nu(\tau)[1+\mathcal{N}(x^i, q, \hat{n}_j, \tau)]}\right)+1\right]^{-1}. \tag{2.29}$$

From Eq. (1.46), and by analogy with Eqs. (1.51) and (1.52) which are valid in the homogeneous universe, we can easily show that the components of T^μ_ν can be written as

$$T^0_0 = -\frac{1}{a^4}\int q^2 dq d\Omega\, \mathscr{E} f_0(q)(1+\Psi)\,, \tag{2.30}$$

$$T^0_i = \frac{1}{a^4}\int q^2 dq d\Omega\, q\hat{n}_i f_0(q)\Psi\,, \tag{2.31}$$

$$T^i_j = \frac{1}{a^4}\int q^2 dq d\Omega\, \frac{q^2\hat{n}_i\hat{n}_j}{\mathscr{E}} f_0(q)(1+\Psi)\,, \tag{2.32}$$

where $\mathscr{E} = aE = \sqrt{q^2+m^2a^2}$ is the comoving energy. Note that in these last equations we have (conventionally) integrated the factor $g/(2\pi)^3$, where g is the number of internal degrees of freedom, in the phase-space distribution function. We have also used the fact that (in Newtonian gauge) $\sqrt{-g} = a^4(1+\psi)(1-3\phi)$, and $dP_1 dP_2 dP_3 = (1-3\phi)q^2 dq d\Omega$.

2.2 The perturbed universe

Let us now derive the Einstein and Boltzmann equations for the perturbed universe. All calculations in this section are based on Ref. [41], and will be performed in *Fourier space* (or "k-space") in order to linearized the Einstein and Boltzmann equations at first order in perturbation. In this thesis, we use the following convention

$$\phi(x,\tau) = \int \frac{d^3k}{(2\pi)^3} e^{ik.x}\cdot\tilde{\phi}(k,\tau)\,, \tag{2.33}$$

where k corresponds to the wavenumber of the perturbation allowing to define a perturbation mode. The comoving wavelength of the mode associated to k is define as $\lambda = 2\pi/\|k\|$. Let us note that while the comoving size of a mode is given by λ, the comoving size of the Universe, the comoving horizon, is given by τ.

2.2.1 Perturbed Einstein's equations

Let us start with the perturbed Einstein equations. The (scalar) perturbation of the metric tensor by $\psi(x,\tau)$ and $\phi(x,\tau)$, or $h(x,\tau)$ and $\eta(x,\tau)$, implies that the Einstein tensor $G_{\mu\nu}$ is also perturbed: $G_{\mu\nu} \mapsto G_{\mu\nu} + \delta G_{\mu\nu}$. As one has seen above, the stress-energy tensor is perturbed as $T_{\mu\nu} \mapsto T_{\mu\nu} + \delta T_{\mu\nu}$, implying that the perturbed Einstein equations read [one eliminates the homogeneous and isotropic contribution thanks to Eq. (1.1)]

$$\delta G^\mu_\nu = 8\pi G\cdot\delta T^\mu_\nu\,. \tag{2.34}$$

This allows us to obtain, in k-space, the following equations [corresponding to the 00, $0i$, ii and ij components of Eq. (2.34) respectively] for the two gauges:

Newtonian gauge:

$$k^2\phi + 3\frac{\dot{a}}{a}\left(\dot{\phi} + \frac{\dot{a}}{a}\psi\right) = -4\pi G a^2 \delta\rho(\text{New}), \tag{2.35}$$

$$k^2\left(\dot{\phi} + \frac{\dot{a}}{a}\psi\right) = 4\pi G a^2(\overline{\rho} + \overline{P})\theta(\text{New}), \tag{2.36}$$

$$\ddot{\phi} + \frac{\dot{a}}{a}(\dot{\psi} + 2\dot{\phi}) + \left(2\frac{\ddot{a}}{a} - \frac{\dot{a}^2}{a^2}\right)\psi + \frac{k^2}{3}(\phi - \psi) = 4\pi G a^2 \delta P(\text{New}), \tag{2.37}$$

$$k^2(\phi - \psi) = 12\pi G a^2(\overline{\rho} + \overline{P})\sigma(\text{New}). \tag{2.38}$$

Synchronous gauge:

$$k^2\eta - \frac{1}{2}\frac{\dot{a}}{a}\dot{h} = -4\pi G a^2 \delta\rho(\text{Syn}), \tag{2.39}$$

$$k^2\dot{\eta} = 4\pi G a^2(\overline{\rho} + \overline{P})\theta\rho(\text{Syn}), \tag{2.40}$$

$$\ddot{h} + 2\frac{\dot{a}}{a}\dot{h} - 2k^2\eta = -24\pi G a^2 \delta P\rho(\text{Syn}), \tag{2.41}$$

$$\ddot{h} + 6\ddot{\eta} + 2\frac{\dot{a}}{a}(\dot{h} + 6\dot{\eta}) - 2k^2\eta = -24\pi G a^2(\overline{\rho} + \overline{P})\sigma\rho(\text{Syn}). \tag{2.42}$$

We recall that θ and σ correspond respectively to the total divergence of the fluid velocities ($\theta = \sum_a ik_j v_a^j$ in Fourier space) and to the total anisotropic stress perturbation, respectively. These four equations allow us to determine the space-time evolution of ϕ and ψ (on the left-hand side of these equations, obtained thanks to δG^μ_ν) as a function of the perturbation parameters of the fluid, that is $\delta\rho$, δP, θ and σ (on the right-hand side of these equations, obtained thanks to δT^μ_ν). Note that deep inside the horizon, where $k \gg aH$, Eq. (2.35) reduces to the Poisson equation:

$$-\frac{k^2}{a^2}\phi = 4\pi G\delta\rho. \tag{2.43}$$

2.2.2 Conservation of the stress-energy tensor

In addition, the stress-energy tensor $T_{\mu\nu}$ must be conserved for a non-interacting fluid, which is expressed through its covariant derivative:

$$\nabla_\mu T^\mu_\nu \equiv \frac{\partial T^\mu_\nu}{\partial x^\mu} + \Gamma^\mu_{\alpha\mu} T^\alpha_\nu - \Gamma^\alpha_{\nu\mu} T^\mu_\alpha = 0, \tag{2.44}$$

where we recall that the $\nu = 0$ component corresponds to the continuity equation, while the $\nu = i$ component corresponds to the Euler's equation. While the Euler equation is trivially zero in the homogeneous and isotropic FLRW universe, since $\partial P/\partial x^i$ is obviously zero, this is no longer true in a non-homogeneous and non-isotropic universe. In the two gauges presented above, the continuity and Euler equations take the following form:

Newtonian gauge:

$$\dot{\delta} = -(1+\omega)(\theta - 3\dot{\phi}) - 3\frac{\dot{a}}{a}\left(\frac{\delta P}{\delta\rho} - \omega\right)\delta\,, \tag{2.45}$$

$$\dot{\theta} = -\frac{\dot{a}}{a}(1-3\omega)\theta - \frac{\dot{\omega}}{1+\omega}\theta + \frac{\delta P/\delta\rho}{1+\omega}k^2\delta - k^2\sigma + k^2\psi\,. \tag{2.46}$$

Synchronous gauge:

$$\dot{\delta} = -(1+\omega)(\theta + \frac{\dot{h}}{2}) - 3\frac{\dot{a}}{a}\left(\frac{\delta P}{\delta\rho} - \omega\right)\delta\,, \tag{2.47}$$

$$\dot{\theta} = -\frac{\dot{a}}{a}(1-3\omega)\theta - \frac{\dot{\omega}}{1+\omega}\theta + \frac{\delta P/\delta\rho}{1+\omega}k^2\delta - k^2\sigma\,. \tag{2.48}$$

These two equations allow us to obtain two coupled differential equations for δ and θ, where δ is simply $\delta\rho/\overline{\rho}$. A number of comments deserve to be made here:

1. Unlike the perturbed Einstein equations, we will apply these two equations to each constituent and not to the sum of the constituents, since these equations depend on the intrinsic nature of the constituents (through the equation of state parameter w, for example).

2. The first equation governing the behaviour of $\dot{\delta}$ corresponds to the perturbed continuity equation, while the second equation governing the behaviour of $\dot{\theta}$ corresponds to the perturbed Euler's equation. As already mentioned in chapter 1 and as we shall see later on, the first two moments of the Boltzmann equation allow us to find these two equations as well.

3. As we will explain later (when we will derive the perturbed Boltzmann equations), these two equations are sufficient to describe the perturbation behaviour of massive species (namely, baryons and dark matter). On the other hand, for non-massive species (namely photons and neutrinos), it is necessary to solve the complete hierarchy of the Boltzmann equations, and not just the first two moments! Typically, each moment will involve a new perturbation parameter, which means that photons and neutrinos have many more perturbation parameters than dark matter and baryons.

4. These two equations are only valid for a fluid without interaction. This is true for neutrinos and dark matter (which decoupled from the other fluids very early in the history of the Universe within the ΛCDM framework). On the other hand, for baryons and photons it is necessary to add an interaction term to the right-hand side of Eq. (2.44), since these two components have interacted before recombination through Thomson scattering.

5. In our case, the interaction terms will only modify the Euler equations and not the continuity equations, insofar as the latter deals with the temporal conservation of the number of particles per unit volume. For the processes in which we are interested (in particular the Thomson scattering) we have no modification in the total number of particles.

We can now use Eqs. (2.45)-(2.48) in order to derive the perturbed continuity and Euler equations for the different cosmological fluids. To do so, let us note that for adiabatic perturbations (see next section), we have the following relationship: $\delta P/\delta\rho = c_s^2$, where c_s is

the adiabatic sound speed of the perturbations. On the other hand, this parameter is defined as $c_s^2 = dP/d\rho = dw/d\rho + w$. Consequently, in an adiabatically perturbed fluid with a constant equation of state parameter, $\delta P/\delta\rho = w$. Given that for photons and massless neutrinos $\omega = 1/3$, and for cold dark matter and baryons $\omega \approx 0$, one has:

Newtonian gauge:

$$\textbf{Cold Dark Matter: } \dot{\delta}_c = -\theta_c + 3\dot{\phi} \quad ; \quad \dot{\theta}_c = -\frac{\dot{a}}{a}\theta_c + k^2\psi\,, \tag{2.49}$$

$$\textbf{Massless Neutrinos: } \dot{\delta}_\nu = -\frac{4}{3}\theta_\nu + 4\dot{\phi} \quad ; \quad \dot{\theta}_\nu = k^2\left(\frac{1}{4}\delta_\nu - \sigma_\nu\right) + k^2\psi\,, \tag{2.50}$$

$$\textbf{Photons: } \dot{\delta}_\gamma = -\frac{4}{3}\theta_\gamma + 4\dot{\phi} \quad ; \quad \dot{\theta}_\gamma = k^2\left(\frac{1}{4}\delta_\gamma - \sigma_\gamma\right) + k^2\psi + an_e\sigma_T(\theta_b - \theta_\gamma)\,, \tag{2.51}$$

$$\textbf{Baryons: } \dot{\delta}_b = -\theta_b + 3\dot{\phi} \quad ; \quad \dot{\theta}_b = -\frac{\dot{a}}{a}\theta_b + c_s^2k^2\delta_b + k^2\psi + \frac{4\overline{\rho}_\gamma}{3\overline{\rho}_b}an_e\sigma_T(\theta_\gamma - \theta_b)\,. \tag{2.52}$$

Synchronous gauge:

$$\textbf{Cold Dark Matter: } \dot{\delta}_c = -\frac{1}{2}\dot{h} \quad ; \quad \dot{\theta}_c = \theta_c = 0\,, \tag{2.53}$$

$$\textbf{Massless Neutrinos: } \dot{\delta}_\nu = -\frac{4}{3}\theta_\nu - \frac{2}{3}\dot{h} \quad ; \quad \dot{\theta}_\nu = k^2\left(\frac{1}{4}\delta_\nu - \sigma_\nu\right)\,, \tag{2.54}$$

$$\textbf{Photons: } \dot{\delta}_\gamma = -\frac{4}{3}\theta_\gamma - \frac{2}{3}\dot{h} \quad ; \quad \dot{\theta}_\gamma = k^2\left(\frac{1}{4}\delta_\gamma - \sigma_\gamma\right) + an_e\sigma_T(\theta_b - \theta_\gamma)\,, \tag{2.55}$$

$$\textbf{Baryons: } \dot{\delta}_b = -\theta_b - \frac{1}{2}\dot{h} \quad ; \quad \dot{\theta}_b = -\frac{\dot{a}}{a}\theta_b + c_s^2k^2\delta_b + \frac{4\overline{\rho}_\gamma}{3\overline{\rho}_b}an_e\sigma_T(\theta_\gamma - \theta_b)\,. \tag{2.56}$$

These equations have a few subtleties that need to be explained:

1. As already mentioned above, the synchronous gauge gives us the freedom to set the frame of reference. Conventionally, we fix the synchronous coordinates to the dark matter rest frame, implying $\theta_c = \dot{\theta}_c = 0$.

2. We have added collision terms from the Thomson interaction to the Euler equations for baryons and photons. These two interaction terms are effective before recombination, and depend on the Thomson cross section σ_T [2] and the proper mean density of electrons n_e. We can see that these terms involve a coupling between the velocity divergence of photons and that of baryons through the factor $(\theta_\gamma - \theta_b)$. To have an explicit derivation of these collision terms from Eq. (1.11), the interested reader can for example refer to chapter 5 of Ref. [9].

[2] The differential cross section is given by

$$\frac{d\sigma}{d\Omega} = 3\sigma_T\frac{1+\cos^2\theta}{16\pi}\,, \tag{2.57}$$

where θ is the scattering angle and $\sigma_T = 0.6652\cdot 10^{-24}\text{cm}^2$.

3. For baryons, in principle $\delta P/\delta\rho = c_s^2 = \omega \ll 1$. However, for sufficiently large k, we cannot neglect the $c_s^2 k^2 \delta_b$ acoustic term for baryons. For dark matter this term is set to zero to the extent that this species does not interact with photons (in the ΛCDM model) and therefore exhibits a perfect non-relativistic behavior (*i.e*, $w_c = 0$).

4. One has neglected σ_c and σ_b since cold dark matter and baryons do not have anisotropic stress perturbation due to their low velocities with respect to the temperature scales considered. As we will see in the following, this is due to the fact that we can neglect the Boltzmann equations of higher order than the Euler equation.

2.2.3 Perturbed Boltzmann's equations

Now, let us perturb the general Boltzmann equation. To do so, we inject the perturbed phase-space distribution function (2.23) into the standard Boltzmann equation (in conformal time):

$$\frac{\partial f}{\partial \tau} + \frac{\partial f}{\partial x^i}\cdot\frac{dx^i}{d\tau} + \frac{\partial f}{\partial q}\cdot\frac{dq}{d\tau} + \frac{\partial f}{\partial \hat{n}^i}\cdot\frac{\hat{n}^i}{d\tau} = C[f]\,. \tag{2.58}$$

As in the homogeneous framework, to solve this equation all we need to do is determine $dx^i/d\tau$, $dq/d\tau$ and $d\hat{n}_i/d\tau$ in the two gauges. Let us emphasize that $\partial f/\partial\hat{n}^i \cdot d\hat{n}^i/d\tau$ is not linear in perturbation and that we can therefore drop it. Finally, with a bit of basic algebra, we can obtain the non-homogeneous and non-isotropic Boltzmann equations in the two gauges:

Newtonian gauge:

$$\frac{\partial\Psi}{\partial\tau} + i\frac{q}{\mathscr{E}}(k\cdot\hat{n})\Psi + \frac{d\ln f_0}{d\ln q}\left[\dot{\phi} - i\frac{\mathscr{E}}{q}(k\cdot\hat{n})\psi\right] = \frac{1}{f_0}C[f]\,, \tag{2.59}$$

Synchronous gauge:

$$\frac{\partial\Psi}{\partial\tau} + i\frac{q}{\mathscr{E}}(k\cdot\hat{n})\Psi + \frac{d\ln f_0}{d\ln q}\left[\dot{\eta} - \frac{\dot{h}+6\dot{\eta}}{2}(k\cdot\hat{n})^2\right] = \frac{1}{f_0}C[f]\,, \tag{2.60}$$

where $\mathscr{E} = aE = \sqrt{p^2 + m^2a^2}$ is the comoving energy.

The case of non-relativistic particles

In the case of non-relativistic particles, we have trivially $q/E \sim q/m \ll 1$. We will therefore keep only the moments of the Boltzmann equation that involve terms in $(q/m)^0$ and $(q/m)^1$, while we will neglect the higher-order terms. By integrating the Boltzmann equation with $\int d^3q/(2\pi)^3$ and $\int d^3q/(2\pi)^3 qq^j/\mathscr{E}$, one obtains the conservation and Euler equations respectively. This can be easily done for dark matter and for baryons. It is easy to see that obtaining the higher moments of the Boltzmann equation would require integrating higher powers of q/E, which implies that these moments are suppressed. This explains why the continuity and Euler equations are sufficient to describe the behaviour of dark matter and baryons.

The case of relativistic particles

The story is different for relativistic particles. In this case, we trivially have $q/E = 1$, implying that the hierarchy of the Boltzmann equations is not truncated by an underlying physical principle. In principle, there are an infinite number of non-zero moments, and we have to resolve the Boltzmann hierarchy completely. However, we have to close the system of equations if we want to solve it, which means we still have to truncate the hierarchy at some point.

In order to simplify the calculations, it is customary to introduce a new quantity, $F(k,\hat{n},\tau)$, which integrates out the q-dependence of the perturbation of the phase space distribution function:

$$F(k,\hat{n},\tau) = \frac{\int q^2 dq\, q\, f_0(q)\, \Psi}{\int q^2 dq\, q\, f_0(q)}\,. \tag{2.61}$$

This quantity allows us to get rid of q, the magnitude of the comoving momentum, but not $\hat{n}$, the direction of the comoving momentum. To do this, we can expand the angular dependence of this quantity thanks to a *Legendre polynomial* decomposition:

$$F(k,\hat{n},\tau) \equiv \sum_{l=0}^{\infty} (-i)^l (2l+1) F_\ell(k,\tau) \mathscr{L}_\ell(\hat{k}\cdot\hat{n})\,, \tag{2.62}$$

where $\mu = \hat{k}\cdot\hat{n}$ is the cosine of the angle given by the direction of a perturbation mode and the momentum direction, and where $\mathscr{L}_\ell(\hat{k}\cdot\hat{n})$'s correspond to the Legendre polynomials. At the end of the day, let us note that the different moments $F_\ell(k,\tau)$ depend neither on q nor on $\hat{n}$, which considerably simplifies the analytical resolution of the Boltzmann equation. Let us now consider two specific cases: massless neutrinos and photons.

Massless neutrinos. For massless neutrinos, we have $P_\nu = 3\rho_\nu$, implying that one obtains from Eqs. (2.30)-(2.32):

$$\delta\rho_\nu = 3\delta P_\nu - \frac{1}{a^4}\int q^2 dq d\Omega\, q f_0(q)\Psi\,, \tag{2.63}$$

$$\delta T^0_{\nu\, i} = \frac{1}{a^4}\int q^2 dq d\Omega\, q\hat{n}_i f_0(q)\Psi\,, \tag{2.64}$$

$$\Sigma^i_{\nu\ j} = \frac{1}{a^4}\int q^2 dq d\Omega\, q\left(\hat{n}_i\hat{n}_j - \frac{1}{3}\delta_{ij}\right) f_0(q)\Psi\,, \tag{2.65}$$

where $\delta T^0_{\nu\, i}$ is the energy flux, and where $\Sigma^i_{\nu\ j} = T^i_{\nu\ j} - P\delta^i_j$ is the anisotropic stress tensor. If we use our definition of $F(k,\hat{n},\tau)$, then one can show that:

$$\delta_\nu = \frac{1}{4\pi}\int d\Omega F(k,\hat{n},\tau) = F_{\nu 0}\,, \tag{2.66}$$

$$\theta_\nu = \frac{3i}{16\pi}\int d\Omega\, k\cdot\hat{n}\, F(k,\hat{n},\tau) = \frac{3}{4}kF_{\nu 1}\,, \tag{2.67}$$

$$\sigma_\nu = -\frac{3}{16\pi}\int d\Omega\left[(k\cdot\hat{n})^2 - \frac{1}{3}\right] F(k,\hat{n},\tau) = \frac{1}{2}F_{\nu 2}\,, \tag{2.68}$$

where $\delta_\nu = \delta\rho_\nu/\overline{\rho}_\nu$, with $\overline{\rho}_\nu = 3\overline{P}_\nu = a^{-4}\int q^2 dq d\Omega\, q f_0(q)$. To obtain these equations, we have used the fact that:

$$F_\ell(k,\tau) = \frac{2\ell+1}{2}\int_{-1}^{1} d\mu\, \mathscr{L}_\ell(\mu) F(k,\hat{n},\tau)\,. \tag{2.69}$$

If we now integrate Eqs. (2.59) and (2.60), by performing the integral

$$\frac{\int q^2\, dq\, q f_0(q) \times [(2.59)\ \text{or}\ (2.60)]}{\int q^2\, dq\, q f_0(q)}\,, \tag{2.70}$$

one can find the perturbed Boltzmann equations in Newtonian and synchronous gauges for massless neutrinos:

Newtonian gauge:

$$\frac{\partial F_\nu}{\partial\tau} + ik\mu F_\nu = 4(\dot{\phi} - ik\mu\psi)\,, \tag{2.71}$$

Synchronous gauge:

$$\frac{\partial F_\nu}{\partial\tau} + ik\mu F_\nu = -\frac{2}{3}\dot{h} - \frac{4}{3}(\dot{h}+6\dot{\eta})\mathscr{L}_2(\mu)\,, \tag{2.72}$$

where $\mathscr{L}_2(\mu) = 1/2(3\mu^2-1)$. It is now possible, by integrating over the various Legendre polynomials and using Eq. (2.69), to determine that:

Synchronous gauge:

$$\dot{\delta}_\nu = -\frac{4}{3}\theta_\nu + 4\dot{\phi}\,, \tag{2.73}$$

$$\dot{\theta}_\nu = k^2\left(\frac{1}{4}\delta_\nu - \sigma_\nu\right) + k^2\psi \tag{2.74}$$

$$\dot{F}_{\nu(\ell>1)} = \frac{k}{2\ell+1}\left[\ell F_{\nu(\ell-1)} - (\ell+1)F_{\nu(\ell+1)}\right]\,, \tag{2.75}$$

Synchronous gauge:

$$\dot{\delta}_\nu = -\frac{4}{3}\theta_\nu - \frac{2}{3}\dot{h}\,, \tag{2.76}$$

$$\dot{\theta}_\nu = k^2\left(\frac{1}{4}\delta_\nu - \sigma_\nu\right)\,, \tag{2.77}$$

$$2\dot{\sigma}_\nu = \frac{8}{15}\theta_\nu - \frac{3}{5}kF_{\nu 3} + \frac{4}{15}\dot{h} + \frac{8}{5}\dot{\eta}\,, \tag{2.78}$$

$$\dot{F}_{\nu(\ell>2)} = \frac{k}{2\ell+1}\left[\ell F_{\nu(\ell-1)} - (\ell+1)F_{\nu(\ell+1)}\right]\,, \tag{2.79}$$

where we have explicitly shown that the equation governing the behaviour of F_ℓ depends on the $(\ell-1)$ and $(\ell+1)$ multipoles. Let us note that to obtain Eqs. (2.75) and (2.79), we used the recursion relation of the Legendre polynomials:

$$(\ell+1)P_{\ell+1}(\mu) = (2\ell+1)\mu P_\ell(\mu) - \ell P_{\ell-1}(\mu)\,. \tag{2.80}$$

We thus obtain an infinite hierarchy of multipoles for massless neutrinos (unlike massive particles). However, we need to close this system if we want to solve it. Therefore, Ref. [41] proposed adopting the following truncation scheme for neutrinos:

$$F_{\nu(\ell_{\max}+1)} \simeq \frac{2\ell_{\max}+1}{k\tau} F_{\nu\ell_{\max}} - F_{\nu(\ell_{\max}-1)}\,. \tag{2.81}$$

This prevents us from setting $F_{\nu(\ell_{\max}+1)} = 0$, which would propagate the error to all the lower multipoles. This truncation scheme then allows us to minimise the propagation of error to the lower multipoles.

Photons. For photons, the method is exactly the same, and all the precedent equations work. The only difference is that it is necessary to add a collision term on the right-hand side of the Boltzmann equations [Eqs. (2.59) and (2.60)] that takes into account the Thomson scattering between photons and baryons before recombination. This collision term takes the following form:

$$\hat{C}[f] = an_e\sigma_T \left[-F_\gamma + F_{\gamma 0} + 4\hat{n}.v_e - \frac{1}{2}(F_{\gamma 2} + G_{\gamma 0} + G_{\gamma 2})\mathscr{L}_2 \right], \tag{2.82}$$

where F_γ is defined by Eq. (2.61), and where v_e is the electron bulk velocity. The last term $\propto \mathscr{L}_2$ quantifies the dependence of the Thomson cross section on the polarisation of the photons, where $G_{\gamma\ell}(k,\hat{n},\tau)$ is the polarization strength, namely the difference between the two linear polarization components of the photons (that we expend in Legendre polynomial decomposition). Let us note that $G_{\gamma\ell}$ is sourced only by the quadrupole of the temperature distribution (see below), namely $F_{\gamma 2}$. With all these tools in hand, it is finally possible to determine the Boltzmann equation for photons, crucial for describing the CMB perturbations:

Newtonian gauge:

$$\dot{\delta}_\gamma = -\frac{4}{3}\theta_\gamma + 4\dot{\phi}\,, \tag{2.83}$$

$$\dot{\theta}_\gamma = k^2\left(\frac{1}{4}\delta_\gamma - \sigma_\gamma\right) + k^2\psi + an_e\sigma_T(\theta_b - \theta_\gamma)\,, \tag{2.84}$$

$$2\dot{\sigma}_\gamma = \frac{8}{15}\theta_\gamma - \frac{3}{5}kF_{\gamma 3} - \frac{9}{5}an_e\sigma_T\sigma_\gamma + \frac{1}{10}an_e\sigma_T(G_{\gamma 0} + G_{\gamma 2})\,, \tag{2.85}$$

$$\dot{F}_{\gamma(\ell>2)} = \frac{k}{2\ell+1}\left[\ell F_{\gamma(\ell-1)} - (\ell+1)F_{\gamma(\ell+1)}\right] - an_e\sigma_T F_{\gamma\ell}\,, \tag{2.86}$$

Synchronous gauge:

$$\dot{\delta}_\gamma = -\frac{4}{3}\theta_\gamma - \frac{2}{3}\dot{h}\,, \tag{2.87}$$

$$\dot{\theta}_\gamma = k^2\left(\frac{1}{4}\delta_\gamma - \sigma_\gamma\right) + an_e\sigma_T(\theta_b - \theta_\gamma)\,, \tag{2.88}$$

$$2\dot{\sigma}_\gamma = \frac{8}{15}\theta_\gamma - \frac{3}{5}kF_{\gamma 3} + \frac{4}{15}\dot{h} + \frac{8}{5}\dot{\eta} - \frac{9}{5}an_e\sigma_T\sigma_\gamma + \frac{1}{10}an_e\sigma_T(G_{\gamma 0} + G_{\gamma 2})\,, \tag{2.89}$$

$$\dot{F}_{\gamma(\ell>2)} = \frac{k}{2\ell+1}\left[\ell F_{\gamma(\ell-1)} - (\ell+1)F_{\gamma(\ell+1)}\right] - an_e\sigma_T F_{\gamma\ell}\,. \tag{2.90}$$

The truncation scheme usually adopted for photons is

$$\dot{F}_{\gamma\ell_{\max}} = kF_{\gamma(\ell_{\max}-1)} - \frac{\ell_{\max}+1}{\tau}F_{\gamma\ell_{\max}} - an_e\sigma_T F_{\gamma\ell_{\max}}\,. \tag{2.91}$$

In the following, we will express the CMB power spectrum as a function of $\Theta(k,\mu,\tau)$, the temperature perturbation. It is therefore convenient to rewrite the previous equations in terms of $\Theta_\ell(k,\tau)$, the Legendre polynomial decompositions of the $\Theta(k,\mu,\tau)$ field [see Eq. (2.62)]. By solving δ_γ, $\delta T^0_{\nu\ i}$ and $\Sigma^i_{\nu\ j}$ [namely Eqs. (2.63)-(2.65)] in terms of $\Theta_\ell(k,\tau)$ instead of $\Psi_\ell(k,\tau)$, one can easily show that:

$$\delta_\gamma = 4\Theta_0 \quad ; \quad \theta_\gamma = 3k\Theta_1 \quad ; \quad \sigma_\gamma = 2\Theta_2\,. \tag{2.92}$$

In addition, we can show that:

$$\begin{aligned} F &= \frac{\int q^2dq\; q\; f_0(q)\;\Psi}{\int q^2dq\; q\; f_0(q)} \\ &= -\frac{\int q^2dq\; q^2\;\frac{\partial f^(0)}{\partial q}\Theta}{\int q^2dq\; q\; f_0(q)} \\ &= 4\Theta\,, \end{aligned} \tag{2.93}$$

where we have used Eq. (2.28) in the second line, and an integration by parts in the third line. We now have a very simple equation connecting $\Theta(k,\mu,\tau)$ and $F(k,\mu,\tau)$, which means that we can re-express Boltzmann's equations in terms of $\Theta(k,\mu,\tau)$. For example, using Eqs. (2.71) and (2.82), the Boltzmann equation for photons in the Newtonian gauge can be written as follows:

$$\dot{\Theta} + (ik\mu + n_e\sigma_T a)\Theta = +\dot{\phi} - ik\mu\,\psi + n_e\sigma_T a\left[\Theta_0 + \mu v_b - \frac{1}{2}\mathscr{L}_2\mu\Pi\right]\,, \tag{2.94}$$

where $\Pi = \Theta_2 + \Theta_{P,2} + \Theta_{P,0}$, with $\Theta_P = G/4$ the polarization field. In this equation, we have used the fact that $\hat{n}.v_e = \mu v_e$, because the baryon velocity is collinear with k (namely the baryon velocity is irrotational).

2.2.4 Partial summary

Thus, the perturbation equations governing the behaviour of the local universe correspond to Eqs. (2.35)-(2.42) on the one hand, which describe the space-time evolution of the metric perturbations with respect to the perturbation parameters of the fluid, and Eqs. (2.49)-(2.56) on the other hand, which govern the behaviour of δ, the energy overdensity field, and θ, the divergence of the velocity fluid, for each constituent. The first set of equations is obtained from the perturbed Einstein equations, while the second set is obtained from the perturbed stress-energy tensor conservation. As already mentioned above, the second set of equations can also be obtained from the first two moments of the Boltzmann equation. These two sets of equations are sufficient for dark matter and baryons, because in the time scales one considers, one respects the condition $T \ll m_{DM}, m_b$, where m_{DM} and m_b corresponds respectively to the mass of a dark matter particle and a baryonic particle. However, for photons and neutrinos, which are relativistic species, one has to complete these two sets of equations with the equations of

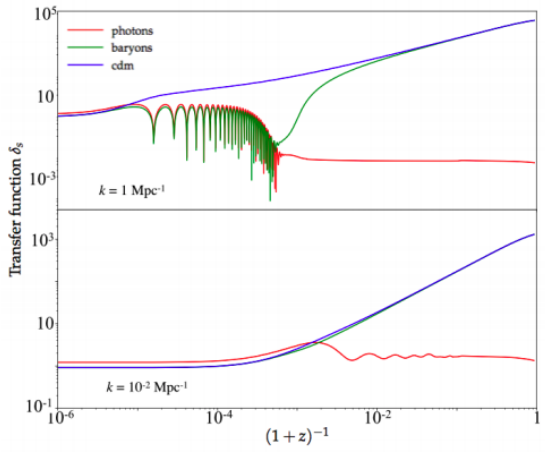

Figure 2.2: Evolution of the energy density perturbations (δ_γ, δ_b and δ_c) with respect to the scale factor ($a/a_0 = (1+z)^{-1}$) for $k = 1$ and 10^{-2} Mpc^{-1}. Taken from Ref. [42].

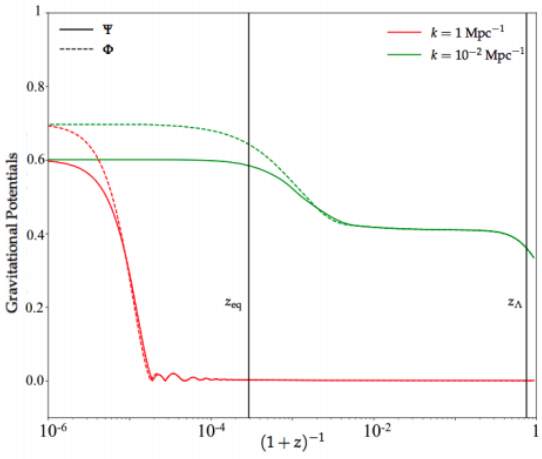

Figure 2.3: Evolution of the metric tensor perturbations (ϕ and ψ) with respect to the scale factor ($a/a_0 = (1+z)^{-1}$) for $k = 1$ and 10^{-2} Mpc^{-1}. Taken from Ref. [42].

the higher-level multipoles $F_l(k,\tau)$, with $l > 1$ (until a certain l which one considers negligible).

All these cosmological perturbation equations can be solved with a Boltzmann code such as `CLASS` [43] or `CAMB` [44]. In Figs. 2.3 and 2.2, one can plot with the `CLASS` code the evolution of the perturbations for $k = 1$ Mpc^{-1}, a mode that entered the horizon during the radiation domination era, and for $k = 10^{-2}$ Mpc^{-1}, a mode that entered the horizon at the beginning of the matter domination era. In Fig. 2.2, we can see that the three perturbation densities are initially equal and constant: this corresponds to the moment when the mode has not yet entered the horizon. Then, one can see that δ_c evolves independently from δ_b and δ_γ, while the latter two evolve together through the Thomson scattering already mentioned earlier. The oscillations correspond precisely to the baryonic acoustic oscillations (BAO), that is, a competition between (i) the thermal pressure between photons and baryons, and (ii) the gravity interaction between baryons and dark matter, resulting in a spatio-temporal oscillation of the perturbations of the fluid composed of photons and baryons. These oscillations stop when the baryons and photons are no longer coupled by the Thomson effect, *i.e.*, from the recombination epoch. After that, δ_γ decreases due to the expansion of the Universe, while under the effect of gravity, δ_c and δ_b increase, allowing the formation of structures. For the mode $k = 10^{-2}$ Mpc^{-1}, the perturbations are initially constant because they are outside the horizon and do not exhibit oscillation afterwards because they enter after the recombination. The behaviour of the perturbations is then identical to the mode $k = 1$ Mpc^{-1}. In Fig. 2.3, we can see that gravitational potentials are strongly suppressed when a mode enters during the radiation era, whereas this is not the case when a mode enters during the matter era. In addition, let us note that the potentials are constant in time during matter era, namely $\phi \sim$ const. These effects will be described in detail in chapter 3. Finally, let us note that the difference between ϕ and ψ at early time is due to the presence of the anisotropic shear of neutrinos, as can be seen from Eq. (2.38). The remainder of this introductory part is devoted to describing in detail the behaviour of these perturbations in the context of the CMB and large-scale structure physics, which implies that we will come back to these figures.

2.3 Initial conditions

As with any physical system, if we wish to characterise its evolution, it is necessary to know (i) the equations which govern the evolution of the system, and (ii) the initial conditions of this system. Having detailed the equations of the perturbed universe, it is now time to look briefly at its initial conditions. The initial conditions refer here to the state of the perturbations well into the radiation domination era, but after nucleosynthesis, insofar as it is from this moment that the five main constituents of our Universe are fully formed (as detailed in chapter 1, Sec. 1.1). It is possible to take this moment as the initial time because only perturbations that have a wavelength greater than the Hubble radius (and which have therefore not yet been affected by sub-horizon physics) are relevant for CMB observations. This section is based mainly on Refs. [9] and [21].

2.3.1 Adiabatic and isocurvature perturbations

First, let us describe the two possible types of perturbation: the adiabatic and isocurvature perturbations.

Adiabatic modes. These modes have two fundamental characteristics: (i) the local state of the energy densities of each of the species at an instant t is the same as that of the background at an instant $t+\delta t(x)$, and (ii) $\delta t(x)$ is the same for all constituents, *i.e.*, at a given point in space, the energy density of each of the species comes from the same background state. It then corresponds to common shift in time of all background quantities in a local area. If we perform a first- order Taylor expansion in $\delta t(x)$, we get

$$\rho_a(x,t) = \overline{\rho}_a(t+\delta t(x)) \simeq \overline{\rho}_a(t) + \delta t(x)\cdot\dot{\overline{\rho}}_a(t)\,. \tag{2.95}$$

This equation, together with condition (ii), implies that

$$\delta t(x) = \frac{\delta\rho_a}{\dot{\overline{\rho}}_a} = \frac{\delta\rho_b}{\dot{\overline{\rho}}_b}\,, \tag{2.96}$$

indicating that this ratio at a given time and a given position in the Universe is the same for all species. If we use the background continuity equation, $\dot{\overline{\rho}}_a = -3H(1+w_a)\overline{\rho}_a$, we can express this ratio as

$$\frac{\delta_a}{(1+w_a)} = \frac{\delta_b}{(1+w_b)}\,. \tag{2.97}$$

From all these properties, we can draw out an important result: at the initial time, the matter overdensities and the radiation overdensities are related by the following relation, wherever we are in the Universe

$$\delta_r(x,t_i) = \frac{4}{3}\delta_m(x,t_i)\,. \tag{2.98}$$

At the end of the day, adiabatic perturbations allow a change in the total energy density $\delta = \sum_a \delta_a$, while the relative ratios in the energy density perturbations remain unperturbed, namely [from Eq. (2.97)]:

$$\delta\left(\frac{\delta_a(x,t_i)}{\delta_b(x,t_i)}\right) = 0\,. \tag{2.99}$$

In addition, we can rewrite the 00 component of Einstein's equations [see Eq. (2.35)], as:

$$\delta = \sum_a \delta_a = -\frac{3}{2}\frac{k^2 a^2}{\dot{a}^2}\phi - \frac{2a}{\dot{a}}\dot{\phi} - 2\phi\,. \tag{2.100}$$

If we neglect the cosmic shear (*i.e.*, $\sigma = 0$), then $\phi = \psi$ by virtue of Eq. (2.38). Furthermore, for super-horizon scales, we have $k \ll \dot{a}/a$ and $\dot{\phi} \simeq 0$ (since $\phi =$ const because no causal physics can modify super-horizon modes), which implies that:

$$\delta = -2\phi = -2\psi\,. \tag{2.101}$$

This equation therefore indicates that adiabatic perturbations, which imply $\delta \neq 0$, modify the local curvature of the Universe. Using Eq. (2.98), we therefore have for adiabatic perturbations in a radiation-dominated universe (*i.e.*, $\delta = \delta_r$)

$$\delta_m(x,t_i) = \frac{3}{4}\delta_r(x,t_i) = -\frac{3}{2}\phi(x,t_i) = -\frac{3}{2}\psi(x,t_i)\,. \tag{2.102}$$

This is the equation that connects density perturbations and metric perturbations at the end of inflation, where the Universe is dominated by radiation, for super-horizon modes. Subsequently, all modes which gradually enter the horizon thereafter possess this property before being affected by sub-horizon physics. For modes entering the horizon during the matter domination era, there is a small subtlety, in that the metric perturbations of the super-horizons modes are slightly suppressed (as we shall shortly see):

$$\phi_{\rm Matter} = \frac{9}{10}\phi_{\rm Radiation}\,. \tag{2.103}$$

Isocurvature modes. Furthermore, given that there are several different species in the Universe, it is in principle possible to obtain perturbations that do not modify the geometry of the Universe: these are the *isocurvature modes*. For these modes, the total energy density is conserved at any point in space, namely $\delta = \sum_a \delta_a = 0$, while the various constituents can be perturbed independently, namely $\delta_a \neq 0$, in such a way that their sum is equal to zero. Therefore, for these perturbations, there are variations in the individual energy densities, but with vanishing curvature perturbation since $\delta = 0$ [see Eq. (2.101)]. The relative ratios in the energy density perturbations is now non-zero, namely $\delta(\delta_a/\delta_b) \neq 0$, and they can be quantify using the *entropy perturbations*:

$$S_{\rm a,b} \equiv \frac{\delta_a(x,t_i)}{(1+w_a)} - \frac{\delta_b(x,t_i)}{(1+w_b)}\,. \tag{2.104}$$

We can define the entropy perturbations with respect to a reference species, that we (conventionally) choose to be the photons. We can therefore define:

$$S_{b,\gamma} = \delta_b - \frac{3}{4}\delta_\gamma\,, \tag{2.105}$$

$$S_{c,\gamma} = \delta_c - \frac{3}{4}\delta_\gamma\,, \tag{2.106}$$

$$S_{\nu,\gamma} = \frac{3}{4}\delta_\nu - \frac{3}{4}\delta_\gamma\,. \tag{2.107}$$

The standard single-field inflation model only predicts adiabatic modes, [3] and this is (remarkably) consistent with CMB data, which do not detect any primordial isocurvature mode. The data are then consistent with $S_{b,\gamma} = S_{c,\gamma} = S_{\nu,\gamma} = 0$. Let us note that pure isocurvature initial perturbations would generate a sine oscillatory behaviour in the CMB fluctuations with a first peak at $\ell \simeq 330$, while pure adiabatic initial perturbations generate a cosine oscillatory behaviour with a first peak at $\ell \simeq 220$ (see bellow). The *Planck* data are compatible with the second scenario, and consequently, in the remainder of this manuscript we only consider adiabatic modes. However, it should be noted that the *Planck* data exclude isocurvature modes as the main contribution of primordial fluctuations, but there is nothing to prevent this type of fluctuations from being subdominant.

2.3.2 Primordial power spectrum

The aim now is to find a appropriate summary statistics that encodes the initial condition of the Universe assuming adiabatic perturbations. To do this, we use the power spectrum and start by giving some properties of this summary statistic.

Power spectrum in cosmology. For a Gaussian field $f(x)$, all the information is contained in the correlation function:

$$\xi(x,x') = \left\langle f(x) f(x') \right\rangle . \tag{2.108}$$

We can then rewrite x' as $x' = x + r$, and Fourier transform the correlation function as

$$\xi(x,r) = \langle f(x) f(x+r) \rangle = \int \frac{d^3k}{(2\pi)^3} \int \frac{d^3k'}{(2\pi)^3} \left\langle \tilde{f}(k) \tilde{f}^*(k') \right\rangle e^{ik\cdot x}\, e^{-ik'\cdot x'}\, e^{-ik'\cdot r} . \tag{2.109}$$

If we now consider a homogeneous universe, then the correlation function depends only on the distance between x and x', and not on the position of x: $\xi(x,r) \to \xi(r)$, where $r = x - x'$. This implies that $\left\langle \tilde{f}(k) \tilde{f}^*(k') \right\rangle \propto \delta_D(k-k')$ in order to eliminate x and x' in the integral. In addition, if we consider an isotropic universe, then the correlation function does not depend on the direction of r: $\xi(r) \to \xi(r)$.

We can now define the power spectrum $P(k)$ of an homogeneous and isotropic field as

$$P(k)\ \delta_D^{(3)}(k-k') = (2\pi)^{-3} \left\langle \tilde{f}(k) \tilde{f}^*(k') \right\rangle , \tag{2.110}$$

where $P(k)$ does not depend on the direction of k because of the isotropy. The power spectrum corresponds to the inverse Fourier transform of the correlation function, since, using Eq. (2.109), we now have:

$$\xi(r) = \int \frac{d^3k}{(2\pi)^3} P(k) e^{-ik\cdot r} \tag{2.111}$$

$$= \int \frac{dk\, k^2}{2\pi^2} P(k) \frac{\sin(kr)}{kr} . \tag{2.112}$$

[3] Indeed, if we only have one perturbed inflaton field, it is not possible to obtain $\delta = 0$ when this field decays. On the other hand, it is possible to obtain isocurvature modes for multi-field inflation models.

We can then obtain the variance of the field simply by setting $r = 0$:

$$\sigma^2 = \xi(r=0) = \int \frac{1}{k}\frac{dk}{2\pi^2} k^3 \, P(k) \tag{2.113}$$

$$= \int d\ln k \; \mathscr{P}_k \,, \tag{2.114}$$

where

$$\mathscr{P}_k = \frac{k^3}{2\pi^2} P(k) \tag{2.115}$$

is the *dimensionless power spectrum*.

Curvature perturbations. The aim now is to find a suitable formulation for the primordial power spectrum, which encodes the initial condition of the Universe. Canonical inflation models only predict Gaussian fields, which implies that we only consider the two-point correlation function (or its Fourier transform) and not the higher-order correlation functions. As already indicated in chapter 1, the initial perturbations come from quantum perturbations in the inflaton field that have been stretched during the inflationary phase. We can then write the inflaton field with an homogeneous part and a perturbation $\delta\phi(x,t)$ as

$$\phi(x,t) = \overline{\phi}(t) + \delta\phi(x,t) \,, \tag{2.116}$$

where $\overline{\phi}(t)$ respects the field equations mentioned in Sec. 1.2.7. If we consider the $\nu = 0$ component of the perturbed conservation equation, we can obtain the perturbed Klein-Gordon equation for $\delta\phi(x,t)$ (in Newtonian gauge):

$$\ddot{\delta\phi} + 2aH\dot{\delta\phi} + k^2\delta\phi = 0 \,. \tag{2.117}$$

It is useful to find a quantity that is conserved on the super-horizon scales for adiabatic fluctuations. When a mode leaves the horizon during inflation, it will later enter the horizon after experiencing a super-horizon life. Finding a quantity that is preserved during this period thus allows us to preserve the information coming directly from inflation. It is therefore possible to define the *curvature perturbation* $\mathscr{R}$, such a conserved quantity (see Ref. [21]), as follows (in Newtonian gauge)

$$\mathscr{R} \equiv \frac{ik_i \delta T^i_{\ 0}(k,\tau) a^2 H(\tau)}{k^2[\rho + P](\tau)} - \psi(k,\tau) \,. \tag{2.118}$$

One can show that this quantity is conserved, namely $\dot{\mathscr{R}} = 0$, at super-horizon scales for adiabatic perturbations (only). During inflation ψ is negligible compared with the first term, while we have

$$\rho + P = \frac{1}{2}\frac{\dot{\phi}^2}{a^2} + V(\phi) + \frac{1}{2}\frac{\dot{\phi}^2}{a^2} - V(\phi) = \frac{\dot{\phi}^2}{a^2} \,. \tag{2.119}$$

In addition, from Eq. (1.77)

$$\delta T^i_{\ 0} = g^{i\nu} \, \partial_\nu \delta\phi \; \partial_0 \phi \tag{2.120}$$

$$= \frac{ik_i \dot{\overline{\phi}} \delta\phi}{a^3} \,, \tag{2.121}$$

implying that

$$\mathscr{R} = -\frac{aH}{\dot{\phi}}\delta\phi\,. \tag{2.122}$$

This equation relates the comoving curvature perturbation to the inflaton perturbations.

In addition, using the continuity equation, we can show that

$$\mathscr{R} = -\frac{5+3w}{3+3w}\psi\,, \tag{2.123}$$

implying that (as already mentioned earlier)

$$\mathscr{R} = -\frac{3}{2}\phi_{\text{Radiation}} = -\frac{5}{3}\phi_{\text{Matter}} \;\;\Rightarrow\;\; \phi_{\text{Matter}} = \frac{9}{10}\phi_{\text{Radiation}}\,. \tag{2.124}$$

Primordial power spectrum. Given that curvature perturbation $\mathscr{R}$ is conserved beyond the horizon and that we know its expression as a function of the inflaton field perturbation $\delta\phi$, it is customary to define the primordial power spectrum as the Fourier transform of the two-point correlation function of the curvature perturbation $\mathscr{R}$. In particular, from Eq (2.122), the variance of the curvature perturbation can be expressed as

$$\left\langle |\,\mathscr{R}_k\,|^2 \right\rangle = \left(\frac{aH}{\dot{\phi}}\right)^2 \left\langle |\,\delta\phi_k\,|^2 \right\rangle, \tag{2.125}$$

where $\left\langle |\,\delta\phi_k\,|^2 \right\rangle$ is the variance of the inflaton field perturbation for a given mode. One can show that (see Ref. [9] or [21])

$$P_{\delta\phi}(k) \simeq \frac{H^2}{2k^3}\,, \tag{2.126}$$

therefore involving

$$P_{\mathscr{R}}(k) = \frac{2\pi G H^2}{\varepsilon k^3} \quad ; \quad \varepsilon = 4\pi G\left(\frac{\dot{\phi}}{aH}\right)^2. \tag{2.127}$$

It is customary to parametrize the dimensionless primordial scalar power spectrum $\mathscr{P}_{\mathscr{R}}(k) = k^3/2\pi^2 \cdot P_{\mathscr{R}}(k)$ as

$$\mathscr{P}_{\mathscr{R}}(k) \equiv A_s\left(\frac{k}{k_*}\right)^{n_s-1}, \tag{2.128}$$

where n_s the *tilt* of the primordial scalar power spectrum, and A_s its *amplitude* at $k = k_*$, where k_* refers to the pivot scale, often set at 0.05 Mpc^{-1}. Note that from Eq. (2.124) we have, during the radiation domination era,

$$\mathscr{P}_{\phi}(k) = \mathscr{P}_{\psi}(k) = \frac{4}{9}\mathscr{P}_{\mathscr{R}}(k)\,. \tag{2.129}$$

The *Planck* data measure $A_s = (2.101 \pm 0.033)\cdot 10^{-9}$ and $n_s = 0.9649 \pm 0.0044$ [11]. These data therefore yield a primordial scalar power spectrum that is almost scale independent, in agreement with the predictions of inflation, which assert an almost constant energy density during the inflationary period. This is one of the greatest successes of the combination between the ΛCDM model and the inflationary paradigm.

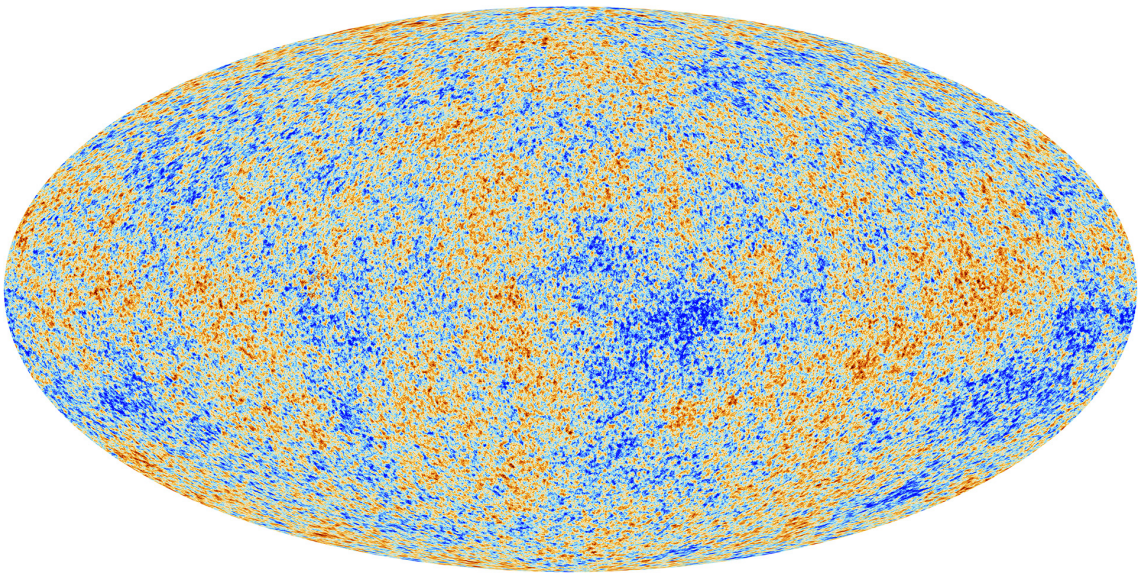

Figure 2.4: Anisotropies (of the order of 10^{-4} to 10^{-5}) of the Cosmic Microwave Background (CMB) observed by *Planck*. Taken from https://www.esa.int/.

2.4 CMB physics

Now that we know the equations of the perturbed universe and have mentioned the initial conditions of the perturbations, it is time to explain the origin of the temperature anisotropies of the CMB observed in Fig. 2.4. This section is based mainly on Ref. [9].

2.4.1 CMB power spectrum

The temperature anisotropies, measured in particular by the *Planck* satellite, are evaluated at time τ_0 (*i.e.*, at the age of the current universe) and at the position x_0^i (*i.e.*, at our position today). In addition, one has seen previously that baryons and photons interact only by the Thomson effect, which implies a conservation of the norm of the photon momentum q during these interactions. It follows that $\Theta(x_0^i, q, \hat{n}, \tau_0) \to \Theta(x_0^i, \hat{n}, \tau_0)$ does not depend on q, and that the anisotropies that one sees in Fig. 2.4 are only generated by a change in $\hat{n}$, the direction of the photon momentum! Then, it is convenient to decompose the temperature anisotropies $\Theta(x_0^i, \hat{n}, \tau_0)$ on a *spherical harmonic basis* (equivalent of the discrete Fourier basis when one has an invariance by rotation) as follows:

$$\Theta(x_0^i, \hat{n}, \tau_0) = \frac{T(\hat{n}) - \overline{T}}{T(\hat{n})} = \sum_{\ell=1}^{+\infty} \sum_{m=-\ell}^{\ell} a_{\ell m}(x_0^i, \tau_0) Y_{\ell m}(\hat{n}) \,, \tag{2.130}$$

where $a_{\ell m}$ are the coefficients associated to the spherical harmonics $Y_{\ell m}$. Here ℓ and m are conjugate to the unit vector $\hat{n}$, and $Y_{\ell m}$ corresponds to the eigenfunctions for an expansion of $\Theta(x_0^i, \hat{n}, \tau_0)$ on the surface of a sphere. The $a_{\ell m}$ coefficients can be obtained from $\Theta(k, \hat{n}, \tau)$ (in Fourier space) thanks to the following relation [which corresponds to the Fourier transform of the inversion of Eq. (2.130)]:

$$a_{\ell m}(x, \tau) = \int \frac{d^3k}{(2\pi)^3} e^{ik.x} \cdot \int d\Omega \, Y^*_{\ell m}(\hat{n}) \Theta(k, \hat{n}, \tau) \,. \tag{2.131}$$

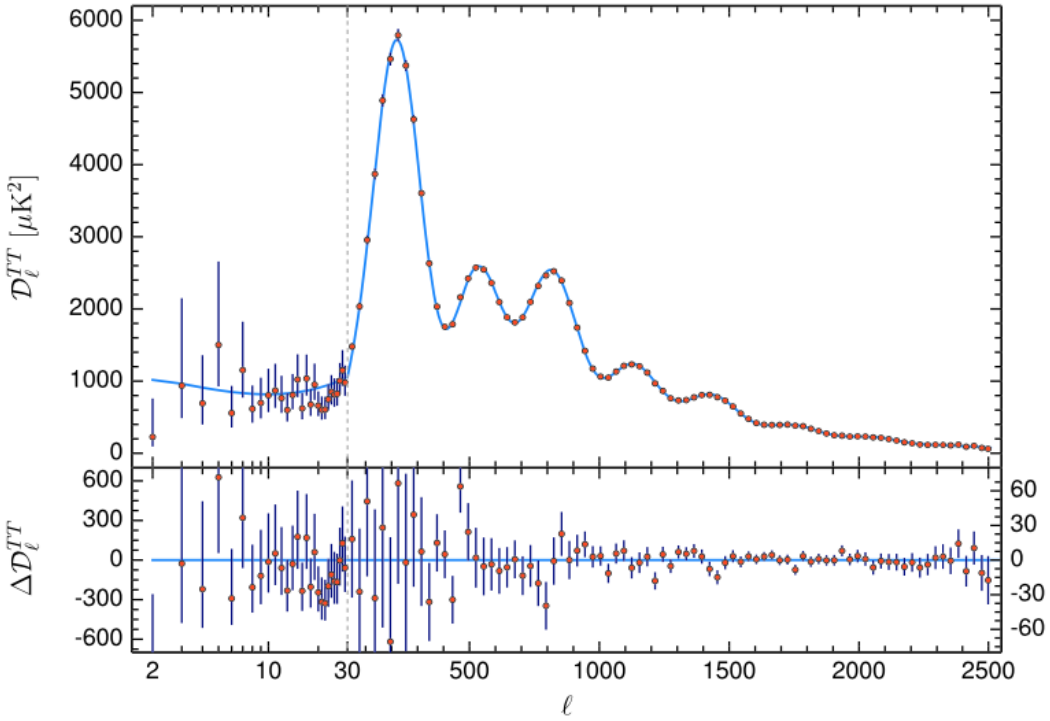

Figure 2.5: CMB temperature power spectrum from the *Planck* data, together with the best-fit of the ΛCDM model. Taken from Ref. [11].

Interestingly, $\langle a_{\ell m}\rangle = 0$, because if we average out the perturbations, we get zero, namely $\langle\Theta(k,\hat{n},\tau)\rangle = 0$. The cosmological information is therefore to be found in the variance of the $a_{\ell m}$ coefficients determined through the two-point correlation function:

$$\langle a_{\ell m} a^*_{\ell' m'}\rangle = \delta_{\ell\ell'}\delta_{mm'}C_\ell\,, \tag{2.132}$$

where C_ℓ is what one calls the *CMB power spectrum* of temperature anisotropies, which corresponds to the real observable of the CMB. It turns out that the CMB perturbations are Gaussian, which implies that all the information is contained in C_ℓ (note, however, that some inflation models predict non-Gaussianities and that it is necessary to study higher-order correlation functions). When ℓ is fixed, each $a_{\ell m}$ has the same variance, which means that the power spectrum can be measured as:

$$C_l^{obs} = \frac{1}{2l+1}\sum_{-l<m<l}|a_{lm}^{obs}|^2\,. \tag{2.133}$$

Given that at ℓ fixed, there are $2\ell+1$ degenerate $a_{\ell m}$, this implies that the smaller ℓ is, the more imprecise the measurement of the power spectrum: this is what we call the *cosmic variance*. This is an uncertainty related to the geometry of the Universe and the fact that we observe fewer large-scale modes than small-scale modes. Fig. 2.5, taken from Ref. [11], represents D_ℓ as a function of ℓ, where D_l^{TT} defined as

$$D_l^{TT} \equiv \frac{\ell(\ell+1)}{2\pi}C_\ell\,, \tag{2.134}$$

where the prefactor allows us to highlight the CMB peaks.

The main objective of what follows will be (i) to relate the power spectrum C_ℓ to $\Theta(x_0^i, \hat{n}, \tau_0)$ and (ii) to find the expression for $\Theta(x_0^i, \hat{n}, \tau_0)$ allowing us to obtain the theoretical expression of C_ℓ. Ultimately, what we want to explain is how to obtain the fit shown in Fig 2.5. To achieve this, it will be necessary, according to Eqs. (2.131) and (2.132), to determine the quantity $\left\langle \Theta(k,\hat{n}) \cdot \Theta^*(k',\hat{n}') \right\rangle$, where now we implicitly assume that we are at $\tau = \tau_0$. This expectation value depends both on the initial conditions of the Universe and the evolution of these initial perturbations up to the last-scattering surface. We have already partially described these two contributions, which prompts us to make the following separation:

$$\Theta(k,\hat{n}) = \mathscr{R}(k) \cdot \mathscr{T}(k,\hat{n}), \tag{2.135}$$

where $\mathscr{R}$ corresponds to the primordial curvature perturbations defined above, while $\mathscr{T}$ is the transfer function allowing us to encode the spatio-temporal evolution of $\Theta(k,\hat{n},\tau)$. Therefore,

$$\left\langle \Theta(k,\hat{n}) \cdot \Theta^*(k',\hat{n}') \right\rangle = \left\langle \mathscr{R}(k) \cdot \mathscr{R}^*(k') \right\rangle \cdot \mathscr{T}(k,\hat{n}) \mathscr{T}^*(k',\hat{n}') \tag{2.136}$$

$$= (2\pi)^3 \delta_D^{(3)}(k-k') P_{\mathscr{R}}(k) \cdot \mathscr{T}(k,\hat{n}) \mathscr{T}^*(k',\hat{n}'). \tag{2.137}$$

Let us note that $\mathscr{T}(k,\hat{n}) = \mathscr{T}(k,\mu)$, with $\mu = \hat{k} \cdot \hat{n}$, because each time k enters the equations it is multiplied by $\hat{n}$ (see the perturbation equations above). By squaring Eq. (2.131), and injecting the last equation, we obtain an equation for the CMB temperature power spectrum which depends on both the transfer function and the primordial power spectrum:

$$C_\ell = \int \frac{d^3k}{(2\pi)^3} P_{\mathscr{R}}(k) \int d\Omega Y^*_{\ell m}(\hat{n}) \mathscr{T}^*(k,\mu) \int d\Omega' Y_{\ell m}(\hat{n}') \mathscr{T}(k,\mu'). \tag{2.138}$$

If we now expand $\mathscr{T}(k,\mu) = \sum_\ell (-i)^\ell (2\ell+1) \mathscr{L}(\mu) \mathscr{T}_\ell(k)$ into a Legendre polynomial decomposition, and inject it into equation (2.138), then we can show that:

$$C_\ell = \frac{2}{\pi} \int_0^{+\infty} dk\, k^2\, P_{\mathscr{R}}(k) \cdot \mid \mathscr{T}_\ell(k) \mid^2, \tag{2.139}$$

where $\mathscr{T}_\ell(k) = \Theta_\ell(k,\tau_0)/\mathscr{R}(k)$. This is a very important result, as this equation allows the CMB temperature power spectrum to be linked with the primordial power spectrum and the transfer function. In other words, if we can obtain a theoretical equation for these two contributions, then we are able to describe the CMB power spectrum in Fig. 2.5. While we have already explained the contribution from the initial conditions [see Eq. (2.128)], we now explain the contribution from the evolution of the temperature perturbations.

2.4.2 The CMB anisotropies

The main objective is here to determine the functional form of $\mathscr{T}_\ell(k)$. To do this, it is necessary to characterise that of $\Theta_\ell(k)$, since the two are directly linked by $\mathscr{R}(k)$. First of all, let us slightly rewrite the inhomogeneous and anisotropic Boltzmann equation for photons in Newtonian gauge (remember that the observables are independent of the gauge considered), corresponding to Eq. (2.94), as:

$$\dot{\Theta} + (ik\mu - \dot{\tau}_{\rm opt})\Theta = \hat{S}, \tag{2.140}$$

where $\hat{S}$ is the source term that generates the $\Theta(k,\mu,\tau)$ perturbations:

$$\hat{S} \equiv \dot{\phi} - ik\mu\psi - \dot{\tau}_{\rm opt}\left[\Theta_0 + \mu v_b - \frac{1}{2}\mathscr{L}_2\mu\Pi\right]. \tag{2.141}$$

In this equation, $\Pi = \Theta_2 + \Theta_{P,2} + \Theta_{P,0}$, with Θ_P the polarization field (see above), and $\tau_{\rm opt}$ is the optical depth, defined as:

$$\tau_{\rm opt} \equiv \int_{\tau}^{\tau_0} d\tau' n_e \sigma_T a, \tag{2.142}$$

$$\Rightarrow\ \dot{\tau}_{\rm opt} = -n_e\sigma_T a, \tag{2.143}$$

where τ_0 is the conformal time of the Universe today. On the other hand, we can rewrite Eq. (2.140) as:

$$e^{-ik\mu\tau+\tau_{\rm opt}}\frac{d}{d\tau}\left[\Theta\, e^{-ik\mu\tau+\tau_{\rm opt}}\right] = \hat{S}, \tag{2.144}$$

allowing us to determine an equation for $\Theta(k,\mu,\tau=\tau_0)$ which depends on the source term $\hat{S}$:

$$\begin{aligned}\Theta(k,\mu,\tau=\tau_0) =& \Theta(k,\mu,\tau=\tau_{\rm init})\, e^{ik\mu(\tau_{\rm init}-\tau_0)}\, {\rm e}^{-\tau_{\rm opt}(\tau_{\rm init})} \\ &+ \int_{\tau_{\rm init}}^{\tau_0} d\tau \hat{S}(k,\mu,\tau)\, e^{ik\mu(\tau-\tau_0)-\tau_{\rm opt}(\tau)},\end{aligned} \tag{2.145}$$

where $\tau_{\rm init} \to 0$ is the initial conformal time, and where τ_0 is the current conformal time. In this equation, we have used the fact that $\tau_{\rm opt}(\tau_0) = 0$ from the definition of this parameter in Eq. (2.142). Interestingly, the first term in Eq. (2.145) tends to zero, since $\tau_{\rm opt}(\tau_{\rm init}) \to \infty$. This implies that Eq. (2.145) simplifies to:

$$\Theta(k,\mu,\tau=\tau_0) = \int_0^{\tau_0} d\tau \hat{S}(k,\mu,\tau)\, e^{ik\mu(\tau-\tau_0)-\tau_{\rm opt}(\tau)}. \tag{2.146}$$

We can now get rid of the μ-dependence and determine the equations for $\Theta_\ell(k,\tau=\tau_0)$ by integrating this equation over the Legendre polynomials. We can show (see Ref. [9]) that the exact solution is

$$\Theta_\ell(k,\tau=\tau_0) = \int_0^{\tau_0} d\tau\, S(k,\tau)\, j_\ell[k(\tau_0-\tau)], \tag{2.147}$$

where j_ℓ are the spherical Bessel function obtained from

$$\int_{-1}^{+1}\frac{d\mu}{2}\mathscr{L}_\ell(\mu)e^{i\mu X} = \frac{1}{(-i)^\ell}j_\ell[X], \tag{2.148}$$

and where we have defined a new source term which does not depend on μ:

$$\begin{aligned}S(k,\tau) \equiv& e^{-\tau_{\rm opt}}\left[\dot{\phi} - \dot{\tau}_{\rm opt}\left(\Theta_0 + \frac{1}{4}\Pi\right)\right] + \frac{d}{d\tau}\left[e^{-\tau_{\rm opt}}\left(\psi - \frac{iv_b\dot{\tau}_{\rm opt}}{k}\right)\right] \\ &- \frac{3}{4k^2}\frac{d^2}{d\tau^2}\left[e^{-\tau_{\rm opt}}\dot{\tau}_{\rm opt}\Pi\right].\end{aligned} \tag{2.149}$$

This is the exact solution for $\Theta_\ell(k,\tau=\tau_0)$. Importantly, we can inject this solution into Eq. (2.139) to obtain the CMB temperature power spectrum from a Boltzmann code. However,

although this equation allows us to obtain the final physical observable of the CMB, it is not very intuitive. In order to have an expression which is a little more physically meaningful, it is useful to simplify it. To do so, it is customary to introduce the visibility function $g(\tau)$, defined as

$$g(\tau) \equiv -\dot{\tau}_{\rm opt} e^{-\tau_{\rm opt}} \quad ; \quad \int_0^{\tau_0} d\tau g(\tau) = 1\,, \tag{2.150}$$

which simply corresponds to the probability of a photon undergoing its last scattering at τ. If we neglect Π, which is very small (compared to ϕ, ψ and Θ_0), then one obtains, in terms of the visibility function,

$$\begin{aligned}\Theta_\ell(k,\tau=\tau_0) \simeq & \int_0^{\tau_0} d\tau g(\tau)\left[\Theta_0(k,\tau)+\psi(k,\tau)\right] j_\ell[k(\tau_0-\tau)] \\ & -\frac{i}{k}\int_0^{\tau_0} d\tau g(\tau) v_b(k,\tau)\frac{d}{d\tau} j_\ell[k(\tau_0-\tau)] \\ & +\int_0^{\tau_0} d\tau e^{-\tau_{\rm opt}}\left[\dot{\psi}(k,\tau)+\dot{\phi}(k,\tau)\right] j_\ell[k(\tau_0-\tau)]\,. \end{aligned} \tag{2.151}$$

The visibility function is very peaked around the last scattering surface conformal time τ_* (since the probability of a photon having its last scattering at τ_* is very high). It follows, together with the fact that $v_b = -i\Theta_1$ at linear order [see Eq. (2.92)], that

$$\begin{aligned}\Theta_\ell(k,\tau=\tau_0) \simeq & \left[\Theta_0(k,\tau_*)+\psi(k,\tau_*)\right] j_\ell[k(\tau_0-\tau_*)] \\ & +3\Theta_1(k,\tau_*)\left(j_{\ell-1}[k(\tau_0-\tau_*)]-(\ell+1)\frac{j_\ell[k(\tau_0-\tau_*)]}{k(\tau_0-\tau_*)}\right) \\ & +\int_0^{\tau_0} d\tau e^{-\tau_{\rm opt}}\left[\dot{\psi}(k,\tau)+\dot{\phi}(k,\tau)\right] j_\ell[k(\tau_0-\tau)]\,. \end{aligned} \tag{2.152}$$

This formula is fairly accurate and agrees with the numerical solution to within about 10% (provided that we take into account a damping term related to the Silk damping in the first term). In order to solve this analytical solution, we need to know the behaviour of Θ_0, Θ_1 and ψ at the time of the last-scattering surface (*i.e.*, at $\tau = \tau_*$). Let us note that the monopole Θ_0 (which encodes the isotropic temperature distribution at a given point in the CMB) is directly linked to the energy density fluctuations δ_γ [$\delta_\gamma = 4\Theta_0$ according to Eq. (2.92)], while the dipole Θ_1 (which encodes, at a given point in the CMB, a particular preferential direction where the temperature is higher) is directly linked to the local velocity of the baryons v_b [$v_b = -i\Theta_1$ according to Eq. (2.92)]. Eq. (2.152) has several terms that are easy to interpret physically. These terms are plotted independently in Fig. 2.6, and are described in the following:

- The first term, known as *Sachs-Wolfe effect*, is the main contribution of the CMB power spectrum and corresponds to the main state of the CMB perturbations at the time of the last-scattering surface. In this term, we need to add the contribution of ψ, which takes into account the *gravitational redshift*, namely the effect of the gravitational potential field $\psi(x,\tau_*)$ on the photon propagation. This term varies as a function of the angular scale l^{-1} through the Bessel functions.

- The second term $\propto v_b$ corresponds to the *Doppler effect term*, which comes from the local velocity of the fluid at the emission time. This term is proportional to the projection of the local baryon peculiar velocity along the photon's line of sight.

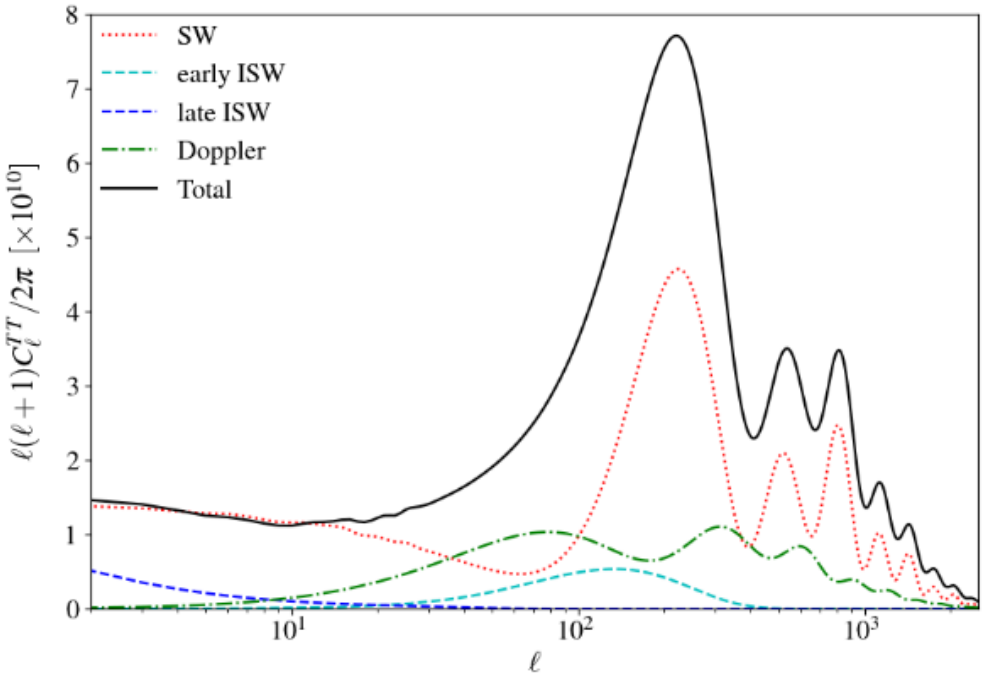

Figure 2.6: Main contributions to the CMB temperature power spectrum. Taken from Ref. [22].

- Finally, the last term, called the *integrated Sachs-Wolf term*, is an integral of the time variation of ψ and ϕ along the CMB photon's trajectory. This term allows us to take into account the gravitational influence of a variation in the metric perturbation along the line of sight. The integrated Sachs-Wolf term can be divided into two contributions (see Fig. 2.5), namely the *early* integrated Sachs-Wolf and the *late* integrated Sachs-Wolf, corresponding to the two main locations where the metric perturbations vary significantly along the line of sight. The first contribution is due to the fact that recombination occurs shortly after matter-radiation equality and that the perturbations of the metric have not had time to stabilise completely after undergoing a decay during the radiation domination period (see next chapter). The second contribution is due to the moment at which the perturbations of the metric began to decay again during the dark energy domination era (see next chapter as well).

2.4.3 A description of the CMB temperature power spectrum

We are now going to give a little more detail about the physics of the CMB and the shape of the power spectrum in Fig. 2.5.

Acoustic oscillations. In order to describe the CMB acoustic oscillations, it is customary to consider the tightly-coupled limit, which corresponds to the limit where the mean free path of a photon is much smaller than the scale λ we consider. This is actually a condition on τ_{opt}, namely $\tau_{\text{opt}} \gg 1$. The main idea behind this condition is that it is necessary to solve only the first two moments of the Boltzmann equation, while all the others are zero. We will therefore consider, in

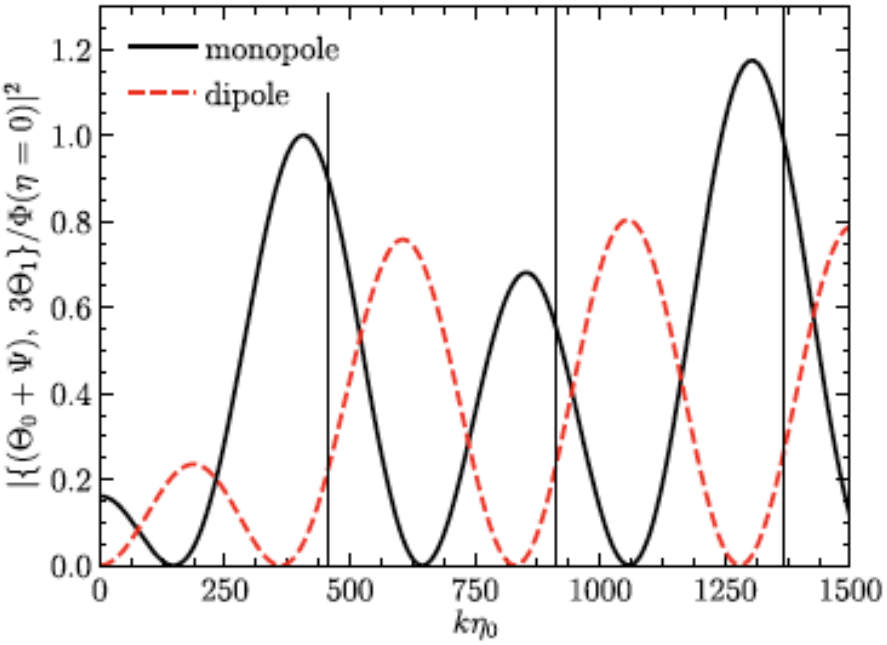

Figure 2.7: The monopole $\Theta_0(k,\tau_*)$ and dipole $\Theta_1(k,\tau_*)$ of the CMB at recombination as a function of the $\ell \sim k\tau_0$ modes. Taken from Ref. [9].

the context of this approximation, the following equations [from Eqs. (2.87), (2.88) and (2.92)]:

$$\dot{\Theta}_0 + k\Theta_1 = \dot{\phi}\,, \tag{2.153}$$

$$\dot{\Theta}_1 - \frac{k}{3}\Theta_0 = \frac{k}{3}\psi + \dot{\tau}_{\rm opt}\left(\Theta_1 - \frac{i}{3}v_b\right). \tag{2.154}$$

We can show with a little bit of algebra (see Ref. [9]) that we obtain the following solution for the $(\Theta_0 - \phi)(k,\tau)$ quantity:

$$\left[\frac{d^2}{d\tau^2} + \frac{\dot{R}}{1+R}\frac{d}{d\tau} + k^2c_s^2\right](\Theta_0-\phi)(k,\tau) = -\frac{k^2}{3}\left[\frac{1}{1+R}\phi + \psi\right](k,\tau)\,, \tag{2.155}$$

where R is the baryon-to-photon energy ratio, and $c_s(\tau)$ is the the sound speed of the perturbations in fluid:

$$R(\tau) \equiv \frac{3\rho_b(\tau)}{4\rho_\gamma(\tau)} \quad \text{and} \quad c_s(\tau) \equiv \sqrt{\frac{1}{3\cdot(1+R(\tau))}}\,. \tag{2.156}$$

Eq. (2.155) is the equation of an harmonic oscillator with a driving force term due to gravity on the right-hand side (so it is a forced harmonic oscillator), and with a drag term in $\dot{\Theta}_0$ in the left-hand side. The drag term creates an asymmetry between the odd and even peaks (see Fig. 2.7) which is controlled by the R parameter. However, the contribution of the drag term $\sim R/[\tau^2(1+R)]$ is subdominant compared to the contribution of the pressure term $\sim k^2c_s^2$ when the modes are within the horizon, namely when $k \gg 1/\tau$. If we ignore this drag term, we

can show that (see Ref. [9])

$$\Theta_0(\boldsymbol{k},\tau)-\phi(\boldsymbol{k},\tau)\simeq[\Theta_0(\boldsymbol{k},\tau=0)-\phi(\boldsymbol{k},\tau=0)]\cos(kr_s) + \frac{k}{\sqrt{3}}\int_0^\tau d\tilde{\tau}[\phi(\boldsymbol{k},\tilde{\tau})-\psi(\boldsymbol{k},\tilde{\tau})]\sin[k(r_s(\tau)-r_s(\tilde{\tau})]\,, \tag{2.157}$$

where we define the sound horizon as

$$r_s\equiv\int_0^\tau d\tilde{\tau}c_s(\tilde{\tau})\,. \tag{2.158}$$

Similarly, we can show that the approximate solution of $\Theta_1(k,\tau)$ respects

$$\Theta_1(\boldsymbol{k},\tau)\simeq\frac{1}{\sqrt{3}}[\Theta_0(\boldsymbol{k},\tau=0)-\phi(\boldsymbol{k},\tau=0)]\sin(kr_s) - \frac{k}{3}\int_0^\tau d\tilde{\tau}[\phi(\boldsymbol{k},\tilde{\tau})-\psi(\boldsymbol{k},\tilde{\tau})]\cos[k(r_s(\tau)-r_s(\tilde{\tau})]\,. \tag{2.159}$$

Importantly, this gives an approximate solution of $\Theta_0(k,\tau_*)$ and $\Theta_0(k,\tau_*)$ in Eq. (2.152). In Fig. 2.7, we represent the two CMB multipoles (using full numerical resolution) at the time of recombination as a function of the ℓ modes. There are a number of important physical points that need to be highlighted here:

- The dipole is totally out of phase with the monopole. This implies that the Sachs-Wolf contribution is out of phase with the Doppler contribution in Eq. (2.152) (see Fig. 2.6). Therefore, this second contribution increases the overall anisotropy level compared to the first contribution alone.

- The main contribution to the $\Theta_0(k,\tau)$ and $\Theta_1(k,\tau)$ solutions is respectively a cosine and sine term multiplied by the initial conditions $\Theta_0(k,\tau=0)+\phi(k,\tau=0)$, that comes directly from inflation.

- The solution of $\Theta_0(k,\tau)$ allows us to estimate the position of the peaks in the CMB power spectrum. In fact, as we can see in Fig. 2.6, the principal contribution of the CMB peak positions comes from the Sachs-Wolf term, which depends directly on $\Theta_0(k,\tau_*)$. From the extrema of $\cos(kr_s)$ in Eq. (2.157), we can determine that:

$$k_{\rm peak}(\tau_*)=\frac{n\pi}{r_s(\tau_*)}\,,\quad \text{with } n=1,2,3,... \tag{2.160}$$

  These peak positions are shown in Fig. 2.7 by solid black lines and are in agreement to within 10% with the numerical resolution.

Finally, it should be noted that $r_s(\tau)$ corresponds to the sound horizon, namely the comoving characteristic distance travelled by a sound wave at τ. At recombination, it is defined as:

$$r_{\rm s}(z_*)=\int_{z_*}^{+\infty}\frac{c_s(z')}{H(z')}dz'\,. \tag{2.161}$$

The sound horizon allows us to define a important quantity of the CMB physics, namely the angular acoustic scale at recombination θ_s, defined as [see Eq (1.69)]:

$$\theta_s=\frac{r_s(z_*)}{D_A(z_*)}, \tag{2.162}$$

where $D_A(z_*) = \int_0^{z_*} dz'/H(z') \propto 1/H_0$ is the comoving angular diameter distance. This quantity corresponds to the apparent angular size of the characteristic distance travelled by a sound wave at τ_* – which is located at a distance r_s from an initial perturbation –, and corresponds to the position of the first CMB peak. The angular acoustic scale is extremely well measured by the *Planck* satellite ($100\theta_s = 1.04110 \pm 0.00031$ [11]) and is perhaps the best measured quantity in modern cosmology.

Diffusion damping. If we are interested in the small scales of the CMB (up to now we have only considered the medium scales), then it is necessary to take into account Θ_2. If we solve the first three moments of the Boltzmann hierarchy, we arrive at an equation of the following type (see Ref. [9]):

$$\Theta_0, \Theta_1 \sim \exp\left\{ ik \int d\tilde{\tau} c_s(\tilde{\tau}) \right\} \exp\left\{ -\frac{k^2}{k_D^2} \right\}, \tag{2.163}$$

where k_D is the damping scale:

$$\frac{1}{k_D^2} \equiv \int_0^{\tau} \frac{d\tilde{\tau}}{6(1+R) n_e \sigma_T a} \left(\frac{R^2}{1+R} + \frac{8}{9} \right). \tag{2.164}$$

So when we solve the Boltzmann hierarchy we bring in a new scale $\lambda_D \sim 1/k_D \sim \sqrt{\tau/n_e \sigma_T a}$ which suppresses the small-scale perturbations. This scale corresponds to the typical (comoving) mean distance travelled by a photon at recombination. Below this scale, the perturbations are washed out by photon diffusion, as we can see in Fig. 2.5. This phenomenon is called *Silk damping*, and occurs at $\ell \gtrsim 800$. Below this scale, perturbations are increasingly suppressed.

Large-scale anisotropies. The last scales we have not yet considered are the very large scales, on the order of the size of today's Hubble horizon. Interestingly, they provide direct access to the initial conditions of the Universe, fixed by inflation, insofar as they have just entered the horizon and have not yet undergone sub-horizon physics. At very large scales, the dominant term in Eq. (2.152) is the Sachs-Wolfe term (see Fig. 2.6):

$$\Theta_\ell(k, \tau = \tau_0) \simeq \left[\Theta_0(k, \tau_*) + \psi(k, \tau_*) \right] j_\ell[k(\tau_0 - \tau_*)]. \tag{2.165}$$

On very large scales, only the first moment of the Boltzmann equation is not negligible, which means that the hierarchy can be reduced to:

$$\dot{\Theta}_0 = \dot{\phi} \Rightarrow \Theta_0(\tau) = \phi(\tau) + C, \tag{2.166}$$

where C is nothing more than an integration constant. If we evaluate this equation at $\tau = 0$, and using the fact that $\Theta_0(\tau = 0) = -\phi(\tau = 0)/2$ [see Eqs. (2.102) and (2.92)] then we get that $C = -3/2\ \phi(\tau = 0) = \mathscr{R}$ [from Eq. (2.124)]. Given that the last-scattering surface at $\tau = \tau_*$ is well inside the matter domination era, we get $\phi(k, \tau_*) = \psi(k, \tau_*) = -3/5\ \mathscr{R}(k)$ [see Eq. (2.124)], giving

$$\Theta_0(k, \tau_*) = \phi(k, \tau_*) + \mathscr{R}(k) = -\frac{2}{3} \phi(k, \tau_*), \tag{2.167}$$

$$\Rightarrow \Theta_0(k, \tau_*) + \psi(k, \tau_*) \simeq \frac{1}{3} \phi(k, \tau_*) \simeq -\frac{\mathscr{R}(k)}{5}. \tag{2.168}$$

This implies that

$$\mathscr{T}_\ell(k) = \frac{\Theta_l(k,\tau_0)}{\mathscr{R}(k)} \simeq -\frac{1}{5}\cdot j_\ell[k(\tau_0-\tau_*)]\,, \tag{2.169}$$

and if we insert this equation into Eq. (2.139), then we obtain

$$C_\ell^{\rm SW} \simeq \frac{2}{25\pi}\int_0^\infty dk\, k^2\, P_{\mathscr{R}}(k)\mid j_\ell[k(\tau_0-\tau_*)]\mid^2\,. \tag{2.170}$$

The primordial power spectrum is given by Eq. (2.128), which can be inserted into the previous equation:

$$C_\ell^{\rm SW} \simeq \frac{4\pi}{25}A_s k_p^{1-n_s}\int_0^\infty dk\, k^{n_s-2}\ \mid j_\ell[k(\tau_0-\tau_*)]\mid^2\,. \tag{2.171}$$

Large scales give direct access to A_s and n_s insofar as the loss of information about the initial conditions is minimised at these scales. For instance, if we consider a scale-independent primordial power spectrum ($n_s = 1$) then one finds that:

$$\ell(\ell+1)\, C_\ell^{\rm SW} \simeq \frac{8}{25}A_s\,, \tag{2.172}$$

providing a precise determination of the A_s value.

2.4.4 Cosmological parameters.

If we want to fit the *Planck* data with the flat-ΛCDM model, we need to use (only) 6 parameters. We list these parameters here and explain their influence on the CMB power spectrum:

- A_s: the variance of primordial curvature perturbations centred around the pivot scale $k_* = 0.05\,{\rm Mpc}^{-1}$. This parameter controls the overall amplitude of the power spectrum. Indeed, from Eq. (2.139), we can easily see that $C_\ell \propto A_s$.

- n_s: the scalar spectral index. If we shift $n_s \to n_s + \beta$, then the power spectrum at small scales is shifted by a factor of $(l/l_*)^\beta$, where $l_* \sim \tau_0 k_*$ is the angular wavenumber associated with the pivot scale. Finally, a change in n_s change the overall slope of the power spectrum (in logarithmic space): the larger n_s is, the steeper the overall shape of the power spectrum.

- $\omega_b = \Omega_b\, h^2$: the dimensionless baryon energy density. This parameter has three main effects on the power spectrum. Firstly, it modifies the position of the peaks. As we saw earlier, the positions of the C_ℓ peaks are given by:

$$l_{\rm peaks} \sim \tau_0\, k_{\rm peaks} \sim \tau_0 \cdot \frac{n\pi}{r_s(\tau_*)}\,. \tag{2.173}$$

  Changing the ω_b parameter will modify the position of the peaks insofar as this parameter will modify the size of the sound horizon through $H(z)$:

$$r_{\rm s}(z_*) = \int_{z_*}^{+\infty}\frac{c_s(z')}{H(z')}dz = \int_{z_*}^{+\infty}\frac{c_s(z')}{100\cdot[{\rm km/s/Mpc}]\sqrt{\sum_a \omega_a(z')}}dz'\,. \tag{2.174}$$

So the larger this parameter, the larger $l_{\rm peaks}$ will be, which means that the CMB temperature power spectrum will shift to the right. Secondly, as we saw earlier, this parameter is included in the drag term in $\dot{\Theta}_0$ of Eq. (2.155). This term sets an asymmetry between even and odd peaks (as we can see in Fig. 2.7), and increasing ω_b will have the effect of increasing this asymmetry. Finally, the last effect is a modification in the damping scale k_D [see Eq. (2.164)]: if we increase ω_b, then we reduce the Silk damping length (and increase k_D), and the CMB temperature power spectrum will be suppressed at larger l.

- $\omega_c = \Omega_c\, h^2$: the dimensionless cold dark matter energy density. Changing this parameter will also result in three main types of change in the power spectrum. Firstly, this parameter has an influence on the position of the peaks, in exactly the same way as the ω_b parameter [see Eq. (2.174)]. Secondly, this parameter will change the driving force term (since the evolution of the gravitational potentials ϕ and ψ are dominated by the cold dark matter) in Eq. (2.155) that governs the behaviour of Θ_0. Finally, increasing the ω_c parameter will bring forward the moment of matter-radiation equality, which has two main influences: (i) it will affect the evolution of perturbations, namely it will increase the matter clustering (which is higher in the matter-dominated universe than in the radiation-dominated universe), and (ii) it will reduce the early integrated Sachs-Wolf effect, because the metric perturbations (or the gravitational potentials) have had more time to stabilise before the last-scattering surface. This last effect is particularly important and leads to a suppression of the power spectrum at $\ell \sim 100$ (around the first peaks).

- H_0: the Hubble parameter today. The main impact of this parameter is to change $D_A(z_*) = \int_0^{z_*} dz'/H(z') \propto 1/H_0$, namely the distance of the last-scattering surface from us. The main effect of this parameter will be to modified the position of the peaks, insofar as $\pi/l_{\rm peaks} \sim \theta_s(\tau_*) \propto H_0 \cdot r_s(\tau_*)$. While ω_b and ω_c influence the position of the CMB peaks through $r_s(\tau_*)$, H_0 also influences the position of the CMB peaks through $D_A(z_*)$. Note that if we replace this parameter with θ_s or Ω_Λ we obtain the same phenomenology.

- $\tau_{\rm reio}$: the reionization optical depth. This parameter allows us to take into account the effect of reionization on CMB radiation: once the Universe has been reionized, CMB photons can once again interact with free electrons from the reionization. This effect changes the CMB perturbation patterns, and it is therefore necessary to take it into account (for both temperature and polarisation). This effect changes the CMB temperature as

$$\overline{T}_\gamma(1+\Theta_\gamma) \;\rightarrow\; \overline{T}_\gamma(1+\Theta_\gamma)e^{-\tau_{\rm reio}} + \overline{T}_\gamma\left(1-e^{-\tau_{\rm reio}}\right) = \overline{T}_\gamma\left(1+\Theta_\gamma e^{-\tau_{\rm reio}}\right), \qquad (2.175)$$

where $e^{-\tau_{\rm reio}}$ is the fraction of photons that are not scattered. Therefore, $\overline{T}_\gamma(1+\Theta_\gamma)e^{-\tau_{\rm reio}}$ corresponds to the temperature of the photons that have not been scattered, while $\overline{T}_\gamma(1-e^{-\tau_{\rm reio}})$ corresponds to the temperature of the photons scattered by the ionised regions. So the greater the τ parameter, the more temperature perturbations are suppressed. This parameter therefore has the same effect as A_s (and is degenerate with the latter) insofar as it controls the overall amplitude of the power spectrum. However, this effect only suppresses modes that are within the horizon at the time of reionization, *i.e.*, at $z \sim 10$. This corresponds to modes $l \gtrsim 50$.

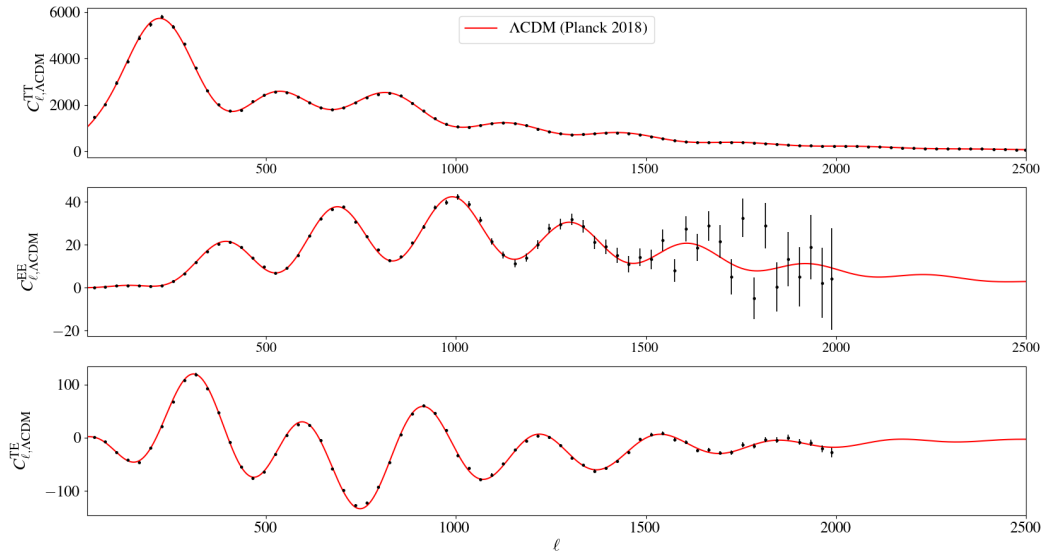

Figure 2.8: Primary CMB power spectra and the ΛCDM best-fit (from Ref. [11]). The data points and associated error bars correspond to those of the *Planck* data.

2.4.5 Other CMB power spectra

In this thesis, we will also use other observables from CMB observations. These include the CMB polarization power spectrum and the lensing power spectrum. We briefly explain these two observables here.

Polarization

It is possible to decompose the polarization of the CMB photons into two modes: the E-modes and the B-modes. It turns out that the B-modes can be sourced solely by the tensor perturbations of the metric, while the E-modes are coupled to the scalar and tensor contributions of the metric perturbations. Tensor perturbations can be generated by primordial gravitational waves predicted by the inflationary paradigm, with a nearly scale-invariant power spectrum, $P_h = A_t (k/k_p)^{n_t}$. A detection of these B-modes would then be a mean of detecting these primordial gravitational waves, and measure the *tensor-to-scalar ratio* $r = A_t/A_s$. This would constitute additional evidence for inflation. Since these modes have never been detected so far, they will not be considered in the remainder of this thesis.

In this thesis, we will use the EE power spectrum, corresponding to the auto-correlation of the E-mode polarization, and the TE power spectrum, which corresponds to the cross-correlation of the E-mode polarization and the temperature perturbations. By analogy with the CMB temperature power spectrum, we define C_ℓ^{EE} and C_ℓ^{TE} as

$$C_\ell^{\mathrm{EE}} = \frac{2}{\pi} \int_0^{+\infty} dk\, k^2\, P_{\mathscr{R}}(k) \cdot \mid \mathscr{T}_\ell^{\mathrm{E}}(k) \mid^2, \tag{2.176}$$

$$C_\ell^{\mathrm{TE}} = \frac{2}{\pi} \int_0^{+\infty} dk\, k^2\, P_{\mathscr{R}}(k) \cdot \mid \mathscr{T}_\ell^{*}(k) \cdot \mathscr{T}_\ell^{\mathrm{E}}(k) \mid, \tag{2.177}$$

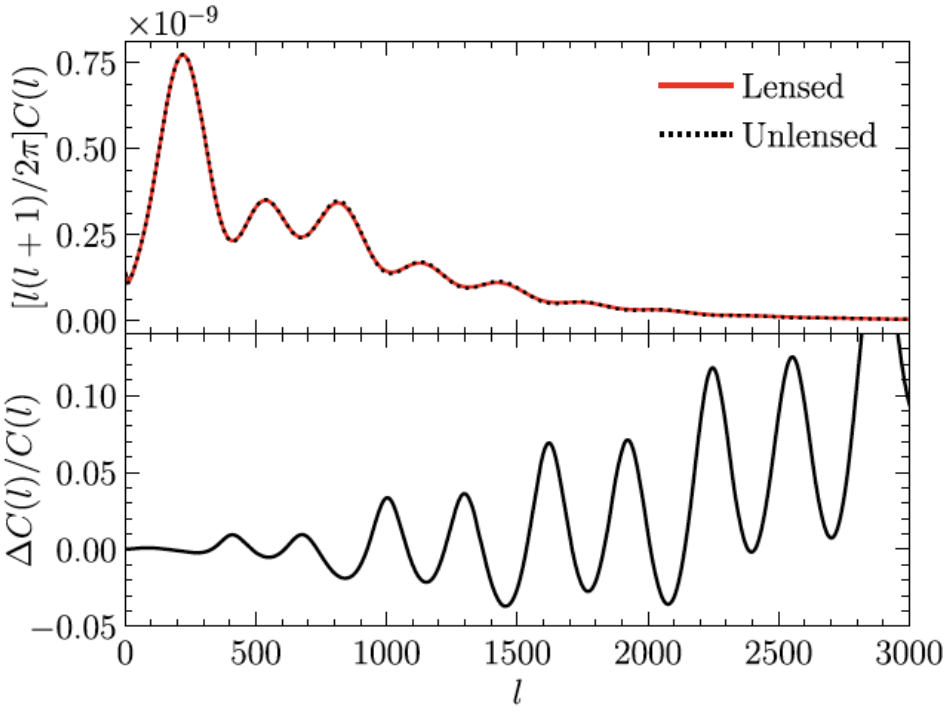

Figure 2.9: CMB temperature power spectrum with and without the lensing correction. Taken from Ref. [9].

where $\mathscr{T}_\ell^{\rm E}(k) = \Theta_{P,\ell}(k,\tau_0)/\mathscr{R}(k)$. In Fig. 2.8, we plot the best-fit of the flat-ΛCDM model obtained from the three primary CMB power spectra measured by *Planck*. In addition, it is possible to obtain an analytical approximation of $\Theta_{P,\ell}(k,\tau_0)$ for a Universe that contains only scalar perturbations [as we did for $\Theta_\ell(k,\tau_0)$]. We can then show (see Ref. [9] for instance) that at small-scales ($k\tau_0 >> 1$) and in the tightly-coupled approximation (where the photon mean free path is much smaller that the scale we consider), we obtain:

$$\Theta_{P,\ell}(k,\tau_0) \simeq \frac{15}{8}\Theta_2(k,\tau_*)\frac{\ell^2 j_\ell(k\tau_0)}{(k\tau_0)^2} \tag{2.178}$$

$$\simeq -\frac{5k}{6\dot{\tau}_{\rm opt}(\tau_*)}\Theta_1(k,\tau_*)\frac{\ell^2 j_\ell(k\tau_0)}{(k\tau_0)^2}\,, \tag{2.179}$$

where we have used the fact that, in the tightly-coupled approximation, $\Theta_2 \simeq -4k\Theta_1/(9\dot{\tau}_{\rm opt})$. A number of important points need to be highlighted here:

- The E-mode polarization is sourced by the quadrupole $\Theta_2(k,\tau_*)$ of the temperature perturbations. Therefore, polarization fluctuations are strongly correlated with the temperature patterns, which implies that we can obtain cosmological information from $C_\ell^{\rm TE}$ (see Fig. 2.8).
- $C_\ell^{\rm EE}$ is smaller than $C_\ell^{\rm TT}$ by a factor of $\sim \Theta_{P,\ell}^2(k,\tau_0)/\Theta_\ell^2(k,\tau_0) \sim (k/\dot{\tau}_{\rm opt}(\tau_*))^2$.
- Since $\Theta_{P,\ell}(k,\tau_0) \propto \Theta_1(k,\tau_*)$, we expect the EE power spectrum to exhibit an oscillatory behaviour out of phase with $\Theta_0(k,\tau_*)$, and by the same token with $C_\ell^{\rm TT}$ (see Fig. 2.8).

Lensing

Photons from the last-scattering surface are affected by several effects as they propagate in the post-CMB universe. We have already mentioned the effect of reionization and the integrated Sachs-Wolf effect. One of the other main effects corresponds to the deflection of photons by large-scale structures localized at $z \lesssim 3$ through the weak lensing effect. The interested reader can refer to Ref. [45] for an in-depth study of this effect.

Fig. 2.9 shows the CMB temperature power spectrum $C_\ell^{\rm TT}$ with and without the lensing correction. We can see that the weak lensing effect has two main impacts: (i) it suppresses the peaks of the CMB temperature power spectrum, and (ii) adds power on very small scales (because the effect of weak lensing is negligible at large scales). The main observable of weak lensing is the two-dimensional deflection field $\hat{d}(\hat{n})$, which is defined as the difference between the direction of the incident photon coming from the CMB, $\hat{n}$, and the direction of the photon after undergoing this effect, $\hat{n}+\hat{d}(\hat{n})$. This effect changes the patterns of the temperature perturbations and it is therefore important to take it into account in order to extract the primary CMB power spectra correctly. We define the lensing potential φ, related to the deflection field according to $\hat{d}(\hat{n}) \equiv \nabla_\perp \varphi$, as

$$\varphi(\hat{n}) = -\int_{\tau_*}^{\tau_0} d\tau \frac{\chi(\tau_*)-\chi(\tau)}{\chi(\tau_*)\chi(\tau)} (\phi+\psi)_{(x=r(\tau)\hat{n},\tau)}\,, \tag{2.180}$$

where χ is the comoving distance defined in chapter 1. Note that weak lensing is sourced by the metric perturbations ϕ and ψ, which in turn depend on the matter density perturbations δ_m via Poisson's equation. It is then possible to extract cosmological information from the harmonic lensing power spectrum $C_\ell^{\varphi\varphi}$, which depends on the matter power spectrum $\sim \langle \delta_m^2 \rangle$.

III

Beyond the linearly perturbed universe and large-scale structure physics

Contents

3.1 The linear matter power spectrum **68**
3.1.1 The (relevant) perturbation equations 69
3.1.2 Solving the perturbation equations 70
3.1.3 The various analytical solutions 72
3.1.4 The transfer function 73
3.1.5 The shape of the matter power spectrum 74
3.1.6 The growth factor 74
3.1.7 Impact of the ΛCDM parameters on the matter power spectrum . . . 75
3.2 Biased tracer statistics in linear perturbation theory **76**
3.2.1 Biased tracers 76
3.2.2 Galaxy density field perturbation 82
3.2.3 The linear galaxy power spectrum 84
3.2.4 Alcock-Paczyński parameters and BAO 87
3.3 Beyond the linear theory **90**
3.3.1 The Vlasov-Poisson system 91
3.3.2 The standard perturbation theory 93
3.3.3 Non-linear matter power spectrum 97
3.4 The effective field theory of large-scale structures **100**
3.4.1 The basics of EFTofLSS 100
3.4.2 The EFTofLSS matter power spectrum 104
3.4.3 The EFTofLSS galaxy power spectrum 109
3.4.4 Additional effects 116

In the previous chapter, we detailed the linear perturbation theory of modern cosmology within the ΛCDM model, which allowed us to describe the physics of the CMB. In particular, we saw how it is possible to fit the full-shape of the CMB power spectra in order to extract cosmological information. The objective is identical in this chapter, but this time for the matter power spectrum. However, compared with CMB physics, there are two major complexities when we want to extract cosmological information from the large-scale structure physics: (i) as we approach small scales, linear perturbation theory breaks down, since the condition $\delta_m \ll 1$ is no longer satisfied, which means that we have to develop a non-linear perturbation theory, (ii) the matter power spectrum cannot be measured directly and we have to consider *biased tracers*, which are massive objects that allow us to track the matter evolution of the Universe. This section has two main objectives. First, we explain the physics associated with the matter and biased tracer power spectra in linear and non-linear frameworks. Secondly, we show how to extract information from the biased tracer power spectrum, both in the linear framework (from the the redshift space distortion information and the BAO imprint on the galaxy power spectrum), and in the non-linear framework (from fitting the biased tracer power spectrum full-shape).

In this chapter, we first describe in Sec. 3.1 the physics associated with the matter power spectrum in the framework of linear perturbation cosmology, while in Sec. 3.2 we explain the biased tracer physics and how it is possible to extract cosmological information at the linear level from the biased tracer power spectrum with the redshift space distortion information and the BAO imprint on the galaxy power spectrum. Then, in Sec. 3.3, we go beyond the linear regime and provide a more accurate description of the matter power spectrum using the standard perturbation theory. Finally, in Sec. 3.4, we deal with the effective field theory of large-scale structures and explain how this theory makes it possible to extract cosmological information from the full-shape of the galaxy power spectrum. This final section introduces the theoretical framework and motivations used throughout this thesis. Let us note that Secs. 3.1, 3.2 and 3.3 are based mainly on Ref. [9].

3.1 The linear matter power spectrum

In this section, we focus on the evolution of perturbations in the matter density field $\delta\rho_m(k,\tau)$, previously defined as

$$\rho_m(k,\tau) = \overline{\rho}_m(\tau) + \delta\rho_m(k,\tau) \tag{3.1}$$

$$= \overline{\rho}_m(\tau)\left[1+\delta_m(k,\tau)\right], \tag{3.2}$$

where $\delta_m = \delta\rho_m/\overline{\rho}_m$. In particular, the material content of the Universe is composed of dark matter, baryons and massive neutrinos, such that

$$\delta_m = \frac{\delta\rho_m}{\overline{\rho}_m} = \frac{\delta\rho_c + \delta\rho_b + \delta\rho_\nu}{\overline{\rho}_c + \overline{\rho}_m + \overline{\rho}_\nu}. \tag{3.3}$$

The main observable we consider in this section is the *(linear) matter power spectrum* $P_m(k)$, *i.e.*, the two-point correlation function of the matter density field perturbation, defined as (see Sec. 2.3.2 of the previous chapter)

$$P_m(k)\delta^3(k-k') = (2\pi)^{-3}\left\langle \delta_m(k)\delta_m(k')\right\rangle. \tag{3.4}$$

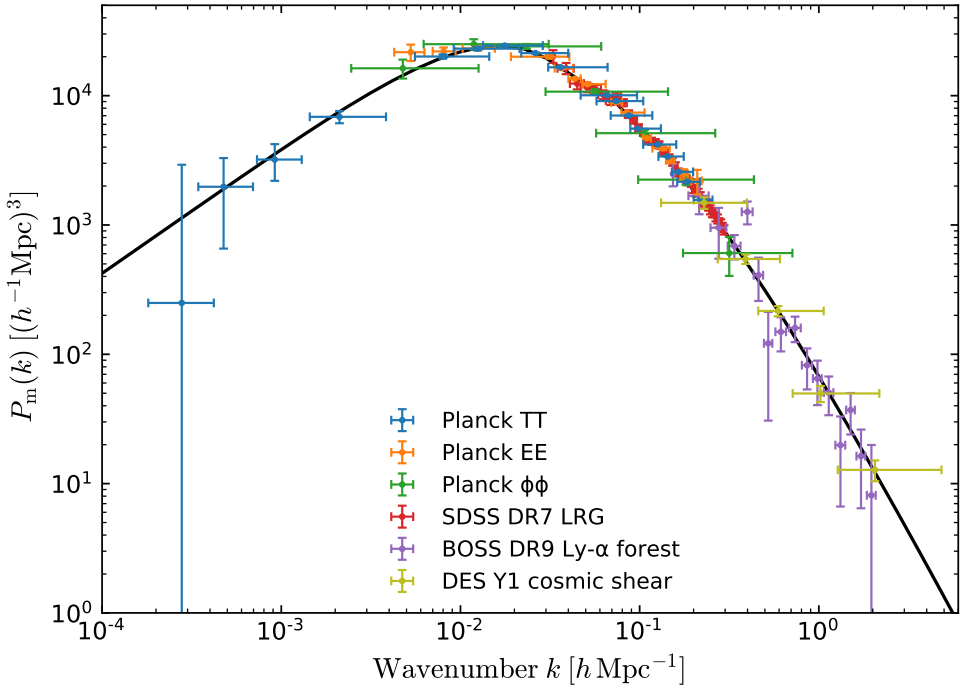

Figure 3.1: Linear matter power spectrum of the ΛCDM model confronted with various probes, namely CMB perturbations (*Planck*), galaxy clustering (SDSS/BOSS) and weak lensing (DES). Credit: ESA and the *Planck* Collaboration.

Fig. 3.1 shows the ΛCDM matter power spectrum, confronted with various experiments, and the aim of this section is to explain its shape and associated physics. This section is based mainly on Ref. [9].

3.1.1 The (relevant) perturbation equations

First of all, we need to specify the set of equations we are going to use to obtain the matter power spectrum. In what follows, we carry out a first fundamental approximation: we consider that matter is composed solely of dark matter, implying that $\delta_m = \delta_c$. In reality, we would need to add the effect of baryons and neutrinos in order to get an accurate description of the matter power spectrum, but here we neglect these effects because they are subdominant. On the other hand, let us note they are taken into account in the numerical resolutions using a Boltzmann code. In addition, we need to consider radiation insofar as it had a decisive impact in the early Universe, namely before matter-radiation equality: the evolution of gravitational potentials at small-scales, *i.e.*, modes that entered the horizon before matter-radiation equality, is dependent on their coupling with radiation in the early universe. Finally, here is the set of equations we are going to consider:

$$\text{Boltzmann radiation}: \quad \begin{cases} \dot{\Theta}_{r,0} + k\Theta r, 1 = \dot{\phi} \\ \dot{\Theta}_{r,1} - \frac{k}{3} = -\frac{k}{3}\phi \end{cases} ; \tag{3.5}$$

$$\text{Boltzmann dark matter}: \quad \begin{cases} \dot{\delta}_c + ikv_c = 3\dot{\phi} \\ \dot{v}_c + \frac{\dot{a}}{a}v_c = -ik\phi \end{cases} ; \tag{3.6}$$

$$\text{Einstein } (00): \quad k^2\phi + 3\frac{\dot{a}}{a}\left(\dot{\phi} + \frac{\dot{a}}{a}\phi\right) = -4\pi G a^2 \delta\rho\,. \tag{3.7}$$

We can make a few brief comments on this set of equations:

- **Boltzmann's equations for radiation**: we consider only Θ_1 and Θ_2, because we saw in the previous chapter that before recombination photons can be characterised by their first two moments (because the others are strongly damped by photon diffusion). The impact of photons on the matter power spectrum is negligible after CMB, which means that we only consider their impact before the last-scattering surface, at $a < a_*$. Therefore, we consider here Eqs. (2.153) and (2.154), namely the first two moments of the Boltzmann hierarchy in the tightly-coupled approximation, where we have dropped the term $\propto \dot{\tau}_{\rm opt}$ which takes into account the interaction with baryons, since we are only interested in dark matter perturbations. Note that we are also considering neutrinos in their relativistic regime here. We neglect the higher order multipoles of neutrinos (namely multipoles higher than $\Theta_{\nu,1}$), so that the first two Boltzmann moments are identical to those of photons. This is why we have used $\Theta_{r,0}$ and $\Theta_{r,1}$ in Eq. (3.5), to avoid confusing them with Θ_0 and Θ_1.

- **Boltzmann's equations for dark matter**: it is simply the equations from Eqs. (2.49). We simply used the fact that, without the neutrino cosmic shear, namely $\sigma_\nu = 0$, then $\phi = \psi$.

- **Time-time component of the Einstein equations**: this corresponds to Eq. (2.35), together with the approximation $\phi = \psi$. Let us note that $\delta\rho \simeq \delta\rho_c + 4\rho_r\Theta_{r,0}$. This equation is used to close the previous two sets of Boltzmann's equations.

3.1.2 Solving the perturbation equations

Unfortunately, there is no analytical solution for δ_c that is valid for all regimes (*i.e.*, on all scales at all times), so it is necessary to solve these equations numerically. In what follows, we nevertheless try to find analytical equations that are valid in some specific regimes, in order to gain physical intuition. The final objective is to explain the shape of the power spectrum shown in Fig. 3.1.

For the CMB, we have isolated two contributions for Θ [the first coming from the initial conditions, and the second from the transfer function, namely $\Theta = \mathscr{R}(k)\cdot\mathscr{T}(k,\hat{n})$]. We can do the same here with the gravitational potential:

$$\phi(k,a) = \psi(k,\tau) = -\frac{3}{5}\mathscr{R}(k)\times T(k)\times\frac{D_+(a)}{a}\,. \tag{3.8}$$

This prescription is made up of three contributions:

- **The primordial curvature perturbation**: as we saw in the previous chapter, it is possible to relate the super-horizon solution of ϕ with the primordial curvature perturbation $\mathscr{R}$ [see Eq. (2.124)] as $\phi = -3/5\cdot\mathscr{R}$. Note that this relationship is valid only for a super-horizon mode that evolves in the matter domination era, and this corresponds to the initial condition of a mode that enters the horizon during this period.

- **The transfer function**: this function $T(k)$ is used to describe the spatial evolution (in k) of the gravitational potential, such that

$$T(k) \equiv \frac{\phi(k, a_{\rm late})}{\phi_{\rm large-scale}(k, a_{\rm late})}\,, \tag{3.9}$$

  where $a_{\rm late}$ means that we consider a period in the matter domination era, and where $\phi_{\rm large-scale}(k, a_{\rm late})$ corresponds to the gravitational potential solution of a mode crossing the horizon in the matter domination era. The transfer function thus corresponds to the solution of the potential for each mode, normalised by the initial solution of that mode in the matter domination period. The transfer function is used to quantify, at fixed time (namely at $a_{\rm late}$), the difference in behaviour between a mode that crossed the horizon during the radiation domination era and a mode that crossed the horizon during the matter domination era.

- **The growth factor**: the growth factor $D_+(a)$ allows to quantify the time dependence of the gravitational potential, such that

$$\frac{D_+(a)}{a} \equiv \frac{\phi(k,a)}{\phi(k, a_{\rm late})}\,. \tag{3.10}$$

  This corresponds to the solution of the potential, for a given scale k, normalised by its value at the time the transfer function is defined, *i.e.*, at $a_{\rm late}$. We will show that for a mode entering the horizon during the matter domination era, the potential is constant in time, implying that $D_+(a) \propto a$ for this period.

We need to bear in mind that we want to solve the solution of δ_c in order to obtain the matter power spectrum. It is then important to find a mathematical relationship between the gravitational potential ϕ and the (dark) matter overdensity δ_c. To do so, we use the Poisson equation [see Eq. (2.43)], valid deep inside the horizon:

$$-\frac{k^2}{a^2}\phi = 4\pi G \delta\rho\,, \tag{3.11}$$

where $\delta\rho = \rho_m \delta_m$ in the matter domination era. Note that the evolution of baryons follows the evolution of dark matter (insofar as they no longer interact with photons after CMB and behave like dark matter), which implies that baryons are taken into account in this equation. By using the fact that $\rho_m = \Omega_m \rho_{\rm crit,0} a^{-3}$ and that $4\pi G \rho_{\rm crit,0} = (3/2) H_0^2$, we obtain

$$\delta_m(k,a) = -\frac{3}{2}\frac{k^2 a}{\Omega_m H_0^2}\phi(k,a) \tag{3.12}$$

$$= \frac{2}{5}\frac{k^2}{\Omega_m H_0^2}\,\mathscr{R}(k)\,T(k)\,D_+(a)\,, \tag{3.13}$$

which is valid only if $a > a_{\rm late}$ and if $k \gg aH$. If we square this equation, we obtain a (relatively accurate) formula for the linear matter power spectrum at late time for $k \gg aH$:

$$P_m(k,a) = \frac{4}{25}\frac{k^4}{\Omega_m^2 H_0^2}\,P_{\mathscr{R}}\,T^2(k)\,D_+^2 \tag{3.14}$$

$$= \frac{8\pi^2}{25}\frac{A_s}{\Omega_m^2}\,\frac{k^{n_s}}{H_0^4 k_*^{n_s-1}}\,D_+^2(a)\,T^2(k)\,, \tag{3.15}$$

where we have used the fact that $P_{\mathscr{R}} = (2\pi^2/k^3)A_s(k/k_*)^{n_s-1}$ [see Eq. (2.128)]. This equation therefore allows us to directly link the matter power spectrum with the gravitational potential. In other words, finding the solution to the gravitational potential, namely if we know $D_+(a)$ and $T(k)$, gives us direct access to the matter power spectrum. The rest of this section focuses on the (approximate) solutions of these two functions.

3.1.3 The various analytical solutions

In order to obtain approximate analytical solutions of the transfer function, it is customary to solve it for two cosmological periods, namely the radiation and matter domination periods, and three regimes, namely the super-horizon regime ($k\tau \ll 1$), the horizon entry ($k\tau \sim 1$) and the sub-horizon regime ($k\tau \gg 1$). Here we give some details of these different regimes, in order to better understand the behaviour of matter throughout the history of the Universe:

- **Super-horizon solution**: if we consider a mode that has always remained in the super-horizon regime, then we have already mentioned in the previous chapter that $\phi_{\rm Matter} = (9/10)\,\phi_{\rm Radiation} = -(3/5)\mathscr{R}$ [see Eq. (2.124)]. This implies that:

$$\frac{\phi(k,\tau)}{\phi(k,0)} = \begin{cases} 1 & \text{if} \quad \tau < \tau_{\rm eq} \\ \frac{9}{10} & \text{if} \quad \tau > \tau_{\rm eq} \end{cases} \tag{3.16}$$

  where ϕ is constant in both radiation and matter domination eras. According to Eq. (2.102), $\delta_m = -(3/2)\phi$ for super-horizon scales (and adiabatic perturbations), implying that δ_m is also constant in time.

- **Modes that crossed the horizon during matter domination era**: for this regime we can neglect the Boltzmann radiation equations, and solve only the Boltzmann dark matter equations. We can show that (see below) $\delta_m \propto a$ when we are in matter domination era. We can then use the Poisson equation (3.11) in order to obtain the time dependence of the gravitational potential:

$$\phi \propto a^2 \cdot \rho_m \cdot \delta_m \propto a^2 \cdot a^{-3} \cdot a \sim \text{constant}\,. \tag{3.17}$$

  Finally, a mode entering the matter domination era will see its gravitational potential remain constant, while δ_m will become $\propto a$. The important result here is that $T(k) \simeq 1$ for modes that have crossed the horizon after matter-radiation equality!

- **Modes that crossed the horizon during radiation domination era**: the last important case concerns the evolution of modes that have crossed the horizon before matter-radiation equality. To do this, we need an equation that describes the evolution of δ_c in the matter domination era for the sub-horizon modes that have corssed the horizon before $\tau_{\rm eq}$. In this regime, photons are negligible, which means that we can use the two Boltzmann dark matter equations, together with the Poisson equation (3.11). It is straightforward to show that combining these equations (see Ref. [9]) leads to the *Meszaros equation*:

$$\frac{d^2\delta_c}{dy^2} + \frac{2+3y}{2y(y+1)}\frac{d\delta_c}{dy} - \frac{3}{2y(y+1)}\delta_c = 0\,, \tag{3.18}$$

  where $y = a/a_{\rm eq} = \rho_m/\rho_r$. This equation governs the evolution of dark matter overdensities for sub-horizon modes when radiation is negligible. We can show that the solution

to the Meszaros equation can be expressed as a linear combination of a growing mode $D_+(a)$ and a decaying mode $D_-(a)$

$$\delta_c(k,a) = C_1 D_+(a) + C_2 D_-(a)\,, \tag{3.19}$$

where

$$D_+(a) = a + \frac{2}{3}a_{\rm eq}\,, \tag{3.20}$$

$$D_-(y) = (y+\frac{2}{3})\ln\frac{\sqrt{1+y}+1}{\sqrt{1+y}} - 1 - 2\sqrt{1+y}\,. \tag{3.21}$$

This expression is valid from $a = a_{\rm eq}$ to $a \lesssim 0.1$, namely after the radiation domination era and before the dark energy domination era, for a mode deep inside the horizon. The important result here is that at late time, when $a \gg a_{\rm eq}$ (and $y \gg 1$), *i.e.*, deep inside matter domination era, $D_+(a) \simeq a$ and $D_-(a) \simeq (a/a_{\rm eq})^{-3/2}$, implying that the $D_-(a)$ solution is subdominant during the matter domination era.

3.1.4 The transfer function

We now give an approximate solution of the transfer function that we can inject into Eq. (3.15) to obtain an estimate of the matter power spectrum. To do this it is necessary (i) to find the δ_c solution in the radiation domination era for a mode which is well within the horizon in this period, and (ii) to equalise it with the solution of Eq. (3.19) in order to find the value of the C_1 coefficient. This term can in fact be determined by performing the following boundary condition: $\delta_c(k, a < a_{\rm eq}) = \delta_c(k, a > a_{\rm eq})$, where $\delta_c(k, a > a_{\rm eq})$ corresponds to Eq. (3.19). It is possible to show (see Ref. [9]) that the solution of δ_c for a mode well within the horizon during radiation domination era can be approximated as

$$\delta_c(k,\tau) \simeq A\mathscr{R}\ln Bk\tau\,, \tag{3.22}$$

where A and B are two integration constants. By equating Eq. (3.19) with Eq. (3.22) as well as their derivatives, we can show that the growing mode behaves like

$$\delta_c(k,a) = \frac{3}{2}A\mathscr{R}(k)\ln\left(\frac{4Be^{-3}a_{\rm eq}}{a_H}\right)D_+(a)\,, \tag{3.23}$$

where a_H is the scale factor when the mode enters the horizon. We have neglected the decaying mode here because, as we showed earlier, it is subdominant at late time. This equation then describes the evolution in the matter domination era of a mode that entered the horizon during the radiation domination era. We can compare this equation with Eq. (3.13), in order to get

$$T(k) = \frac{15}{4}\frac{\Omega_m H_0^2}{k^2 a_{\rm eq}}A\ln\left(\frac{4Be^{-3}a_{\rm eq}}{a_H}\right). \tag{3.24}$$

Finally, we can obtain a final approximation for the transfer function

$$T(k) \simeq \begin{cases} 1 & \text{for} \quad k \ll k_{\rm eq} \\ 12.0\frac{k_{\rm eq}^2}{k^2}\ln\left(0.12\frac{k}{k_{eq}}\right) & \text{for} \quad k \gg k_{\rm eq} \end{cases}, \tag{3.25}$$

where for the regime $k \ll k_{\rm eq}$ we have used the result obtained above [see Eq. (3.17)]. For the regime $k \gg k_{\rm eq}$, we have used the fact that $k_{\rm eq} = \sqrt{2\Omega_m}H_0 a_{\rm eq}^{-1/2}$.

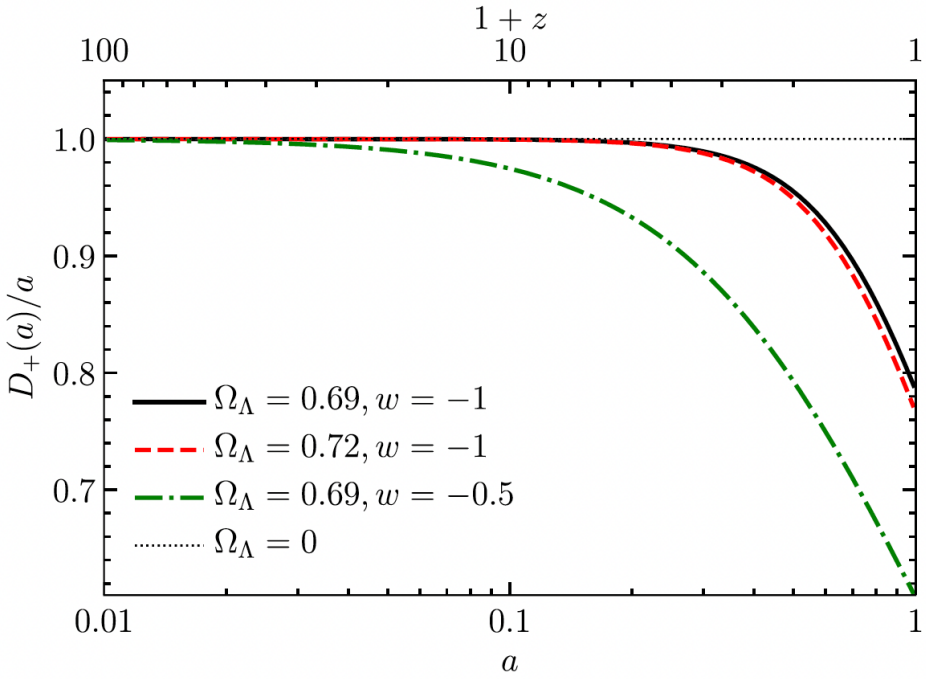

Figure 3.2: Evolution of the growth factor divided by the scale factor $D_+(a)/a$ as a function of the scale factor a. Note that this figure only concerns time-scales that are well into the matter domination era (and dark energy domination era). This figure shows also the evolution of the growth factor as a function of several values of Ω_Λ, the current dark energy density fraction, and w, the dark energy equation of state parameter. Taken from Ref. [9].

3.1.5 The shape of the matter power spectrum

We now have all the tools to understand the shape of the matter power spectrum in Fig. 3.1. If we inject Eq. (3.25) in Eq. (3.15), then we obtain

$$P_m \sim k^{n_s} T^2(k) \sim \begin{cases} k^{n_s} & \text{for} \quad k \ll k_{\rm eq} \\ k^{n_s}\, k^{-4} & \text{for} \quad k \gg k_{\rm eq} \end{cases} . \tag{3.26}$$

Given that $n_s \simeq 1$, we get

$$P_m \sim \begin{cases} k & \text{for} \quad k \ll k_{\rm eq} \\ k^{-3} & \text{for} \quad k \gg k_{\rm eq} \end{cases} . \tag{3.27}$$

This is a fairly precise description of the linear matter power spectrum of Fig. (3.1)!

3.1.6 The growth factor

Having quantified the scale dependence of the matter power spectrum through the transfer function, we now need to determine its time dependence by determining an approximate analytical solution for the growth factor. This is the last ingredient we need to fully characterise the behaviour of the matter power spectrum in Eq. (3.15). To do this, we can con-

sider these two equations

$$\frac{d}{d\tau}\left[a\dot{\delta}_m(k,\tau)\right] = -ak^2\phi(k,\tau)\,, \tag{3.28}$$

$$k^2\phi(k,\tau) = -4\pi G a^2 \rho_m \delta_m(k,\tau)\,, \tag{3.29}$$

where the first equation corresponds to the time derivative (with respect to τ) of the dark matter continuity equation [see Eq. (3.6)] multiplied by a, and combined with the dark matter Euler equation [see Eq. (3.6)], where we neglect $\dot{\phi}$ and v_c. The second equation is simply the Poisson equation for a mode deep inside the horizon. It is then straightforward to get the following differential equation, which is nothing more than the Meszaros equation [see Eq. (3.18)]

$$\frac{d^2\delta_m}{da^2} + \frac{d\ln(a^3H)}{da}\frac{d\delta_m}{da} - \frac{3}{2}\frac{\Omega_m H_0^2}{2a^5H^2}\delta_m = 0\,. \tag{3.30}$$

In the presence of dark energy (which we have not yet considered), the solution is

$$D_+(a) = \frac{5}{2}\frac{\Omega_m H(a)}{H_0}\int_0^a \frac{da'}{(a'H(a')/H_0)^3}\,. \tag{3.31}$$

We plot in Fig. 3.2 the evolution of $D_+(a)/a$ as a function of a from this equation. We can see that we obtain the aforementioned solution $D_+(a) = a$ in the matter domination era. When dark energy starts to dominate, at $1+z \simeq 1.3$ for $\Omega_\Lambda = 0.69$ and $w = -1$, then we have a decay of the growth factor, and therefore of the matter overdensities δ_m.

Finally, let us note that it is customary to define the *growth rate* f, which quantifies the variation of the growing mode $D_+(a)$ as a function of the scale factor a

$$f(a) \equiv \frac{d\ \ln D_+(a)}{d\ \ln a} \simeq [\Omega_m(a)]^{0.55}\,, \tag{3.32}$$

where the last equality comes from a fitting formula which is remarkably accurate within the ΛCDM framework.

3.1.7 Impact of the ΛCDM parameters on the matter power spectrum

To close the section on the linear matter power spectrum, we describe the impact of the 6 ΛCDM parameters on this observable:

- A_s: from Eq. (3.15), where $P_m \propto A_s$, it is clear that this parameter controls the amplitude of the matter power spectrum, as it does for the CMB power spectra.

- n_s: from Eq. (3.26), it is clear that this parameter controls the tilt of the matter power spectrum, as it does for the CMB power spectra.

- ω_c: given that $k_{\rm eq} = \sqrt{2\omega_m}a_{\rm eq}^{-1/2}$, this parameter controls the location of the turn-over (and therefore of the total matter power spectrum). The more we increase this parameter, the more the power spectrum shifts to the right.

- ω_b: this parameter mainly controls the behaviour of the BAO in the matter power spectrum, in particular its amplitude and the position of the peaks (see similar discussion for the CMB temperature power spectrum). We have not yet discussed the BAO in the matter power spectrum, but we shall do so later. In addition, ω_b slightly controls the location of the turn-over in the same way as ω_c.

- H_0: this parameter, like A_s, controls the overall amplitude of the matter power spectrum. We saw earlier that dark energy suppresses the growth factor (see Fig 3.2), and that this suppression is identical for all the scales considered (because the growing mode does not depend on k). Since H_0 is directly linked to Ω_Λ, this parameter also controls the suppression of the power spectrum. The greater this parameter, the more the matter power spectrum is suppressed.

- $\tau_{\rm reio}$: trivially, this parameter has no influence on the matter power spectrum, insofar as it quantifies the effect of reionization on photons.

3.2 Biased tracer statistics in linear perturbation theory

In the previous section of this chapter, we detailed the behaviour of the matter power spectrum, as we did for CMB in chapter 2. We saw that the CMB power spectra can be determined directly from observations, since we can measure the temperature distribution (as well as the polarization) of the photons coming from the last scattering surface. However, matter is mainly composed of invisible dark matter, which makes it impossible to measure the matter power spectrum directly (apart from lensing). Therefore, it is necessary to use *biased tracers* in order to probe the large-scale matter distribution. The biased tracers correspond to observable objects made of matter which track the matter evolution described earlier without behaving in exactly the same way as the whole matter distribution (due to their dynamics, geometry, composition, distribution, *etc.*). In this thesis, we use two types of biased tracers, namely galaxies and quasars. For instance, Fig. 3.3 shows the distribution of galaxies observed by the SDSS Collaboration. In this figure, we can directly determine the two point correlation function of the galaxy distribution, and therefore infer the *galaxy power spectrum*. In other words, galaxy redshift surveys (such as SDSS) measure the 3D positions of each galaxy, and then derive the 3D galaxy power spectrum. The main objective of the rest of this chapter is to relate the biased tracer power spectrum, *i.e.*, what is measured by the large-scale structure Collaborations, with the linear matter power spectrum defined above, in order to extract cosmological information from large-scale structure data. In this section, we carry out this work within the framework of the linear perturbation theory, while in the following sections we perform it in the mildly non-linear regime in order to (significantly) improve the accuracy of the theoretical prediction of the biased tracer power spectrum. In the following we use galaxies as an example of biased tracers, but everything we claim is valid for other biased tracers, such as quasars. This section is based mainly on Ref. [9].

3.2.1 Biased tracers

In order to obtain the galaxy power spectrum, four elements need to be taken into account in order to relate it to the matter power spectrum: (i) the fact that the galaxy clustering is *biased* with respect to the matter clustering, (ii) the *redshift space distortion*, (iii) the *Alcock-Paczyński*

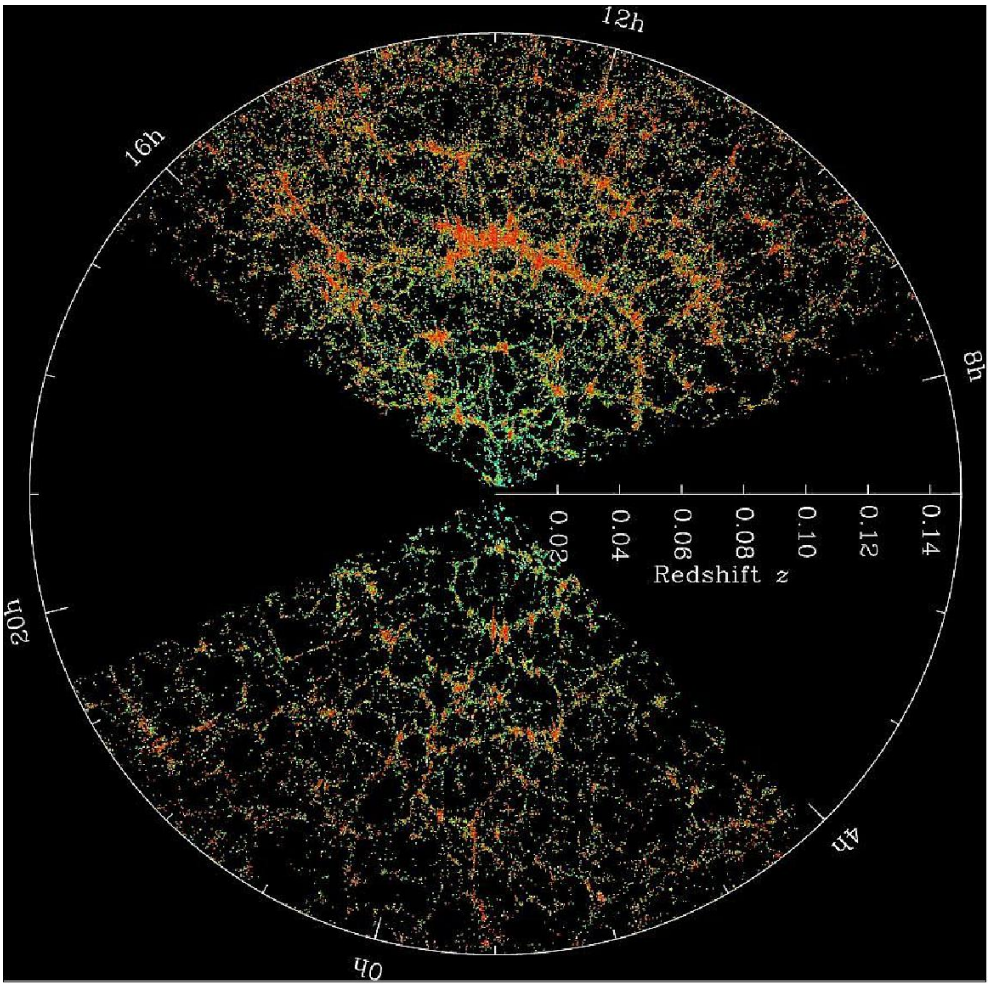

Figure 3.3: Galaxy distribution observed by the SDSS collaboration as a function of angle and redshift. In the remainder of this thesis we will use data directly from these observations. Credit: SDSS Collaboration.

effect, and (iv) the *stochastic behaviour* of galaxy clustering. These four features are specific to the biased tracers used and therefore do not concern the matter distribution. In the following, we describe these four effects in detail.

Bias parameter

In this section (because we are still in the framework of linear perturbation theory), we assume that there is a linear relationship between the galaxy density field perturbations and the matter density field perturbations:

$$\delta_g(x,\tau) = b_1(\tau)\cdot\delta_m(x,\tau)\,, \tag{3.33}$$

where b_1 is the *linear bias parameter*, which encodes the specific behaviour of galaxy clustering with respect to the specific behaviour of matter clustering. In other words, the density perturbation of matter is not the same as the density perturbation of galaxies, and we need to takes it into account thanks to the b_1 parameter. This parameter depends on the object under consideration (type of galaxy, quasars, *etc.*) as well as the redshift.

Redshift space distortion

If the frame of reference of galaxies were the same as the frame of reference of matter, then we would simply have the following relationship: $P_g(k,\tau) = b_1^2 \cdot P_m(k,\tau)$. However, things are not quite so simple, because the measured redshift of galaxies contains a contribution from the expansion of the Universe as well as a Doppler shift due to the particular galaxy velocities. Cosmological redshift is key to measuring distances in the Universe, and it is therefore necessary to subtract the redshift contribution of the particular velocity of the galaxies in order to be able to deduce the distance of the galaxies from us. Furthermore, the galaxy velocity field is correlated with the galaxy density field, which implies that the galaxy velocities are not random and will therefore modify the galaxy statistics. This means that we cannot use the standard reference frame of cosmology (as has always been the case up to now) and that it is necessary to make a change of coordinate that corrects the position of the galaxies by taking into account the Doppler effect.

The observed redshift $z_{\rm obs}$ of the light emitted from a distant object sitting on a cosmological background is given by:

$$1 + z_{\rm obs} = (1+z)(1+\delta z_{\rm pec})\,, \tag{3.34}$$

where $\delta z_{\rm pec} \simeq v(z)\cdot\hat{n}/c$, with c the speed of light, arises from the peculiar velocity v of the object in the direction of the line-of-sight $\hat{n}$ with respect to its local cosmological background (labelled with redshift z). Eq. (3.34) follows straightforwardly from noticing that: (i) the peculiar velocity of the object with respect to the local comoving background induces a redshift $1+\delta z_{\rm pec} \equiv \lambda_c/\lambda_e$, where λ_e is the emitted physical wavelength while λ_c is the wavelength seen in the local comoving frame, (ii) the cosmological expansion induces another redshift $1+z \equiv \lambda_o/\lambda_c$ between the wavelength λ_o that we observe today in our local inertial frame with respect to the wavelength λ_c, (iii) the total redshift is the shift between the physical emitted wavelength λ_e and the observed one λ_o: $1+z_{\rm obs} = \lambda_o/\lambda_e$. For what follows, it is convenient to rewrite Eq. (3.34) as:

$$z_{\rm obs} = z + (1+z)\delta z_{\rm pec}\,. \tag{3.35}$$

Let us recall that the comoving distance $\chi(z)$ from us at redshift $z=0$ to the observed object sitting on a cosmological background at redshift z, is given by:

$$\chi(z) \equiv \int \frac{dt}{a} = \int_a^{a_0} \frac{da'}{a'^2 H(a')} = \int_0^z \frac{dz'}{H(z')}\,. \tag{3.36}$$

The line-of-sight distance associated to the volume distortion from the peculiar velocity v of the object measured in its local comoving frame at redshift z is given by $\delta\chi'(\delta z_{\rm pec}) \simeq \delta z_{\rm pec}/H(z)$, assuming that the change in the background $d(H^{-1}(z))/dz$ around z is small with respect to $\delta z_{\rm pec}$. Seen from our local comoving frame, this distance is rescaled by $a_0/a \equiv (1+z)$, then yielding:

$$\delta\chi \equiv (1+z)\frac{\delta z_{\rm pec}}{H(z)} \simeq (1+z)\frac{v(z)\cdot\hat{n}}{H(z)}\,, \tag{3.37}$$

assuming that the velocity is non-relativistic such that $\delta z_{\rm pec} \simeq v(z)\cdot\hat{n}/c$. Thus, we get that the comoving coordinate in redshift space $s \equiv \chi(z_{\rm obs})$ is related to the comoving coordinate

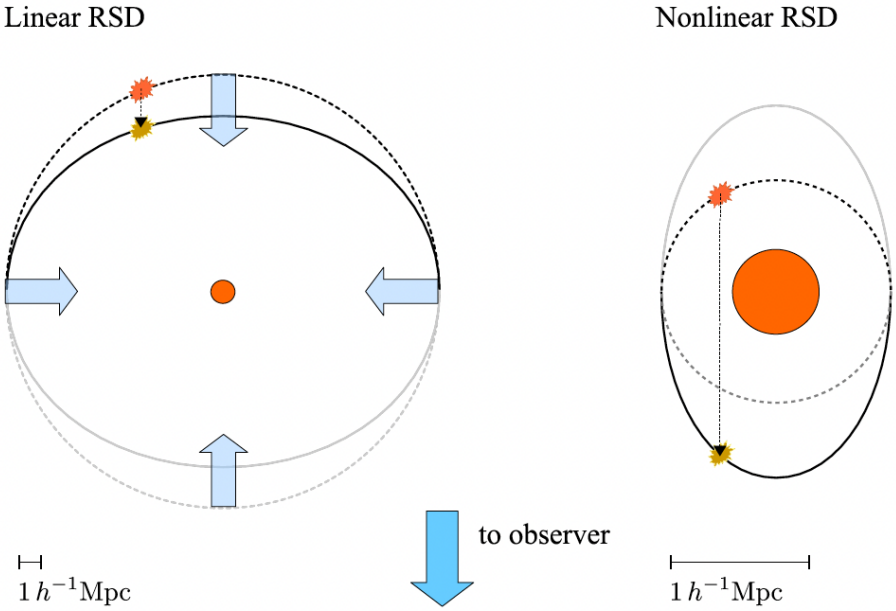

Figure 3.4: The effect of redshift space distortion on galaxy clustering in the linear and non-linear regimes. The observer is located far away below this figure. In the linear regime (considered here), an overdense region in real space (shown in dashed line) is compressed along the line of sight in redshift space (shown in solid line). The arrows indicate the direction of galaxy velocities within the cluster. Taken from Ref. [9].

in real space $x \equiv \chi(z)$ through:

$$s(z) \simeq x(z) + (1+z)\frac{v(z)\cdot\hat{n}}{H(z)}\hat{n} = x + \frac{v\cdot\hat{n}}{aH}\hat{n}\,. \tag{3.38}$$

In this equation, x is the true three-dimensional position of a given galaxy obtained by correcting the measured distance $s(z)$ for the Doppler effect, and $v\cdot\hat{n} = v_{\parallel}$ is the projection of the galaxy velocity along the line of sight.

Before moving on to the other effects, let us describe what *redshift space distortion* (RSD) is, and its impact on galaxy clustering. The problem is the following: let us consider a overdense galaxy region (typically a galaxy cluster), where all the galaxies are attracted towards the center. The galaxies that are closest to an observer located far from the galaxy cluster will therefore move away from the observer, so that the Doppler effect will add an additional redshift to the cosmological one. These galaxies are therefore perceived as being further away from the observer. Similarly, the most distant galaxies move towards the observer, so the contribution of the Doppler effect will be a blueshift. These galaxies are therefore perceived as being closer to the observer. The redshift space distortion effect is illustrated in Fig 3.4, and we can understand intuitively that the number density of galaxies is larger in redshift space than in real space (because the number of galaxies is conserved between the real space volume, in dashed line, and the redshift space volume, in solid line).

We can anticipate a little by mentioning the effect of RSD for non-linear scales. For these scales, the galaxy velocities become large as the typical distance considered decreases (because

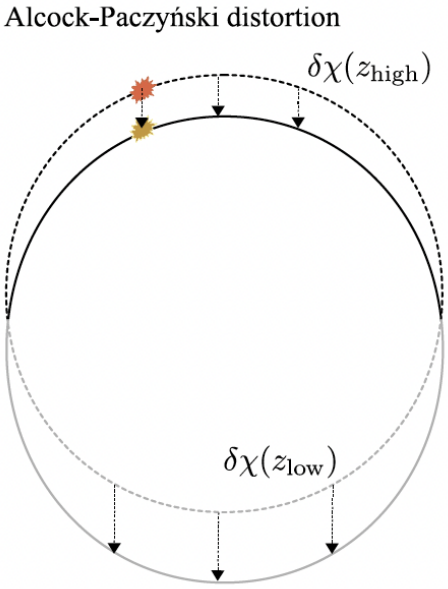

Figure 3.5: The effect of the Alcock-Paczyński distortion on galaxy clustering. Taken from Ref. [9].

we are in the non-linear regime), which implies that the $v_\parallel/aH$ term becomes larger than the typical distance separating two galaxies. In Fig 3.4, we can see that this implies (i) an elongation (and not a compression as in the linear case) of the overdense volume when we go from real space coordinates to redshift space coordinates, and (ii) that the quadrupole moment of the galaxy power spectrum has the opposite sign to the linear case (because the galaxies have swapped places relative to the centre of the overdensity) [9]. This phenomenon therefore leads to an elongation of the galaxy clusters along the line of sight at small scale. In the type of diagram shown in Fig 3.3, the galaxy clusters are then elongated towards the centre. For this reason, this phenomenon is often referred to as *fingers of god* in the literature.

Alcock-Paczyński effect

Eq. (3.38) allows us to connect the redshift space coordinates $s(z)$ with the real space coordinates $x(z)$, where $x(z)$ corresponds to the comoving distance in real space along the line of sight, *i.e.*, $x(z) = \chi(z)\cdot\hat{n}$. It follows that if we want to determine the redshift space coordinates $s(z)$ of a galaxy (in order to match the observations) then we need to know the real space comoving distance of this galaxy *a posteriori*. We therefore need to have an idea of the expansion history of the Universe before we can measure it with the galaxy in question (remember that this measurement is necessarily made in redshift space in order to eliminate the contribution of the Doppler effect).

Consequently, it is necessary to postulate a fiducial cosmology, *i.e.*, a fiducial value of $H_0^{\rm fid}$ and $\Omega_m^{\rm fid}$, which allows us to assume a comoving distance before having measured it:

$$\chi^{\rm fid}(z) = \int_0^z \frac{dz'}{H_0^{\rm fid}\sqrt{\Omega_m^{\rm fid}a^{-3} + (1-\Omega_m^{\rm fid})}}\,. \tag{3.39}$$

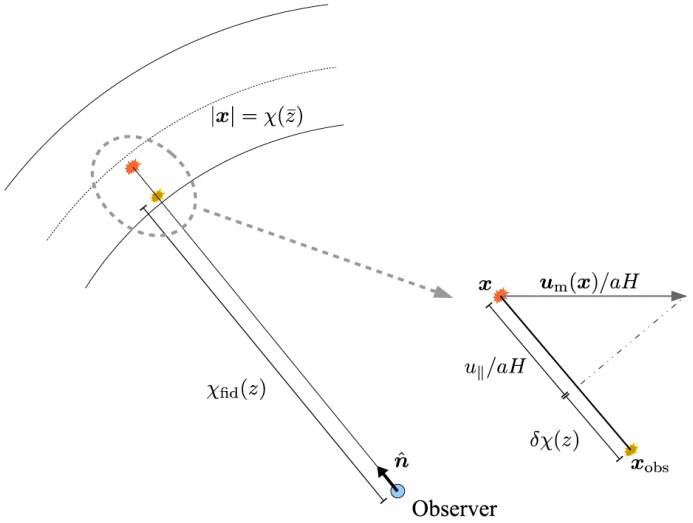

Figure 3.6: Effects of the redshift space distortion (or Doppler) and Alcock-Paczyński contributions on the observed comoving distance. Taken from Ref. [9].

This fiducial comoving distance is related to the actual one in the following way:

$$\chi^{\rm fid}(z) = \chi(z) + \delta\chi(z)\,. \tag{3.40}$$

The impact of the fiducial cosmology on galaxy clustering is known as the *Alcock-Paczyński (AP) effect*. We will see that this effect plays a key role in extracting cosmological information from the BAO imprint on the galaxy power spectrum. In any case, it is therefore necessary to perform the transformation $\boldsymbol{x}(z) \to \boldsymbol{x}(z) + \delta\chi(z)\,\hat{n}$ in the redshift space coordinates $\boldsymbol{s}(z)$:

$$\boldsymbol{s}(z) = \boldsymbol{x}(z) + \frac{v_{\parallel}}{aH}\hat{n} \;\to \boldsymbol{s}(z) = \boldsymbol{x}(z) + \left(\delta\chi(z) + \frac{v_{\parallel}}{aH}\right)\hat{n}\,. \tag{3.41}$$

Fig. 3.5 shows the effect of the Alcock-Paczyński distortion on galaxy clustering. At the lowest order, all the galaxies are displaced from their true position (obtained with the true cosmology) by a quantity $\delta\chi \cdot \hat{n}$, parallel to the line of sight. However, in reality, $\delta\chi$ is not constant with redshift (because the distance-redshift relation evolves independently between the true and fiducial cosmologies), which implies that the furthest galaxies are not moved by the same distance as the nearest galaxies.

Finally, the redshift space distortion and the AP effect are two contributions that must be taken into account in the observed comoving distance in order to reconstruct the actual expansion history of the Universe. Fig 3.6 summarises these two contributions and their additive effect on the observed distance.

Stochastic behaviour of galaxies

Because galaxies are discrete tracers, the two-point correlation function of the galaxy field is not zero if we remove gravity (*i.e.*, if we remove any physical correlation). This leads us to model a noise term P_N in the galaxy power spectrum which takes into account statistic correlations that have no physical origin. In this section, we consider that galaxies are Poisson-sampled

from the underlying (continuous) matter field, which leads to the following modification in the linear galaxy power spectrum:

$$P_g(k,\tau) \to P_g(k,\tau) + P_N \quad ; \quad P_N = \frac{1}{\bar{n}_g}\,, \tag{3.42}$$

where $\bar{n}_g$ is the mean number density of galaxies. The noise term P_N, called *shot noise*, is scale-independent, and this approximation only works (as we shall see later) at very large scales.

3.2.2 Galaxy density field perturbation

Following Refs. [46, 47] (see also Refs. [48, 49]), we can derive the relation between the density field in redshift space (that we denote with a subscript "r") at comoving redshift-space coordinate $\boldsymbol{s}$ with the density and velocity fields in real space at comoving real-space coordinate $\boldsymbol{x}$. As we saw earlier in Fig. 3.4, the number of galaxies is conserved between a volume in real space and a volume in redshift space. Therefore, mass conservation between the infinitesimal volume d^3x in real space and the infinitesimal volume d^3s in redshift space implies:

$$\rho_g(\boldsymbol{x})d^3x = \rho_{g,r}(\boldsymbol{s})d^3s = \rho_{g,r}(\boldsymbol{s})\left|\frac{\partial \boldsymbol{s}}{\partial \boldsymbol{x}}\right| d^3x\,, \tag{3.43}$$

where $\left|\frac{\partial \boldsymbol{s}}{\partial \boldsymbol{x}}\right| \equiv J$ denotes the Jacobian of the transformation. The overdensity field in redshift space thus transforms as:

$$1+\delta_{g,r}(\boldsymbol{s}) = \left|\frac{\partial \boldsymbol{s}}{\partial \boldsymbol{x}}\right|^{-1} (1+\delta_g(\boldsymbol{x}))\,. \tag{3.44}$$

In Fourier space, the overdensity relation between redshift space and real space then reads:

$$\begin{aligned}
\delta_{g,r}(\boldsymbol{k}) &\equiv \int d^3s\, e^{-i\boldsymbol{k}\cdot\boldsymbol{s}}\delta_{g,r}(\boldsymbol{s}) \\
&= \delta_g(\boldsymbol{k}) + \int d^3x\, e^{-i\boldsymbol{k}\cdot\boldsymbol{x}}\left(e^{-i\boldsymbol{k}\cdot\hat{n}\,\frac{\boldsymbol{v}}{aH}\cdot\hat{n}} - 1\right)(1+\delta_g(\boldsymbol{x})) \\
&= b_1\delta_m(\boldsymbol{k}) + \int d^3x\, e^{-i\boldsymbol{k}\cdot\boldsymbol{x}}\left(e^{-i\boldsymbol{k}\cdot\hat{n}\,\frac{\boldsymbol{v}}{aH}\cdot\hat{n}} - 1\right)(1+b_1\delta_m(\boldsymbol{x}))\,.
\end{aligned} \tag{3.45}$$

Note that in this equation we have not introduced $\delta\chi$ from Eq. (3.41), which takes into account the AP effect, because we only want to consider the correction due to the peculiar velocity. We will look later at the effect of $\delta\chi$ on the galaxy power spectrum. Eq. (3.45) connects $\delta_{g,r}(\boldsymbol{k})$, the galaxy overdensities in redshift space and in Fourier space, with δ_m and v, the matter overdensity field and the galaxy velocity field in real space. As we are working in the linear regime, it is possible to simplify this equation by noting that $v_\parallel/aH \ll 1$: [1]

$$\delta_{g,r}(\boldsymbol{k}) \simeq b_1\delta_m(\boldsymbol{k}) + \int d^3x\, e^{-i\boldsymbol{k}\cdot\boldsymbol{x}}\left(-i\boldsymbol{k}\cdot\hat{n}\,\frac{\boldsymbol{v}(x)\cdot\hat{n}}{aH}\right)\,. \tag{3.46}$$

Alternatively, we can derive the same relation from the Lagrangian description that relates both the density in real space and the density in redshift space to the density at some initial

[1] This means that the galaxy velocities are significantly lower than the expansion velocity of the Universe. We saw earlier that when this condition is not met, we have to consider the non-linear regime.

time. In real space, the position of the object in Lagrangian coordinate x, at time t, is given by its initial position q and the displacement $m(q,t)$ from its initial position:

$$x(q,t) = q + m(q,t)\,, \tag{3.47}$$

where x are the Eulerian coordinates used above. For dark matter, the overdensity field is given by:

$$1 + \delta_m(x,t) = \int d^3q\, \delta_D(x - q - m(q,t))\,. \tag{3.48}$$

For biased tracers, this becomes:

$$1 + \delta_g(x,t) = \int d^3q\, F_L\, \delta_D(x - q - m(q,t))\,, \tag{3.49}$$

where $F_L \equiv F_L\left[\delta(q,t), \partial^2\delta(q,t), \dots\right]$ is the Lagrangian halo biasing function. Fourier transforming the above, the real-space galaxy overdensity reads:

$$(2\pi)^3\delta_D(k) + \delta_g(k,t) = \int d^3q\, F_L\, e^{-ik\cdot(q+m(q,t))}\,. \tag{3.50}$$

In redshift space, the position in Lagrangian coordinates is given by:

$$s(q,t) = q + m(q,t) + \left(\frac{\dot{m}(q,t)}{aH}\cdot\hat{n}\right)\hat{n}\,. \tag{3.51}$$

Eq. (3.50) thus becomes:

$$\begin{aligned}(2\pi)^3\delta_D(k) + \delta_{g,r}(k,t) &= \int d^3q\, F_L\, e^{-ik\cdot\left(q+m(q,t)+\left(\frac{\dot{m}(q,t)}{aH}\cdot\hat{n}\right)\hat{n}\right)} \\ &= \int d^3x\,(1+\delta_g(x))e^{-ik\cdot x}e^{-ik\cdot\hat{n}\,\frac{v}{aH}\cdot\hat{n}}\,,\end{aligned} \tag{3.52}$$

where we have used Eq. (3.49) to go to the second line. We thus find the same relation between the overdensities in redshift space and real space:

$$\delta_{g,r}(k) = \delta_g(k) + \int d^3x\, e^{-ik\cdot x}\left(e^{-ik\cdot\hat{n}\,\frac{v}{aH}\cdot\hat{n}} - 1\right)(1+\delta_g(x))\,. \tag{3.53}$$

In order to determine the galaxy power spectrum in redshift space as a function of the matter power spectrum in real space, it is necessary to find a relationship that relates v with δ_m in order to inject it into the equation Eq. (3.46), which we rewrite here for the sake of clarity:

$$\delta_{g,r}(k) \simeq b_1\delta_m(k) + \int d^3x\, e^{-ik\cdot x}\left(-ik\cdot\hat{n}\,\frac{v(x)\cdot\hat{n}}{aH}\right)\,. \tag{3.54}$$

To do so, we can notice that at late time (*i.e.*, $z \lesssim 10$), baryons cool down and then have the same dynamics as cold dark matter, which implies that $\delta_c = \delta_b$ and $v_c = v_b$. We can then use the perturbed continuity equation:

$$\dot{\delta}_m + ik\cdot v_m = 3\dot{\phi}\,, \tag{3.55}$$

where $\delta_m = \delta_c + \delta_b$ and $v_m = v_c + v_b$. For sub-horizon modes, one can neglect the right-hand side (since the potential is constant in matter domination era, as already mentioned in Sec. 3.1.3). Using the fact that $\dot{\delta}_m = (\dot{D}_+/D_+) \cdot \delta_m$ [since, from Eq. (3.19), $\delta_c(k,a) = C_1(k) \cdot D_+(a)$], one can express the matter velocity in terms of the matter density perturbation as

$$v_m(k,\tau) = \frac{ik}{k^2}\frac{\dot{D}_+}{D_+}\delta_m(k,\tau) = aHf\frac{ik}{k^2}\delta_m(k,\tau)\,, \tag{3.56}$$

where $f = d\ln D_+/d\ln a$ is the linear growth rate [see Eq. (3.32)]. This relationship is only valid within the framework of linear perturbation theory, *i.e.*, on a very large scale.

However, if we assume that the tracer velocity field is unbiased, [2] then the peculiar velocity of galaxies v in Eq. (3.54) is nothing more than the matter velocity v_m at the location of the galaxies in question, implying that $v = v_m$. If we now inject Eq. (3.56) into Eq. (3.54), we obtain

$$\begin{aligned}\delta_{g,r}(\boldsymbol{k}) &\simeq b_1\delta_m(\boldsymbol{k}) + \int d^3x e^{-i\boldsymbol{k}\cdot\boldsymbol{x}}\left(-i\boldsymbol{k}\cdot\hat{n}\,\tfrac{1}{aH}\right)\int\frac{d^3k'}{(2\pi)^3}e^{i\boldsymbol{k}'\boldsymbol{x}}aHf\frac{ik'}{k'^2}\delta_m(k')\cdot\hat{n}\\ &= b_1\delta_m(\boldsymbol{k}) + f\int\frac{d^3k'}{(2\pi)^3}\,\delta_m(k')\left(\boldsymbol{k}\cdot\hat{n}\cdot\frac{\boldsymbol{k}'}{k'^2}\cdot\hat{n}\right)\int d^3x e^{i(\boldsymbol{k}'-\boldsymbol{k})\cdot\boldsymbol{x}}\,,\end{aligned} \tag{3.57}$$

where the last integral leads to $(2\pi)^3\,\delta_D^{(3)}(\boldsymbol{k}'-\boldsymbol{k})$. As a result, we end up with

$$\delta_{g,r}(\boldsymbol{k}) = \left[b_1 + f\mu^2\right]\,\delta_m(\boldsymbol{k})\,, \tag{3.58}$$

where $\mu = \hat{n}\cdot\hat{k}$ is the cosine of the angle between the wavevector $\boldsymbol{k}$ and line of sight $\hat{n}$. Note that to obtain this result, we have implicitly carried out the *distant-observer* approximation, namely the approximation that the observer sees all the galaxies along the direction $\hat{n}$. This direction often corresponds to the direction of the centre of the sky area probed by the large-scale structure survey in question.

3.2.3 The linear galaxy power spectrum

It is now trivial to obtain the linear galaxy power spectrum in redshift-space [by squaring Eq. (3.58)], found by Nicholas Kaiser in 1987 [50], as a function of the linear matter power spectrum

$$P_{g,r}(\boldsymbol{k},\mu,a) = \left[b_1 + f\mu^2\right]^2 P_m(\boldsymbol{k},a) + \frac{1}{\bar{n}_g}\,, \tag{3.59}$$

where we (artificially) add the shot noise contribution (see Sec. 3.2.1). As previously stated, galaxy overdensities are stronger in redshift space than in real space (where $P_g = b_1^2 P_m$), since $f\mu^2 \geq 0$. Note that this does not apply to a perturbation perpendicular to the line of sight (since $\mu = 0$ in this case). In addition, it should be remembered that Eq. (3.59) only takes into account the effect of redshift space distortion on the galaxy power spectrum and not the AP

[2] We will come back to this assumption later, as it follows directly from the equivalence principle of general relativity.

effect (which we deal with below).

However, it is not possible to accurately fit the measured galaxy power spectrum with this formula (see Fig. 3.16). In fact, this formula is only valid on very large scales, and therefore cannot be used to fit the full shape galaxy power spectrum, but only very small modes. To overcome this issue, we can extract information from the galaxy power spectrum using the $f\sigma_8$ information, instead of fitting the galaxy power spectrum full-shape. The σ_8 parameter corresponds to the root mean square of matter fluctuations on an $8h^{-1}$Mpc scale, defined as

$$\sigma_8^2 = \int \frac{k^3}{2\pi^2} P_m(k) W_8^2(k) d\ln k \,, \tag{3.60}$$

where $P_m(k)$ is the linear matter power spectrum, and $W_8(k)$ is a window function describing a sphere (in Fourier space) with a (historically chosen) radius of 8 h^{-1}Mpc. There are several choices for the window function $W_8(k)$, but the most popular one is undoubtedly the Fourier transform of the top-hat window function:

$$W_8(k) = 3\frac{\sin(kR) - kR\cos(kR)}{(kR)^3} \,, \tag{3.61}$$

where $R = 8\,h^{-1}$Mpc. As already mentioned, and as we shall discuss in detail in the introduction of part III, this parameter is subjected to a tension within the ΛCDM model between its local determination and its distant determination under the assumption of the ΛCDM model. In all cases, the large-scale structure surveys give us the opportunity to measure this parameter in combination with f, the linear growth rate. To do this, we need to get rid of the μ dependence of the galaxy power spectrum using a Legendre polynomials decomposition:

$$P_g(k,\mu) = \sum_\ell P_{g,\ell}(k) \mathscr{L}_\ell(\mu) \,, \tag{3.62}$$

$$P_{g,\ell}(k) = \frac{2\ell+1}{2} \int_{-1}^{1} d\mu\, P_g(k,\mu)\, \mathscr{L}_\ell(\mu) \,. \tag{3.63}$$

The first three non-zero multipoles are the monopole ($\ell = 0$), the quadrupole ($\ell = 2$) and the hexadecapole ($\ell = 4$). Using the parameter $\beta = f/b_1$, one has:

$$P_{g,\ell=0}(k) = \left(1 + \frac{2}{3}\beta + \frac{1}{5}\beta^2\right) b_1^2 P_m(k) \,, \tag{3.64}$$

$$P_{g,\ell=2}(k) = \left(\frac{4}{3}\beta + \frac{4}{7}\beta^2\right) b_1^2 P_m(k) \,, \tag{3.65}$$

$$P_{g,\ell=4}(k) = \frac{8}{35}\beta^2 b_1^2 P_m(k) \,. \tag{3.66}$$

There are a number of important points to be made here:

- All odd multipoles are equal to zero. In real space, the Universe is isotropic, but in redshift space this isotropy is broken, because we have now a privileged direction, that of the line of sight (see Fig. 3.4). However, there remains a residual symmetry, a consequence of the isotropy in real space, which is the invariance of the direction along the line of sight. In other words, the power spectrum must be invariant under the $\mu \to -\mu$ transformation, which implies that all odd multipoles are zero (because they involve odd powers of μ).

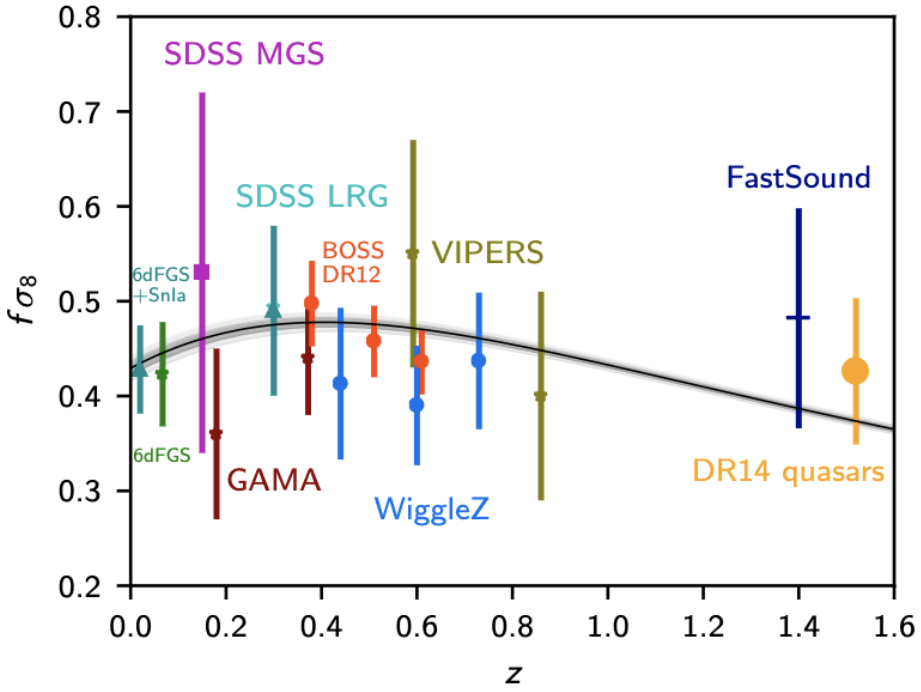

Figure 3.7: Various $f\sigma_8$ measurements from different clustering experiments using the method explained here. Grey bands correspond to the 68% and 95% C.L. of the ΛCDM fit to the *Planck* data (using the TT, EE, TE and lensing power spectra). Taken from Ref. [11].

- We can quantify the impact of the redshift space distortion on the monopole by taking $f = 1$ [valid for a matter dominated Universe, as shown by Eq. (3.32)] and $b_1 = 2$ (valid for the BOSS CMASS galaxy sample at $z = 0.57$). Then, the ratio $P_{g,\ell=0}(k)/[b_1^2 P_m(k)] \sim 1.4$, which means that the RSD modifies the monopole (*i.e.*, the isotropic part of the linear galaxy power spectrum) by 40%, which is a significant effect!

- Last but not least, if we integrate these multipoles as $\int \frac{k^3}{2\pi^2} W_8^2(k) d\ln k$, then Eqs.(3.64)-(3.66) are modified as $P_m(k) \to \sigma_8^2$. This modification allows us to use the σ_8 parameter instead of using the unknown (in the sense that we cannot measure it) matter power spectrum. These three multipoles allow us to obtain several combinations of f and b_1 in order to disentangle the effects of each of these parameters on the galaxy power spectrum. This then provides us a measure of $f\sigma_8$ and $b_1\sigma_8$, where the former contains cosmological information and the latter galaxy information. The $b_1\sigma_8$ combination is therefore considered more as a nuisance parameter.

In Fig. 3.7, we show the measurement of $f\sigma_8$ from different experiments, together with the ΛCDM fit to the *Planck* data. We can see that the ΛCDM model provides good agreement between the clustering data and the CMB data for the $f\sigma_8$ information. Note that in the remainder of this thesis we will be making considerable use of data from SDSS/BOSS DR12, commonly referred to as "BOSS", and SDSS/BOSS DR14, commonly referred to as "eBOSS" (and a little from MGS and 6dFGS as well).

3.2.4 Alcock-Paczyński parameters and BAO

Measuring $f\sigma_8$, commonly referred to as *redshift space distortion information*, is therefore a first way of extracting cosmological information from the galaxy power spectrum in the linear regime (although often some non-linear corrections are made to determine $f\sigma_8$). There is actually a second popular way of extracting cosmological information in the linear regime using the BAO part of the galaxy power spectrum. Previously, we had only taken into account the effect of redshift space distortion on the power spectrum and not the AP effect. It is now time to understand how it is possible to determine the true cosmology using the BAO part of the galaxy power spectrum, and to extract cosmological information from it.

As we explained earlier, it is necessary to assume a fiducial cosmology in Eq. (3.38) in order to connect the redshift space coordinates $s(z)$ with the real space coordinates $x(z)$, where $x(z) = \chi(z)\cdot\hat{n}$. In particular, we need this fiducial cosmology in order to transform the observed galaxy position in the system (θ, ϕ, z), where θ and ϕ are the angles used to position the galaxy in the sky, into a 3D position in real space, $x_{\rm obs} = (x^1_{\rm obs}, x^2_{\rm obs}, x^3_{\rm obs})$. We can easily show that the 3D position in real space obtained from the fiducial cosmology is related to the true one according to

$$\left(x^1, x^2\right) = \left[1 - \frac{\delta\chi(z)}{\chi^{\rm fid}(z)}\right]\left(x^1_{\rm obs}, x^2_{\rm obs}\right), \tag{3.67}$$

$$x^3 = \left[1 - \frac{\delta H(\bar{z})}{H^{\rm fid}(\bar{z})}\right] x^3_{\rm obs}, \tag{3.68}$$

where $\delta\chi(z) = \chi^{\rm fid}(z) - \chi(z)$, $\delta H(z) = H(z) - H^{\rm fid}(z)$, and $\bar{z}$ is the central redshift of the sky area probed. To obtain the second relationship, we used the fact that $x^3_{\rm obs} = \chi^{\rm fid}(\bar{z}) \simeq \bar{z}/H^{\rm fid}(\bar{z})$ and $x^3 \simeq \bar{z}/H(\bar{z})$. Note that the transverse distortion [quantified by the transverse coordinates (x^1, x^2)] is different from the distortion along the line of sight (quantified by the parallel coordinate x^3). The AP effect then generates a general elliptical distortion (see Fig. 3.5). It is customary to parametrize the system of Eqs. (3.67)-(3.68) as:

$$x(x_{\rm obs}) = \left([1-\alpha_\perp]x^1_{\rm obs}, [1-\alpha_\perp]x^2_{\rm obs}, [1-\alpha_\parallel]x^3_{\rm obs}\right), \tag{3.69}$$

$$\alpha_\perp = \left.\frac{\delta\chi}{\chi^{\rm fid}}\right|_{z=\bar{z}} \quad ; \quad \alpha_\parallel = \left.\frac{\delta H}{H^{\rm fid}}\right|_{z=\bar{z}}, \tag{3.70}$$

where $\alpha_\perp$ and $\alpha_\parallel$ are the two AP parameters evaluated at $z = \bar{z}$, assuming that the redshift slice is narrow. We can then express the true values of the comoving distance and the Hubble parameter as a function of the AP parameters as

$$\chi(\bar{z}) = \chi^{\rm fid}(\bar{z})[1+\alpha_\perp], \tag{3.71}$$

$$H(\bar{z}) = H^{\rm fid}(\bar{z})[1+\alpha_\parallel]. \tag{3.72}$$

Therefore, if we can measure the AP parameters, then we can directly infer the true values of H and χ, which is crucial information for knowing the (true) expansion history.

We now have all the tools we need to correct the galaxy power spectrum of the AP effect. To do this, we need to evaluate the galaxy power spectrum at $z = \bar{z}$, and at the corrected wavevector:

$$P_g(k_{\rm obs}, \mu, \bar{z}) = \left[b_1 + f\mu^2\right]^2 P_m(k, \bar{z})\Big|_{k=\left([1+\alpha_\perp]k^1_{\rm obs}, [1+\alpha_\perp]k^2_{\rm obs}, [1+\alpha_\parallel]k^3_{\rm obs}\right)} + \frac{1}{\bar{n}_g}. \tag{3.73}$$

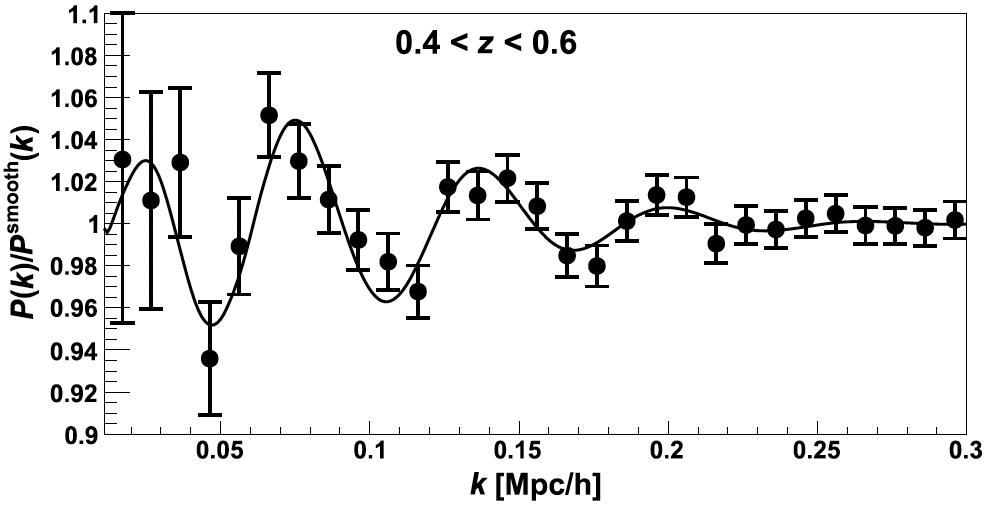

Figure 3.8: Ratio between the galaxy power spectrum $P(k)$ and the smooth galaxy power spectrum $P^{\text{smooth}}(k)$, namely $P(k)$ without the BAO feature, for the monopole of the BOSS CMASS sample. The solid line corresponds to the ΛCDM model with a correction for the AP effect (by adjusting $\alpha_\perp$ and $\alpha_\parallel$), which produces a general shift along the k dimension. Taken from Ref. [51] (with an adaptation from Ref. [9]).

We thus obtain a formula for the linear galaxy power spectrum that depends directly on $\boldsymbol{k}_{\text{obs}}$, the wavevector obtained with the fiducial cosmology, since $\boldsymbol{k}$ has been corrected for the AP effect using the $\alpha_\perp$ and $\alpha_\parallel$ parameters. In other words, correcting the AP effect in the galaxy power spectrum means shifting the wavevector according to the correct cosmology. Note that Eq. (3.73) takes into account all the aforementioned effects, *i.e.*, the contribution of the biased tracer, the redshift space distortion, the Alcock-Paczyński distortion and the stochastic contribution.

We now explain how we can measure AP parameters using the galaxy power spectrum, in order to infer the true value of $H(\bar{z})$ and $\chi(\bar{z})$. To do so, we can use the *baryonic acoustic oscillation* (BAO) imprint on the linear matter power spectrum. In Fig. 2.2, we mentioned the fact that the baryon density field underwent an oscillatory behaviour for modes that entered the horizon before the last-scattering surface epoch. Consequently, when we take baryons into account, the matter power spectrum has low amplitude oscillations around $k_{\text{eq}} \sim 0.1\,h\text{Mpc}^{-1}$, as shown in Fig. 3.8. These oscillations are small, because the baryon fraction is low compared with that of dark matter, but these oscillations are well measured. The physical origin of these oscillations is therefore the same as those of the CMB, namely the propagation of sound waves in the primordial plasma. We saw earlier that the apparent angular size of the characteristic distance travelled by a sound wave at τ_* (corresponding to the position of the first CMB peak) is quantified by the angular acoustic scale at recombination θ_s [see Eq. (2.162)]: $\theta_s = r_s(z_*)/D_A(z_*)$. This scale is determined at the moment when photons decouple from baryons, *i.e.*, at $z = z_*$. However, there are many more photons than baryons in the Universe, since $\eta \equiv n_b/n_\gamma = 6.0 \cdot 10^{-10}$. This means that it is much less likely that a photon interact with a baryon (from the point of view of photons) than a baryon interact with a photon (from the point of view of baryons). However, when the photons decouple from the baryons, at $z = z_*$, the baryons continue to interact significantly with

the photons. It is therefore necessary to introduce a new period at which baryons decouple from photons, namely the baryon-drag epoch $z_{\rm drag} = 1059.94 \pm 0.30 < z_* = 1089.92 \pm 0.25$ (according to *Planck* [11]). We can then define the sound horizon seen at baryon-drag epoch $r_s(z_{\rm drag})$, and therefore the angular acoustic scale at this time. In particular, galaxy survey measure the combinations $r_s(z_{\rm drag})H(z)$ and $r_s(z_{\rm drag})/D_A(z)$, which can be summarized as

$$\theta_g = \frac{r_s(z_{\rm drag})}{D_V(\bar{z})} \,, \tag{3.74}$$

where $D_V(z) = [D_A^2(z) \cdot z/H(z)]^{1/3}$ is the volume average of the comoving distances in the directions parallel ($\chi \simeq z/H$) and perpendicular (D_A) to the line of sight. The angle θ_g typically summarizes the information from the BAO. In Fig 3.9, we show various angular acoustic scale measurements, obtained from different clustering experiment, and we show that the current values of θ_s are in good agreement with the ΛCDM fit to the *Planck* data. The angular acoustic scale (either the one from the last-scattering surface or the one from the galaxy surveys) is a standard ruler, as already mentionned in chapter 1 [see Eq. (1.69)]. Indeed, the comoving sound horizon at baryon-drag epoch $r_s(z_{\rm drag}) = 147.09 \pm 0.26$ Mpc and at recombination $r_s(z_*) = 144.43 \pm 0.26$ Mpc (according to *Planck* [11]) correspond to two physical processes whose intrinsic distance is known in a given cosmological model (in this case ΛCDM). The second advantage of the comoving sound horizon at baryon-drag epoch is that it is fixed (insofar as it depends on the history before the baryon-drag epoch), and therefore does not depend on the redshift of the galaxy survey. Finally, note that by analogy with the CMB [see Eq. (2.160)], the position of the peaks are located at (see Fig. 3.8)

$$k_{\rm peak}(\tau_{\rm drag}) = \frac{n\pi}{r_s(\tau_{\rm drag})} \,, \quad \text{with } n = 1, 2, 3, \dots . \tag{3.75}$$

If we go back to Eq. (3.73), the standard ruler established by the BAO is used to calibrate the position of the galaxy power spectrum along the k axis. In other words, according to the true cosmology we should have the first peak at $k \sim \pi/r_s(z_{\rm drag}) \sim 0.02\,h{\rm Mpc}^{-1}$ (see Fig. 3.8), but we detect it at an apparent scale $k_{\rm obs}(k)$ which is different from k, because of the fiducial cosmology. Given that $r_s(z_{\rm drag})$ is extremely well measured by the CMB (which makes it a standard ruler) it is then possible to determine the real position of the peaks [see Eq. (3.75)]. This allows us to correct the position of the galaxy power spectrum along the k axis and to have access to $\alpha_\perp$ and $\alpha_\parallel$, since in Eq. (3.73) we have a direct relationship between $\boldsymbol{k}$ and $\boldsymbol{k}_{\rm obs}$ that depends solely on the AP parameters. We can then infer the true value of $H(\bar{z})$ and $D_A(\bar{z})$ from Eqs. (3.71) and (3.72). It should be pointed out that this method is very robust insofar as the BAO physics is very well characterised and we know *a posteriori* the intrinsic value of the characteristic distance of the BAO oscillations in the galaxy power spectrum. In Fig. 3.10, we show the measurement of $H(\bar{z})$ from different clustering experiments, together with the ΛCDM fit to the *Planck* data. We can see that the ΛCDM model provides again a good agreement between the clustering data and the CMB data for this parameter.

We have seen here two methods for extracting cosmological information from the galaxy power spectrum at linear order: (i) the redshift space distortion information $f\sigma_8$ and (ii) the extraction of the AP parameters from the BAO shape. These two methods will be used frequently in this thesis, and one of the main objectives will be to go further and extract cosmological

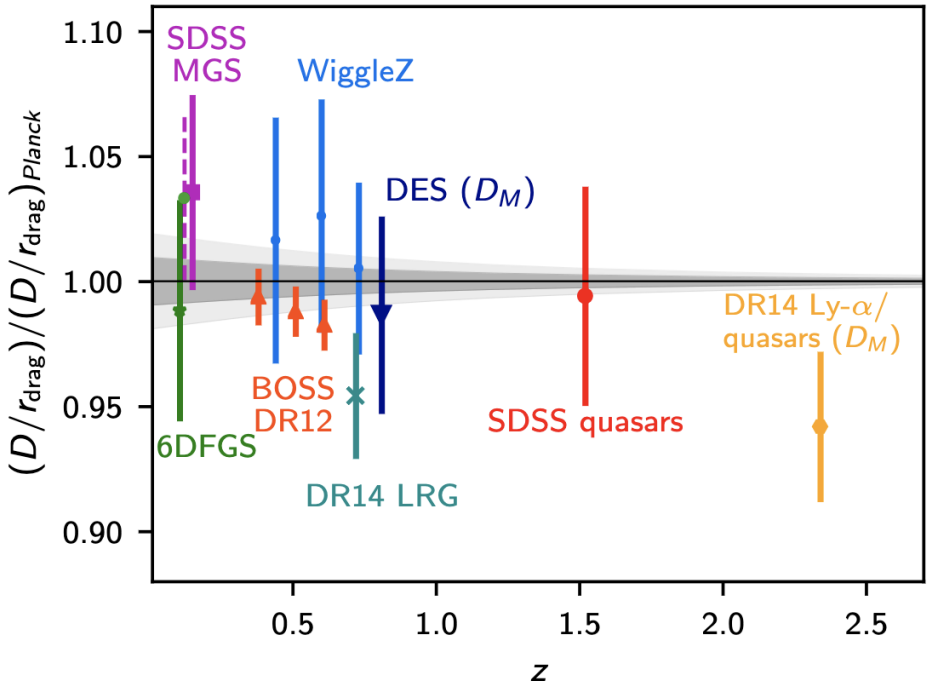

Figure 3.9: Various angular acoustic scale measurements, obtained from different clustering experiments, normalized to the corresponding parameter obtained by the ΛCDM fit of the *Planck* data. What is shown here is $1/\theta_g = D_V(z)/r_s(z_{\rm drag})$. Grey bands correspond to the 68% and 95% C.L. of the ΛCDM fit to the *Planck* data (using the TT, EE, TE and lensing power spectra). Taken from Ref. [11].

information by fitting the full shape of the galaxy power spectrum, exactly as we have done with the CMB power spectra. Let us note that the combination of this two methods used here will be referred to as "BAO/$f\sigma_8$" in the remainder of this thesis, which corresponds to the measurement of $f\sigma_8$ (see Fig. 3.7), $H(\bar{z})$ (see Fig. 3.10) and $D_A(\bar{z})$.

3.3 Beyond the linear theory

Up to now, we have remained solely within the linear perturbation framework. In particular, in the CMB theory we have always used the linear regime, and this was justified by the fact that we always have $\delta_a \ll 1$ and $\phi, \psi \ll 1$. This implies, as we have seen, that the linear regime is sufficient to accurately fit the CMB data and derive cosmological information from the full shape of the CMB power spectra. However, things are not that simple at late time. As we have seen, in the framework of linear perturbation theory, we extract cosmological information from the galaxy power spectrum with the redshift space distortion (*i.e.*, $f\sigma_8$) and the BAO shape (*i.e.*, $\alpha_\perp$ and $\alpha_\parallel$). We have to use these two "tricks" because it is not possible to fit the galaxy power spectrum precisely with linear perturbation theory. Indeed, as we approach small scales, linear perturbation theory breaks down, since the condition $\delta_m \ll 1$ is no longer satisfied. It is possible to determine the non-linear scale $k_{\rm NL}$ at which non-linearities become so important that we leave the linear framework. To do so, we can use the variance of the matter overdensity

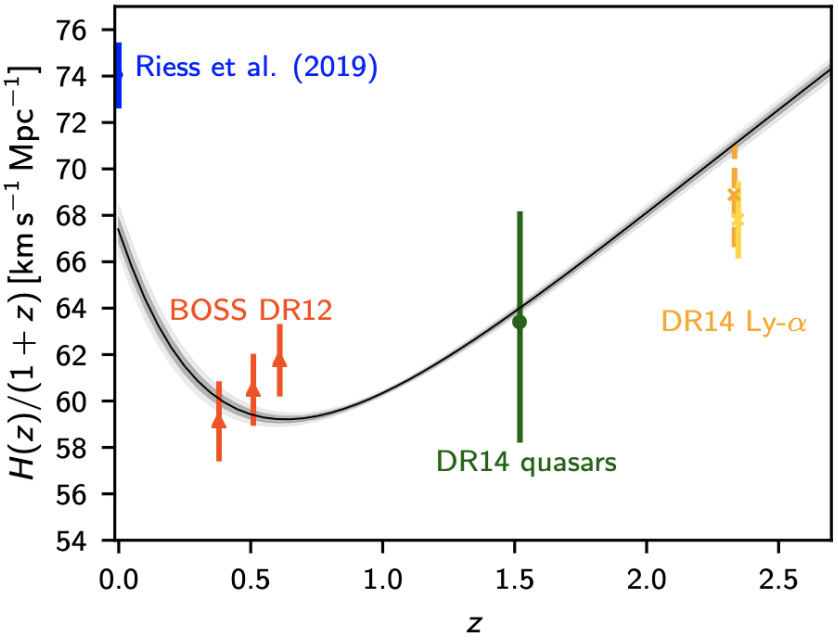

Figure 3.10: Various measurements of the comoving Hubble parameter $aH(\bar{z})$ from different clustering experiments using the method explained here. Note that parameter $r_s(z_{\rm drag})$ has been calibrated using *Planck* data in order to extract $\alpha_{\parallel}$ and then $H(\bar{z})$, as explained in the main text. The blue point corresponds to the local Hubble determination from the SNIa calibrated with the cepheids, leading to the so-called Hubble tension (see introduction of part III). Grey bands correspond to the 68% and 95% C.L. of the ΛCDM fit to the *Planck* data (using the TT, EE, TE and lensing power spectra). Taken from Ref. [11].

field [see Eq. (2.114)] generated by the neighbouring modes closely centred on k, with $\Delta \to 0$:

$$\sigma^2 \equiv \frac{1}{\Delta}\int_{\ln k-\Delta/2}^{\ln k+\Delta/2} d\ln k' \; \mathscr{P}_m(k',a) \simeq \mathscr{P}_m(k,a) = \frac{k^3 P_m(k,a)}{2\pi^2}\,. \tag{3.76}$$

The linear regime corresponds to the regime where $\mathscr{P}_m(k,a) \ll 1$, namely when the variance of the density field perturbation is low, while non-linearities start to become important when $\mathscr{P}_m(k,a) \gtrsim 1$. We can easily show that when $\mathscr{P}_m(k,a) \sim 1$, then $k_{\rm NL}(a=a_0) \sim 0.25\,h{\rm Mpc}^{-1}$. As we will see in the rest of this thesis, being able to describe the matter and galaxy power spectra precisely up to $k = 0.25\,h{\rm Mpc}^{-1}$ makes it possible to obtain a very rich amount of cosmological information. However, although in linear perturbation theory each k mode evolves independently, this is no longer the case in the non-linear framework (see below). This implies that each mode is in fact coupled with the other modes, and that an inaccurate description of the large modes (typically $k \gtrsim k_{\rm NL}$) will lead to a significant theoretical error on the small modes (typically $k \lesssim k_{\rm NL}$), even if they are located in the linear regime. It is therefore necessary to take these non-linearities into account in order to have an accurate description of the galaxy power spectrum on large scales, and this is the purpose of the end of this chapter. This section is based mainly on Ref. [9].

3.3.1 The Vlasov-Poisson system

First of all, let us define the system of equations we are dealing with in this section. In the linear framework, we considered the continuity, Euler and Poisson equations

[see Eqs. (3.5)-(3.7)]:

$$\dot{\delta}_m + ikv_m = 3\dot{\phi}\,, \tag{3.77}$$

$$\dot{v}_m + \frac{\dot{a}}{a}v_m = -ik\psi\,, \tag{3.78}$$

$$k^2\phi + 3\frac{\dot{a}}{a}\left(\dot{\phi} + \psi\frac{\dot{a}}{a}\right) = -4\pi G a^2 \rho_m \delta_m\,. \tag{3.79}$$

In the previous section, we set $\phi = \psi$, because we neglected the neutrino cosmic shear. We are still going to do this here, as we are going to deal with non-linearities and not with the impact of neutrinos on the power spectrum (which in all cases leads to a percent-level correction). In addition, previously we dropped the second term of the left-hand side of the Poisson equation because we were in the sub-horizon regime. This is still the case here and we also apply this approximation in the non-linear framework. Indeed, for sub-horizon modes, the potential is constant (see above), which means that $\dot{\phi} \sim (\dot{a}/a)\,\phi \sim 0$. Thus, in this section, we do not modify the gravity equations compared to the linear regime: (i) the perturbations of the metric are in any case very small (because ϕ has been constant since the radiation domination era), implying that we can continue to work at linear order, and (ii) we can still apply the approximation previously made for the Poisson equation.

However, in this section we want a Boltzmann equation for matter that is no longer restricted to small perturbations and therefore to large scales, because we are breaking the approximation $\delta_m \ll 1$ (remember that $\delta_m \propto a$ in the matter dominated era). Starting from the collisionless Boltzmann equation [see Eq. (1.8)]

$$\frac{df}{dt} = \frac{\partial f}{\partial t} + \frac{\partial f}{\partial x^i}\cdot\frac{dx^i}{dt} + \frac{\partial f}{\partial p^i}\cdot\frac{dp^i}{dt} = 0\,, \tag{3.80}$$

we obtained, in the linear regime, the first two moments, namely Eqs. (3.77) and (3.78). In particular, we had decomposed p^i as $p^i = p\cdot\hat{p}^i$ and removed the contribution of $\hat{p}^i$, which was necessarily non-linear (see Sec. 1.1). Here, this approximation is no longer valid, so we are keeping p^i. In the non-relativistic ($m \gg p$) and sub-horizon ($\dot{\psi} = 0$) regime, we can show from the geodesic equation that (see Ref. [9]):

$$\frac{dx^i}{dt} = \frac{p^i}{am}\,, \tag{3.81}$$

$$\frac{dp^i}{dt} = -Hp^i - \frac{m}{a}\partial_i\psi\,. \tag{3.82}$$

By injecting these equations into the Boltzmann equation, we obtain the so-called *Vlasov equation*

$$\frac{df}{dt} = \frac{\partial f}{\partial t} + \frac{\partial f}{\partial x^i}\cdot\frac{p^i}{am} - \frac{\partial f}{\partial p^i}\cdot\left[Hp^i + \frac{m}{a}\partial_i\psi\right] = 0\,. \tag{3.83}$$

Together with the Poisson equation,

$$k^2\psi = -4\pi G a^2\rho_m\delta_m\,, \tag{3.84}$$

we get the *Vlasov-Poisson* system, a 7-dimensional system which is non-linear via the coupling between f and ψ (even if it assumes a linear perturbation in the metric). The remainder of this section is devoted to solving this equation using the perturbation theory method.

To do so, one needs to deduce the non-linear continuity and Euler equations. One obtains the continuity equation by taking the zeroth moment of the Vlasov equation, namely by doing the operation $\int d^3p/(2\pi)^3 \times$ (3.83), multiplied by m. Similarly, one obtains the Euler equation by taking the first moment of the Vlasov equation, namely by doing the operation $\int d^3p/(2\pi)^3\, p^j \times$ (3.83). Without any particular difficulty, it can be shown (see Ref. [9]) that in real space, the Vlasov-Poisson system reduces to

$$\dot{\delta} + \theta = -\delta\theta - v^j \partial_j \delta\,, \tag{3.85}$$

$$\dot{\theta} + aH\theta + \nabla^2\psi = -v^j \partial_j \theta - \partial_i v^j \cdot \partial_j v^i\,, \tag{3.86}$$

$$\nabla^2\psi = \frac{3}{2}\Omega_m(a)(aH)^2\delta\,, \tag{3.87}$$

where $\Omega_m(a) = \Omega_m a^{-3}$. Note that we have omitted the subscript "m" here for the sake of clarity, as we will only be dealing with matter in the remainder of this chapter. In addition, we are not considering velocity dispersion for dark matter, *i.e.*, $\sigma_m = 0$ in this set of equations. We have now considerably reduced the problem, as we have moved from a 7-dimensional differential equation system to a 4-dimensional differential equation system, since we have integrated over p^i. However, this system is non-linear and no simple resolution is possible. In the following we use a method, the *standard perturbation theory*, to obtain a (first) suitable resolution of this system.

3.3.2 The standard perturbation theory

The fundamental principle of the standard perturbation theory is to expand the matter overdensity field and the matter velocity field as follows

$$\delta(\boldsymbol{x},\tau) = \delta^{(1)}(\boldsymbol{x},\tau) + \delta^{(2)}(\boldsymbol{x},\tau) + \ldots + \delta^{(n)}(\boldsymbol{x},\tau)\,, \tag{3.88}$$

$$\theta(\boldsymbol{x},\tau) = \theta^{(1)}(\boldsymbol{x},\tau) + \theta^{(2)}(\boldsymbol{x},\tau) + \ldots + \theta^{(n)}(\boldsymbol{x},\tau)\,, \tag{3.89}$$

where $\delta^{(1)}(\boldsymbol{x},\tau)$ is the linear solution we have dealt with so far. The idea is therefore to perturb the linear solution up to an order n, where $\delta^{(n)}$ and $\theta^{(n)}$ involve n powers of the linear solution $\delta^{(1)}$. Whereas $\delta^{(2)} \sim (\delta^{(1)})^2$, $\delta^{(3)} \sim (\delta^{(1)})^3$, and so on, in such a way that each order is suppressed relative to the previous one (hence the name *perturbation theory*).

Let us go back to the linear system in order to see how to obtain the higher-order solution $\delta^{(2)}$. At linear order, we have the following set of equations [see Eqs. (3.85) and (3.86)]:

$$\dot{\delta} + \theta = 0\,, \tag{3.90}$$

$$\dot{\theta} + aH\theta + \nabla^2\psi = 0\,, \tag{3.91}$$

$$\nabla^2\psi = \frac{3}{2}\Omega_m(a)(aH)^2\delta\,. \tag{3.92}$$

We have already solved this system, and according to Eqs. (3.19) and (3.56), we get

$$\delta^{(1)}(\boldsymbol{x},\tau) = D_+(\tau)\delta_0(\boldsymbol{x})\,, \tag{3.93}$$

$$\theta^{(1)}(\boldsymbol{x},\tau) = -\dot{\delta}^{(1)}(\boldsymbol{x},\tau) = -aHf\delta^{(1)}(\boldsymbol{x},\tau)\,, \tag{3.94}$$

where we have kept only the growing solution D_+ and removed the decaying solution D_- (since the second solution is largely subdominant in the matter domination era). In the first equation, $\delta_0(\boldsymbol{x}) = \delta^{(1)}(\boldsymbol{x},\tau_{\rm ref})/D_+(\tau_{\rm ref})$ corresponds to the overdensity field at a (arbitrary) given time (remember that fixing $\tau_{\rm ref} = \tau_{\rm eq}$ enabled us to link this solution valid in the matter domination era to the solution valid in the radiation domination era, in order to determine an approximate form of the transfer function).

The fact that we have obtained the linear solution by neglecting the non-linear terms, together with the fact that we have perturbed in Eqs. (3.88) and (3.89) the matter overdensity field and the matter velocity field, suggest that to obtain the non-linear solutions at second order in perturbation, namely $\delta^{(2)}(\boldsymbol{x},\tau)$ and $\theta^{(2)}(\boldsymbol{x},\tau)$, we can evaluate the right-hand side of Eqs. (3.85) and (3.86) as follows:

$$\dot{\delta}^{(2)} + \theta^{(2)} = -\delta^{(1)}\theta^{(1)} - (v^{(1)})^j\partial_j\delta^{(1)}\,, \tag{3.95}$$

$$\dot{\theta}^{(2)} + aH\theta^{(2)} + \nabla^2\psi^{(2)} = -(v^{(1)})^j\partial_j\theta^{(1)} - \partial_i(v^{(1)})^j\cdot\partial_j(v^{(1)})^i\,, \tag{3.96}$$

$$\nabla^2\psi^{(2)} = \frac{3}{2}\Omega_m(a)(aH)^2\delta^{(2)}\,. \tag{3.97}$$

Here we have injected the linear solution into the non-linear terms, in the same way as we neglected these terms to obtain the linear solution. This iterative procedure allows us to linearise Eqs. (3.85) and (3.86) for each order in perturbation and obtain a solution that depends on the previous order. We can see that $\delta^{(2)}$ and $\theta^{(2)}$ are sourced by terms of the order of $\sim(\delta^{(1)})^2$, which implies that $\delta^{(n)} \sim (\delta^{(1)})^n$. On the other hand, note that the Poisson equation is linear and that such a procedure is not required, since it is true to any order.

The natural next step is to determine the form of the system composed of Eqs. (3.95)-(3.97) in Fourier space (after all, what we want is to compute the power spectrum). While for the left-hand sides it is trivial (and identical to the linear case), for the right-hand sides it is slightly more complicated: the products of perturbations in real space take the form of a convolution in Fourier space. We can show that we then obtain the following set of equations [using Eqs. (3.94) and (3.97)]

$$\dot{\delta}^{(2)} + \theta^{(2)} = \int\frac{d^3k_1}{(2\pi)^3}\int\frac{d^3k_2}{(2\pi)^3}(2\pi)^3\delta_D^{(3)}(\boldsymbol{k}-\boldsymbol{k}_1-\boldsymbol{k}_2)\cdot aHfD_+^2\left[1+\frac{\boldsymbol{k}_1\cdot\boldsymbol{k}_2}{k_1^2}\right]\delta_0(\boldsymbol{k}_1)\delta_0(\boldsymbol{k}_2)\,, \tag{3.98}$$

$$\dot{\theta}^{(2)} + aH\theta^{(2)} + \frac{3}{2}\Omega_m(a)(aH)^2\delta^{(2)} = -\int\frac{d^3k_1}{(2\pi)^3}\int\frac{d^3k_2}{(2\pi)^3}(2\pi)^3\delta_D^{(3)}(\boldsymbol{k}-\boldsymbol{k}_1-\boldsymbol{k}_2) \times(aHfD_+)^2\left[\frac{\boldsymbol{k}_1\cdot\boldsymbol{k}_2}{k_1^2}+\frac{(\boldsymbol{k}_1\cdot\boldsymbol{k}_2)^2}{k_1^2k_2^2}\right]\delta_0(\boldsymbol{k}_1)\delta_0(\boldsymbol{k}_2)\,. \tag{3.99}$$

This equation is an ordinary differential equation that can be solved (relatively) easily. Using the derivative with respect to the growth factor D_+ instead of the derivative with respect to the

conformal time τ, by performing the transformation

$$\frac{d}{d\tau} \to \frac{d\ln a}{d\tau}\cdot\frac{d\ln D_+}{d\ln a}\frac{d}{d\ln D_+} = aHf\frac{d}{d\ln D_+}\,, \tag{3.100}$$

we obtain (see Ref. [9])

$$\frac{d}{d\ln D_+}\delta^{(2)} + \hat{\theta}^{(2)} = D_+^2 S_\delta(\boldsymbol{k})\,, \tag{3.101}$$

$$\frac{d}{d\ln D_+}\hat{\theta}^{(2)} + \left(\frac{3}{2}\frac{\Omega_m(a)}{f^2} - 1\right)\hat{\theta}^{(2)} + \frac{3}{2}\frac{\Omega_m(a)}{f^2}\delta^{(2)} = D_+^2 S_\theta(\boldsymbol{k})\,, \tag{3.102}$$

where $\hat{\theta} \equiv \theta/aHf$, and where $S_\delta(\boldsymbol{k})$ and $S_\theta(\boldsymbol{k})$ are time-independent source terms

$$S_\delta(\boldsymbol{k}) = \int\frac{d^3k_1}{(2\pi)^3}\int\frac{d^3k_2}{(2\pi)^3}(2\pi)^3\delta_D^{(3)}(\boldsymbol{k}-\boldsymbol{k}_1-\boldsymbol{k}_2)\cdot\left[1+\frac{\boldsymbol{k}_1\cdot\boldsymbol{k}_2}{k_1^2}\right]\delta_0(\boldsymbol{k}_1)\delta_0(\boldsymbol{k}_2)\,, \tag{3.103}$$

$$S_\theta(\boldsymbol{k}) = -\int\frac{d^3k_1}{(2\pi)^3}\int\frac{d^3k_2}{(2\pi)^3}(2\pi)^3\delta_D^{(3)}(\boldsymbol{k}-\boldsymbol{k}_1-\boldsymbol{k}_2)\cdot\left[\frac{\boldsymbol{k}_1\cdot\boldsymbol{k}_2}{k_1^2}+\frac{(\boldsymbol{k}_1\cdot\boldsymbol{k}_2)^2}{k_1^2k_2^2}\right]\delta_0(\boldsymbol{k}_1)\delta_0(\boldsymbol{k}_2)\,. \tag{3.104}$$

Let us note that in a matter domination era $\Omega_m(a)/f^2 \simeq \Omega_m(a)/[\Omega_m(a)]^{0.55\times2} \simeq 1$, and that we use this approximation now (which allows us to linearise this system of equations in D_+).

The next step is therefore to solve this system of equations. To do this, we perform the following ansatz:

$$\delta^{(2)}(\boldsymbol{k}, D_+) = A_\delta(\boldsymbol{k})D_+^p\,, \tag{3.105}$$

$$\hat{\theta}^{(2)}(\boldsymbol{k}, D_+) = A_\theta(\boldsymbol{k})D_+^p\,, \tag{3.106}$$

which is a power-low solution in D_+ with a k-dependant amplitude. By inserting this solution into Eqs. (3.101) and (3.102), we can show that the only viable solution is $p = n = 2$ (the other solutions are valid for a finite set of times). It is then straightforward to show that:

$$A_\delta(\boldsymbol{k}) = \frac{5}{7}S_\delta(\boldsymbol{k}) - \frac{2}{7}S_\theta(\boldsymbol{k})\,, \tag{3.107}$$

$$A_\theta(\boldsymbol{k}) = -\frac{3}{7}S_\delta(\boldsymbol{k}) + \frac{4}{7}S_\theta(\boldsymbol{k})\,. \tag{3.108}$$

By incorporating these solutions into Eqs. (3.105) and (3.106), we can determine the final form of the second-order density field perturbation $\delta^{(2)}$ and the second-order velocity field $\theta^{(2)}$ in Fourier space:

$$\delta^{(2)}(\boldsymbol{k},\tau) = D_+^2(\tau)\int\frac{d^3k_1}{(2\pi)^3}\int\frac{d^3k_2}{(2\pi)^3}(2\pi)^3\delta_D^{(3)}(\boldsymbol{k}-\boldsymbol{k}_1-\boldsymbol{k}_2)\cdot F_2(\boldsymbol{k}_1,\boldsymbol{k}_2)\delta_0(\boldsymbol{k}_1)\delta_0(\boldsymbol{k}_2)\,, \tag{3.109}$$

$$\theta^{(2)}(\boldsymbol{k},\tau) = -aHfD_+^2(\tau)\int\frac{d^3k_1}{(2\pi)^3}\int\frac{d^3k_2}{(2\pi)^3}(2\pi)^3\delta_D^{(3)}(\boldsymbol{k}-\boldsymbol{k}_1-\boldsymbol{k}_2)\cdot G_2(\boldsymbol{k}_1,\boldsymbol{k}_2)\delta_0(\boldsymbol{k}_1)\delta_0(\boldsymbol{k}_2)\,, \tag{3.110}$$

where $F_2(\boldsymbol{k}_1,\boldsymbol{k}_2)$ and $G_2(\boldsymbol{k}_1,\boldsymbol{k}_2)$ are respectively the second-order density kernel and second-order velocity kernel, symmetrized in $\boldsymbol{k}_1$ and $\boldsymbol{k}_2$ [52]:

$$F_2(\boldsymbol{k}_1,\boldsymbol{k}_2) = \frac{5}{7} + \frac{2}{7}\frac{(\boldsymbol{k}_1\cdot\boldsymbol{k}_2)^2}{k_1^2k_2^2} + \frac{1}{2}\frac{\boldsymbol{k}_1\cdot\boldsymbol{k}_2}{k_1k_2}\left(\frac{k_1}{k_2}+\frac{k_2}{k_1}\right), \tag{3.111}$$

$$G_2(\boldsymbol{k}_1,\boldsymbol{k}_2) = \frac{3}{7} + \frac{4}{7}\frac{(\boldsymbol{k}_1\cdot\boldsymbol{k}_2)^2}{k_1^2k_2^2} + \frac{1}{2}\frac{\boldsymbol{k}_1\cdot\boldsymbol{k}_2}{k_1k_2}\left(\frac{k_1}{k_2}+\frac{k_2}{k_1}\right). \tag{3.112}$$

This result is very important because it allows to (partially) derive the next leading order of the matter power spectrum. We carried out several steps to arrive at this result, which, for the sake of clarity, are recalled here:

1. Linearize the Vlasov-Poisson system at order n by injecting the $n-1$ solution into the non-linear terms [see Eqs. (3.95)-(3.97)].
2. Get this set of equations in Fourier space [see Eqs. (3.101) and (3.102)].
3. Insert the ansatz $\delta^{(n)}(k,D_+), \hat{\theta}^{(n)}(k,D_+) \propto D_+^p$ into this set of equations, where $p=n$.

We can iteratively use exactly the same steps to determine the higher-order contributions to δ and θ. Finally, we obtain for all orders:

$$\begin{aligned}\delta^{(n)}(\boldsymbol{k},\tau) =& D_+^n(\tau)\left(\prod_{i=1}^{n}\int\frac{d^3k_1}{(2\pi)^3}\right)(2\pi)^3\delta_D^{(3)}\left(\boldsymbol{k}-\sum_{i=1}^{n}\boldsymbol{k}_i\right)\\ &\times F_n(\boldsymbol{k}_1,...,\boldsymbol{k}_n)\delta_0(\boldsymbol{k}_1)...\delta_0(\boldsymbol{k}_n),\end{aligned} \tag{3.113}$$

$$\begin{aligned}\theta^{(n)}(\boldsymbol{k},\tau) =& -aHfD_+^n(\tau)\left(\prod_{i=1}^{n}\int\frac{d^3k_1}{(2\pi)^3}\right)(2\pi)^3\delta_D^{(3)}\left(\boldsymbol{k}-\sum_{i=1}^{n}\boldsymbol{k}_i\right)\\ &\times G_n(\boldsymbol{k}_1,...,\boldsymbol{k}_n)\delta_0(\boldsymbol{k}_1)...\delta_0(\boldsymbol{k}_n).\end{aligned} \tag{3.114}$$

The difficulty is then to determine the kernels for each order, and obviously the higher the order, the more complicated it is (see Ref. [53]). Let us note that at linear order, for $n=1$, we have trivially $F_1 = G_1 = 1$, so that the integral reduces to $\delta_0(\boldsymbol{x})$, to recover Eqs. (3.93) and (3.94). In addition, we find again that $\delta^{(n)} \sim (\delta^{(1)})^n$. Using the method described above to the next order, namely $\delta^{(3)}$, we find the third-order density kernel

$$\begin{aligned}F_3(\boldsymbol{k}_1,\boldsymbol{k}_2,\boldsymbol{k}_3) =& \frac{1}{18}\left[7\frac{\boldsymbol{k}_1\cdot(\boldsymbol{k}_1+\boldsymbol{k}_2+\boldsymbol{k}_3)}{k_1^2}F_2(\boldsymbol{k}_2,\boldsymbol{k}_3) + (\boldsymbol{k}_1\cdot\boldsymbol{k}_2)\frac{|\,\boldsymbol{k}_1+\boldsymbol{k}_2\,|^2}{k_1^2k_2^2}G_2(\boldsymbol{k}_2,\boldsymbol{k}_3)\right]\\ &+\frac{1}{18}G_2(\boldsymbol{k}_1,\boldsymbol{k}_2)\left[7\frac{(\boldsymbol{k}_1+\boldsymbol{k}_2)\cdot(\boldsymbol{k}_1+\boldsymbol{k}_3)}{|\,\boldsymbol{k}_1+\boldsymbol{k}_2\,|^2} + \frac{|\,\boldsymbol{k}_1+\boldsymbol{k}_2+\boldsymbol{k}_3\,|^2}{k_3^2\,|\,\boldsymbol{k}_1+\boldsymbol{k}_2\,|^2}(\boldsymbol{k}_1+\boldsymbol{k}_2)\cdot\boldsymbol{k}_3\right].\end{aligned} \tag{3.115}$$

Before moving on to the power spectrum, there are two important points to make:

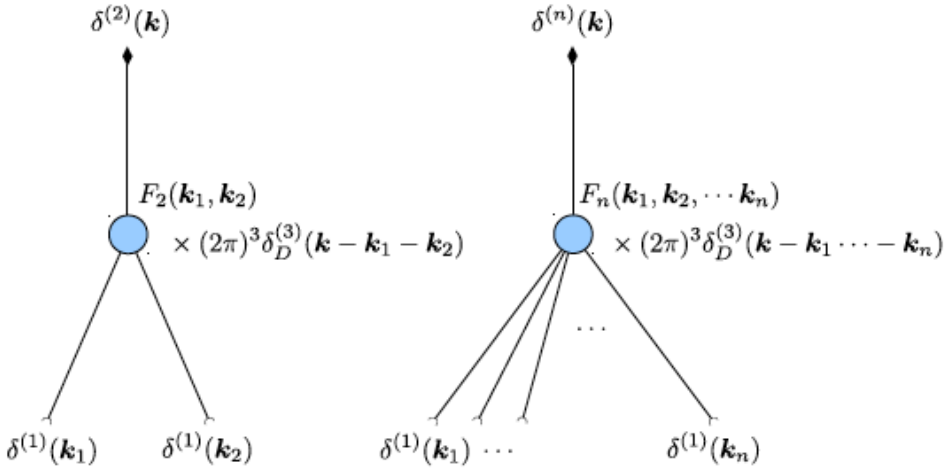

Figure 3.11: Diagrams showing the construction of the second-order and nth-order overdensity fields from the linear solution $\delta^{(1)}$ connected with each other thanks to the interaction kernels F_n. Taken from Ref. [9].

- Whereas at linear order we have $\delta^{(1)}(k,\tau) = D_+(\tau)\delta_0(k)$, which implies that each mode evolves independently from the others, this is not the case at non-linear order. In Eq. (3.113), $\delta^{(n)}(k,\tau)$ now depends on n integrals over $k_1,...,k_n$, implying that each mode is coupled to other modes. For example, at second order, finding the solution of $\delta^{(2)}(k,\tau)$ for a given mode k means integrating over all the modes k_1 and k_2 that satisfy condition $\boldsymbol{k} = \boldsymbol{k}_1 + \boldsymbol{k}_2$. This is due directly to the non-linear terms in Eqs. (3.95) and (3.96), which couple two $\delta^{(1)}(k,\tau)$ together evaluated at different k [*i.e.*, $\delta^{(1)}(k_1,\tau)$ with $\delta^{(1)}(k_2,\tau)$], and therefore couple the modes together.

- We can draw an analogy with quantum field theory. Here, the $\delta^{(1)}$'s, *i.e.*, the linear solutions, correspond to the *free fields* of the problem which can interact with each other to give higher order terms. The kernels are then the *transition amplitudes* between n linear fields and one non-linear field. For example, $\delta^{(2)}$ is constructed by joining two different $\delta^{(1)}$'s (evaluated at two different wavenumbers) with an F_2 kernel. We can then construct diagrams, which are analogous to Feynman diagrams, as shown in Fig. 3.11.

3.3.3 Non-linear matter power spectrum

We now have all the tools to determine the (mildly) non-linear matter power spectrum from the standard perturbation theory. First of all, let us note that the expectation value of an odd number of Gaussian random fields is zero [for instance, if f is such a field, then $\langle f(k_1)f(k_2)f(k_3)\rangle = 0$]. Let us determine the contribution to the matter power spectrum of a nth-order overdensity field $\delta^{(n)}$ correlated with a n'th-order overdensity field $\delta^{(n')}$. Given that $\delta^{(n)} \sim (\delta^{(1)})^n$ and that $\delta^{(1)}$ is a Gaussian random field, $n+n'$ must be even to contribute to the matter power spectrum, otherwise it would involve an correlation of an odd number of $\delta^{(1)}$. At the end of the day, the non-zero contributions to the matter power spectrum can be expressed as

$$P_{nn'}(k)\delta_D^{(3)}(k-k') = (2\pi)^{-3}\left\langle \delta^{(n)}(k)\delta^{(n')}(k')\right\rangle \quad ; \quad n+n' = 2,4,6,... \tag{3.116}$$

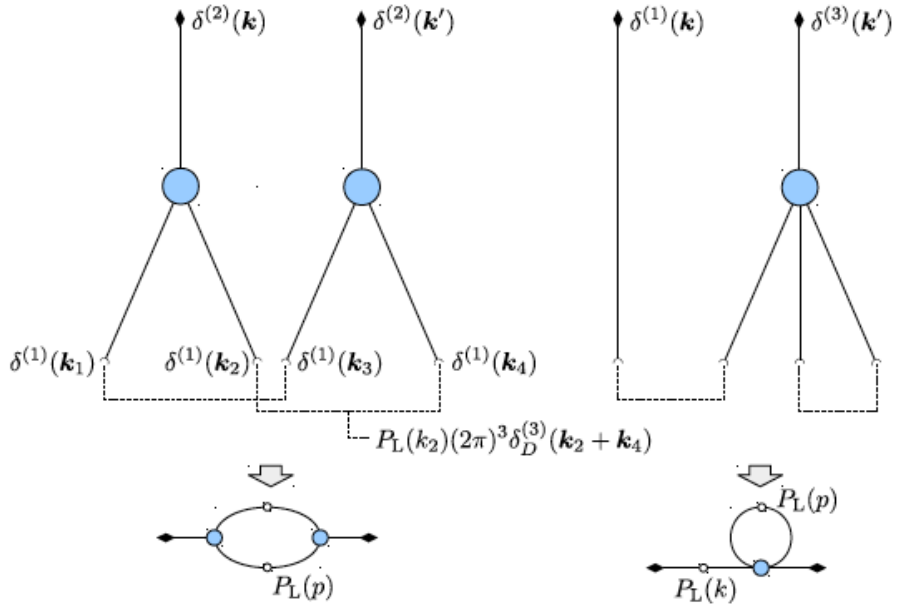

Figure 3.12: Diagrams showing the construction of the NLO contributions to the matter power spectrum. The diagram on the left represents the contraction of $\delta^{(2)}$ with $\delta^{(2)}$ that leads to P_{22}, while the diagram on the right represents the contraction of $\delta^{(1)}$ with $\delta^{(3)}$ that leads to P_{13}. Note that we have two different possibilities of constructing P_{22}, while we have three different possibilities of constructing P_{13}. $P_{\rm L}$ corresponds to what we call P_{11} in the main text. Finally, the bottom diagrams correspond to a condensed form of the top diagrams where the free fields have been connected. Each loop corresponds to an integral over the wavevector $\boldsymbol{p}$ [see Eqs. (3.119) and (3.120)]. Taken from Ref. [9].

On the other hand, we are interested here in the *next-to-leading order* (NLO) correction to the matter power spectrum, where the leading order corresponds to the linear matter power spectrum as previously determined, namely

$$P_{11}(k)\delta^3(k-k') = (2\pi)^{-3}\left\langle \delta^{(1)}(k)\delta^{(1)}(k')\right\rangle , \tag{3.117}$$

where the subscript "11" indicates that we have correlated $\delta^{(1)}$ with $\delta^{(1)}$. In the language of quantum field theory, this corresponds to the *tree-level* contribution to the matter power spectrum, *i.e.*, the contraction between two free fields. Consequently, the NLO contribution must satisfy the condition $n+m=4$, in order to obtain $P_{\rm NLO} \sim \left\langle (\delta^{(1)})^4 \right\rangle$. [3] There are two ways of doing this: either we can contract $\delta^{(2)}$ with $\delta^{(2)}$, which corresponds to the P_{22} contribution, or we can contract $\delta^{(1)}$ with $\delta^{(3)}$, which corresponds to the P_{13} contribution, as shown in Fig. 3.12. The aim is to always contract the free fields with each other to form pairs, and each of these pairs then corresponds to a linear power spectrum P_{11}, implying that $P_{\rm NLO} \sim P_{11}^2$. These contractions lead to loop Feynmann diagrams (see Fig. 3.12), and this is why the NLO power spectrum is referred to as the *one-loop power spectrum*. Finally, by adding the NLO contribution, we obtain

$$P_m(k,\tau) = P_{11}(k,\tau) + P_{22}(k,\tau) + 2P_{13}(k,\tau)\,, \tag{3.118}$$

[3] Let us note that the *next-to-next-to leading order* (NNLO) contribution is obtained through $n+n'=6$.

where the factor 2 in front of P_{13} corresponds to a symmetry factor (since $P_{13} = P_{31}$), and where

$$P_{22}(k,\tau) = 2\int \frac{d^3p}{(2\pi)^3}\left[F_2(\boldsymbol{p},\boldsymbol{k}-\boldsymbol{p})\right]^2 P_{11}(p,\tau)P_{11}(|\,\boldsymbol{k}-\boldsymbol{p}\,|,\tau)\,, \tag{3.119}$$

$$P_{13}(k,\tau) = 3P_{11}(k,\tau)\int \frac{d^3p}{(2\pi)^3}F_3(\boldsymbol{p},-\boldsymbol{p},\boldsymbol{k})P_{11}(p,\tau)\,. \tag{3.120}$$

Let us note that these integrals can only be computed numerically because (as we have seen) the linear matter power spectrum has no simple analytical expression that is valid for all scales and all periods. As indicated in Fig. 3.12, each loop corresponds to an integral over the wavevector $\boldsymbol{p}$ (as in quantum field theory), explaining why $P_{22} \sim \int P_{11}^2$ and $P_{13} \sim P_{11}\int P_{11}$. According to Fig. 3.12, this implies that $P_{22}(k,\tau)$ allows us to describe how two short-scale modes, namely $\boldsymbol{k}$ and $\boldsymbol{p}-\boldsymbol{k}$, generate a large-scale mode $\boldsymbol{k}$, while $P_{13}(k,\tau)$ is used to quantify the modification of the matter power spectrum determined at a given $\boldsymbol{k}$ mode by a short-scale modes $\boldsymbol{p}$ (in the limit where $\boldsymbol{k} \ll \boldsymbol{p}$). Here are the steps for obtaining Eqs. (3.119) and (3.120):

1. Insert the solutions of $\delta_{(1)}$, $\delta_{(2)}$ and $\delta_{(3)}$ from Eq. (3.113) into Eq. (3.116) to get P_{22} and P_{13}.

2. Use the *Wick's theorem*, which states that the n-point correlation function is obtained through all terms involving all possible combinations of the n fields into two-point correlation functions. Therefore, the Fourier transform of the four-point correlation function reads

$$\begin{aligned}\langle\delta_0(\boldsymbol{k}_1)\delta_0(\boldsymbol{k}_2)\delta_0(\boldsymbol{k}_3)\delta_0(\boldsymbol{k}_4)\rangle =&(2\pi)^6\delta_D^{(3)}(\boldsymbol{k}_1-\boldsymbol{k}_2)\delta_D^{(3)}(\boldsymbol{k}_3-\boldsymbol{k}_4)P(k_1)P(k_3)\\ &+(2\pi)^6\delta_D^{(3)}(\boldsymbol{k}_1-\boldsymbol{k}_3)\delta_D^{(3)}(\boldsymbol{k}_2-\boldsymbol{k}_4)P(k_1)P(k_2)\\ &+(2\pi)^6\delta_D^{(3)}(\boldsymbol{k}_1-\boldsymbol{k}_4)\delta_D^{(3)}(\boldsymbol{k}_2-\boldsymbol{k}_3)P(k_1)P(k_2)\,.\end{aligned} \tag{3.121}$$

3. Evaluate the different possibilities of constructing P_{22} and P_{13}. From Fig. 3.12, one can see that one has two different possibilities of constructing P_{22}, and three different possibilities of constructing P_{13}. This is the origin of the prefactors in Eqs. (3.119) and (3.120).

The perturbation theory breaks down when the NLO contribution becomes similar to that of the tree-level. To estimate the scale from which this theory is no longer valid, we can consider the following quantity (using the fact that the kernels are of the order of unity):

$$\frac{P_{\rm NLO}}{P_{11}} \sim \int \frac{d^3p}{(2\pi)^3}P_{11}(p) = \int_0^{\ln k} d\ln p\,\mathscr{P}(p)\,, \tag{3.122}$$

which is nothing more the variance of the linear matter power spectrum until the k mode (we integrate until $\ln k$ because the kernels are suppressed for $k > p$). This quantity is very approximately similar to the quantity used to determine $k_{\rm NL}(a=a_0) \sim 0.25h{\rm Mpc}^{-1}$ [see Eq. (3.76)]. Therefore, the one-loop perturbation theory breaks down around the non-linear scale. Finally, to close this section, it should be noted that the main effect of the standard perturbation theory with respect to the linear theory is an enhancement of the power spectrum at small scales, and that this enhancement becomes more and more pronounced as the scale decreases (see Fig. 3.13).

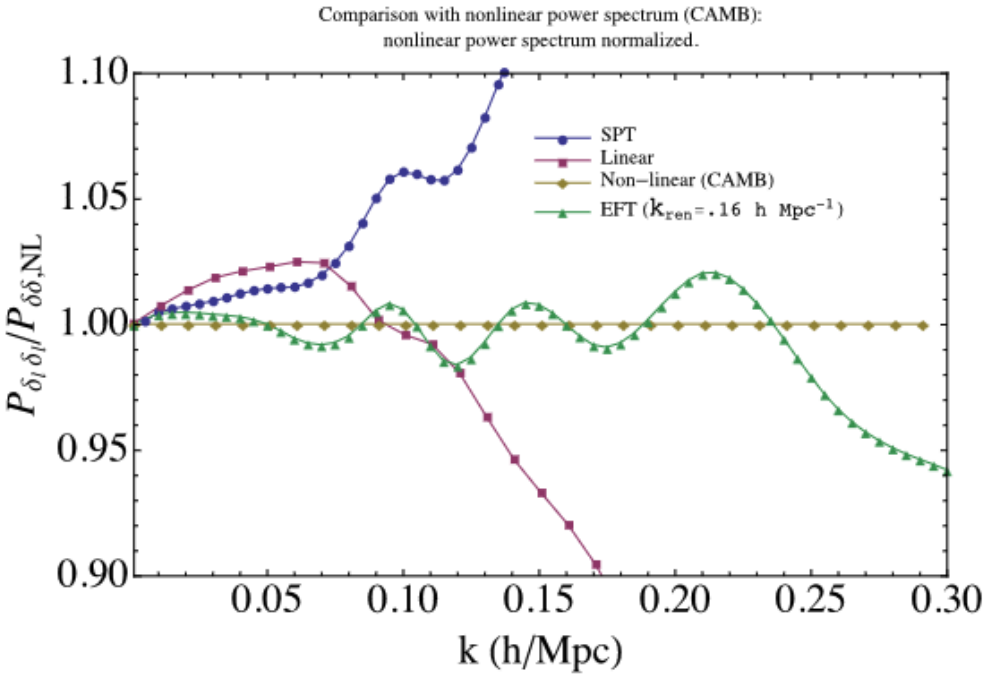

Figure 3.13: Comparison between the matter power spectrum obtained from the linear theory (see Sec. 3.1), the standard perturbation theory referred to as "SPT" (see Sec. 3.3), the effective field theory of large-scale structures (see Sec. 3.4), and from an Nbody simulation incorporated in the CAMB code [44] referred to as "Non-linear (CAMB)" in the figure. All these predictions are normalised to that of the Nbody simulation, used here as a reference. Taken from Ref. [54].

3.4 The effective field theory of large-scale structures

In the previous section, we presented a perturbative method for obtaining a (mildly) non-linear equation of the matter power spectrum at the NLO (or one-loop) order. Although this method is a decisive first step in obtaining an accurate non-linear matter power spectrum formulation, it suffers from a number of inconsistencies that lead to a very imprecise description of the large-scale structure data. As shown in Fig. 3.13, the standard perturbation theory prediction is very far from the Nbody prediction, and it turns out that the matching is just as bad as for linear theory! In this section, we therefore consider a theory, the *effective field theory of large-scale structures* (EFTofLSS), that corrects the inaccuracies of the standard perturbation theory. Fig. 3.13 shows that the EFTofLSS prediction agrees with the Nbody prediction at percent level up to $k \simeq 0.25h\text{Mpc}^{-1}$.

3.4.1 The basics of EFTofLSS

We now need to understand the main issues of the standard perturbation theory that need to be overcome in order to obtain an accurate description of the matter power spectrum. We identify here three problems of the standard perturbation theory:

1. **No well-defined expansion parameter.** In the standard perturbation theory there is no well-defined expansion parameter, in the sense that the expansion parameter used, namely δ, can be arbitrarily large. When this is the case, at small scales, linear theory is

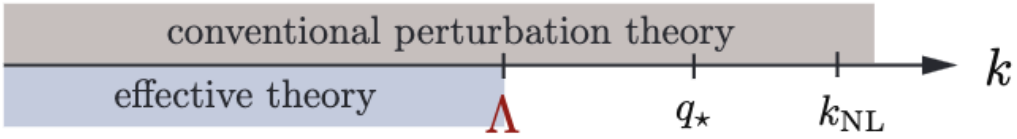

Figure 3.14: Summary of the different scales considered in the EFTofLSS. Standard perturbation theory includes the non-linear modes that break down the perturbative expansion, whereas the EFTofLSS only considers the $k < \Lambda$ modes in the loop integrals. Taken from Ref. [55].

no longer at all well defined and expansion around this solution becomes inappropriate (in the sense that we can obtain inconsistencies such as $\delta^{(2)} > \delta^{(1)}$).

2. **Ideal fluid approximation.** In standard perturbation theory, we assume that cold dark matter behaves like an ideal fluid. Remember that for dark matter, we have set the pressure to zero, which implies that the dark matter stress-energy tensor $T^c_{\mu\nu} = \mathrm{diag}\,[-\overline{\rho}_c(\boldsymbol{x},t),0,0,0]$. In addition, let us recall that at linear order, the general Euler's equation is written in the following form [see Eq. (2.46)]:

$$\dot{\theta} = -\frac{\dot{a}}{a}(1-3\omega)\theta - \frac{\dot{\omega}}{1+\omega}\theta + \frac{\delta P/\delta\rho}{1+\omega}k^2\delta - k^2\sigma + k^2\psi\,. \tag{3.123}$$

By setting $P = w = 0$, we obtained $\dot{\theta}_c = -\frac{\dot{a}}{a}\theta_c + k^2\psi$ at linear order. In particular, in the Euler's equation, we have neglected the contribution of the stress tensor (the spatial part of the stress-energy tensor), which encodes the pressure forces, in order to set the $\delta P/\delta\rho = c_s^2$ term to zero. This term, however, was not set to zero for baryons because at very small scales we could not neglect the baryon pressure caused by Thomson scattering. However, for our system, it is not possible to neglect the contribution of the dark matter stress tensor at small scales (as was the case for baryons in CMB physics). It is therefore necessary to introduce generalised pressure forces, which do not come from the usual pressure of a gas composed of colliding atoms, but correspond to effective gravitational effects created by small-scale perturbations. At very small scales, under the effect of gravity, dark matter particles virialize to form bound structures. This happens at $R_{\rm vir} \sim 3h^{-1}\,$Mpc, which corresponds to the typical size of a virialized halo. It is therefore crucial to take into account the UV displacements (*i.e.*, the small-scale displacements) due to the virialization of dark matter particles, which standard perturbation theory does not do. In other words, we obtain an enhancement of the matter power spectrum when we do not take this effect into account, insofar as this effect suppresses the displacement of the dark matter particles that are confined in the halos (see below).

3. **Integration over UV modes.** The last problem stems from the previous one: since we are not able to adequately capture UV physics, then it is not adequate to integrate the one-loop terms over UV modes. In particular, the loop integrals of Eqs. (3.119) and (3.120) are evaluated up to infinity, and therefore integrate over modes of the non-linear regime, where the fluid description breaks down.

All these elements imply that this perturbative theory does not converge: in particular, the two-loop term is of the same order of magnitude as the one-loop term, while the three-loop

term is larger than the two-loop term! We now show how it is possible to solve these issues with the effective field theory of large-scale structures, in order to avoid the break down of the (relevant) theory.

Solution to the first issue: the cutoff scale

To solve the first problem, the EFTofLSS proposes to make a substantial distinction between short-scale modes δ_s and long-scale modes δ_l, by separating them using a cutoff scale Λ:

$$\delta(\boldsymbol{k}) = \delta_l(\boldsymbol{k}) + \delta_s(\boldsymbol{k}), \tag{3.124}$$

$$\delta_l(\boldsymbol{k}) = \delta(\|\boldsymbol{k}\| < \Lambda^{-1}) \quad ; \quad \delta_s(\boldsymbol{k}) = \delta(\|\boldsymbol{k}\| > \Lambda^{-1}). \tag{3.125}$$

The cutoff scale is chosen according to two criteria. First, it must be chosen in such a way that the δ_l modes are always small, namely $\delta_l \lesssim \mathscr{O}(1)$ for $k \lesssim \Lambda^{-1}$, so that we can continue to work in a perturbative framework. Knowing that at the approach of the non-linear scale $k_{\rm NL}$, δ starts to be significantly large, it is necessary to adopt a cutoff scale which respects the condition $\Lambda^{-1} \lesssim k_{\rm NL}$. We are therefore going to solve the Vlasov-Poisson system only for δ_l, which cannot be arbitrarily large (in contrast to standard perturbation theory). We will therefore smooth the Vlasov equation and solve it only for the long-scale modes. Second, we want to build an effective field theory, namely we want to describe large-scale physics by capturing all the relevant degrees of freedom from small-scale physics. The small-scale modes will be integrated out in order to obtain a description of the large-scale physics which will depend on the UV physics through several couplings. To achieve this, the cutoff scale must be chosen from the scale at which the microphysics effects become significant. As we explained when we introduced the second problem of the standard perturbation theory, dark matter can no longer be treated as an ideal fluid from the scale where we have a virialization of dark matter particles, *i.e.*, at $R_{\rm vir}$. This suggests that the cutoff scale is chosen such that $\Lambda \sim \mathscr{R}_{\rm vir} \sim 3h^{-1}\,{\rm Mpc}$. On the other hand, the non-linear scale $k_{\rm NL}$ (which is not the same as the one defined in standard perturbation theory) in EFTofLSS has a very specific physical origin: it is the characteristic distance travelled by a dark matter particle since the primordial instants. We expect the physics to become non-linear below $1/k_{\rm NL}$ insofar as these scales are subjected to physical effects that no longer derive from the physics of large-scale structures. Therefore, we take $1/k_{\rm NL} \sim vH^{-1}$, where v is the (non-relativistic) speed of a dark matter particle, leading to $k_{\rm NL} \sim 0.7h\,{\rm Mpc}^{-1}$. Fig. 3.14 summarises these different scales and the benefits of introducing the cutoff scale Λ compared to the standard perturbation theory.

We therefore need to define a *smoothing function* in order to smooth out the observables when $k > \Lambda^{-1}$. To do so, we define the *Gaussian smoothing* as

$$W_\Lambda(\boldsymbol{x}) = \left(\frac{\Lambda}{\sqrt{2\pi}}\right)^3 e^{-\frac{1}{2}\Lambda^2 x^2}, \tag{3.126}$$

$$W_\Lambda(\boldsymbol{k}) = e^{-\frac{1}{2}\frac{k^2}{\Lambda^2}}. \tag{3.127}$$

In Fourier space, we can check that $W \to 1$ when $k \ll \Lambda^{-1}$, implying that the large-scale modes are not affected by this smoothing function. In real space, all observables are then smoothed by a convolution with the Gaussian smoothing, such that

$$\mathscr{O}_l(\boldsymbol{x},\tau) = [\mathscr{O}]_\Lambda(\boldsymbol{x},\tau) = \int d^3x' W_\Lambda(\boldsymbol{x}-\boldsymbol{x}')\mathscr{O}(\boldsymbol{x}',\tau). \tag{3.128}$$

This equation is used to define δ_l in Eq. (3.124). This procedure also allows us to smooth the other quantities that enter the Vlasov equation such that

$$\frac{df}{dt} \to \left[\frac{df}{dt}\right]_\Lambda . \tag{3.129}$$

It is interesting to note at this point that each higher-order of the Vlasov equation is suppressed by $k/k_{\rm NL}$, given that each moment adds a contribution of order $(v^i/H)\partial^i \sim (1/k_{\rm NL})k$ compared to the previous moment.

Solution to the second issue: The EFT Vlasov-Poisson system

We therefore solve the Vlasov-Poisson system only for the long-scale modes δ_l. However, it is necessary to incorporate the small-scale physics, induced by δ_s, in order to determine its impact on the large-scale physics. This also leads us to solve our second problem, by introducing a (effective) stress tensor τ^{ij} to encode the (generalized) pressure forces induced by the virialization of dark matter particles. The system under consideration is then (see Ref. [54])

$$\dot{\delta}_l + \theta_l = -\delta\theta_l - v^j\partial_j\delta_l\,, \tag{3.130}$$

$$\dot{\theta}_l + aH\theta_l + \nabla^2\psi_l = -v^j\partial_j\theta_l - \partial_i v_l^j\cdot\partial_j v_l^i - \partial_j\left(\frac{1}{\rho_l}\partial_i\left[\tau^{ij}\right]_\Lambda\right), \tag{3.131}$$

$$\nabla^2\psi_l = \frac{3}{2}\Omega_m(a)(aH)^2\delta_l\,, \tag{3.132}$$

where we have highlighted in bold the new contribution from the effective stress tensor. This system does depend on the long-scale modes (solution to the first problem) and includes the contribution from the spatial part of the stress-energy tensor coming from the UV physics (solution to the second problem). This contribution is a generalisation of the $c_s^2k^2\delta$ term in Eq. (3.123). The stress tensor induced by the short-scale fluctuations is also smooth out, and is defined as

$$[\tau^{ij}]_\Lambda = k_l^{ij} + \Phi_l^{ij}\,, \tag{3.133}$$

where k_l^{ij} and Φ_l^{ij} are respectively the *kinetically-induced* and the *gravitationally-induced* contributions to this tensor, defined as (see Ref. [54])

$$k_l^{ij} = \sigma_l^{ij} - \rho_l v_l^i v_l^j\,, \tag{3.134}$$

$$\Phi_l^{ij} = -\frac{1}{8\pi G a^2}\left[w_l^{kk}\delta^{ij} - 2w_l^{ij} - \partial_k\phi_l\partial^k\phi_l\delta^{ij} + 2\partial^i\phi_l\partial^j\phi_l\right]. \tag{3.135}$$

The w_l^{ij} smooth tensor has the following form

$$w_l^{ij}(\vec{x}) = \int d^3x' W_\Lambda(\vec{x}-\vec{x}')\left[\partial^i\phi(\vec{x}')\partial^j\phi(\vec{x}') - \sum_n \partial^i\phi_n(\vec{x}')\partial^j\phi_n(\vec{x}')\right]. \tag{3.136}$$

In this equation, we consider all the terms allowed by the symmetries of general relativity, *i.e.*, the rotation symmetry and the equivalence principle. Note that because of this second symmetry, we cannot have terms $\propto \phi$ and $\propto \partial_i\phi$ in the stress-energy tensor (since these quantities can be eliminated by a change of gauge).

So now we have an effective dark matter fluid obtained by considering only large-scale modes with small perturbations. However, the dynamics of this effective fluid depends on a stress tensor which encodes the microphysics, and we need to integrate out the UV physics in order to get rid of any explicit dependence on δ_s. To do so, and since we have smoothed out the effective stress tensor, we can perform a first-order Taylor expansion in δ_l:

$$\langle [\tau^{ij}]_\Lambda \rangle_{\delta_l} = \langle [\tau^{ij}]_\Lambda \rangle_0 + \left. \frac{\partial \langle [\tau^{ij}]_\Lambda \rangle_{\delta_l}}{\partial \delta_l} \right|_0 \delta_l + \dots , \tag{3.137}$$

where we can show that at linear order it takes the following form (see Ref. [55])

$$\langle [\tau^{ij}]_\Lambda \rangle_{\delta_l} = \overline{P}\delta^{ij} + \overline{\rho}\left[c_s^2 \delta_l \delta^{ij} - \frac{c_{bv}^2}{Ha}\delta^{ij}\partial_k v_l^k - \frac{3}{4}\frac{c_{sv}^2}{Ha}\left(\partial^j v_l^i + \partial^i v_l^j - \frac{2}{3}\delta^{ij}\partial_k v_l^k \right) \right] + \Delta\tau^{ij} + \dots . \tag{3.138}$$

The first term corresponds to the large-scale effective background pressure generated by small-scale fluctuations, while the term in $c_s^2 \rho \delta_l$ corresponds to the equivalent of the sound speed term mentioned above. The parameters c_{bv} and c_{sv} are two coefficients related to the viscosity of the fluid. In particular, $c_{bv}^2 = \zeta H/\rho_b$ and $c_{sv} = \eta 4H/(3\rho_b)$, where ζ and η are respectively the bulk and the shear viscosity. Finally, one adds a stochastic component $\Delta\tau^{ij}$. The physical origin of this term is the following: small-scale physics is not entirely correlated with large-scale physics, insofar as it depends on underlying physical processes that do not depend on large-scale physics (as is the case with virialization, for example). This term therefore encodes the difference between the actual value of the effective stress energy tensor and its expectation value. We have then the following properties: $\langle \delta_l \Delta\tau^{ij} \rangle = 0$, since $\Delta\tau^{ij}$ is not correlated with δ_l. Let us note that if we remove this term, one obtains the standard Navier-Stokes equations. All these coefficients in the effective stress tensor (namely P, c_s, c_{bv} and c_{sv}) depend on the small-scale physics, as well as the cutoff scale Λ, and cannot therefore be determined with the EFTofLSS itself. However, these parameters can be measured with an Nbody simulation, and Ref. [54] explains how to extract the value of these coefficients from such a simulation.

Solution to the third issue: the loop integral cut-off

Solving the third problem follows directly from solving the first. To avoid integrating UV modes, the EFTofLSS only considers the $k < \Lambda^{-1}$ modes in the loop integrals (unlike the standard perturbation theory), as shown in Fig. 3.14. To do so, we are going to consider the *smoothed power spectrum* in standard perturbation theory loop integrals [see Eqs. (3.119) and (3.120)]:

$$P_{11,l}(k,\tau,\Lambda) = W^2(k) P_{11}(k,\tau) , \tag{3.139}$$

in order to perform this cutoff. Let us finally note that the one-loop matter power spectrum will depend on Λ, insofar as all the smooth variables depend on this quantity. The dependence on Λ will be eliminated thanks to counterterms, as we shall see later.

3.4.2 The EFTofLSS matter power spectrum

Having presented the conceptual basis of the EFTofLSS, and in particular the main differences with the standard perturbation theory, we can now determine the matter power spectrum

obtained using this theory. One can Fourier transform Eqs. (3.130) and (3.131) exactly as we did with standard perturbation theory. By injecting Eq. (3.138) in Eq. (3.131), we find

$$\dot{\delta}_l^{(2)} + \theta_l^{(2)} = \int \frac{d^3k_1}{(2\pi)^3} \int \frac{d^3k_2}{(2\pi)^3} (2\pi)^3 \delta_D^{(3)}(\boldsymbol{k} - \boldsymbol{k}_1 - \boldsymbol{k}_2) \times aHfD_+^2 \left[1 + \frac{\boldsymbol{k}_1 \cdot \boldsymbol{k}_2}{k_1^2}\right] \delta_{0,l}(\boldsymbol{k}_1) \delta_{0,l}(\boldsymbol{k}_2)\,, \tag{3.140}$$

$$\dot{\theta}_l^{(2)} + aH\theta_l^{(2)} + \frac{3}{2}\Omega_m(a)(aH)^2\delta_l^{(2)} = -\int \frac{d^3k_1}{(2\pi)^3} \int \frac{d^3k_2}{(2\pi)^3} (2\pi)^3 \delta_D^{(3)}(\boldsymbol{k} - \boldsymbol{k}_1 - \boldsymbol{k}_2) \times (aHfD_+)^2 \left[\frac{\boldsymbol{k}_1 \cdot \boldsymbol{k}_2}{k_1^2} + \frac{(\boldsymbol{k}_1 \cdot \boldsymbol{k}_2)^2}{k_1^2 k_2^2}\right] \delta_{0,l}(\boldsymbol{k}_1) \delta_{0,l}(\boldsymbol{k}_2) + c_s^2 k^2 \delta_l^{(1)} - \frac{c_v^2 k^2}{aH} \theta_l^{(1)}\,, \tag{3.141}$$

where $c_v^2 = c_{sv}^2 + c_{bv}^2$. For the moment we neglect the contribution of the stochastic parameter $\Delta\tau^{ij}$, but we shall come back to that later. We can easily see that Eqs. (3.140) and (3.141) are equivalent to Eqs. (3.98) and (3.99) of the standard perturbation theory in the limit where $c_s^2 = c_v^2 = 0$ and $\delta_l^{(2)} \to \delta^{(2)}$. The additional difficulty compared with Eqs. (3.98) and (3.99) is that the parameters c_s^2 and c_v^2 are now time-dependent. Let us now talk about the pressure terms in Eq. (3.141). The term $\propto c_s^2$ is the sound speed term, which is equivalent to the term in the Euler's equation for baryons [see Eq. (2.52)], while the term $\propto c_v^2$ is the viscosity term. We are going to solve these terms perturbatively, in the same way as we solved the non-linear terms in standard perturbation theory. Since the large-scale Vlasov equations at linear order do not include these terms, then we inject the linear solutions $\delta_l^{(1)}$ and $\theta_l^{(1)}$ into these terms. In addition, using the fact that $\theta^{(1)} = -aHf\delta^{(1)}$ [see Eq. (3.94)], we can rewrite the stress tensor contribution of Eq. (3.141) as

$$c_s^2 k^2 \delta_l^{(1)} - \frac{c_v^2 k^2}{aH} \theta_l^{(1)} = \left[c_s^2 + f c_v^2\right] k^2\, \delta_l^{(1)} = c_{\rm comb}^2(a)\, k^2\, D_+(a) \delta_{0,l}(\boldsymbol{k})\,, \tag{3.142}$$

where we have defined

$$c_{\rm comb}^2(a) = c_s^2(a) + f\, c_v^2(a)\,. \tag{3.143}$$

This parameter is the relevant combination of c_s^2, c_{bv}^2 et c_{sv}^2 at one-loop order. Finally, the resulting term of Eq. (3.142) is treated perturbatively with respect to the solution of the standard perturbation theory (SPT), such that we now perform the following expansion:

$$\delta_{m,l} = \underbrace{\delta_l^{(1)}}_{\text{Tree-level}} + \underbrace{\delta_l^{(2)} + \delta_l^{(3)}}_{\text{One-loop SPT}} + \underbrace{\delta_l^{(c_{\rm comb}^2)}}_{\text{EFT contribution}} + \ldots\,. \tag{3.144}$$

Finally, we already know the solutions of the first three elements, where $\delta_l^{(2)}$ and $\delta_l^{(3)}$ have simply been smoothed with respect to the standard perturbation theory solution. In addition, the solution for $\delta_l^{(c_{\rm comb}^2)}$ reads [54]

$$\delta_l^{(c_{\rm comb}^2)}(k,a) = -k^2 \int_0^a d\tilde{a}\, G(a,\tilde{a},\Lambda)\, c_{\rm comb}^2(\tilde{a},\Lambda)\, D_+(\tilde{a})\, \delta_{0,l}(\boldsymbol{k})\,, \tag{3.145}$$

where $G(a,\tilde{a})$ is the density Green function for the second order linear differential operator. It is necessary to introduce this function because the $c^2_{\rm comb}(a)$ parameter depends on the scale factor! In reality, we would have had to do the same for $\delta_l^{(2)}$ and $\delta_l^{(3)}$ if we had not set $\Omega_m(a)/f(a)^2 = 1$ in Eq. (3.102). In this equation, all the functions that multiplied $\delta_l^{(2)}$ did not depend on time, implying that in a universe that is not Einstein-de-Sitter, *i.e.*, with $\Omega_m(a)/f(a)^2 \neq 1$, then the solutions of $\delta_l^{(2)}$ and $\delta_l^{(3)}$ also depend on the density Green function.

At the end of the day, by analogy with Eq. (3.118), the EFT one-loop matter power spectrum reads

$$P_m(k,\tau) = P_{11}(k,\tau) + P^{\Lambda}_{22}(k,\tau) + 2P^{\Lambda}_{13}(k,\tau) + 2P^{\Lambda}_{c^2_{\rm comb}}(k,\tau)\,, \tag{3.146}$$

where $P^{\Lambda}_{22}(k,\tau)$ + $P^{\Lambda}_{13}(k,\tau)$ are the same as those of the standard perturbation theory, namely Eqs. (3.119) and (3.120), with the only difference is that we now integrate the smooth matter power spectrum, which means that we only integrate over the $p < \Lambda$ modes. The new contribution to the matter power spectrum, which comes from the EFT theory, is defined (at leading order) by

$$P^{\Lambda}_{c^2_{\rm comb}}(k,\tau)\delta^3_D(k-k') = (2\pi)^{-3}\left\langle \delta_l^{(c^2_{\rm comb})}(k,\tau)\delta_l^{(1)}(k',\tau)\right\rangle, \tag{3.147}$$

leading to the following solution [using Eq. (3.145)]

$$\begin{aligned} P^{\Lambda}_{c^2_{\rm comb}}(k,a)\delta^3_D(k-k') &= -\frac{1}{(2\pi)^3}k^2 D_+(a)\left[\int_0^a d\tilde{a}\, G(a,\tilde{a})\, c^2_{\rm comb}(\tilde{a},\Lambda)\, D_+(\tilde{a})\right]\left\langle \delta_{0,l}(\boldsymbol{k})\delta_{0,l}(\boldsymbol{k}')\right\rangle \\ P^{\Lambda}_{c^2_{\rm comb}}(k,\tau) &\equiv -c^2_{s,\rm eff}(a,\Lambda)\, k^2 P_{11}(k,\tau)\,, \end{aligned} \tag{3.148}$$

where $c^2_{s,\rm eff}(a,\Lambda)$ is often referred to as *effective sound speed*. First, note that the factor two in Eq. (3.146) in front of $P^{\Lambda}_{c^2_{\rm comb}}(k,\tau)$ comes from the fact that Eq. (3.147) is symmetric by an inversion of $\delta_l^{(c^2_{\rm comb})}$ and $\delta_l^{(1)}$. Second, the contribution of $P^{\Lambda}_{c^2_{\rm comb}}(k,\tau)$ is negative, since c_s^2 and c_v^2 suppress the gravitational collapse, which reduces the clustering of matter on at small scales. This additional term therefore suppresses the matter power spectrum at small scales, as expected form Fig. 3.13.

We now need to deal with one final issue: the Λ-dependence of Eq. (3.146). Let us recall that $P^{\Lambda}_{22}(k,\tau)$ and $P^{\Lambda}_{13}(k,\tau)$ depend on Λ through the smoothing of the linear matter power spectrum $P_{11,l}(k,\tau,\Lambda)$, while $P^{\Lambda}_{c^2_{\rm comb}}(k,\tau)$ depends on Λ through the parameter $c^2_{\rm comb}$ (since we have integrated out the small-scale modes). It is therefore necessary to remove any dependency on Λ (which is just a calculation artefact). Let us first consider the term $P^{\Lambda}_{13}(k,\tau)$. According to Refs. [56, 57], we separate the loop integral of this term into two parts:

$$\begin{aligned} P^{\Lambda}_{13}(k,\tau) = 3\,P_{11}(k,\tau)&\int_0^{p_{\rm trust}}\frac{d^3p}{(2\pi)^3}F_3(\boldsymbol{p},-\boldsymbol{p},\boldsymbol{k})P_{11}(p,\tau) \\ &+3\,P_{11}(k,\tau)\int_{p_{\rm trust}}^{\Lambda}\frac{d^3p}{(2\pi)^3}F_3(\boldsymbol{p},-\boldsymbol{p},\boldsymbol{k})P_{11}(p,\tau)\,. \end{aligned} \tag{3.149}$$

Remember that integrating over the smooth matter power spectrum is equivalent to integrating the usual matter power spectrum up to Λ. Therefore, in the previous equation, if we carry out the $\Lambda \to \infty$ limit, we find exactly the equation of the standard perturbation theory [see Eq. (3.120)]. Here, we have created an artificial separation between a part which is integrated up to a mode of trust $p_{\rm trust}$ (*i.e.*, this integral is carried out over scales which EFT is known to be valid), and an integral which depends on Λ and can potentially incorporate UV modes. The final result must not depend on Λ, insofar as the value of Λ must not affect the total matter power spectrum. It follows that we must then remove this integral, *i.e.*, $P_{13}^{\Lambda}(k,\tau)$ must be renormalized. To simplify the problem, let us assume that $p_{\rm trust} \gg k$ (in other words, we compute the matter power spectrum for a k mode which is on a much larger scale than that of $p_{\rm trust}$), which implies that (according to Refs. [56, 57]):

$$3P_{11}(k,\tau)\int_{p_{\rm trust}\gg k}^{\Lambda}\frac{d^3p}{(2\pi)^3}F_3(\boldsymbol{p},-\boldsymbol{p},\boldsymbol{k})P_{11}(p,\tau) = -\frac{61}{630\pi^2}k^2P_{11}(k,\tau)\int_{p_{\rm trust}\gg k}^{\Lambda}dp\,P_{11}(p,\tau)\,, \tag{3.150}$$

which is the UV limit of $P_{13}^{\Lambda}(k,\tau)$ which may possibly diverge. Remarkably, this UV limit has the same k-dependence as $P^{\Lambda}_{c^2_{\rm comb}}(k,\tau)$ [see Eq. (3.148)], which makes this quantity a good candidate for renormalizing $P_{13}^{\Lambda}(k,\tau)$. This implies that we can intuitively represent $P^{\Lambda}_{c^2_{\rm comb}}(k,\tau)$ as an interaction between $\delta^{(1)}$ and $\delta^{(3)}$ that renormalizes $P_{13}^{\Lambda}(k,\tau)$, as shown in Fig. 3.15. We can then separate the parameter $c^2_{s,\rm eff}(a,\Lambda)$ of Eq. (3.148) into two contributions: a contribution which does not depend on Λ and which constitutes a renormalization parameter, and a counterterm which depends on Λ:

$$c^2_{s,\rm eff}(a,\Lambda) = c^2_{s,\rm eff\,ren}(a,p_{\rm trust}) + c^2_{s,\rm eff\,ctr}(a,\Lambda)\,, \tag{3.151}$$

where the second contribution must necessarily cancel out the UV contribution of $P_{13}^{\Lambda}(k,\tau)$, namely:

$$c^2_{s,\rm eff\,ctr}(a,\Lambda) = -\frac{61}{630\pi^2}\int_{p_{\rm trust}\gg k}^{\Lambda}dp\,P_{11}(p,\tau)\,. \tag{3.152}$$

Finally, the contribution $2P_{13}^{\Lambda}(k,\tau) + 2P^{\Lambda}_{c^2_{\rm comb}}(k,\tau) = 2P_{13}^{\Lambda}(k,\tau) - 2c^2_{s,\rm eff}k^2P_{11}(k,\tau)$ in Eq. (3.146) no longer depends on Λ, implying that the $c^2_{s,\rm eff}$ parameter renormalizes $P_{13}^{\Lambda}(k,\tau)$. The parameter $c^2_{s,\rm eff\,ren}(a,p_{\rm trust})$ is finite and does not depend on the value of Λ (even if $\Lambda \to \infty$), while the other contribution is cancelled. This contribution to the effective sound speed must either be fitted to the data or extracted from the Nbody simulations. In the remainder of this thesis we will focus on the first method.

Finally, the last quantity that needs to be renormalised is $P_{22}^{\Lambda}(k,\tau)$. This renormalization is performed with the stochastic parameter $\Delta\tau^{ij}$ introduced into the effective stress tensor in Eq. (3.138). As already indicated, this term is not correlated with δ_l, which implies that $\langle\delta_l\Delta\tau^{ij}\rangle = 0$. The only contribution of this term to the matter power spectrum therefore comes from its self-correlation. It is then necessary to add a new stochastic contribution $\delta_l^{(\rm stoch)}$ to Eq. (3.144), which scales at $k^2\Delta\tau^{ij}$ [we can easily see it by injecting the $\Delta\tau^{ij}$ contribution of Eq. (3.138) into Eq. (3.131)]. Consequently, the new contribution to the matter power spectrum in Eq. (3.146) is

$$P^{\Lambda}_{\rm stoch}(k,\tau)\delta_D^3(k-k') = (2\pi)^{-3}\left\langle\delta_l^{(\rm stoch)}(k,\tau)\delta_l^{(\rm stoch)}(k',\tau)\right\rangle\,, \tag{3.153}$$

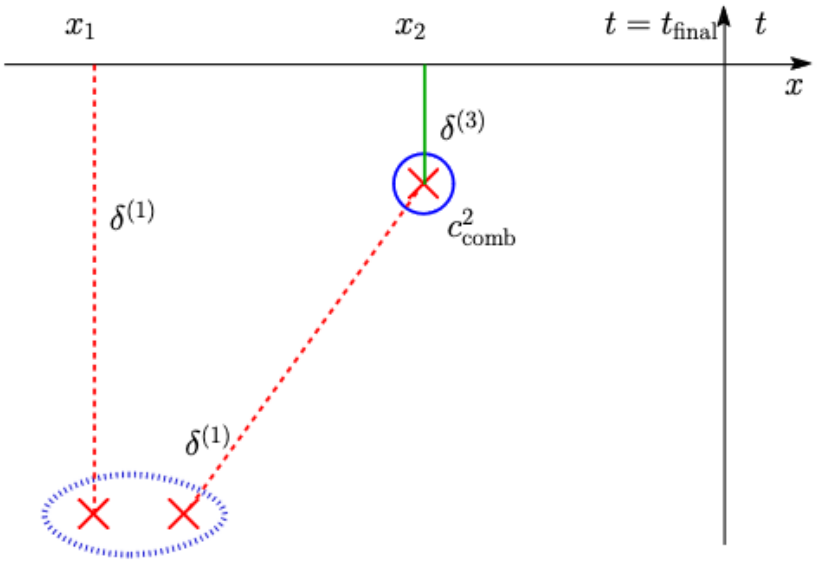

Figure 3.15: Diagram showing the construction of the one-loop counterterm contribution to the matter power spectrum. Taken from Ref. [54].

with a solution of the following form

$$P^{\Lambda}_{\rm stoch}(k,a) = R_{\rm stoch}(a,\Lambda)^7 \cdot k^4 \,, \tag{3.154}$$

where $R_{\rm stoch}(a,\Lambda)$ has the unit of a length (see Ref. [56]). In addition, using the same approach as in Eq. (3.150), we can show that UV contribution of $P^{\Lambda}_{22}(k,\tau)$ reduces to:

$$P^{\rm UV}_{22}(k,\tau) = 2\int^{\Lambda}_{p_{\rm trust}\gg k} \frac{d^3p}{(2\pi)^3}\left[F_2(\boldsymbol{p},\boldsymbol{k}-\boldsymbol{p})\right]^2 P_{11}(p,\tau)P_{11}(|\,\boldsymbol{k}-\boldsymbol{p}\,|,\tau) \tag{3.155}$$

$$= k^4\left[\frac{9}{196\pi^2}\int^{\Lambda}_{p_{\rm trust}\gg k}\frac{dp}{p^2}P_{11}(p,\tau)\right] , \tag{3.156}$$

which has the same k-dependency as $P_{\rm stoch}(k,\tau)$! We can then make the same separation as for $c^2_{s,\rm eff}(a,\Lambda)$ in Eq. (3.151) for $R_{\rm stoch}(a,\Lambda)$ and then remove the Λ-dependence of $P_{22}(k,\tau)$, by imposing $R_{\rm stoch\,ctr}(a,\Lambda)^7 = -P^{\rm UV}_{22}(k,\tau)/k^4$. The stochastic term therefore allows us to renormalize this one-loop contribution, but we did not include the $P^{\Lambda}_{\rm stoch}(k,\tau)$ contribution in Eq. (3.146), which is actually a higher-order term than the one-loop.

This last point is worth clarifying. The linear matter power spectrum is a power law in k [see Eq. (3.27)], so that:

$$P_{11}(k) = \frac{1}{k^3_{\rm NL}}\left(\frac{k}{k_{\rm NL}}\right)^n , \tag{3.157}$$

where $n \sim 1$ at very small k [see Eq. (3.27)], *i.e.*, in the linear regime. Consequently, we have that

$$\mathscr{P}_{11}(k) \equiv \frac{k^3}{2\pi^2}P_{11}(k) = \left(\frac{k}{k_{\rm NL}}\right)^{n+3} \sim \left(\delta^{(1)}\right)^2 , \tag{3.158}$$

implying that $\delta^{(1)} \sim (k/k_{\rm NL})^2$ at $k \gg k_{\rm NL}$. Finally, one obtains (see Ref. [56]):

$$\mathscr{P}_m(k) \sim \underbrace{\left(\frac{k}{k_{\rm NL}}\right)^{n+3}}_{\rm Tree-level} + \underbrace{\left(\frac{k}{k_{\rm NL}}\right)^{2(n+3)}}_{\rm One-loop} + \underbrace{\left(\frac{k}{k_{\rm NL}}\right)^{n+5}}_{\rm Counterterm\ c^2_{comb}} + \underbrace{\left(\frac{k}{k_{\rm NL}}\right)^{7}}_{\rm Stochastic}, \tag{3.159}$$

where we have used the fact that $\mathscr{P}_{22} \sim \mathscr{P}_{13} \sim \mathscr{P}_{11}^2$ for the one-loop contribution, $\mathscr{P}_{c^2_{\rm comb}} \sim k^2 \mathscr{P}_{11}$ for the counterterm contribution, and $\mathscr{P}_{\rm stoch} \sim k^3 \cdot P_{\rm stoch} \sim k^3 \cdot k^4$ for the stochastic contribution. In the mildly non-linear regime (just after the turn over $k_{\rm eq}$), one has $n \simeq -1.5$, implying that:

$$\mathscr{P}_{11} \gg \mathscr{P}_{22} \sim \mathscr{P}_{13} \sim \mathscr{P}_{c^2_{\rm comb}} \gg \mathscr{P}_{\rm stoch}\,, \tag{3.160}$$

explaining why we have not included the stochastic contribution in Eq. (3.146). Let us note that, in the general case, we have for the L-loop order:

$$\mathscr{P}_{L-loop} = \left(\frac{k}{k_{\rm NL}}\right)^{(L+1)(n+3)}. \tag{3.161}$$

3.4.3 The EFTofLSS galaxy power spectrum

The aim now is to determine a formulation for the EFTofLSS galaxy power spectrum. To do this, it is necessary (as was the case in Sec. 3.2 for the linear galaxy power spectrum) to consider (i) the redshift-space distortion effect, and (ii) the corrections related to the biased tracers (*i.e.*, the fact that the galaxy distribution is not the same as the matter distribution).

Redshift-space distortion in EFTofLSS

Let us start with the redshift-space distortion. All calculations in this subsection are taken from Ref. [48]. Since we want to determine the galaxy power spectrum in the (mildly) non-linear regime, we need to take into account the non-linear effects of the redshift-space distortion (see discussion related to Fig. 3.4). We previously determined that the galaxy overdensity field in redshift-space and in Fourier space reads [see Eq. (3.53)]:

$$\delta_{g,r}(\boldsymbol{k}) = \delta_g(\boldsymbol{k}) + \int d^3x\, e^{-i\boldsymbol{k}\cdot\boldsymbol{x}} \left(e^{-i\boldsymbol{k}\cdot\hat{n}\frac{\boldsymbol{v}}{aH}\cdot\hat{n}} - 1\right)(1+\delta_g(\boldsymbol{x}))\,. \tag{3.162}$$

In order to find the Kaiser formula, we had carried out a Taylor expansion up to first order:

$$e^{-i\boldsymbol{k}\cdot\hat{n}\frac{\boldsymbol{v}}{aH}\cdot\hat{n}} = 1 - i\boldsymbol{k}\cdot\hat{n}\,\frac{\boldsymbol{v}}{aH}\cdot\hat{n} + \ldots. \tag{3.163}$$

We also used the distant observer approximation, which states that $\hat{n}$ is the same for all the galaxies in the survey under consideration. We use here the same approximation, and in particular we will consider that $\hat{n} = \hat{z}$, implying that $\boldsymbol{k}\cdot\hat{n} = k_z$ and $\boldsymbol{v}\cdot\hat{n} = v_z$. The difference with the linear calculation is that now we have to Taylor expand up to cubic order (as we did previously for the matter overdensity field):

$$e^{-i\frac{k_z}{aH}v_z(\boldsymbol{x})} = 1 - i\frac{k_z}{aH}v_z(\boldsymbol{x}) + \frac{i^2}{2}\left(\frac{k_z}{aH}\right)^2 v_z(\boldsymbol{x})^2 - \frac{i^3}{3!}\left(\frac{k_z}{aH}\right)^3 v_z(\boldsymbol{x})^3 + \ldots, \tag{3.164}$$

which is nothing more than an expansion in the velocity field $v_z(\boldsymbol{x})$. Therefore, to determine the one-loop galaxy power spectrum, we need to consider the following equation for the galaxy overdensity field:

$$\delta_{g,r}(\boldsymbol{k}) = \delta_g(\boldsymbol{k}) + \int d^3x \left[-i\frac{k_z}{aH} v_z(\boldsymbol{x}) + \frac{i^2}{2}\left(\frac{k_z}{aH}\right)^2 v_z(\boldsymbol{x})^2 - \frac{i^3}{3!}\left(\frac{k_z}{aH}\right)^3 v_z(\boldsymbol{x})^3 + \dots \right] + \int d^3x \left[-i\frac{k_z}{aH} v_z(\boldsymbol{x})\delta_g(\boldsymbol{x}) + \frac{i^2}{2}\left(\frac{k_z}{aH}\right)^2 v_z(\boldsymbol{x})^2\delta_g(\boldsymbol{x}) + \dots \right], \tag{3.165}$$

which can be rewritten in condensed form, using the notation $[f]_{\boldsymbol{k}} = \int d^3x e^{-i\boldsymbol{k}\boldsymbol{x}} f(\boldsymbol{x})$ [48], as

$$\delta_{g,r}(\boldsymbol{k}) = \delta_g(\boldsymbol{k}) - i\frac{k_z}{aH} v_z(\boldsymbol{k}) + \frac{i^2}{2}\left(\frac{k_z}{aH}\right)^2 [v_z(\boldsymbol{x})^2]_{\boldsymbol{k}} - \frac{i^3}{3!}\left(\frac{k_z}{aH}\right)^3 [v_z(\boldsymbol{x})^3]_{\boldsymbol{k}} - i\frac{k_z}{aH}[v_z(\boldsymbol{x})\delta_g(\boldsymbol{x})]_{\boldsymbol{k}} + \frac{i^2}{2}\left(\frac{k_z}{aH}\right)^2 [v_z(\boldsymbol{x})^2\delta_g(\boldsymbol{x})]_{\boldsymbol{k}} + \dots, \tag{3.166}$$

where the two first terms lead directly to the Kaiser formula. However (as we saw above), the product of two fields located at the same point in space depends very strongly on the UV physics. These terms must therefore be renormalized to remove any dependence on UV physics. One obtains (using the equivalence principle) (see Ref. [48]):

$$[v_z(\boldsymbol{x})^2]_{R,\boldsymbol{k}} = [v_z(\boldsymbol{x})^2]_{\boldsymbol{k}} + \left(\frac{aH}{k_{\mathrm{R}}^{-1}}\right)^2 [c_1 + c_2\delta(\boldsymbol{k})] + \left(\frac{aH}{k_{\mathrm{R}}^{-1}}\right)^2 c_3\frac{k_z^2}{k^2}\delta(\boldsymbol{k}) + \dots, \tag{3.167}$$

$$[v_z(\boldsymbol{x})^3]_{R,\boldsymbol{k}} = [v_z(\boldsymbol{x})^3]_{\boldsymbol{k}} + 3\left(\frac{aH}{k_{\mathrm{R}}^{-1}}\right)^2 c_1 v_z(\boldsymbol{k}) + \dots, \tag{3.168}$$

$$[v_z(\boldsymbol{x})\delta(\boldsymbol{x})]_{R,\boldsymbol{k}} = [v_z(\boldsymbol{x})\delta(\boldsymbol{x})]_{\boldsymbol{k}} + \left(\frac{aH}{k_{\mathrm{R}}^{-1}}\right)^2 c_4\frac{k_z}{k_M}\delta(\boldsymbol{k}) + \dots, \tag{3.169}$$

$$[v_z(\boldsymbol{x})^2\delta(\boldsymbol{x})]_{R,\boldsymbol{k}} = [v_z(\boldsymbol{x})^2\delta(\boldsymbol{x})]_{\boldsymbol{k}} + \left(\frac{aH}{k_{\mathrm{R}}^{-1}}\right)^2 c_1\delta(\boldsymbol{k}) + \dots. \tag{3.170}$$

Let us note a few important points about these equations:

- We have four counterterms, c_1, c_2 c_3 and c_4, whose role is to eliminate the UV dependence of the field product operators $[...]_{\boldsymbol{k}}$ in order to get UV-independent operators $[...]_{R,\boldsymbol{k}}$. These counterterms thus come purely from the Taylor expansion in v_z due to the redshift-space distortion. We therefore call them *RSD counterterms*.
- The aH/k_{R}^{-1} factor has been conventionally chosen so that the counterterms are of the order of unity.
- k_{R}^{-1} is the renormalization scale of the velocity products appearing in the redshift-space expansion. Physically it corresponds to the the typical scale associated with the velocity dispersion of the galaxies.
- The renormalized operators $[...]_{R,\boldsymbol{k}}$ are written directly as a function of the dark matter overdensity field δ and not as a function of the galaxy overdensity field δ_g, because in the end it is the relevant field that need to be used to relate the galaxy power spectrum to the matter power spectrum.

Now, if we perform the two point correlation function of Eq. (3.166), and using the renormalized operators, then one can show that (see Ref. [48])

$$P_{g,r}(k,\mu) = P_{g,r}^{\rm NLO}(k,\mu) + P_{g,r}^{\rm RSD\,ctr}(k,\mu)\,, \tag{3.171}$$

where $P_{g,r}^{\rm NLO}(k,\mu)$ is the galaxy power spectrum obtained using the non-renormalized operators [which is nothing more than the two-point correlation function of Eq. (3.166)], and where $P_{g,r}^{\rm RSD\,ctr}(k,\mu)$ is the contribution of the RSD counterterms to the galaxy power spectrum. One can easily show that this contribution reads (see Ref. [48]):

$$P_{g,r}^{\rm RSD\,ctr}(k,\mu) = 2\left(1+f\mu^2\right)\left(c_{r,1}\mu^2 + c_{r,2}\mu^4\right)\left(\frac{k}{k_R}\right)^2 P_{11}(k,\mu)\,, \tag{3.172}$$

where

$$c_{r,1} = c_1 + c_2 - 2c_4\,, \tag{3.173}$$

$$c_{r,2} = c_1 + c_3\,. \tag{3.174}$$

Note that the c_i parameters have been modified as: $c_i \to -2\pi^2 D_+^2(a)c_i$. Finally, only two combinations of these RSD counterterms are suitable for the one-loop galaxy power spectrum, namely $c_{r,1}$ and $c_{r,2}$.

Biased tracers in EFTofLSS

Now we need to determine $P_{g,r}^{\rm NLO}(k,\mu)$ in Eq. (3.171), which depends solely on the δ_g and v_z fields. The new difficulty lies in the relationship between δ_g and δ in order to find an expression for $P_{g,r}^{\rm NLO}(k,\mu)$ that depends on the linear matter power spectrum. To do this, it is possible to choose several parametrizations that leave the theory invariant. In particular, in this thesis we consider two different parametrization: the "West coast" (WC) parametrization [58] implemented in the `PyBird` code [59], and the "East coast" (EC) parametrization [60] implemented in the `CLASS-PT` code [61, 62]. However, note that the form of the countreterms must necessarily be equivalent between the two parametrizations. One of the aims of chapters 5 and 6 will be to compare these parametrizations, since they lead to different cosmological results. It is crucial to understand the origin of these deviations, since these two parameterisations are mathematically equivalent.

In order to obtain the one-loop galaxy power spectrum, one needs to consider all the possible operators in the bias expansion that do not violate the equivalence principle. As with the matter overdensity and velocity fields, we need to consider the expansion up to third order. For example, the bias expansion in the EC parametrization reads [60, 61]:

$$\delta_g = \tilde{b}_1\delta + \frac{\tilde{b}_2}{2}\delta^2 + \frac{\tilde{b}_3}{6}\delta^3 + b_{\mathscr{G}_2}\mathscr{G}_2 + b_{\delta\mathscr{G}_2}\delta\mathscr{G}_2 + b_{\mathscr{G}_3}\mathscr{G}_3 + b_{\Gamma_3}\Gamma_3 + R_*^2\partial^2\delta + \varepsilon\,, \tag{3.175}$$

where

- $\tilde{b}_1$, $\tilde{b}_2$ and $\tilde{b}_3$ are the bias expansion parameters of the matter overdensity field. In particular, $\tilde{b}_1$ corresponds to the linear bias parameter, as defined in the Kaiser formula, while $\tilde{b}_2$ and $\tilde{b}_3$ are the second and third order non-linear bias parameters of the matter overdensity field.

- ε is a stochastic field uncorrelated with the matter overdensity field. It has the same meaning as the one introduced in the effective stress tensor (see above).

- $b_{\mathscr{G}_2}$, $b_{\delta\mathscr{G}_2}$ and $b_{\mathscr{G}_3}$ correspond to the bias parameters which encode the dependence of δ_g on the gravitational potential ϕ. Because of the equivalence principle, it is not possible to have terms in ϕ and $\partial\phi$, which implies that there is no dependence of the potential at linear order. $\mathscr{G}_2$ is the *Galileon operator* defined as:

$$\mathscr{G}_2(\phi) \equiv (\partial_i\partial_j\phi)^2 - (\partial_i^2\phi)^2\,, \tag{3.176}$$

  while

$$\Gamma_3 \equiv \mathscr{G}_2(\phi) - \mathscr{G}_2(\phi_v)\,, \tag{3.177}$$

  where ϕ_v is the velocity potential (defined as $\nabla^2\phi_v = -\theta/aH$ [60]).

- One finally needs to add the contribution of $\partial^2\delta$ (the contribution $\partial\delta$ does not respect the equivalence principle) in the bias expansion.

Note that after renormalization, the contributions from $\tilde{b}_3$, $\delta\mathscr{G}_2$ and b_{Γ_3} disappear. In addition, the $R_*^2\partial^2\delta$ contribution (which is $\propto k^2$ in Fourier space) is degenerated with the effective sound speed of the one loop matter power spectrum $c^2_{s,\text{eff}}$, which means that in the following we consider a new parameter, called c_{ct}, which is a linear combination of these two parameters, namely $c^2_{\text{ct}} \sim c^2_{s,\text{eff}} + R_*^2$. Finally, in addition to the two RSD counterterms, we will have four bias parameter ($\tilde{b}_1$, $\tilde{b}_2$, $b_{\delta\mathscr{G}_2}$ and b_{Γ_3}), the c_{ct} parameter and stochastic parameters coming from the two-point correlation function of ε.

In the following, we will consider the WC parametrization, written in the basis $\{b_1, b_2, b_3, b_4\}$, which is related to the previous basis $\{\tilde{b}_1, \tilde{b}_2, b_{\mathscr{G}_2}, b_{\Gamma_3}\}$ [60] in the following way [63]:

$$\begin{aligned} b_1 &= \tilde{b}_1\,,\\ b_2 &= \tilde{b}_1 + \frac{7}{2}b_{\mathscr{G}_2}\,,\\ b_3 &= \tilde{b}_1 + 15b_{\mathscr{G}_2} + 6b_{\Gamma_3}\,,\\ b_4 &= \frac{1}{2}\tilde{b}_2 - \frac{7}{2}b_{\mathscr{G}_2}\,. \end{aligned} \tag{3.178}$$

The WC parametrization is the one mainly used in this thesis.

Finally, note that the final one-loop galaxy power spectrum in redshift-space is obtained by injecting the bias expansion [see Eq. (3.175)] into the $P^{\text{NLO}}_{g,r}(k,\mu)$ term of Eq. (3.171), which depends only on the δ_g and v_z fields.

Final expression of the galaxy power spectrum

We now turn to the final equation of the EFTofLSS galaxy power spectrum, obtained in Ref. [64]. In this section, we give all the relevant details about this equation that will be used throughout the manuscript. In particular, Eq. (3.180), implemented in the `PyBird` code, is the fundamental equation that we consider throughout this thesis, and it

is the one that will be used each time we perform a full-shape analysis of clustering data (unless otherwise indicated). The main idea behind this equation is to obtain a formulation of the EFTofLSS galaxy power spectrum that depends only on the linear matter power spectrum. It is therefore possible to determine the latter using a Boltzmann code, and then to infer the mildly non-linear galaxy power spectrum by applying this equation in a second step.

First of all, let us recall that at linear order the galaxy power spectrum in redshift space is given by the famous Kaiser formula [see Eq. (3.59)]: [4]

$$P_{g,r}(z,k,\mu) = \left[b_1(z) + f\mu^2\right]^2 P_{11}(z,k) \equiv Z_1(\mu)^2 P_{11}(z,k)\,, \tag{3.179}$$

where $P_{11}(z,k)$ corresponds to the linear matter power spectrum that can be calculated with a Boltzmann code such as `CLASS` [43] or `CAMB` [44], f is the growth factor, $b_1(z)$ is the linear galaxy bias parameter, and $\mu = \hat{z}\cdot\hat{k}$ is the cosine of the angle between the line-of-sight $\boldsymbol{z}$ and the wavevector of the Fourier mode $\boldsymbol{k}$. At one-loop order, for the WC parametrization, the formula is improved to [64]:

$$\begin{aligned} P_{g,r}(k,\mu) &= Z_1(\mu)^2 P_{11}(k) + 2Z_1(\mu)P_{11}(k)\left(c_{\rm ct}\frac{k^2}{k_{\rm M}^2} + c_{r,1}\mu^2\frac{k^2}{k_{\rm R}^2} + c_{r,2}\mu^4\frac{k^2}{k_{\rm R}^2}\right) \\ &+ 2\int\frac{d^3q}{(2\pi)^3}\,Z_2(\boldsymbol{q},\boldsymbol{k}-\boldsymbol{q},\mu)^2 P_{11}(|\boldsymbol{k}-\boldsymbol{q}|)P_{11}(q) + 6Z_1(\mu)P_{11}(k)\int\frac{d^3q}{(2\pi)^3}\,Z_3(\boldsymbol{q},-\boldsymbol{q},\boldsymbol{k},\mu)P_{11}(q) \\ &+ \frac{1}{\bar{n}_g}\left(c_{\varepsilon,0} + c_\varepsilon^{\rm mono}\frac{k^2}{k_{\rm M}^2} + 3c_\varepsilon^{\rm quad}\left(\mu^2-\frac{1}{3}\right)\frac{k^2}{k_{\rm M}^2}\right), \end{aligned} \tag{3.180}$$

where $k_{\rm M}^{-1} \simeq k_{\rm NL}^{-1}$ is the scale controlling the spatial derivative expansion, with size given by the host halo typical extension [65], while $k_{\rm R}^{-1}$ is the renormalization scale of the velocity products appearing in the redshift-space expansion (see above) [48]. We discuss these scales more in details in Sec. 4.1.2. In the following, we give a description of the different terms of Eq. (3.180):

- The first term corresponds to the Kaiser term (3.179).
- The second term proportional to $k^2 Z_1(\mu)P_{11}(k)$ corresponds to the contribution of the one loop-order counterterms. $c_{\rm ct}$ is a linear combination of the dark matter sound speed $c^2_{s,\rm eff}$ coming from the one-loop matter power spectrum [see Eq. (3.148)] and a higher-derivative bias (see above) [65], while $c_{r,1}$ and $c_{r,2}$ represent the redshift-space counterterms (see also above) [48]. Let us note that in our analyses, we do not consider $c_{r,2}$ (which belongs to a μ^4-term), since we do not include the hexadecapole. Without the latter, this term is degenerate with $c_{r,1}$.
- The second line corresponds to the one-loop perturbation contribution, which depends on four galaxy bias parameters appearing in Eqs. (3.181)-(3.183): b_i, with $i = [1,4]$ (see above for their explicit definition).
- Finally, the last line, inversely proportional to the mean galaxy number density $\bar{n}_g$, corresponds to the stochastic contribution, which depends on three stochastic terms: $c_{\varepsilon,0}$, $c_\varepsilon^{\rm mono}$ and $c_\varepsilon^{\rm quad}$. The first term describes a constant shot noise as in the linear theory [see

[4] Note that for the sake of simplicity we have not indicated the redshift dependency of $Z_1(\mu)$.

Sec. 3.2], while the other two terms correspond to the scale-dependant stochastic contributions of the monopole and the quadrupole. This comes from the two-point correlation function of the stochastic parameter ε.

In Eq. (3.180), Z_n corresponds to the redshift-space galaxy density kernels of order n (see *e.g.*, [64]). The equations of Z_1, Z_2, and Z_3 are given by:

$$Z_1(q_1) = K_1(q_1) + f\mu_1^2 G_1(q_1) = b_1 + f\mu_1^2\,, \tag{3.181}$$

$$Z_2(q_1,q_2,\mu) = K_2(q_1,q_2) + f\mu_{12}^2 G_2(q_1,q_2) + \frac{1}{2} f\mu q \left(\frac{\mu_2}{q_2} G_1(q_2) Z_1(q_1) + \text{perm.}\right), \tag{3.182}$$

$$\begin{aligned} Z_3(q_1,q_2,q_3,\mu) &= K_3(q_1,q_2,q_3) + f\mu_{123}^2 G_3(q_1,q_2,q_3) \\ &\quad + \frac{1}{3} f\mu q \left(\frac{\mu_3}{q_3} G_1(q_3) Z_2(q_1,q_2,\mu_{123}) + \frac{\mu_{23}}{q_{23}} G_2(q_2,q_3) Z_1(q_1) + \text{cyc.}\right), \end{aligned} \tag{3.183}$$

where $\mu = q\cdot\hat{z}/q$, $q = q_1 + \cdots + q_n$, and $\mu_{i_1\ldots i_n} = q_{i_1\ldots i_n}\cdot\hat{z}/q_{i_1\ldots i_n}$, $q_{i_1\ldots i_m} = q_{i_1} + \cdots + q_{i_m}$. G_i are the standard perturbation theory velocity kernels (see Sec. 3.3), while K_i are the galaxy density kernels, reading as [65, 66, 67]:

$$K_1 = b_1\,, \tag{3.184}$$

$$K_2(q_1,q_2) = b_1 \frac{q_1\cdot q_2 (q_1^2+q_2^2)}{2q_1^2 q_2^2} + b_2\left(F_2(q_1,q_2) - \frac{q_1\cdot q_2(q_1^2+q_2^2)}{2q_1^2q_2^2}\right) + b_4\,, \tag{3.185}$$

$$\begin{aligned} K_3(q,-q,k) &= \frac{b_1}{504k^3q^3}\left(-38k^5q + 48k^3q^3 - 18kq^5 + 9(k^2-q^2)^3 \log\left[\frac{k-q}{k+q}\right]\right) \\ &\quad + \frac{b_3}{756k^3q^5}\left(2kq(k^2+q^2)(3k^4 - 14k^2q^2 + 3q^4) + 3(k^2-q^2)^4 \log\left[\frac{k-q}{k+q}\right]\right) \\ &\quad + \frac{b_1}{36k^3q^3}\left(6k^5q + 16k^3q^3 - 6kq^5 + 3(k^2-q^2)^3 \log\left[\frac{k-q}{k+q}\right]\right), \end{aligned} \tag{3.186}$$

where F_2 is the symmetrized standard perturbation theory second-order density kernel (see Sec. 3.3 together with Ref. [53]), and the third-order kernel is written in its UV-subtracted version and is integrated over $k\cdot\hat{q}$. Finally, in the redshift-space galaxy power spectrum at one-loop [*i.e.*, Eq. (3.180)], one obtains a total of ten EFT parameters, namely three counterterms, four galaxy bias parameters and three stochastic parameters.

In this thesis, we consider the multipoles of the galaxy power spectrum, obtained through a Legendre polynomials decomposition of the total galaxy power spectrum [as we did for the Kaiser formula in Eqs. (3.64)-(3.66)]:

$$P_g(z,k,\mu) = \sum_{\ell=0} \mathscr{L}_\ell(\mu) P_\ell(z,k)\,, \tag{3.187}$$

where $\mathscr{L}_\ell$ represents the Legendre polynomial of order ℓ, and $P_\ell(z,k)$ are the multipoles of the galaxy power spectrum defined as:

$$P_\ell(z,k) = \frac{2\ell+1}{2}\int_{-1}^{1} d\mu\, \mathscr{L}_\ell(\mu) P_g(z,k,\mu)\,. \tag{3.188}$$

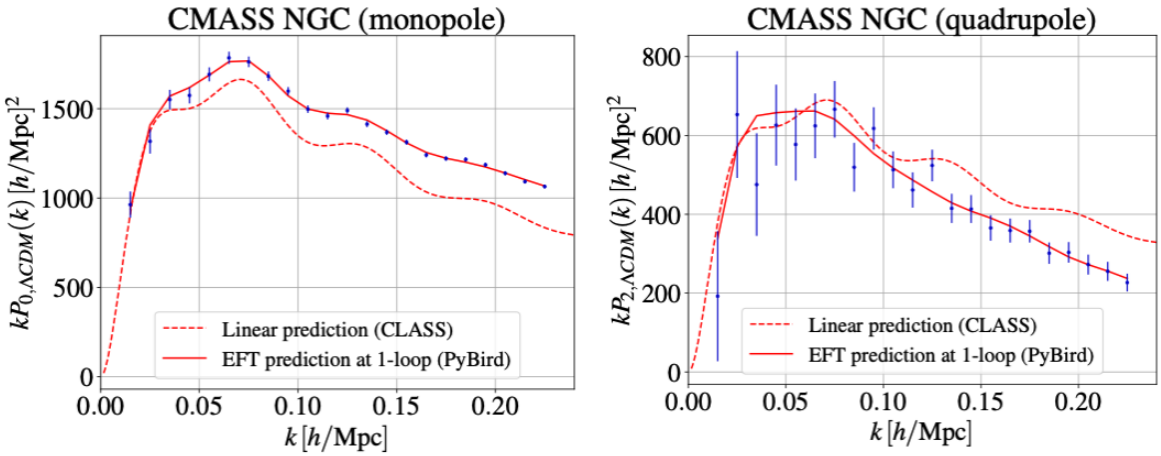

Figure 3.16: Fit of the monopole and quadrupole of the galaxy power spectrum, either from the linear perturbation theory [*i.e.*, using the monopole and the quadrupole of the Kaiser formula from Eqs. (3.64) and (3.65)] or from the EFTofLSS [*i.e.*, using Eq. (3.180) implemented in the `PyBird` code]. The data shown here correspond to the CMASS NGC skycut of the BOSS data.

Given that most of the signal-to-noise ratio resides in the monopole ($\ell = 0$) and the quadrupole ($\ell = 2$), we consider only these two moments in our analyses, and in practice, we evaluate the loop corrections using the FFTLog method [68]. In Fig. 3.16, we plot the predictions from the linear perturbation theory [using the monopole and the quadrupole of the Kaiser formula from Eqs. (3.64) and (3.65)] and from the EFTofLSS [using Eq. (3.180) implemented in the `PyBird` code] when confronted with the galaxy power spectrum of the BOSS data. We can see that this theory fits the galaxy power spectrum very precisely up to $k_{\mathrm{max}} \sim 0.20 - 0.25\,h\mathrm{Mpc}^{-1}$ (whereas this is not at all the case for the linear perturbation theory). In chapter 4, we shall detail precisely how to determine k_{max}, and we shall quantify the goodness of the fit more precisely.

Galaxy correlation function

In chapter 4, we also consider the redshift-space galaxy correlation function instead of the power spectrum. The correlation function at one loop order corresponds to the inverse Fourier transform of the galaxy power spectrum given in Eq. (3.180):

$$\xi_g(z,s,\mu_s) = \int \frac{d^3\boldsymbol{k}}{(2\pi)^3}\, e^{i\boldsymbol{k}\cdot\boldsymbol{q}} P_g(z,k,\mu_s)\,, \tag{3.189}$$

and, similarly to the galaxy power spectrum, one considers a Legendre polynomials decomposition:

$$\xi_g(z,s,\mu_s) = \sum_{\ell=0} \mathscr{L}_\ell(\mu_s)\xi_\ell(z,s)\,. \tag{3.190}$$

We can relate the correlation function multipoles to the power spectrum multipoles through a spherical-Bessel transform:

$$\xi_\ell(s) = i^\ell \int \frac{dk}{2\pi^2} k^2 P_\ell(k) j_\ell(ks)\,, \tag{3.191}$$

where j_ℓ is the spherical-Bessel function of order ℓ. As with the power spectrum, we make use of the monopole ($\ell = 0$) and the quadrupole ($\ell = 2$) of the correlation function in the following. As the Fourier transform of power-laws are simply Dirac-δ function in configuration space, the stochastic contributions in Eq. (3.180) drop out from the correlation function prediction [69]. In practice, we also evaluate the correlation function using the FFTLog method [70, 69].

3.4.4 Additional effects

In this final subsection, we briefly discuss both theoretical (for IR resummation) and experimental corrections made to Eq. (3.180). In particular, we will use these corrections throughout this thesis, whenever we perform a full shape analysis with EFTofLSS.

IR-resummation

As the long-wavelength displacements are non-perturbative in our Universe, we need to resum them to all orders to accurately describe the scales around the BAO scale [71]. The IR-resummation of the galaxy power spectrum up to the N-loop order is defined as [48, 72, 59]:

$$P^\ell(k)_{|N} = \sum_{j=0}^{N} \sum_{\ell'} 4\pi(-i)^{\ell'} \int dq\, q^2\, Q^{\ell\ell'}_{||N-j}(k,q)\, \xi^{\ell'}_j(q)\,, \tag{3.192}$$

where $P^\ell(k)_{|N}$ corresponds to the resummed power spectrum, and $\xi^\ell_j(k)$ are the j-loop order pieces of the Eulerian (*i.e.*, non-resummed) correlation function, respectively. The effects from the bulk displacements are encoded in $Q^{\ell\ell'}_{||N-j}(k,q)$, given by:

$$Q^{\ell\ell'}_{||N-j}(k,q) = \frac{2\ell+1}{2} \int_{-1}^{1} d\mu_k \frac{i^{\ell'}}{4\pi} \int d^2\hat{q}\, e^{-i\boldsymbol{q}\cdot\boldsymbol{k}}\, F_{||N-j}(\boldsymbol{k},\boldsymbol{q}) \mathscr{L}_\ell(\mu_k) \mathscr{L}_{\ell'}(\mu_q)\,, \tag{3.193}$$

$$F_{||N-j}(\boldsymbol{k},\boldsymbol{q}) = T_{0,r}(\boldsymbol{k},\boldsymbol{q}) \times T^{-1}_{0,r\,||N-j}(\boldsymbol{k},\boldsymbol{q})\,,$$

$$T_{0,r}(\boldsymbol{k},\boldsymbol{q}) = \exp\left\{ -\frac{k^2}{2} \left[\Xi_0(q)(1 + 2f\mu_k^2 + f^2\mu_k^2) + \Xi_2(q) \left((\hat{k}\cdot\hat{q})^2 + 2f\mu_k\mu_q(\hat{k}\cdot\hat{q}) + f^2\mu_k^2\mu_q^2 \right) \right] \right\},$$

where $\Xi_0(q)$ and $\Xi_2(q)$ are defined as:

$$\Xi_0(q) = \frac{2}{3} \int \frac{dp}{2\pi^2} \exp\left(-\frac{p^2}{\Lambda^2_{\rm IR}} \right) P_{11}(p) \left[1 - j_0(pq) - j_2(pq) \right], \tag{3.194}$$

$$\Xi_2(q) = 2 \int \frac{dp}{2\pi^2} \exp\left(-\frac{p^2}{\Lambda^2_{\rm IR}} \right) P_{11}(p)\, j_2(pq)\,. \tag{3.195}$$

In practice, we evaluate the IR-resummation using the FFTLog method [59].

Additional modeling effects

On top of the description of the biased tracers in redshift space, we account for a number of observational effects, as described in Ref. [58]: the Alcock-Paszynski effect [73] (see Sec. 3.2), the window functions as implemented in Ref. [74] (we describe this correction in detail in App. D.1), and binning. For a given redshift data slice, we evaluate our predictions at one effective redshift rather than accounting for the redshift evolution. In particular, we take the

EFT parameters as constant within the redshift slice. The accuracy of this approximation has been checked in Ref. [75] in the context of the BOSS survey. We have checked that this approximation leads to negligible shifts in the determined cosmological parameters from eBOSS, as expected from the size of the survey compared to the one of BOSS. Tests and further considerations on observational effects are given in Sec. 4.1.3 of chapter. 4. Moreover, we have shown above that the correction for uncertainties in the redshift determination is degenerate with some EFT counterterms (see below), and therefore that our formalism naturally accounts for it.

Part II

The effective field theory of large-scale structures applied to (e)BOSS data and its consistency within the ΛCDM model

The distribution of matter at large scales contains a wealth of cosmological information, from the initial conditions of the Universe to the gravitational collapse of late-time objects. The program of cosmic microwave background (CMB) experiments has now matured to a state where ΛCDM parameters have been measured to percent level with the *Planck* satellite [11], and with similar precision by subsequent experiments, *e.g.*, ACT [76] and SPT [77, 78]. At the same time, the data volume gathered by large-scale structure (LSS) surveys has been continuously growing. As those surveys probe vastly different epochs in the history of the Universe, they allow for a crucial consistency test of the ΛCDM model and have delivered independent cosmological determinations at precision comparable to CMB measurements, see *e.g.*, the recent results from the photometric surveys DES [79] and KIDS [80], or from the spectroscopic surveys BOSS [81]. In addition, LSS data have become paramount to break degeneracies of the ΛCDM model and extensions when combined with CMB.

The large amount of LSS data available provides us with new opportunities to extract additional cosmological information, by making use of the full-shape of summary statistics built from clustering data. Among the spectroscopic surveys, the extended baryon oscillation spectroscopic survey (eBOSS), combined with previous phases of the sloan digital sky survey (SDSS), has mapped more than 11 billion years of cosmic history, providing an unprecedented map of the matter clustering in the Universe [82] through different tracers of the underlying matter density distribution, *e.g.*, galaxies, quasars or the lyman-α forest. To extract cosmological information from these surveys, the (e)BOSS Collaboration follows the convention of compressing information from these surveys into simple parameters that can be easily compared with cosmological models. These are usually expressed in the form of the Alcock-Paczynski (AP) parameters measured from the BAO angles [73] and the $f\sigma_8$ parameter, where f is the growth factor, measured from redshift-space distortions (RSD) [50], as already explained in detail in Sec. 3.2. The combination of these two pieces of information is referred to as "BAO/$f\sigma_8$" in this thesis. However, the large amount of LSS data available provides us with new opportunities to extract additional cosmological information, by making use of the full-shape of summary statistics built from clustering data. Given the increasing data volume and the variety of tracers probed, new methods to make reliable predictions for the full-shape are necessary to extract the cosmological parameters in a robust and systematic ways.

Thankfully, the underlying density and velocity fields of any tracer respect a set of symmetries in the long-wavelength limit known as Galilean invariance [83, 84, 85]. Moreover, we are interested in objects that are non-relativistic, allowing us to define a *nonlinear scale* as the average distance travelled by the objects during the age of the Universe, under which the underlying fields and their dynamics can be smoothed out [55] (see Sec. 3.4). Building on those considerations, the effective field theory of large-scale structures (EFTofLSS) has emerged as a systematic way to organize the expansions in fluctuations and derivatives of the density and velocity fields of the observed tracers at long wavelengths [55, 54, 71, 65, 48], as explained in detail in Sec. 3.4. [5] The prediction at the one-loop order for the power spectrum

[5] The first formulation of the EFTofLSS was carried out in Eulerian space in Refs. [54, 55] and in Lagrangian space in [86]. Once this theoretical framework was established, many efforts were made to improve this theory and make it predictive, such as the understanding of renormalization [87, 88], the IR-resummation of the long displacement fields [48, 89, 71, 90, 70, 91], and the computation of the two-loop matter power spectrum [92, 93]. Then, this theory was developed in the framework of biased tracers (such as galaxies and quasars) in Refs. [65, 60, 66, 67, 64, 94]. See also the introduction footnote in, *e.g.*, Ref. [95] for relevant related works on the EFTofLSS.

of biased tracers in redshift space from the EFTofLSS [64] (see also Ref. [96]) has been used to analyze the full-shape of BOSS clustering data in Refs. [58, 97]. These works have shown that: (i) higher wavenumbers beyond the linear regime in good theoretical control can be accessed, bringing additional cosmological information (see also Ref. [98]), and (ii) with reliable predictions, as the cosmological parameters (together with the nuisance parameters) are scanned the template can be varied instead of being held fixed, exploiting the full information of the full-shape beyond the one from geometrical distortions (see Refs. [99, 100] for earlier works where the full-shape predictions, yet not from the EFTofLSS, were varied at each point in parameter space). EFT analyses of BOSS data have already provided precise and robust determination of ΛCDM parameters [58, 97, 101, 102, 103, 69, 104, 105]. Some EFT analyses of BOSS data have also included the bispectrum at tree-level [58, 62] and at one-loop [95] (see also Ref. [106]), pushing down uncertainties on ΛCDM parameters and setting new bounds from the LSS on non-Gaussianities [107, 108, 109]. See also, *e.g.*, Refs. [110, 111, 112, 113, 114, 115] for results from BOSS and/or eBOSS full-shape analyses using methods different from the EFTofLSS.

Furthermore, clustering data have the potential to play a key role in shedding light on the Hubble and S_8 tensions (see introduction of part III). In particular, an agreement between clustering and CMB data would have, under the assumption that there is no systematic error, significant impact on the interpretation of these tensions. Regarding the S_8 tension, this would hint that the origin lies in the scales beyond the (large) scales included in clustering or CMB analyses (see *e.g.*, Ref. [116]). As for the H_0 tension, a resolution would then require modifications to the concordance model that can lift both the values measured in the CMB and in the LSS.

The second part of this thesis corresponds to my overall contribution to the EFTofLSS analysis applied to (e)BOSS data within the framework of the ΛCDM model (and its canonical extensions). In chapter 4 (adapted from Ref. [117]), we present the first application of the EFTofLSS to eBOSS QSO data and we established a systematic method for applying it to different LSS data to obtain robust results. In this chapter, we show (i) that this analysis allows us to improve the ΛCDM constraints from LSS data and to obtain competitive constraints with CMB data (and especially with the *Planck* data), and (ii) that current LSS data are compatible with the flat-ΛCDM model and provide interesting constraints on the canonical extensions of the ΛCDM model. Then, in chapter 5 (adapted from Ref. [105]), we seek to verify the self-consistency of this theory within the ΛCDM model, in particular between different EFTofLSS theoretical parametrizations that have been proposed in the literature and that seemed to provide different constraints on cosmological parameters. We perform a series of analyses of the BOSS full-shape data, varying one-by-one (in order of importance) the prior choices, the BOSS measurements used (full-shape and post-reconstructed BAO parameters), the scale cuts and the number of multipoles included. Importantly, we find that cosmological constraints are sensitive to the choice of prior on the EFT parameter space, and that this choice drives most of the differences in the results. Finally, in chapter 6 (adapted from Ref. [118]), we explore this difference in parametrization and priors using a profile likelihood analysis. In particular, the goal is to understand the impact of the EFT priors on the inferred cosmological parameters and how this will change with more constraining data. This work demonstrates the importance of combining Bayesian and frequentist approaches for a in depth inference from current and future LSS data.

IV

Cosmological inference from the EFTofLSS: the eBOSS QSO full-shape analysis

Contents

4.1 Analysis pipeline **124**
4.1.1 Cosmological inference setup 124
4.1.2 Scale cut from governing scales 127
4.1.3 Assessing systematics beyond the EFT reach 129
4.1.4 Including redshift error in EFTofLSS 131
4.2 Constraints on flat ΛCDM **133**
4.2.1 Flat ΛCDM from the EFT analysis of eBOSS 136
4.2.2 Comparison with several LSS probes 137
4.2.3 Comparison with Planck 140
4.3 Extensions to the flat ΛCDM model **141**
4.3.1 $\Omega_k\Lambda$CDM 141
4.3.2 w_0CDM 144
4.3.3 $\nu\Lambda$CDM 146
4.3.4 $N_{\rm eff}\Lambda$CDM 147
4.4 Conclusions **148**

This chapter is based on:

T. Simon, P. Zhang and V. Poulin, *Cosmological inference from the EFTofLSS: the eBOSS QSO full-shape analysis*, **JCAP 07 (2023) 041**, arXiv:2210.14931.

In this chapter, we analyze the eBOSS quasars (QSO) full-shape using the prediction from the EFTofLSS. There are two main motivations behind this work. First, the EFTofLSS has only been used to analyze BOSS luminous red galaxies (LRG) and more recently eBOSS emission line galaxies (ELG) [119]. As QSO are different tracers than LRG, and selected by SDSS at an overall higher redshift than LRG, the eBOSS QSO full-shape analysis complements previous BOSS full-shape analysis, providing yet another important consistency test of ΛCDM at a different epoch and for another tracer (while also allowing us to test the assumptions behind the EFTofLSS such as the Galilean invariance symmetries). Second, the eBOSS QSO full-shape once combined with other cosmological probes can shed light on extensions to ΛCDM model. Here, we explore four one-parameter extensions to the flat ΛCDM model, namely the curvature density fraction Ω_k, the dark energy equation of state w_0, neutrino masses $\sum m_\nu$, and the effective number of relativistic species $N_{\rm eff}$. We compare the obtained limits with the ones from *Planck* and with the ones from the standard BAO/$f\sigma_8$ technique, in order to assess both the consistency of the results and the potential improvements brought by the EFT analysis.

This chapter is organized as follow. In Sec. 4.1, we describe the EFT analysis pipeline for eBOSS QSO that we built. In particular, we present the dataset, likelihood, and prior chosen for our analysis in 4.1.1. In 4.1.2, we assess the highest wavenumbers $k_{\rm max}$ that can be included in the analysis of eBOSS QSO full-shape data by making use of a general method that consists in evaluating the size of the theoretical error through the insertion of the dominant next-to-next leading order terms in the EFTofLSS prediction at one-loop. In 4.1.3, we address known observational systematic effects and provide tests against simulations, while in 4.1.4 we perform a new calculation to include the redshift error (which is significant for QSOs) in EFTofLSS. In Sec. 4.2, we present and discuss the constraints on flat ΛCDM from the EFT analysis of the eBOSS QSO full-shape, both in Fourier and configuration space, and in combination with other cosmological probes. Results on extensions to ΛCDM are presented and discussed in Sec. 4.3. A summary of our results and concluding remarks are given in Sec. 4.4. Additional material can be found in App. A.1, which is dedicated to exploring the impact of fixing the spectral tilt n_s and the baryons abundance ω_b in the base-ΛCDM analysis of the eBOSS QSO full-shape.

4.1 Analysis pipeline

In this chapter, we use the WC parametrization as presented in Sec. 3.4.3. In particular, the galaxy power spectrum equation we use is that of Eq. (3.180).

4.1.1 Cosmological inference setup

Data. In this work, we use various sets of cosmological observations, comparing results of the EFTofLSS applied to (e)BOSS data with those from *Planck* CMB data, and their combination. We make use of the following datasets:

- **eBOSS DR16 QSO**: The main novelty of this work is the full-shape analysis of the quasars (QSO) from the extended Baryon Oscillation Spectroscopic Survey (eBOSS) [82]. The QSO catalogs are described in Ref. [120]. The covariances are built from the EZmocks described in Ref. [121]. There are about 343 708 quasars selected in the redshift range $0.8 < z < 2.2$, making for a sample of about $0.6{\rm Gpc}^3$ at an effective redshift of $z_{\rm eff} = 1.52$, cut into two skies, NGC and SGC. We analyze the full-shape of

the eBOSS QSO power spectrum multipoles, $\ell = 0, 2$, namely the monopole and the quadrupole, measured in Ref. [122]. [1] The covariances and the window functions we use are also from [122]. We use data (and associated covariance matrices) deconvolved from the window functions, such that one does need to apply them to the prediction [58, 122]. We analyze the correlation function multipoles measured in Ref. [123]. [2] When not explicitly mentioned, our eBOSS results are obtained with the power spectrum.

- **BOSS DR12 LRG**: We compare and combine the eBOSS QSO with BOSS luminous red galaxies (LRG) [81]. The BOSS catalogs are described in Ref. [124]. The covariances are built from the patchy mocks described in Ref. [125]. The BOSS data are cut into two redshift bins, LOWZ and CMASS, spanning ranges $0.2 < z < 0.43$ ($z_{\rm eff} = 0.32$), $0.43 < z < 0.7$ ($z_{\rm eff} = 0.57$), respectively, with north and south galactic skies for each, respectively denoted NGC and SGC. We use the EFT likelihood of the full-shape of the BOSS LRG power spectrum pre-reconstructed multipoles, $\ell = 0, 2$ (namely the monopole and the quadrupole), measured and described in Ref. [69], together in cross-correlation with post-reconstruction BAO compressed parameters obtained in Ref. [59] on the post-reconstructed power spectrum measurements of Ref. [126].

- **ext-BAO**: We also combine the data from eBOSS and BOSS with external BAO (ext-BAO) measurements, namely data from 6dFGS at $z = 0.106$ and SDSS DR7 at $z = 0.15$ [127, 128, 81], and the joint constraints from eBOSS DR14 [3] Ly-α absorption auto-correlation at $z = 2.34$ and cross-correlation with quasars at $z = 2.35$ [130, 131].

- **Pantheon**: We also include the Pantheon18 SNIa catalogue, [4] spanning redshifts $0.01 < z < 2.3$ [133]. We stress that here we are only using the uncalibrated luminosity distance to Pantheon18 SNIa.

- **Planck**: Finally, we compare constraints obtained from different LSS surveys combinations with the *Planck* results obtained from analyzing the high-ℓ TTTEEE + lowE + lensing [11]. We use the nuisance parameters marginalized *Planck* `lite` likelihood when performing the MCMC, but switch to the full likelihood to derive the best-fit.

We dub "LSS" the combination of eBOSS + BOSS + ext-BAO + Pantheon to refer to an analysis that is independent of *Planck* (or any CMB data).

Likelihood and prior. To describe the eBOSS QSO full-shape data, we use the following likelihood $\mathscr{L}$:

$$-2\log(\mathscr{L}) = (D - T(\theta)) \cdot C^{-1} \cdot (D - T(\theta)) - 2\log p(\theta)\,. \tag{4.1}$$

Here D is the data vector, constructed from the measurements of the monopole and quadrupole of the power spectrum or the correlation function; $T(\theta)$ is the corresponding EFTofLSS prediction, containing also additional modeling effects, as described in Sec. 3.4, where θ designates generically all parameters– cosmological and EFT ones– entering in T; C^{-1} is the inverse

[1] Publicly available at: `https://fbeutler.github.io/hub/deconv_paper.html`.

[2] Publicly available at: `https://svn.sdss.org/public/data/eboss/DR16cosmo/tags/v1_0_1/dataveccov/lrg_elg_qso/QSO_xi/`.

[3] These data were recently updated in Ref. [129] and are consistent with those used in this work.

[4] We note that, as this work was completed, the new Pantheon+ data became available [132]. Given that the datasets are broadly consistent we do not expect major changes in our conclusions.

covariance built from the mocks mentioned in previous paragraph; $p(\theta)$ is the prior that we describe next. For our baseline ΛCDM analysis of the LSS data, we vary three cosmological parameters within uninformative large flat prior: $\{\omega_{cdm}, h, \log(10^{10}A_s)\}$, corresponding respectively to the physical cold dark matter abundance, the reduced Hubble constant, and the log-amplitude of the primordial fluctuations. We fix the physical baryons abundance $\omega_b = 0.02233$, as motivated by big-bang nucleosynthesis estimates [134], and the spectral tilt $n_s = 0.965$ to *Planck* preferred value [11]. The impact on the posteriors of letting these parameters free to vary is discussed in App. A.1. Let us stress that every time *Planck* data are used, we free ω_b and n_s, and co-vary the optical depth to reionization $\tau_{\rm reio}$. For better comparison with the literature, we present most of our cosmological results on the fractional matter abundance, the reduced Hubble constant, and the clustering amplitude, respectively $\{\Omega_m, h, \sigma_8\}$. We also explore one-parameter extensions to this baseline ΛCDM analysis, freeing either the fractional curvature density Ω_k, the equation of state parameter of a smooth dark energy field w_0, the sum of the neutrino masses $\sum m_\nu$, or the effective number of relativistic species $N_{\rm eff}$. For all runs performed, unless specified, we use *Planck* prescription for the neutrinos, taking two massless and one massive species with $m_\nu = 0.06eV$ [11]. For the EFT parameters, we analytically marginalized over the parameters appearing only linearly in our predictions with a Gaussian prior centered on 0 of width $\sim \mathcal{O}(b_1)$ in order to keep them within physical range [58]. As for the remaining ones, b_1 and c_2, we use flat prior $[0,4]$ and $[-4,4]$ while scanning them. We refer to chapters 5 and 6 for a detailed description of our choice of priors, that is dubbed "West-coast" prior therein. For eBOSS, we use $\bar{n}_g = 2\cdot 10^{-5}(h\,\mathrm{Mpc}^{-1})^3$ as estimated from Ref. [135], while for BOSS, we use $\bar{n}_g = 4\cdot 10^{-4}(h\,\mathrm{Mpc}^{-1})^3$ as estimated from Ref. [81]. The values chosen for $k_{\rm M}$ and $k_{\rm R}$ is discussed in Sec. 4.1.2. We assign one set of EFT parameters per sky cut (NGC or SGC) and per redshift bin for BOSS and eBOSS. To obtain the best-fits, we follow the App. C of Ref. [59] and minimize the full likelihood, but without scanning over the parameters appearing only linearly in our predictions, as described therein. When analyzing both BOSS and eBOSS full-shapes, we simply add their corresponding likelihoods, as there is no overlap. We also simply add the likelihoods when combining with ext-BAO, Pantheon, or *Planck*, neglecting potential small correlation.

Posterior sampling. We sample the posteriors from our likelihood using the Metropolis-Hasting algorithm from `MontePython` [136, 137]. [5] The linear power spectra are computed with the `CLASS` Boltzmann code [43]. [6] The full-shape prediction from the EFTofLSS [corresponding to Eq. (3.180)] with additional modeling effects are computed using `PyBird` [59]. [7]

Credible interval and best-fit. As we will see in chapters 5 and 6 in the context of the full-shape analysis of BOSS data with the EFTofLSS, shifts between the means of the 1D marginalized posteriors with respect to the most-likely values can arise due to prior volume effects. Therefore, when presenting the cosmological results, on top of providing the 68%-credible intervals, we also systematically provide the corresponding most-likely values. Those latter are sensitive to the prior weight but are not affected by the prior volume projection effect (see chapters 5 and 6). Let us also caution about the determination of the best-fit values quoted in this work, as they can be subject to some uncertainty, given the flatness of the likelihood of eBOSS

[5] https://github.com/brinckmann/montepython_public
[6] http://class-code.net
[7] https://github.com/pierrexyz/pybird

QSO full-shape around its maximum in some particular directions. For example, we find for eBOSS alone $\Delta\chi^2 \lesssim 0.2$ when moving by $\sim 1\sigma$ in the direction of Ω_m or σ_8, where σ is the error bars read from the 68%-credible intervals. As a complete profile likelihood analysis is beyond the scope of this work, we leave this to future investigation. See, *e.g.*, Ref. [138] for discussions on how to mitigate those uncertainties.

4.1.2 Scale cut from governing scales

In this section, we determine the scale cut of the full-shape analysis of eBOSS QSOs directly from the data by considering the impact of higher-order corrections to our one-loop prediction. We additionally validate our likelihood against simulations in order to cross-check the value of the scale cut, as well as test for additional modeling uncertainties independent of the EFTofLSS formalism. We summarize here the scale cut values that we use, and for which we find that the determination of the cosmological parameters is safe from significant systematic shifts due to the theory error:

- When analyzing the eBOSS QSO power spectrum, we include $k \in [0.01, 0.24] h\,\mathrm{Mpc}^{-1}$.
- When analyzing the eBOSS QSO correlation function, we include $s \in [20, 160]\,\mathrm{Mpc}\,h^{-1}$ (which are all the scales provided in the public data).
- For completeness, we recall that in the analysis of BOSS LRG power spectrum, we include $k \in [0.01, 0.23]\,h\,\mathrm{Mpc}^{-1}$ for CMASS, while we include $k \in [0.01, 0.20]\,h\,\mathrm{Mpc}^{-1}$ for LOWZ [101, 59].

Let us remark that it may come as a surprise that the maximal wavenumber of the analysis for eBOSS QSO are so close to the one of BOSS. Indeed, naively, given that eBOSS data are at higher redshift, therefore with smaller nonlinearities, and are of smaller volume than BOSS data, one may expect that the EFTofLSS prediction at one loop could allow to include (in a controlled manner) deeper scales in the eBOSS full-shape analysis, *i.e.*, $k_{\mathrm{max}}^{\mathrm{eBOSS}} > k_{\mathrm{max}}^{\mathrm{BOSS}}$. In fact, the scales at which the theory error starts to become important is similar in both analyses. This is because, although eBOSS error bars are larger, the theory error is dominated by terms that renormalize products of velocities in the redshift-space expansion and that happen to be larger for eBOSS QSOs than BOSS LRGs. We expand over this issue in the following.

Governing scales in eBOSS QSOs. In Eq. (3.180) appear three scales governing the EFT expansions: the nonlinear scale, k_{NL}^{-1}, the spatial extension of the observed objects, k_{M}^{-1}, and the "dispersion" scale, k_{R}^{-1}. The nonlinear scale k_{NL}^{-1} can be understood as the typical distance matter particles travel during the (finite) age of the Universe $\sim \mathscr{H}^{-1}$. It is thus about $k_{\mathrm{NL}}^{-1} \sim v/\mathscr{H}$, where $v \ll 1$, as we are dealing with non-relativistic matter. For the long-wavelength modes of interest, $k \sim \mathscr{H}$, this implies $k/k_{\mathrm{NL}} \ll 1$. Therefore, this allows us to organize the expansion of the galaxy density field δ_g in long-wavelength "smoothed" fluctuations, *e.g.*, $\delta_g \sim \partial^2\phi/\mathscr{H}^2 \sim (k/k_{\mathrm{NL}})^2 \ll 1$ [55]. In particular, at next-to-leading order, this scale appears explicitly in the counterterm $\propto (\partial^2/k_{\mathrm{NL}}^2)\partial^2\phi/\mathscr{H}^2 \sim c_{s,\mathrm{eff}}^2 (k^2/k_{\mathrm{NL}}^2)\delta^{(1)}$ renormalizing the dark matter field δ at short distances [54]. The spatial extension of the observed objects k_{M}^{-1} is instead controlling the spatial derivative expansion [65]. At leading order in derivatives, δ_g receives a contribution of the form of $\delta_{hd} \sim (\partial^2/k_{\mathrm{M}}^2)\partial^2\phi/\mathscr{H}^2 \sim R_*^2 (k^2/k_{\mathrm{M}}^2)\delta^{(1)}$. For halos, k_{M}^{-1} is typically of a few Mpc's, and similarly for LRGs residing in halos, or QSOs residing in LRGs. Therefore,

in the galaxy power spectrum, Eq. (3.180), given $k_{\rm NL} \sim k_{\rm M}$, the counterterm proportional to $c_{\rm ct}^2 \sim c_{s,\rm eff}^2 + R_*^2$ is then the linear combination of the two aforementioned contributions, arising from the renormalization of the dark matter field at short distances and from the spatial derivatives expansion (see Sec. 3.4). Finally, the products of velocity operators, appearing in the redshift space expansion, are renormalized by counterterms entering with yet another scale, $k_{\rm R}^{-1}$ [72, 139], *e.g.*, $\delta_g \supset \frac{1}{2}\mu^2 k^2 (v\cdot\hat{z})^2 \supset \frac{1}{2} c_{r,1} \mu^2 (k/k_{\rm R})^2 \delta^{(1)}$, where $c_{r,1}$ is defined in Eq. (3.180). In practice, these scales can be measured directly from the data with associated EFT parameters $\sim \mathcal{O}(1)$. As explained above, since for biased tracers, the dark matter counterterm is degenerate with the higher-derivative term with $k_{\rm NL}^{-1} \sim k_{\rm M}^{-1}$, we only measure $k_{\rm M}$ and $k_{\rm R}$. For BOSS, it was found that $k_{\rm M} \sim 0.7h\,{\rm Mpc}^{-1}$ and $k_{\rm R} \sim 0.35h\,{\rm Mpc}^{-1}$ [58, 139]. [8] We find for eBOSS similar value for the scale $k_{\rm M} \sim 0.7h\,{\rm Mpc}^{-1}$, which is expected since QSOs are residing in LRGs. In contrast, we measure that $k_{\rm R}^{\rm eBOSS} \sim 0.7 k_{\rm R}^{\rm BOSS}$, such that $c_{r,1} \sim \mathcal{O}(1)$. Such measurement indicates that the "velocity dispersion" along the line-of-sight is larger in eBOSS QSOs than in BOSS LRGs, which could point to the possibility that QSOs populate preferentially satellite galaxies rather than central galaxies (see also Ref. [140] suggesting likewise from the perspective of halo occupation distribution). For all analyses in this chapter, we choose the following values for the renormalization scales, ensuring that $c_{\rm ct}$, $c_{r,1}$ are measured well within their Gaussian prior $\mathcal{N}(0,2)$:

$$\begin{aligned} k_{\rm M}^{\rm BOSS} &= 0.7h\,{\rm Mpc}^{-1}, \qquad & k_{\rm R}^{\rm BOSS} &= 0.35h\,{\rm Mpc}^{-1}, \\ k_{\rm M}^{\rm eBOSS} &= 0.7h\,{\rm Mpc}^{-1}, \qquad & k_{\rm R}^{\rm eBOSS} &= 0.25h\,{\rm Mpc}^{-1}. \end{aligned} \tag{4.2}$$

Next-to-next-to-leading order. Given the scale estimates above, the theory error associated to the higher order terms not included in our baseline analysis is dominated by the terms associated to $k_{\rm R}^{-1} > k_{\rm NL}^{-1}, k_{\rm M}^{-1}$. Thus, the size of the theory error can be estimated by the size of the largest contributions at next-to-next-to-leading order (NNLO), which are given by the counterterms [139]:

$$P_{\rm NNLO}(k,\mu) = \frac{1}{4} b_1 \left(c_{r,4} b_1 + c_{r,6}\mu^2\right) \mu^4 \frac{k^4}{k_{\rm R}^4} P_{11}(k)\,, \tag{4.3}$$

where $c_{r,4}$ and $c_{r,6}$ are the $\mathcal{O}(1)$-parameters controlling the size of the NNLO counterterms. Following Ref. [69], we measure the shift in each 1D posterior upon adding of the NNLO term given by Eq. (4.3) as a function of $k_{\rm max}$. The scale cut is determined as the highest scale $k_{\rm max}$ included in the analysis such that the theory error is safely small.

$k_{\rm max}$ vs. theory error. In Tab. 4.1, we show as a function of $k_{\rm max}$ the shifts upon adding the NNLO term, Eq. (4.3), to the one-loop prediction, Eq. (3.180), on the 1D posteriors of the three baseline cosmological parameters, Ω_m, h, and σ_8, and two EFT parameters, b_1 and c_2. Given the scale estimates above, we put a Gaussian prior $\mathcal{N}(0,4)$ on the NNLO parameters $c_{r,4}$ and $c_{r,6}$ to keep their size within physical range with a conservative choice. The posteriors are obtained as described in previous subsection, additionally marginalizing over $c_{r,4}$ and $c_{r,6}$ when including the NNLO term in the prediction. At $k_{\rm max} \leq 0.27h\,{\rm Mpc}^{-1}$, the shift in all parameters is small. At $k_{\rm max} = 0.30h\,{\rm Mpc}^{-1}$, the shift starts to become appreciable in Ω_m, to about 0.5σ, where σ is the 68% CL. Therefore, staying on the conservative side and within

[8] Note that here we have adjusted the value of $k_{\rm R}$, redefining accordingly the associated EFT parameters.

$\Delta^{\rm shift}_{\rm NNLO}/\sigma^{\rm eBOSS}_{\rm stat}$				
$k_{\rm max}$ [$h\,{\rm Mpc}^{-1}$]	0.21	0.24	0.27	0.30
$\Omega_{\rm m}$	0.00	-0.04	0.05	-0.47
h	-0.02	-0.07	-0.06	0.09
σ_8	-0.04	-0.15	-0.03	-0.20
$b_1^{\rm N}$	0.02	0.09	0.02	-0.09
$c_2^{\rm N}$	0.02	0.06	0.00	-0.18
$b_1^{\rm S}$	0.02	0.08	0.06	0.01
$c_2^{\rm S}$	-0.02	-0.07	0.04	0.00

Table 4.1: Relative shifts of the cosmological and EFT parameters from the addition of the NNLO to the base-ΛCDM fit to eBOSS for different values of $k_{\rm max}$ in $h\,{\rm Mpc}^{-1}$.

the EFT regime of validity, we take as our final choice for the scale cut $k_{\rm max} = 0.24h\,{\rm Mpc}^{-1}$, where no appreciable shift is observed. Let us note that the same conclusion is reached when considering the shift in the best-fit values upon inclusion of the NNLO: at $k_{\rm max} = 0.24h\,{\rm Mpc}^{-1}$, we find $\lesssim 0.25\sigma$ on all cosmological parameters. Formally the EFT expansions are convergent only for $k < \min(k_{\rm NL}, k_{\rm M}, k_{\rm R}) = k_{\rm R}$. Therefore, for eBOSS, this reinforce our choice of $k_{\rm max} = 0.24h\,{\rm Mpc}^{-1}$, as it is smaller than the EFT breakdown scale, $k_{\rm R} \sim 0.25h\,{\rm Mpc}^{-1}$. However, we note that this $k_{\rm max}$ is rather close to $k_{\rm R}$. Consequently, the associated parameter controlling this expansion is close to unity, and the whole tower of counterterms (at all order) proportional to powers of $k_{\rm R}^{-1}$ can in principle be of the same order as the linear power spectrum around $k_{\rm max}$. Nevertheless, the theory error should ultimately be compared with the observational error to gauge whether the computation is sufficiently under control. In practice, we find that despite being very close the EFT breakdown scale, for our truncated expansion at one-loop, the shift in parameters presented in Tab. 4.1 is much smaller than the observational error up to $k_{\rm max} \lesssim k_{\rm R}$, and it is safe to take $k_{\rm max} = 0.24h\,{\rm Mpc}^{-1}$. In addition, an analysis to higher $k_{\rm max}$ than the one found here is not precluded by the size of $k_{\rm R}^{-1}$. Indeed, the multipoles can be rotated to form new linear combinations where the terms associated to $k_{\rm R}^{-1}$ are suppressed [139]. As shown in Ref. [139], not much cosmological constraint is gained by such analysis for BOSS data volume (see also [141]). Similarly, we find that the addition to higher wavenumbers in the full-shape analysis of eBOSS QSOs does not improve significantly the constraints. For simplicity, we thus present the results from the multipoles instead of the rotated ones.

4.1.3 Assessing systematics beyond the EFT reach

Our method to determine the scale cut is convenient as it does not rely on simulations (except the ones used to built the covariance). We have simply taken the scale cut as being the $k_{\rm max}$ for which the theory error controlled by the largest NNLO contribution, Eq. (4.3), is negligible at the level of the posteriors. This is a well-defined procedure relying only on estimates of the scales entering in the EFT expansions. However, it does not allow for testing the modeling aspects beyond the EFTofLSS prediction, as *e.g.*, the additional observational effects described at the end of Sec. 3.4. In order to assess the accuracy of these extra modeling aspects, in particular the window functions, we perform the following two tests.

Test against simulations. We fit the full-shape of the mean over all EZmock realizations. As described in Sec. 4.1.1, those mocks are built to simulate eBOSS observational characteristics such as the sky mask, redshift selection, systematics weights and veto, etc. Results from this

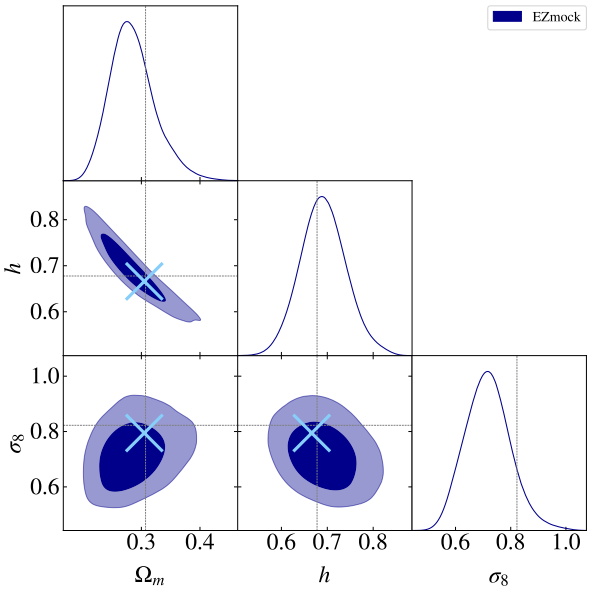

Figure 4.1: Triangle plot (1D and 2D posterior distributions) of the cosmological parameters reconstructed when fitting the mean of all EZmock realizations, analyzed up to $k_{\rm max} = 0.24h\,{\rm Mpc}^{-1}$. The crosses correspond to the best-fit values while the dashed lines correspond to the truth of the simulation.

fit are shown in Fig. 4.1. We find that up to $k_{\rm max} = 0.24h\,{\rm Mpc}^{-1}$, the best-fit values of the cosmological parameters of interest (Ω_m, h, and σ_8) are shifted with respect to the truth of the simulations by $\lesssim 1/3 \cdot \sigma$. [9] This shows that our modeling of the observational effects in eBOSS are under good control, and our previous determination of the scale cut $k_{\rm max} = 0.24h\,{\rm Mpc}^{-1}$ is corroborated by our fit to simulations. Before moving on, a comment on the 1D posteriors of the reconstructed cosmological parameters is in order. Although the best-fit parameters agree well with the fiducial model, we see that the mean of the posterior is shifted with respect to the fiducial by up to 1.3σ (on σ_8). The fact that the mean is shifted with respect to the best-fit represents a clear illustration of the *prior volume projection effects*, as mentioned in Sec. 4.1.1 and discussed throughout in chapter 5: this motivates us to consider the 68%-credible intervals *together* with the corresponding best-fit values, especially when comparing results from two different experiments.

Fourier vs. configuration space. In the following section, we compare the results obtained when fitting the correlation function or the power spectrum of eBOSS QSO. This allows us to assess the potential systematic error associated to the estimators and the differences in the modeling discussed at the end of Sec. 3.4. In particular, the effect of the mask cancels in the correlation function estimator, which makes it free from potential inaccuracies associated to the modeling of the window function. In the following, we will demonstrate that the posteriors of Ω_m, h, and σ_8 are consistent at $< 0.4\sigma$ between the Fourier and the configuration space analyses (see Tab. 4.2 and Fig. 4.4 for details). Bearing in mind that the information content in the power spectrum and the correlation is not exactly the same in the BAO part and due to effectively different scale cuts, such consistency provides a conservative bound on the level of

[9] Hereinafter, when comparing results from the *same* dataset, σ is taken as the error bar read from the 68%-credible interval, regardless of whether we compare the posterior means or best-fits.

the aforementioned systematics. For more discussions on the comparison between the analyses of the power spectrum or the correlation function, see Ref. [69].

Additional systematic errors? Last, we caution that the tests conducted in this work only assess the systematics arising at the level of the summary statistics: the cosmological results are also dependent on the choices made at the level of map-making and catalog selection, which are beyond the scope of the present study. We also mention that there are sub-leading contributions that we have not included in our predictions, in particular wide-angle and relativistic effects, line-of-sight dependent effects, and corrections to fiber collisions. The wide-angle and relativistic effects have been shown to be negligible for current surveys at $k_{\rm min} = 0.01h\,{\rm Mpc}^{-1}$ in, *e.g.*, Refs. [142, 74, 143, 144]. Similarly, the line-of-sight dependent effects have been shown to lead to a relatively small impact on the determination of the cosmological parameters in the context of the EFT analysis of BOSS in the App. D of Ref. [69] (see also Ref. [145]). However, these conclusions are dependent on the choice of prior on the size of the tidal alignment biases. While for LRGs selected by BOSS, such estimate can be found in Ref. [146], QSOs selected by eBOSS lack, to our knowledge, an estimate of the size of tidal alignments. If no estimate can be derived for QSOs, the bispectrum can mitigate those effects (see *e.g.*, Ref. [147]). We leave this to future work. Finally, the fiber collisions can be treated using the effective window method put forward in Ref. [148]. This correction has been implemented in the EFT analysis of BOSS in Ref. [58]. The largest corrections are degenerate with the EFT counterterms [148], and are therefore automatically accounted for in our analysis. The remaining corrections, the so-called uncorrelated part [148], can also be straightforwardly included. However, they were shown to be negligible for BOSS volume [58]: we therefore also neglect them in the current analysis. Finally, we are now going to show that our analysis is free from errors in the redshift determination of eBOSS QSOs as the corrections to the prediction happen to be degenerate with some EFT counterterms.

4.1.4 Including redshift error in EFTofLSS

The broadness of the emission lines of the quasars from the eBOSS QSO data, due to the rotating gas located around the black hole, increases the uncertainties in the determination of their redshift, see *e.g.*, Ref. [149]. Here, we show that the leading corrections coming from these redshift errors are, under minor assumptions concerning their distribution, degenerate with EFT counterterms (justifying that our analysis is free from those potential systematics). Note that this discussion is only relevant for biased tracers that have a significant redshift error, as is the case for quasars. For galaxies, on the other hand, the redshift is very well determined, and this discussion is not useful. Note that this calculation is entirely new and that it can be used for other data with significant redshift uncertainty.

Integrating redshift errors into the galaxy power spectrum The uncertainties in the determination of the redshift can be tracked by introducing an independent variable, $\delta z_{\rm sys}$, in Eq. (3.34):

$$1 + z_{\rm obs} = (1+z)(1+\delta z_{\rm pec} + \delta z_{\rm sys})\,. \tag{4.4}$$

For convenience, we define an associated "fake" velocity variable given by $\delta z_{\rm sys} \equiv v_{\rm sys}(z)/c$. In what follows, we perform the same derivation as in Sec. 3.2.1 (where we dealt with red-

shift space distortion), but with the replacement $\boldsymbol{v}\cdot\hat{n} \to \boldsymbol{v}\cdot\hat{n} + v_{\rm sys}$. Therefore, in the presence of redshift errors, the relation between the overdensities in redshift space and real space, Eq. (3.53), is modified to:

$$\delta^{\rm sys}_{g,r}(\boldsymbol{k}) = \delta_g(\boldsymbol{k}) + \int d^3x e^{-i\boldsymbol{k}\cdot\boldsymbol{x}} \left(e^{-i\boldsymbol{k}\cdot\hat{n}\frac{\boldsymbol{v}}{\mathscr{H}}\cdot\hat{n}} e^{-i\boldsymbol{k}\cdot\hat{n}\frac{v_{\rm sys}}{\mathscr{H}}} - 1 \right) (1+\delta_g(\boldsymbol{x}))\,. \tag{4.5}$$

We want to understand the leading corrections to our predictions from the presence of redshift errors. To see this, we can Taylor-expand $e^{-i\boldsymbol{k}\cdot\hat{n}\frac{v_{\rm sys}}{\mathscr{H}}} = 1 - i(\boldsymbol{k}\cdot\hat{n})\,\mathscr{H}^{-1}\,v_{\rm sys} - \frac{1}{2}(\boldsymbol{k}\cdot\hat{n})^2\,\mathscr{H}^{-2}\,v^2_{\rm sys} + \dots$ in the above equation. After some straightforward manipulations, Eq. (4.5) becomes:

$$\delta^{\rm sys}_{g,r}(\boldsymbol{k}) = \delta_{g,r}(\boldsymbol{k}) + \varepsilon_{\rm sys}(\boldsymbol{k})\,\delta_D(k) + \varepsilon_{\rm sys}(\boldsymbol{k})\,\delta_{g,r}(\boldsymbol{k}) + \dots\,, \tag{4.6}$$

where $\delta_{g,r}(\boldsymbol{k})$ is the redshift-space galaxy density field without redshift error given by Eq. (3.53). In addition, we have introduced the notation

$$\varepsilon_{\rm sys}(\boldsymbol{k}) \equiv -i\mu k\mathscr{H}^{-1}\,v_{\rm sys} - \frac{1}{2}\mu^2k^2\mathscr{H}^{-2}\,v^2_{\rm sys}\,, \tag{4.7}$$

with $\mu \equiv (\boldsymbol{k}\cdot\hat{n})/|\boldsymbol{k}|$. The "…" represents higher-order corrections in powers of $\varepsilon_{\rm sys}$. Assuming that, by definition, $v_{\rm sys}$ is a scale-independent variable that correlates only with itself, the power spectrum picks, at leading orders in derivatives, corrections going as:

$$\begin{aligned} P^{\rm sys}_{g,r}(k,\mu) = P_{g,r}(k,\mu) &- 2i\mu k\frac{\bar{v}_{\rm sys}}{\mathscr{H}}\sigma_0^2 - 2i\mu k\frac{\bar{v}_{\rm sys}}{\mathscr{H}}(b_1+f\mu^2)^2P_{11}(k) \\ &- \mu^2k^2\frac{\sigma^2_{v,\rm sys}}{\mathscr{H}^2}(\delta_D(k)+3\sigma_0^2) - 2\mu^2k^2\frac{\sigma^2_{v,\rm sys}}{\mathscr{H}^2}(b_1+f\mu^2)^2P_{11}(k) + \dots\,, \end{aligned} \tag{4.8}$$

where we have introduced the following notation: $\bar{v}_{\rm sys} \equiv \langle v_{\rm sys}|v_{\rm sys}\rangle$, $\sigma^2_{v,\rm sys} \equiv \langle v_{\rm sys}v_{\rm sys}|v_{\rm sys}v_{\rm sys}\rangle$, and $\sigma_0^2 \equiv P_{g,r}(0)$.

Application to eBOSS QSO full-shape analysis From this derivation, we can make several observations:

- The first two correction terms at the first line of Eq. (4.8), are purely imaginary, and thus do not appear in the even multipoles that we use in our analysis. Moreover, those terms are significant only if the determination of the redshifts is biased on average, *i.e.*, $\langle v_{\rm sys}|v_{\rm sys}\rangle \neq 0$. [10]
- Therefore, as anticipated and according to Eq. (3.180), we see that the leading corrections to uncertainties in the redshift determination are degenerate with EFT counterterms going like $\sim \mu^2k^2$ (namely, the terms in $c_\varepsilon^{\rm quad}$) or $\sim \mu^2k^2P_{11}(k)$ (namely, the terms in $c_{r,1}$). Therefore, albeit a potential adjustment in the prior for the coefficients associated to those counterterms to accomodate this new effect, our predictions are unchanged in the presence of redshift errors.

[10] One could imagine measuring the redshift error bias by searching in the odd multipoles such signal, that may be clean from other known contributions such as relativistic or wide-angle effects that present a different scaling dependence, see *e.g.*, Refs. [74, 150]. Besides, in principle, the odd window function multipoles that are imaginary also mix imaginary contributions in the power spectrum to the even multipoles of the power spectrum. We leave those explorations to future work.

- Beyond the leading corrections, there could be a term going like $\sim k^3 P_{11}(k)$ from the contraction of $\langle v^3_{\rm sys} | v^3_{\rm sys} \rangle$, that is not degenerate with counterterms in the EFT. However, again, this term is purely imaginary, and thus does not appear in the even multipoles that we use in our analysis. Moreover, this term is significant only if the distribution of the redshift errors has some level of assymetry.

- We can get insights on the size of the corrections by inspecting the distribution of the redshift errors. From Ref. [151], we learn that the variance of the estimated distribution of eBOSS QSO redshift errors corresponds roughly to $\sigma^2_{v,\rm sys} \sim (300\text{km/s})^2$. This tells us that the size of the correction is about

$$\frac{\sigma^2_{v,\rm sys}}{\mathscr{H}^2(z)} \sim \frac{(1+z_{\rm eBOSS})^2 (300\ \text{km/s})^2}{(\Omega_m \cdot (1+z_{\rm eBOSS})^3 + \Omega_\Lambda)\,(100\,h\ \text{km/s/Mpc})^2} \sim 10\ (\text{Mpc}\,h^{-1})^2\ . \tag{4.9}$$

  Despite this being slightly larger than the size of $c_\varepsilon/k^2_{\rm M} \sim 4\ (\text{Mpc}\,h^{-1})^2$, σ^2_0 is smaller than $1/\bar{n}_g \sim 2\cdot 10^5\ (\text{Mpc}\,h^{-1})^3$ for eBOSS, and therefore, the first correction term at the second line of Eq. (4.8) is smaller than the corresponding EFT counterterm going as $\sim \mu^2 k^2$. Furthermore, Eq. (4.9) also tells us that $b_1^2\ \sigma^2_{v,\rm sys}\,\mathscr{H}^{-2} \sim 40\ (\text{Mpc}\,h^{-1})^2$ is about 1.6 times smaller than $b_1\, c_{r,1}/k^2_{\rm R} \sim 64\ (\text{Mpc}\,h^{-1})^2$, *i.e.*, the typical size of the EFT counterterm going as $\sim \mu^2 k^2 P_{11}$ that is degenerate with the last correction in the second line of Eq. (4.8). Thus, corrections to redshift uncertainties are well accounted in our analysis given the prior we put on those counterterms. [11]

- The next-to-leading correction to the even multipoles is going like $\sim \mu^4 k^4 P_{11}(k)$, which is degenerate with EFT counterterms at two loop [see Eq. (4.3)]. From Ref. [151] (see in particular figs. 4 and 5), we see that the redshift errors distribution of eBOSS QSO sample departs visibly from a Gaussian by the presence of fat tails. Naively, this indicates that higher moments of the distribution are suppressed, and in particular, $\langle v^4_{\rm sys} | v^4_{\rm sys} \rangle \ll \sigma^4_{v,\rm sys}$. Thus, the higher-order corrections to redshift uncertainties, *e.g.*, $\sim \mu^4 k^4 \frac{\langle v^4_{\rm sys} | v^4_{\rm sys} \rangle}{\mathscr{H}^4} P_{11}(k)$, become quickly negligible with respect to the EFT counterterms that share similar scale dependence, *e.g.*, the NNLO counterterms of Eq. (4.3), that are themselves already higher order and thus safely small with respect to the error bars of the data at the scales analyzed.

We conclude that, given the presence of EFT counterterms that share similar scale dependence with corrections from redshift errors and large enough priors to encompass these effects, our analysis is unaffected by uncertainties in the determination of eBOSS QSO redshifts.

4.2 Constraints on flat ΛCDM

In this section, we present results on the flat ΛCDM model from the EFT analysis of the full-shape of eBOSS QSOs. We perform combined analyses with different sets of LSS surveys, namely BOSS full-shape, ext-BAO, Pantheon, as well as with *Planck* data, as described in Sec. 4.1.1. We remind that for our base-ΛCDM analysis, we fix the baryon abundances to the mean value measured by BBN experiments, the spectral tilt n_s to *Planck* preferred value, and

[11] Note that here we have assumed that redshift uncertainties are thought to arise in the determination of the peculiar velocity of the objects, as given by Eq. (4.4). If instead we attribute them as a global error, such as $z_{\rm obs} = z + (1+z)\delta z_{\rm pec} + \delta z_{\rm sys}$, the size of the corrections to our observables will be reduced by a factor $1+z$.

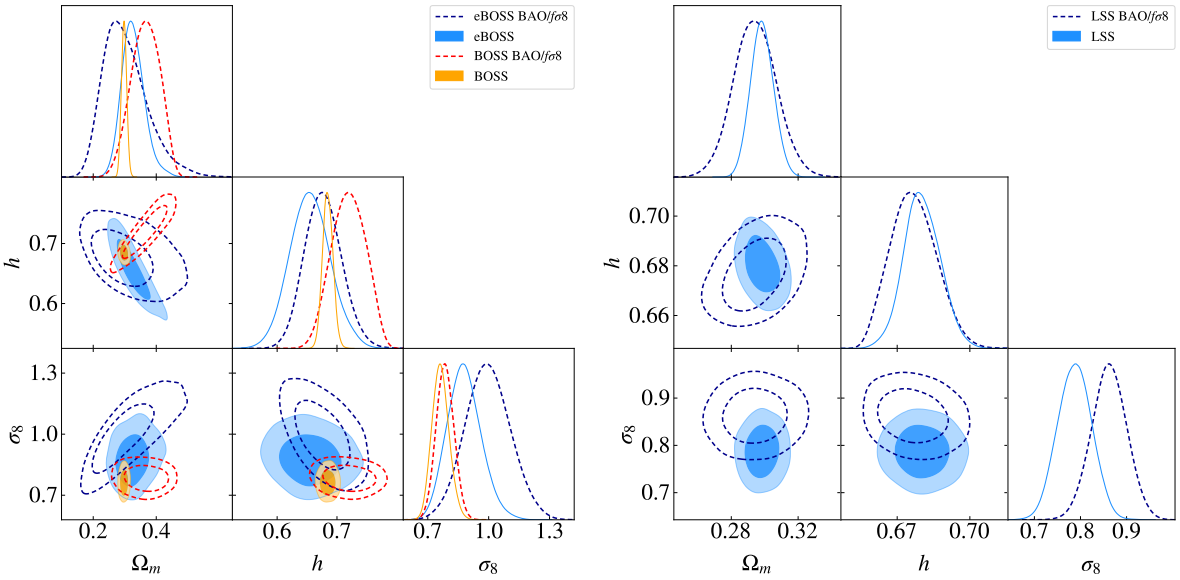

Figure 4.2: Triangle plots (1D and 2D posterior distributions) of the cosmological parameters reconstructed either from the EFT full-shape analysis or from the compressed BAO/$f\sigma_8$ parameters. In the *left panel*, we have represented these two analyses for eBOSS and BOSS, while in the *right pannel* we have combined these two datasets and added the ext-BAO and Pantheon data. In this figure and for the rest of this chapter, when not explicitly mentioned, eBOSS and BOSS refer to the EFT full-shape analysis of the power spectrum multipoles.

the neutrino total mass to its minimal value, as explained in Sec. 4.1.1. In App. A.1, we show the impact on the cosmological results letting the baryon abundance to vary within a Gaussian prior motivated by BBN experiments and freeing n_s. The free neutrino mass case, together with other one-parameter extensions to our base-ΛCDM model, are presented in the next section.

As a preliminary analysis and to gauge the impact of the EFT analysis of eBOSS, we show in Fig. 4.2 the results from the analyses of eBOSS, BOSS and their combination (LSS, referring to eBOSS + BOSS + ext-BAO + Pantheon), using either the combination of BAO and redshift space distortion information (BAO/$f\sigma_8$) as measured by the eBOSS Collaboration [152] or the EFT full-shape likelihood built in this work. One can see that, as expected, the EFT analysis allows us to gain significant constraining power over the conventional BAO/$f\sigma_8$ information. For eBOSS, the error bars of Ω_m and σ_8 are reduced by a factor ~ 2.0 and ~ 1.3, respectively. For BOSS, the error bars of Ω_m and h are reduced by ~ 5.4 and ~ 3.2, respectively. Finally, for their combination, we find that the error bars of Ω_m and h are reduced by ~ 2.0 and ~ 1.25, respectively. We also note that the EFT likelihood leads to a lower mean for σ_8 than the BAO/$f\sigma_8$ analysis: $\sim 1\sigma$ for eBOSS and $\sim 2\sigma$ for the full combination of LSS datasets. Note that, as can be seen in $\Omega_m - \sigma_8$ plane, the results obtained with BOSS and eBOSS are in better agreement in the EFT analysis than in the template-based BAO/$f\sigma_8$ analysis (which shows a difference of low statistical significance). This may be traced in part to the lower mean value of σ_8 inferred in the EFT analysis of eBOSS, which in addition may be subject to some prior volume projection effects as we comment on later.

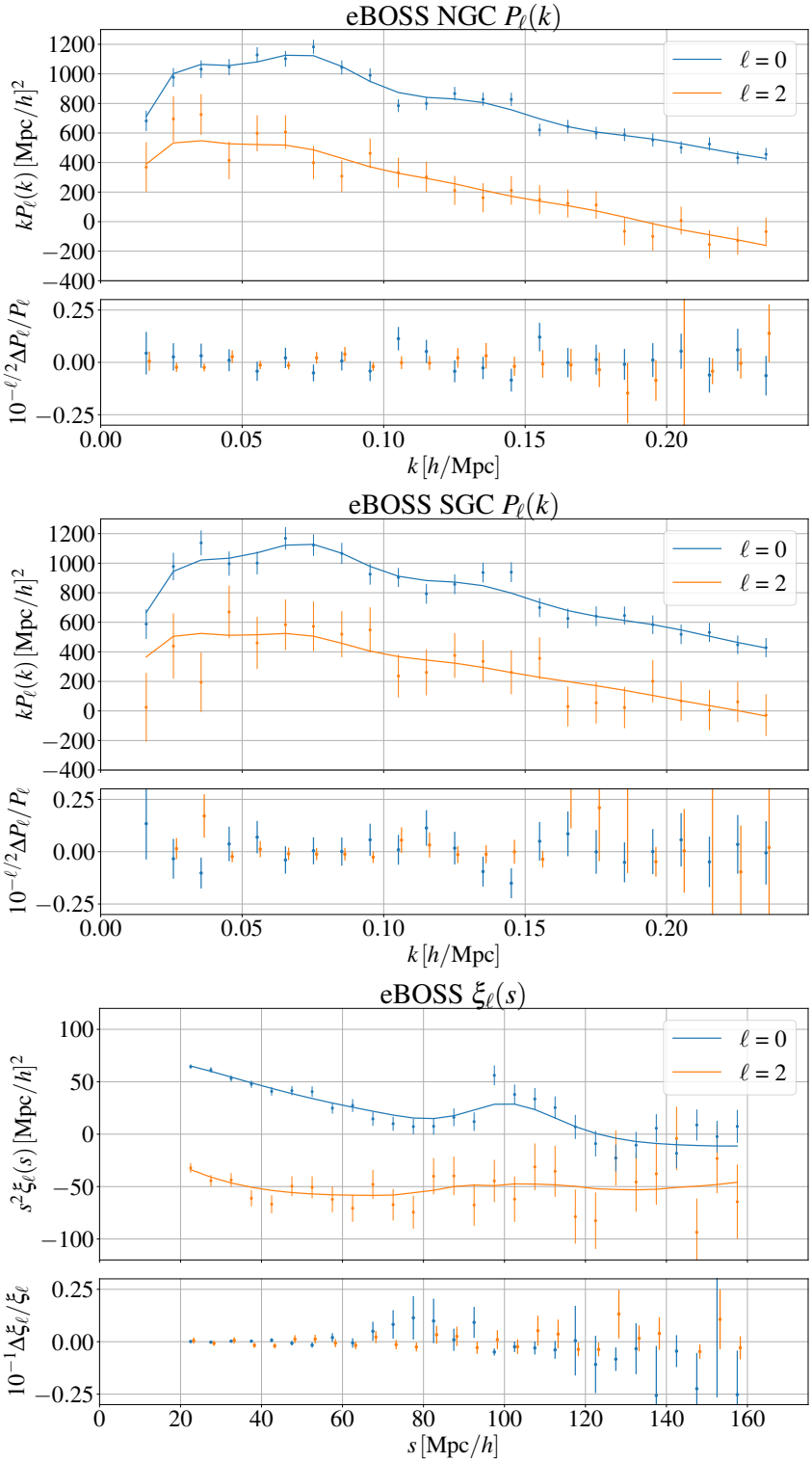

Figure 4.3: *Upper* - Best-fit predictions of the monopole and quadrupole of the power spectrum $P_\ell(k)$ for the NGC sky cut of eBOSS QSOs against the data. We also plot the residuals with respect to the data. *Middle* - Same but with the eBOSS SGC sky cut. *Lower* - Same but with the eBOSS correlation function $\xi_\ell(s)$ measured on the combination of NGC-SGC sky cuts.

best-fit $\mu^{+\sigma_u}_{-\sigma_l}$	BOSS	eBOSS	eBOSS $\xi_\ell(s)$	eBOSS + BOSS	BOSS + ext.BAO + Pan	eBOSS + BOSS + ext.BAO + Pan
$\Omega_{\rm m}$	0.2981 $0.2978^{+0.0082}_{-0.0083}$	0.331 $0.327^{+0.031}_{-0.039}$	0.306 $0.311^{+0.032}_{-0.037}$	0.2986 $0.2981^{+0.0077}_{-0.0079}$	0.2986 $0.2979^{+0.0075}_{-0.0076}$	0.2991 $0.2985^{+0.0066}_{-0.0071}$
h	0.6839 $0.6846^{+0.0086}_{-0.0086}$	0.646 $0.655^{+0.033}_{-0.034}$	0.648 $0.655^{+0.026}_{-0.031}$	0.6814 $0.6827^{+0.0078}_{-0.0085}$	0.6813 $0.6812^{+0.0078}_{-0.0079}$	0.6793 $0.6803^{+0.0072}_{-0.0078}$
σ_8	0.811 $0.763^{+0.038}_{-0.045}$	0.943 $0.880^{+0.076}_{-0.089}$	0.922 $0.888^{+0.084}_{-0.085}$	0.840 $0.787^{+0.036}_{-0.039}$	0.809 $0.762^{+0.038}_{-0.044}$	0.840 $0.788^{+0.037}_{-0.037}$
$\omega_{\rm cdm}$	0.1164 $0.1166^{+0.0047}_{-0.0047}$	0.1154 $0.1162^{+0.0077}_{-0.0079}$	0.106 $0.110^{+0.010}_{-0.010}$	0.1157 $0.1160^{+0.0038}_{-0.0043}$	0.1156 $0.1153^{+0.0042}_{-0.0042}$	0.1150 $0.1152^{+0.0035}_{-0.0037}$
$\ln(10^{10}A_s)$	3.08 $2.95^{+0.12}_{-0.12}$	3.42 $3.26^{+0.20}_{-0.21}$	3.49 $3.36^{+0.21}_{-0.24}$	3.16 $3.02^{+0.11}_{-0.11}$	3.08 $3.03^{+0.12}_{-0.12}$	3.17 $3.17^{+0.10}_{-0.10}$
S_8	0.808 $0.761^{+0.040}_{-0.046}$	0.991 $0.918^{+0.089}_{-0.123}$	0.931 $0.903^{+0.096}_{-0.115}$	0.838 $0.785^{+0.037}_{-0.040}$	0.807 $0.759^{+0.039}_{-0.045}$	0.839 $0.786^{+0.038}_{-0.038}$
$\chi^2_{\rm min}$	157.9	57.1	53.9	217.8	1191.1	1251.0
$N_{\rm data}$	170	92	56	262	1224	1316
p-value	0.13	0.94	0.20	0.47	0.50	0.64

Table 4.2: Cosmological results (best-fit, posterior mean, and 68% CL) of different combinations of LSS data, including BOSS and eBOSS, for our base-ΛCDM model. For each dataset we also report its best-fit $\chi^2_{\rm min}$, the number of data bins $N_{\rm data}$, and the associated p-values. In the following, "LSS" refers to eBOSS + BOSS + ext-BAO + Pantheon.

Parameter	eBOSS - BOSS		BOSS - Planck		eBOSS - Planck		(eBOSS + BOSS) - Planck		LSS - Planck	
	b-f	μ	b-f	μ	b-f	μ	b-f	μ	b-f	μ
$\Omega_{\rm m}$	0.89	0.76	-1.60	-1.58	0.42	0.30	-1.61	-1.62	-1.67	-1.68
h	-1.08	-0.84	1.05	1.08	-0.79	-0.53	0.84	0.93	0.66	0.72
σ_8	1.41	1.25	-0.03	-1.13	1.56	0.82	0.72	-0.63	0.75	-0.63
$\omega_{\rm cdm}$	-0.11	-0.05	-0.75	-0.69	-0.58	-0.47	-1.04	-0.95	-1.32	-1.26
$\ln(10^{10}A_s)$	1.43	1.30	0.26	-0.76	1.82	1.05	1.04	-0.19	1.17	-0.09
S_8	1.55	1.33	-0.55	-1.57	1.43	0.77	0.11	-1.15	0.13	-1.15

Table 4.3: σ-deviations between the ΛCDM cosmological parameters reconstructed from eBOSS, BOSS, their combination, and *Planck*. For a given cosmological parameter, the σ-deviation metric is computed, assuming Gaussian errors, as $(\mu_1-\mu_2)/\sqrt{\sigma_1^2+\sigma_2^2}$, where μ_i are either the means (μ) or the best-fits (b-f) obtained from the two experiments $i=1,2$, while σ_i are the associated error bars read from the 68%-credible intervals.

4.2.1 Flat ΛCDM from the EFT analysis of eBOSS

Goodness of fit. Before commenting over the reconstructed cosmological parameters, let us first assess the goodness of fit. We plot in Fig. 4.3, using the best-fit parameters listed in Tab. 4.2, the theoretical prediction of the monopole and quadrupole of the power spectrum, as well as the correlation function, against the data. One can see that there are not particular features in the residuals. We list in Tab. 4.2 the $\chi^2_{\rm min}$ and degrees of freedom of each fit. Assuming that all data points and parameters are uncorrelated, we find that the p-values associated with the different fits are acceptable both for our analyses in Fourier and configuration space, which tell us that our model is a good description of the data, up to the scale cut chosen in Sec. 4.1.2.

68%-credible interval. The 1D and 2D posterior distributions from eBOSS, analysed alone or in combination with other LSS probes, are shown in Fig. 4.4, with the corresponding 68%-credible intervals and best-fit values given in Tab. 4.2. We also display posteriors obtained with *Planck* data for comparison. As it can be read off from Tab. 4.2, from eBOSS alone, we reconstruct at 68% CL within the base-ΛCDM model, Ω_m, h, and σ_8 to 11%, 5%, and 9% precision, respectively. The eBOSS full-shape analysis in configuration space leads to comparable

error bars at $\lesssim 20\%$ (and consistency on Ω_m, h, and σ_8 at $< 0.4\sigma$, as already commented in Sec. 4.1.2). The corresponding posteriors are shown in the lower right panel of Fig. 4.4.

4.2.2 Comparison with several LSS probes

Consistency across LSS probes. The EFT analysis of eBOSS QSOs provides independent measurements of ΛCDM parameters in a different redshift range than previous EFT analyses (recalling that $z_{\rm eff} \simeq 1.5$), and from yet another tracer. It is therefore interesting, as a consistency check of ΛCDM (and the assumptions behind the EFTofLSS), to compare the results with other cosmological probes. In Tab. 4.3, we present the σ-deviations on the cosmological parameters reconstructed from BOSS, eBOSS, and *Planck*, analyzed under ΛCDM. [12] As already mentioned in Sec. 4.1.2 and discussed throughout in chapter 5, the EFT analysis, given the prior chosen in Sec. 4.1.1, can lead to potentially important prior volume projection effects (which do not affect the best-fit values). Therefore, we present in Tab. 4.3 the σ-deviation on the cosmological parameters between two experiments comparing both their means and their best-fits (shown in Tab. 4.2 and in the left upper panel of Fig. 4.4). Given those two metrics, we find that all cosmological parameters are consistent at $\lesssim 1.6\sigma$ between eBOSS and BOSS. Note that the value of H_0 is $\sim 1\sigma$ lower for eBOSS than for BOSS, while σ_8, as well as $\ln(10^{10}A_s)$ and S_8, are $\sim 1.5\sigma$ higher.

Combining LSS probes. We present constraints from combining eBOSS + BOSS data in Fig. 4.4. Posteriors are also given in Tab. 4.2. Combining eBOSS with BOSS, we reconstruct Ω_m, h, and σ_8 to 3%, 1%, and 5% precision at 68% CL. This represents an improvement of about 10% over BOSS alone. If the improvement in the constraints within ΛCDM is somewhat marginal, in the next section we show that the addition of eBOSS can play a significant role in extended models, in particular in constraining the total neutrino mass. For better comparison with the official eBOSS analysis [82], we also present in Fig. 4.4 results obtained when combining with a compilation of independent BAO data dubbed "ext-BAO" and the Pantheon SN1a sample. These additional data, on top of eBOSS + BOSS, further improves the constraints on Ω_m and h by about 10% (see upper right panel of Fig. 4.4).

Comparison with other works. Our joint constraints on flat ΛCDM from eBOSS + BOSS using the EFTofLSS can be compared with constraints from previous full-shape analysis, *e.g.*, from Refs. [112, 113, 114], with the caveat that there are some differences in the modeling, the data combination considered, the scale cuts, and the priors on the cosmological parameters ω_b and n_s. Concretely, we find that when considering similar data we are consistent at $\lesssim 0.4\sigma$ on all cosmological parameters with Ref. [112] when freeing ω_b and n_s (see App. A.1). [13] With the

[12] While for BOSS and eBOSS, we remind that we analyze them fixing ω_b and n_s, for *Planck*, we let them vary and additionally vary $\tau_{\rm reio}$. See App. A.1 for results with n_s free and a BBN prior on ω_b.

[13] In Ref. [112], our constraints can be compared with the results for "BOSS + eBOSS" with "Wide priors" from their Tab. 2, as they consider the same redshift bins of BOSS LRG LOWZ + CMASS and eBOSS QSO that we analyze. However, their analysis is carried in configuration-space wedges restricted to scales $20 < s/[{\rm Mpc}/h] < 160$ instead. Their model uses a different parameterization for the galaxy biases, no counterterms, and a different treatment for the BAO smearing than our IR-resummation. Albeit small differences in the treatment of the BAO smearing, redshift-space distortions, and nuisance parametrization, we believe that the modeling in [112] is effectively not so different than Eq. (3.194), for the following reason. Although they do not include counterterms, in configuration space, the stochastic terms are absent as they are just Dirac-δ distributions at vanishing seperation, as we explained in Sec. 3.4. Plus, the remaining counterterms are very steep and thus potentially negligible at the

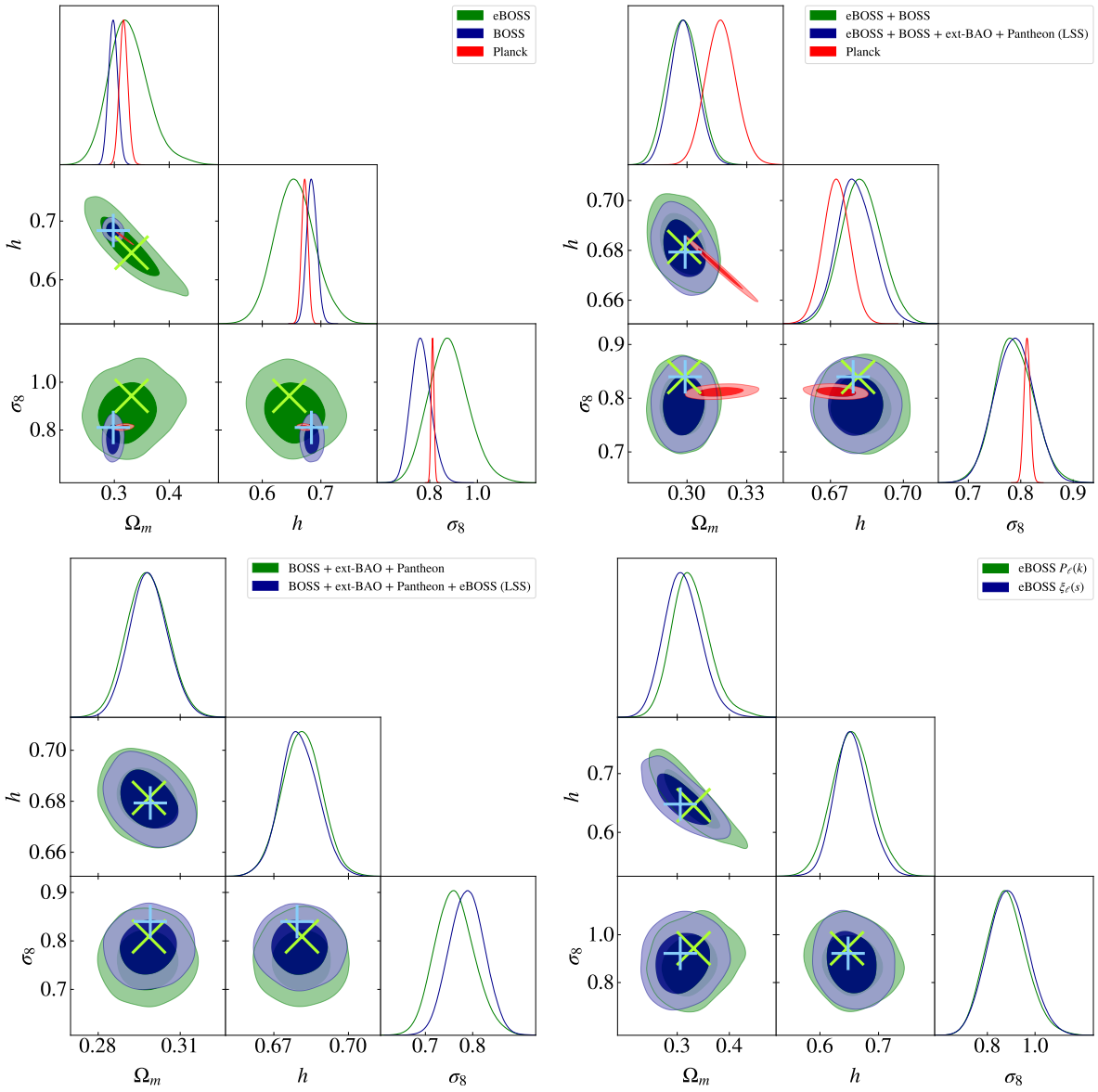

Figure 4.4: Triangle plots (1D and 2D posterior distributions) of the cosmological parameters reconstructed from the base-ΛCDM analyses performed in this work of the following datasets: *Upper left* - eBOSS compared to BOSS or *Planck*. *Upper right* - eBOSS + BOSS and eBOSS + BOSS + ext-BAO + Pantheon, (*i.e.*, the LSS dataset). *Planck* is shown for comparison. *Lower left* - eBOSS + BOSS + ext-BAO + Pantheon with and without eBOSS, to gauge the impact of the addition of eBOSS. *Lower right* - eBOSS power spectrum $P_\ell(k)$ or correlation function $\xi_\ell(s)$. The crosses represent the best-fit values.

results of Ref. [114], we find consistency at 0.3σ, 0.1σ, 1.9σ on Ω_m, h, σ_8, with fixed ω_b and n_s. [14] Finally, we find consistency at 1.1σ, 1.7σ, 2σ on Ω_m, h, σ_8 with the results of Ref. [113], with fixed ω_b and n_s. [15] This tells us that, despite the various choices of those analyses, our results are in broad agreement with these results. It would be interesting to understand better how the small differences we find arise. We leave this to future work.

best-fit $\mu^{+\sigma_u}_{-\sigma_l}$	LSS + Planck
$\Omega_{\rm m}$	0.3081 $0.3081^{+0.0052}_{-0.0052}$
h	0.6787 $0.6789^{+0.0039}_{-0.0040}$
σ_8	0.8096 $0.8095^{+0.0057}_{-0.0057}$
$\omega_{\rm cdm}$	0.1188 $0.1189^{+0.0009}_{-0.0009}$
$\ln(10^{10}A_s)$	3.052 $3.051^{+0.013}_{-0.015}$
S_8	0.820 $0.820^{+0.010}_{-0.010}$
n_s	0.9665 $0.9674^{+0.0036}_{-0.0038}$
$\tau_{\rm reio}$	0.0592 $0.0585^{+0.0064}_{-0.0075}$
$\chi^2_{\rm min}$	4026.4

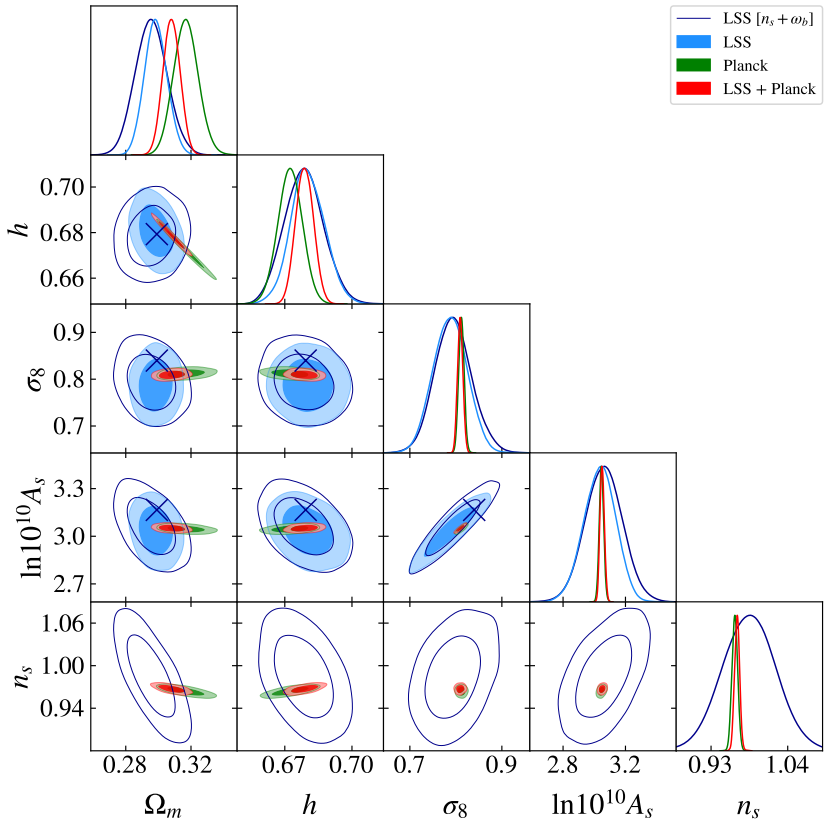

Figure 4.5: *Left* - Cosmological results (best-fit, posterior mean, and 68% CL) of eBOSS + BOSS + ext-BAO + Pantheon in combination with *Planck*. We also report the best-fit $\chi^2_{\rm min}$ of this analysis. *Right* - Triangles plots (1D and 2D posterior distributions) of the cosmological parameters reconstructed from eBOSS + BOSS + ext-BAO + Pantheon (referred as LSS), *Planck*, or their combination, within the base-ΛCDM model. When *Planck* is analyzed, n_s and ω_b are set free. The empty contours correspond to the LSS analysis of App. A.1 where we let n_s free and ω_b vary within a BBN prior. The blue crosses represent the LSS best-fit values for our base-ΛCDM model.

scales analyzed. This is not the case in Fourier space: there, the counterterms are substantial contributions at the scales analyzed.

[14] Our results can be compared with the "BBN + ShapeFit" analysis from Tab. 8 in Ref. [114]. They consider the two redshift bins BOSS LRG $0.2 < z < 0.6$ and $0.4 < z < 0.6$, eBOSS LRG $0.6 < z < 1$, but the same eBOSS QSO redshift bins than us, with scale cuts $0.02 < k/[h/\text{Mpc}] < 0.15$ for the LRG bins and $0.02 < k/[h/\text{Mpc}] < 0.30$ for the QSO bins. They use a different model to describe the perturbation theory contributions and no counterterms, as well as a different approach that extends the template-based BAO/$f\sigma_8$ analysis with a new "shape parameter", from which cosmological constraints can then be derived.

[15] Our results can be compared with the case "3 surveys" in Ref. [113] with "ω_b & n_s" prior from their Tab. 3. They consider as redshift bins BOSS LRG low-z ($0.2 < z < 0.5$), eBOSS LRG ($0.6 < z < 1$) instead of CMASS, but the same eBOSS QSO sample, with scale cuts respectively $0.02 < k/[h/\text{Mpc}] < 0.15$, $0.02 < k/[h/\text{Mpc}] < 0.15$, and $0.02 < k/[h/\text{Mpc}] < 0.30$. They use a different model on the perturbation theory contributions and no counterterms.

4.2.3 Comparison with Planck

Consistency with Planck. The combination of eBOSS + BOSS allows to determine Ω_m and h at a precision similar to *Planck*, with error bars only larger by 5% and 50% respectively. Once ext-BAO and Pantheon are included, we obtain lower error bar of 5% and higher error bar of 40% for Ω_m and h respectively. Indeed, it is known that there is a rather large geometric degeneracy between Ω_m and h in the CMB, as displayed in Fig. 4.4, while LSS data benefit from measuring the BAO (and additional shape features) over volumes (*i.e.*, in two directions, parallel and perpendicular to the line-of-sight), and covering a large range of redshifts. In contrast, the amplitude parameter σ_8 is constrained roughly ~ 6 times better by *Planck*. Given the two metrics used in Tab. 4.3, we find that all cosmological parameters are consistent at $\lesssim 1.8\sigma$ between *Planck* and the various combinations of LSS data. More specifically, as it can be seen from Tab. 4.3 and in the upper right panel of Fig. 4.4, we find that the combination of eBOSS + BOSS leads to cosmological parameters consistent at $\lesssim 1.0\sigma$ with the ones inferred from *Planck*, except for Ω_m where we find a ~ 1.6 σ-deviation. These conclusions are unchanged with the inclusion of ext-BAO and Pantheon. The consistency between LSS and CMB experiments represent a nontrivial check of the ΛCDM model, given that those are different experiments in the target objects they probe, their technical design (and associated systematic errors), and the redshift range they cover. Further considerations on consistency of beyond-ΛCDM models are discussed in Sec. 4.3.

S_8 and H_0 tension. From the analyses presented here, we find no tension on H_0 or S_8 between LSS and *Planck*. Nevertheless, let us remark that, since the error bars on the cosmological parameters inferred from the LSS data are larger than the ones obtained by *Planck*, our results are in reasonable agreement with the lensing measurements of S_8. While *Planck* is known to be in 3σ tension with KIDS [80], we find here agreement at about $\sim 1.8\sigma$, considering either the best-fit value of eBOSS + BOSS or LSS. As for H_0, we find that the inferred value is, depending on the addition of ext-BAO + Pantheon to the EFT analyses of BOSS + eBOSS, in $\sim 3.6-4.0\sigma$ tension with the one obtained by SH0ES [153]. This level of tension is comparable to that recently determined in Ref. [154] with updated BBN predictions and the recently-developed ShapeFit analysis [114]. Yet, we stress that this CMB-independent determination of H_0 does not marginalize over the sound horizon information, as advertised in Refs. [155, 156, 157, 158], and therefore should not be interpreted as a constraint against models affecting the pre-recombination era in order to resolve the Hubble tension.

Combination with Planck. In Fig. 4.5, we show the results from the combination of eBOSS + BOSS + ext-BAO + Pantheon with *Planck*. Compared to *Planck* alone, the constraints on Ω_m and h are improved by $\sim 30\%$, as we can clearly see that LSS data break the partial degeneracy present in the CMB in the $\Omega_m - h$ plane. This is further accompanied by an improvement in the constraints on ω_{cdm}, S_8, and n_s of about 28%, 24%, and 13%, respectively. On the other hand, the amplitude parameter σ_8 and A_s are not significantly impacted, as they are very tightly constrained by *Planck* alone. Note that the best-fit values are not far from the mean with respect to the error bars for all cosmological parameters, as expected from the relatively large data volume of *Planck* which lead to posteriors that are much more Gaussian (see Refs. [105, 138] for related discussions).

4.3 Extensions to the flat ΛCDM model

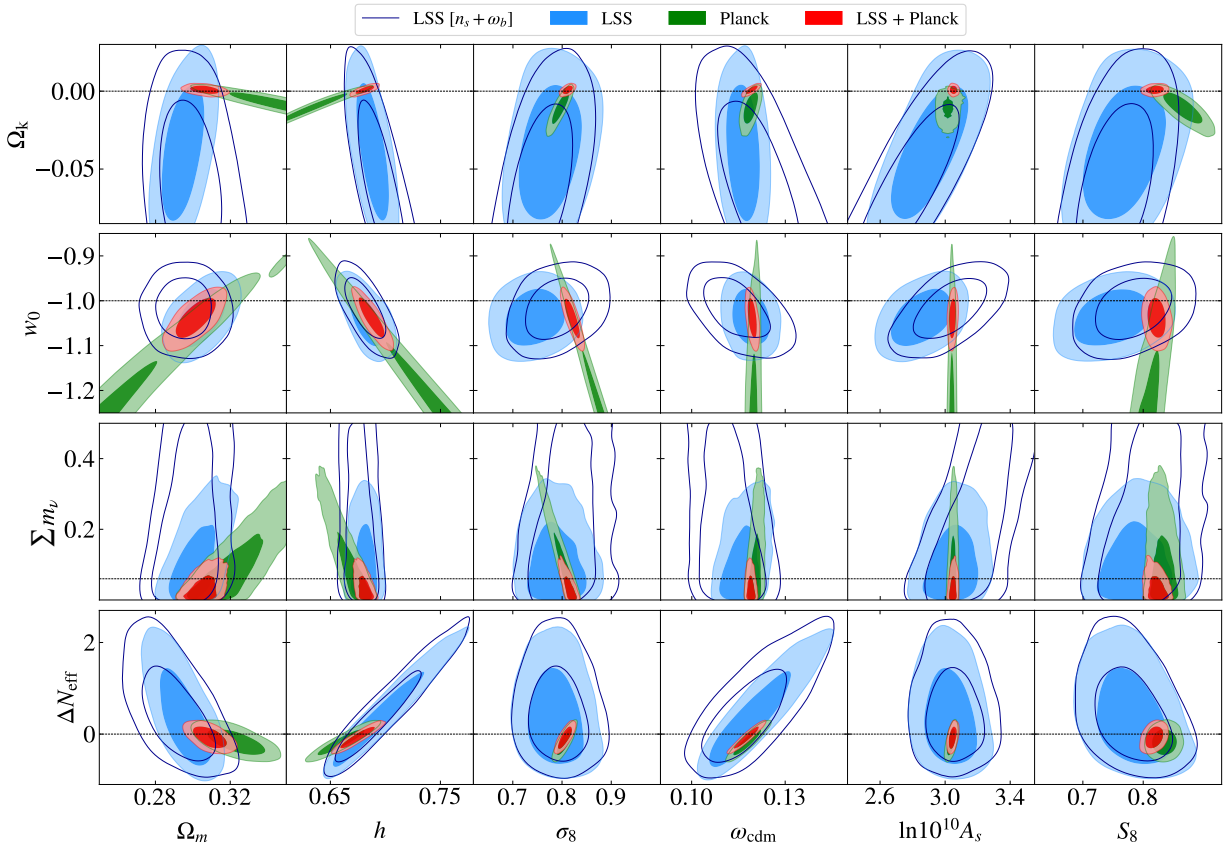

Figure 4.6: 2D posterior distributions of cosmological parameters in several model extensions to ΛCDM reconstructed from analyzing LSS data (*i.e.*, eBOSS + BOSS + ext-BAO + Pantheon), with and without freeing n_s and ω_b, compared with *Planck* and their combination.

In this section, we present the results of analyses of several extensions to the flat ΛCDM model, namely the curvature density fraction Ω_k, the equation of state of dark energy w_0, the neutrino mass $\sum m_\nu$, and the number of relativistic degrees of freedom $N_{\rm eff}$. For each model, we list in Tab. 4.4 the results of LSS analyses with and without eBOSS to highlight the role of the EFT likelihood of eBOSS QSO data in constraining these extensions. In App. A.1, we provide the results of analyses including the variation of n_s (within a uninformative flat prior) and ω_b (within a BBN prior), and show the differences with the baseline analyses that fix these parameters. We also combine the LSS datasets with *Planck* and provide reconstructed parameters in Tab. 4.5. For comparison (and although not explicitly listed), we perform the same series of analyses using the BAO/$f\sigma_8$ information for the eBOSS and BOSS data. Finally, in Fig. 4.6 we plot, for each model, the 2D posterior distributions obtained from analyzing the combination of the LSS datasets (with and without the n_s and ω_b variations) compared to *Planck*, and their combination.

4.3.1 Ω_kΛCDM

In this section, we consider the ΛCDM model with the addition of the curvature density fraction, Ω_k, by imposing a large flat prior on this parameter. We derive $\Omega_k = -0.032^{+0.028}_{-0.031}$ at

BOSS + ext-BAO + Pantheon				
best-fit $\mu^{+\sigma_u}_{-\sigma_l}$	$\Omega_k\Lambda$CDM	w_0CDM	$\nu\Lambda$CDM	$N_{\rm eff}\Lambda$CDM
$\Omega_{\rm m}$	0.2962 $0.2955^{+0.0079}_{-0.0074}$	0.2987 $0.2967^{+0.0080}_{-0.0085}$	0.2982 $0.3049^{+0.0094}_{-0.0110}$	0.298 $0.291^{+0.010}_{-0.010}$
h	0.6853 $0.6886^{+0.0099}_{-0.0110}$	0.681 $0.684^{+0.010}_{-0.011}$	0.6811 $0.6826^{+0.0080}_{-0.0082}$	0.685 $0.714^{+0.026}_{-0.044}$
σ_8	0.801 $0.749^{+0.044}_{-0.043}$	0.810 $0.762^{+0.042}_{-0.044}$	0.810 $0.763^{+0.039}_{-0.044}$	0.809 $0.758^{+0.041}_{-0.046}$
$\omega_{\rm cdm}$	0.1161 $0.1172^{+0.0046}_{-0.0043}$	0.1155 $0.1158^{+0.0046}_{-0.0047}$	0.1154 $0.1179^{+0.0047}_{-0.0055}$	0.1168 $0.1256^{+0.0078}_{-0.0150}$
$\ln(10^{10}A_s)$	3.01 $2.84^{+0.16}_{-0.17}$	3.09 $2.95^{+0.14}_{-0.13}$	3.09 $3.00^{+0.12}_{-0.13}$	3.08 $2.95^{+0.12}_{-0.12}$
S_8	0.796 $0.744^{+0.045}_{-0.044}$	0.808 $0.758^{+0.044}_{-0.044}$	0.808 $0.769^{+0.040}_{-0.045}$	0.806 $0.748^{+0.044}_{-0.048}$
Ω_k	-0.023 $-0.032^{+0.028}_{-0.031}$	–	–	–
w_0	–	-0.998 $-1.015^{+0.042}_{-0.042}$	–	–
$\sum m_\nu$ [eV]	–	–	0.052 < 0.429	–
$\Delta N_{\rm eff}$	–	–	–	0.09 $0.82^{+0.62}_{-1.08}$
$\chi^2_{\rm min}$	1190.8	1191.1	1191.1	1191.1
$\Delta\chi^2_{\rm min}$	-0.3	0	0	0

eBOSS + BOSS + ext-BAO + Pantheon (LSS)				
best-fit $\mu^{+\sigma_u}_{-\sigma_l}$	$\Omega_k\Lambda$CDM	w_0CDM	$\nu\Lambda$CDM	$N_{\rm eff}\Lambda$CDM
$\Omega_{\rm m}$	0.2952 $0.2945^{+0.0072}_{-0.0081}$	0.2987 $0.3042^{+0.0084}_{-0.0096}$	0.2962 $0.3017^{+0.0076}_{-0.0097}$	0.3029 $0.2950^{+0.0099}_{-0.0093}$
h	0.6858 $0.6882^{+0.0098}_{-0.0094}$	0.680 $0.683^{+0.011}_{-0.011}$	0.6789 $0.6810^{+0.0078}_{-0.0072}$	0.664 $0.696^{+0.017}_{-0.039}$
σ_8	0.824 $0.775^{+0.032}_{-0.050}$	0.835 $0.744^{+0.040}_{-0.041}$	0.838 $0.787^{+0.035}_{-0.040}$	0.843 $0.787^{+0.033}_{-0.043}$
$\omega_{\rm cdm}$	0.1158 $0.1165^{+0.0041}_{-0.0031}$	0.1150 $0.1189^{+0.0043}_{-0.0038}$	0.1142 $0.1164^{+0.0040}_{-0.0044}$	0.1107 $0.1199^{+0.0061}_{-0.0120}$
$\ln(10^{10}A_s)$	3.04 $2.90^{+0.14}_{-0.15}$	3.15 $2.86^{+0.13}_{-0.13}$	3.14 $3.04^{+0.10}_{-0.11}$	3.18 $3.03^{+0.11}_{-0.11}$
S_8	0.817 $0.768^{+0.040}_{-0.047}$	0.833 $0.749^{+0.041}_{-0.043}$	0.833 $0.789^{+0.036}_{-0.041}$	0.847 $0.780^{+0.039}_{-0.039}$
Ω_k	-0.034 $-0.039^{+0.028}_{-0.029}$	–	–	–
w_0	–	-1.002 $-1.038^{+0.041}_{-0.041}$	–	–
$\sum m_\nu$ [eV]	–	–	0.002 < 0.274	–
$\Delta N_{\rm eff}$	–	–	–	-0.37 $0.40^{+0.44}_{-0.91}$
$\chi^2_{\rm min}$	1250.0	1250.9	1250.6	1250.8
$\Delta\chi^2_{\rm min}$	-1.0	-0.1	-0.4	-0.2

Table 4.4: *Upper* - Cosmological results (best-fit, posterior mean, and 68% CL) from BOSS + ext-BAO + Pantheon for several model extensions to ΛCDM. Note that we quote the 95% CL bound for $\sum m_\nu$. For each dataset we also report its best-fit χ^2, and the $\Delta\chi^2$ with respect to the analogous ΛCDM best-fit model. *Lower* - Same, but this time with the addition of eBOSS data.

LSS + Planck				
best-fit $\mu^{+\sigma_u}_{-\sigma_l}$	$\Omega_k\Lambda$CDM	w_0CDM	$\nu\Lambda$CDM	$N_{\rm eff}\Lambda$CDM
$\Omega_{\rm m}$	0.3069 $0.3065^{+0.0051}_{-0.0054}$	0.3015 $0.3013^{+0.0071}_{-0.0073}$	0.3039 $0.3058^{+0.0055}_{-0.0059}$	0.3080 $0.3090^{+0.0063}_{-0.0054}$
h	0.6809 $0.6813^{+0.0059}_{-0.0055}$	0.6877 $0.6878^{+0.0076}_{-0.0081}$	0.6825 $0.6809^{+0.0045}_{-0.0044}$	0.680 $0.675^{+0.010}_{-0.011}$
σ_8	0.8100 $0.8109^{+0.0068}_{-0.0069}$	0.821 $0.821^{+0.011}_{-0.010}$	0.8203 $0.8144^{+0.0098}_{-0.0071}$	0.811 $0.806^{+0.009}_{-0.010}$
$\omega_{\rm cdm}$	0.1192 $0.1192^{+0.0013}_{-0.0012}$	0.1195 $0.1194^{+0.0009}_{-0.0010}$	0.1192 $0.1189^{+0.0009}_{-0.0009}$	0.1191 $0.1177^{+0.0027}_{-0.0026}$
$\ln(10^{10}A_s)$	3.050 $3.051^{+0.014}_{-0.015}$	3.045 $3.046^{+0.013}_{-0.015}$	3.043 $3.048^{+0.014}_{-0.015}$	3.052 $3.047^{+0.014}_{-0.017}$
S_8	0.819 $0.820^{+0.010}_{-0.010}$	0.823 $0.822^{+0.010}_{-0.010}$	0.826 $0.822^{+0.010}_{-0.010}$	0.821 $0.818^{+0.010}_{-0.010}$
n_s	0.9650 $0.9665^{+0.0042}_{-0.0043}$	0.9646 $0.9659^{+0.0038}_{-0.0039}$	0.9658 $0.9673^{+0.0037}_{-0.0037}$	0.9665 $0.9650^{+0.0062}_{-0.0070}$
$\tau_{\rm reio}$	0.0581 $0.0582^{+0.0068}_{-0.0081}$	0.0555 $0.0555^{+0.0068}_{-0.0074}$	0.0548 $0.05716^{+0.0070}_{-0.0076}$	0.0593 $0.0581^{+0.0073}_{-0.0074}$
Ω_k	0.0007 $0.0008^{+0.0018}_{-0.0017}$	–	–	–
w_0	–	-1.040 $-1.039^{+0.029}_{-0.029}$	–	–
$\sum m_\nu$ [eV]	–	–	9×10^{-5} <0.093	–
$\Delta N_{\rm eff}$	–	–	–	0.02 $-0.07^{+0.15}_{-0.16}$
$\chi^2_{\rm min}$	4025.9	4025.0	4023.3	4026.1
$\Delta\chi^2_{\rm min}$	-0.5	-1.4	-3.1	-0.3

Table 4.5: Cosmological results (best-fit, posterior mean, and 68% CL) from LSS + *Planck* for several model extensions to ΛCDM. Note that we quote 95% CL bound for $\sum m_\nu$. For each dataset we also report its best-fit χ^2, and the $\Delta\chi^2$ with respect to the analogous ΛCDM best-fit model.

68% CL (with a best-fit value at -0.023) from the analysis without eBOSS, while we derive $\Omega_k = -0.039^{+0.028}_{-0.029}$ at 68% CL (with a best-fit value at -0.034) for the analysis with eBOSS. These analyses allow us to highlight several important points for the LSS analysis:

- With the LSS data only, we find Ω_k compatible with zero curvature at 1.2σ (considering the best-fit). When we vary n_s and ω_b (see App. A.1), this compatibility is increased to 0.6σ.

- The addition of eBOSS data does not significantly reduce the 68% constraints on Ω_k. However it improves the constraint at 95% CL from $-0.032^{+0.062}_{-0.057}$ to $-0.039^{+0.054}_{-0.052}$, which corresponds to an improvement of $\sim 10\%$.

- The EFT analysis significantly improves the constraints on Ω_k (by $\sim 50\%$) compared to the conventional BAO/$f\sigma_8$ analysis ($-0.037^{+0.067}_{-0.053}$ at 68% C.L., with a best-fit value at -0.006).

- Note that, as visible on Fig. 4.6, we find no tension between LSS and *Planck* when curvature is allowed to vary as long as CMB lensing is included in the fit to *Planck*: at 95% CL, *Planck* finds $\Omega_k = -0.011^{+0.013}_{-0.012}$ while our combination of LSS data leads to $\Omega_k = -0.039 \pm 0.053$.

When combining LSS and *Planck*, we reconstruct $\Omega_k = 0.0008^{+0.0018}_{-0.0017}$ at 68% CL and $\Omega_k = 0.0008 \pm 0.0034$ at 95% CL (with a best-fit value at -0.0007), which allows us to highlight that:

- The combination of LSS and *Planck* leads to a strong constraint on the Ω_k parameter, thanks to the redshift leverage between LSS probes and the last-scattering surface, allowing the breaking of degeneracies in the Ω_k-Ω_m and Ω_k-H_0 planes.

- The combination with *Planck* data excludes the (slightly favored) negative values of Ω_k reconstructed from LSS data alone, and we find that cosmological data are in very good agreement with $\Omega_k = 0$.

- Our constraints are better at 10% than the *Planck* + BAO constraints of Ref. [11] (0.0007 ± 0.0037 at 95% CL), and are similar within 5% to the constraints obtained from the ShapeFit method (0.0015 ± 0.0016 at 68% CL) [114][16] or from the equivalent combined analysis including instead standard BAO/$f\sigma_8$ method (0.0013 ± 0.0017 at 68% CL) derived in our work. See also Ref. [159] for a work presenting CMB-independent constraints on spatial curvature from beyond the standard BAO/$f\sigma_8$ that also support a flat universe.

4.3.2 w_0CDM

We now turn to the dark energy equation of state w_0 in the context of smooth quintessence, *i.e.*, a quintessence field with no perturbations, and carry out two analyses: one in which we impose a large flat prior on w_0, and another in which we restrict $w_0 \geq -1$ to stay in the physical region. With the former prior, we obtain $w_0 = -1.015 \pm 0.042$ at 68% CL (with a best-fit value at -0.998) for the analysis without eBOSS, and $w_0 = -1.038 \pm 0.041$ at 68% CL (with a best-fit value at -1.002) for the analysis with eBOSS. We can conclude that:

- With the LSS data, we find no evidence for a universe with $w_0 \neq -1$. This conclusion does not change when considering the variation of n_s and ω_b.

- The inclusion of eBOSS data does not improve the constraints at 68% CL and at 95% CL. This is expected as the effective redshift of the eBOSS data, namely $z = 1.52$ (which is significantly higher than the effective redshift of the BOSS data, $z = 0.32 - 0.57$), is well above the beginning of the dark energy dominated universe, $z_\Lambda \sim 0.3$.

- The EFT analysis improves the constraints on w_0 by $\sim 20\%$ compared to the BAO/$f\sigma_8$ analysis ($-0.961^{+0.054}_{-0.042}$ at 68% CL, with a best-fit value at -0.931). This improvement can be understood as follow. Roughly, for each mode k in our analysis, the amplitudes of the monopole and the quadrupole are given by $b_1^2 D^2 A_s \mathscr{T}(k)$ and $4/3 \cdot b_1 f D^2 A_s \mathscr{T}(k)$, respectively, where D is the growth factor and $\mathscr{T}(k)$ describes a k-dependence fixed by the transfer function of the linear power spectrum, roughly scaling as $\mathscr{T}(k) \propto (1 + \log(k/k_{\rm eq}))^2 (k/k_*)^{n_s - 4}$, where k_* is the pivot scale. The transfer function captures modes that have re-entered the horizon during radiation domination, $k > k_{\rm eq}$, where $k_{\rm eq} \sim 0.01 h\,{\rm Mpc}^{-1}$ is the radiation-matter equality scale, and are log-enhanced (see *e.g.*, Ref. [158]). The ratio of the monopole and quadrupole allows to obtain

[16] We note that this comparison should be taken with caution, as we do not use the same exact dataset as in Ref. [114]. In particular, authors therein consider the eBOSS LRG sample, which is not the case in our analysis, while we consider the Pantheon data, which is not the case in their analysis.

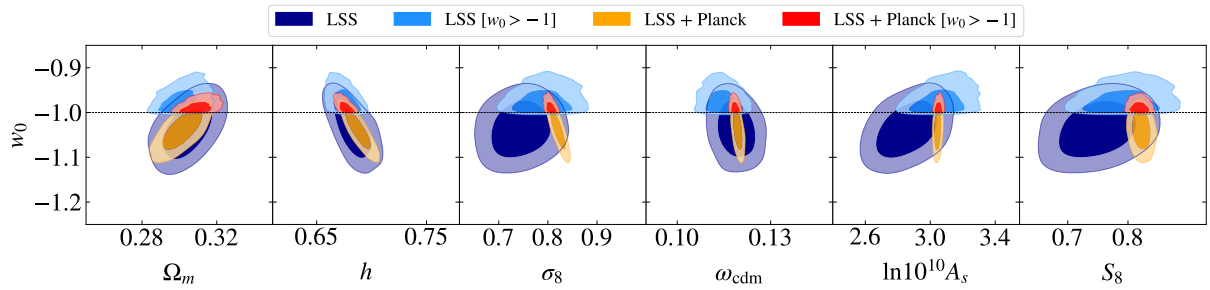

Figure 4.7: 2D posterior distributions of LSS (*i.e.*, eBOSS + BOSS + ext-BAO + Pantheon), and the combination between LSS and *Planck* for the w_0CDM model. For both analyses, we show the results with the uninformative prior on w_0 and with the $w_0 \geq -1$ prior.

$f\sigma_8 \propto fD^2 A_s$, but does not contain information on $\mathscr{T}(k)$. The EFT analysis allows us to make use of the k-dependence of the full-shape that contains information beyond the (scale-independent) BAO/$f\sigma_8$ analysis, in particular about $k_{\rm eq} \propto \Omega_m h^2$, in turn providing an extra handle on $\Omega_m h^2$ with no degeneracy with w_0. This allows to break the $w_0 - \Omega_m$ degeneracy that remains with BAO/$f\sigma_8$, and therefore to improve constraints on w_0 [59, 160].

- The constraints we derived in this work are much better than *Planck* ($w_0 = -1.57^{+0.50}_{-0.40}$ at 95% CL for the high-ℓ TT, TE, EE + lowE + lensing analysis [11]), which is expected as (the primary) *Planck* CMB data is largely unable to constrain the behaviour of the Universe at low redshift.

When combining the LSS data with *Planck*, we obtain $w_0 = -1.039 \pm 0.029$ at 68% CL and $w_0 = -1.039^{+0.055}_{-0.059}$ at 95% CL (with a best-fit value at -1.040), which allows us to highlight that:

- The w_0 best-fit value is $\sim 1.4\sigma$ below -1, with $\Delta\chi^2 = -1.4$ with respect to the ΛCDM model.

- The addition of LSS data select values of w_0 close to -1, located in the 2-σ region reconstructed from *Planck* data.

- Our constraints are better at 43% than the *Planck* + BAO constraints of Ref. [11] (-1.04 ± 0.10 at 95% CL) and better than the constraints reported using ShapeFit ($-1.093^{+0.048}_{-0.044}$ at 68% CL) [114] at 37%. However, these constraints are similar at $< 1\%$ to the equivalent combined analysis including instead the standard BAO/$f\sigma_8$ (-1.043 ± 0.030 at 68% CL), indicating the improvement mostly comes from our inclusion of Pantheon data, when combining with *Planck*.

In Fig. 4.7, we show results of the analyses with the $w_0 \geq -1$ prior, to restrict the parameter space in the physical region of smooth quintessence (see *e.g.*, discussions in Ref. [160]). We obtain $w_0 < -0.932$ at 95% CL for the LSS analysis, while the constraint improves to $w_0 < -0.965$ at 95% CL for the LSS + *Planck* analysis. In addition, one can see that this new prior shifts the 2D posteriors inferred from the LSS data in a non-negligible way, while it remains globally stable for the LSS + *Planck* analysis. Note that, for these analyses, $\Delta\chi^2 = 0$ with respect to ΛCDM, since we obtain best-fit values of $w_0 = -1$.

4.3.3 $\nu\Lambda$CDM

We now turn to variation of the total neutrino mass $\sum m_\nu$. Following the convention used by *Planck*, we consider one massive neutrino and two massless ones. We derive $\sum m_\nu < 0.429eV$ at 95% (with a best-fit value at $0.052eV$) from the analysis without eBOSS, while we derive $\sum m_\nu < 0.274eV$ (with a best-fit value at $0.002eV$) from the analysis that includes eBOSS. We can conclude that:

- A non-zero value of the total neutrino mass is not favored.
- The eBOSS data improve the upper limit on the sum of neutrino masses by $\sim 40\%$ with respect to the analysis of LSS data without eBOSS. This significant improvement is due to the fact that the neutrino energy density is higher at the epoch probed by eBOSS QSO than at the epoch probed by BOSS.
- The EFT analysis significantly improves the constraints on $\sum m_\nu$ (by a factor of ~ 18) over the BAO/$f\sigma_8$ constraint ($\sum m_\nu < 4.84eV$ at 95% CL, with a best-fit value at $0.74eV$). This is expected as BAO/$f\sigma_8$ gains constraining mostly from the geometrical impact of massive neutrinos (as the determination of $f\sigma_8$ assumes scale-independence), which is largely degenerate with the CDM density. The inclusion of the full-shape of the power spectrum breaks that degeneracy. The reason is the following: the EFT full-shape analysis allows to exploit the scale-dependence of the power spectrum that contains both information on the characteristic power suppression induced by neutrinos at the perturbation level, as well as on $k_{\rm eq} \propto \Omega_m h^2$ (through the log-enhancement at small-scales), therefore breaking the degeneracy with neutrino masses at the background level.
- The LSS constraint derived in this work is only $\sim 10\%$ weaker than the *Planck* constraint ($\sum m_\nu < 0.241eV$) obtained from high-ℓ TT, TE, EE + lowE + lensing [11].

We note here that unlike the other model extension, co-varying n_s and ω_b has a significant impact on the reconstructed parameters, as seen in App. A.1. In particular, we find $\sum m_\nu < 0.777eV$ at 95% CL from the full combination of LSS datasets, which is 2.8 times weaker than what we found when fixing those parameters. We show in App. A.1 that (perhaps unsurprisingly) this relaxation is due to the marginalization over n_s, which is strongly degenerate with the power suppression induced by a non-zero neutrino mass.

When combining LSS with *Planck*, we derive the strong constraint $\sum m_\nu < 0.093eV$ at 95% CL. We conclude that:

- This analysis disfavors the inverse hierarchy at $\sim 2.2\sigma$, as the minimal sum of neutrino masses allowed by oscillation experiments is $\sim 0.1eV$ [15].
- The best-fit value of $\sum m_\nu$ is very close to $0eV$, with $\Delta\chi^2_{\rm min} = -3.1$ compared to the base-ΛCDM analysis which sets the mass of a neutrino at $0.06eV$. Note that the contribution to the $\Delta\chi^2_{\rm min}$ is about -2 from *Planck* and -1 from eBOSS + BOSS data. Taken at face value, our analysis therefore seems to slightly favor a universe *without* massive neutrinos compared to the base-ΛCDM model, in agreement with what was found for high-ℓ TT, TE, EE + lowE + BAO analysis in Ref. [11] (where the best-fit is $0.0009eV$), and may be connected to the lensing amplitude anomaly, see *e.g.*, discussions in Ref. [138].

- This constraint is better than the *Planck* high-ℓ TT, TE, EE + lowE + BAO constraint [11]: $\sum m_\nu < 0.120eV$. However, our constraint is slightly weaker than the ShapeFit constraint [114]: $\sum m_\nu < 0.082eV$. This may be due to their inclusion of eBOSS LRG data in addition to QSO. Nevertheless, these constraints are competitive with recent constraints from the Ly-α forest power spectrum [161]. Note that the bound on the total neutrino mass derived in this work is somewhat relaxed with respect the one derived from the equivalent combined analysis including instead standard BAO/$f\sigma_8$: $\sum m_\nu < 0.080eV$ (derived in this work). Such relaxation was already observed when combining *Planck* with the EFT likelihood of BOSS [162] (see also Ref. [59]). Importantly, this does not imply that the EFT likelihood has less statistical power than the BAO/$f\sigma 8$ likelihood, but rather results from the differences in the modeling of the power spectrum in the mildly nonlinear regime in the presence of massive neutrinos.

We perform two complementary analyses where we consider the sum of the neutrino masses either under the assumption of normal ($\sum m_{\nu,\mathrm{NH}}$) or inverted ($\sum m_{\nu,\mathrm{IH}}$) hierarchy. In summary, we find that:

- For the normal hierarchy (NH), $\sum m_{\nu,\mathrm{NH}} < 0.469eV$ at 95 % CL for the analysis without eBOSS, and $\sum m_{\nu,\mathrm{NH}} < 0.308eV$ with eBOSS (with a best-fit value compatible with the prior lower bound). This represents a $\sim 50\%$ stronger constraint thanks to eBOSS. When varying n_s and ω_b, we get $\sum m_{\nu,\mathrm{NH}} < 0.633eV$, which is ~ 2 times larger than the analysis where these two parameters are kept fix. Yet, the combination of LSS + *Planck* leads to $\sum m_{\nu,\mathrm{NH}} < 0.134eV$ (with a best-fit value compatible with the prior lower bound, *i.e.*, $0.06eV$).

- Similarly, for the inverse hierarchy (IH) we reconstruct $\sum m_{\nu,\mathrm{IH}} < 0.337eV$ for the LSS analysis and $\sum m_{\nu,\mathrm{IH}} < 0.177eV$ in combination with *Planck* (with a best-fit value compatible with the prior lower bound for both analyses, *i.e.*, $0.1eV$).

- We obtain, for LSS + *Planck*, $\Delta\chi^2_{\mathrm{min}} = +3.7$ between the analysis with the NH and the one assuming two massless neutrinos. This is because the LSS + *Planck* analysis has a preference for zero mass (see above).

- Similarly, we obtain, for LSS + *Planck*, $\Delta\chi^2_{\mathrm{min}} = +7.1$ between the analysis with the IH and the one with two massless neutrinos. Interestingly, we find $\Delta\chi^2_{\mathrm{min}} = +3.4$ between the IH and NH analyses, implying that the IH is disfavoured by LSS + *Planck* compared to the NH, as already mentioned above (see Refs. [163, 164] for detailed discussions about preference against the IH from a compilation of data).

4.3.4 $N_{\mathrm{eff}}\Lambda$CDM

Finally, we co-vary the effective number of relativistic species, N_{eff}. Here we consider $\Delta N_{\mathrm{eff}} = N_{\mathrm{eff}} - 3.044$, where 3.044 is the standard model prediction [165]. We derive $\Delta N_{\mathrm{eff}} = 0.82^{+0.62}_{-1.08}$ at 68% CL (with a best-fit value at 0.09) from the analysis without eBOSS, while we derive $\Delta N_{\mathrm{eff}} = 0.40^{+0.44}_{-0.91}$ at 68% CL (with a best-fit value at -0.37) for the analysis with eBOSS. These analyses allow us to conclude that:

- The inclusion of eBOSS data changes the best-fit value of ΔN_{eff}, favoring a negative value, while the analysis without eBOSS favored a positive one. Nevertheless, constraints with

and without eBOSS are in statistical agreement, with a significantly stronger constraints on $\Delta N_{\rm eff}$ (by $\sim 30\%$) once eBOSS is included. The clear improvement in this constraint is due to the fact that $\Delta N_{\rm eff}$ leaves an impact on the matter power spectrum by affecting the BAO and the amplitude on scales $k > k_{\rm eq}$, where $k_{\rm eq}$ is the equality scale: the presence of additional energy density affects the expansion rate of the Universe, reducing the sound horizon and delaying the onset of matter domination (see *e.g.*, Ref. [166] for a review). The addition of a data point at $z \sim 1.5$ thus improves the constraints.

- Interestingly, the conventional BAO/$f\sigma_8$ analysis is unable to constrain this parameter since it is mostly sensitive to the background radiation density that is negligible at low-redshift. The EFT therefore provides a new way of probing the contribution of extra relativistic species using BOSS and eBOSS data.

- Current LSS constraint is weaker than the *Planck* constraint ($\Delta N_{\rm eff} = -0.15^{+0.36}_{-0.38}$ at 95% CL from high-ℓ TT, TE, EE + lowE + lensing [11]), but it would be interesting to test whether higher accuracy LSS data can provide an independent constraint competitive with that obtained from the next generation CMB data.

When we combine the LSS analysis with *Planck* data, we reconstruct $\Delta N_{\rm eff} = -0.07^{+0.15}_{-0.16}$ at 68% CL and $\Delta N_{\rm eff} = -0.07^{+0.30}_{-0.29}$ at 95% CL (with a best-fit value at 0.02). We conclude that:

- This is compatible with the standard model value and this represents a significant improvement over the results from *Planck* alone.

- Our constraints are better by 12% than the *Planck* + BAO constraints of Ref. [11] ($-0.06^{+0.34}_{-0.33}$ at 95% CL) and by 20% than the ShapeFit constraints (0.07 ± 0.38 at 95% CL) [114]. In addition, we note that our full-shape constraints are also slightly better than those obtained with the equivalent combined analysis including instead the standard BAO/$f\sigma_8$ ($0.05^{+0.33}_{-0.31}$ at 95% CL.).

4.4 Conclusions

In this chapter, we have performed the first EFT analysis of the eBOSS QSO full-shape data. We have combined this analysis with other LSS data in order to obtain independent constraints from *Planck*. As results are in good agreement with *Planck*, we have combined LSS and CMB probes in order to break the degeneracies present in the CMB, especially within models beyond ΛCDM. We summarise our main results here.

Determining the scale cut. In order to adequately study the eBOSS QSOs data, we have determined the maximum scale $k_{\rm max}$ at which the EFT full-shape analysis is valid. This scale is chosen such that the theoretical error is smaller than the data error bars and does not cause a significant shift in the cosmological results. By fitting the full-shape of the mean over all EZmock realizations with the EFTofLSS at one-loop, as well as with the addition of the dominant next-to-next-leading order terms, we determine that for a scale cut $k_{\rm max} = 0.24h\,{\rm Mpc}^{-1}$, the shift in all cosmological and EFT parameters is below a reasonable threshold (of $< 1/3\sigma$). In addition, cosmological results obtained using the correlation function of eBOSS QSO are in overall good agreement. It is interesting to note that the scale cut for eBOSS QSO full-shape is restricted by a rather large "dispersion" scale $k_{\rm R} \sim 0.25h\,{\rm Mpc}^{-1}$, entering the renormalization of the products

of velocity operators appearing in the redshift-space expansion of the density field. This might provide indication that quasars selected by the eBOSS are preferentially populating satellite galaxies rather than central ones, as also argued from the perspective of halo occupation [140].

eBOSS QSOs flat ΛCDM cosmological results. The EFT analysis of eBOSS QSOs provides independent measurements of the ΛCDM parameters in a different redshift range ($z \sim 1.5$) than previous EFT analyses, and from yet another tracer. Interestingly, we find good consistency between the EFT analysis of eBOSS QSO and the BOSS LRG data. For the H_0 parameter in particular, we find consistency at $\sim 1.0\sigma$ between these two datasets. Additionally, we find that eBOSS favors a higher value for σ_8 (and S_8) at $\sim 1.5\sigma$ than the ones reconstructed using BOSS or *Planck*. Therefore, in general, the combination of eBOSS to the other cosmological probes tend to lift the value of the clustering amplitude. The addition of the EFT likelihood of eBOSS QSOs on top of the EFT likelihood of BOSS LRG (as well as in combination with ext-BAO + Pantheon) improves the 68% CL error bars by about 10%.

Consistency with Planck. Interestingly, we found that all cosmological parameters are consistent at $\lesssim 1.0\sigma$ between eBOSS + BOSS and *Planck* data, except Ω_m that is consistent at $\sim 1.6\sigma$. This consistency is a non-trivial check of the ΛCDM model and the many associated assumptions, as we considered very different data both in terms of redshift and in terms of the objects being probed. This may hint that the S_8 tension, unless causes by a systematic error, is restricted to scales smaller than $k \sim 0.2h\,\mathrm{Mpc}^{-1}$, or originate only at very late times (see *e.g.*, Refs. [167, 168, 169, 170]).

Extensions of the flat ΛCDM model. In addition to further testing the ΛCDM model, we have assessed that eBOSS data help improving constraints on extended cosmological models in which the late-time background dynamics departs from flat ΛCDM. Using a combination of LSS datasets, *i.e.*, eBOSS + BOSS + ext-BAO + Pantheon, we obtain competitive constraints on the curvature density fraction $\Omega_k = -0.039 \pm 0.029$, the dark energy equation of state $w_0 = -1.038 \pm 0.041$, the effective number of relativistic species $N_{\rm eff} = 3.44^{+0.44}_{-0.91}$ at 68% CL, and the sum of neutrino masses $\sum m_\nu < 0.274eV$ at 95% CL. These constraints represent a significant improvement over the standard BAO/$f\sigma_8$ method. First, Ω_k and w_0 are better constrained by 50% and 20% respectively (at 68% CL). Second, the application of the EFT to BOSS and eBOSS allows to tremendously improve constraints on the $\sum m_\nu$ (by a factor ~ 18) as the EFT allows to gain sensitivity to the power suppression of neutrinos, while conventional analysis are mostly sensitive to their effect on the angular diameter distance. In the same vein, the EFT likelihoods of eBOSS and BOSS allows for a novel independent determination of the effective number of relativistic species, while $N_{\rm eff}$ is basically unconstrained from the standard BAO/$f\sigma_8$ analysis that is mostly sensitive to the (almost negligible) background contribution of radiation at late-times. Including *Planck* data, contraints significantly improve thanks to the large lever arm in redshift between LSS and CMB measurements. In particular, we obtain $\Omega_k = 0.0008 \pm 0.0018$ and $w_0 = -1.039 \pm 0.029$ at 68% CL. In addition, we obtain the stringent constraint $\sum m_\nu < 0.093eV$, competitive with recent Lyman-α forest power spectrum bound [161], and $N_{\rm eff} = 2.97 \pm 0.16$ at 68% CL ($\Delta N_{\rm eff} < 0.23$ at 2σ). Note that, unlike the limits obtained using LSS data only, similar results are obtained when considering conventional BAO/$f\sigma_8$ data, due to the fact that *Planck* constraining power still largely dominates over that of BOSS and eBOSS. However, we expect that for significantly larger volume of data with,

e.g., DESI [171] or Euclid [172], the EFT analysis will allow to improve over conventional analysis even when combining with *Planck*.

Our work demonstrates that eBOSS QSO data can help breaking model degeneracies in certain extensions to ΛCDM, as they sit at an intermediate redshift between BOSS and *Planck*. Furthermore, we have shown the importance of going beyond conventional BAO/$f\sigma_8$ analysis with the EFTofLSS in order to constrain simple extensions to ΛCDM without the inclusion of *Planck* data. We leave for future work the application of the EFT full-shape analysis of eBOSS QSO data to more sophisticated beyond-ΛCDM physics, such as, *e.g.*, early dark energy (see chapter 7) and decaying dark matter (see chapter 9). Our analysis can also be extended to the eBOSS LRG [173, 174] and eBOSS ELG data [175] (see Ref. [119] for an EFT analysis of eBOSS ELG), which can provide new consistency tests of the ΛCDM model, and refine our ways to look for deviations from ΛCDM.

Note that after this work, Ref. [176] carried out an EFT full-shape analysis of the eBOSS QSO data using the `CLASS-PT` code [61]. Our results are broadly consistent.

V

Consistency of EFTofLSS analyses of the BOSS data

Contents

5.1 The role of EFT priors **153**
5.1.1 The two EFT priors 155
5.1.2 Prior weight and volume projection effects 156
5.1.3 Pipeline validation check 157
5.2 Impact of EFT priors in ΛCDM **159**
5.2.1 Highlighting the role of the priors 159
5.2.2 How to beat the prior weights and volume effects 162
5.3 Comparison of BOSS measurements **165**
5.3.1 Contenders 166
5.3.2 The matchups 166
5.3.3 Measurements comparison summary 169
5.4 Comparison of Reconstructed BAO **169**
5.4.1 Inconsistency between post-reconstructed measurements 169
5.4.2 Comparison of extraction methods of reconstructed BAO parameters 171
5.5 Conclusions **172**

This chapter is based on:

T. Simon, P. Zhang, V. Poulin and T. L. Smith, *Consistency of effective field theory analyses of the BOSS power spectrum*, **Phys. Rev. D 107 (2023) 123530**, arXiv:2208.05929.

In this chapter, we perform a thorough comparison of the cosmological constraints derived from the full-shape analysis of BOSS power spectrum from the EFTofLSS, in order to assess the consistency of the various analyses presented in the literature. Indeed, a proper comparison between these various analyses is still lacking, and the implication for the robustness of the constraints has yet to be established. The EFT implementation and BOSS data we will focus on in this study are packaged in the `PyBird` likelihood, based on the EFT prediction and likelihood from `PyBird` [1] [59] (as in chapter 4) and the `CLASS-PT` likelihood, based on the EFT prediction from `CLASS-PT` [2] [61] and likelihood from Ref. [62]. [3] Cosmological constraints in ΛCDM obtained from these two likelihoods for the BOSS full-shape analysis with a big-bang nucleosynthesis (BBN) prior were originally presented in Ref. [69] and Ref. [62]. While results are in broad agreement, differences occur at the 1σ level between the two approaches for BOSS data, in particular on the primordial power spectrum amplitude A_s and the cold dark matter density $\omega_{\rm cdm}$, that can have an impact on the variance of matter fluctuations on a $8h^{-1}$Mpc scale, σ_8. As a result, the level of the tension on the $S_8 \equiv \sigma_8(\Omega_m/0.3)^{0.5}$ parameter compared to the CMB prediction can vary between these analyses, from mild to insignificant, which is particularly relevant to understand the scale-dependence of the growing "S_8 tension" [177, 79, 178, 116, 40]. Moreover, it casts some doubts on the robustness (and potentially on the validity) of the constraints derived on ΛCDM (and extensions) from the EFTofLSS applied to BOSS data. Note that we are not performing an eBOSS analysis here, as chapter 4 was chronologically completed after this chapter. The aim here is to study the consistency of the EFTofLSS within the ΛCDM model between the various analyses available in the literature, in the context of a particular case, namely the analysis of BOSS data.

In this work, we aim at understanding what drives the differences seen at the level of the posteriors of the cosmological parameters for the BOSS data. There are several analyses choices that differ between the two pipelines, from the choice of prior on the EFT parameters, for which several prescriptions have been suggested in the literature, to the BOSS measurements themselves. Specifically, we ask: (i) *How sensitive are cosmological constraints derived from the full-shape analysis of BOSS power spectrum to those effects?*; (ii) *How do the various BOSS data measurements used in previous full-shape analysis, that are obtained with different estimators, split in different redshift bins, or combined with various post-reconstructed measurements, impact the cosmological results?*

To answer those questions, we perform a series of analyses of the BOSS full-shape data, varying one-by-one (in order of importance) the prior choices, the BOSS measurements used (full-shape and post-reconstructed BAO parameters), the scale cuts and the number of multipoles [4] included. Importantly, we find that cosmological constraints are sensitive to the choice of prior on the EFT parameter space, and the two different choices of prior used in the `PyBird` and `CLASS-PT` analyses drive most of the differences in the results. On the other hand, the different BOSS full-shape measurements leads to at most 0.6σ difference among all

[1] https://github.com/pierrexyz/pybird

[2] https://github.com/michalychforever/CLASS-PT

[3] https://github.com/oliverphilcox/full_shape_likelihoods

[4] By multipoles, we refer to the Legendre polynomial $\mathscr{L}_\ell$ decomposition in multipoles $P_\ell(k)$ of the 3D power spectrum $P(k,\mu)$, *i.e.*, $P(k,\mu) = \sum_\ell \mathscr{L}_\ell(\mu) P_\ell(k)$, where k is the norm of the mode $\boldsymbol{k}$ and μ is the cosine of its angle with the line-of-sight. In this work we consider multipoles restricted to the first even ones, namely $\ell = \{0,2\}$ (the monopole and the quadrupole), or $\ell = \{0,2,4\}$ (including also the hexadecapole).

cosmological parameters, while the different post-reconstructed BAO measurements can affect constraints by up to 0.9σ. Yet, when the choices of prior and data are the same, we show that the two pipelines agree at better than 0.2σ, which consists in an important validation check of the two public likelihoods available.

For all analyses in this chapter, we work within ΛCDM. Except when combined with *Planck* [179], we impose a Gaussian prior on $\omega_b \sim \mathcal{N}(0.02268, 0.00038)$. [5] We scan over the physical dark matter density ω_{cdm}, the reduced Hubble constant h, the log-amplitude of the primordial fluctuations $\ln(10^{10}A_s)$, and the spectral tilt n_s, with large flat prior. We fix the total neutrino mass to minimal following *Planck* prescription [179]. We sample our posteriors using the Metropolis-Hasting algorithm in `MontePython` [136] with convergence given by the Gelman-Rubin criterion $R-1<0.01$. Finally, we extract the maximum a posteriori (MAP) parameters from the procedure highlighted in appendix of Ref. [183], and triangle plots are produced using `GetDist` [184].

Our chapter is organized as follows. In Sec. 5.1, we review the two prior choices on the EFT parameters used in previous analyses with the two aforementioned likelihoods, and discuss the various prior effects at play in the determination of the cosmological parameters from the Bayesian analysis. In Sec. 5.2, we assess the impact from those prior choices on the cosmological constraints from the EFT analysis of BOSS power spectrum. We scrutiny the impacts given various BOSS data measurements of the pre-reconstructed two-point functions in Sec. 5.3, and of the post-reconstructed ones in Sec. 5.4. Finally, we summarize our findings and conclude in Sec. 5.5. In App. B.1, we quantify the (minor) differences introduced due to choices of scale cuts and number of multipoles included in the analyses. For completeness, we provide a comparison of the two likelihoods in their respective baseline configurations in App. B.2.

5.1 The role of EFT priors

The one-loop prediction to the galaxy power spectrum in redshift space depends on a number of EFT parameters. Those are marginalized over in order to obtain constraints on the cosmological parameters. There are various ways that the EFT prediction can be parametrized, but all are equivalent at the one-loop order, in the sense that they are simply changes of basis (*i.e.*, linear transformations) of each others. However, differences can appear at the level of the posteriors, as soon as one needs to impose priors on the EFT parameters. There are two effects that can arise from the choice of priors. Let us give a precise definition for a given parameter Ω of interest (a cosmological parameter) and one nuisance "EFT" parameter c. The generalization to more parameters is straightforward. Considering a Gaussian prior $e^{-\frac{1}{2}(c/\sigma)^2}$ on c, we identify the following effects on the 1D posterior of Ω:

- *The prior weight effect*: this refers to how much the prior is weighting in the likelihood given that the true value of c will be different than the central value of our prior: $e^{-\frac{1}{2}((c-\hat{c})/\sigma)^2}$, with $\hat{c}$ the true value. This can lead to a shift of the most-likely value of Ω away from its true value.

[5] This prior is inspired from BBN experiments [180], based on the theoretical prediction of [181], the experimental Deuterium fraction of [12] and the experimental Helium fraction of [182].

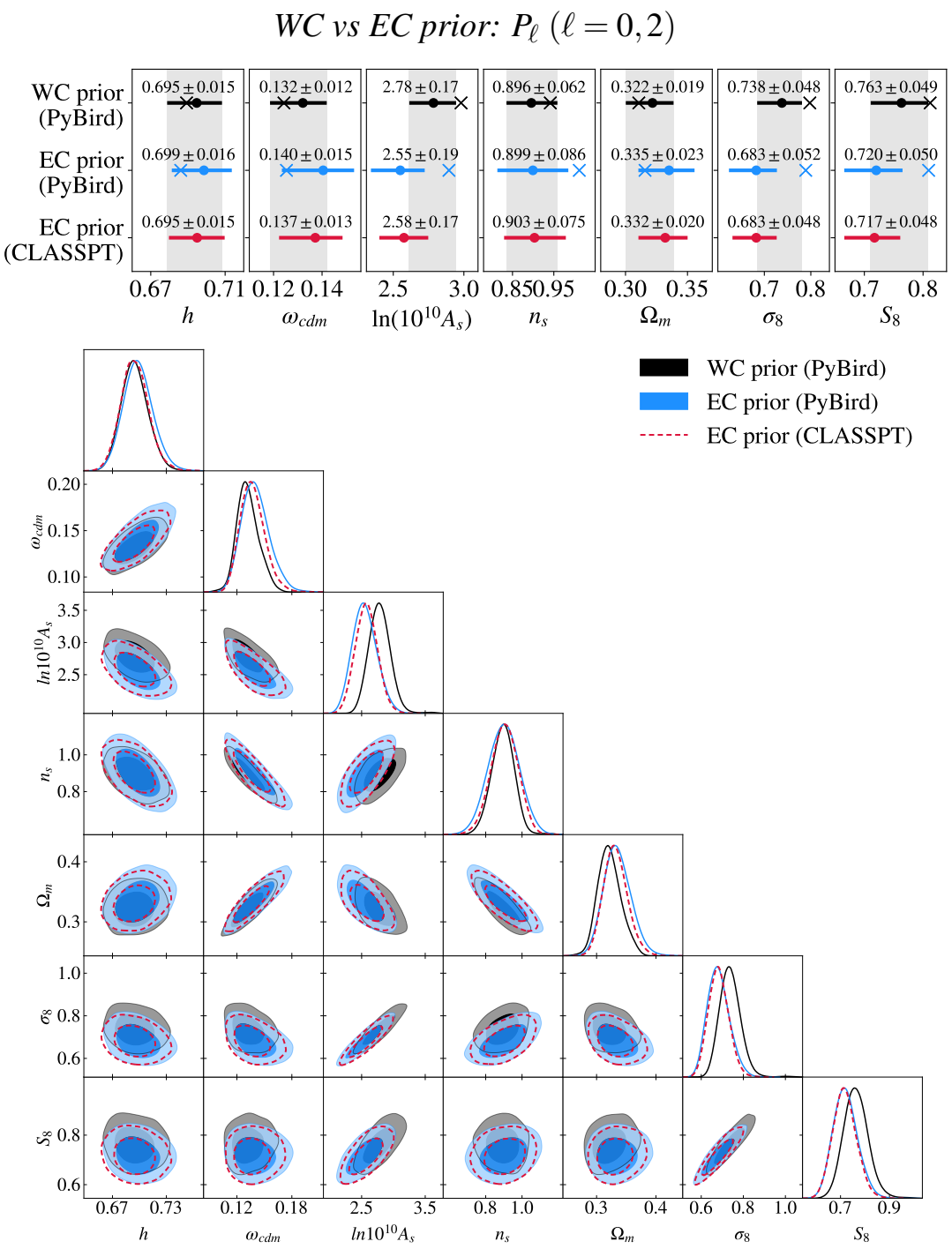

Figure 5.1: Comparison of ΛCDM results (1D and 2D credible intervals) from the full-shape analyses of BOSS power spectrum using the `PyBird` likelihood or the `CLASS-PT` likelihood. Here we use the same data measurements, $P_{\rm QUAD}^{z_1/z_3}$ as specified in Tab. 5.4, and same analysis configuration: we fit two multipoles, $\ell = 0, 2$, and use $k_{\rm max} = 0.20/0.25 h\,{\rm Mpc}^{-1}$ for the z_1/z_3 redshift bins. Given the same prior choice, the EC prior, we reproduce from the `PyBird` likelihood the results from the `CLASS-PT` likelihood to very good agreement (see blue and red posteriors): we obtain shifts $\lesssim 0.2\sigma$ on the means and the errors bars similar at $\lesssim 15\%$. Given that the two pipelines have been developed independently, this comparison provides a validation check of their implementation. In contrast, the WC and the EC prior choices lead to substantial differences on the 1D marginalized posteriors (see black and blue posteriors). The gray bands on the 1D posteriors are centered on the results obtained with the WC priors. The MAP (depicted by the crosses) are however in better agreement.

- *The prior volume projection effect*: this refers to the marginalization integral over c given its prior: $\int dc\, e^{-\frac{1}{2}((c-\hat{c})/\sigma)^2} \ldots$ As the likelihood will be a function of Ω and c, that usually enter in the model not just linearly but also as $\Omega \times c$, etc., the posterior of Ω will be non-Gaussian. The effect is a shift of the mean of Ω away from its most-likely value.

Here, we quantify the impact on the inferred cosmological parameters that different choices in the prior of the EFT parameters can have upon marginalization.

5.1.1 The two EFT priors

There has been several prescriptions for the EFT parameter priors that have been suggested in the literature. Generally, one would like to keep EFT parameters within physical range, such that the one-loop contributions cannot be larger than the tree-level part given the perturbative nature of the EFTofLSS. The simplest way to implement this requirement is to ask the EFT parameters controlling the loop contributions to be $\sim \mathcal{O}(b_1)$, where b_1 is the linear bias. We here compare two choices of prior on the EFT parameters made in the original analyses with the `PyBird` likelihood and the `CLASS-PT` likelihood. Following Ref. [98], we dub those prior choices "West coast" (WC) prior and "East coast" (EC) prior, respectively. Let us describe the differences between these two parametrizations. We recall that the redshift space galaxy power spectrum at one-loop for the WC parametrization is given in Eq. (3.180).

WC prior. The WC prior is designed to encompass the region physically-allowed by the EFTofLSS [65]. For each sky cut, we assign one set of EFT parameters, and impose the following priors to keep them within physical range [160]:

- $b_1 \sim$ flat $[0,4]$,
- $c_2 = (b_2+b_4)/\sqrt{2} \sim$ flat $[-4,4]$,
- $\{b_3, c_{\rm ct}, 2c_{r,1}, c_{\varepsilon,0}, c_\varepsilon^{\rm quad}\} \sim \mathcal{N}(0,2)$,
- $\{c_4 = (b_2-b_4)/\sqrt{2}, c_{r,2}, c_\varepsilon^{\rm mono}\} \sim 0$,

where $\mathcal{N}(m,\sigma)$ is a Gaussian prior centered on m with a standard deviation σ. Here b_1 is the linear bias and b_2, b_3, b_4 are the nonlinear EFTofLSS biases [65, 66, 67]. $c_{\rm ct}$ is dark-matter / higher-derivative counterterm coefficient appearing in front of $\sim k^2/k_{\rm M}^2 P_{\rm lin}(k)$ [54, 65]. $c_{r,1}, c_{r,2}$ are the counterterm coefficients renormalizing products of velocity operators appearing the expansion of the density field in redshift space [48, 64, 139], that are appearing in front of $\sim k^2/k_{\rm R}^2 P_{\rm lin}(k)$. $c_{\varepsilon,0}, c_\varepsilon^{\rm mono}, c_\varepsilon^{\rm quad}$ are the stochastic term coefficients [64], respectively of the shot noise $\bar{n}^{-1}$, monopole $\sim k^2/k_{\rm M}^2$ and quadrupole $\sim k^2/k_{\rm M}^2$. The renormalization scales are measured to be $k_{\rm NL} = k_{\rm M} = 0.7h\,{\rm Mpc}^{-1}$ and $k_{\rm R} = 0.35h\,{\rm Mpc}^{-1}$ [139], and the mean galaxy density is set to $\bar{n} = 4\cdot 10^{-4}({\rm Mpc}\,h^{-1})^3$. The EFT parameters set to 0 have too low signal-to-noise ratio to be measured from BOSS two-point function (namely, c_4 and $c_\varepsilon^{\rm mono}$), or are degenerate with already present EFT parameters when using only two multipoles (namely $c_{r,2}$) [58]. [6] In total, the WC prior consists of 9 EFT parameters per sky cut when fitting two

[6] Notice than when we perform checks adding the hexadecapole, we then free $c_{r,2}$ with a prior $\sim \mathcal{N}(0,2)$ as the degeneracy is broken.

multipoles, and 10 when fitting three multipoles. We also perform checks freeing c_4 and $c_\varepsilon^{\rm mono}$, as well as adding the next-to-next-leading order redshift-space counterterm $\tilde{c}$ (defined in the following). In this case, both priors have the same number of EFT parameters and an equivalent set of associated theoretical predictions.

EC prior. The EC prior is motivated by the coevolution model and simulations [185] (and see Refs. therein). The basis of galaxy biases $\{\tilde{b}_1, \tilde{b}_2, b_{\mathscr{G}_2}, b_{\Gamma_3}\}$ developed in Ref. [60] is related to the EFTofLSS basis as (see, *e.g.*, [63]):

$$\begin{aligned} b_1 &= \tilde{b}_1, \quad b_2 = \tilde{b}_1 + \frac{7}{2} b_{\mathscr{G}_2}, \\ b_3 &= \tilde{b}_1 + 15 b_{\mathscr{G}_2} + 6 b_{\Gamma_3}, \quad b_4 = \frac{1}{2}\tilde{b}_2 - \frac{7}{2} b_{\mathscr{G}_2}. \end{aligned} \tag{5.1}$$

As for the counterterms and the stochastic terms, although almost all scaling functions are present in the two likelihoods, there are differences in their definition, leading to differences in their prior. In particular, in the EC prior, $k_{\rm M}$ or $k_{\rm R}$ are absorbed in the definition of the counterterm coefficients c_0, c_2, c_4, while $k_{\rm NL}^{-0/2}\bar{n}^{-1}$ appears explicitly in front of their k^0/k^2 stochastic terms, with choice $k_{\rm NL} = 0.45h\,{\rm Mpc}^{-1}$ and $\bar{n} \simeq 3\cdot 10^{-4}({\rm Mpc}\,h^{-1})^3$. Furthermore, the EC prior also includes in their baseline a next-to-next-leading order term $\sim \tilde{c}\,k^4 P_{\rm lin}(k)$. The EC prior on the EFT parameters consists of [62]:

- $\tilde{b}_1 \sim$ flat $[0,4]$,
- $\{\tilde{b}_2, b_{\mathscr{G}_2}\} \sim \mathcal{N}(0,1), b_{\Gamma_3} \sim \mathcal{N}(\frac{23}{42}(b_1-1),1)$,
- $c_0/[{\rm Mpc}\,h^{-1}]^2 \sim \mathcal{N}(0,30)$, $c_2/[{\rm Mpc}\,h^{-1}]^2 \sim \mathcal{N}(30,30)$, $c_4/[{\rm Mpc}\,h^{-1}]^2 \sim \mathcal{N}(0,30)$,
- $\{c_{\varepsilon,0}, c_\varepsilon^{\rm mono}, c_\varepsilon^{\rm quad}\} \sim \mathcal{N}(0,2)$,
- $\tilde{c}/[{\rm Mpc}\,h^{-1}]^4 \sim \mathcal{N}(500,500)$.

In total, the EC prior consists of 11 EFT parameters per sky cut when fitting two multipoles, and an extra one, c_4, when fitting three multipoles.

5.1.2 Prior weight and volume projection effects

The EC and WC basis are merely linear combinations of the other ones. However, we stress that the two prior choices are not equivalent, for two reasons. First, given the definition above, the allowed ranges of variation are not equivalent. As a result, they can lead to different *prior weight effect* (on the likelihood of the cosmological parameters of interest) as defined previously. This raises two important questions regarding the prior choice and the prior weight effect: *Is one prior choice more restrictive* (i.e., *more informative) than the other one? How significantly does the prior choice disfavor physically-allowed region, and lead to potential bias in the measured cosmological parameters?* Second, the *metric* on the parameter space is different: although one can go from one basis to the other through linear transformations, we do not keep the jacobians of the transformations, *i.e.*, the integral measures that enter in the marginalization. If the posteriors are Gaussian, *e.g.*, in the limit where the parameters are well determined, this is

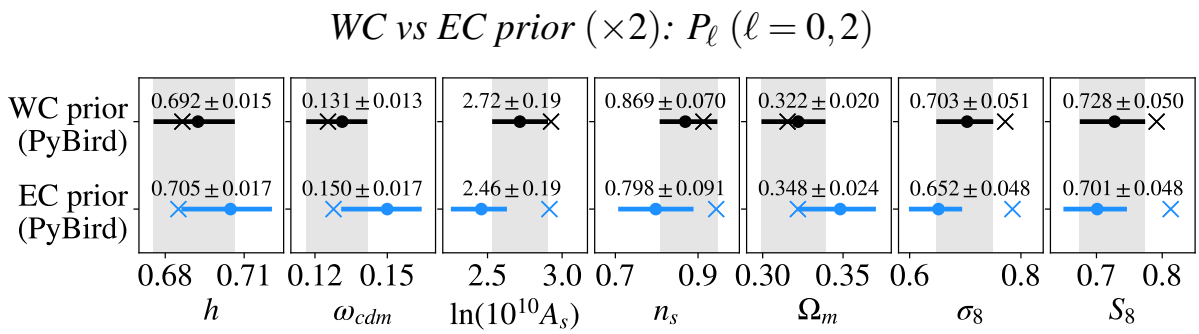

Figure 5.2: Same figure as the top panel of Fig. 5.1, but this time increasing the allowed prior width for the EFT parameters by a factor of two. The shifts between the mean and the MAP are $\lesssim 1.4\sigma$ for the WC prior and $\lesssim 2.7\sigma$ for the EC prior. This should be compared with the shifts we obtain for the usual EFT prior width, namely $\lesssim 1.2\sigma$ for the WC prior and $\lesssim 2.0\sigma$ for the EC prior.

not so much an issue. However, in our case, the posteriors are non-Gaussian. This is obvious in the case of the cosmological parameters, but it is also the case for EFT ones, as for example b_1 enters quadratically in the prediction. In fact, even the EFT parameters that enter at most linearly in the prediction, and thus quadratically in the likelihood, do not lead to Gaussian posteriors as they often (if not always) correlate with other parameters, such as b_1, A_s, etc. Given the relatively large number of EFT parameters to marginalize over, this might lead to a rather large *prior volume projection effect* that affects the marginalized posteriors, as defined previously. Given the non-Gaussianity of the posteriors, a natural question to ask is therefore: *do the differences in the parametrization, producing effectively different integral measures upon marginalization, lead to discrepancies on the measured value of the cosmological parameters?* In the following, we perform a detailed analysis to address those issues.

5.1.3 Pipeline validation check

Before comparing the results from the two prior choices, let us first present an important check. To test the validity of the two pipelines, we implement in the `PyBird` likelihood the EC prior. On the same data and at same configuration (same number of multipoles and same $k_{\rm max}$), we obtain the posteriors shown in Fig. 5.1 (see also Fig. B.1 of App. B.1 for the equivalent analyses with three multipoles). The residual differences are $\lesssim 0.2\sigma$ on the 1D posteriors of the cosmological parameters. Beyond serving as validation check of those two pipelines built independently, this also means that the different IR-resummation schemes, that differ at the two-loop level, are indeed not leading to appreciable shifts in the posteriors, as expected from the size of theory error (compared to BOSS error bars) at the scales we analyze. [7]

[7] `PyBird` implements the original IR-resummation scheme proposed in Ref. [71], generalized to redshift space in Ref. [72], and made numerically practical in Ref. [59]. In this approach, the bulk displacements are resummed directly on the full shape, and higher-order terms that are neglected are proven to be small at each order in perturbations [71] (see also [90]). `CLASS-PT` implements instead the IR-resummation scheme proposed in Ref. [91], and generalized to redshift space in Ref. [186]. This alternative scheme has been shown to be an approximation of the former one in Ref. [70], where one consider only the resummation of the bulk displacements around the BAO peak, $r_{\rm BAO} \sim 110{\rm Mpc}\,h^{-1}$. For this scheme to be made practical, one further relies on a wiggle-no-wiggle split procedure to isolate the BAO part. These approximations were shown to be smaller than the two-loop contribution in Ref. [61].

Parameter	WC pr.	EC pr.	WC pr. $\times 2$	EC pr. $\times 2$
h	0.6893	0.6861	0.6865	0.6850
$\omega_{\rm cdm}$	0.1243	0.1253	0.1254	0.1277
$\ln(10^{10}A_s)$	2.980	2.894	2.926	2.915
n_s	0.941	1.011	0.913	0.944
$\Omega_{\rm m}$	0.3107	0.3158	0.3155	0.3219
σ_8	0.7979	0.7891	0.7718	0.7848
S_8	0.8120	0.8096	0.7915	0.8129
b_1	1.977	–	1.962	–
c_2	0.4058	–	-0.0478	–
c_4	–	–	3.999	–
b_3	0.7003	–	-0.1567	–
c_{ct}	-0.2901	–	0.0927	–
$c_{r,1}$	-0.6575	–	1.246	–
$c_{\varepsilon,0}$	1.706	–	2.131	–
$c_\varepsilon^{\rm mono}$	–	–	3.919	–
$c_\varepsilon^{\rm quad}$	-0.3780	–	0.1944	–
$\tilde{c}/[{\rm Mpc}/h]^4$	–	–	134.3	–
$\tilde{b}_1$	–	2.181	–	2.038
$\tilde{b}_2$	–	-1.382	–	-2.725
$b_{\mathscr{G}_2}$	–	0.0977	–	-0.2013
b_{Γ_3}	–	0.0571	–	-0.3848
$c_0/[{\rm Mpc}/h]^2$	–	19.06	–	23.27
$c_2/[{\rm Mpc}/h]^2$	–	43.88	–	36.07
$c_{\varepsilon,0}$	–	0.3509	–	0.5684
$c_\varepsilon^{\rm mono}$	–	-0.0440	–	0.4738
$c_\varepsilon^{\rm quad}$	–	0.6255	–	0.4041
$\tilde{c}/[{\rm Mpc}/h]^4$	–	160.3	–	111.5
$\chi^2_{\rm min}$	352.6	343.7	336.0	336.4
$N_{\rm data}$	344			

Table 5.1: MAP of the cosmological parameters and EFT parameters corresponding to the analyses of Fig. 5.1, obtained either with the WC or the EC prior. For clarity, we only show the EFT parameters associated to the NGC z_3 sky cut. We also report the associated effective χ^2 values. Here we quote the MAP, as defined in the main text, which is *not* the values obtained maximizing the likelihood where the EFT parameters that enter the model linearly are marginalized over analytically. The MAP can be obtained with such likelihood [59] (see also Ref. [95]), but it is not sufficient to simply maximize this likelihood.

Parameter	WC (→ Pr. ×2)	EC (→ Pr. ×2)
h	0.4 σ ($\to 0.4\sigma$)	0.8 σ ($\to 1.1\sigma$)
$\omega_{\rm cdm}$	0.6 σ ($\to 0.4\sigma$)	1.0 σ ($\to 1.3\sigma$)
$\ln(10^{10}A_s)$	-1.2 σ ($\to -1.1\sigma$)	-1.3 σ ($\to -2.4\sigma$)
n_s	-0.7 σ ($\to -0.6\sigma$)	-1.3 σ ($\to -1.6\sigma$)
$\Omega_{\rm m}$	0.5 σ ($\to$ 0.3 σ)	0.8 σ ($\to 1.1\sigma$)
σ_8	-1.2 σ ($\to -1.3\sigma$)	-2.0 σ ($\to$ -2.7 σ)
S_8	-1.0 σ ($\to -1.3\sigma$)	-1.8 σ ($\to$-2.3 σ)

Table 5.2: A summary of prior volume projection effects on the posterior mean: distance of the mean from the MAP. σ is taken as the 68% C.L. error bars. The number in parenthesis give the distance when multiplying the prior width by two.

Parameter X	ΔX(MAP)	$\to$ Pr. ×2
h	0.2 σ	$\to$ 0.1 σ
$\omega_{\rm cdm}$	-0.1 σ	$\to$ -0.2 σ
$\ln(10^{10}A_s)$	0.5 σ	$\to$ 0.1 σ
n_s	0.9 σ	$\to$ -0.4 σ
$\Omega_{\rm m}$	-0.2 σ	$\to$ -0.3 σ
σ_8	0.2 σ	$\to$ -0.3 σ
S_8	0.1 σ	$\to$ -0.4 σ

Table 5.3: A summary of prior weight effects on the MAP: distance $(X^{\rm WC} - X^{\rm EC})$ between the MAP obtained with the WC and EC prior in units of σ, the average of the 68%-CL error bars derived from the two priors. The number in the right column give the distance when multiplying the prior width by two.

5.2 Impact of EFT priors in ΛCDM

5.2.1 Highlighting the role of the priors

To illustrate the impact of the prior choice, we compare the marginalized posteriors of the cosmological parameters within ΛCDM obtained with one or another prior choice (WC or EC), using the exact same data measurements, at the exact same scale cut and number of multipoles. In Fig. 5.1, we show the results when analyzing $P_{\rm QUAD}^{z_1/z_3}$ as specified in Tab. 5.4, with the same analysis configuration, namely we fit two multipoles, $\ell = 0,2$, and use $k_{\rm max} = 0.20/0.25h\,{\rm Mpc}^{-1}$ for the z_1/z_3 redshift bins. Additional comparisons with different data configurations are provided in App. B.1, Figs. B.1 and B.2. Let us quote the largest shifts for two analysis configurations:

- Fitting $\ell = 0,2$ at $k_{\rm max} = 0.25h\,{\rm Mpc}^{-1}$ in z_3 (*i.e.*, the `PyBird` native configuration), we find differences $< 0.5\sigma$ on all cosmological parameters between the two likelihoods, except larger ones on $\ln(10^{10}A_s)$, σ_8, and S_8, of 1.2σ, 1.1σ and 0.9σ.

- Fitting $\ell = 0,2,4$ at $k_{\rm max} = 0.20h\,{\rm Mpc}^{-1}$ in z_3 (*i.e.*, the `CLASS-PT` native configuration), we find differences $< 0.5\sigma$ on all cosmological parameters between the two likelihoods, except large ones on $\ln(10^{10}A_s)$, Ω_m, σ_8 and S_8, of 1.2σ, 0.7σ, 1σ, and 0.7σ.

This shows that the choice of prior on the EFT parameters can lead to differences in the posteriors. These can arise either from prior weights, in the sense that the allowed ranges are informing (potentially disfavoring) the "true" value that the EFT parameters want to take; or the

prior volume lead to important projection effects, given the large number of EFT parameters that we marginalize over.

Prior volume projection effects. One way to estimate the prior volume projection effects is to compare the MAP values in Tab. 5.1 to the 68%-credible intervals in Fig. 5.1 (as already mentioned in chapter 4). We summarize those shifts in Tab. 5.2. In particular, one can compute the shifts of the mean to the MAP, where the MAP is (by definition) *not* affected by prior volume projection effects. Here we refer to the "MAP" as the most likely value obtained by maximizing the likelihood of the data together with a conditional probability distribution given by the prior chosen for the EFT (nuisance) parameters. We stress that to obtained such MAP, the nuisance parameters are not marginalized over, *i.e.*, they are not integrated over given their prior probability distribution. With the EC prior, we find for some cosmological parameters that the MAP values are not lying within the 68%-credible intervals: for example, we find shifts of $\sim 2\sigma$ on $\ln(10^{10}A_s)$, σ_8, or S_8. With the WC prior, we find that the MAP and the mean are consistent at $\lesssim 1.2\sigma$ for all cosmological parameters. These shifts are particularly relevant when assessing the level of tension with the σ_8 and S_8 measurements from *Planck* (as already mentioned in chapter 4). While it might appear that σ_8 measured from EFTBOSS data are systematically lower than those deduced from *Planck* under ΛCDM, we find here that a large part of the apparent tension comes from a projection effect that shift the σ_8 value by 1.2σ and 2σ for the WC and EC prior respectively compared to the MAP (and by a similar amount for S_8). In fact, the MAP we derived for both priors (see Tab. 5.1) is in very good agreement with the reconstructed value from *Planck* TTTEEE+lowE+lensing under ΛCDM, $\sigma_8 = 0.8111 \pm 0.0060$ [11].

Finding smaller prior volume projection effects with the WC prior than with the EC prior is consistent with the fact that the prior widths for the EFT parameters are, in general, slightly more restrictive in the WC prior than in the EC prior (see discussion in Sec. 5.1). To further demonstrate the prior volume effect, we increasing the prior widths for the EFT parameters by a factor of two. One can see from Fig. 5.2 and Tab. 5.2 that the prior volume projection effects grow as expected: the mean-to-MAP distances are now up to $\sim 1.3\sigma$ with the WC prior and up to $\sim 2.7\sigma$ with the EC prior, with σ_8 suffering again from the largest projection effect. A similar analysis was recently performed in Ref. [187] in the context of ΛCDM and a model of dark energy with a free-to-vary equation of state w and interaction rate with dark matter. Working with the EC priors defined above, they show that broadening the width of the priors can strongly affect posteriors distributions of cosmological parameters, in good agreement with our findings. A more complete diagnosis would be to look at the profile likelihoods, that are however computationally challenging to obtain. We discuss this frequentist approach in Sec. 5.2.2, while this will be the main focus of chapter 6.

Prior weight effects. One simple way to quantify the effect due to the prior weight is to consider the MAP from the two prior choices, given in Tab. 5.1. Indeed, these are not affected by the projection effects discussed above, which only occur when performing the marginalization integrals over the EFT parameters (within their priors), and therefore are mostly biased by the prior weight effect (barring computational errors / inaccuracies). In

Tab. 5.3, we quantify the consistency between the most-likely values of all cosmological parameters X derived with the two prior choices (EC or WC), by computing the distance $(X^{\rm WC} - X^{\rm EC})/\sigma$, where σ is taken as the average of the 68%-CL error bars derived from the two priors. [8] One can see that they are different at $\lesssim 1\sigma$, with the largest difference being for n_s. It is also informative to compare the $\min\chi^2$ values, in order to check whether the fit is acceptable for both priors. From Tab. 5.1, we see that with the EC prior, the ΛCDM model leads to a slight better $\min\chi^2$ at $\Delta\chi^2 \sim 9$ than with the WC prior, but also introduces 2 extra free parameters per sky cut. Assuming all data points and parameters to be uncorrelated, we estimate that both prior choices lead to a comparable goodness-of-fit, with a $p-$value $\simeq 5\%$.

Finally, to further demonstrate the role of the prior in informing the determination of the cosmological parameters, we enlarge the allowed range for the EFT parameters in both prior choices by a factor of two. [9] We now find that the $\min\chi^2$ values are comparable: 336.0 and 336.4 from the WC and the EC prior, respectively, with corresponding p-values $\simeq 7\%$. More importantly, the most-likely values of the cosmological parameters are now compatible at $\lesssim 0.4\sigma$ (compared to $\lesssim 1\sigma$ before enlargement).

Summary. On the one hand, we have shown that prior volume projection effects lead to shifts up to $\sim 1\sigma$ and $\sim 2\sigma$ on the posterior means from the WC and EC prior, respectively (see Tab. 5.2). As already mentioned in chapter 4, this effect is particularly noticeable in shifting downward the mean value of σ_8, which lead to an apparent small tension with *Planck* under ΛCDM (at 1.5σ and 2.5σ for the WC and EC prior respectively), compared to the MAP that is in good agreement with *Planck* at $\lesssim 0.5\sigma$ for all prior choices. The prior weight effects, on the other hand, are responsible for differences in the most-likely values up to $\sim 1\sigma$ between the two prior choices. Additionally, the ΛCDM model provides an acceptable description of the data regardless of the prior. Let us stress that the effects from the prior that we have found here are sizeable (with respect to the error bars) only because current data are of relatively small volume (and therefore larger statistical errors). In the following, we argue that those effects becomes less relevant as soon as more data are added in the cosmological analysis.

Before moving on, we make the following comment. One may wonder if the present study allows us to draw lesson on how to choose appropriately priors on the EFT parameters. We have demonstrated that the two EFT priors allow for the same maximal likelihood point once enlarged enough. This is expected since we stress again that the two parametrizations are equivalent, as they are related by a change of basis to each other: as such, once the prior is large enough, the prior weight becomes negligible with respect to the likelihood of the data, and the maximal likelihood point is recovered. Therefore, one possible criteria to choose the prior is to require that the size of the one-loop contribution stays smaller than the tree-level, such that the perturbative nature of the theory is preserved. Progress in this direction are ongoing. Nev-

[8] In principle, it would be more accurate to estimate the consistency between the best-fits via a profile likelihood (see chapter 6). We take the 68%-credible intervals obtained from the posterior distribution as a simple proxy, although these are potentially affected by the projection effects mentioned above.

[9] For the WC prior, we also free c_4 and $c_\varepsilon^{\rm mono}$ with range 4, and add the next-to-next leading redshift-space counterterm $\tilde{c}$ as in the EC prior, such that the two priors have equivalent sets of associated theoretical predictions. Indeed, in this case, both priors have the same number of EFT parameters and an equivalent set of associated theoretical predictions.

ertheless, we anticipate than none of the choice for the EFT parameters satisfying such criteria will be immune to the prior volume projection effects given BOSS data volume. We therefore now move on to look at the situation given larger data volume.

5.2.2 How to beat the prior weights and volume effects

Forthcoming surveys data. While we have established that effects from the prior are of utmost importance for BOSS, one may ask whether these will still be important given a larger data volume, *e.g.*, from forthcoming surveys such as DESI [171] or Euclid [172]. To answer this question, following Ref. [95], we measure effect from the prior by fitting synthetic data generated with our prediction on the MAP of the data. The results are presented in Fig. 5.3 for the WC prior as well as for the EC prior. For the volume of BOSS, one can see as expected that the prior effects are important, as the posterior means are far away from the truth, namely a $\lesssim 1.2\sigma$ shift for the WC prior and a $\lesssim 2.0\sigma$ shift for the EC prior. However, by re-scaling the covariance of BOSS by 16, which corresponds roughly to the volume of the forthcoming galaxy surveys, one can see that the prior effects are less important: the shifts of the mean to the truth are now $\lesssim 0.5\sigma$ for the WC prior and $\lesssim 0.7\sigma$ for the EC prior. There are several caveats to this simple exercise. First, here we have simply rescaled the covariance of BOSS, and used the synthetic data generated from the MAP to BOSS data. These are far from the specifications of forthcoming surveys in terms of targeting, shot noise, redshifts, etc., although we anticipate that this should not change the conclusions. Maybe more importantly, keeping in mind that the $k_{\rm max}$ is determined as the highest scale at which the theory error remains under control with respect to the statistical error, the $k_{\rm max}$ will presumably not be as high for larger data volume. Therefore, the size of the error bars seen in Fig. 5.3 are likely underestimated. This in principle can allow for more effects from the prior, which remain to be precisely quantified. We refer to App. C of Ref. [98] as well as Ref. [139] for more realistic prospects of the EFT analysis on a DESI-like surveys with the WC prior. Finally, the forthcoming data will be cut into very different redshift bins than the ones of BOSS. If one assigns one set of EFT parameters per redshift bin in the analysis, the thinner is the slicing, the bigger the prior volume will get. If this becomes an issue, one can imagine to be more informative, for example add a correlation on the EFT parameters from one redshift bin to another, given that one expects them to not be so different. This effectively reduces the number of EFT parameters to marginalize over, *i.e.*, reduces the prior volume and the associated projection effects. We refer to Ref. [95] for a practical implementation of such correlated prior in an EFT analysis of BOSS data.

Combining with CMB. In Fig. 5.4, we show the combination of the EFT analysis of BOSS power spectrum, using either the WC or the EC prior, with *Planck* TTTEEE+lowE+lensing data [11]. The inclusion of *Planck* data brings the two analyses into good agreement: we observe at most shifts $\lesssim 0.5\sigma$ on the means, and the errors bars are similar at $\lesssim 5\%$. The *Planck* data represents a considerable data volume with respect to BOSS, such that it is not surprising that the cosmological constraints are dominated by *Planck*. As such, all prior effects observed earlier are then less prone to bias the cosmological results.

Profile Likelihood. Although we have shown that increasing the data volume, either from the survey or by combining with CMB experiments, help to mitigate prior effects, the question of

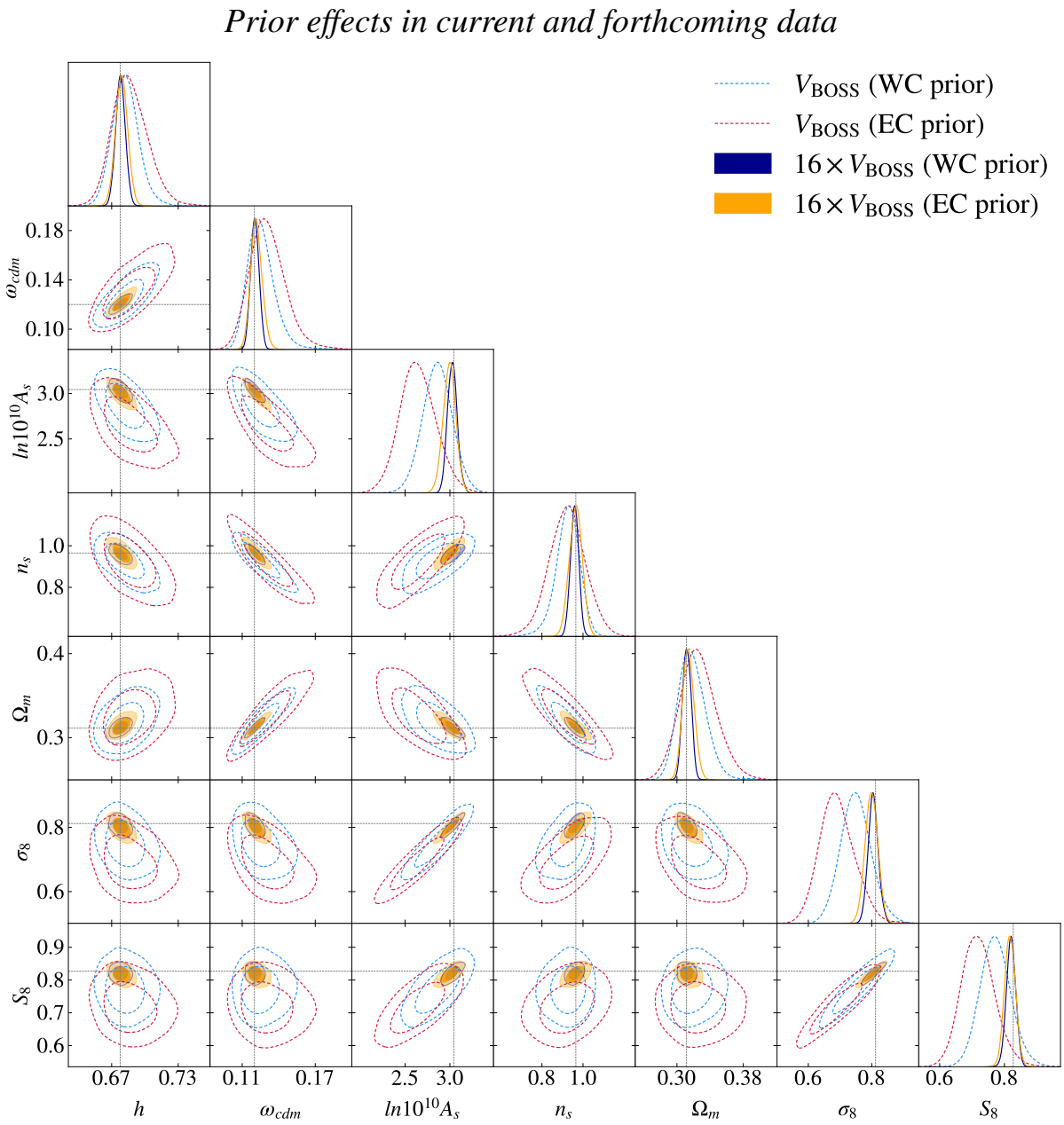

Figure 5.3: ΛCDM results (1D and 2D credible intervals) from the same likelihood as Fig. 5.1, `PyBird`, but on noiseless synthetic data generated with the EFT prediction close to the MAP of BOSS. In particular, we use the same covariance as for the BOSS analysis, represented by $V_{\rm BOSS}$. We perform this analysis either with the WC prior or the EC prior. The vertical lines represent the truth. For BOSS data volume, $V_{\rm BOSS}$, we observe shifts in the 1D posteriors from the prior effects up to $\sim 1.2\sigma$ for the WC prior, and up to $\sim 2.0\sigma$ for the EC prior. For forthcoming survey-like data volume, $\sim 16\times V_{\rm BOSS}$, we see that the cosmological parameters are instead recovered at $\lesssim 0.5\sigma$ with the WC prior and $\lesssim 0.7\sigma$ with the EC prior.

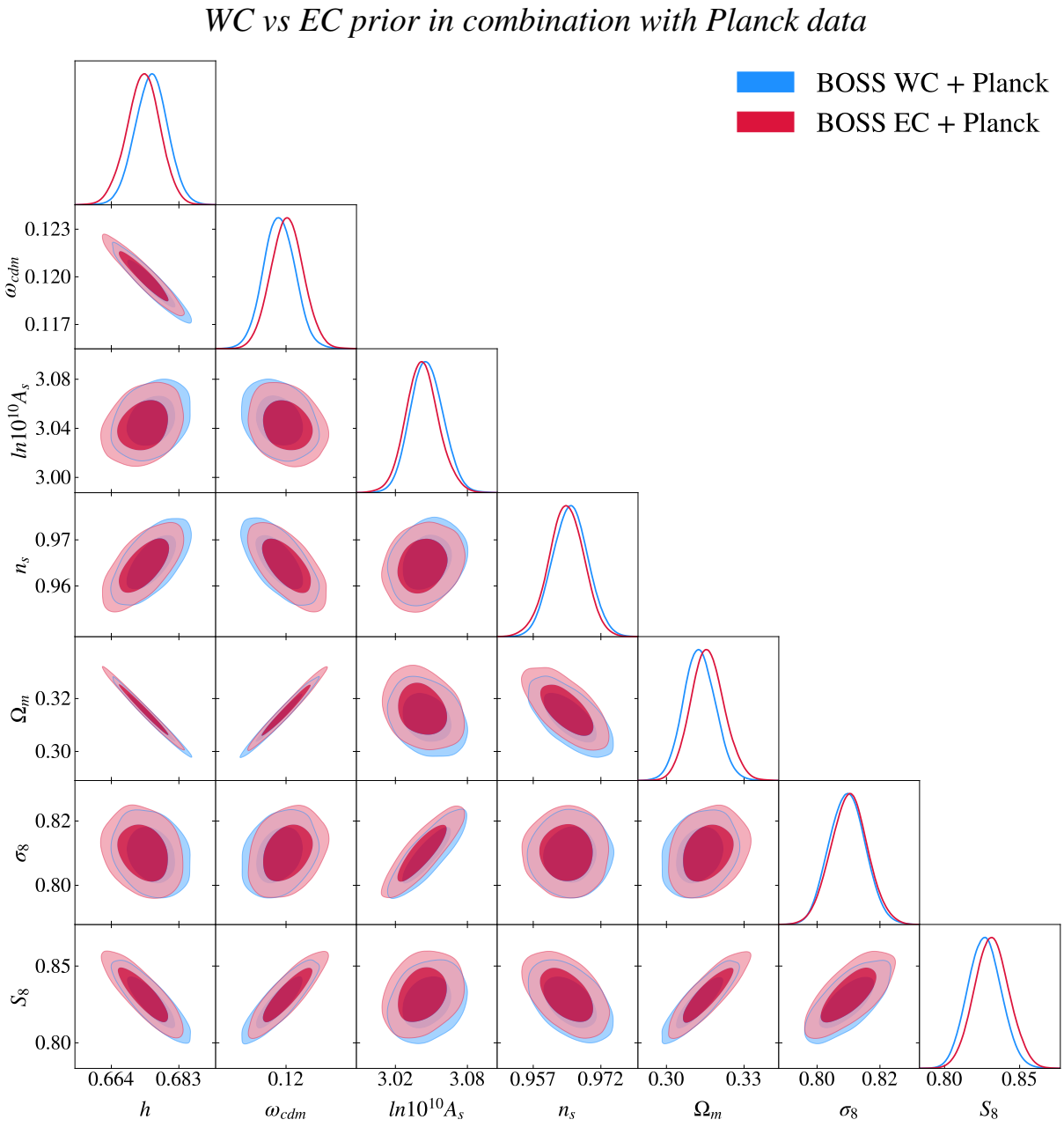

Figure 5.4: Once combined with *Planck* TT,TE,EE+lowE+lensing [11], the full-shape analysis of BOSS with the EC and WC prior choices lead to similar results within $\lesssim 0.5\sigma$ on all cosmological parameters.

Pre-reconstructed measurements					
	Ref.	Estimator	Code	Redshift split	Window
$\mathscr{P}_{\rm FKP}^{\rm LZ/CM}$	[191]	FKP	`Rustico` [191]	LOWZ / CMASS	Inconsistent norm.
$P_{\rm FKP}^{\rm LZ/CM}$	[69]	FKP	`PowSpec` [192] / `nbodykit` [193]	LOWZ / CMASS	Consistent norm.
$\xi^{\rm LZ/CM}$	[69]	Landy & Slazay	`FCFC` [194]	LOWZ / CMASS	Window-free
$P_{\rm FKP}^{z_1/z_3}$	[122]	FKP	–	z_1 / z_3	Consistent norm.
$P_{\rm QUAD}^{z_1/z_3}$	[62]	Quadratic	`Spectra without Windows` [195]	z_1 / z_3	Window-free

Post-reconstructed measurements					
	Ref.	–	–	Redshift split	Method
$\alpha_{rec}^{\rm LZ/CM}$	[126]	–	–	LOWZ / CMASS	[59]
$\alpha_{rec}^{z_1/z_3}$	[51]	–	–	z_1 / z_3	[59]
$\beta_{rec}^{z_1/z_3}$	[51]	–	–	z_1 / z_3	[102]

Table 5.4: Comparison of pre-reconstructed and post-reconstructed BOSS two-point function measurements: reference, estimator, code of the measurements, redshift split [LOWZ: $0.2 < z < 0.43$ ($z_{\rm eff} = 0.32$), CMASS: $0.43 < z < 0.7$ ($z_{\rm eff} = 0.57$); z_1: $0.2 < z < 0.5$ ($z_{\rm eff} = 0.38$), z_3: $0.5 < z < 0.7$ ($z_{\rm eff} = 0.61$)], and window function treatment. For the post-reconstructed measurements, while we instead provide under "Method" the references presenting the algorithm used to extract the reconstructed BAO parameters and how the cross-correlation with the pre-reconstructed measurements is performed, "Ref." now refers to the public post-reconstructed measurements used. The SDSS-III BOSS DR12 galaxy sample data are described in Refs. [81, 125]. The pre-reconstructed measurements are from BOSS catalogs DR12 (v5) combined CMASS-LOWZ [124].

how to extract reliable cosmological summary statistics from smaller data volume remains. One possibility is to go back to the frequentist approach: instead of sampling the likelihood to obtain posteriors that we then marginalize to get credible intervals, we can simply look at the profile likelihoods and read the confidence intervals. In the context of *Planck* CMB data, Ref. [138] showed that the frequentist analysis yields similar distribution as the Bayesian analysis within ΛCDM. However, it as already been pointed out that this is not necessarily the case for beyond-ΛCDM model, such as early dark energy [188, 189, 190]. As we have illustrated, this can have several advantages over the Bayesian approach: one is free to choose very agnostic prior, *i.e.*, broad prior ranges, thus avoiding potential bias from the prior weight, without paying the price of being subject to large prior volume projection effects, as the confidence intervals are not derived upon marginalization. It this will be the main focus of chapter 6.

5.3 Comparison of BOSS measurements

On top of various EFT prior choices, there are various BOSS two-point function measurements (that can be) used in full-shape analyses. Here, we present a detailed comparison on the posteriors obtained from the EFT analysis given various BOSS measurements. In particular, we ask what are the differences that can occur given the various treatments of the window functions. The characteristics of each measurements are listed in Tab. 5.4, while a more in-depth description is available in Sec. 5.3.1. All analyses in this section are performed using the same pipeline: same prior choice on the EFT parameters, same scale cuts, and same number of multipoles, to ensure that we are only sensitive to differences due to the various measurements under scrutiny.

5.3.1 Contenders

Here we compare four pre-reconstructed and two post-reconstructed two-point function measurements from the BOSS sample, summarized in Tab. 5.4:

- $P_{\rm FKP}^{\rm LZ/CM}$: pre-reconstructed power spectrum measured for the full-shape analysis (abbreviated "FS" analysis in the following) presented in Ref. [69]. The corresponding window functions were consistently normalized with $Q_0(s \to 0) \sim 0.9$ at vanishing separation, matching the measurements normalization (see App. D.1).

- $\xi^{\rm LZ/CM}$: pre-reconstructed correlation function measured for the FS analysis presented in Ref. [69]. The correlation function estimator is free from window function effects.

- $P_{\rm FKP}^{z_1/z_3}$: pre-reconstructed power spectrum measured in Ref. [122]. The corresponding window functions were consistently normalized matching the corresponding measurements normalization. We analyze $P_{\rm FKP}^{z_1/z_3}$ by deconvolving the window functions from the theory prediction by redefinition of the data vector and covariances at the level of the likelihood, as described in Ref. [122]. The window functions furthermore include the integral constraints [196].

- $P_{\rm QUAD}^{z_1/z_3}$: pre-reconstructed power spectrum measured using the quadratic "window-free" estimator of [195].

- $\alpha_{rec}^{\rm LZ/CM}$: BAO transverse and parallel parameters measured in Ref. [59] from post-reconstructed power spectrum measured in Ref. [126].

- $\alpha_{rec}^{z_1/z_3}$: BAO transverse and parallel parameters measured in this work (following methodology described, *e.g.*, in Ref. [51]) from post-reconstructed power spectrum measured in Ref. [51].

$P_{\rm FKP}^{\rm LZ/CM}$, $\xi^{\rm LZ/CM}$, and $\alpha_{rec}^{\rm LZ/CM}$ are cut into LOWZ and CMASS redshift bins, $0.2 < z < 0.43$ ($z_{\rm eff} = 0.32$), $0.43 < z < 0.7$ ($z_{\rm eff} = 0.57$), respectively. $P_{\rm FKP}^{z_1/z_3}$, $P_{\rm QUAD}^{z_1/z_3}$ and $\alpha_{rec}^{z_1/z_3}$ are cut into z_1 and z_3 redshift bins, $0.2 < z < 0.5$ ($z_{\rm eff} = 0.38$) and $0.5 < z < 0.7$ ($z_{\rm eff} = 0.61$), respectively. The scale cut for BOSS FS analysis has been determined on large-volume high-fidelity HOD simulations in Refs. [101, 98, 59, 69] and from a theory-error estimate in Ref. [69] for LOWZ / CMASS split to $(k_{\rm min}, k_{\rm max}) = (0.01, 0.20/0.23) h\,{\rm Mpc}^{-1}$ in Fourier space and $(s_{\rm min}, s_{\rm max}) = (25/20, 200)\,{\rm Mpc}\,h^{-1}$ in configuration space. When the data are split into z_1 and z_3 instead, we rescale $k_{\rm max}$, using Eq. (40) of [58], in order to have an equivalence with the LOWZ / CMASS separation. Especially, since z_3 is effectively slightly higher redshift and with less data volume than CMASS, we re-scale the associated $k_{\rm max}$ to $k_{\rm max}^{z_3} = 0.25 h\,{\rm Mpc}^{-1}$, while we keep $k_{\rm max}^{z_1} = 0.20 h\,{\rm Mpc}^{-1}$. Finally, we precise that the reconstructed BAO parameters are always combined with a FS analysis of pre-reconstructed measurements. $\alpha_{rec}^{\rm LZ/CM}$ and $\alpha_{rec}^{z_1/z_3}$ listed above for completeness will be compared in the next section.

5.3.2 The matchups

We now compare the cosmological results from a FS analysis within ΛCDM of the various BOSS data presented previously. Summary of the cosmological results are given in Fig. 5.5. We divide the contenders into the following matchups:

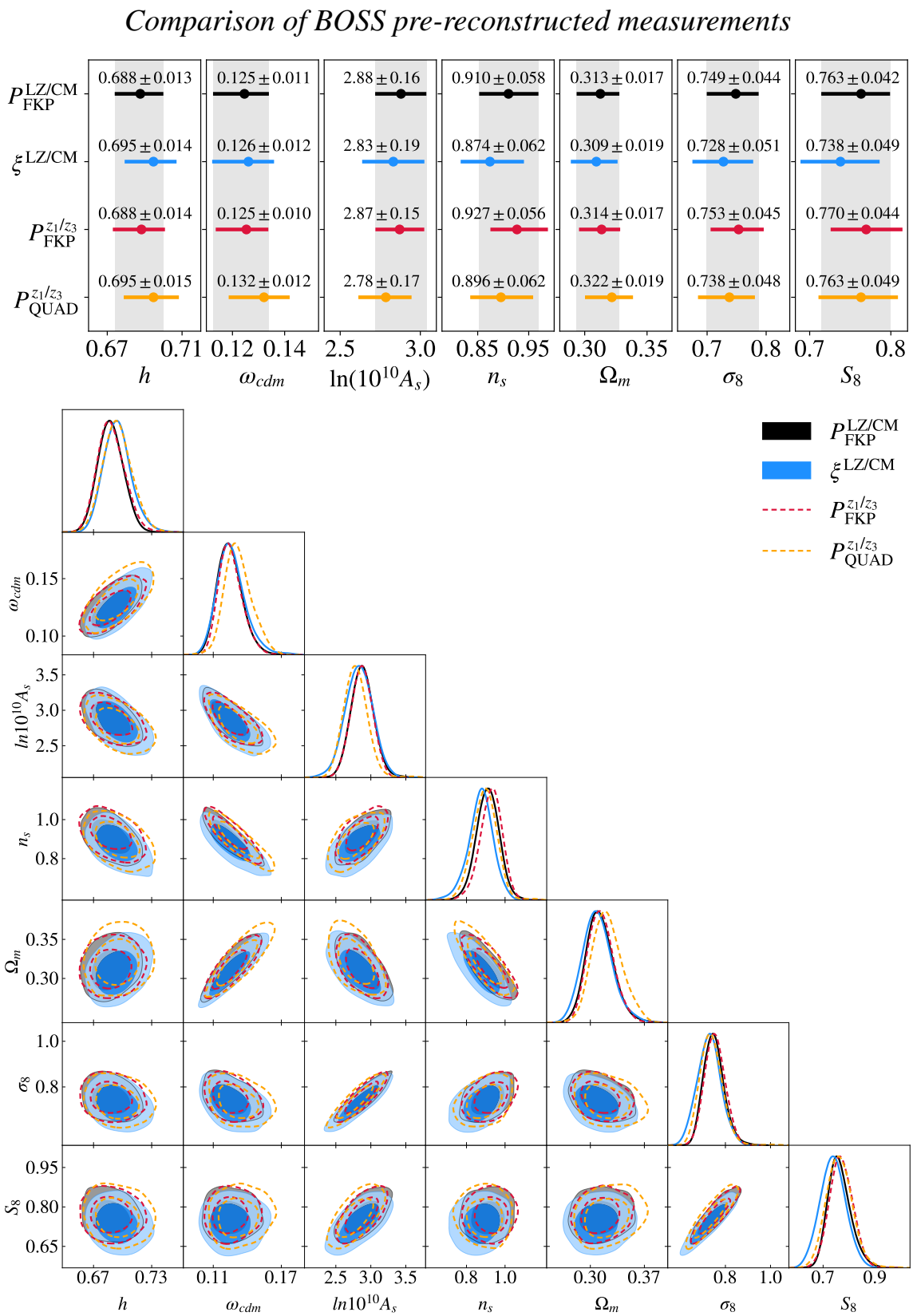

Figure 5.5: Comparison of ΛCDM results (1D and 2D credible intervals) from BOSS full-shape analyses of various pre-reconstructed two-point function measurements ($P_{\rm FKP}^{\rm LZ/CM}$, $\xi^{\rm LZ/CM}$, $P_{\rm FKP}^{z_1/z_3}$, $P_{\rm QUAD}^{z_1/z_3}$). Details on the naming convention and relevant information are summarized in Tab. 5.4. The gray bands on the 1D posteriors are centered on the results obtained with $P_{\rm FKP}^{\rm LZ/CM}$.

$P_{\rm FKP}^{\rm LZ/CM}$ vs. $\xi^{\rm LZ/CM}$ (*i.e.*, the Fourier vs. configuration space matchup). Such matchup was already presented in Ref. [69] but with varying neutrino masses. Here we re-do the same comparison with one massive neutrino fixed to minimal mass, finding similar conclusions: the difference in the 1D posteriors is about $\lesssim 0.6\sigma$ for all cosmological parameters. Importantly, as seen in Fig. 5.6, the consistency is brought to better agreement when the same reconstructed BAO parameters $\alpha_{rec}^{\rm LZ/CM}$ is added to both: $\lesssim 0.2\sigma$ for all cosmological parameter, except on σ_8, S_8, and n_s, which are consistent at about $0.3-0.5\sigma$. Contrary to the other comparisons made here, the cosmological information between the two compared statistics is effectively quite different due to two reasons. First, the BAO signal is fully analyzed in configuration space, as it shows up as a peak around $110{\rm Mpc}\,h^{-1}$, while the BAO wiggles in Fourier space above the scale cut are not analyzed. Second, the scale cuts are effectively different (see more discussions in Ref. [69]). Therefore, the addition of the same reconstructed BAO parameters effectively bring closer the BAO information content between the Fourier and configuration space analysis. However, we still expect some level of differences on the posteriors as the information content is not equivalent in the two analyses. In particular, as the correlation function is free from the window functions effect, such match between the two analyses tells us that the effect from the window function (normalization) is under relatively good control. $P_{\rm FKP}^{\rm LZ/CM}$ and $\xi^{\rm LZ/CM}$ are thus declared both consistent.

$P_{\rm FKP}^{\rm LZ/CM}$ vs. $P_{\rm FKP}^{z_1/z_3}$ (*i.e.*, the LOWZ / CMASS vs z_1 / z_3 redshift split matchup). We find that $P_{\rm FKP}^{\rm LZ/CM}$ and $P_{\rm FKP}^{z_1/z_3}$ and their respective window functions (consistently normalized), measured independently, are rather consistent ($\lesssim 0.3\sigma$). Here $P_{\rm FKP}^{z_1/z_3}$ is analyzed by deconvolving the window from the theory predictions at the level of the likelihood as described in Ref. [122]. Furthermore, [122] adds to the window of $P_{\rm FKP}^{z_1/z_3}$ the integral constraints [196]. Therefore, finding consistency between $P_{\rm FKP}^{\rm LZ/CM}$ and $P_{\rm FKP}^{z_1/z_3}$ gives us several important information: (i) it allows us to check the accuracy of the deconvolution procedure on BOSS data; (ii) it tells us that the integral constraints have minor effects on the cosmological results from BOSS; and (iii) that the LOWZ / CMASS and z_1 / z_3 splits (and their respective scale cuts) lead to consistent cosmological measurements. $P_{\rm FKP}^{\rm LZ/CM}$ vs. $P_{\rm FKP}^{z_1/z_3}$ are thus declared both consistent.

$P_{\rm FKP}^{\rm LZ/CM}$ vs. $P_{\rm QUAD}^{z_1/z_3}$ (*i.e.*, window vs. window-free matchup). This comparison was initially performed in Ref. [195] but using the `CLASS-PT` likelihood. Thanks to the `PyBird` likelihood, we find similar trend using the WC prior, with $P_{\rm QUAD}^{z_1/z_3}$ leading to differences of about $0.5-0.6\sigma$ on h, $\omega_{\rm cdm}$, $\ln\left(10^{10}A_s\right)$ and Ω_m. Similarly, $P_{\rm FKP}^{z_1/z_3}$ and $P_{\rm QUAD}^{z_1/z_3}$ are consistent at $\lesssim 0.6\sigma$ on all cosmological parameters. While Ref. [195] argues that the $P_{\rm QUAD}^{z_1/z_3}$ analysis is "formally equivalent" to the $P_{\rm FKP}^{z_1/z_3}$ window-deconvolved analysis, we observe that the inverse covariance (schematically $W^T\cdot C^{-1}\cdot W$, where W is the window function matrix, see again Ref. [122]) in the deconvolved analysis is different than the inverse covariance built from measurements using the window-free quadratic estimator. Another potential difference is the fact that $P_{\rm FKP}^{z_1/z_3}$ is shot-noise subtracted while $P_{\rm QUAD}^{z_1/z_3}$ is not. However, putting a prior centered on 1 instead of 0 (in unit of $\bar{n}^{-1}$) for the shot noise in the analysis $P_{\rm QUAD}^{z_1/z_3}$ only shifts $\ln\left(10^{10}A_s\right)$ by $\sim 0.2\sigma$. Finally, we note that both $P_{\rm FKP}^{\rm LZ/CM}$ and $P_{\rm QUAD}^{z_1/z_3}$ are consistent with $\xi^{\rm LZ/CM}$ at $\lesssim 0.6\sigma$.

5.3.3 Measurements comparison summary

All in all, all BOSS pre-reconstructed full-shape measurements not affected by a window function normalization issue (see App. D.1 for a discussion about this issue and its impact on the cosmological parameters), namely $P_{\rm FKP}^{\rm LZ/CM}$, $\xi^{\rm LZ/CM}$, $P_{\rm FKP}^{z1/z3}$, and $P_{\rm QUAD}^{z1/z3}$, measured from different estimators as figuring in Tab. 5.4, lead to broadly consistent results at $< 0.8\sigma$ on the 1D posteriors for all cosmological parameters, and with similar error bars within $\lesssim 10\%$ (see Fig. 5.5). To be more precise, taking $P_{\rm FKP}^{\rm LZ/CM}$ as reference, the 1D posterior distribution of parameters reconstructed from $\xi^{\rm LZ/CM}$, $P_{\rm FKP}^{z1/z3}$, and $P_{\rm QUAD}^{z1/z3}$ are consistent at $\lesssim 0.6\sigma$, 0.3σ, and 0.6σ, respectively. The addition of the same post-reconstructed BAO signal (by cross-correlation) to $P_{\rm FKP}^{\rm LZ/CM}$ and $\xi^{\rm LZ/CM}$ brings them in consistency at $\lesssim 0.2\sigma$ for all cosmological parameters, with the exception of residual shifts of $\sim 0.3-0.5\sigma$ on σ_8, S_8, or n_s, as it can be seen on Figs. 5.5.

To summarize, we list the differences seen at the level of the posteriors (within ΛCDM), ordered from the most to the least important one, and the respective choices of measurements that they stem from:

- up to 0.6σ among all cosmological parameters from the choice of the power spectrum estimators ($P_{\rm FKP}^{\rm LZ/CM}$ vs. $P_{\rm QUAD}^{z1/z3}$);
- about $0.3-0.5\sigma$ on σ_8, S_8, or n_s, from the choice of Fourier-space analysis or configuration-space analysis ($P_{\rm FKP}^{\rm LZ/CM}+\alpha_{rec}^{\rm LZ/CM}$ vs. $\xi^{\rm LZ/CM}+\alpha_{rec}^{\rm LZ/CM}$);
- $\lesssim 0.3\sigma$ on all cosmological parameters from the choice of the redshift bin split in either LOWZ and CMASS or z_1 and z_3 ($P_{\rm FKP}^{\rm LZ/CM}$ vs. $P_{\rm FKP}^{z1/z3}$), as defined in Tab. 5.4.

Besides the effects mentioned here, there are subleading ones affecting those comparisons that we have discussed above: the addition of the integral constraints in the analysis of FKP measurements or subtracting the shot noise in the power spectrum measurements lead to shifts of at most $\lesssim 0.2\sigma$. We now turn to the comparisons of reconstructed BAO parameters combined with the full-shape analysis.

5.4 Comparison of Reconstructed BAO

5.4.1 Inconsistency between post-reconstructed measurements

We here compare the two BOSS post-reconstructed measurements through the BAO parameters extracted with the same methods, as defined in previous section and in Tab. 5.4: $\alpha_{rec}^{\rm LZ/CM}$ vs. $\alpha_{rec}^{z1/z3}$. The results of this comparison are shown in Fig. 5.6. We find that adding the reconstructed signals $\alpha_{rec}^{\rm LZ/CM}$ and $\alpha_{rec}^{z1/z3}$ to $P_{\rm FKP}^{\rm LZ/CM}$ and $P_{\rm FKP}^{z1/z3}$, respectively, lead to substantial differences on the mean of h, at about 0.9σ. This is to be contrasted with the consistency on h that was better than $< 0.1\sigma$ between $P_{\rm FKP}^{\rm LZ/CM}$ and $P_{\rm FKP}^{z1/z3}$ before the addition of the reconstructed BAO parameters. Indeed, the addition of the two reconstructed BAO measurements to the full-shape analysis shift h in the opposite directions (see Fig. 5.6). Given that the reconstruction algorithm used for both reconstructed measurements is essentially the same, this is an unexpected result. Exploring the reconstruction algorithm is beyond the scope

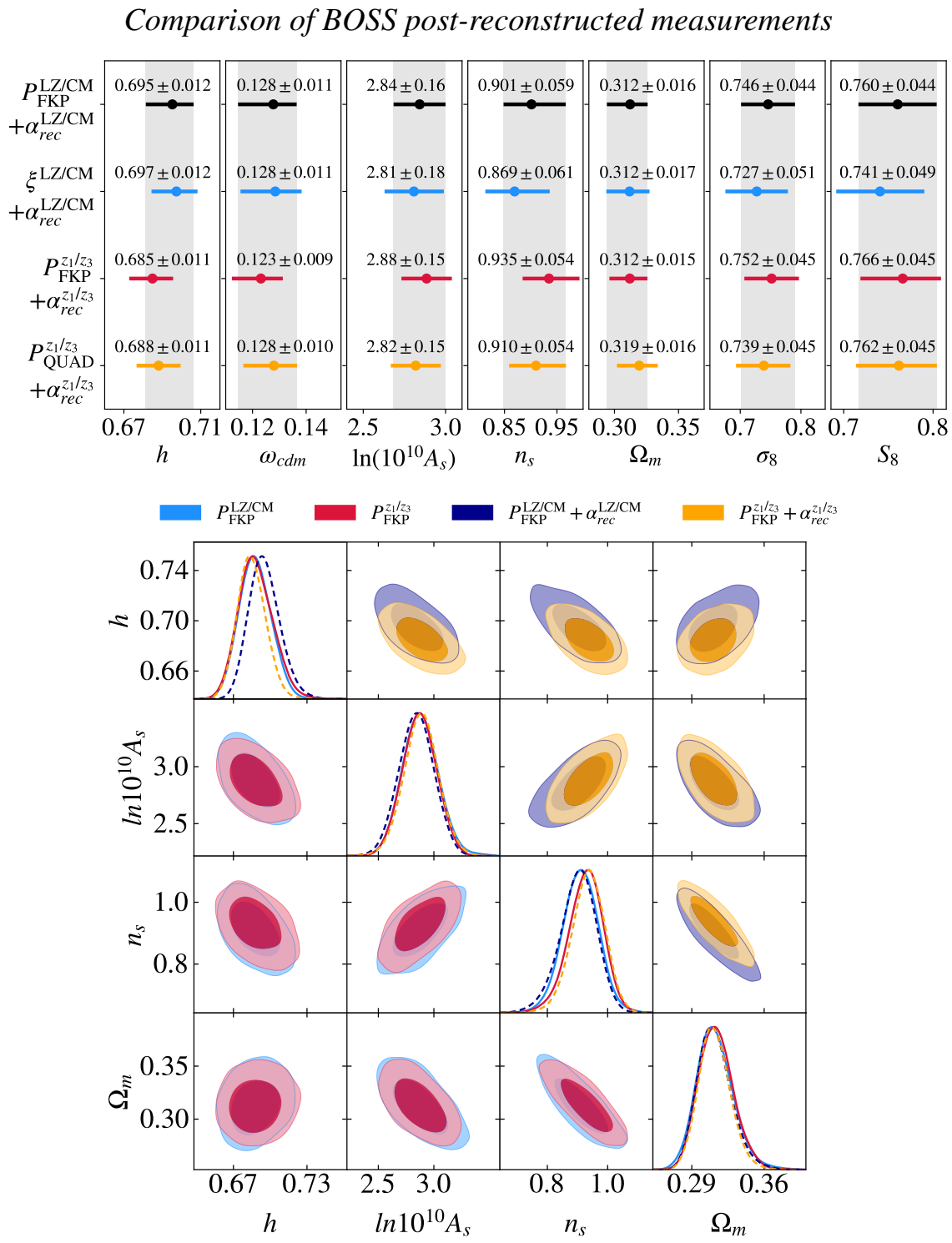

Figure 5.6: *Upper panel:* same as the 1D posterior distributions of Fig. 5.5 but combined with various post-reconstructed BAO parameters: $\alpha_{rec}^{\rm LZ/CM}$, $\alpha_{rec}^{z_1/z_3}$. The gray bands are centered on the results obtained with $P_{\rm FKP}^{\rm LZ/CM}+\alpha_{rec}^{\rm LZ/CM}$. *Lower panel:* 2D posteriors from the full-shape analyses of BOSS power spectrum with two choices of redshift splits: $P_{\rm FKP}^{\rm LZ/CM}$, $P_{\rm FKP}^{z_1/z_3}$. We also show their combinations with $\alpha_{rec}^{\rm LZ/CM}$ and $\alpha_{rec}^{z_1/z_3}$, respectively. Details on the naming convention and relevant information are summarized in Tab. 5.4. While the two choices of redshift split lead to consistent results at $\lesssim 0.1\sigma$ on h, the addition of the BAO parameters, that extracted from the two available BOSS post-reconstructed measurements in Fourier space, lead to differences on h of $\sim 0.9\sigma$.

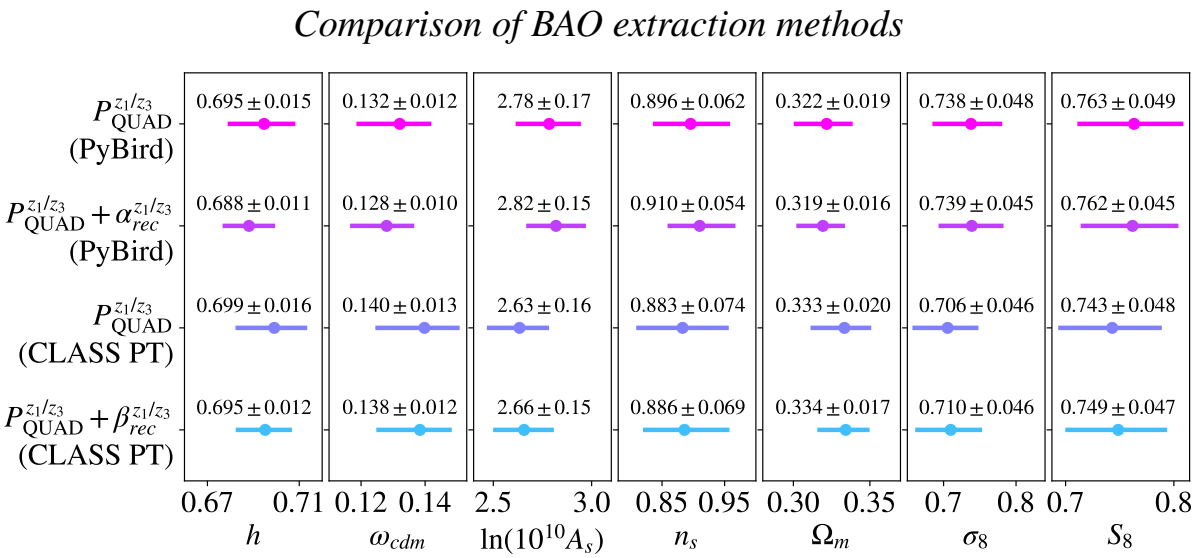

Figure 5.7: Comparison of ΛCDM results (1D credible intervals) from BOSS full-shape analyses using the `PyBird` likelihood or the `CLASS-PT` likelihood. The differences between the two likelihoods consist in the choices of prior on the EFT parameters, the number of multipoles analyzed and the value of $k_{\rm max}$. For the same pre-reconstructed measurements $P^{z_1/z_3}_{\rm QUAD}$, although not analyzed with the same likelihood, one can see the differences from different BAO parameters, α^{z_1/z_3}_{rec} and β^{z_1/z_3}_{rec}, due to different extraction methods, since they are from the same post-reconstructed measurements. Relevant information regarding the measurements and their notations are summarized in Tab. 5.4.

of this work, and we leave a careful scrutiny of the reconstructed measurements to future work. We observe that full-shape analyses combining the pre-reconstructed power spectrum either with reconstructed signal from configuration space [103], or with the bispectrum analyzed at one loop up to $k_{\rm max} \sim 0.23h\,{\rm Mpc}^{-1}$ (which comprises most of the additional information brought by the reconstructed signal) [95], find shifts in h in the same direction (and by a similar amount) as what we obtain when we add $\alpha^{\rm LZ/CM}_{rec}$, rather than α^{z_1/z_3}_{rec}. Although the comparisons are far from straightforward given differences in the analysis setups, we take them as mild evidence that $\alpha^{\rm LZ/CM}_{rec}$ is more consistent than α^{z_1/z_3}_{rec} with what one should expect from the addition of the information from the reconstructed measurements. We nevertheless warn the reader that further studies are required to clarify this discrepancy. We note that the addition of the reconstructed BAO parameters also has an impact on n_s, since we have a shift of 0.6σ between $P^{\rm LZ/CM}_{\rm FKP}+\alpha^{\rm LZ/CM}_{rec}$ and $P^{z_1/z_3}_{\rm FKP}+\alpha^{z_1/z_3}_{rec}$, while the other parameters does not shift appreciably.

5.4.2 Comparison of extraction methods of reconstructed BAO parameters

After comparing the two available BOSS post-reconstructed measurements using the same BAO extraction methods, $\alpha^{\rm LZ/CM}_{rec}$ and α^{z_1/z_3}_{rec}, we now compare two sets of BAO parameters from the same post-reconstructed measurements, α^{z_1/z_3}_{rec} and β^{z_1/z_3}_{rec}, but extracted from two different methods as defined in the following. The reconstructed BAO parameters are not

obtained using the same methodology: in the PyBird likelihood, the BAO parameters ($\alpha_{rec}^{\rm LZ/CM}$ or $\alpha_{rec}^{z_1/z_3}$) are obtained following the standard method as described in, *e.g.*, Ref. [51], while in the CLASS-PT likelihood, the BAO parameters ($\beta_{rec}^{z_1/z_3}$) are obtained following the method put forward in Ref. [102]. The two methods are similar in spirit as they both focus on extracting the information from the reconstructed signal using only knowledge of "the position of BAO peak" through the Alcock-Paszinki parameters, as the broadband shape (and the BAO amplitude with respect to the broadband) is marginalized over. However, they differ slightly in their design. In particular we note that in the CLASS-PT likelihood, some nuisance parameters such as the shot noise are not included in the model to fit the reconstructed power spectrum. Instead, an approximation for the theory error at high k (where the shot noise contribution starts to be significant) is added to the data covariance to account for, among others, the shot noise contribution, which should be equivalent to the procedure in used by PyBird likelihood. [10]

In Fig. 5.7, we can see the differences on the cosmological parameters arising from the two extraction methods. We compare $\alpha_{rec}^{z_1/z_3}$ with $\beta_{rec}^{z_1/z_3}$, that we remind that are from the same post-reconstructed measurements, combined with the same pre-reconstructed measurements $P_{\rm QUAD}^{z_1/z_3}$, analyzed respectively with the PyBird or the CLASS-PT likelihood. Here are the takeaways:

- The addition of $\beta_{rec}^{z_1/z_3}$ to $P_{\rm QUAD}^{z_1/z_3}$ in the CLASS-PT likelihood shifts h in the same direction as the addition of $\alpha_{rec}^{z_1/z_3}$ to $P_{\rm QUAD}^{z_1/z_3}$ in the PyBird likelihood, of about $1/3\cdot\sigma$ and $1/2\cdot\sigma$, respectively. This is expected, as the BAO parameters of $\beta_{rec}^{z_1/z_3}$ and $\alpha_{rec}^{z_1/z_3}$ are based on the same post-reconstructed measurements obtained in Ref. [51] as seen in Tab. 5.4.

- The error bar reduction from the addition of the BAO parameters are quite comparable between the PyBird likelihood and the CLASS-PT likelihood. Indeed, taking the same pre-reconstructed measurements, $P_{\rm QUAD}^{z_1/z_3}$, we find that the errors on h, $\ln(10^{10}A_s)$, n_s, Ω_m, and σ_8 are reduced respectively by 23%, 13%, 14%, 18%, and 12% in the PyBird likelihood when adding $\alpha_{rec}^{z_1/z_3}$, while they are reduced by 22%, 3%, 7%, 16%, and 0% in the CLASS-PT likelihood when adding $\beta_{rec}^{z_1/z_3}$. Therefore, keeping in mind that $\alpha_{rec}^{z_1/z_3}$ ans $\beta_{rec}^{z_1/z_3}$ are based on the same post-reconstructed measurements, we see that differences in the methods to extract and cross-correlate the BAO parameters lead to similar error bars within $\sim 10\%$.

To conclude, given the same post-reconstructed measurements, we do not find appreciable differences between the two extraction methods of reconstructed BAO parameters.

5.5 Conclusions

The developments of the predictions for the galaxy clustering statistics from the EFTofLSS have made possible the study of BOSS data beyond the conventional analyses dedicated to extracting BAO and RSD information. The analyses available in the literature lead

[10] There is an additional difference in the methodology, however, shown to be not relevant at the level of the constraints: $\beta_{rec}^{z_1/z_3}$ are obtained in Ref. [102] by marginalizing over the damping of the BAO wiggles, while $\alpha_{rec}^{\rm LZ/CM}$ or $\alpha_{rec}^{z_1/z_3}$ are obtained following [51] using a fixed damping amplitude parameter. As shown in Ref. [102], this does not lead to significant differences in the determination of the BAO parameters and their covariances.

to differences on the reconstructed cosmological parameters that can be at the 1σ level. Given that they all come from the same BOSS data, this may be consider surprising and unsatisfactory. However, the analyses vary at a number of levels: the EFT parameters prior choices, the power spectrum estimator used for the measurements, the reconstructed BAO algorithm, the scale cut and the number of multipoles. In this chapter, we have identified the analyses choices that can impact the cosmological constraints, and quantify the shifts in the full-shape analysis of BOSS power spectrum within ΛCDM. We summarize our findings below.

In Sec. 5.1, we have looked at two choices of prior used in previous BOSS full-shape analysis, the so-called "West-coast" (WC) and "East-coast" (EC) priors, that have been implemented in the `PyBird` and `CLASSPT` pipeline, respectively. Most importantly, we have identified that the prior assigned on the EFT parameters plays a non-negligible role in the determination of the cosmological parameters, for two reasons.

- First, in the Bayesian analysis, the marginalized constraints of the cosmological parameters are subject to prior volume projection effects from the marginalization over the EFT parameters, as the resulting posteriors are non-Gaussian. We find that that prior volume projection effects shift the posterior mean from the MAP up to $\sim 1\sigma$ with the WC prior and up to $\sim 2\sigma$ with the EC prior across all cosmological parameters.

- Second, from a frequentist perspective, we have found that the prior weight shift the MAP between the two analyses at $\lesssim 1\sigma$, with the $\min \chi^2$ different at $\Delta\chi^2 \sim 9$. Once the prior range are enlarged by two, the MAP become consistent at $\lesssim 0.4\sigma$, and the $\min \chi^2$ are now comparable at $\Delta\chi^2 = 0.4$. However, at the same time, the prior volume projection effect increases by up to $\sim 33\%$ depending on the prior choice and the cosmological parameters.

- Nevertheless, we checked that when the pipelines follow the same prescription, results are in agreement at better than 0.2σ. We conclude that the results between the two analyses are consistent, up to the various level of prior volume projection effects and prior weight effect, resulting from their respective choice of basis and more-or-less informative prior for the EFT parameters.

We have then suggested several ways to mitigate the prior effects.

- First, one can simply abandon the Bayesian view and come back to the frequentist one, for which the confidence intervals are not affected by prior volume projection effects as they are derived from profile likelihoods rather than from marginalized posteriors (see chapter 6).

- Setting aside the philosophical debate between Bayesian and frequentist, we have argued that for forthcoming larger data volume, all those prior effects will eventually become less important (with respect to the error bars). In fact, the prior effects in the EFT analysis of BOSS have been realized only recently [95] because in the past, most of the validations, if not all, were performed with large-volume simulations. [11]

[11] Note one exception in Ref. [62], where a large-volume simulation is analyzed with a covariance corresponding to BOSS total volume. Here the shift to the truth, that represents a sum of the theory error + prior effect, is find to be $\lesssim 0.4\sigma$ on all cosmological parameters. This is different than the shift we find in Fig. 5.3, as in their case, there is only one sky, while in our case, we keep four skies as for the real analysis of BOSS data, with four independent sets of EFT parameters. When analyzing one-sky of synthetic data with covariance corresponding to BOSS total volume, we find $< 1/5 \cdot \sigma$.

- Additionally, for the time being with BOSS, we have shown that when combined with *Planck*, the results are less sensitive to those prior effects and the results are in good agreement.

For completeness, we have also scrutinized the impact on the cosmological constraints given various BOSS measurements. From the most significant to the least one, we have found:

- a difference of about 0.9σ on h between the two public BOSS pre-reconstructed measurements in Fourier space ($\alpha_{rec}^{\rm LZ/CM}$ vs. $\alpha_{rec}^{z_1/z_3}$). This might constitute a warning that one should not use reconstructed measurements until this is clarified (see Sec. 5.4 for more discussions);
- a difference of up to 0.6σ among all cosmological parameters between the FKP and quadratic estimators of the power spectrum ($P_{\rm FKP}^{\rm LZ/CM}$ vs. $P_{\rm QUAD}^{z_1/z_3}$);
- a difference of about $0.3-0.5\sigma$ on σ_8, S_8, and n_s, between the Fourier-space analysis and the configuration-space analysis ($P_{\rm FKP}^{\rm LZ/CM}+\alpha_{rec}^{\rm LZ/CM}$ vs. $\xi^{\rm LZ/CM}+\alpha_{rec}^{\rm LZ/CM}$);
- Finally, a difference of $\lesssim 0.3\sigma$ on all cosmological parameters between the choices of redshift bin split in either LOWZ and CMASS or z_1 and z_3 ($P_{\rm FKP}^{\rm LZ/CM}$ vs. $P_{\rm FKP}^{z_1/z_3}$).

Besides the former EFT analyses of BOSS power spectrum using the `PyBird` likelihood or `CLASSPT` likelihood, let us also mention the work of Ref. [103] using another likelihood based on yet another public code developed independently, `Velocileptors` [197, 198]. `Velocileptors` also implements predictions from a Lagrangian version of the EFTofLSS, which is equivalent, up to higher-order terms, to the Eulerian version of the EFTofLSS with IR-resummation [71, 198]. It would also be interesting to perform comparison with the `Velocileptors` likelihood with the prior choice used in the BOSS analysis of Ref. [103]. See some discussions in App. B.2, and more importantly Ref. [199] that reaches similar conclusions as our current work on the prior volume projection effects in the EFT analysis within ΛCDM but with the `Velocileptors` pipeline. Given that all analyses are equivalent in their parametrization (*i.e.*, provide equivalent sets of fitting functions), all prior choices are equally motivated as long as they encompass the physically-allowed region of the EFT. For the current level of precision of the data, the various prior choices lead to various level of prior projection volume effect, but the results, *i.e.*, MAP or multidimensional posteriors, are essentially the same.

We end the discussion with a closer look at S_8 and σ_8 in light of the BOSS full-shape analysis. At face-value, the 68%-credible interval on S_8 and σ_8 in this work are systematically lower than the value measured by *Planck* under ΛCDM, with a statistical significance of $\sim 1.4\sigma$ (2.2σ) and $\sim 1.5\sigma$ (2.5σ) respectively for the WC (EC) priors. However, we have argued that part of this (small) discrepancy is due to a downwards shift compared to the MAP due to prior volume projection effect (as already mentioned in chapter 4). These are more important for the EC prior ($\sim 2\sigma$) than the WC prior ($\sim 1.2\sigma$), and increase when doubling the widths of the EFT priors. In fact, the MAP values for S_8 and σ_8 (Tab. 5.1) measured with both priors are in good agreement with *Planck* under ΛCDM, which infers $\sigma_8 = 0.8111 \pm 0.006$ [11] (see also [95, 200]). Nevertheless, the values reconstructed from our analyses are also consistent with lower measurements of S_8 from lensing observations, see, *e.g.*, [201, 177, 79]. In fact, the analysis of BOSS data is done in the perturbative regime, *i.e.*, we restrict

the analysis at $k_{\rm max} \sim 0.2h\,{\rm Mpc}^{-1}$ where the EFTofLSS applies and in that sense, most of the cosmological information is from the large scales. In contrast, measurements of S_8 from lensing experiments rely on the modeling of small scales (way) beyond the nonlinear scales, where our EFT approach does not apply. Our reconstruction suggests that the deviation mostly occurs on scales smaller than those probed by our analysis (or at very low-$z < 0.3$), although because of large error bars, it is still compatible with a relatively low-S_8 on large scales, as hinted by the cross-correlation of DES and CMB lensing [202]. For more discussion on the scale-dependence of the S_8 tension, we refer to Refs. [178, 200].

Although the detailed comparisons we have performed in this chapter help quantifying at some level the systematic uncertainties associated with the measurements, we stress that we have not studied those related to BOSS galaxy catalog itself, which would require much more work. It will also be interesting to perform similar analysis for the bispectrum [95, 62] as well as the recent eBOSS datasets [82], that can provide interesting additional constraining power on ΛCDM and extensions.

VI

Frequentist investigation of EFTofLSS analyses of the BOSS and eBOSS data

Contents

6.1 Analysis Methods **178**
6.1.1 Profile Likelihood and Markov Chain Monte Carlo 179
6.1.2 Datasets and analysis choices 181
6.2 The EFTofLSS parametrizations **182**
6.2.1 Different parametrizations 183
6.2.2 Priors 184
6.3 Consistency of EFTofLSS from profile likelihood analyses **185**
6.3.1 EC vs. WC parametrizations and comparison to MCMC 185
6.3.2 Role of EFT "priors" in the frequentist setting 187
6.3.3 Effect of more constraining data 189
6.4 Profile likelihood results on cosmological parameters **190**
6.5 Conclusions **194**

This chapter is based on:

E. Brinch Holm, L. Herold, **T. Simon**, E. Ferreira, S. Hannestad, V. Poulin, and T. Tram, *Bayesian and frequentist investigation of prior effects in EFTofLSS analyses of full-shape BOSS and eBOSS data*, **Phys. Rev. D 108 (2023) 123514**, arXiv:2309.04468.

We have shown in chapter 5 that the parameter structure of the EFTofLSS may impact the results of Bayesian analyses through prior effects, especially when the data has weak constraining power. As a consequence, chapter 5 showed that different – yet theoretically equivalent – choices of the EFT parametrization result in discrepant Bayesian credible intervals and in point-estimate shifts sometimes on the order of 1σ, particularly affecting the amplitude of matter fluctuations, σ_8. Additionally, Ref. [187] found the priors on the EFT parameters to be informative and motivate a more comprehensive study of the effects of the parameter structure of the EFT sector. Ref. [199] argue that prior effects lead to a shift in $f\sigma_8$ in BOSS full-shape analyses based on an EFT implementation using the `Velocileptors` code [197, 198, 103], partially explaining the difference with template fitting methods. Ref. [203] find that confidence intervals based on the profile likelihood method on a modified gravity scenario are inflated with respect to the Bayesian posterior and that volume effects shift the likelihood peaks. Moreover, Refs. [204, 205] show that the use of a Jeffreys prior on the EFT parameters can mitigate biases in the standard EFT analysis.

Motivated by these previous results, in this chapter, we complement the results of the standard Bayesian analysis, as performed in chapters 4 and 5, with a profile likelihood analysis. The profile likelihood is a frequentist method based only on the maximum likelihood estimate (MLE) and, therefore, inherently reparametrization invariant and prior independent. Our goal is to understand the impact of priors on the EFT parameters on the inferred cosmological parameters and how this will change with more constraining data. In particular, we wish to answer the question, already raised in chapter 6): *does the seemingly low σ_8 value reconstructed from a Bayesian analysis of BOSS data under the EFTofLSS come from prior effects inherent to the Bayesian framework, rather than the true data likelihood?* Ultimately, our analysis demonstrates the importance of combining Bayesian and frequentist approaches for a fully nuanced inference from current and future LSS data.

This chapter is structured as follows. In Sec. 6.1, we describe the respective analysis methods employed in the Bayesian and frequentist approaches and introduce the datasets used. In Sec. 6.2, we outline the EFTofLSS approach and give a detailed description of the two predominantly employed EFT parametrizations to be scrutinized. In Sec. 6.3.1, we compare the two EFT parametrizations using the profile likelihood and contrast them to the MCMC results. In Sec. 6.3.2, we study the influence of prior effects and discuss the issue that the EFT parameters take on extreme values in the frequentist setting. In Sec. 6.3.3, we show that discrepancies between frequentist and Bayesian approaches subside with increasingly constraining data. Finally, we provide a profile likelihood analysis of the ΛCDM concordance model for the parameters σ_8, h, Ω_m, n_s and $\ln\left(10^{10}A_s\right)$ with data from the BOSS and eBOSS surveys using the EFTofLSS formalism in Sec. 6.4 and conclude in Sec. 6.5. In App. C.1, we illustrate the impact of changing the prior width on the profile likelihood of σ_8 and we discuss the values of the EFT parameters in our analysis. In Apps. C.2 and C.3 we show additional material, namely a comparison between profile results and MCMC results, and global best-fitting parameters for several datasets.

6.1 Analysis Methods

The structure of the EFT parameters and their priors may impact the constraints on cosmological parameters derived from Bayesian inference. In particular, given a fixed choice of

parametrization, we may classify the prior impact in terms of two separate effects, as was already done in chapter 5:

- The *prior weight effect*: Since the Bayesian posterior is proportional to the product of the prior and likelihood, non-flat priors will affect the posterior in a direct way when they do not align with the likelihood. This can manifest in, for example, a shift of the posterior peak or a scaling of its width.

- The *prior volume effect*: Bayesian marginalization of the full-dimensional posterior involves integrating out the nuisance dimensions. Since in addition to the value of the posterior, an integral is sensitive to the volume in these directions, large parameter regions (of possibly non-maximal posterior values) are emphasized compared to smaller regions (of possibly larger posterior values).

Importantly, the volume effect can occur even with flat priors and is, therefore, an inescapable feature of the Bayesian method. Therefore, it becomes relevant to study the extent to which one's results are affected by volume effects. Since the profile likelihood is directly inferred from the likelihood, it is inherently independent of priors [206] and is, therefore, an ideal tool for this. In Sec. 6.1.1, we briefly review the use of profile likelihoods for inference, and in Sec. 6.1.2 we describe our analysis pipeline.

6.1.1 Profile Likelihood and Markov Chain Monte Carlo

The profile likelihood is a method in frequentist statistics, maximizes the likelihood over nuisance parameters (as opposed to marginalization, which is the commonly used method in Bayesian statistics). By splitting the full parameter space Θ into two categories, θ of N parameters and ν of M (nuisance) parameters, the profile likelihood of θ is obtained by maximization over all parameters in the complementary set of (nuisance) parameters ν for fixed θ [206],

$$L(\theta) = \max_{\nu} L(\theta, \nu), \tag{6.1}$$

where $L(\theta, \nu)$ represents the full likelihood function. Since the above is a MLE in the reduced parameter space θ, the profile likelihood is invariant under reparametrizations of the reduced parameter space θ [206]. The reparametrization invariance of the profile likelihood will be particularly useful when comparing the different EFT parametrizations in Sec. 6.3.1, which is more challenging with Bayesian methods since these can depend on the particular parametrization of the model and prior choices. In addition, the profile likelihood is inherently prior independent, thus automatically avoiding prior volume effects.

Frequentist methods like the profile likelihood are commonly used in particle physics but rarely used for cosmological inference. They recently gained more interest in the context of models beyond ΛCDM, which often contain many model parameters that are not well constrained by the data [188, 207, 190, 208, 189, 209, 210, 211], and in the context of efficient marginalization [212].

To obtain parameter constraints in θ, we employ the Neyman construction, valid in the limit of a Gaussian likelihood of the data (also called the "graphical construction") [213]: from the profile likelihood $L(\theta)$, α confidence regions are given by the solution to $\Delta\chi^2(\theta) < F^{-1}(\alpha, N)$,

where F^{-1} is the inverse of the χ^2 cumulative distribution function with N degrees of freedom. For example, in the one-dimensional case $\theta = \theta$, the 68% (95%) confidence intervals correspond to the values of θ for which $\Delta\chi^2(\theta) < 0.99$ (3.84). These confidence levels are exact when the likelihood is Gaussian, or, in the asymptotic limit of a large dataset [214]. In this limit, the quantity $\Delta\chi^2(\theta) \equiv -2\log(L(\theta)/L_{\rm max})$ follows a χ^2 distribution with N degrees of freedom [206] and the graphical method corresponds to the exact Neyman construction. Since for the BOSS and eBOSS datasets Gaussian likelihoods are employed, the graphical construction is exact, whereas parts of the *Planck* likelihood are non-Gaussian [215] and we acknowledge that the graphical confidence intervals may be approximate. If the profile likelihood has a substantial overlap across a physical boundary of the parameter, an alternative Neyman construction needs to be used, also known as the Feldman-Cousins prescription [216]. However, since the parameters studied in this work are well away from their physical boundaries, the Neyman construction is sufficient.

Computing the profile likelihood amounts to optimizations in the reduced parameter space ν. Since evaluating the likelihood function $L(\theta, \nu)$ involves running the Einstein-Boltzmann solver, numerical gradients are noisy and inefficient [138]. For the optimization, we therefore use *simulated annealing* [217], a gradient-free stochastic optimization algorithm (see [218] for efficient computation of profile likelihoods using an emulator and see [219] for earlier approaches). The simulated annealing algorithm is based on chains with iteratively decreasing temperatures and step sizes, where the temperature $T > 0$ modulates the likelihood function as $L(\theta, \nu) \to L(\theta, \nu)^{1/T}$. Large temperatures smoothen the likelihood landscape, whereas small temperatures enhance peak structures. Thus, the chains are able to escape local optima while eventually being localized in a likelihood peak at low temperatures. Simulated annealing performs well against the noisy cosmological likelihood landscapes with many local optima [220], but may depend moderately on the particular temperature schedule employed. In practice, we inform the simulated annealing process with proposal covariance matrices and best-fits obtained from the corresponding MCMC analyses. Since the minimizations for each point in the profile are started from the global best-fit obtained from the MCMC, poor convergence would likely lead to an *underestimation* of the width of the confidence interval, which would not have a strong impact on the conclusions in this work as we find very large confidence intervals with the profile likelihood. We ensure convergence and combat local optima by running each optimization several times. Due to the limited accuracy of the global best-fits caused by the finite sampling of the profile, we present the best-fit points in this work as the optimum of the parabola fitted to the point of highest likelihood and its two neighboring points. Our implementation of the simulated annealing algorithm [1] interfaces the `MontePython` [137, 136] inference code with the Einstein-Boltzmann solver `CLASS` [221], [2] which models the CMB coefficients and linear matter power spectra, and with `PyBird` [59], [3] which models the full-shape of the galaxy power spectra from the EFTofLSS. It is identical to the implementation used in Refs. [210, 211].

For all MCMCs performed in this study, we use the Metropolis-Hastings algorithm from `MontePython`, and we assume our MCMC chains to be converged with the Gelman-Rubin

[1] Publicly available at: https://github.com/AarhusCosmology/montepython_public/tree/2211.01935.

[2] Publicly available at: http://class-code.net.

[3] Publicly available at: https://github.com/pierrexyz/pybird.

criterion $R-1<0.05$.

In the following, we quote frequentist confidence intervals as the MLE $\pm\ 1\sigma$ obtained via the graphical Neyman method and we quote Bayesian credible intervals as the posterior mean $\pm\ 1\sigma$ obtained from the MCMC posterior. We will employ the following metric as a measure of the discrepancy between two approximately Gaussian posteriors or likelihoods,

$$\sigma\text{-distance} \equiv \frac{|\theta_i - \theta_j|}{\sqrt{\sigma^2_{\theta,i} + \sigma^2_{\theta,j}}}, \tag{6.2}$$

where θ_i is the i'th point estimate of the parameter θ and $\sigma_{\theta,i}$ the corresponding standard deviation. The point estimates and standard deviations may be derived either from a posterior or from a profile likelihood. In the case that the two intervals are derived from the same model and the same statistical method (Bayesian or frequentist), but different datasets, the σ-distance coincides with the Gaussian tension metric employed, for example, in Ref. [183]. When the point estimates are from different statistical paradigms, we instead normalize only by the Bayesian uncertainty,

$$\sigma\text{-distance} \equiv \frac{|\theta_{\text{Bayes.}} - \theta_{\text{freq.}}|}{\sigma_{\theta,\text{Bayes.}}}, \tag{6.3}$$

which can be interpreted as the significance of the bias between mean and MLE in units of the Bayesian error bars induced by the prior effects.

6.1.2 Datasets and analysis choices

In this chapter, we perform various MCMC and profile likelihood analyses using different datasets:

- **BOSS DR12 LRG**: In our main analysis, we consider the BOSS luminous red galaxies data (LRG) [81] (see Ref. [124] for a description of the catalogues), with covariances built from the patchy mocks described in Ref. [125]. The BOSS data are divided into four sky cuts, corresponding to two galactic skies, denoted NGC and SGC, cut into to two redshift bins: LOWZ, which corresponds to the redshift range $0.2<z<0.43$ ($z_{\text{eff}}=0.32$), and CMASS, which corresponds to the redshift range $0.43<z<0.7$ ($z_{\text{eff}}=0.57$). For LOWZ we analyse the galaxy power spectrum up to $k_{\text{max}}=0.20h\,\text{Mpc}^{-1}$, while for CMASS we analyse it up to $k_{\text{max}}=0.23h\,\text{Mpc}^{-1}$. In this study, we use the EFT likelihood of the full shape of the BOSS LRG power spectrum pre-reconstructed multipoles, including the monopole and the quadrupole, measured and described in Ref. [69] and referred to as "BOSS." We also consider "BOSS+BAO," which additionally includes the cross-correlation of the pre-reconstructed measurements with post-reconstruction BAO compressed parameters obtained in Ref. [59] on the post-reconstructed power spectrum measurements of Ref. [126].

- **eBOSS DR16 QSO**: We also consider the quasars (QSO) data from the extended Baryon Oscillation Spectroscopic Survey (eBOSS) [82] (see Ref. [120] for a description of the catalogues), with covariances built from the EZmocks described in Ref. [121]. The eBOSS data are divided into two sky cuts, corresponding to two galactic skies, denoted

NGC and SGC, in the redshift range $0.8 < z < 2.2$ ($z_{\rm eff} = 1.52$). We analyse the eBOSS QSO galaxy power spectrum up to $k_{\rm max} = 0.24h\,{\rm Mpc}^{-1}$. In this study, we use the EFT likelihood of the full shape of the eBOSS QSO power spectrum pre-reconstructed multipoles from chapter 4 and the measurements of Ref. [122], including the monopole and the quadrupole, which is referred to as "eBOSS".

- **BBN likelihood**: As in chapter 5, unless specified otherwise, we impose a Gaussian likelihood on $\omega_b \sim \mathcal{N}(0.02268, 0.00038)$, where $\mathcal{N}(\bar{x}, \sigma_x)$ denotes a Gaussian centered on $\bar{x}$ with standard deviation σ_x, coming from BBN experiments [180]. This likelihood is based on the theoretical prediction of [181], the experimental Helium fraction of [182] and the experimental Deuterium fraction of [12].

- ***Planck***: Finally, we compare the BOSS and eBOSS results with the low-l CMB TT, EE, and the high-l TT, TE, EE data, as well as the gravitational lensing potential reconstruction from *Planck* 2018 [11], referred to as "*Planck*."

For the BOSS and eBOSS analyses, we vary five cosmological parameters:

$$\{\omega_{\rm cdm},\, \omega_b,\, h,\, \ln\left(10^{10}A_s\right),\, n_s\}, \tag{6.4}$$

corresponding to the physical cold dark matter and baryon energy density, the reduced Hubble constant, the log-amplitude of the primordial fluctuations and the scalar spectral index, respectively. [4] For the MCMC, we assume large flat priors, and for the profile likelihood, we scan a parameter range that covers at least the 95% confidence interval. For the LSS data, unless specified otherwise, we always include the BBN likelihood mentioned above. To facilitate comparison with previous studies, we present our cosmological results on $\{\sigma_8,\, h,\, \Omega_m,\, n_s,\, \ln\left(10^{10}A_s\right)\}$, corresponding respectively to the clustering amplitude, the reduced Hubble constant, the fractional matter abundance as well as the scalar spectral index and amplitude of primordial fluctuations from (6.4). Finally, for all analyses performed we use the *Planck* convention for the neutrinos, namely we take two massless and one massive species with $m_\nu = 0.06$ eV [11].

6.2 The EFTofLSS parametrizations

To model the full shape of the BOSS and eBOSS power spectra, we use the EFTofLSS theoretical prediction at one-loop order [see Eq. (3.180)]. In the literature, several prescriptions have been proposed for the EFT parameters. In line with Ref. [98] and chapter 5, we consider the two most commonly used parametrizations, namely the "West coast" (WC) parametrization, the one used in the `PyBird` [59] likelihood, and the "East coast" (EC) parametrization, the one used in the `CLASS-PT` [61, 62] likelihood. [5] In this section, we describe these two EFT parametrizations and the associated priors. Note that we have already described these two parametrizations in the previous chapter (see Sec. 5.1), but we recall them here for the sake of clarity and given that there are some minor differences between the two analyses.

[4] For runs that include *Planck* data, we also vary $\tau_{\rm reio}$, the re-ionization optical depth, within a large flat prior.

[5] Let us note that there exists another EFT likelihood implemented in the public code `Velocileptors` [197, 198, 103], with different prior choices on the EFT parameters.

6.2.1 Different parametrizations

WC parametrization

In Eq. (3.180), we expressed the power spectrum in the framework of the WC parametrization using 10 EFT terms: 4 bias parameters (b_i, with $i = [1,4]$), 3 counterterms ($c_{\rm ct}$, $c_{r,1}$ and $c_{r,2}$), and 3 stochastic terms ($c_{\varepsilon,0}$, $c_\varepsilon^{\rm mono}$ and $c_\varepsilon^{\rm quad}$). In this study, we set to zero [58] the parameters $c_{r,2}$ (degenerated with $c_{r,1}$, as we do not include the hexadecapole), implying that we end up with 9 EFT parameters for each sky cut of the BOSS LRG and eBOSS QSO data. In the `PyBird` likelihood, instead of using b_2 and b_4, we use linear combinations of these parameters: $c_2 = (b_2 + b_4)/\sqrt{2}$ and $c_4 = (b_2 - b_4)/\sqrt{2}$. Given that b_2 and b_4 are almost completely anti-correlated (at $\sim 99\%$ according to Ref. [58]), the standard procedure is to set $c_4 = 0$. In addition, $c_\varepsilon^{\rm mono}$ is also set to zero in the `PyBird` baseline analysis since the functions that are multiplied by this parameter were found to be small compared to the signal-to-noise ratio associated with the BOSS volume [222, 58]. In this study, we include c_4 and $c_\varepsilon^{\rm mono}$ as free parameters in our analysis when comparing the WC parametrization with the EC parametrization in Sec. 6.3.1, which ensures mathematical equivalence between the EC and WC parametrizations. On the other hand, for our cosmological results (where we only use the WC parametrization) we adopt the standard `PyBird` convention and set $c_4 = c_\varepsilon^{\rm mono} = 0$ to facilitate easier comparison with previous works. In Sec. 6.3.1, we find that fixing or freeing c_4 and $c_\varepsilon^{\rm mono}$ changes the frequentist confidence intervals for σ_8, indicating that the effect of these two EFT parameters is not negligible.

Note that we treat these nuisance parameters as independent across each of the four sky cuts, giving a total of 28 EFT nuisance parameters in our standard BOSS analysis (and 14 for the eBOSS analysis) when fixing $c_4 = c_\varepsilon^{\rm mono} = 0$.

Within the WC parametrization, we set $k_{\rm M} = 0.7h\,{\rm Mpc}^{-1}$, $k_{\rm R} = 0.35h\,{\rm Mpc}^{-1}$ and $\bar{n}_g = 4\cdot 10^{-4}({\rm Mpc}/h)^3$ for the BOSS LRG data [139], and $k_{\rm M} = 0.7h\,{\rm Mpc}^{-1}$, $k_{\rm R} = 0.25h\,{\rm Mpc}^{-1}$ and $\bar{n}_g = 2\cdot 10^{-5}({\rm Mpc}/h)^3$ for the eBOSS QSO data (see chapter 4) in Eq. (3.180).

EC parametrization

We now turn to the EC parametrization which is used by the `CLASS-PT` likelihood [61]. In the following, we list the differences between the two parametrizations, and comment on how to switch from one to the other:

- **Bias parameters**: the EC parametrization uses the $\{\tilde{b}_1, \tilde{b}_2, b_{\mathscr{G}_2}, b_{\Gamma_3}\}$ basis [60], which is related to the previous basis $\{b_1, b_2, b_3, b_4\}$ in the following way [63]:

$$\begin{aligned} b_1 &= \tilde{b}_1\,, \\ b_2 &= \tilde{b}_1 + \frac{7}{2} b_{\mathscr{G}_2}\,, \\ b_3 &= \tilde{b}_1 + 15 b_{\mathscr{G}_2} + 6 b_{\Gamma_3}\,, \\ b_4 &= \frac{1}{2}\tilde{b}_2 - \frac{7}{2} b_{\mathscr{G}_2}\,. \end{aligned} \tag{6.5}$$

  These two bases are equivalent and describe the one-loop contribution.

	WC Priors		EC Priors	
Parameter type	Parameter	MCMC prior	Parameter	MCMC prior
Bias	b_1	flat $[0,4]$	$\tilde{b}_1$	flat $[0,4]$
	c_2	flat $[-4,4]$	$\tilde{b}_2$	$\mathcal{N}(0,1)$
	c_4 $(*)$	flat $[-4,4]$	$b_{\mathscr{G}_2}$	$\mathcal{N}(0,1)$
	b_3	$\mathcal{N}(0,2)$	b_{Γ_3}	$\mathcal{N}(\frac{23}{42}(b_1-1),1)$
Counterterms	c_{ct}	$\mathcal{N}(0,2)$	$c_0/[\mathrm{Mpc}/h]^2$	$\mathcal{N}(0,30)$
	$c_{r,1}$	$\mathcal{N}(0,2)$	$c_2/[\mathrm{Mpc}/h]^2$	$\mathcal{N}(30,30)$
Stochastic	$c_{\varepsilon,0}$	$\mathcal{N}(0,2)$	$c_{\varepsilon,0}$	$\mathcal{N}(0,2)$
	$c_\varepsilon^{\mathrm{mono}}$ $(*)$	$\mathcal{N}(0,2)$	$c_\varepsilon^{\mathrm{mono}}$	$\mathcal{N}(0,2)$
	$c_\varepsilon^{\mathrm{quad}}$	$\mathcal{N}(0,2)$	$c_\varepsilon^{\mathrm{quad}}$	$\mathcal{N}(0,2)$

Table 6.1: Standard priors on the EFT parameters in the WC and EC parametrizations used for MCMC analyses in this chapter. In the WC parametrization, b_1 and c_2 vary within flat priors, whereas in the EC parametrization, $\tilde{b}_1$ varies within a flat prior, $\tilde{b}_2$ and $b_{\mathscr{G}_2}$ vary within Gaussian priors, while Gaussian priors are imposed on the other parameters before analytically marginalizing them. In the profile likelihood analyses, we mimic the case without priors by multiplying all priors by a factor 100. The two parameters with $(*)$ are set to 0 for our cosmological results, but we include them for the comparison with the EC parametrization in Sec. 6.3.1 to ensure perfect equivalence between the two parametrizations. $\mathcal{N}(\bar{x},\sigma_x)$ corresponds to a Gaussian prior on the parameter x with a mean value of $\bar{x}$ and a standard deviation of σ_x. We emphasize that we treat these parameters as an independent set in each sky cut.

- **Counterterms**: in the EC parametrization, the definition of the counterterms $\{c_0, c_2, c_4\}$ changes slightly with respect to the WC parametrization $\{c_{ct}, c_{r,1}, c_{r,2}\}$: k_{M} and k_{R} are now absorbed in the counterterm coefficients, such that $c_0 \propto c_{ct}/k_{\mathrm{M}}^2$, $c_2 \propto c_{r,1}/k_{\mathrm{R}}^2$ and $c_4 \propto c_{r,2}/k_{\mathrm{R}}^2$. Note that in the EC parametrization, these counterterms are not unitless. In this analysis, we fix $c_4 = 0$ as we do not include the hexadecapole.

- **Stochastic terms**: we use the same definition for the stochastic parameters as for the WC parametrization. Further, the EC parametrization uses $k_{\mathrm{M}} = 0.45h\,\mathrm{Mpc}^{-1}$ and $\bar{n} \simeq 3\cdot 10^{-4}(\mathrm{Mpc}\,h^{-1})^3$.

Note that the EC baseline parametrization includes a next-to-next leading order parameter, $\tilde{c}$, in front of a term in $\sim k^4 P_{11}(k)$. In order to be consistent with the WC parametrization, we do not include this term in this analysis, which implies that we end up with 9 EFT parameters that are equivalent to the WC ones.

In this chapter, in line with chapter 5, the results of the EC parametrization are obtained with `PyBird`, which supports both the EC and WC parametrizations. This facilitates exploration of the differences in the inferred cosmological parameters introduced by the priors and parametrizations of the EFT parameters without the need to take into account differences in data and codes, namely the different implementations in `CLASS-PT` and `PyBird` (we invite the interested reader to refer to chapter 5 for such a comparison).

6.2.2 Priors

In the left half of Tab. 6.1, we summarize the MCMC standard priors used for the 9 parameters in the `PyBird` code. In general, given the perturbative nature of the theory, the

one-loop contribution should be smaller than the tree-level contribution. The latter is given by the Kaiser formula, which depends on the linear bias b_1, implying that the other EFT parameters should be in $\sim \mathcal{O}(b_1)$. In the standard WC analysis, *i.e.*, $c_4 = c_\varepsilon^{\rm mono} = 0$, the parameters b_1 and c_2 vary within flat priors, while the other EFT parameters, *i.e.*, those which enter linearly into Eq. (3.180), are analytically marginalized with Gaussian priors following the procedure of App. C of Ref. [59].

In the right half of Tab. 6.1, we summarize the MCMC standard priors used for the 9 parameters in the `CLASS-PT` likelihood. The main difference to the WC priors is that the EC priors are mainly based on simulations [185]. In the standard EC analysis, $\tilde{b}_1$ varies within a flat prior, and $\tilde{b}_2$ and $b_{\mathcal{G}_2}$ vary within Gaussian priors, while the other EFT parameters are analytically marginalized within Gaussian priors. [6]

For the profile likelihood analysis, in theory, we do not need to include priors. However, for practical reasons related to the implementation of the EFT likelihood, we mimic the case without priors by multiplying the bounds of the flat priors and the standard deviation of the Gaussian priors in Tab. 6.1 by 100. In App. C.1 we check that this leads to an effectively flat prior. Lastly, we refrain from applying the analytical marginalization from appendix C of Ref. [58], commonly used in the standard analysis. Instead, we use the analytical approximation (without marginalization) from the same reference to estimate, at each point in the optimizations, the best-fitting values of the EFT parameters that have Gaussian priors in the standard configuration, having checked explicitly that this approximation works to good precision even with flat priors.

6.3 Consistency of EFTofLSS from profile likelihood analyses

In this section, we compare the two EFTofLSS parametrizations introduced in Sec. 6.2.1, contrast them to the standard MCMC results, explore the impact of the Bayesian priors, and illustrate explicitly the effect of more constraining data. We take the example of the amplitude of matter clustering, [7] σ_8, which was found to be particularly affected by prior effects (see Ref. [187] and chapter 5).

6.3.1 EC vs. WC parametrizations and comparison to MCMC

In Fig. 6.1, we compare the one-dimensional marginalized MCMC posteriors $P(\sigma_8)$ to the profile likelihoods $L(\sigma_8)$, which are normalized by their individual MLEs. We use BOSS full-shape data combined with reconstructed BAO data based on the WC (blue) and EC (orange) parametrizations, respectively. We find that the Bayesian MCMC posteriors differ from the frequentist profile likelihoods in both WC and EC parametrizations, respectively, indicating that priors and/or marginalization have an impact on the constraints on σ_8 in the Bayesian analysis, as was already pointed out in chapter 5.

[6] Note that alternative renormalization approaches can help to inform well-motivated priors from theory, see *e.g.* [223].

[7] Note that the definition of σ_8, which is in units of Mpc/h, depends also on the background cosmology and, therefore, alternative measures of the amplitude of matter fluctuations have been proposed [224, 112, 115, 225].

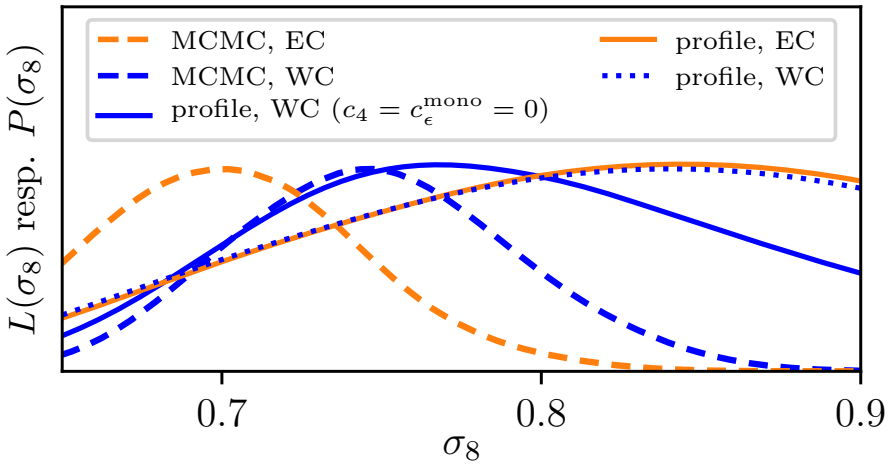

Figure 6.1: Marginalized MCMC posteriors (dashed) and profile likelihoods (solid) of σ_8 within the WC (blue) and EC parametrizations (orange), for BOSS+BAO data. The two statistical approaches and two parametrizations yield different intervals for σ_8. If c_4 and $c_\varepsilon^{\rm mono}$ are allowed to vary in the WC parametrization, the MCMC posteriors do not agree (dashed lines), while the WC-profile likelihood (blue dotted) agrees with the EC-profile likelihood (orange solid), confirming that the two mathematically equivalent parametrizations lead to the same likelihood. In the remainder of this chapter, we adopt the WC-standard convention ($c_4 = c_\varepsilon^{\rm mono} = 0$, blue solid).

In the WC parametrization, the standard configuration includes setting $c_4 = c_\varepsilon^{\rm mono} = 0$. Mathematically, the WC parametrization is only equivalent to the EC parametrization if c_4 and $c_\varepsilon^{\rm mono}$ are taken as free parameters (see Sec. 6.2.1). However, even if c_4 and $c_\varepsilon^{\rm mono}$ are free to vary, the MCMC posteriors in the two parametrizations (dashed lines), using the recommended standard priors in Tab. 6.1, do *not* yield the same credible interval:

$$\begin{aligned} \sigma_8 &= 0.748^{+0.043}_{-0.048} \quad \text{(MCMC, WC)}, \\ \sigma_8 &= 0.700 \pm 0.044 \quad \text{(MCMC, EC)}. \end{aligned} \tag{6.6}$$

Chapter 5 showed that this difference, which corresponds to a σ-distance of $0.7\,\sigma$ (as defined in Eq. 6.2), can be attributed to the different prior configurations in the WC and EC parametrizations (and not to differences in the implementation of the codes).

The profile likelihoods, on the other hand, do not depend on priors, since they are constructed solely from the MLE, and are reparametrization invariant. Therefore, two profile likelihoods from the same dataset will agree if the underlying models are equivalent, *i.e.*, if the range of their possible predictions coincide. We explicitly confirm that if c_4 and $c_\varepsilon^{\rm mono}$ are free to vary, the profile likelihood in the WC parametrization (blue dotted) agrees with the profile likelihood in the EC parametrization (orange solid) up to numerical accuracy:

$$\begin{aligned} \sigma_8 &= 0.850 \pm 0.119 \quad \text{(profile, WC)}, \\ \sigma_8 &= 0.850 \pm 0.117 \quad \text{(profile, EC)}. \end{aligned} \tag{6.7}$$

Note that in Fig. 6.1, we show the individually normalized profiles, but we checked that the absolute values of the likelihood at each point are also approximately equal with maximum

differences of $\Delta\chi^2 < 0.2$, which can be attributed to uncertainties in the optimization. This consistency check at the example of σ_8 confirms the mathematical equivalence of the WC and EC parametrizations.

Since the recommended standard configuration in the WC parametrization includes setting $c_4 = c_\varepsilon^{\rm mono} = 0$, we use this as the baseline setting for both Bayesian and frequentist analyses in the remainder of this chapter to facilitate comparison with previous work. The profile likelihood in the baseline configuration (blue solid line in Fig. 6.1, $c_4 = c_\varepsilon^{\rm mono} = 0$) yields:

$$\sigma_8 = 0.7699 \pm 0.0851 \quad \text{(profile, WC-base)}, \tag{6.8}$$

which differs from the profile likelihood with free c_4, $c_\varepsilon^{\rm mono}$ in the WC parametrization (blue dotted) by $0.6\,\sigma$. Fixing c_4 and $c_\varepsilon^{\rm mono}$ also leads to a reduction of the width of the frequentist confidence interval by 30%. This indicates that c_4 and $c_\varepsilon^{\rm mono}$ have an impact on the inference for σ_8, which cannot be neglected for the profile likelihood analysis. Explicitly checking the best-fit values of these two EFT parameters close to the global MLE, *i.e.*, the minimum of the profile likelihood, reveals that these parameters take on non-zero values as large as $c_4 \approx 57$ and $c_\varepsilon^{\rm mono} \approx 38$ (depending on the particular sky cut), pointing to an important role played by these two parameters and motivating closer inspection of the impact of analysis choices regarding the EFT parameters, which we present in the next section.

6.3.2 Role of EFT "priors" in the frequentist setting

It is instructive to look at the values attained by the EFT parameters in the frequentist framework, which requires varying all parameters in very large flat ranges. Let us recall that the EFT parameters in the WC parametrization should be of order unity in order to conserve the perturbative nature of the EFTofLSS [139]. Yet, we find that they take on extreme values at most points in the profile. For example, Fig. C.2 in App. C.1 shows the values of the EFT parameters at each point in the σ_8 profile with the baseline configuration (WC, $c_4 = c_\varepsilon^{\rm mono} = 0$), which finds values like $b_3 \approx 26$ and $c_{\rm ct} \approx 23$. Similarly large values appear in the σ_8 profile using the EC configuration, where we find as large values as $b_2 \approx 53$ and $b_{\mathcal{G}_3} \approx 38$. This indicates that the profile likelihood includes parts of the EFT parameter space in the analysis in which the EFT prediction is no longer valid. In the Bayesian analysis this issue is addressed by imposing narrow Gaussian priors on the EFT parameters (see Tab. 6.1). However, as we will now show, imposing a specific (subjective) prior has a direct impact on the inferred uncertainty in σ_8.

Indeed, the intervals from the profile likelihoods in Fig. 6.1 are broader than the intervals from the MCMC posteriors by factors of 2.6 to 2.7 (for c_4, $c_\varepsilon^{\rm mono}$ free). To explore whether this significant loss in constraining power can be explained by the information content of the priors in the Bayesian analysis, we construct a profile likelihood subject to the same "priors" as the Bayesian analysis: If the non-flat Bayesian priors were well-founded, they could in principle be promoted to likelihoods, be interpreted as genuine data, and thus used in the profile likelihood construction.

In Fig. 6.2, we show the impact of including Gaussian likelihoods on the EFT parameters, which correspond to the standard priors in the WC (top, black solid line, with free c_4, $c_\varepsilon^{\rm mono}$) and EC parametrization (bottom, red solid line), as quoted in Tab. 6.1. Including the Gaussian

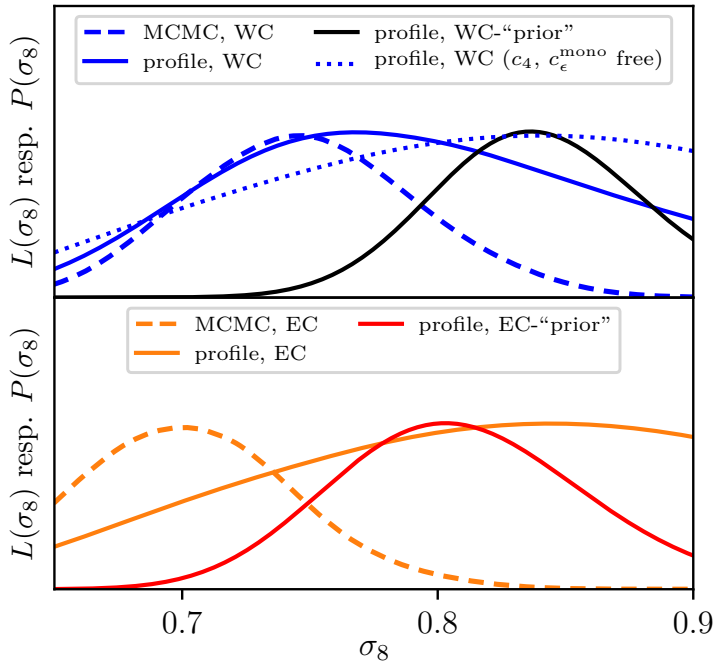

Figure 6.2: Same as Fig. 6.1 but including profile likelihoods with Gaussian data likelihoods on the EFT parameters, which correspond to the standard WC (top, black line) and EC priors (bottom, red line). The Gaussian likelihoods lead to a reduction of the width of the profiles almost to the level of the MCMC posterior and to small shifts of the MLE. However, the posterior and profile do still not overlap, which can be explained by prior volume effects in the Bayesian inference.

data likelihoods gives the following frequentist confidence intervals:

$$\begin{aligned} \sigma_8 &= 0.817 \pm 0.049 \quad \text{(profile, WC-"priors")}, \\ \sigma_8 &= 0.783 \pm 0.060 \quad \text{(profile, EC-"priors")}. \end{aligned} \tag{6.9}$$

We observe a strong increase in constraining power, reducing the width of the frequentist intervals almost to the level of the Bayesian intervals, indicating that the priors on the EFT parameters are informative. We also observe a slight shift in the global MLE toward the mean of the posterior as a result of including the Gaussian likelihoods on the EFT parameters. However, the shift thus introduced is not enough to reconcile the frequentist and Bayesian results; we observe a σ-distance of about $1\,\sigma$ for both the WC and EC parametrizations. This is an indication that there is not only a prior *weight* effect, which is a direct result of the multiplication of the prior, but also a prior *volume* effect, which is a result of the marginalization (see Sec. 6.1) of some of the model parameters. This is in agreement with Ref. [199], which finds similar results for $f\sigma_8$ using a profile likelihood analysis based on `Velocileptors` [197, 198, 103] (see *e.g.* their Fig. 3). Moreover, Ref. [204] find that the posteriors of several EFT parameters, *e.g.*, c_4, $c_\epsilon^{\rm mono}$, b_3, $c_{\rm ct}$ among others, are dominated by the prior information (see their Fig. 8), reinforcing our conclusions that the priors on the EFT parameters are informative. In App. C.1, we go one step further and illustrate the impact of changing the prior width on the profile likelihood of σ_8.

We conclude this section with the observation that both statistical approaches come with disadvantages in the context of BOSS+BAO data. While the results of the Bayesian analysis

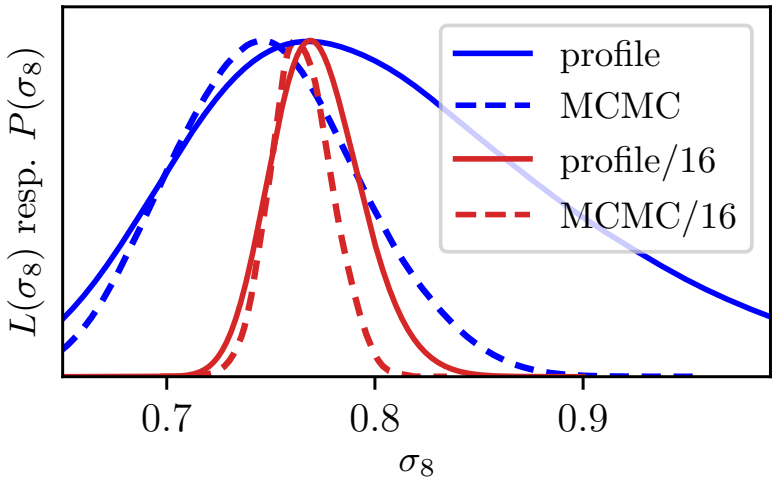

Figure 6.3: Profile likelihoods (solid) and marginalized MCMC posteriors (dashed) of σ_8 in the WC parametrization under BOSS+BAO data (blue) and the same data but with a data covariance divided by 16 (red). This illustrates how more constraining power reduces the difference between the Bayesian and frequentist approaches.

depend on informative (subjective) priors and are influenced by volume effects, the frequentist analysis takes into account parts of the EFT parameter space in which the theory is no longer valid, which reflects a significant loss of constraining power. As a way forward, we explore the impact of using more constraining data than the BOSS+BAO data in the next section.

6.3.3 Effect of more constraining data

In the asymptotic limit of infinite data, the likelihood will dominate the Bayesian prior, and prior effects will vanish accordingly [206]. Consequently, Bayesian and frequentist constraints will converge to the same answer as the model is better constrained by data.

To illustrate this point, we rescaled the BOSS covariance matrix by a factor 16, simulating a prospective situation with less uncertainties or, equivalently, a larger data volume, roughly corresponding to that of future galaxy surveys such as DESI [171] or Euclid [172]. In Fig. 6.3, we compare the constraints on σ_8 from the rescaled data covariance to those obtained from the unscaled data covariance using both MCMC and profile likelihoods, normalized to their MLE. Note that from now on, we show only results in the WC parametrization, using the default configuration $c_4 = c_\varepsilon^{\rm mono} = 0$. The constraints on σ_8 as well as the σ-distances, as defined in Eq. (6.3), are given in Table 6.2.

With the reduced data covariance, the profile and posterior are narrower and roughly centered around the same value of σ_8. When reducing the data covariance, the posterior mean value obtained from the MCMC moves closer to the MLE (*i.e.*, the maximum of the profile likelihood), while the MLE is unchanged since the case with reduced data covariance is based on the same power-spectra data. Table 6.2 shows that the consistency improves from 0.49σ to 0.33σ when we reduce the data covariance.

	BOSS + BAO	BOSS/16 + BAO
MCMC (mean $\pm 1\sigma$)	0.748 ± 0.045	0.765 ± 0.015
profile (bf. $\pm 1\sigma$)	0.770 ± 0.085	0.770 ± 0.018
σ-distance	0.49σ	0.33σ

Table 6.2: Constraints on σ_8 from the marginalized MCMC posteriors and profile likelihoods of Fig. 6.3. The last row gives the σ-distances between the MCMC/profile constraints.

This improved consistency between the best-fit and the posterior mean of the MCMC shows that the prior influence decreases as the data volume increases, as already pointed out in chapter 5. Thus, discrepancies between Bayesian and frequentist methods can be seen as due to a lack of data, which will improve as more data is obtained in the future. Furthermore, one may hope that more data will aid in constraining the EFT parameters helping to avoid extreme values at which the EFT is no longer valid, though this is not guaranteed. Hence, we can look to future galaxy surveys to improve the situation for EFTofLSS analyses using either statistical method.

6.4 Profile likelihood results on cosmological parameters

In this section, we present profile likelihood results from the EFTofLSS applied to BOSS, eBOSS and *Planck* data for five selected ΛCDM parameters, σ_8, h, Ω_m, n_s, and A_s, and compare to the credible intervals from the Bayesian MCMC. While lacking more constraining data, comparison of frequentist and Bayesian methods can help to gain a more nuanced view of the data. For both frequentist and Bayesian setups we use the standard WC parametrization (setting $c_4 = c_\varepsilon^{\text{mono}} = 0$) of the `PyBird` likelihood and for the MCMC the default prior configuration from Ref. [58] as above.

Bayesian results. Firstly, Fig. 6.4 shows the one-dimensional marginalized posterior distributions and the 68% and 95% two-dimensional marginalized posteriors obtained from our MCMC analyses for the BOSS, BOSS + BAO, eBOSS, and *Planck* data (see Sec. 6.1.2 for details). The general picture, which corroborates previous results using the WC parametrization of the EFTofLSS [58], is that the parameter constraints from BOSS and eBOSS show overall agreement with *Planck* data up to $1.6\,\sigma$. All σ-distances, as defined in Eq. 6.2, are summarized in Table 6.4. We confirm that BOSS+BAO data prefers slightly lower values of σ_8 than *Planck* data at a significance of $1.4\,\sigma$. Note that this difference is larger in the EC parametrization corresponding to a σ-distance of $2.5\,\sigma$ (see Sec. 6.3.1). Moreover, we find that BOSS+BAO data prefers slightly larger values of h than *Planck* at a significance of $1.6\,\sigma$ and eBOSS prefer slightly larger values of n_s and A_s than *Planck* at a significance of $1.4\,\sigma$ to $1.5\,\sigma$, while having a weaker constraining power compared to BOSS data. The inclusion of the reconstructed BAO data does not alter the constraints from BOSS significantly, the most significant being a 0.4σ shift on h. [8]

Frequentist results. Fig. 6.5 shows the profile likelihood results for the cosmological parameters σ_8, h, Ω_m, n_s, and A_s. For each of the parameters, the top panels show the profile

[8] Compared to previous analyses, especially in chapter 4, we do not set n_s to the *Planck* value, which explains why our LSS constraints are somewhat weaker and why we have a stronger inconsistency between eBOSS and BOSS.

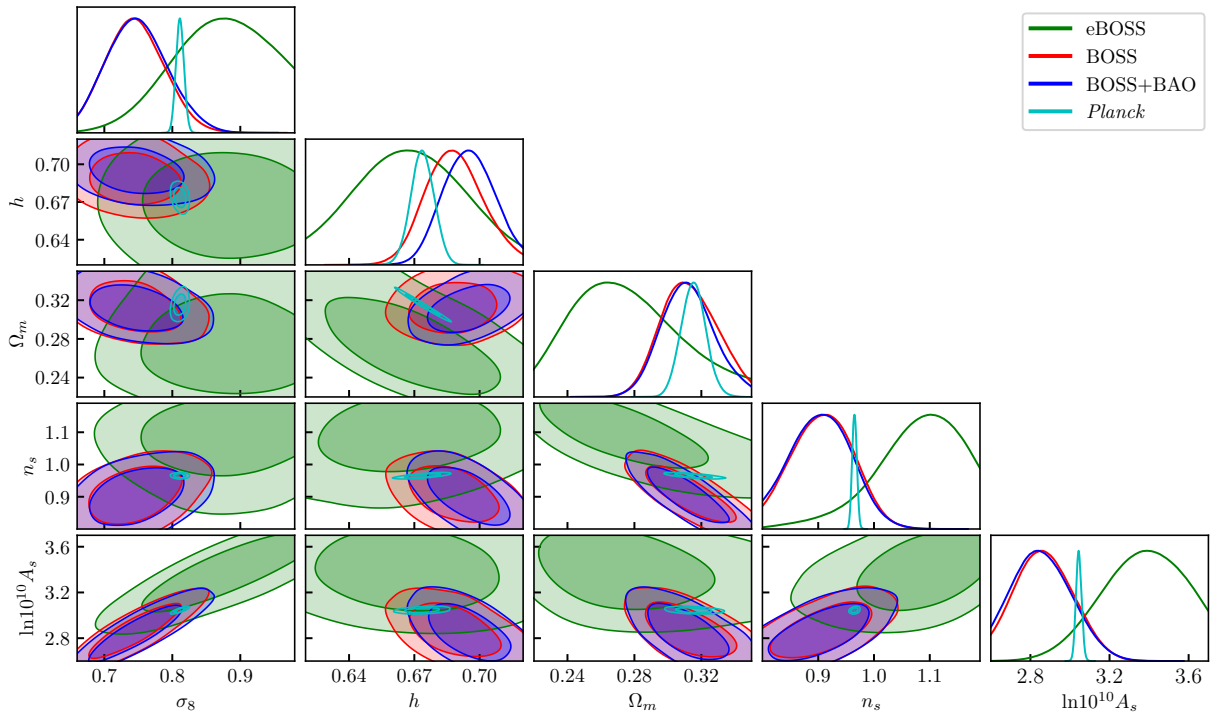

Figure 6.4: MCMC posteriors for five selected ΛCDM parameters using four different datasets, described in Sec. 6.1.2.

likelihoods in terms of the $\Delta\chi^2$, such that according to the Neyman construction for a Gaussian likelihood the intersections with $\Delta\chi^2 = 1$ (3.84), shown as the dashed (dotted) horizontal line, gives the 68% (95%) confidence interval. The bottom panels show such constructed confidence intervals, along with the corresponding credible intervals obtained from the MCMC analyses. Note that the confidence intervals for *Planck* have been constructed from fitting the $\Delta\chi^2$ to a parabola, which is the fit shown in the figure. This is appropriate since the ΛCDM profiles are Gaussian under *Planck* data [138]. For a visual comparison, individual profiles and posteriors for each parameter and data combination can be found in Fig. C.3 of App. C.2. Our constraints are summarized in Table 6.3, and the global best-fitting parameters in the BOSS+BAO and eBOSS datasets are given in App. C.3. In Tab. 6.4, we indicate the σ-distances between several combinations of experiments for either the MCMC or the profiles, while in Tab. 6.5, we display the σ-distances between posterior mean and MLE for each dataset. In the following, we will discuss the profile results and compare them to the MCMC results for each dataset individually.

BOSS & the "σ_8-discrepancy." Our profile likelihood confidence intervals for the BOSS+BAO data are in good agreement with the confidence intervals from *Planck* data for all five cosmological parameters at less than $1.4\,\sigma$ and we find no indication for a tension. Removing the reconstructed BAO data leads only to sub-σ shifts, the largest being in h, which is 0.7σ larger when including the reconstructed BAO data (as is the case for the MCMC analysis). When comparing to the credible intervals from the MCMC, the most striking feature is that the confidence intervals from the profile are much wider, *e.g.*, the 68% profile confidence intervals are wider by a factor of 1.4 to 1.9 than the MCMC credible intervals. As already discussed in Sec. 6.3.2, this cannot fully be attributed to prior volume effects, and is consequently an indication that the priors on the EFT parameters in the Bayesian approach are

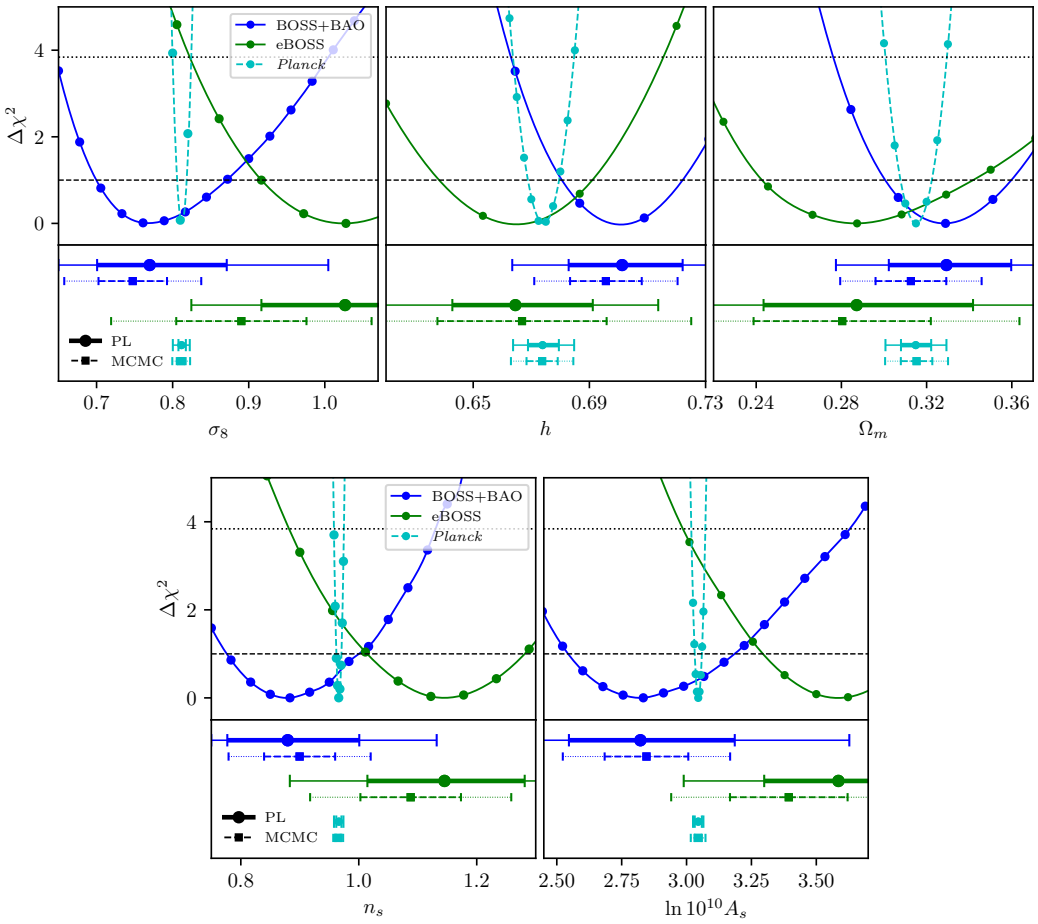

Figure 6.5: Profile likelihoods for five selected ΛCDM parameters using the three main datasets described in Sec. 6.1.2. For each of the parameters, the top subplots show the profile likelihoods in terms of the quantity $\Delta\chi^2(\theta) = -2\log(L(\theta)/L_{\max})$, where $L_{\max}$ is the MLE. The bottom subplots show the 68% and 95% confidence intervals derived from the profiles (solid) as well as the 68% and 95% credible intervals obtained from the Bayesian analysis (dashed) of Fig. 6.4. The profile constraints differ from the MCMC constraints for BOSS+BAO and eBOSS data, while the *Planck* constraints are roughly unchanged. We find no indication for a tension between any of the considered datasets.

informative and lead to tighter constraints on the cosmological parameters. The point estimates of profile and MCMC differ only slightly; we find σ-distances between posterior mean and MLE, as defined in Eq. 6.3, up to 1σ, namely $\sim 0.5\sigma$ on h and σ_8, and $\sim 1\sigma$ on Ω_m (see Tab. 6.5). As discussed in Sec. 6.3.2, note that in our BOSS and BOSS+BAO results, we observe that the EFT parameters take on extreme values, which reflects in considerably larger uncertainties and questions the validity of the EFTofLSS in our profile likelihood analysis. Our results corroborate previous findings (see Refs. [204] as well as chapters 4 and 5) that there is no indication for a "σ_8 discrepancy" between BOSS and *Planck* data. While in the Bayesian analysis the σ-distance between σ_8 posteriors of BOSS+BAO data based on the WC (EC) parametrization and *Planck* is $1.4\,\sigma$ ($2.5\,\sigma$), this is reduced to $0.49\,\sigma$ ($0.33\,\sigma$) for the profile. This reduction of the σ-distance is mainly due to the increase of the errorbar by a factor of 1.9 (2.7) along with a shift of the MLE compared to the posterior mean to slightly larger values of σ_8. These results suggest treating the somewhat curious $2.5\,\sigma$ discrepancy in σ_8 obtained in the

		σ_8	h	Ω_m	n_s	$\ln 10^{10} A_s$
BOSS	PL	0.8025 ± 0.0925	0.6816 ± 0.0209	0.3197 ± 0.0291	0.9499 ± 0.1349	3.0304 ± 0.3167
	MCMC	0.7443 ± 0.0433	0.6889 ± 0.0136	0.3137 ± 0.0174	0.9050 ± 0.0576	2.8610 ± 0.1543
BOSS + BAO rec.	PL	0.7699 ± 0.0851	0.7013 ± 0.0183	0.3293 ± 0.0281	0.8795 ± 0.1078	2.8222 ± 0.2918
	MCMC	0.7476 ± 0.0450	0.6957 ± 0.0123	0.3126 ± 0.0170	0.8997 ± 0.0602	2.8455 ± 0.1612
eBOSS	PL	1.0267 ± 0.1179	0.6645 ± 0.0233	0.2872 ± 0.0490	1.1454 ± 0.1326	3.5852 ± 0.3065
	MCMC	0.8903 ± 0.0856	0.6668 ± 0.0291	0.2804 ± 0.0416	1.0880 ± 0.0853	3.3940 ± 0.2266
Planck	PL	0.8122 ± 0.0063	0.6742 ± 0.0054	0.3151 ± 0.0074	0.9663 ± 0.0044	3.0453 ± 0.0139
	MCMC	0.8112 ± 0.0058	0.6737 ± 0.0054	0.3153 ± 0.0074	0.9651 ± 0.0042	3.0446 ± 0.0142

Table 6.3: 68% C.L. constraints obtained in this work. Profile likelihood (PL) constraints represent the best-fit and confidence interval from the Neyman construction described in Sec. 6.1.1; the quantity in $\pm$ is the average of the absolute difference between the lower and upper bounds and the best-fit (noting that the profiles are largely Gaussian). The MCMC constraints represent the mean of the marginalized one-dimensional posterior and its associated 68% credible interval.

		σ_8	h	Ω_m	n_s	$\ln 10^{10} A_s$
BOSS+BAO vs. *Planck*	PL	0.49σ	1.33σ	0.48σ	0.78σ	0.70σ
	MCMC	1.40σ	1.63σ	0.15σ	1.08σ	1.23σ
eBOSS vs. *Planck*	PL	1.82σ	0.39σ	0.56σ	1.34σ	1.76σ
	MCMC	0.92σ	0.23σ	0.83σ	1.44σ	1.54σ
BOSS+BAO vs. eBOSS	PL	1.77σ	1.18σ	0.74σ	1.53σ	1.72σ
	MCMC	1.48σ	0.91σ	0.72σ	1.80σ	1.87σ

Table 6.4: σ-distances, as defined in Eq. 6.2, for five selected parameters between different datasets.

	σ_8	h	Ω_m	n_s	$\ln 10^{10} A_s$
BOSS+BAO	0.50σ	0.46σ	0.98σ	0.34σ	0.14σ
eBOSS	1.59σ	0.08σ	0.16σ	0.67σ	0.84σ
Planck	0.16σ	0.08σ	0.03σ	0.29σ	0.05σ

Table 6.5: Distance between posterior mean and best-fit in units of the standard deviation, σ, of the posterior, as defined in Eq. 6.3.

MCMC analysis using the EC parametrization cautiously since it depends on the EC convention of the EFT parameter priors and on prior-volume effects inherent to the Bayesian framework.

eBOSS. The profile likelihood confidence intervals from eBOSS data show mild discrepancies with *Planck* and BOSS+BAO data for some parameters, *e.g.*, σ_8 is $1.82\,\sigma$ ($1.77\,\sigma$) higher than for *Planck* (BOSS+BAO) and $\ln 10^{10} A_s$ is $1.82\,\sigma$ ($1.72\,\sigma$) higher than for *Planck* (BOSS+BAO), which is similar to the MCMC analyses (see Tab. 6.4). Otherwise, the parameter constraints of eBOSS are within around $\lesssim 1.5\,\sigma$ of the constraints from *Planck* and BOSS+BAO. When comparing to the MCMC constraints, we find that the width of the 68% confidence intervals of the profile is a factor 1.2 to 1.6 wider than the credible intervals of the MCMC. The best-fit obtained from the profile is within 1σ of the posterior mean obtained from the MCMC except for the parameter σ_8, where the best-fit is at a $1.59\,\sigma$ higher value than the posterior mean. However, as with BOSS data, we also find extreme values of the EFT parameters under eBOSS data.

Planck. For comparison, we also constructed profile likelihoods for *Planck* data. We find very good agreement between the constraints from profile likelihoods and MCMC for *Planck* data. The width of the confidence and credible intervals agree within less than 8% and the shifts between best-fit and posterior mean are less than $0.3\,\sigma$. This corroborates the results in Ref. [138], which used *Planck* 2013 intermediate results and also found very good agreement between both methods. The good agreement between the profile likelihood and MCMC are expected due to the high constraining power of *Planck* data, which dominates over any prior information. We note that for all cosmological parameters, the *Planck* constraints are in-between the BOSS and eBOSS ones, indicating no tension between the CMB and the galaxy clustering data.

6.5 Conclusions

Motivated by previous Bayesian studies that found a prior dependence of the inferred cosmological parameters from BOSS full-shape data using the EFTofLSS [187, 203, 105, 204], in this work, we present frequentist profile likelihood constraints to view this matter from a different statistical point of view. In particular, two of the commonly used parametrizations of the EFTofLSS, the WC [59] and EC parametrizations [61], give different constraints on the cosmological parameters of up to $\sim 1\,\sigma$ in a Bayesian analysis (see chapter 5).

Using the profile likelihood, we find that the WC and EC parametrizations yield the same confidence interval for σ_8, confirming that the two parametrizations are mathematically equivalent, *i.e.*, they describe the same space of model predictions for the galaxy power spectrum multipoles (see Fig. 6.1 in Sec. 6.3.1). [9] However, we find that the profile likelihood gives constraints on σ_8 that are factors of > 2 wider than the constraints based on the MCMC posterior. Moreover, we observed that several of the EFT parameters take on extreme values during the profile likelihood analysis, indicating that the frequentist analysis takes into account parts of the EFT parameter space beyond the intended use of the theory, in which the perturbative nature might be broken. This issue is addressed in the Bayesian case by imposing narrow Gaussian priors on the EFT parameters. If these priors were well founded, *e.g.*, motivated from theory, simulations, or other observations, the priors could in principle be promoted to data likelihoods in the frequentist analysis. Although the priors on the EFT parameters are not rigorously motivated, we explore the effect of including Gaussian data likelihoods in the frequentist analysis, which correspond to the priors in the Bayesian analysis. We find that the inclusion of the Gaussian likelihoods on the EFT parameters reduces the width of the constraints almost to the level of the ones inferred from the MCMC posterior and keeps the EFT parameters in the intended range (see Fig. 6.2 in Sec. 6.3.2). However, it also leads to a shift of the confidence interval of σ_8. This demonstrates that the priors on the EFT parameters in the Bayesian analysis are informative and influence the inferred cosmological parameters.

As a way forward, we explore the impact that data from future surveys like DESI [226] will have by considering BOSS+BAO data with a data covariance matrix rescaled by 16 (see Fig. 6.3 in Sec. 6.3.3). We find that the constraints from Bayesian and frequentist approaches converge to the same interval for σ_8 as the likelihood dominates over the prior information,

[9] This equivalence requires the free variation of two EFT parameters in the WC parametrization (c_4 and $c_\varepsilon^{\rm mono}$, see Sec. 6.2), which are typically fixed to zero in the standard WC convention. Instead, we find a strong correlation between these parameters and σ_8, motivating further study.

suggesting that the issues discussed above will subside with more data.

Finally, we construct frequentist confidence intervals for five selected ΛCDM parameters, σ_8, h, Ω_m, n_s, $\ln 10^{10} A_s$, and compare the constraints from different datasets, including BOSS, eBOSS and *Planck* (see Sec. 6.4). With the profile likelihood, we find that the constraints from BOSS and *Planck* for all five parameters are within $1.4\,\sigma$, finding no indication of a tension. In particular, while the MCMC posterior prefers intervals for σ_8, which are $1.4\,\sigma$ ($2.5\,\sigma$) lower than the *Planck* value for the WC (EC) EFT parametrization, the intervals from the profile likelihood are only $0.5\,\sigma$ ($0.3\,\sigma$) lower than the *Planck* constraint. The reduction of the σ-distances can be mainly attributed to the wide confidence intervals from the profile likelihood, but in the case of σ_8, also to shifts of the MLE closer to the *Planck* value than the posterior mean. In line with chapters 4 and 5, we find that the parameter σ_8 is most subject to prior effects. This indicates that the slight "σ_8 discrepancy" seen in the Bayesian results using the EC parametrization is due to the particular choice of priors. On the other hand, although our main profile likelihood analysis makes use of the WC baseline parametrization of the EFTofLSS without priors, we do not expect major changes in our conclusions regarding the state of the σ_8 tension from resorting to the use of "priors" or a different parametrization.

Our results clearly show the advantages and disadvantages of frequentist and Bayesian parameter inference. Since the frequentist inference does not include priors that confine the EFT parameters to the regime intended by the theory, we observe that the data prefers several EFT parameters to take on extreme values, possibly breaking the perturbativeness of the theory. The lack of prior further leads to significantly wider confidence intervals. This loss of constraining power reflects the purely data driven frequentist approach, which is completely agnostic about which model parameters are deemed more likely *a priori*. On the other hand, the priors in the Bayesian inference are informative and have an impact on the inferred cosmological parameters. This is important since it is not straightforward to define well motivated priors on the EFT parameters, which is reflected in the fact that the WC and EC parametrizations use different standard configurations for the EFT priors.

Looking towards the future, which will bring more constraining datasets, we can expect these points of discussion to subside as the data will dominate over any subjective preference introduced by the analysis setup. While waiting for better data, our results indicate that the use of frequentist along with Bayesian methods are valuable in order to obtain a fully nuanced view of the data.

Part III

Constraining models beyond ΛCDM with the effective field theory of large-scale structures

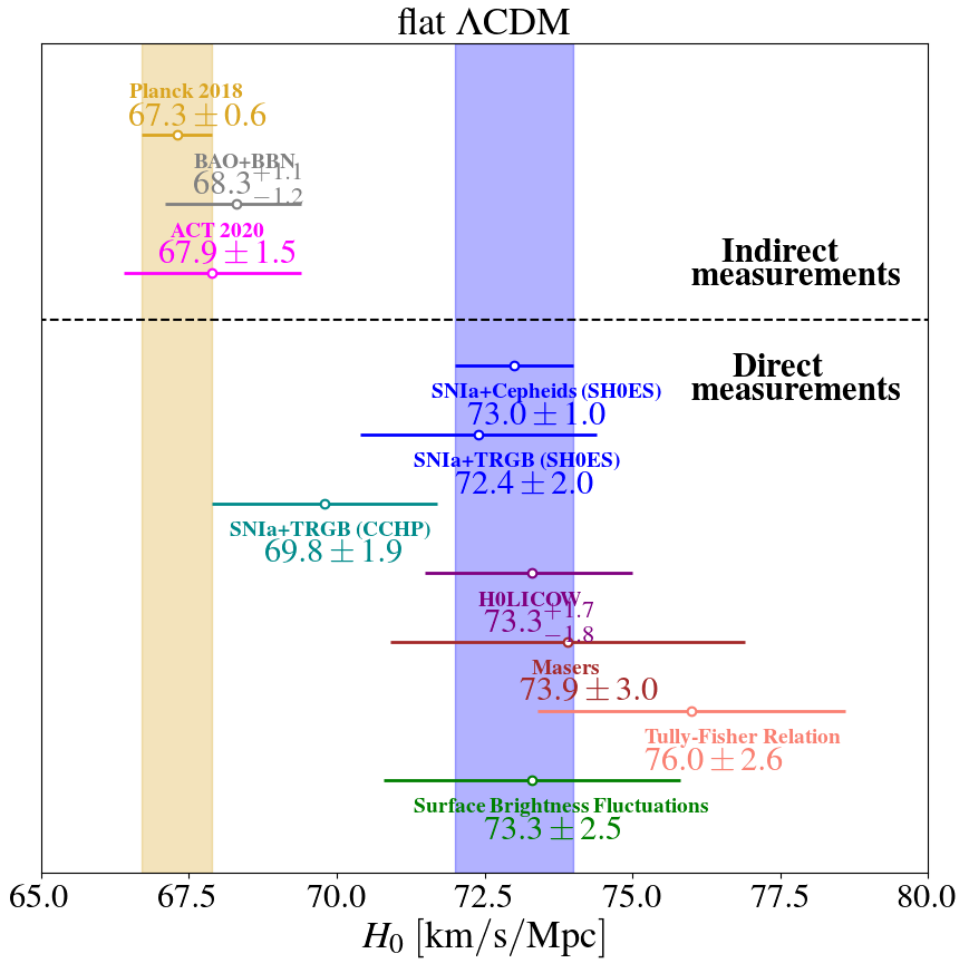

Figure 6.6: 68% CL constraints on the H_0 parameter either from indirect measurements (coming from CMB experiments) or from direct measurements in the local universe. The yellow band corresponds to the Planck value [11], while the blue band refers to the SH0ES value using the Cepheid-calibrated cosmic distance ladder [153, 227] (which is the canonical value we consider in the following analyses). I would like to thank Guillermo Franco Abellàn and Vivian Poulin for this figure.

In the previous part of this thesis, we showed that there is very good agreement between the ΛCDM parameters reconstructed from the clustering data analysed with the EFTofLSS and the CMB data, in particular those from *Planck*. However, in recent years, several tensions between probes of the early and late universe analyzed under the ΛCDM model have emerged. The Hubble tension [228] refers to the inconsistency between local measurements of the current expansion rate of the Universe, *i.e.*, the Hubble constant H_0, and the value inferred from early universe data using the ΛCDM model. This tension is predominantly driven by the *Planck* Collaboration's observation of the cosmic microwave background (CMB), which predicts a value in ΛCDM of $H_0 = 67.27 \pm 0.60$ km/s/Mpc [11], and the value measured by the SH0ES Collaboration using the Cepheid-calibrated cosmic distance ladder, whose latest measurement yields $H_0 = 73 \pm 1$ km/s/Mpc [153, 227]. Taken at face value, these observations alone result in a $\sim 5\sigma$ tension. [10] Experimental efforts are underway to establish whether this

[10] A new calibration including cluster cepheids and Gaia EDR3 parallaxes further increase the tension to 5.3σ [227].

discrepancy can be caused by yet unknown systematic effects (appearing in either the early or late universe measurements [229, 230], or both). It appears that various attempts to alter the modeling of dust extinction are not successful in altering the Hubble constant [231, 232, 233], nor is there support for different populations of type Ia supernova (SNIa) at low$-z$ and high$-z$ causing significant impact [234, 235, 236, 237]. In fact, the SH0ES team recently provided a comprehensive measurement of the H_0 parameter to 1.3% precision, addressing these potential systematic errors, and concluded that there is "*no indication that the discrepancy arises from measurement uncertainties or [over 70] analysis variations considered to date*" [153]. On the side of the CMB, it has been noted that *Planck* data carry a number of anomalies of low statistical significance that may play a role in this tension [238, 239, 11, 240, 241]. Nevertheless, the appearance of this discrepancy across an array of probes (although not always with strong statistical significance) suggests that a single systematic effect may not be sufficient to resolve it. For a very short summary of alternative methods, let us mention that, on the one hand, there exists a variety of different techniques for calibrating ΛCDM at high redshifts and subsequently inferring the value of H_0, which do not involve *Planck* data. For instance, one can use alternative CMB datasets such as WMAP, ACT, or SPT. We can even remove observations of the CMB altogether and combine measurements of big bang nucleosynthesis (BBN) with data from baryonic acoustic oscillation (BAO) [242, 243], as shown in Fig. 3.10, or from the full-shape of the galaxy power spectrum analysed with the EFTofLSS, as shown in chapter 4, resulting in H_0 values in good agreement with *Planck*. On the other hand, alternative methods for measuring the local expansion rate have been proposed in the literature, in an attempt at removing any bias introduced from cepheid and/or SNIa observations. The Chicago-Carnegie Hubble program (CCHP), which calibrates SNIa using the tip of the red giant branch (TRGB), obtained a value of $H_0 = 69.8 \pm 0.6\ (\text{stat}) \pm 1.6\ (\text{sys})$ km/s/Mpc [244, 245], in between the *Planck* CMB prediction and the SH0ES calibration measurement, and a reanalysis of the CCHP data by Anand *et al.* yields $H_0 = 71.5 \pm 1.9$km/s/Mpc [246]. The SH0ES team, using the parallax measurement of $\omega-$Centauri from Gaia DR3 to calibrate the TRGB, obtained $H_0 = 72.1 \pm 2.0$km/s/Mpc [247, 248]. Additional methods intended to calibrate SNIa at large distances include surface brightness fluctuations of galaxies [249], Miras [250], or the Baryonic Tully Fisher relation [251]. There also exists a variety of observations that do not rely on observations of SNIa – these include, *e.g.*, time delay of strongly lensed quasars [252, 253], maser distances [254], or gravitational waves as "standard sirens" [255]. For recent reviews on the topic, we refer the reader to Refs. [256, 40], while a summary is given in Fig. 6.6.

Along with experimental developments to confirm the Hubble tension, a lot of effort has been given to explain these discrepancies with some new physical mechanism, often in the form of extensions to the ΛCDM model that may be connected to the (still unknown) nature of dark matter or dark energy. It has been argued that the most promising category of solutions to resolve the H_0 tension involves physics in the pre-recombination era leading to a decrease of the sound horizon at recombination [257, 258, 259, 260, 261, 183], such as models involving dark radiation and/or new neutrino properties [262, 263, 264, 265, 266, 267, 268, 269, 270, 271, 272, 273], early dark energy (EDE) [274, 275, 276, 277, 278, 279, 280], modified gravity [281, 282, 283, 284, 285, 286, 287, 288, 289, 290, 291, 292, 293, 294, 295, 296, 297, 298, 299, 300], or exotic recombination [301, 302, 303, 304, 305] (for review of EDE models see Ref. [280], and for a review of models that could resolve the Hubble tension see Refs. [256, 183]).

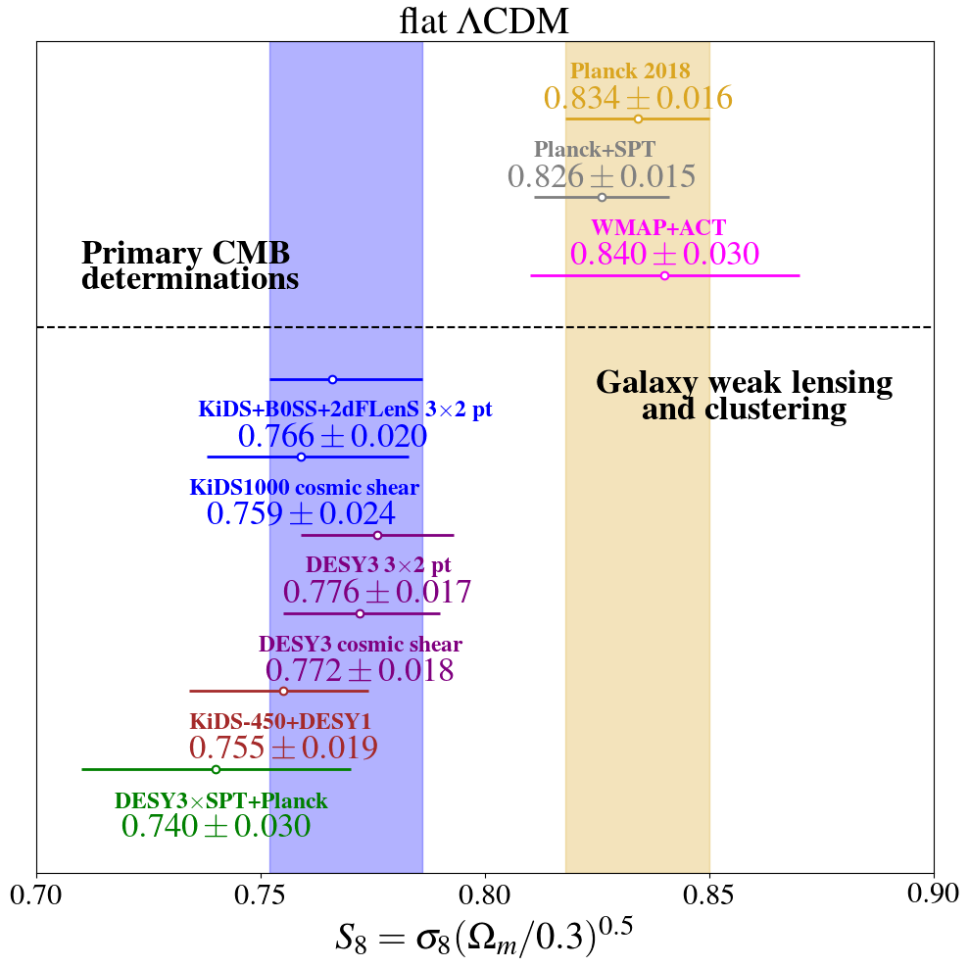

Figure 6.7: 68% CL constraints on the S_8 parameter either from indirect measurements (coming from CMB experiments) or from direct measurements in the local universe (coming from weak lensing surveys). The yellow band corresponds to the Planck value [11], while the blue band refers to the combined analysis between the weak lensing observations from KiDS-1000, the galaxy clustering observations from BOSS and the galaxy-galaxy lensing observations from KiDS-1000, BOSS, and the spectroscopic 2-degree Field Lensing Survey (2dfLenS) [177]. I would like to thank Guillermo Franco Abellàn and Vivian Poulin for this figure.

Additionally, within ΛCDM, the parameter $S_8 \equiv \sqrt{\sigma_8(\Omega_m/0.3)}$, where σ_8 [11] is the root mean square of matter fluctuations on an $8h^{-1}$Mpc scale and Ω_m the (fractional) matter density today, inferred from CMB [11, 76] is about $2-3\sigma$ larger than that deduced from weak lensing surveys [12] such as the CFHTLenS [201], HSC [307], KiDS-1000 [177, 80], DESY3 [79], as well as from *Planck* Sunyaev-Zeldovich cluster abundances [11, 308] and

[11] We recall that σ_8 is defined as follows:

$$\sigma_8^2 = \int \frac{k^3}{2\pi^2} P_m(k) W_8^2(k) d\ln k\,, \tag{6.10}$$

where $P_m(k)$ is the linear matter power spectrum, and $W_8(k)$ is a window function describing a sphere (in Fourier space) with a (historically chosen) radius of 8 h^{-1}Mpc.

[12] More precisely, there even exists a "lensing is low" anomaly when comparing galaxy clustering and weak lensing data within the ΛCDM cosmology [306, 178, 116].

SPT [309]. The early and late measurements of S_8 are summarised in Fig. 6.7. In particular, the *Planck* [11] data indicate $S_8 = 0.834 \pm 0.016$, while the combined analysis between the weak lensing observations from KiDS-1000, the galaxy clustering observations from BOSS and the galaxy-galaxy lensing observations from KiDS-1000, BOSS, and the spectroscopic 2-degree Field Lensing Survey (2dFLenS), namely the so-called "3×2pt" analysis, [13] indicates 0.766 ± 0.020 [177]. Note that the S_8 values of the other CMB experiments, in particular ACT [76] and SPT [309], are compatible with the value of *Planck*, while all the weak lensing measurements lead to lower values than in the CMB experiments. In addition, the 3×2pt analysis breaks down the degeneracy between σ_8 and Ω_m compared with the weak lensing analysis alone, showing that the tension comes from σ_8 rather than Ω_m. Finally, let us note that the constraints on S_8 derived solely from galaxy clustering data with the EFTofLSS (but also with the BAO/$f\sigma_8$ information and other techniques) are compatible with *Planck* and weak lensing values. In chapter 4, we indeed found that $S_8 = 0.785^{+0.037}_{-0.040}$, with a best-fit at 0.838, for BOSS + eBOSS.

As for the H_0 tension, it has yet to be understood whether the S_8 tension is due to systematic effects [116], or physics beyond ΛCDM. Among the systematics that could explain the low value of the late time determination of S_8, we can cite for instance the intrinsic alignment of galaxies [310] or the effect of baryons at very small scales (namely the baryonic feedback) [311, 200]. Note that recently an analysis (released after the studies carried out in this thesis) combining KiDS-1000 data and DESY3 data [312] found a value of $S_8 = 0.790^{+0.018}_{-0.014}$ (with a best-fit at 0.801), showing a lower discrepancy of 1.7σ. This analysis took several systematic effects into account and succeeded in reducing this tension, perhaps indicating the need to explore this direction further. However, this discrepancy might also be the first clue about the intrinsic nature of the ΛCDM dark sector. The resolution of the S_8 tension (because it is due to σ_8 rather than Ω_m) requires a suppression in the matter power spectrum for $k \sim 0.1 - 1\ h\mathrm{Mpc}^{-1}$ in order to reduce the value of the σ_8 parameter, which can be achieved through a number of models that take into account new hypothetical properties of dark matter and/or dark energy [313, 314, 315, 316, 317, 305, 318, 319, 320, 167, 321, 322].

Interestingly, the models which can alleviate one or both tensions tend to leave signatures in the matter power spectrum on large scales that can be probed by large-scale structures surveys. While models that resolve the S_8 tension need to suppress the matter power spectrum, models that resolve the Hubble tension often require the ΛCDM parameters to be readjusted, which has an effect on the matter power spectrum. [14] An EFTofLSS analysis has already been applied to several models beyond ΛCDM, such as neutrino masses and effective number of relativistic species [101, 162, 323, 324, 273, 203], dark energy [59, 160, 187], curvature [325, 326] (see chapter 4 as well), early dark energy [327, 328, 329, 330], non-cold dark matter [169, 331], interacting dark energy [332], and more [333, 298, 334, 335]. In addition, the EFTofLSS has made possible the development of a new consistency test of the ΛCDM and alternative models based on a sound horizon-free analysis [155, 156, 157], providing a new way to probe beyond ΛCDM models [158].

[13] This refers to the 2-point statistic combination of cosmic shear, galaxy-galaxy lensing and galaxy clustering.

[14] For example, we will see later that the early dark energy model has a higher value of n_s and $\omega_{\rm cdm}$ than the ΛCDM model, which has a significant impact on the matter power spectrum (see Sec. 3.1).

The third part of this thesis is dedicated to the study of constraints derived from an EFTofLSS analysis applied to BOSS and eBOSS data, combined with other cosmological probes, on some models beyond ΛCDM. In chapters 7 (adapted from Ref. [330]) and 8 (adapted from Ref. [336]), we deal respectively with the axion-like early dark energy and acoustic (early) dark energy models proposed to resolve the Hubble tension, while in chapter 9 (adapted from Ref. [169]), we study the constraints on two decaying cold dark matter scenarios, including one that could resolve the S_8 tension.

VII

EFTofLSS' take on the Hubble tension and the early dark energy

Contents

7.1 Early Dark Energy Model and Data **207**
7.1.1 Review of the EDE model 207
7.1.2 Data and method 210
7.1.3 Details on the BOSS measurements and EFT likelihoods 212
7.2 Updated EFTBOSS constraints on EDE **213**
7.2.1 Preliminary study 213
7.2.2 Constraints from various BOSS data 214
7.2.3 Primary CMB-free constraints on EDE 217
7.3 EFTBOSS combined with CMB data **217**
7.3.1 EFTBOSS+*Planck*TTTEEE 217
7.3.2 EFTBOSS+*Planck*TT650TEE+ACT 220
7.3.3 EFTBOSS+*Planck*TTTEE+ACT 221
7.3.4 Impact of Pantheon+ data 222
7.4 Conclusions **225**
7.4.1 EFTBOSS constraints on EDE alone 225
7.4.2 *Planck*+EFTBOSS constraints on EDE 226
7.4.3 ACT+EFTBOSS constraints on EDE 226
7.4.4 Final comments 227

This chapter is based on:

T. Simon, P. Zhang, V. Poulin and T. L. Smith, *Updated constraints from the effective field theory analysis of the BOSS power spectrum on early dark energy*, **Phys. Rev. D 107 (2023) 063505**, arXiv:2208.05930.

In this chapter, we reassess the constraints on early dark energy (EDE) from the full shape of the most recent measurements of the power spectrum (or correlation function) of BOSS in light of a correction to the normalization of BOSS window functions (presented in App. D.1). EDE has been shown to reduce the Hubble tension to the $\sim 1.5\sigma$ level, with an energy density representing at most a fraction $f_{\rm EDE}(z_c) \sim 12\%$ at the critical redshift $z_c \sim 3500$ after which the fields start to dilute away [274, 275, 276, 183]. There exists a variety of EDE models that can similarly reduce the tension to the $1.5-2.5\sigma$ level [337, 277, 338, 279, 339]. Recently, several groups have reported "hints" of EDE within ACT data at the $\sim 3\sigma$ level, alone or in combination with WMAP (or, equivalently, *Planck* temperature data restricted to $\ell < 650$) and *Planck* polarization data [340, 341], as well as with SPT-3G data [342, 343].

However, it has also been pointed out that EDE leaves an impact in the matter power spectrum that can be constrained thanks to the EFTofLSS applied to BOSS data or through measurements of the parameter S_8. Typically, in the EDE cosmology that resolves the Hubble tension, the amplitude of fluctuations σ_8 is slightly larger due to increase in $\omega_{\rm cdm}$ and n_s, which are necessary to counteract some of the effects of the EDE on the CMB power spectra [275, 344, 345]. As a result, the S_8 tension tends to increase by $\sim 0.5\sigma$ in the EDE cosmology, and large-scale structure (LSS) measurements may put pressure on the EDE model [344]. Additionally, it has been argued that the full-shape analysis of the galaxy power spectrum of BOSS disfavors the EDE model as an efficient resolution of the H_0 tension [328, 327]. Indeed, in order to adjust the BAO data seen either in 3D or 2D at different comoving distances in a galaxy clustering survey (typically at $z \sim 0.1-1$), it requires in the EDE cosmology an increase in $\omega_{\rm cdm}$ [1] [275, 304], which can affect the fit to the full-shape [344, 327, 328]. Thus, galaxy clustering data can provide a way to break the degeneracy introduced by EDE, in particular, due to the constraints it provides on $\omega_{\rm cdm}$ and σ_8.

Although these effects are certainly relevant in constraining EDE, the original interpretation of the additional constraining power suggested in Refs. [327, 328] was disputed in Refs. [346, 347]. There, it was argued that the apparent constraining power from the BOSS full-shape analysis may be artificially amplified by (i) the impact of the prior volume artificially favoring ΛCDM in the Bayesian context (later verified with a profile likelihood approach [2] [188, 189]); (ii) a potential $\sim 20\%$ mismatch in the overall amplitude (typically parametrized by the primordial power spectrum amplitude A_s) between BOSS and *Planck*, rather than additional constraints on $\omega_{\rm cdm}$. In parallel, it had already been pointed out in Ref. [329] that the effective field theory of LSS applied to BOSS data does not rule out the new EDE model.

In App. D.1, we explore the impact of the correction to the normalization of the BOSS data window function within ΛCDM and show that it leads to a 1σ shift upward in the value of A_s, now in better agreement with *Planck*. [3] Given that previous analyses, *e.g.*, Refs. [327, 328], have used the measurements inconsistently normalized between the power spectrum and the window function (as already acknowledged in Ref. [157] for their previous analyses), the constraints from EDE are expected to change with these corrected BOSS measurements. While

[1] A similar increase is required to keep the CMB peaks' height fixed [275], in particular, through the ISW effect [345].

[2] For further discussion about the mitigation of projection and prior volume effect, see Ref. [190].

[3] Note that, in chapter 5, we argue that the remaining difference on the amplitude might be explained by projection effects from the prior volume associated with the marginalization of the EFT parameters.

Refs. [327, 328] concluded that the BOSS data, combined with *Planck* data, disfavored the EDE model as a potential candidate to solve the H_0 tension, we find here that the conclusions reached strongly depend on the normalization of the window functions used in the BOSS measurements.

This chapter is structured as follows: In Sec. 7.1, we review the EDE model and data considered in this work. In particular, we detail the possible choices of BOSS measurements and EFT likelihoods. In Sec. 7.2, we assess the constraining power of corrected BOSS data alone on the EDE resolution to the Hubble tension and discuss differences between the constraints derived from the various BOSS data and EFTofLSS likelihoods. In Sec. 7.3, we derive constraints on EDE from the EFTBOSS data combined with either *Planck* data (with and without SH0ES) or ACT data. We also show the impact of the new Pantheon+ SN1a catalog [132] on the constraints on EDE. We eventually present our conclusions in Sec. 7.4. App. D.1 presents details on how to consistently normalize the window function with the power spectrum measurements. App. D.2, provides additional comparison between EFTofLSS likelihoods within the EDE model. Finally, App. D.3 lists additional relevant information about χ^2 statistics.

7.1 Early Dark Energy Model and Data

7.1.1 Review of the EDE model

Background dynamics

The EDE model corresponds to an extension of the ΛCDM model, where the existence of an additional subdominant oscillating scalar field ϕ is considered. The EDE field dynamics is described by the Klein-Gordon equation of motion (at the homogenous level),

$$\ddot{\phi} + 3H\dot{\phi} + V_{n,\phi}(\phi) = 0\,, \tag{7.1}$$

where $V_n(\phi)$ is a modified axion-like potential defined as

$$V_n(\phi) = m^2 f^2 \left[1 - \cos(\phi/f)\right]^n . \tag{7.2}$$

f and m correspond to the decay constant and the effective mass of the scalar field, respectively, while the parameter n controls the steepness of the potential (see Fig. 7.1), and the rate of dilution after the field becomes dynamical (see Fig. 7.2). Let us note that the $n = 1$ case corresponds to the standard axion potential. In the following, we will use the redefined field quantity $\Theta = \phi/f$ for convenience, such that $-\pi \leq \Theta \leq +\pi$. In Fig. 7.1, we plot the axion-like EDE potential for several values of n.

Within this framework, the EDE energy density $\rho_\phi = -T^0_0$ and the EDE pressure $P_\phi = T^i_i$ take the following form:

$$\rho_\phi = \frac{1}{2}\dot{\phi}^2 + V_n(\phi)\,, \tag{7.3}$$

$$P_\phi = \frac{1}{2}\dot{\phi}^2 - V_n(\phi)\,, \tag{7.4}$$

implying that the EDE equation of state parameter is defined as

$$w_\phi = \frac{P_\phi}{\rho_\phi} = \frac{\frac{1}{2}\dot{\phi}^2 - V_n(\phi)}{\frac{1}{2}\dot{\phi}^2 + V_n(\phi)}\,. \tag{7.5}$$

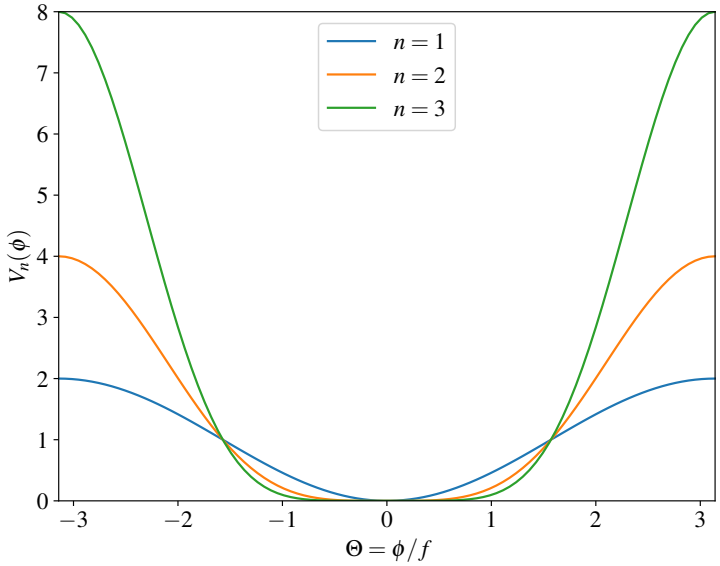

Figure 7.1: The axion-like EDE potential for $n = 1$ (*i.e.* the standard axion potential), $n = 2$ and $n = 3$ (*i.e.* our baseline model). Let us note that here $m = f = 1$.

At early times, when $H \gg m$, during the *slow-roll* phase (that consists in neglecting the kinetic energy $\dot{\phi}^2$ and the acceleration $\ddot{\phi}$ of the EDE field as for inflation), the scalar field ϕ is frozen at its initial value since the Hubble friction prevails, which implies that the EDE behaves like a form of dark energy and that its contribution to the total energy density increases relative to the other components. When the Hubble parameter drops below a critical value ($H \sim m$), the field starts evolving toward the minimum of the potential and becomes dynamical. The EDE contribution to the total budget of the Universe is maximum around a critical redshift z_c, after which the energy density starts to dilute with an approximate equation of state w_ϕ [348, 349],

$$w_\phi = \begin{cases} -1 & \text{if } z > z_c \\ \frac{n-1}{n+1} & \text{if } z < z_c \end{cases} . \tag{7.6}$$

In the following, we will fix $n = 3$ as it was found that the data are relatively insensitive to this parameter provided $2 \lesssim n \lesssim 5$ [276]. Instead of the theory parameters f and m, we make use of z_c and $f_{\rm EDE}(z_c) = \rho_\phi(z_c)/\rho_{\rm tot}(z_c)$, which is the fraction of EDE at z_c, determined through a shooting method [276]. We also include the initial field value Θ_i as a free parameter, whose main role once $f_{\rm EDE}(z_c)$ and z_c are fixed is to set the dynamics of perturbations right around z_c, through the EDE sound speed c_s^2 (see chapter 8). Thus, Θ_i controls the frequency of the background field oscillations, as can be seen in Fig. 7.2. This parameter also plays a role in the value of $f_{\rm EDE}(z_c)$, which can be approximated as [276]

$$f_{\rm EDE}(z_c) \sim \frac{V_n(\Theta_i)}{\rho_{\rm tot}(z_c)} = \frac{m^2 f^2}{\rho_{\rm tot}(z_c)}[1 - \cos(\Theta_i)]^n . \tag{7.7}$$

Perturbation dynamics

The perturbation of the EDE field $\delta\phi(k,t)$, around its homogeneous solution $\bar{\phi}(t)$, is defined by $\phi(k,t) = \bar{\phi}(t) + \delta\phi(k,t)$. The axion-like EDE model we consider in this work does not rely

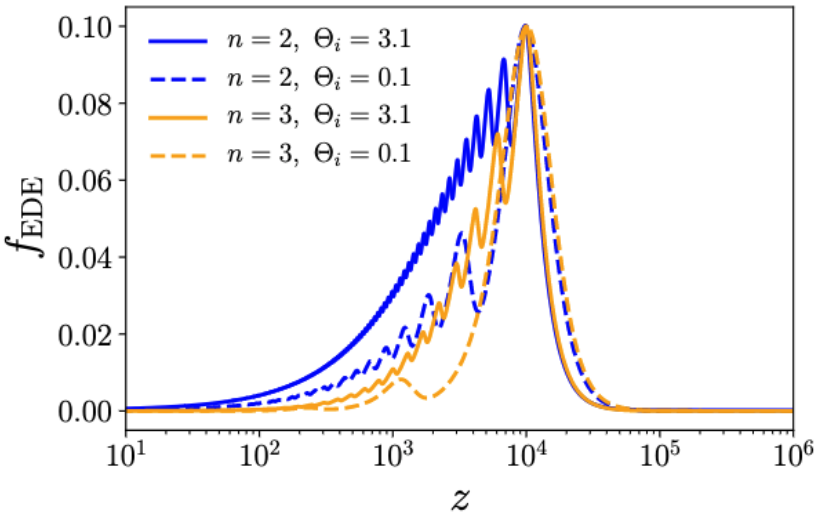

Figure 7.2: Impact of n and Θ_i on the evolution of the total energy density fraction. Taken from [276].

on a fluid approximation (like in Ref. [275]), since we solve the exact perturbed Klein-Gordon equation (at linear order) for a scalar field, which is expressed in synchronous gauge as [41]:

$$\delta\phi_k'' + 2H\delta\phi_k' + \left[k^2 + a^2 V_{n,\phi\phi}\right]\delta\phi_k = -h'\frac{\phi'}{2}, \tag{7.8}$$

where the prime denotes derivatives with respect to conformal time.

The EDE resolution of the Hubble tension and LSS data

The EDE field will provide a small contribution to the expansion rate $H(z)$ around z_c (we will focus on $\sim 10^3 - 10^4$ in the context of the Hubble tension), which causes a modification of the sound horizon at the recombination

$$r_{\rm s}(z_{\rm rec}) = \int_{z_{\rm rec}}^{+\infty} \frac{c_s(z')}{H(z')} dz', \tag{7.9}$$

where c_s corresponds to the sound speed of the photon-baryon fluid acoustic waves. The sound horizon is observationally determined through the angular acoustic scale at recombination θ_s, defined as

$$\theta_s = \frac{r_s(z_{\rm rec})}{D_A(z_{\rm rec})}, \tag{7.10}$$

where $D_A(z_{\rm rec}) = \int_0^{z_{\rm rec}} dz'/H(z') \propto 1/H_0$ is the comoving angular diameter distance. Given that θ_s is determined from *Planck* CMB power spectra with a very high accuracy, the change in the sound horizon must be compensated by a readjustment of the angular diameter distance in order to keep the angular acoustic scale constant. This readjustment is automatically done by increasing H_0 (and additional shift in $\omega_{\rm cdm}$ and n_s to compensate effect of EDE on the growth of perturbations), which can, by design, bring the CMB measurements and the late-time estimate of the Hubble constant from the SH0ES Collaboration into agreement. In this chapter, we address the question of whether the current full shape of galaxy clustering data analyzed using the

EFTofLSS, can accommodate EDE. Indeed, on the one hand, the sound horizon seen at baryon-drag epoch $r_s(z_{\rm drag})$ is measured through another angular acoustic scale in galaxy surveys,

$$\theta_g = \frac{r_s(z_{\rm drag})}{D_V(z_{\rm eff})}\,, \tag{7.11}$$

where $z_{\rm eff}$ is the effective redshift of the survey, and $D_V(z) = (D_A^2(z)\frac{c\cdot z}{H(z)})^{1/3}$ is a volume average of the comoving distances in the directions parallel and perpendicular to the line of sight, with c the speed of light. The angle θ_g typically summarizes the information from the BAO, and measuring it with high precision has the potential to break the degeneracy between $r_s(z_{\rm drag})$ and H_0 introduced by the EDE. In practice, BAOs from BOSS were shown to be well fit in combination with *Planck* and SH0ES when allowing for EDE [275], at the cost of a larger $\omega_{\rm cdm}$ [350], which can simultaneously allow for the CMB peaks' height to be kept fixed [275] through the ISW effect [345]. However, the full-shape of the galaxy power spectrum also contains additional information. For example, the amplitude of the small-scale galaxy power spectrum at $k > k_{\rm eq}$, where $k_{\rm eq}$ is the wavenumber entering the horizon at matter/radiation equality, contains information about ω_m, h, and the spectral tilt n_s [58, 101]. As the values of ω_{cdm} and n_s are uplifted to compensate the growth of perturbations in the presence of EDE, the full shape of the galaxy power spectrum (with ω_b fixed by CMB or a BBN prior) is also modified in that respect. In the following, we quantify if these modifications from the EDE as a resolution of the H_0 tension are consistent with current cosmological data, including the full-shape galaxy power spectrum from BOSS modeled with the EFT.

7.1.2 Data and method

We analyze the EDE model in light of recent cosmological observations through a series of Markov chain Monte Carlo (MCMC) analyses using the Metropolis-Hastings algorithm from `MontePython-v3` [4] code [137, 136] interfaced with our modified [5] version of `CLASS` [6] [221]. In this work, we carry out various analyses from a combination of the following datasets:

- **PlanckTTTEEE:** The low-l CMB TT, EE, and the high-l TT, TE, EE data from *Planck* 2018 [11].
- **PlanckTT650TEEE:** Same dataset as *Planck* TTTEEE, but in this case the TT power spectrum has a multipole range restricted to $l < 650$.
- **Lens:** The CMB gravitational lensing potential reconstructed from *Planck* 2018 temperature and polarization data [179]. When used without high-l TT, TE, EE data, we use the CMB-marginalized version of the likelihood. [7]
- **ACT:** The temperature and polarization angular power spectrum of the CMB from the Atacama Cosmology Telescope (ACT DR4) [351].
- **BBN:** The BBN measurement of ω_b [180] that uses the theoretical prediction of [181], the experimental deuterium fraction of [12], and the experimental helium fraction of [182].

[4] `https://github.com/brinckmann/montepython_public`.
[5] `https://github.com/PoulinV/AxiCLASS`.
[6] `https://lesgourg.github.io/class_public/class.html`.
[7] We thank Oliver Philcox for his help with correcting a bug in the standard Plik implementation.

- **BAO:** The measurements of the BAO from the CMASS and LOWZ galaxy samples of BOSS DR12 at $z = 0.38$, 0.51, and 0.61 [81], which we refer to as BOSS BAO DR12, and the BAO measurements from 6dFGS at $z = 0.106$ and SDSS DR7 at $z = 0.15$ [127, 128], which we refer to as BOSS BAO low$-z$.

- **BOSS $f\sigma_8$ DR12:** We also sometimes include the redshift space distortion at $z = 0.38$, 0.51, and 0.61, which we refer to as $f\sigma_8$ [81], taking into account the cross-correlation with BAO measurements.

- **EFTBOSS:** The full-shape analysis of the BOSS power spectrum from the EFTofLSS, namely, $P_{\rm FKP}^{\rm LZ/CM}$ [69], cross-correlated with reconstructed BAO, namely, $\alpha_{\rm rec}^{\rm LZ/CM}$ [126]. The measurements are defined in Tab. 5.4 of chapter 5. The SDSS-III BOSS DR12 galaxy sample data and covariances are described in Refs. [81, 125]. The measurements, obtained in Ref. [69], are from BOSS catalogs DR12 (v5) combined CMASS-LOWZ [8] [124] and are divided in redshift bins LOWZ $0.2 < z < 0.43$ ($z_{\rm eff} = 0.32$) and CMASS $0.43 < z < 0.7$ ($z_{\rm eff} = 0.57$), with north and south Galactic skies for each, respectively, denoted NGC and SGC. For the EDE analyses, we analyze the full shape of CMASS NGC, CMASS SGC, and LOWZ NGC, cross-correlated with post-reconstruction BAOs. The analysis includes the monopole and quadrupole between $(k_{\rm min}, k_{\rm max}) = (0.01, 0.20/0.23)h\,{\rm Mpc}^{-1}$ in Fourier space and $(s_{\rm min}, s_{\rm max}) = (25/20, 200)\,{\rm Mpc}\,h^{-1}$ in configuration space [101, 59, 69] for LOWZ / CMASS. The theory prediction and likelihood are made available through `PyBird`. We also compare `PyBird` to `CLASS-PT`. More details on the differences between these likelihoods are given *e.g.* in Sec. 5.1 of chapter 5. When computing constraints with `CLASS-PT`, we use the galaxy power spectrum monopole, quadrupole, and hexadecapole, for $0.01 \leqslant k \leqslant 0.2\ h{\rm Mpc}^{-1}$ as well as the real-space extension Q_0, up to $k_{\rm max} = 0.4\ h{\rm Mpc}^{-1}$, and the post-reconstructed BAO parameters. We use the standard `CLASS-PT` priors on the bias parameters.

- **Pan18:** The Pantheon SNIa catalog, spanning redshifts $0.01 < z < 2.3$ [133]. We will also study in Sec. 7.3.4 the impact of the newer Pantheon+ catalog, favoring a larger Ω_m [132], on our conclusions.

- **SH0ES:** The SH0ES determination of $H_0 = 73.04 \pm 1.04$ km/s/Mpc from cepheid calibrated SNIa, modeled as a Gaussian likelihood. [9]

We will refer to the combination of *Planck*TTTEEE+BAO+Pan18 as BaseTTTEEE, and to BaseTT650TEEE when replacing *Planck*TTTEEE with *Planck*TT650TEEE. In the absence of CMB TTTEEE data, we refer to the dataset EFTBOSS+BBN+Lens+BAO+Pan18 as BaseEFTBOSS. For all runs performed, we use *Planck* conventions for the treatment of neutrinos, that is, we include two massless and one massive species with $m_\nu = 0.06$ eV [11]. In addition, we impose a large flat prior on the dimensionless baryon energy density ω_b, the dimensionless cold dark matter energy density $\omega_{\rm cdm}$, the Hubble parameter today H_0, the logarithm of the variance of curvature perturbations centered around the pivot scale $k_p = 0.05\ {\rm Mpc}^{-1}$ (according to the *Planck* convention), $\ln\left(10^{10}\mathscr{A}_s\right)$, the scalar spectral index n_s, and the reionization optical depth

[8] `https://data.sdss.org/sas/dr12/boss/lss/`.
[9] For discussions about this modeling, see Refs. [260, 261, 183]

$\tau_{\rm reio}$. Regarding the three free parameters of the EDE model, we impose a logarithmic prior on z_c and flat priors for $f_{\rm EDE}(z_c)$ and Θ_i,

$$\begin{aligned} 3 &\leq \log_{10}(z_c) \leq 4, \\ 0 &\leq f_{\rm EDE}(z_c) \leq 0.5, \\ 0 &\leq \Theta_i \leq \pi\,. \end{aligned}$$

We define our MCMC chains to be converged when the Gelman-Rubin criterion $R-1<0.05$, except for runs combining *Planck*+EFTBOSS+ACT, for which we use a relaxed criterion of $R-1<0.1$ due to the complicated nature of the parameter space for the MCMC to explore. [10] Finally, we extract the best-fit parameters from the procedure highlighted in the appendix of Ref. [183], and we produce our figures thanks to `GetDist` [184].

7.1.3 Details on the BOSS measurements and EFT likelihoods

In this chapter, we perform a thorough comparison of the constraints derived from the EFTBOSS data, in order to assess the consistency of the various analyses presented in the literature. Indeed, there are various BOSS two-point function measurements available to perform full-shape analyses, as well as a different EFT code. As described in more detail in chapter 5, the BOSS DR12 data can be divided into two different sets of redshift splitting (LOWZ/CMASS vs z_1/z_3). Furthermore, depending on the estimator, the data are sometimes analyzed by convolving the theory model with a window function, or not. For a window-free analysis, one way is to use the configuration-space correlation function ξ, another is to use a quadratic estimator, which we denote with the subscript "QUAD." Finally, there are different ways to analyze the post-reconstructed parameters, which are then combined with the EFTBOSS data, denoted by $\alpha_{\rm rec}$ and $\beta_{\rm rec}$. These different datasets include slightly different amounts of information (due to different scale cuts) but they all represent reasonable choices on how to analyze the BOSS DR12 observations.

The characteristics of each measurement are listed in Tab. 5.4 of chapter 5 and more details can be found in Sec. 5.3 of this chapter. The EFT implementation and BOSS data we will focus on in this study are packaged in the `PyBird` likelihood, based on the EFT prediction and likelihood from `PyBird` [11] [59], and the `CLASS-PT` likelihood, based on the EFT prediction from `CLASS-PT` [12] [61] and likelihood from Ref. [62]. [13] Details about the `PyBird` and `CLASS-PT` likelihoods are presented in Sec. 5.1 of chapter 5. Here, let us simply mention that `CLASS-PT` implements the IR-resummation scheme proposed in Ref. [91] and generalized to redshift space in Ref. [186]. This is different than that implemented in `PyBird`, proposed in Ref. [71], generalized to redshift space in Ref. [72], and made numerically efficient in Ref. [59]. The `CLASS-PT` scheme has been shown to be an approximation of the one used in `PyBird` in Ref. [70], where one considers only the resummation of the bulk displacements around the BAO peak, $r_{\rm BAO}\sim 110{\rm Mpc}\,h^{-1}$. For this scheme to be made practical, one further relies on a wiggle-no-wiggle split procedure to isolate the BAO part. Although this scheme

[10] Most parameters are converged at 0.01-0.05, the parameter with the worse convergence is Θ_i, which is often unconstrained or multimodal in the analyses.

[11] https://github.com/pierrexyz/pybird.

[12] https://github.com/michalychforever/CLASS-PT.

[13] https://github.com/oliverphilcox/full_shape_likelihoods.

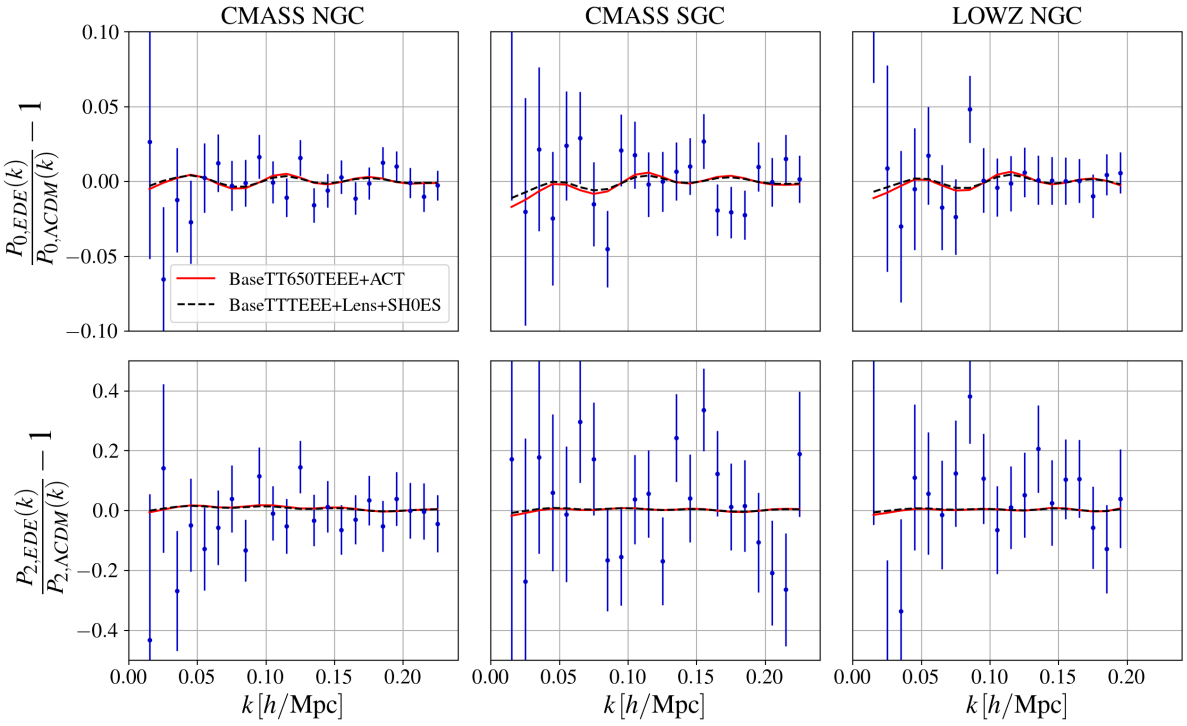

Figure 7.3: Residuals of the monopole and quadrupole of the galaxy power spectrum in two EDE models (see. Tab. 7.1) with respect to the ΛCDM model (obtained from the baseTTTEEE+Lens+EFTBOSS analysis, see chapter 9) for the three sky cuts of the EFTBOSS data.

has been shown to work fairly well within ΛCDM for cosmologies not too far from the one of *Planck*, we cautiously observe that in far-away cosmologies as the ones probed in EDE, the BAO peak location happens to be dramatically modified, and it thus remains to be checked that the approximations still hold in these cases. For our prior choice (on $f_{\rm EDE}$), we have checked that at least the wiggle-no-wiggle split procedure as implemented in `CLASS-PT` is as numerically stable as for a fiducial case where the BAO peak is $\sim 110\mathrm{Mpc}\,h^{-1}$.

In addition, in chapter 5, we have checked the validity of the two pipelines by implementing in the `PyBird` likelihood the exact same prior as those used in the `CLASS-PT` likelihood, and we found agreement on the 1D posteriors of the cosmological parameters at $\lesssim 0.2\sigma$ in ΛCDM, where these residual differences can be attributed to the different implementations of the IR-resummation mentioned above.

7.2 Updated EFTBOSS constraints on EDE

7.2.1 Preliminary study

In the recent literature, there has been a number of analyses showing hints of EDE and allowing for a resolution of the Hubble tension [275, 277, 340, 341, 342, 343]. In this preliminary study, we will take the results of two representative analyses. First, the baseline analysis of BaseTTTEEE+Lens+SH0ES data (second column of Tab. 7.2)

	BaseTTTEEE+Lens +SH0ES (EDE)	BaseTT650TEEE +ACT (EDE)	BaseTTTEEE+Lens +EFTBOSS (ΛCDM)
$\chi^2_{\rm CMASS\ NGC}$	39.3	39.1	40.3
$\chi^2_{\rm CMASS\ SGC}$	45.2	46.0	44.0
$\chi^2_{\rm LOWZ\ NGC}$	34.4	35.1	33.5
$\chi^2_{\rm EFTBOSS}$	118.9	120.2	117.8
$\Delta\chi^2_{\rm min}({\rm EDE}-\Lambda{\rm CDM})$	+1.1	+ 2.4	–
$p-$value (%)	16.7	14.7	18.5
$N_{\rm data}$	132		

Table 7.1: χ^2 of each sky cut of the EFTBOSS dataset for the EDE best-fit models extracted from a fit to BaseTTTEEE+Lens+SH0ES and BaseTT650TEEE+ACT and the ΛCDM model from a fit to BaseTTTEEE+Lens+EFTBOSS. We also indicated the $\Delta\chi^2$ with respect to the ΛCDM best-fit model. The associated p-value is calculated assuming that the data points are uncorrelated and taking $3\cdot 9$ EFT parameters in each fit (given that the cosmology is fixed).

has a best-fit of $f_{\rm EDE}(z_c) = 0.122$, $H_0 = 71.89$ km.s^{-1}.Mpc^{-1}. Second, the analysis of BaseTT650TEEE+ACT (first column of Tab. 7.3) favors an EDE model with significantly larger values of $f_{\rm EDE}(z_c)$ and H_0 compared to the BaseTTTEEE+Lens+SH0ES, namely, $f_{\rm EDE}(z_c) = 0.159$, $H_0 = 73.30$ km.s^{-1}.Mpc^{-1} (see also [340, 342, 341, 343]). In this section, we will gauge how these two specific models fair against BOSS data following Refs. [327, 328].

Using the best-fit parameters listed in Tab. 7.2 (second column) and Tab. 7.3 (first column), we perform a preliminary study where we determine the χ^2 of the EFTBOSS data (using our fiducial $P_{\rm FKP}^{\rm LZ/CM} + \alpha_{\rm rec}^{\rm LZ/CM}$ data) after optimizing only the EFT parameters (since the cosmological parameters are fixed here). Using the `PyBird` code, we show in Tab. 7.1 the χ^2 associated with the EFTBOSS data, and we plot in Fig. 7.3 the residuals with respect to ΛCDM from the BaseTTTEEE+Lens+EFTBOSS analysis [14]. We also show the BOSS data residuals for comparison with respect to the same model. First, one can see that the changes in the residuals between those various fits are almost imperceptible by eye with respect to BOSS error bars. We find that the χ^2 of the BOSS data is degraded by $+1.1$ for BaseTTTEEE+Lens+SH0ES (to be compared with $\sim +2.5$ in Ref. [328]) and $+2.4$ for BaseTT650TEEE+ACT, compared to the best-fit χ^2 of EFTBOSS data in the ΛCDM model. Despite this small χ^2 degradation, we note that the p-value of BOSS data in the EDE models that resolve the Hubble tension is still very good. Nevertheless, we anticipate that the EFTBOSS data could have a non-negligible constraining power in combination with BaseTT650TEEE+ACT, while its impact should be small in the context of the BaseTTTEEE+Lens+SH0ES analysis.

7.2.2 Constraints from various BOSS data

As is done in chapter 5 for ΛCDM, we compare the constraints on EDE from the various BOSS two-point function measurements, described in Tab. 5.4 of chapter 5, in combination with the BBN prior on ω_b.

[14] When combined with EFTBOSS, we do not include the BOSS BAO+$f\sigma_8$ data.

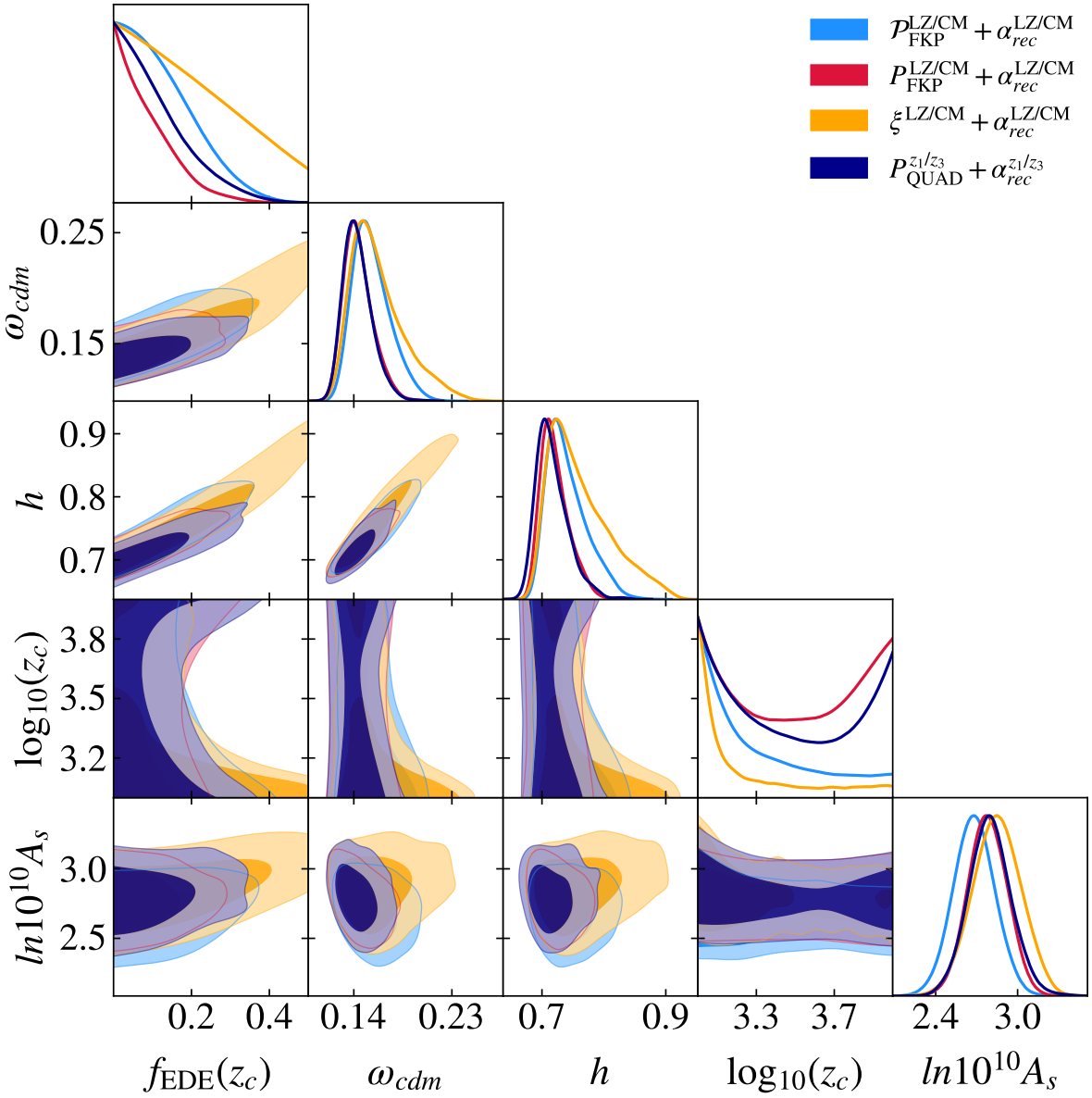

Figure 7.4: Comparison of 2D posteriors of a subset of parameters in the EDE model reconstructed from BOSS full-shape analyses using `PyBird` baseline likelihood, with a BBN prior on ω_b, of various pre-reconstructed two-point function measurements and handling of the window functions ($\mathscr{P}_{\rm FKP}^{\rm LZ/CM}, P_{\rm FKP}^{\rm LZ/CM}, \xi^{\rm LZ/CM}, P_{\rm QUAD}^{z_1/z_3}$) combined with various post-reconstructed BAO parameters ($\alpha_{\rm rec}^{\rm LZ/CM}$, $\alpha_{\rm rec}^{z_1/z_3}$). We recall that $\mathscr{P}_{\rm FKP}^{\rm LZ/CM}+\alpha_{\rm rec}^{\rm LZ/CM}$ corresponds to the BOSS FKP measurements analyzed with the EFT predictions convolved with inconsistently normalized window functions. The main EDE analyses of this work are based on EFTBOSS, which corresponds to $P_{\rm FKP}^{\rm LZ/CM}+\alpha_{\rm rec}^{\rm LZ/CM}$. We choose to show only the cosmological parameters that are not completely prior dominated.

The comparison of the 2D posteriors is shown in Fig. 7.4, while the 1D posteriors of $\{f_{\rm EDE}(z_c), h, \omega_{\rm cdm}, \ln(10^{10}A_s), n_s, \Omega_m\sigma_8, S_8\}$ are shown in Fig. 7.5. In these figures, we also display the results from the BOSS data analyzed with the EFT predictions convolved with inconsistently normalized window functions, namely, $\mathscr{P}_{\rm FKP}^{\rm LZ/CM}+\alpha_{\rm rec}^{\rm LZ/CM}$, which disfavor the EDE model when they are combined with *Planck* data [327, 328] (see the discussion in App. D.1 for the impact of inconsistent normalization within the ΛCDM model). Interest-

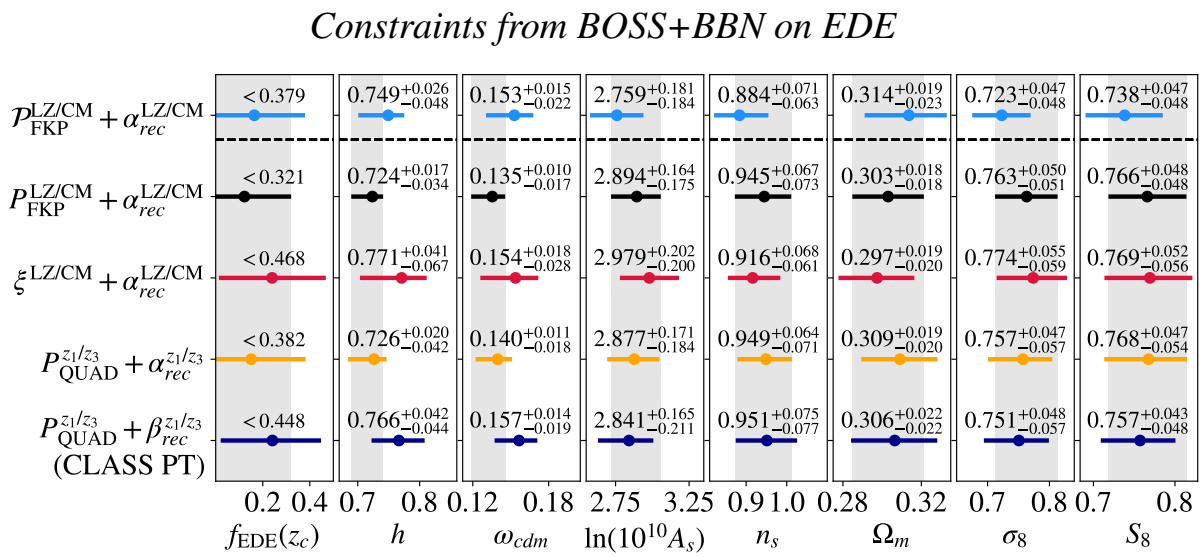

Figure 7.5: Comparison of 1D credible intervals in the EDE model reconstructed from BOSS full-shape analyses using `PyBird` baseline likelihood, with a BBN prior on ω_b, of various pre-reconstructed two-point function measurements and handling of the window functions ($\mathscr{P}^{\rm LZ/CM}_{\rm FKP}$, $P^{\rm LZ/CM}_{\rm FKP}$, $\xi^{\rm LZ/CM}$, $P^{z_1/z_3}_{\rm QUAD}$) combined with various post-reconstructed BAO parameters ($\alpha^{\rm LZ/CM}_{\rm rec}$, $\alpha^{z_1/z_3}_{\rm rec}$, and $\beta^{z_1/z_3}_{\rm rec}$). We recall that $\mathscr{P}^{\rm LZ/CM}_{\rm FKP}+\alpha^{\rm LZ/CM}_{\rm rec}$ corresponds to the BOSS FKP measurements analyzed with the EFT predictions convolved with inconsistently normalized window functions. The gray region corresponds to the EFTBOSS data that we use in our main analysis, namely, $P^{\rm LZ/CM}_{\rm FKP}+\alpha^{\rm LZ/CM}_{\rm rec}$. In the last line, we also show the results of $P^{z_1/z_3}_{\rm QUAD}+\beta^{z_1/z_3}_{\rm rec}$ analyzed using the `CLASS-PT` baseline likelihood. Relevant information regarding the measurements and their notations are summarized in Tab. 5.4 of chapter 5. We choose to show only the cosmological parameters that are not prior dominated. For $f_{\rm EDE}$, we quote instead the 2σ bound.

ingly, using the `PyBird` likelihood, the ΛCDM parameters are broadly consistent between $P^{\rm LZ/CM}_{\rm FKP}+\alpha^{\rm LZ/CM}_{\rm rec}$ and $P^{z_1/z_3}_{\rm QUAD}+\alpha^{z_1/z_3}_{\rm rec}$, as we have a shift of $\lesssim 0.3\sigma$ on ΛCDM parameters between these two measurements. However, we find that $P^{\rm LZ/CM}_{\rm FKP}+\alpha^{\rm LZ/CM}_{\rm rec}$ leads to stronger constraints on EDE, namely, [15] $f_{\rm EDE}(z_c)<0.321$, while $P^{z_1/z_3}_{\rm QUAD}+\alpha^{z_1/z_3}_{\rm rec}$ yields $f_{\rm EDE}(z_c)<0.382$.

Concerning $\xi^{\rm LZ/CM}+\alpha^{\rm LZ/CM}_{\rm rec}$, we find different constraints, even for the ΛCDM parameters: comparing $\xi^{\rm LZ/CM}+\alpha^{\rm LZ/CM}_{\rm rec}$ to $P^{\rm LZ/CM}_{\rm FKP}+\alpha^{\rm LZ/CM}_{\rm rec}$, we find shifts of $\lesssim 1.2\sigma$, whereas comparing $\xi^{\rm LZ/CM}+\alpha^{\rm LZ/CM}_{\rm rec}$ to $P^{z_1/z_3}_{\rm QUAD}+\alpha^{z_1/z_3}_{\rm rec}$, we find shifts of $\lesssim 1.0\sigma$. Let us note that the constraints on ΛCDM parameters reconstructed from $\xi^{\rm LZ/CM}+\alpha^{\rm LZ/CM}_{\rm rec}$ are weaker than those of $P^{\rm LZ/CM}_{\rm FKP}+\alpha^{\rm LZ/CM}_{\rm rec}$ and $P^{z_1/z_3}_{\rm QUAD}+\alpha^{z_1/z_3}_{\rm rec}$, which is consistent with what was found within the ΛCDM model in chapter 5 (see also Ref. [69] and explanations therein). Regarding the EDE parameters, we obtain weaker constraints on $f_{\rm EDE}$, namely $f_{\rm EDE}(z_c)<0.468$. It is worth noting that, for the same likelihood, the constraints on $f_{\rm EDE}(z_c)$ can be up to $\sim 35\%$ different depending on the data (especially between $P^{\rm LZ/CM}_{\rm FKP}+\alpha^{\rm LZ/CM}_{\rm rec}$ and $\xi^{\rm LZ/CM}+\alpha^{\rm LZ/CM}_{\rm rec}$). However, regardless of the data we consider, the BOSS full-shape (analyzed on their own with a BBN prior) within EDE leads to reconstructed values of H_0 that are compatible with what is obtained by the SH0ES Collaboration.

[15] Per convention, we cite one-sided bound at 95% C.L. and two-sided ones at 68% C.L.

This conclusion also holds for the CLASS-PT baseline (last line of Fig. 7.5), which is less constraining than the PyBird likelihood for the EDE model. Indeed, we obtain $f_{\rm EDE}(z_c) < 0.448$, which is $\sim 15\%$ weaker than the constraint obtained with the PyBird likelihood, even for similar data ($P^{z_1/z_3}_{\rm QUAD}$). Furthermore, we note that the $f_{\rm EDE}(z_c)$ constraint reconstructed from $P^{\rm LZ/CM}_{\rm FKP} + \alpha^{\rm LZ/CM}_{\rm rec}$, analyzed with the PyBird likelihood, is $\sim 35\%$ weaker than the constraint obtained from $P^{z_1/z_3}_{\rm QUAD} + \beta^{z_1/z_3}_{\rm rec}$, analyzed with the CLASS-PT likelihood. We conclude that the standard PyBird analysis setup (which consists of our baseline setup) shows a higher constraining power than the standard CLASS-PT analysis. Let us note that, for the H_0 parameter, we obtain a value 1.4σ higher than the *Planck* value ($h = 0.6851^{+0.0076}_{-0.014}$ at 68% CL) with the PyBird analysis setup, and a value 1.8σ higher with the CLASS-PT analysis setup, which indicates a reasonably good consistency between *Planck* and BOSS regarding H_0. For a more detailed discussion, including other data combinations, of the differences between PyBird and CLASS-PT for the EDE model, we refer to App. D.2. We, however, warn that the cosmological constraints from EFTBOSS at the level of the 1D posteriors might be affected by prior effects, as discussed in chapters 5 and 6 in the context of ΛCDM.

7.2.3 Primary CMB-free constraints on EDE

To fully gauge the constraining power of a primary CMB-free analysis, on top of the fiducial EFTBOSS data and BBN prior, we now include other BOSS BAO measurements, *Planck* lensing and the Pantheon18 datasets. We recall that this dataset is simply called BaseEFTBOSS, and we plot the associated reconstructed 2D posteriors in Fig. 7.6 (blue contours). We compare our results with the posteriors reconstructed from a BaseTTTEEE+Lens+SH0ES (red contours) and BaseTT650TEEE+ACT (orange contours) analysis. One can see that, while the primary CMB-free analysis does not favor EDE (in the absence of a SH0ES prior), constraints are relatively weak and the reconstructed posteriors from the BaseEFTBOSS data are not in tension with those reconstructed from the BaseTTTEEE+Lens+SH0ES and BaseTT650TEEE+ACT analyses. Nevertheless, we note a clear narrowing of the constraints in the $\{f_{\rm EDE}(z_c), \log_{10}(z_c)\}$ parameter space around $\log_{10}(z_c) \sim 3.5$, indicating that BOSS gains constraining power right around matter-radiation equality. To extract a meaningful CMB-independent bound on $f_{\rm EDE}(z_c)$, we perform an additional analysis now restricting the $\log_{10}(z_c)$ range to $\log_{10}(z_c) \in [3.4, 3.7]$, which corresponds to the region favored to resolve the Hubble tension. We find that the combination of EFTBOSS+BBN+Lens+BAO+Pan18 (*i.e.*, BaseEFTBOSS) leads to $f_{\rm EDE}(z_c) < 0.2$ (95% C.L.) and $h = 0.710^{+0.015}_{-0.025}$, which does not exclude the EDE models resolving the Hubble tension. When performing the same analysis with CLASS-PT, we find significantly weaker constraints, with $f_{\rm EDE}(z_c) < 0.284$ (95% C.L.) and $h = 0.726^{+0.02}_{-0.04}$. Constraints from CLASS-PT are shown in App. D.2, Fig. D.2.

7.3 EFTBOSS combined with CMB data

7.3.1 EFTBOSS+*Planck*TTTEEE

We now turn to studying the constraining power of EFTBOSS data in combination with primary CMB datasets. We start by performing joint analyses with the full *Planck*TTTEEE datasets. All relevant χ^2 statistics are given in App. D.3, Tabs. D.1 and D.2, while the reconstructed posteriors and best-fit values of parameters are given in Tab. 7.2. In the left

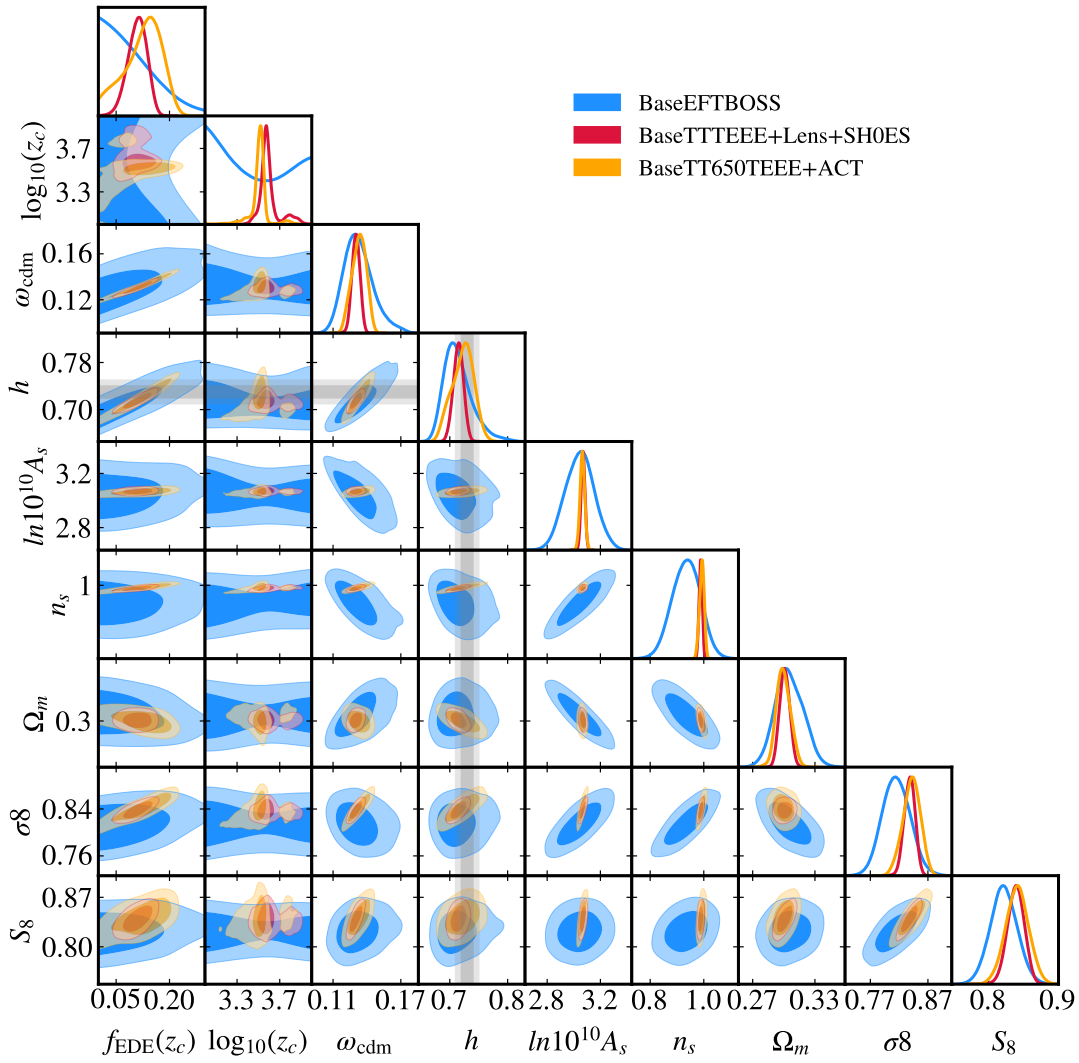

Figure 7.6: 2D posterior distributions reconstructed from the BaseEFTBOSS dataset compared with the posterior reconstructed from BaseTTTEEE+Lens+SH0ES and BaseTT650TEEE+ACT. We recall that BaseEFTBOSS refers to EFTBOSS+BBN+Lens+BAO+Pan18, BaseTTTEEE refers to *Planck*TTTEE+BAO+Pan18, and BaseTT650TEEE to *Planck*TT650TEE+BAO+Pan18.

panel of Fig. 7.7, we compare constraints obtained with the consistently and inconsistently normalized EFTBOSS data to that obtained with the compressed BAO/$f\sigma_8$ data. One can see that the correction of the normalization of the window function leads the new EFTBOSS data to have a constraining power only slightly stronger than the compressed BAO/$f\sigma_8$ data. We derive a BaseTTTEEE+Lens+EFTBOSS constraint of $f_{\rm EDE}(z_c) < 0.083$, to be compared with $f_{\rm EDE}(z_c) < 0.088$ from BaseTTTEEE+Lens+$f\sigma_8$, while the EFTBOSS data with wrong normalization incorrectly lead to $f_{\rm EDE}(z_c) < 0.054$.

Moreover, as was already pointed out in various works [347, 346, 183, 188], posteriors are highly non-Gaussian with long tails toward high-H_0, and therefore these constraints should be interpreted with care. This is further attested by the fact that the best-fit point lies at the 2σ limit of our constraints (*e.g.*, $f_{\rm EDE}$ at the best-fit is 0.082 for BaseTTTEEE+Lens+EFTBOSS). We defer to future work to compare constraints derived here with a Bayesian analysis to those

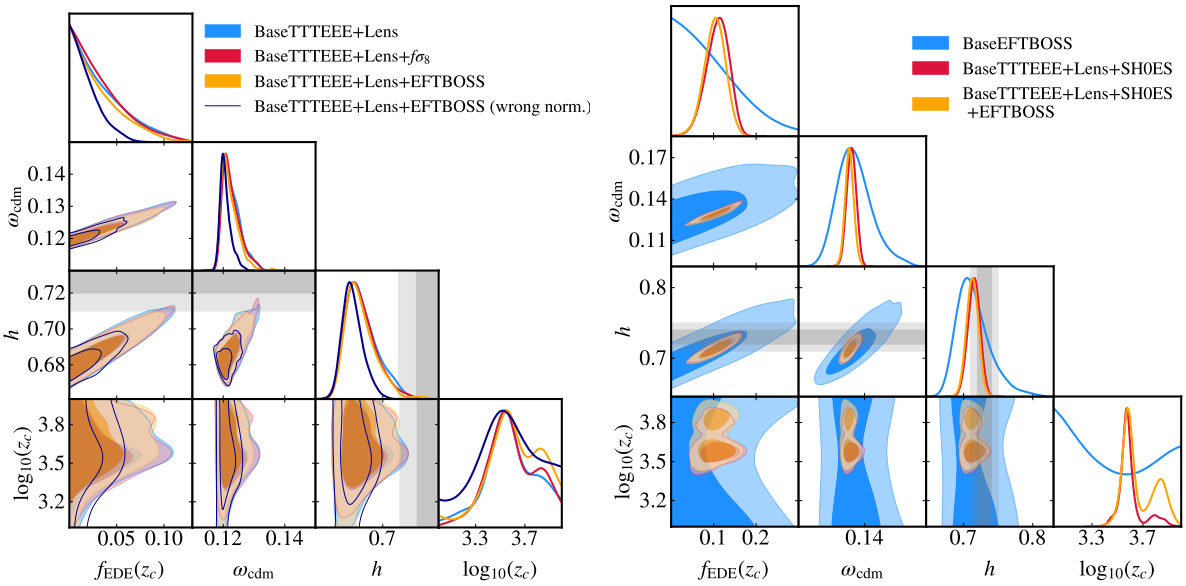

Figure 7.7: *Left panel:* 2D posterior distributions from BaseTTTEEE+Lens, BaseTTTEEE+Lens+$f\sigma_8$, and BaseTTTEEE+Lens+EFTBOSS. We also show the results from the EFTBOSS data with a wrong normalization for comparison. *Right panel:* 2D posterior distributions from BaseEFTBOSS and BaseTTTEEE+Lens+SH0ES, with and without EFTBOSS data. We recall that BaseTTTEEE refers to *Planck*TTTEE+BAO+Pan18, while BaseEFTBOSS refers to EFTBOSS+BBN+Lens+BAO+Pan18.

derived with a profile likelihood approach (*e.g.*, [188, 189]), which will be affected by our update to the survey window function calculation.

As advocated recently, we will gauge the level of the Hubble tension by computing the tension metric $Q_{\rm DMAP} \equiv \sqrt{\chi^2(\text{w/ SH0ES}) - \chi^2(\text{w/o SH0ES})}$ [352, 183], which agrees with the usual Gaussian metric tension for Gaussian posteriors, but better captures the non-Gaussianity of the posterior.

Once the SH0ES prior is included in the BaseTTTEEE+Lens+EFTBOSS analysis, we reconstruct $f_{\rm EDE}(z_c) = 0.103^{+0.027}_{-0.023}$ with $h = 0.713 \pm 0.009$ and find the tension metric $Q_{\rm DMAP} = 2.1\sigma$ (while we find 4.8σ in ΛCDM), see Tab. 7.2 and Fig. 7.7, right panel. This is only a minor difference compared to the results without BOSS $f\sigma_8$ or full-shape information, for which we get $f_{\rm EDE}(z_c) = 0.109^{+0.030}_{-0.024}$ with $h = 0.715 \pm 0.009$ and the $Q_{\rm DMAP}$ metric gives a 1.9σ tension between SH0ES and other datasets. [16] Similarly, when the $f\sigma_8$ information is included, we find a 2.0σ tension with $f_{\rm EDE}(z_c) = 0.102^{+0.030}_{-0.024}$ and $h = 0.712 \pm 0.009$.

Analyses with `CLASS-PT` are presented in App. D.2, and similar results are found. Therefore, current full-shape EFTBOSS data provide little additional constraining power ($\sim 10\%$) on the EDE model over *Planck* and $f\sigma_8$. We conclude that the EFTBOSS data are in agreement with the model reconstructed when including a SH0ES prior, as the preliminary study suggested, and BOSS data do not exclude the EDE resolution to the Hubble tension.

[16] This is different than what was reported in Ref. [183], because of an updated H_0 prior with tighter error bars.

	BaseTTTEEE+Lens		BaseTTTEEE+Lens+$f\sigma_8$		BaseTTTEEE+Lens+EFTBOSS	
H_0 prior?	no	yes	no	yes	no	yes
$f_{\rm EDE}(z_c)$	$< 0.091 (0.088)$	$0.109(0.122)^{+0.030}_{-0.024}$	$< 0.088 (0.057)$	$0.102(0.118)^{+0.030}_{-0.024}$	$< 0.083 (0.082)$	$0.103(0.116)^{+0.027}_{-0.023}$
$\log_{10}(z_c)$	unconstrained (3.55)	$3.599(3.568)^{+0.029}_{-0.081}$	unconstrained (3.78)	$3.603(3.569)^{+0.037}_{-0.11}$	unconstrained (3.82)	$3.67(3.83)^{+0.21}_{-0.15}$
θ_i	unconstrained (2.8)	$2.65(2.73)^{+0.22}_{-0.025}$	unconstrained (2.94)	$2.58(2.76)^{+0.33}_{+0.034}$	unconstrained (2.9)	$2.73(2.89)^{+0.19}_{-0.065}$
h	$0.688(0.706)^{+0.006}_{-0.011}$	$0.715(0.719) \pm 0.009$	$0.687(0.694)^{+0.006}_{-0.011}$	$0.712(0.718) \pm 0.009$	$0.687(0.700)^{+0.006}_{-0.011}$	$0.713(0.715) \pm 0.009$
$\omega_{\rm cdm}$	$0.1227(0.1281)^{+0.0018}_{-0.0036}$	$0.1303(0.1319) \pm 0.0035$	$0.1227(0.1246)^{+0.0016}_{-0.0036}$	$0.1296(0.1314) \pm 0.0035$	$0.1221(0.1269)^{+0.0015}_{-0.0033}$	$0.1288(0.1297) \pm 0.0032$
$10^2\omega_b$	$2.258(2.266)^{+0.018}_{-0.020}$	$2.283(2.303) \pm 0.020$	$2.258(2.266)^{+0.017}_{-0.021}$	$2.282(2.279) \pm 0.021$	$2.257(2.275)^{+0.017}_{-0.020}$	$2.287(2.301) \pm 0.023$
$10^9 A_s$	$2.122(2.135) \pm 0.032$	$2.153(2.145) \pm 0.032$	$2.119(2.119)^{+0.029}_{-0.033}$	$2.146(2.164) \pm 0.031$	$2.113(2.120) \pm 0.032$	$2.144(2.144) \pm 0.032$
n_s	$0.9734(0.9823)^{+0.0053}_{-0.0076}$	$0.9883(0.9895) \pm 0.0060$	$0.9730(0.9809)^{+0.0048}_{-0.0074}$	$0.9868(0.9899) \pm 0.0062$	$0.9715(0.9827)^{+0.0049}_{-0.0076}$	$0.9867(0.9921) \pm 0.0065$
$\tau_{\rm reio}$	$0.0570(0.0574)^{+0.0069}_{-0.0076}$	$0.0582(0.0579) \pm 0.0075$	$0.0564(0.0553) \pm 0.0072$	$0.0572(0.059) \pm 0.0073$	$0.0562(0.0553) \pm 0.0073$	$0.0586(0.0599)^{+0.0068}_{-0.0076}$
S_8	$0.831(0.839)^{+0.011}_{-0.013}$	$0.839(0.843) \pm 0.012$	$0.831(0.833)^{+0.011}_{-0.012}$	$0.838(0.843) \pm 0.013$	$0.826(0.836) \pm 0.011$	$0.833(0.835) \pm 0.012$
Ω_m	$0.3084(0.3041) \pm 0.0058$	$0.3008(0.3005) \pm 0.0048$	$0.3089(0.3074) \pm 0.0054$	$0.3019(0.3003) \pm 0.0051$	$0.3077(0.3065) \pm 0.0054$	$0.2998(0.3004) \pm 0.0050$
total $\chi^2_{\rm min}$	3799.2	3802.9	3801.8	3806.1	3912.7	3917.3
$\Delta\chi^2_{\rm min}$	-3.8	-23.7	-3.9	-23.0	-4.7	-22.7
$Q_{\rm DMAP}$	1.9σ		2.0σ		2.1σ	

Table 7.2: Mean (best-fit) $\pm 1\sigma$ (or 2σ for one-sided bounds) of reconstructed parameters in the EDE model confronted to various datasets, including *Planck*TTTEEE.

	BaseTT650TEEE+ACT	BaseTT650TEEE+ACT +$f\sigma_8$	BaseTT650TEEE+ACT +EFTBOSS	BaseTT650TEEE+ACT +Lens+EFTBOSS
$f_{\rm EDE}(z_c)$	$0.128(0.159)^{+0.064}_{-0.039}$	$0.116(0.148)^{+0.059}_{-0.046}$	$0.093(0.148)^{+0.047}_{-0.066}$	$< 0.172 (0.148)$
$\log_{10}(z_c)$	$3.509(3.521)^{+0.048}_{-0.033}$	$3.505(3.514)^{+0.056}_{-0.049}$	$3.493(3.514)^{+0.080}_{-0.093}$	$3.486(3.514)^{+0.091}_{-0.13}$
θ_i	$2.63(2.77)^{+0.24}_{+0.023}$	$2.53(2.78)^{+0.37}_{+0.094}$	$2.54(2.78)^{+0.47}_{0.065}$	$2.41(2.78)^{+0.65}_{0.12}$
h	$0.723(0.733)^{+0.021}_{-0.017}$	$0.718(0.728) \pm 0.018$	$0.713(0.730)^{+0.017}_{-0.021}$	$0.708(0.725)^{+0.015}_{-0.022}$
$\omega_{\rm cdm}$	$0.1332(0.1369)^{+0.0071}_{-0.0059}$	$0.1320(0.1355) \pm 0.0062$	$0.1285(0.1355)^{+0.0057}_{-0.0067}$	$0.1276(0.1355)^{+0.0047}_{-0.0074}$
$10^2\omega_b$	$2.268(2.267) \pm 0.019$	$2.266(2.261) \pm 0.020$	$2.265(2.266) \pm 0.020$	$2.263(2.265) \pm 0.019$
$10^9 A_s$	$2.144(2.148) \pm 0.037$	$2.136(2.144) \pm 0.038$	$2.128(2.147) \pm 0.040$	$2.127(2.143) \pm 0.034$
n_s	$0.9928(0.9963)^{+0.0092}_{-0.0078}$	$0.9910(0.9936)^{+0.0090}_{-0.0081}$	$0.9885(0.9936) \pm 0.0091$	$0.9865(0.9936) \pm 0.0086$
$\tau_{\rm reio}$	$0.0520(0.0508) \pm 0.0077$	$0.0511(0.0506) \pm 0.0079$	$0.0519(0.0506) \pm 0.0077$	$0.0523(0.0506) \pm 0.0072$
S_8	$0.842(0.846) \pm 0.016$	$0.841(0.845) \pm 0.017$	$0.830(0.838) \pm 0.016$	$0.831(0.837)^{+0.013}_{-0.014}$
Ω_m	$0.2996(0.2982)^{+0.0061}_{-0.0072}$	$0.3013(0.2995) \pm 0.0068$	$0.2990(0.2995) \pm 0.0069$	$0.3008(0.2995) \pm 0.0059$
total $\chi^2_{\rm min}$	3571.9	3575.8	3688.3	3698.4
$\Delta\chi^2$(EDE$-\Lambda$CDM)	-14.6	-13.3	-12.0	-11.1

Table 7.3: Mean (best-fit) $\pm 1\sigma$ (or 2σ for one-sided bounds) of reconstructed parameters in the EDE model confronted to various datasets, including *Planck*TT650TEEE+ACT.

7.3.2 EFTBOSS+*Planck*TT650TEE+ACT

We now turn to the combination of *Planck* data with ACT. We start with a restricted version of *Planck* temperature data at $\ell < 650$ (chosen to mimic WMAP and perform a consistency test between CMB datasets), combined with *Planck* polarization and ACT data. This data combination [17] is known to favor [18] EDE at $\sim 3\sigma$ [340, 341, 342, 343], with large values of $f_{\rm EDE}(z_c) = 0.128^{+0.064}_{-0.039}$ and $h = 0.723^{+0.021}_{-0.017}$ (see Tab. 7.3, first column). In Ref. [343], it was shown that BOSS $f\sigma_8$ and *Planck* lensing data decreased the preference [19] to 2.6σ. We now test whether the EFT analysis of BOSS data can put further pressure on this hint of EDE, as our preliminary study indicates. All relevant χ^2 statistics are given in App. D.3, Tab. D.3, while we give the reconstructed posteriors of parameters in Tab. 7.3. We show in Fig. 7.8 (left panel) the 2D posterior distribution $\{f_{\rm EDE}(z_c), \omega_{\rm cdm}, h, \log_{10}(z_c)\}$ reconstructed from the analysis of BaseTT650TEEE+ACT compared with that reconstructed with the addition of either $f\sigma_8$ or

[17] The preference persists until *Planck*TT data at $\ell \gtrsim 1300$ are included, while the inclusion of SPT-3G TEEE data has little impact (in fact, slightly strengthening the hint of EDE) [343].

[18] As discussed by the ACT Collaboration [340], it is still a possibility that the apparent preference for EDE arises from remaining systematic errors in the data.

[19] In the following, the preference is computed assuming the $\Delta\chi^2$ follows a χ^2 distribution with three degrees of freedom. We stress that this is just an approximation, as the true number of degrees of freedom is more complicated to estimate due to $\log_{10}(z_c)$ and θ_i becoming ill defined when $f_{\rm EDE} \to 0$.

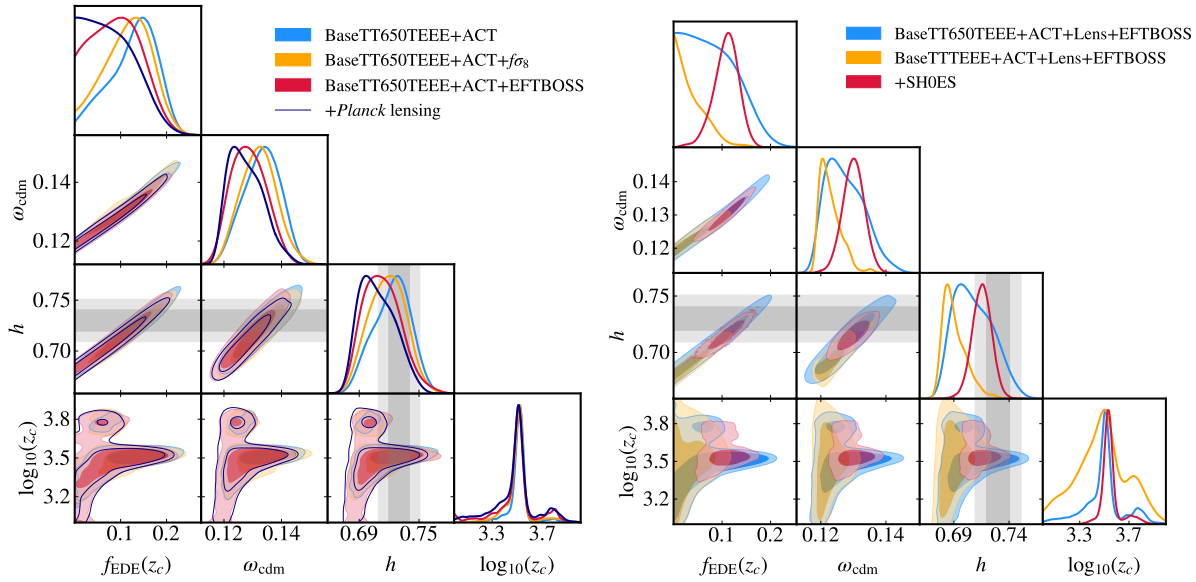

Figure 7.8: *Left Panel:* 2D posterior distributions from BaseTT650TEEE+ACT in combination with $f\sigma_8$, EFTBOSS, and *Planck* lensing. We recall that BaseTT650TEEE refers to *Planck*TT650TEEE+BAO+Pan18 data. *Right Panel:* 2D posterior distributions from ACT+Lens+EFTBOSS in combination with either BaseTT650TEEE or BaseTTTEEEE with and without SH0ES.

EFTBOSS data.

One can see that, in this case, the EFTBOSS data do reduce the preference for EDE, with $f_{\rm EDE}$ now compatible with zero at 1σ. For the BaseTT650TEEE +ACT+Lens+EFTBOSS dataset, represented by the dark blue line on Fig. 7.8 (left panel), we find a weak upper limit $f_{\rm EDE} < 0.172$ and $h = 0.708^{+0.015}_{-0.022}$, with best-fit values $f_{\rm EDE} \simeq 0.148$ and $h \simeq 0.725$ in good agreement with the SH0ES determination. Quantifying the preference over ΛCDM, we find a $\Delta\chi^2 = -11.1$ in favor of EDE (2.5σ), decreased from -14.6 without EFTBOSS and *Planck* lensing data. The χ^2 of EFTBOSS data is degraded by $+1.7$ in the EDE model compared to ΛCDM, while the improvement in the fit of ACT and *Planck*TT650TEEE is fairly stable, with $\Delta\chi^2({\rm ACT}) = -7.6$ and $\Delta\chi^2(\textit{Planck}{\rm TT650TEEE}) = -6.1$, respectively. Additionally, we note that, for this more extreme EDE model, the full EFTBOSS data provide stronger constraints than the conventional BAO/$f\sigma_8$ data. Although current data do not fully erase the preference for EDE over ΛCDM, this confirms that BOSS data, and more generally measurement of the matter power spectrum in the late Universe, provide an important probe of large EDE fraction in the early Universe. We find similar results with `CLASS-PT` (see App. D.2 for details), attesting that once BOSS data are combined with CMB data, the results obtained are robust to reasonable choices in the EFT analysis.

7.3.3 EFTBOSS+*Planck*TTTEE+ACT

Except for consistency tests, there are no good reasons to remove part of the high-ℓ *Planck* TT data. In the following, we present results of combined analyses of *Planck*TTTEEE+ACT+EFTBOSS (*i.e.*, including full *Planck* data) in Tab. 7.4 and Fig. 7.8 (right panel). All relevant χ^2 statistics are given in App. D.3, Tab. D.4. We quantify the

	BaseTTTEEE+ACT+Lens+EFTBOSS	
H_0 prior?	no	yes
$f_{\rm EDE}(z_c)$	$< 0.110 (0.074)$	$0.108(0.124)^{+0.028}_{-0.021}$
$\log_{10}(z_c)$	$3.48(3.51) \pm 0.21$	$3.552(3.531)^{+0.026}_{-0.065}$
θ_i	unconstrained	$2.77(2.81)^{+0.13}_{-0.070}$
h	$0.691(0.7)^{+0.006}_{-0.013}$	$0.715(0.72) \pm 0.009$
$\omega_{\rm cdm}$	$0.1229(0.1267)^{+0.0017}_{-0.0042}$	$0.1300(0.1322)^{+0.0035}_{-0.0031}$
$10^2\omega_b$	$2.247(2.248)^{+0.015}_{-0.017}$	$2.260(2.255) \pm 0.018$
$10^9 A_s$	$2.126(2.133)^{+0.028}_{-0.032}$	$2.153(2.156) \pm 0.030$
n_s	$0.9758(0.9795)^{+0.0049}_{-0.0080}$	$0.9873(0.9893) \pm 0.0058$
$\tau_{\rm reio}$	$0.0540(0.0534) \pm 0.0070$	$0.0548(0.0539) \pm 0.0070$
S_8	$0.829(0.843)^{+0.010}_{-0.012}$	$0.837(0.843) \pm 0.012$
Ω_m	$0.3061(0.3052) \pm 0.0054$	$0.2997(0.3) \pm 0.0047$
total $\chi^2_{\rm min}$	4157.6	4159.8
$\Delta\chi^2_{\rm min}$(EDE $-$ ΛCDM)	-6.4	-26.1
$Q_{\rm DMAP}$	1.5σ	

Table 7.4: Mean (best-fit) $\pm 1\sigma$ (or 2σ for one-sided bounds) of reconstructed parameters in the EDE model confronted to BaseTTTEEE+ACT+Lens+EFTBOSS, with and without SH0ES.

residual tension with SH0ES using the $Q_{\rm DMAP}$ metric introduced previously. In that case, we find that the preference for EDE without SH0ES is strongly reduced, in agreement with previous works, but the 2σ upper limit on $f_{\rm EDE} < 0.110$ is much weaker than in the BaseTTTEEE+Lens+EFTBOSS analysis presented previously, $f_{\rm EDE} < 0.083$. As a result, the tension metric between BaseTTTEEE+ACT+Lens+EFTBOSS and SH0ES is released to 1.5σ compared to 4.7σ in ΛCDM (and 2.1σ without ACT data). When the SH0ES prior is included, we find $f_{\rm EDE} = 0.108^{+0.028}_{-0.021}$ and $h = 0.715 \pm 0.009$ (in very good agreement with the results presented earlier without ACT), with no degradation in the χ^2 of EFTBOSS. This confirms that the EFTBOSS data can accommodate the amount of EDE required to resolve the Hubble tension (with $f_{\rm EDE} \sim 0.1$ and $h \sim 0.72$), but constrain more extreme EDE contributions.

7.3.4 Impact of Pantheon+ data

To finish, we perform an analysis with the new Pantheon+ SNIa catalog [132], which is known to favor a higher $\Omega_m = 0.338 \pm 0.018$, to illustrate the impact that these new data have on the EDE model. We perform analyses of four datasets in combination with Pantheon+, following our baseline data, namely, BaseEFTBOSS, BaseTTTEEE+Lens+EFTBOSS(+SH0ES), and BaseTT650TEEE+ACT+Lens+EFTBOSS. The results of these analyses are presented in Tab. 7.5 and in Fig. 7.9, while all relevant χ^2 statistics are given in App. D.3, Tab. D.5. First, without information from the primary CMB, we find that the combination of EFTBOSS+BBN+Lens+BAO+PanPlus (*i.e.*, BaseEFTBOSS+PanPlus) leads to a weak constraint on $f_{\rm EDE}(z_c) < 0.228$ with $h = 0.717^{+0.015}_{-0.026}$ in good agreement with SH0ES. In fact, even within ΛCDM we find $h = 0.694^{+0.012}_{-0.014}$, which is not in significant tension with SH0ES. This data combination was recently argued to constrain new physics solution to the Hubble tension that affects the sound horizon, due to the fact that measurement of h based on the scale of matter-radiation equality $k_{\rm eq}$ (which can be extracted by marginalizing over the sound horizon

	BaseEFTBOSS +PanPlus	BaseTTTEEE+Lens +EFTBOSS+PanPlus	BaseTTTEEE+Lens +EFTBOSS+PanPlus+SH0ES	BaseTT650TEEE+ACT+Lens +EFTBOSS+PanPlus
$f_{\rm EDE}(z_c)$	$< 0.228(0.01)$	$< 0.079(0.056)$	$0.123(0.141)^{+0.030}_{-0.018}$	$< 0.137(0.11)$
$\log_{10}(z_c)$	unconstrained (3.91)	$3.59(3.57)^{+0.25}_{-0.21}$	$3.64(3.57)^{+0.23}_{-0.13}$	$< 3.5(3.5)$
θ_i	unconstrained(2.98)	unconstrained(2.74)	$2.59(2.77)^{+0.31}_{+0.064}$	unconstrained(2.78)
h	$0.717(0.692)^{+0.015}_{-0.026}$	$0.684(0.692)^{+0.006}_{-0.001}$	$0.719(0.724)^{+0.009}_{-0.008}$	$0.700(0.714)^{+0.013}_{-0.019}$
$\omega_{\rm cdm}$	$0.142(0.131)^{+0.010}_{-0.014}$	$0.1222(0.1251)^{+0.0015}_{-0.0028}$	$0.1317(0.1346) \pm 0.0031$	$0.1258(0.1306)^{+0.0039}_{-0.0058}$
$10^{-2}\omega_b$	$2.276(0.023)^{+0.035}_{-0.039}$	$2.251(2.254) \pm 0.018$	$2.291(2.275)^{+0.020}_{-0.024}$	$2.258(2.259) \pm 0.019$
$10^9 A_s$	$1.88(1.929)^{+0.16}_{-0.20}$	$2.114(2.148) \pm 0.029$	$2.155(2.157)^{+0.030}_{-0.036}$	$2.120(2.135) \pm 0.033$
n_s	$0.873(0.889) \pm 0.049$	$0.9700(0.9752)^{+0.0046}_{-0.0071}$	$0.9911(0.9912)^{+0.0062}_{-0.0071}$	$0.9827(0.9877) \pm 0.0081$
$\tau_{\rm reio}$	–	$0.0562(0.0558) \pm 0.0069$	$0.0582(0.0554) \pm 0.0077$	$0.0519(0.0516)^{+0.0065}_{-0.0075}$
S_8	$0.815(0.824) \pm 0.018$	$0.832(0.837) \pm 0.010$	$0.840(0.847) \pm 0.012$	$0.831(0.839)^{+0.012}_{-0.011}$
Ω_m	$0.321(0.324) \pm 0.013$	$0.3116(0.3093) \pm 0.0056$	$0.3000(0.3014) \pm 0.0047$	$0.3041(0.3016) \pm 0.0061$
total $\chi^2_{\rm min}$	1537.9	4304.0	4187.0	4085.1
$\Delta\chi^2_{\rm min(EDE\text{-}ACDM)}$	0	-1.1	-32.3	-9.2

Table 7.5: Mean (best-fit) $\pm 1\sigma$ (or 2σ for one-sided bounds) of reconstructed parameters in the EDE model confronted to various datasets, including the recent PanPlus SNIa catalog.

information [20]) is in tension with the SH0ES measurement [195, 62, 157]. In our analysis, we stress that we do not marginalize over the sound horizon in the EFTBOSS analysis. We do not expect that removing part of the data through the marginalization procedure would make BOSS data appear in strong tension with SH0ES, at least in EDE. Rather, we expect that constraints would significantly weaken. We leave for future work to test whether the determination of h from $k_{\rm eq}$ is robust to changes in the cosmological model.

When combining with *Planck*TTTEEE, we find that constraints on EDE are increased by $\sim 5\%$ with respect to the analogous analysis with Pantheon18, with $f_{\rm EDE}(z_c) < 0.079$. This can be understood by noting that the larger Ω_m favored by Pantheon+, coupled with the positive correlation between $f_{\rm EDE}(z_c) - h$, can lead to high $\omega_m = \Omega_m h^2$ which are constrained by CMB data. However, once the SH0ES cepheid calibration of SNIa is included, we find a strong preference for EDE, with $f_{\rm EDE}(z_c) = 0.123^{+0.030}_{-0.018}$ (*i.e.*, nonzero at more than 5σ) and a $\Delta\chi^2({\rm EDE} - \Lambda{\rm CDM}) = -32.3$ (compared to -22.7 with Pantheon18). The cost in χ^2 for *Planck*TTTEEE+Lens and EFTBOSS compared to the analysis without the SH0ES calibration is small, with $\chi^2(Planck)$ increasing by $+2.3$ and $\chi^2({\rm EFTBOSS})$ increasing by $+0.9$, which further attests to the non-Gaussianity of the posterior in the absence of the SH0ES calibration. The $Q_{\rm DMAP}$ tension metric introduced earlier cannot be used as easily, due to the fact that the SH0ES data are now modeled in a more involved way, making use of a correlation matrix connecting SNIa calibrators and high$-z$ SNIa [153], rather than the simple Gaussian prior on h.

Finally, when combining with *Planck* TT650TEEE and ACT, we find that the preference for EDE seen within ACT data further decreases to $\Delta\chi^2 = -9.2$ (2.2σ) and we derive a limit $f_{\rm EDE}(z_c) < 0.137$, with $h = 0.700^{+0.013}_{-0.019}$ and a $\lesssim 2\sigma$ tension with SH0ES. We defer to future work to further test the ability of EDE (and other promising models) to resolve the Hubble tension in light of this new Pantheon+ SNIa catalog.

[20] More precisely, in Refs [195, 62, 157], the marginalization over the sound horizon information is intended as a consistency test to be performed within ΛCDM.

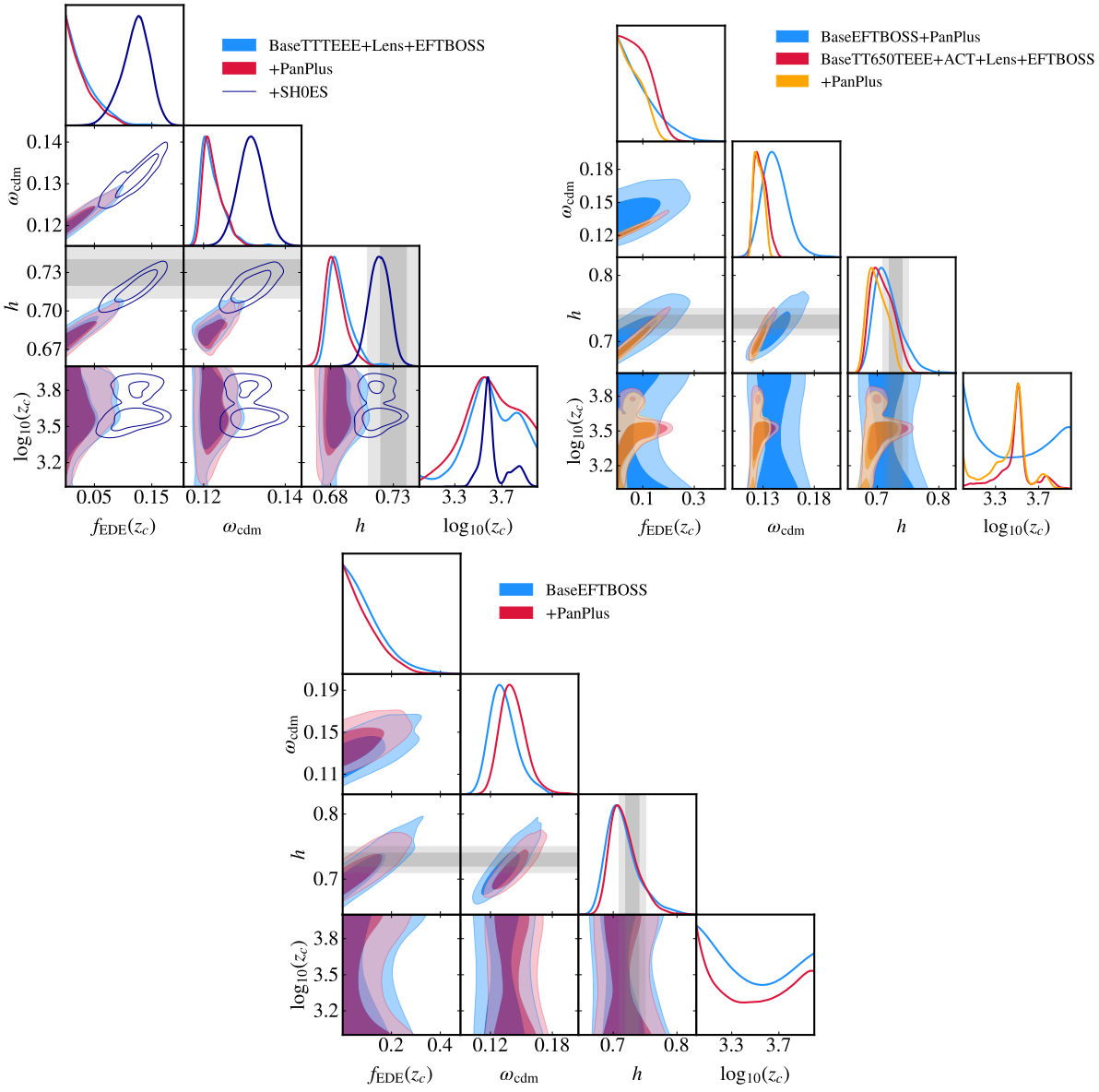

Figure 7.9: *Top left panel:* 2D posterior distributions from BaseTTTEEE+Lens+EFTBOSS in combination with either Pantheon18 or Pantheon+ data, and the SH0ES cepheid calibration. We recall that BaseTTTEEE refers to *Planck*TTTEEE+BAO+Pan18 data. *Top right panel:* 2D posterior distributions from BaseEFTBOSS and BaseTT650TEEE+ACT+Lens+EFTBOSS, in combination with either Pantheon18 or Pantheon+ data. We recall that BaseTT650TEEE refers to *Planck*TT650TEEE+BAO+Pan18 data, while BaseEFTBOSS refers to EFTBOSS+BBN+Lens+BAO+Pan18. *Bottom panel:* 2D posterior distributions from BaseEFTBOSS, with either Pantheon18 or Pantheon+ data.

7.4 Conclusions

The developments of the predictions for the galaxy clustering statistics from the EFTofLSS have made possible the study of BOSS data beyond the conventional analyses dedicated to extracting BAO and $f\sigma_8$ information. There has been in the recent literature a number of studies aiming at measuring the ΛCDM parameters at precision comparable with that of *Planck* CMB data (see, *e.g.*, Refs. [58, 97, 101, 59, 160, 103, 69, 62]). Additionally, it was shown that BOSS full-shape data, when analyzed using the one-loop predictions from the EFTofLSS (here called EFTBOSS data), can lead to strong constraints on extension to the ΛCDM model. In particular, the EDE model, currently one of the most promising models to resolve the Hubble tension [275, 183], was shown to be severely constrained by EFTBOSS data [327, 328]. However, it was subsequently argued that part of the constraints may come from a mismatch in the primordial power spectrum A_s amplitude between EFTBOSS and *Planck* [346].

Recently, it was found that the original EFTBOSS data used in these analyses were affected by an inconsistency between the normalization of the survey window function and the one of the data measurements, which led to a mismatch in A_s. A proper reanalysis of the EFTBOSS data constraints on the EDE model was lacking until now.

In this chapter, we have performed a thorough investigation of the constraints on EDE in light of the correctly normalized EFTBOSS data and estimated the shifts introduced on the reconstructed cosmological parameters and their errors between various analysis strategies. A similar analysis within the ΛCDM model is presented in Sec. 5.3 of chapter 5. Our results are summarized in the following.

7.4.1 EFTBOSS constraints on EDE alone

We have shown in Sec. 7.2.2 that, regardless of the BOSS data or the likelihood we consider, the BOSS full-shape (analyzed on their own with a BBN prior) leads to reconstructed values of H_0 that are compatible with what is obtained by the SH0ES Collaboration. Yet, the various EFTBOSS measurements, as well as the `PyBird` and `CLASS-PT` likelihoods, do not have the same constraining power on EDE:

- When using the `PyBird` likelihood, we found $f_{\rm EDE}(z_c) < 0.321$ when analyzing $P_{\rm FKP}^{\rm LZ/CM} + \alpha_{\rm rec}^{\rm LZ/CM}$, while analyzing $P_{\rm QUAD}^{z_1/z_3} + \alpha_{\rm rec}^{z_1/z_3}$ yields $f_{\rm EDE}(z_c) < 0.382$, a $\sim 20\%$ difference.

- When using the same BOSS data, namely, $P_{\rm QUAD}^{z_1/z_3}$, we have found that the `PyBird` likelihood gives $f_{\rm EDE}(z_c) < 0.382$, while the `CLASS-PT` likelihood gives $f_{\rm EDE}(z_c) < 0.448$, *i.e.*, a $\sim 15\%$ difference.

- Restricting our analysis to the range of critical redshift $\log_{10}(z_c) \in [3.4, 3.7]$ that can resolve the Hubble tension, we have shown that the combination of EFTBOSS+BBN+Lens+BAO+Pan18, leads to the constraints $f_{\rm EDE}(z_c) < 0.2$ (95% C.L.) and $h = 0.710^{+0.015}_{-0.025}$, which does not exclude the EDE models resolving the Hubble tension.

- The inclusion of the recent Pantheon+ data does not affect this conclusion as we find $h = 0.717^{+0.015}_{-0.026}$. We do not expect that marginalizing over the sound horizon as done in Refs. [195, 62, 157] would alter our conclusions, as it would simply remove information from the data. This question will be thoroughly explored elsewhere.

7.4.2 *Planck*+EFTBOSS constraints on EDE

In combination with *Planck* TTTEEE data, we have shown that constraints on EDE have changed due to the correction of the normalization of the window function:

- The combination of *Planck*TTTEEE+Lens+BAO +Pan18+EFTBOSS leads to $f_{\rm EDE}(z_c) < 0.083$, which is a $\sim 10\%$ improvement over the constraints without BOSS data and a $\sim 5\%$ improvement over the constraints with conventional BAO/$f\sigma_8$ data. Yet, this is much weaker than the constraints reported with the incorrect normalization, namely, $f_{\rm EDE} < 0.054$. We quantify that the Hubble tension is reduced to the 2.1σ level in the EDE cosmology (1.9σ without EFTBOSS) compared to 4.8σ in the ΛCDM model, and we find $f_{\rm EDE}(z_c) = 0.103^{+0.027}_{-0.023}$ at $z_c = 3970^{+255}_{-205}$ when the SH0ES prior is included.

- Replacing Pantheon18 by the new Pantheon+ data improves the constraints on EDE to $f_{\rm EDE}(z_c) < 0.079$. Yet, the inclusion of the SH0ES cepheid calibration leads to $f_{\rm EDE}(z_c) = 0.123^{+0.030}_{-0.018}$ at $z_c = 4365^{+3000}_{-1100}$, *i.e.*, a nonzero $f_{\rm EDE}(z_c)$ at more than 5σ with $\Delta\chi^2({\rm EDE}-\Lambda{\rm CDM}) = -32.3$. The cost in χ^2 for *Planck*TTTEEE+Lens and EFTBOSS compared to the analysis without the SH0ES calibration is small, with $\chi^2(Planck)$ increasing by $+2.3$ and $\chi^2({\rm EFTBOSS})$ increasing by $+0.9$, which attests to the non-Gaussianity of the posterior in the absence of the SH0ES calibration. This deserves to be studied further through a profile likelihood approach [188, 189].

7.4.3 ACT+EFTBOSS constraints on EDE

Finally, we have studied the impact of EFTBOSS data on the recent hints of EDE observed within ACT DR4 data:

- EFTBOSS reduces the preference for EDE over ΛCDM seen when analyzing ACT DR4, alone or in combination with restricted *Planck*TT data. The combination of *Planck*TT650TEEE+Lens+BAO+Pan18+ACT+EFTBOSS leads to a mild constraints on $f_{\rm EDE}(z_c) < 0.172$ with $\Delta\chi^2({\rm EDE}-\Lambda{\rm CDM}) = -11.1$, to be compared with $f_{\rm EDE}(z_c) = 0.128^{+0.064}_{-0.039}$ without EFTBOSS+Lens, with $\Delta\chi^2({\rm EDE}-\Lambda{\rm CDM}) = -14.6$.

- The inclusion of Pantheon+ data further restricts $f_{\rm EDE}(z_c) < 0.137$, with $\Delta\chi^2({\rm EDE}-\Lambda{\rm CDM}) = -9.2$.

- When full *Planck* data are included, we derived a constraint $f_{\rm EDE}(z_c) < 0.110$, which is $\sim 30\%$ weaker than without ACT data. When all CMB data are included in combination with EFTBOSS, the Hubble tension is reduced to 1.5σ in the EDE model, to be compared with 4.7σ in ΛCDM. The inclusion of the SH0ES prior leads to $f_{\rm EDE}(z_c) = 0.108^{+0.028}_{-0.021}$ at $z_c = 3565^{+220}_{-495}$.

We conclude that EFTBOSS data do not exclude EDE as a resolution to the Hubble tension, where we consistently find $f_{\rm EDE}(z_c) \sim 10-12\%$ at $z_c \sim 3500-4000$, with $h \sim 0.72$, when

the cepheid calibration is included in the analyses. However, EFTBOSS data do constrain very high EDE fraction as seen when analyzing ACT DR4 data.

7.4.4 Final comments

There are a number of relevant caveats to stress regarding our analyses. First, we note that the reconstructed S_8 values from the various analyses that favor EDE are $\sim 2.8-3.2\sigma$ higher than those coming from weak lensing measurement (and their cross-correlation with galaxy clustering) such as DES [79] and KiDS [177]. As was already pointed out in the past, this indicates that weak lensing data (and the existence of a S_8 tension) could be used to further restrict the existence of EDE. Nevertheless, it has been noted that solutions to the S_8 tension may be due to systematic effects [116] or nonlinear modeling including the effect of baryons at very small scales [200] or to a more complete dynamics in the dark sector [353, 354]. In fact, models that resolve the S_8 tension leave the EDE resolution unaffected [335, 355] such that, although perhaps theoretically unappealing, it is possible that solutions to the H_0 and S_8 lie in different sectors. We leave for future work a robust study of EDE in light of the combination of EFTBOSS and weak lensing data, which will require better handling of the modeling of physical effects at scales beyond the range of validity of our EFT. Second, it will be very important to extend this work to include the bispectrum, which was recently analyzed at the one-loop level within ΛCDM [95, 108]. Additional constraints on EDE may also arise from measurements of the age of old objects such as globular clusters of stars [356, 357], or the halo mass function at high$-z$ [358]. Interestingly, using N-body simulations, Ref. [358] showed that EDE predicts 50% more massive clusters at $z = 1$ and twice more galaxy-mass halos at $z = 4$ than ΛCDM. These predictions can be tested by observations from the James Webb Space Telescope and the first publicly available data are, in part, better fit by EDE than ΛCDM [359].

To close this work, we mention that we find here in agreement with previous literature, that the cosmological data including SH0ES prefer a higher value for the spectral tilt n_s in the EDE model than in ΛCDM, with $n_s \sim 1$ allowed at $\lesssim 2\sigma$ depending on the combination of data considered. Of interest here, we see that the inclusion of EFTBOSS data does not significantly pull back n_s to lower value, and when analyzed alone (with a BBN prior) also independently favors a value of n_s consistent with scale independence at $\sim 1\sigma$. A value of n_s close to that of the Harrison–Zeldovich spectrum, when put in perspective of CMB measurements of the tensor-to-scalar ratio, would dramatically change the status of the preferred inflationary models [360] (see also Refs. [361, 362, 363]). Therefore, if EDE is firmly detected with future cosmological data, beyond serving as resolution of the H_0 tension, it would also have important consequences for early Universe physics.

It should be noted that a similar analysis was subsequently carried out using eBOSS data in Ref. [364] (of which I am one of the authors).

VIII

EFTofLSS' take on the Hubble tension and the acoustic dark energy

Contents

8.1 The model and the data **230**
8.1.1 Review of the ADE model 230
8.1.2 Review of the axion-like EDE model 232
8.1.3 Data and analysis methods 233
8.2 Cosmological results **235**
8.2.1 Impact of the EFTofLSS analysis 236
8.2.2 Impact of the Pantheon+ data 238
8.3 Model variations **241**
8.3.1 Variation of c_s^2 241
8.3.2 The cADE model 243
8.4 Conclusions **243**

This chapter is based on:

T. Simon, *Can acoustic early dark energy still resolve the Hubble tension?*, **submitted to Phys. Rev. D**, arXiv:2310.16800.

In this chapter, we reassess the constraints on the acoustic dark energy (ADE) and axion-like EDE models (paying particular attention to the former) and their ability to resolve the Hubble tension, by successively evaluating the impact of the effective field theory (EFT) full-shape analysis applied to the BOSS LRG [81] and eBOSS QSO [82] data, and the impact of the Pantheon+ data [132]. On the one hand, we make use of developments of the one-loop prediction of the galaxy power spectrum in redshift space from the effective field theory of large-scale structures (EFTofLSS) applied to the BOSS [58] and eBOSS [117] data (see chapter 4) in order to constrain the ADE model. This study is similar to what was carried out for the axion-like EDE in chapter 7 (see also Refs. [327, 346, 328]), which showed that this latter model leaves signatures in the galaxy power spectrum on large scales that can be probed by the BOSS data. On the other hand, we update the constraints on the ADE model by considering the Pantheon+ data from Ref. [132]. It has already been shown in chapter 7 that the combination of the Pantheon+ data with a SH0ES prior provides better constraints on the axion-like EDE model than the equivalent analysis including Pantheon data. This can be interpreted as a consequence of the fact that the Pantheon+ data prefers a value of $\Omega_m = 0.334 \pm 0.018$ which is higher than that of the Pantheon data. Together with the measured value of $H_0 = 100 \cdot h$ km/s/Mpc by SH0ES, it leads to an increased value of $\omega_{\rm cdm} = \Omega_{\rm cdm} \cdot h^2$ (see Ref. [365]), which cannot be fully compensated by the presence of EDE, therefore degrading slightly the fit to CMB data.

In Sec. 8.1, we provide a review of the ADE and axion-like EDE models, as well as a description of the analysis method and the datasets to which these models will be subjected. In Sec. 8.2, we present the constraints of the ADE model and compare them to the axion-like EDE case, while in Sec. 8.3 we consider some additional variations of the model under study. In Apps. E.1 and E.2, we provide additional material.

8.1 The model and the data

8.1.1 Review of the ADE model

In this chapter, we focus on the acoustic dark energy (ADE) model proposed in Ref. [337] (see Ref. [280] for a general introduction). In this model, the ADE equation of state parameter, $w_{\rm ADE}(a) = P_{\rm ADE}(a)/\rho_{\rm ADE}(a)$, is modelled as

$$w_{\rm ADE}(a) = \frac{1+w_f}{\left[1+(a_c/a)^{3(1+w_f)/p}\right]^p} - 1\,. \tag{8.1}$$

In Fig. 8.1, we plot the evolution of $w_{\rm ADE}$ as a function of the cosmological redshift z. This figure clearly illustrates that in this model the critical redshift $z_c = (a_0 - a_c)/a_c$ sets a transition in the ADE equation of state from $w_{\rm ADE} \to -1$, when $z \gg z_c$, to $w_{\rm ADE} \to w_f$, when $z \ll z_c$. Therefore, this parametrization allows the ADE component to behave in a similar way to dark energy before the critical redshift (exactly like the axion-like EDE model), while it allows the late-time value of the ADE equation of state to be set thanks to the parameter w_f. As shown in Fig. 8.1, the rapidity of this transition is controlled by the parameter p, which is set at $p = 1$ for our baseline model, corresponding to the modelling of the time averaged background equation of state of the axion-like EDE model [349]. Similarly to the axion-like EDE case where $w_{\rm EDE}(z \ll z_c) = 1/2$ (see chapter 7), the ADE dilutes faster than the radiation (*i.e.*, $w_f > w_r$)

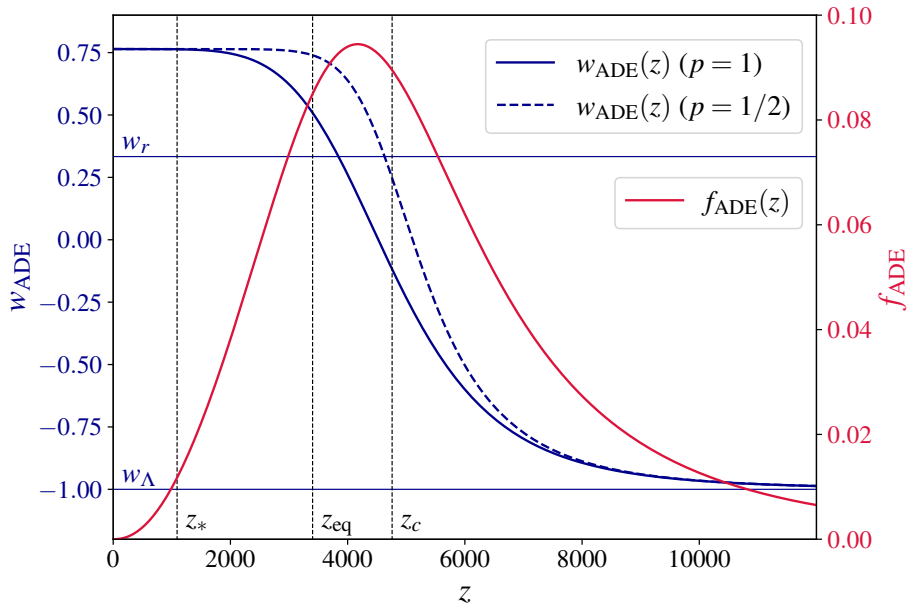

Figure 8.1: Evolution of the ADE equation of state parameter, $w_{\rm ADE}$, as well as the ADE fractional energy density, $f_{\rm ADE}(z_c)$, as a function of the cosmological redshift z. To perform this plot, we use the best-fit values of the BAO/$f\sigma_8$ + Pan + M_b analysis (see Tab. 8.1). For the ADE equation of state parameter, we set $p = 1$, which corresponds to our baseline setup, and $p = 1/2$, which corresponds to the setup of Ref. [337]. The horizontal lines correspond to the radiation and dark energy equation of state parameters, w_r and w_Λ, respectively, while the dashed vertical lines correspond to the redshift of recombination z_*, the redshift of the matter-radiation equality $z_{\rm eq}$, and the ADE critical redshift z_c.

below the critical redshift, in order to suppress the contribution of this component to the total budget of the Universe at the moment of the CMB.

Let us note that the parametrization of Eq. (8.1) can be achieved in the K-essence class of dark energy models. In particular, the dark component is here a perfect fluid represented by a minimally-coupled scalar field ϕ with a general kinetic term [366]. For the specific case of a constant sound speed c_s^2, the Lagrangian density is written as [367]:

$$P(X,\phi) = \left(\frac{X}{A}\right)^{\frac{1-c_s^2}{2c_s^2}} X - V(\phi)\,, \tag{8.2}$$

where $X = -\nabla^2\phi/2$ and A is a constant density scale [337]. In this category of models, $w_{\rm ADE} \to c_s^2$ if the kinetic term dominates, whereas $w_{\rm ADE} \to -1$ if the potential $V(\phi)$ dominates. The main advantage of the ADE model over the axion-like EDE model is that the former provides a general class of exact solutions, while the latter requires a specific set of initial conditions to achieve a similar phenomenology [337].

Since the ADE equation of state parameter changes over time, the conservation equation gives

$$\rho_{\rm ADE}(a) = \rho_{\rm ADE,0} e^{3\int_a^1 [1+w_{\rm ADE}(a')]da'/a'}\,, \tag{8.3}$$

which allows us to define the ADE fractional energy density as

$$f_{\rm ADE}(a) = \frac{\rho_{\rm ADE}(a)}{\rho_{\rm tot}(a)}\,. \tag{8.4}$$

In Fig. 8.1, we also plot the evolution of $f_{\rm ADE}$ as a function of the cosmological redshift z. We notice that this parameter is maximal around the ADE equation of state transition, sets by the critical redshift z_c, namely when $f_{\rm ADE}(z \sim z_c)$. Then, this parameter becomes subdominant at the time of recombination, with $f_{\rm ADE}(z_*) \sim 1\%$ [368].

Finally, the ADE model we are considering is described by the three following parameters

$$\{z_c, f_{\rm ADE}(z_c), w_f\}\,. \tag{8.5}$$

Ref. [337] also considers the variation of a fourth parameter that determines the behavior of the ADE perturbations, namely their rest frame sound speed $c_s^2(k,a)$. Unlike the standard axion-like EDE model (see bellow), we assume for this model the scale independence of this parameter, *i.e.*, $c_s^2(k,a) = c_s^2(a)$, which is equivalent to assuming a perfect fluid with a linear dispersion relation. In addition, because of the sharp transition of the $w_{\rm ADE}$ parameter, the impact of the ADE component on the perturbed universe is localised in time, which implies that we can approximate this parameter as a constant. Thus, Ref. [337] varies this parameter to its critical redshift value, namely $c_s^2 = c_s^2(a = a_c)$, in addition to the three other parameters listed above. In our baseline model, we consider that $c_s^2 = w_f$, insofar as it has been shown to be a good approximation near the best-fit [337]. However, in Sec. 8.3, we consider two model variations of our baseline model: (i) the c_s^2ADE model, where we free these two parameters independently, and (ii) the cADE model, where we set $c_s^2 = w_f = 1$. Let us note that it exists a second difference between Refs. [337, 369] and our baseline analysis, since these references set $p = 1/2$, which leads to a sharper transitions than ours (with $p = 1$), as shown in Fig. 8.1. However, the impact of this parameter on cosmological results is very minor, and we have verified that we obtain the same results as Ref. [369] with $p = 1$.

8.1.2 Review of the axion-like EDE model

For comparison, we also consider the axion-like early dark energy (EDE) model [274, 275, 276] (see Sec. 7.1 of chapter 7). Let us note here that the axion-like EDE sound speed $c_s^2(a,k) = \delta P_{\rm EDE}(k,a)/\delta\rho_{\rm EDE}(k,a)$ is scale- and time-dependent, and is entirely determined by the three EDE parameters $(z_c, f_{\rm EDE}(z_c), \Theta_i)$. In the fluid approximation, one can estimate the a and k dependencies of this parameter as [349, 275]:

$$c_s^2(a,k) = \begin{cases} 1\,, & a \leq a_c\,, \\ \dfrac{2a^2(n-1)\varpi^2(a)+k^2}{2a^2(n+1)\varpi^2(a)+k^2}\,, & a > a_c\,, \end{cases} \tag{8.6}$$

where ϖ corresponds to the angular frequency of the oscillating background field, which has a time dependency fixed by z_c, n and Θ_i (see Ref. [349]). Let us note however that the axion-like EDE model we consider in this work does not rely on this fluid approximation, and instead solves the exact (linearized) Klein-Gordon equation for a scalar field, which is expressed in synchronous gauge as [41]:

$$\delta\phi_k'' + 2H\delta\phi_k' + \left[k^2 + a^2 V_{n,\phi\phi}\right]\delta\phi_k = -h'\frac{\phi'}{2}\,, \tag{8.7}$$

where the prime denotes derivatives with respect to conformal time.

8.1.3 Data and analysis methods

We perform Monte Carlo Markov Chain (MCMC) analyses, confronting the ADE model with recent cosmological observations. To do so, we make use of the Metropolis-Hastings algorithm from `MontePython-v3` [1] code [136, 137] interfaced with our modified `CLASS` [370, 221] version. [2] In this chapter, we perform various analyses from a combination of the following datasets:

- **Planck:** The low-ℓ CMB temperature and polarization auto-correlations (TT, EE), and the high-ℓ TT, TE, EE data [215], as well as the gravitational lensing potential reconstruction from *Planck* 2018 [179].
- **ext-BAO:** The low-z BAO data gathered from 6dFGS at $z = 0.106$ [127], SDSS DR7 at $z = 0.15$ [128].
- **BOSS BAO/$f\sigma_8$:** BAO measurements, cross-correlated with the redshift space distortion measurements, from the CMASS and LOWZ galaxy samples of BOSS DR12 LRG at $z = 0.38$, 0.51, and 0.61 [81].
- **eBOSS BAO/$f\sigma_8$:** BAO measurements, cross-correlated with the redshift space distortion measurements, from the CMASS and LOWZ quasar samples of eBOSS DR16 QSO at $z = 1.48$ [82].
- **EFTofBOSS:** The EFTofLSS analysis of BOSS DR12 LRG, cross-correlated with the reconstructed BAO parameters [126]. The SDSS-III BOSS DR12 galaxy sample data and covariances are described in [81, 125]. The measurements, obtained in [69], are from BOSS catalogs DR12 (v5) combined CMASS-LOWZ [124], and are divided in redshift bins LOWZ, $0.2 < z < 0.43$ ($z_{\rm eff} = 0.32$), and CMASS, $0.43 < z < 0.7$ ($z_{\rm eff} = 0.57$), with north and south galactic skies for each, respectively denoted NGC and SGC. From these data we use the monopole and quadrupole moments of the galaxy power spectrum. The theory prediction and likelihood for the full-modeling information are made available through `PyBird` [59].
- **EFTofeBOSS:** The EFTofLSS analysis (see chapter 4) of eBOSS DR16 QSOs [82]. The QSO catalogs are described in [120] and the covariances are built from the EZ-mocks described in [121]. There are about 343 708 quasars selected in the redshif range $0.8 < z < 2.2$, with $z_{\rm eff} = 1.52$, divided into two skies, NGC and SGC [122, 123]. From these data we use the monopole and quadrupole moments of the galaxy power spectrum. The theory prediction and likelihood for the full-modeling information are made available through `PyBird`.
- **Pantheon:** The Pantheon catalog of uncalibrated luminosity distance of type Ia supernovae (SNeIa) in the range $0.01 < z < 2.3$ [133].
- **Pantheon+:** The newer Pantheon+ catalog of uncalibrated luminosity distance of type Ia supernovae (SNeIa) in the range $0.001 < z < 2.26$ [132].

[1] `https://github.com/brinckmann/montepython_public`.
[2] `https://github.com/PoulinV/AxiCLASS`.

- **Pantheon+/SH_0ES:** The Pantheon+ catalog cross-correlated with the absolute calibration of the SNeIa from SH0ES [153].
- M_b: Gaussian prior from the most up-to-date late-time measurement of the absolute calibration of the SNeIa from SH0ES, $M_b = -19.253 \pm 0.027$ [153], corresponding to $H_0 = (73.04 \pm 1.04)$ km/s/Mpc.

We choose *Planck* + ext-BAO + BOSS BAO/$f\sigma_8$ + eBOSS BAO/$f\sigma_8$ + Pantheon (optionally with the M_b prior) as our baseline analysis, called, for the sake of simplicity, "BAO/$f\sigma_8$ + Pan." In order to assess the impact of the EFT full-shape analysis of the BOSS and eBOSS data on the ADE resolution of the Hubble tension, we compare the baseline analysis with an equivalent analysis that includes the EFTofBOSS and EFTofeBOSS likelihoods instead of the BOSS and eBOSS BAO/$f\sigma_8$ likelihoods. This analysis is called "EFT + Pan." Finally, in order to gauge the influence of the new Pantheon data, we replace the Pantheon likelihood with the Pantheon+ likelihood. This analysis, referred to as "EFT + PanPlus," is compared with the aforementioned EFTofLSS analysis. In App. E.1, we show explicitly that the addition of the M_b prior on top of the Pantheon+ likelihood is equivalent to the use of the full "Pantheon+/SH0ES" likelihood as provided in Ref. [153].

For all runs performed, we impose large flat priors on $\{\omega_b, \omega_{\rm cdm}, H_0, A_s, n_s, \tau_{\rm reio}\}$, which correspond, respectively, to the dimensionless baryon energy density, the dimensionless cold dark matter energy density, the Hubble parameter today, the variance of curvature perturbations centered around the pivot scale $k_p = 0.05$ Mpc^{-1} (according to the *Planck* convention), the scalar spectral index, and the reionization optical depth. Regarding the free parameters of the ADE model, we impose logarithmic flat priors on z_c, and flat priors on $f_{\rm ADE}(z_c)$ and $w_{\rm ADE}$,

$$\begin{aligned} 3 &\leq \log_{10}(z_c) \leq 4.5\,, \\ 0 &\leq f_{\rm ADE}(z_c) \leq 0.2\,, \\ 0 &\leq w_f \leq 3.6\,. \end{aligned}$$

Note that we have verified that a wider prior on w_f does not impact our results. When we compare the ADE model with the axion-like EDE model, we use the following priors for the latter:

$$\begin{aligned} 3 &\leq \log_{10}(z_c) \leq 4\,, \\ 0 &\leq f_{\rm EDE}(z_c) \leq 0.5\,, \\ 0 &\leq \Theta_i \leq \pi\,. \end{aligned}$$

In this work, we use *Planck* conventions for the treatment of neutrinos, that is, we include two massless and one massive species with $m_\nu = 0.06$ eV [11]. In addition, we use `Hmcode` [311] to estimate the non-linear matter clustering solely for the purpose of the CMB lensing. We define our MCMC chains to be converged when the Gelman-Rubin criterion $R - 1 < 0.05$. Finally, we extract the best-fit parameters from the procedure highlighted in the appendix of Ref. [183], and we produce our figures thanks to `GetDist` [184].

In this chapter, we compare the models with each other using two main metrics. Firstly, in order to assess the ability of an extended model $\mathscr{M}$ to fit all the cosmological data, we compute the Akaike Information Criterion (AIC) of this model relative to that of the ΛCDM. This metric is defined as follows

$$\Delta{\rm AIC} = \chi^2_{{\rm min},\mathscr{M}} - \chi^2_{{\rm min},\Lambda{\rm CDM}} + 2\cdot(N_{\mathscr{M}} - N_{\Lambda{\rm CDM}})\,, \tag{8.8}$$

where $\mathscr{M} \in \{\text{ADE}, \text{EDE}, c_s^2\text{ADE}, \text{cADE}\}$, and where $N_{\mathscr{M}}$ stands for the number of free parameters of the model. This metric enables us to determine whether the fit within a particular model $\mathscr{M}$ significantly improves that of ΛCDM by penalizing models with a larger number of degrees of freedom. Secondly, in order to gauge the ability of the extended model $\mathscr{M}$ to solve the Hubble tension for a given combination of data $\mathscr{D}$ (which does not include the M_b prior), we also compute the residual Hubble tension thanks to the difference of the maximum a posteriori (DMAP) [352], determined by

$$Q_{\text{DMAP}} = \sqrt{\chi^2_{\text{min},\mathscr{M}}(\mathscr{D}+M_b) - \chi^2_{\text{min},\mathscr{M}}(\mathscr{D})}\,. \tag{8.9}$$

This metric allows us to determine how does the addition of the M_b prior to the dataset $\mathscr{D}$ impact the fit within a particular model $\mathscr{M}$. Ref. [183] asserts that a model is a good candidate for solving the Hubble tension if it meets these two conditions: $\Delta AIC < -6.91$ and $Q_{\text{DMAP}} < 3\sigma$. Finally, we also consider the Gaussian tension (GT), computed as

$$\text{GT} = \frac{\overline{H_0}(\text{SH}_0\text{ES}) - \overline{\text{H}_0}(\mathscr{D})}{\sqrt{\sigma^2_{H_0}(\text{SH}_0\text{ES}) + \sigma^2_{H_0}(\mathscr{D})}}\,, \tag{8.10}$$

where $\overline{H_0}$ and σ_{H_0} correspond to the mean and standard deviation of the Hubble parameter today determined from the SH_0ES experiment and the dataset $\mathscr{D}$ (within the model $\mathscr{M}$). The Gaussian tension is certainly the most direct metric for quantifying the Hubble tension, but the main problem with this metric is that it is unable to favor a complex model whose some parameters become irrelevant in the ΛCDM limit. If a probability density function deviates from Gaussian in a complex model (as is the case for EDE models), only the Gaussian ΛCDM limit has significant statistical weight [183, 346].

8.2 Cosmological results

In this section, we discuss the cosmological constraints of the ADE model and its ability to solve the Hubble tension by successively evaluating the impact of the EFT full-shape analysis of the BOSS and eBOSS data (compared with the standard BAO/$f\sigma_8$ analysis) and the impact of the new Pantheon data (compared with the equivalent older data) on this model. The cosmological constraints are shown in Tab. 8.1, while the χ^2_{min} values associated with each likelihood are presented in Tab. E.1 of App. E.2. In Tab. 8.1, we also display the $\Delta\chi^2_{\text{min}}$ and the associated ΔAIC with respect to ΛCDM, as well as the Q_{DMAP} for several combinations of data.

Our baseline combination of data, denoted "BAO/$f\sigma_8$ + Pan," refers to *Planck* + ext-BAO + BOSS BAO/$f\sigma_8$ + eBOSS BAO/$f\sigma_8$ + Pantheon, corresponding roughly to that used in Ref. [369]. [3] For this analysis, combined with the M_b prior, we find $f_{\text{ADE}}(z_c) = 0.081 \pm 0.018$ and $H_0 = 71.24 \pm 0.68$ km/s/Mpc for the ADE model, leading to a residual Hubble tension of $Q_{\text{DMAP}} = 2.6\sigma$ and a preference over ΛCDM of ΔAIC $= -22.3$ (see Tab. 8.1). Note that this χ^2 improvement is mainly driven by the SH_0ES data (as is also the case in the remainder of this paper), implying that this preference over ΛCDM will no longer be significant if the Hubble tension arises from systematic associated with the data. Let us underline that with

[3] Note that this analysis used another SH_0ES prior, $H_0 = 74.03 \pm 1.42$ km/s/Mpc, from Ref. [371], and does not take into account the redshift space distortion information (but only the BAO).

	BAO/$f\sigma_8$ + Pan		EFT + Pan		EFT + PanPlus	
M_b prior?	no	yes	no	yes	no	yes
$f_{\rm ADE}(z_c)$	$< 0.060(0.034)$	$0.081(0.090) \pm 0.018$	$< 0.049(0.010)$	$0.068(0.076) \pm 0.019$	$< 0.036(0.011)$	$0.073(0.082) \pm 0.020$
$\log_{10}(z_c)$	*unconst.*(3.748)	$3.655(3.677) \pm 0.093$	*unconst.*(3.713)	$3.676(3.686)^{+0.095}_{-0.120}$	*unconst.*(3.957)	$3.692(3.724)^{+0.098}_{-0.120}$
w_f	$> 0.49(0.69)$	$0.79(0.76)^{+0.10}_{-0.12}$	$> 0.59(0.70)$	$0.78(0.75)^{+0.11}_{-0.13}$	$> 0.61(0.57)$	$0.76(0.73) \pm 0.13$
H_0	$68.44(69.04)^{+0.47}_{-0.93}$	$71.24(71.49) \pm 0.68$	$68.16(68.26)^{+0.41}_{-0.53}$	$71.01(71.31) \pm 0.73$	$68.03(68.16)^{+0.43}_{-0.53}$	$71.13(71.29) \pm 0.73$
$\omega_{\rm cdm}$	$0.1212(0.1239)^{+0.0012}_{-0.0030}$	$0.1291(0.1305) \pm 0.0027$	$0.1196(0.1202)^{+0.0009}_{-0.0015}$	$0.1267(0.1280) \pm 0.0027$	$0.1201(0.1211)^{+0.0011}_{-0.0015}$	$0.1278(0.1294) \pm 0.0028$
$10^2\omega_b$	$2.259(2.269)^{+0.016}_{-0.023}$	$2.304(2.309) \pm 0.021$	$2.254(2.252)^{+0.014}_{-0.017}$	$2.303(2.306) \pm 0.022$	$2.250(2.258) \pm 0.018$	$2.306(2.311) \pm 0.022$
$10^9 A_s$	$2.123(2.119) \pm 0.030$	$2.159(2.152) \pm 0.031$	$2.111(2.111) \pm 0.030$	$2.148(2.151)^{+0.028}_{-0.032}$	$2.111(2.116)^{+0.028}_{-0.036}$	$2.151(2.150)^{+0.028}_{-0.033}$
n_s	$0.9711(0.9748)^{+0.0041}_{-0.0074}$	$0.9900(0.9925) \pm 0.0061$	$0.9684(0.9686)^{+0.0040}_{-0.0048}$	$0.9878(0.9904) \pm 0.0060$	$0.9679(0.9697)^{+0.0038}_{-0.0047}$	$0.9890(0.9906) \pm 0.0063$
$\tau_{\rm reio}$	$0.0583(0.0540)^{+0.0063}_{-0.0075}$	$0.0588(0.0561)^{+0.0066}_{-0.0077}$	$0.0572(0.0573) \pm 0.0070$	$0.0590(0.0584)^{+0.0067}_{-0.0077}$	$0.0570(0.0574) \pm 0.0072$	$0.0585(0.0573)^{+0.0065}_{-0.0077}$
S_8	$0.828(0.834)^{+0.011}_{-0.013}$	$0.843(0.846) \pm 0.013$	$0.820(0.823) \pm 0.010$	$0.832(0.835) \pm 0.012$	$0.825(0.830)^{+0.010}_{-0.011}$	$0.836(0.842) \pm 0.013$
Ω_m	$0.3083(0.3089) \pm 0.0054$	$0.3011(0.3018) \pm 0.0050$	$0.3074(0.3078) \pm 0.0050$	$0.2983(0.2983) \pm 0.0047$	$0.3096(0.3107)^{+0.0047}_{-0.0053}$	$0.2994(0.3014) \pm 0.0047$
$\Delta\chi^2_{\rm min}$	-3.9	-28.3	-1.4	-24.9	-1.3	-27.8
ΔAIC	+2.1	-22.3	+4.6	-18.9	+4.7	-21.8
$Q_{\rm DMAP}$	2.6σ		2.9σ		3.6σ	
$Q_{\rm DMAP}$(EDE)	1.5σ		2.4σ		2.5σ	
$Q_{\rm DMAP}(\Lambda{\rm CDM})$	5.6σ		5.6σ		6.3σ	

Table 8.1: Mean (best-fit) $\pm 1\sigma$ (or 2σ for one-sided bounds) of reconstructed parameters in the ADE model confronted to various datasets. All datasets include *Planck* + ext-BAO data, while we consider either the BAO/$f\sigma_8$ information or the EFT full-shape analysis for the BOSS and eBOSS data, and we consider either the Pantheon data or the Pantheon+ data (with and without the M_b prior). We also display for all datasets the $\Delta\chi^2_{\rm min}$ with respect to ΛCDM, the associated ΔAIC, as well as the $Q_{\rm DMAP}$. Finally, $Q_{\rm DMAP}(\Lambda{\rm CDM})$ and $Q_{\rm DMAP}({\rm EDE})$ corresponds the $Q_{\rm DMAP}$ of the ΛCDM and axion-like EDE models for the equivalent datasets.

our baseline combination of data, the ADE model satisfies both Ref. [183] conditions. In addition, we find for the ADE model that GT $= 3.7\sigma$ for our original combination of data. We are now assessing how the EFTofLSS on the one hand, and the new data from Pantheon+ on the other hand, change these conclusions.

8.2.1 Impact of the EFTofLSS analysis

In the top panel of Fig. 8.2, we show the reconstructed 2D posteriors of the ADE model for the analysis with the BOSS and eBOSS BAO/$f\sigma_8$ likelihoods (namely the BAO/$f\sigma_8$ + Pan analysis), as well as for the analysis with the EFTofBOSS and EFTofeBOSS likelihoods (namely the EFT + Pan analysis), either with or without the M_b prior. To isolate the effect of the EFT full-shape analysis, we carry out these analyses using only the older Pantheon data.

For the analyses without the M_b prior, the addition of the EFT likelihood has a non-negligible impact on the $f_{\rm ADE}(z_c)$, w_f, and H_0 constraints. The upper bound of the ADE fractional energy density and the lower bound of w_f are indeed both improved by $\sim 20\%$, while the standard deviation of H_0 is reduced by $\sim 35\%$.

When we consider the M_b prior, EFTofBOSS and EFTofeBOSS do not improve the parameter constraints of this model over the BAO/$f\sigma_8$ information. However, these likelihoods shift $f_{\rm ADE}(z_c)$ and H_0 towards smaller values of 0.7σ and 0.3σ, [4] respectively. The EFT full-shape analysis of the BOSS and eBOSS data therefore slightly reduces the ability of this model to resolve the Hubble tension, and the $Q_{\rm DMAP}$ changes from 2.6σ to 2.9σ when EFT likelihoods are considered (see Tab. 8.1). In particular, the $\chi^2_{\rm min}$ associated with the M_b prior is degraded by 1.0 compared to the BAO/$f\sigma_8$ analysis. In addition, the preference for this

[4] Since we are considering here the same experiments (with different methods for extracting cosmological constraints), we use the following metric: $2\cdot(\theta_i-\theta_j)/(\sigma_{\theta,i}+\sigma_{\theta,j})$, where θ_i and $\sigma_{\theta,i}$ are respectively the mean value and the standard deviation of the parameter θ for the dataset i.

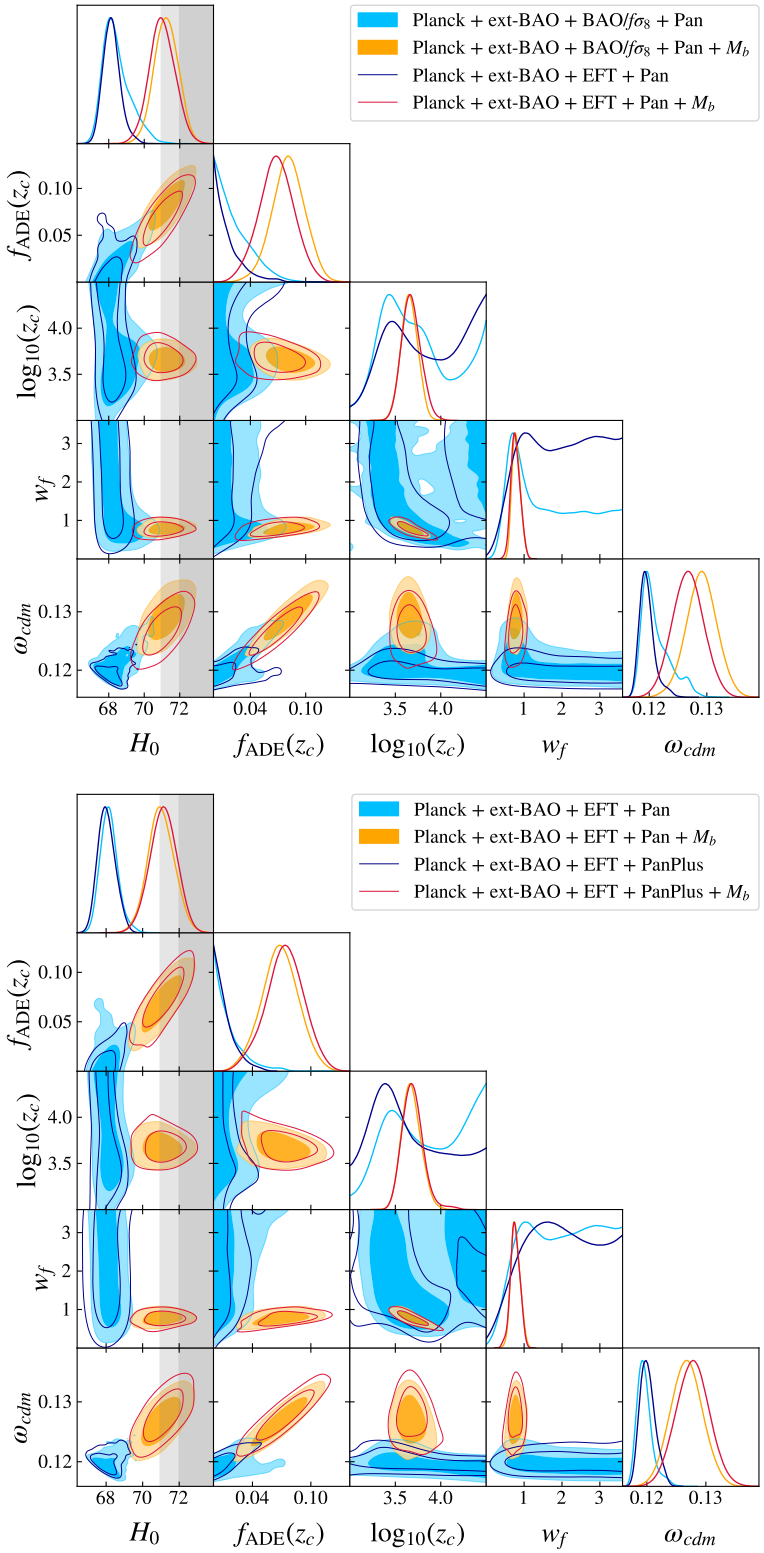

Figure 8.2: *Top panel*: 2D posterior distributions reconstructed from the BAO/$f\sigma_8$ + Pan dataset compared with the 2D posterior distributions reconstructed from the EFT + Pan dataset, either with or without the M_b prior. *Bottom panel*: 2D posterior distributions reconstructed from the EFT + Pan dataset compared with the 2D posterior distributions reconstructed from the EFT + PanPlus dataset, either with or without the M_b prior. The gray bands correspond to the H_0 constraint associated with the M_b prior, $H_0 = (73.04 \pm 1.04)$ km/s/Mpc [153].

model over the ΛCDM model is slightly reduced, given that the ΔAIC changes from -22.3 to -18.9 when the EFT likelihood is added (see Tab. 8.1). Note that at this point, the ADE model still satisfies both conditions of Ref. [183], even though $Q_{\rm DMAP} \sim 3\sigma$. However, the Gaussian tension changes from 3.7σ to 4.3σ when EFT likelihoods are considered, which can be explained by the fact that the $f_{\rm ADE}(z_c)$ parameter is better constrained by the EFT + Pan dataset.

For the axion-like EDE case, we find for the equivalent analyses (see Tab. E.1 of App. E.2) that the $Q_{\rm DMAP}$ changes from 1.5σ to 2.4σ, and that the ΔAIC changes from -29.1 to -22.9, when EFT likelihoods are added. [5] The ADE model slightly better supports the addition of the EFT likelihood compared to the EDE model, insofar as the $Q_{\rm DMAP}$ and ΔAIC are more stable (see Tab. 8.1). However, the EDE model remains a better model to solve the Hubble tension, with $Q_{\rm DMAP} = 2.4\sigma$ for the EFT + Pan analysis, compared to $Q_{\rm DMAP} = 2.9\sigma$ for the ADE model, and has a better fit to the data when the M_b prior is added, with $\Delta{\rm AIC} = -22.9$, compared to $\Delta{\rm AIC} = -18.9$ for the ADE model. For a detailed discussion of the EFTofLSS impact on the EDE model in the framework of the BOSS data, please refer to chapter 7. [6]

8.2.2 Impact of the Pantheon+ data

Let's now turn to the impact of the latest Pantheon data, namely the Pantheon+ data, on the ability of this model to resolve the Hubble tension. In the bottom panel of Fig. 8.2, we show the reconstructed 2D posteriors of the ADE model for the analyses with the old Pantheon data (*i.e.*, the EFT + Pan analysis), as well as for the analyses with the updated data (*i.e.*, the EFT + PanPlus analysis). To isolate the effect of the Pantheon+ data, we carry out these analyses using only the EFT full-shape analysis of the BOSS and eBOSS data.

The analysis with the Pantheon+ data, but without any SH0ES prior, improves significantly the 95% C.L. constraints on $f_{\rm ADE}(z_c)$ by $\sim 30\%$. This implies that H_0 is shifted down by 0.2σ [7] compared to the analysis with the old Pantheon data. Although the ADE model prefers a higher value of $\omega_{\rm cdm}$ than ΛCDM (because ADE slows down the evolution of the growing modes), the larger Ω_m favored by the Pantheon+ data ($\Omega_m = 0.334 \pm 0.018$ [132]) leads to a large $\omega_{\rm cdm} = \Omega_{\rm cdm} \cdot h^2$ which is not sufficiently compensated for by ADE. Then, to offset the high value of Ω_m, the current Hubble parameter decreases slightly, as well as $f_{\rm ADE}(z_c)$, since the latter is positively correlated with H_0.

When the M_b prior is included, non-zero contribution of ADE are favored. One may have expected that the tighter constraints from Pantheon+ may reduce the contribution of $f_{\rm ADE}$ and the value of H_0. These are in fact stable when compared to analyses with the older Pantheon

[5] The similar analysis in chapter 7, which does not include the eBOSS data, determined that $Q_{\rm DMAP} = 2.0\sigma$ for the BAO/$f\sigma_8$ + Pan analysis and that $Q_{\rm DMAP} = 2.1\sigma$ for the EFT + Pan analysis (see Tab. D.2 in chapter 7). This difference is due solely to the eBOSS data: the χ^2 of the eBOSS BAO/$f\sigma_8$ likelihood is improved when the M_b prior is added (which decreases the $Q_{\rm DMAP}$ of the BAO/$f\sigma_8$ + Pan analysis), while the χ^2 is degraded for the EFTofeBOSS likelihood when the M_b prior is added (which increases the $Q_{\rm DMAP}$ of the EFT + Pan analysis).

[6] Note that chapter 7 used an H_0 prior equivalent to the M_b prior, and did not consider the EFTofeBOSS likelihood (as well as the eBOSS BAO/$f\sigma_8$ likelihood). Note that the impact of eBOSS data on the axion-like EDE is studied in Ref. [364].

[7] Since we are considering here different experiments, we use the following metric: $(\theta_i - \theta_j)/\sqrt{\sigma^2_{\theta,i} + \sigma^2_{\theta,j}}$, where θ_i and $\sigma_{\theta,i}$ are respectively the mean value and the standard deviation of the parameter θ for the dataset i.

data, with similar error bars between the EFT + Pan + M_b and EFT + PanPlus + M_b analyses. Thus, if we rely solely on the posterior distributions, we could argue that the Pantheon+ data do not change the conclusion about the ADE resolution of the Hubble tension. However, it turns out that the ADE model is not able to accommodate at the same time the large value of H_0 and Ω_m that are favored by the Pantheon+ data once they are calibrated with M_b. Indeed, the best-fit value $H_0 = 71.29$ km/s/Mpc is 1.7σ lower than the SH0ES constraint [$H_0 = (73.04 \pm 1.04)$ km/s/Mpc], while the best-fit value $\Omega_m = 0.3014$ is 1.8σ lower than the Pantheon+ constraint [$\Omega_m = 0.334 \pm 0.018$]. Therefore, the ADE model does not provide a good fit to the M_b prior ($\chi^2_{M_b} = 6.42$ as shown in Tab. E.1 of App. E.2), while the fit to the Pantheon+ data is worsen (by +1.6) with the inclusion of the M_b prior. These degradations of $\chi^2_{\rm min}$ [8] imply that the $Q_{\rm DMAP}$ changes from 2.9σ (5.6σ for ΛCDM) to 3.6σ (6.3σ for ΛCDM) when we consider the Pantheon+ data (see Tab. 8.1), which severely limits the ability of this model to resolve the H_0 tension. One of the two criteria of Ref. [183], namely $Q_{\rm DMAP} < 3\sigma$, is indeed no longer fulfilled. However, while the Pantheon+ data and the M_b prior from Ref. [153] seriously restrict the ability of the ADE model to resolve the Hubble tension, these data improve the preference for this model over ΛCDM, since the ΔAIC changes from -18.9 to -21.8. We nevertheless caution over-interpreting this preference, given that the $Q_{\rm DMAP}$ indicates that combining these datasets is not statistically consistent. In addition, the Gaussian tension GT $= 4.4\sigma$ is stable with respect to the EFT + Pan dataset. [9]

In the left panel of Fig. 8.4, we show the 2D posterior distributions of the axion-like EDE model reconstructed from the EFT + PanPlus + M_b dataset, while the associated cosmological constraints are displayed in Tab. 8.2. For the axion-like EDE case, we find that the $Q_{\rm DMAP}$ changes from 2.4σ to 2.5σ, and that the ΔAIC changes from -22.9 to -29.1, between the old and the new Pantheon data analysis (see Tab. E.1 of App. E.2 for the individual $\chi^2_{\rm min}$). This model better supports these new data, since the $Q_{\rm DMAP}$ is stable (and especially the $\chi^2_{\rm min}$ of the SH0ES prior), while the ΔAIC, as in the case of the ADE model, decreases significantly. Whereas with the addition of the EFT data we had a slight preference for EDE over ADE, with the Pantheon+ data the preference for this model becomes clearly apparent: in the axion-like EDE model, $H_0 = 71.67 \pm 0.77$ km/s/Mpc with $Q_{\rm DMAP} = 2.5\sigma$, while in the ADE model, $H_0 = 71.13 \pm 0.73$ km/s/Mpc with $Q_{\rm DMAP} = 3.6\sigma$. In addition, the axion-like EDE model provides a better overall fit than the ADE model, with $\Delta AIC({\rm EDE} - {\rm ADE}) = +7.3$. The two main contributions to this difference come from the *Planck* data (and in particular the high-ℓ TTTEEE likelihood), where $\Delta\chi^2({\rm EDE} - {\rm ADE}) = +3.7$, and from the SH0ES prior, where $\Delta\chi^2({\rm EDE} - {\rm ADE}) = +2.7$. The axion-like EDE model is capable of better compensating the effect of large values of H_0 and $\Omega_{\rm m}$ (and therefore $\omega_{\rm cdm}$) on the CMB compared to the ADE model.

In order to understand why the axion-like EDE model performs better than ADE, we plot in Fig. 8.3 the CMB power spectra residuals with respect to the ΛCDM best-fit for these two models. On this figure, we also plot (in green dashed) the CMB power spectra residuals of the ADE model, where we set the ΛCDM parameters to the axion-like EDE best-fit, and the z_c and w_f parameters to the ADE best-fit. The last ADE parameter, namely $f_{\rm ADE}(z_c)$, is dermined

[8] Let us note that the $\chi^2_{\rm min}$ of the other likelihoods are stable between the Pantheon and Pantheon+ analyses, and therefore play no role in the change in $Q_{\rm DMAP}$ between these two analyses.

[9] Note that for the same dataset, we obtain GT $= 3.8\sigma$ for the axion-like EDE model and GT $= 4.8\sigma$ for the ΛCDM model.

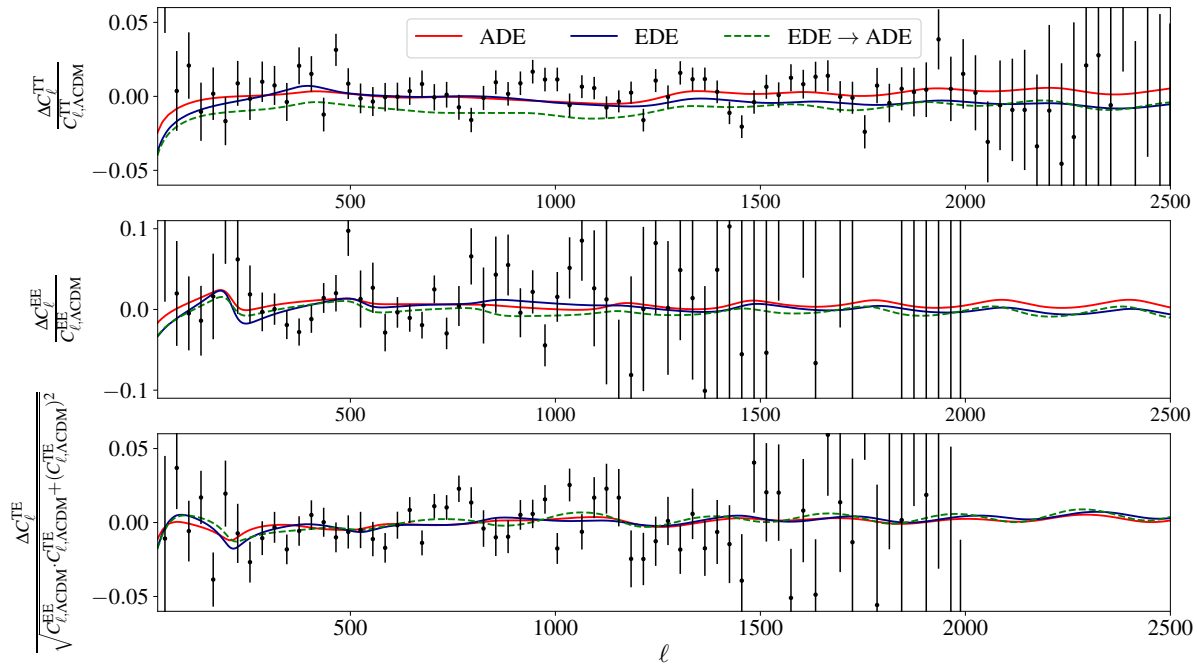

Figure 8.3: CMB power spectra residuals with respect to ΛCDM for the ADE (red) and axion-like EDE (black) models. All cosmological parameters of the ΛCDM, ADE, and axion-like EDE models have been set to their EFT + PanPlus best-fits, while the displayed data (nomalized to the ΛCDM best-fit) correspond to the *Planck* 2018 data [215]. Finally, for the plot entitled "EDE → ADE," we set the ΛCDM parameters to the axion-like EDE best-fit, while the z_c and w_f parameters are set to the ADE best-fit. The last ADE parameter, namely $f_{\rm ADE}(z_c) = 0.095$, is determined such that the values of $100\theta_s = 1.042$ and $r_s = 140.53$ Mpc are the same as for the EDE best-fit.

such that the values of the angular acoustic scale at recombination, θ_*, and the comoving sound horizon at recombination, r_*, are the same as for the EDE best-fit. In other words, this plot would represent the best-fit of the ADE model if the latter could reduce the Hubble tension to the same level as the axion-like EDE model. In this figure, the main difference between the ADE and ADE → EDE plots stems from the suppression (particularly at low ℓ) of the $C_\ell^{\rm TT}$ power spectrum for the EDE → ADE analysis. This suppression typically corresponds to the effect of a large value of $\omega_{\rm cdm}$ (and also n_s), showing that the ADE model is not able to compensate for a high value of $\Omega_{\rm cdm}h^2$ in the same way as the axion-like EDE model. This is explained by the fact that the EDE model allows the sound speed to decrease in the k range associated with $\ell < 500$, making it easier to compensate for the effect of increasing $\Omega_{\rm cdm}h^2$ in the low-ℓ TT power spectrum. Let us note that the effect of the increase in $\Omega_{\rm cdm}h^2$ is more significant for the modes that have re-entered the horizon at the time when $f_{\rm ADE}$ is decreasing, and therefore no longer significantly suppresses the evolution of the growing modes. In order to compensate for this effect, it is therefore helpful to decrease c_s^2 for $l < 500$, insofar as a reduction in this parameter leads to an enhancement in the Weyl potential (see Ref. [337]). Note that these results are compatible with Ref. [337], but interestingly the limitation in the value of $\Omega_{\rm cdm}h^2$ does not arise from the CMB polarization as in that reference (which considered *Planck* 2015 data), but from the CMB temperature.

	EDE	c_s^2ADE	cADE
$f_{\rm ADE/EDE}(z_c)$	$0.116(0.128)^{+0.023}_{-0.021}$	$0.103(0.080)^{+0.028}_{-0.046}$	$0.079(0.087)\pm0.019$
$\log_{10}(z_c)$	$3.69(3.84)^{+0.20}_{-0.16}$	$3.61(3.73)^{+0.12}_{-0.10}$	$3.540(3.532)\pm0.058$
Θ_i	$2.77(2.88)^{+0.15}_{-0.072}$	–	–
w_f	–	*unconst.*(0.71)	–
c_s^2	–	$>0.701(0.72)$	–
H_0	$71.67(71.84)\pm0.77$	$70.76(71.23)\pm0.70$	$70.95(71.23)\pm0.73$
$\omega_{\rm cdm}$	$0.1303(0.1309)\pm0.0030$	$0.1257(0.1294)\pm0.0024$	$0.1273(0.1286)\pm0.0028$
$10^2\omega_b$	$2.294(2.312)\pm0.024$	$2.304(2.310)\pm0.020$	$2.305(2.308)\pm0.021$
10^9A_s	$2.149(2.143)^{+0.027}_{-0.034}$	$2.152(2.150)^{+0.030}_{-0.036}$	$2.149(2.158)\pm0.031$
n_s	$0.9898(0.9951)\pm0.0061$	$0.9882(0.9902)\pm0.0065$	$0.9849(0.9874)\pm0.0057$
$\tau_{\rm reio}$	$0.0590(0.0590)^{+0.0063}_{-0.0079}$	$0.0592(0.0573)^{+0.0069}_{-0.0080}$	$0.0573(0.0583)^{+0.0066}_{-0.0078}$
S_8	$0.836(0.836)\pm0.011$	$0.831(0.842)\pm0.012$	$0.836(0.841)\pm0.012$
Ω_m	$0.2995(0.2997)\pm0.0047$	$0.2985(0.3018)\pm0.0049$	$0.3000(0.3001)\pm0.0047$
$\Delta\chi^2_{\rm min}$	-35.1	-27.9	-24.1
ΔAIC	-29.1	-19.9	-20.1
$Q_{\rm DMAP}$	2.5σ	3.6σ	3.9σ

Table 8.2: Mean (best-fit) $\pm1\sigma$ (or 2σ for one-sided bounds) of reconstructed parameters in the EDE, c_s^2ADE, and cADE models confronted to the *Planck* + ext-BAO + EFT + PanPlus + M_b dataset, *i.e.*, the most up-to-date dataset. We also display for each model the $\Delta\chi^2_{\rm min}$ with respect to ΛCDM, the associated ΔAIC, as well as the $Q_{\rm DMAP}$.

8.3 Model variations

8.3.1 Variation of c_s^2

In the previous sections, we fixed $c_s^2(a_c) = w_f$ instead of varying these two parameters independently. In the right panel of Fig. 8.4, we show the 2D posterior distributions reconstructed from the EFT + PanPlus + M_b dataset for our baseline ADE model by relaxing this assumption, while in Tab. 8.2 we display the associated cosmological constraints. To do so, we have applied the prior of Refs. [337, 369] to c_s^2, namely

$$0 \leq c_s^2 \leq 1.5\,.$$

In the following, we simply call this extended model "c_s^2ADE," for which we still consider that $p = 1$. Interestingly, and in line with Ref. [337], the assumption $c_s^2 = w_f$ does not change our conclusions, especially regarding the Hubble tension: we obtain $Q_{\rm DMAP} = 3.6\sigma$, which is similar to that of our baseline ADE model (see Tab. E.1 of App. E.2 for the χ^2 values). In this specific case, we obtain $H_0 = 70.76 \pm 0.70$ km/s/Mpc, which is 0.5σ lower than the H_0 value from our baseline ADE model. This is due to projection effects caused by the non-Gaussian posteriors of c_s^2 and w_f, and we notice that the best-fit value ($H_0 = 71.23$ km/s/Mpc) is very close to that of the ADE model. Thus, the relaxation of this hypothesis does not resolve the Hubble tension, while the ΔAIC worsens somewhat in this model because of the additional parameter ($\Delta AIC = -20.1$ instead of -21.8 for our baseline ADE model). In addition, as shown in Fig. 8.5, the best-fit point of the ADE model in the $c_s^2 - w_f$ plane lies in the 68% C.L. reconstructed from the c_s^2ADE model, and is very close to the best-fit point of this model. This implies that setting $c_s^2 = w_f$ is a good approximation around the best-fit of the c_s^2ADE model.

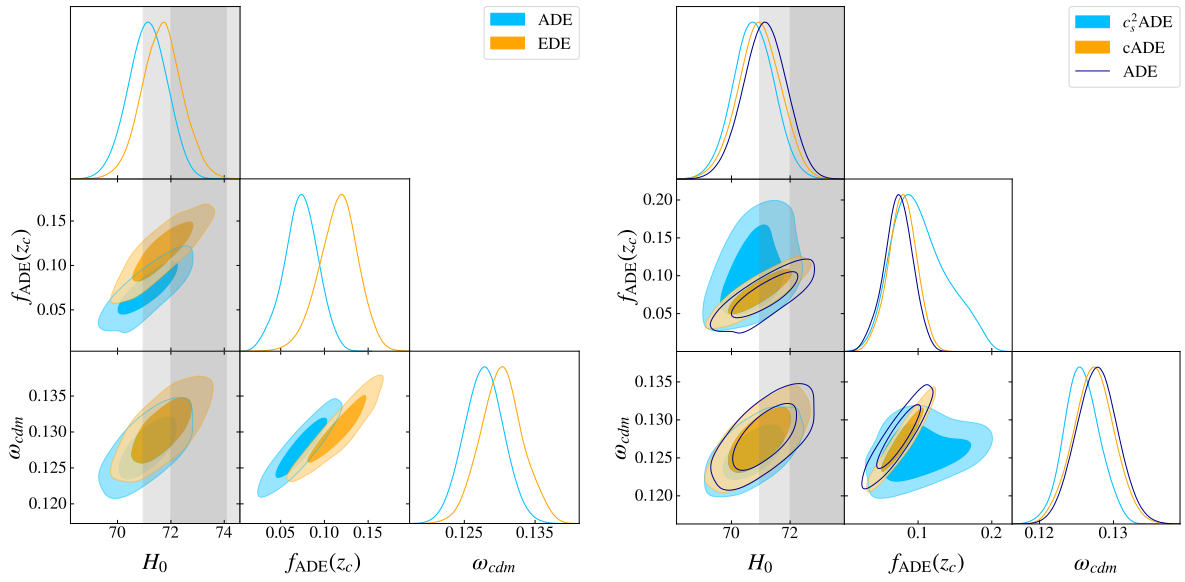

Figure 8.4: *Left panel*: 2D posterior distributions reconstructed from the *Planck* + ext-BAO + EFT + PanPlus + M_b dataset, *i.e.*, the most up-to-date dataset, for our baseline ADE model and the standard axion-like EDE model. *Right panel*: 2D posterior distributions reconstructed from the *Planck* + ext-BAO + EFT + PanPlus + M_b dataset for the c_s^2ADE model (namely our baseline ADE model with the variation of c_s^2), the cADE model (namely our baseline ADE model with $c_s^2 = w_f = 1$), and our baseline ADE model. The gray bands correspond to the H_0 constraint associated with the M_b prior, $H_0 = (73.04 \pm 1.04)$ km/s/Mpc [153].

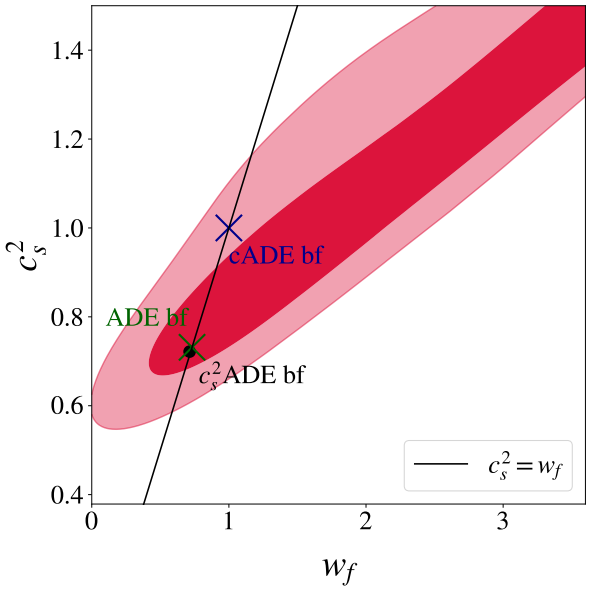

Figure 8.5: 2D posterior distribution of the $c_s^2 - w_f$ plane reconstructed from the *Planck* + ext-BAO + EFT + PanPlus + M_b dataset for the c_s^2ADE model. The solid line corresponds to $c_s^2 = w_f$, while the blue and green crosses correspond respectively to the cADE model and the best-fit of our baseline ADE model. The black circle represents the best-fit of the c_s^2ADE model.

8.3.2 The cADE model

Refs. [337] and [369] showed that the special case where $c_s^2 = w_f = 1$ made it possible to solve the Hubble tension. In this particular model, called "cADE," the ADE component is a canonical scalar which goes from a frozen phase ($w = -1$) to a kinetion phase ($w = 1$) around matter-radiation equality. This model is particularly interesting because it allows the Hubble tension to be resolved with only two more parameters than the ΛCDM model [namely $f_{\rm ADE}(z_c)$ and $\log_{10}(z_c)$]. However, while in Ref. [337] the case $c_s^2 = w_f = 1$ is within the 68% C.L. of the c_s^2 and w_f parameters (see Fig. 1 of this reference), one can see in Fig. 8.5 that this particular case is no longer located in the 1σ region. [10] In the right panel of Fig. 8.4, we display the 2D posterior distributions of the cADE model reconstructed from the EFT + PanPlus + M_b dataset, while in Tab. 8.2 we display the associated cosmological constraints. We can clearly see that this particular model is unable to resolve the Hubble tension with current data, since we obtain $H_0 = 70.95 \pm 0.73$ km/s/Mpc and $f_{\rm ADE}(z_c) = 0.079 \pm 0.019$, with a $Q_{\rm DMAP} = 3.9\sigma$ (compared to $Q_{\rm DMAP} = 3.6\sigma$ for our baseline ADE model).

8.4 Conclusions

In this chapter, we have updated the constraints on the acoustic dark energy model by first assessing the impact of the EFT full-shape analysis applied to the BOSS LRG and eBOSS QSO data, and secondly the impact of the latest Pantheon+ data.

- When we consider the full-shape analysis of the BOSS and eBOSS data, combined with *Planck*, ext-BAO measurements, Pantheon data from [133], and SH0ES data from [153], we obtain $H_0 = 71.01 \pm 0.73$ km/s/Mpc with a residual Hubble tension of 2.9σ (compared to 2.4σ for the axion-like EDE model and 5.6σ for the ΛCDM model).

- We have demonstrated that the EFTofLSS analysis slightly reduces the ability of this model to resolve the Hubble tension compared to the BAO/$f\sigma_8$ analysis, which has a residual tension of 2.6σ (with $H_0 = 71.24 \pm 0.68$ km/s/Mpc).

- Although the axion-like EDE model remains a better solution to the Hubble tension after using the EFTofBOSS and EFTofeBOSS likelihoods, we have shown that the EFTofLSS analysis has a stronger impact on this model.

- Importantly, when we replace the Pantheon data with the Pantheons+ data from [132], the ADE model no longer resolves the Hubble tension at a suitable level, leading to a 3.6σ residual tension (compared to 2.5σ for the EDE model and 6.3σ for the ΛCDM model).

- Whereas with the EFTofLSS analysis we had only a slight preference for EDE over ADE, with the new data from Pantheon+ and SH0ES, the preference for this model becomes clearly apparent, due to the fact that axion-like EDE manages to compensate a higher $\Omega_{\rm cdm}h^2$ in *Planck* data thanks to the scale-dependence of the sound speed.

[10] Let us note that Refs. [337] and [369] set $p = 1/2$, while we set $p = 1$, but this difference does not change the results.

- Finally, we have verified that relaxing the assumption $c_s^2 = w_f$ does not alter our conclusions, justifying this choice. In addition, for the cADE model (where $c_s^2 = w_f = 1$), we have obtained $H_0 = 70.95 \pm 0.73$ km/s/Mpc with a $Q_{\rm DMAP} = 3.9\sigma$, implying that one can no longer solve the Hubble tension with this constrained ADE model, contrary to previous results [337, 369].

Let us add a few words about the $S_8 \equiv \sigma_8 \cdot \sqrt{\Omega_m/0.3}$ tension (see *e.g.*, Ref. [40] for a review). EDE-like models are known to slightly increase the amplitude of fluctuations σ_8 with respect to ΛCDM [275, 344, 345], due to an increase in $\omega_{\rm cdm}$ and n_s. In particular, increasing $\omega_{\rm cdm}$ brings forward matter-radiation equality $a_{\rm eq}$, leaving more time for growing modes (that are subhorizon at $a_{\rm eq}$) to evolve in the matter era. Considering our most up-to-date dataset (*i.e.*, "EFT+PanPlus+M_b"), we obtain a Gaussian tension [11] on S_8 of 3.2σ, 3.5σ and 3.8σ for the ΛCDM, ADE and axion-like EDE models, respectively. It is interesting to note that the better the model is able to resolve the Hubble tension, the higher the S_8 tension. In order to resolve these two tensions simultaneously in the context of EDE cosmologies, it is therefore necessary to find a mechanism that reduces the growth of small-scale modes, as could be achieved by an interaction between EDE and DM [372].

In this work, we have shown that the new data from Pantheon and SH0ES, and to a lesser extent the EFTofLSS applied to the BOSS and eBOSS data, can have a decisive impact on models which aim to resolve the Hubble tension. We leave for future work the study of the impact on the Hubble tension of such an analysis applied to other early dark energy models, such as new early dark energy [277, 278], Rock 'n' Roll dark energy [373], or early modified gravity [298, 374].

[11] We use here the Gaussian metric $(\theta_i - \theta_j)/\sqrt{\sigma^2_{\theta,i} + \sigma^2_{\theta,j}}$, where θ_i and $\sigma_{\theta,i}$ are respectively the mean value and the standard deviation of the parameter θ for the dataset i. For the week lensing determination of the S_8 parameter, we use the simple weighted mean and uncertainty of $S_8^{\rm GT} = 0.766^{+0.020}_{-0.014}$ from the combination of KiDS-1000×dFLensS+BOSS, $S_8 = 0.769^{+0.016}_{-0.012}$ [177], and DES-Y3, $S_8 = 0.775^{+0.026}_{-0.024}$ [79].

IX

EFTofLSS' take on the S_8 tension and the decaying dark matter

Contents

9.1 Nonlinear power spectrum in DCDM cosmologies **247**
9.1.1 Dark radiation decay products (DCDM → DR model) 247
9.1.2 Warm dark matter decay products (DCDM → WDM+DR model) . . 251
9.2 A comprehensive MCMC analysis of the DCDM models **256**
9.2.1 Data and method 256
9.2.2 Dark radiation decay products 258
9.2.3 Warm dark matter decay products 260
9.3 Conclusions **265**

This chapter is based on:

T. Simon, G. F. Abellán, P. Du, V. Poulin and Y. Tsai, *Constraining decaying dark matter with BOSS data and the effective field theory of large-scale structures*, **Phys. Rev. D 106 (2022) 023516**, arXiv:2203.07440.

Decaying cold dark matter (DCDM) models, in which dark matter is unstable on a cosmological timescale and decays into invisible products, have been proposed as potential resolutions to cosmic tensions [375, 376, 377, 378, 167, 168]. In the past it was found that DM models with purely radiation decay products can neither resolve the Hubble tension nor the S_8 tension [379, 380, 381, 382, 383, 384, 385], while DM models with massive decay products can resolve the S_8 tension, as the massive particle produced during the decay acts as a WDM component, reducing power on scale below the free-streaming length at late times [167, 168]. Beyond recent observational tensions, the study of these models is important from the particle physics point of view, as it addresses the question of the stability of DM on long cosmological timescales. In the literature, there are many models involving the existence of DM decays at late times, such as models with R-parity violation [386, 387], super weakly interacting massive particles (super WIMPs) [388, 389, 390, 391], sterile neutrinos [392, 393], models with an additional U(1) gauge symmetry [394, 395, 396, 397], or more recently a model of decaying warm dark matter [398]. Besides cosmic tensions, some DCDM models were proposed as a way to explain the excess of events in the electronic recoils reported by the Xenon1T collaboration [399, 400, 401, 167, 168]. In addition, DCDM models with massive daughters have also been suggested as a potential solution to the small (subgalactic) scales structure problem of CDM (*e.g.*, [402, 403, 404, 405, 406, 407, 408, 409, 396]).

In this chapter, we deal with DCDM with two types of decay products: (i) the DCDM $\to$ DR model, where the decay products is only composed of a (massless) dark radiation (DR) component, and (ii) the DCDM $\to$ WDM+DR model, where the decay products are one massive WDM component and one DR component. Previous works have limited themselves to the impact of DCDM decay at the background and linear perturbations level, deriving constraints (and hints) on these models from a combination of *Planck* CMB, BAO and uncalibrated luminosity distance to SN1a data. Here, we go beyond previous works by making use of the effective field theory of large-scale structures (EFTofLSS) to describe the mildly nonlinear regime of the galaxy clustering power spectrum and derive improved constraints thanks to the EFTofLSS applied to BOSS data. The main objectives of this chapter are: (i) perform the first-ever computation of the mildly nonlinear regime in DCDM models with massive and massless decay products through the EFTofLSS; (ii) test whether current BOSS data can lead to stronger constraints on these models; and (iii) check whether these constraints can put pressure on DCDM models that resolve the S_8 tension.

This chapter is structured as follows: in Sec. 9.1, we introduce the models and present the nonlinear power spectrum computed with the EFTofLSS; in Sec. 9.2, we present the results of comprehensive Monte Carlo Markov chain analyses of the DCDM model and discuss the implications of these constraints for the S_8 tension; we eventually conclude in Sec. 9.3. App. F.1 is dedicated to comparing results of the EFTofLSS with N-body simulations in the DCDM$\to$DR model, while App. F.2 details the scope of our computation in the DCDM$\to$WDM+DR model. Finally Apps. F.3, F.4 and F.5 present additional results of the MCMC analyses for completeness.

9.1 Nonlinear power spectrum in DCDM cosmologies

In this section, we review the models of decaying dark matter considered in this work, and present the first computation of the nonlinear power spectra in these cosmologies. We consider two different DCDM models (both are limited to decay into the dark sector): one in which a fraction of dark matter decays into massless particles, and the second one in which all of the dark matter experiences two-body decay into massive and massless particles.

9.1.1 Dark radiation decay products (DCDM → DR model)

Presentation of the model

In the first model we consider, the cold DM sector is partially composed of an unstable particle (denoted as DCDM) that decays into a noninteracting relativistic particle (denoted as DR). The rest of the DM is considered stable and we refer to it as the standard CDM. In addition to the standard six ΛCDM parameters, there are two free parameters describing the lifetime of DCDM τ (or equivalently the decay width $\Gamma = \tau^{-1}$), as well as the fraction of DCDM to total dark matter at the initial time $a_{\rm ini} \to 0$:

$$f_{\rm dcdm} \equiv \frac{\omega_{\rm dcdm}(a_{\rm ini})}{\omega_{\rm tot,dm}(a_{\rm ini})}, \tag{9.1}$$

with $\omega_{\rm tot,\,dm} \equiv \omega_{\rm dcdm} + \omega_{\rm cdm}$. With these definitions, in the limit of large τ and/or small $f_{\rm dcdm}$, one recovers the ΛCDM model.

The evolution of the homogeneous energy densities of the decaying dark matter and dark radiation is given by (see *e.g.* Refs. [410, 375, 381]):

$$\dot{\bar{\rho}}_{\rm dcdm} + 3\mathscr{H}\bar{\rho}_{\rm dcdm} = -a\Gamma\bar{\rho}_{\rm dcdm}, \tag{9.2}$$

$$\dot{\bar{\rho}}_{\rm dr} + 4\mathscr{H}\bar{\rho}_{\rm dr} = a\Gamma\bar{\rho}_{\rm dcdm}, \tag{9.3}$$

where $\mathscr{H}$ is the conformal Hubble parameter,

$$\mathscr{H}^2(a) = \frac{8\pi G a^2}{3}\sum_i \bar{\rho}_i(a), \tag{9.4}$$

with

$$\sum_i \bar{\rho}_i(a) = \bar{\rho}_{\rm cdm}(a) + \bar{\rho}_{\rm dcdm}(a) + \bar{\rho}_{\rm dr}(a) + \bar{\rho}_\gamma(a) + \bar{\rho}_\nu(a) + \bar{\rho}_b(a) + \bar{\rho}_\Lambda. \tag{9.5}$$

To describe the evolution of the linearly perturbed universe, we consider the usual synchronous gauge, where the scalar part of the perturbed metric is written as [41]

$$ds^2 = a^2(\tau)\left[-d\tau^2 + (\delta_{ij} + h_{ij}(x,t))dx^i dx^j\right]. \tag{9.6}$$

Here τ is the conformal time, and $h_{ij}(x,\tau)$ is defined as

$$h_{ij}(x,\tau) = \int d^3k e^{ik.x}[\hat{k}_i\hat{k}_j h(k,\tau) + \left(\hat{k}_i\hat{k}_j - \frac{1}{3}\delta_{ij}\right) 6\eta(k,\tau)]\,. \tag{9.7}$$

h denotes the trace of h_{ij}, while η corresponds to the other traceless scalar degree of freedom of the metric perturbation in Fourier space. Additionally, we consider the frame comoving with the DCDM (and CDM) fluid, such that $\theta_{\rm dcdm} = \partial_i v^i_{\rm dcdm} = 0$, where $\theta_{\rm dcdm}$ is the divergence of the DCDM velocity $v^i_{\rm dcdm}$. As a result, the energy density perturbation of the DCDM component, $\delta_{\rm dcdm} \equiv \rho_{\rm dcdm}/\bar{\rho}_{\rm dcdm} - 1$, follows the same evolution as standard CDM:

$$\dot{\delta}_{\rm dcdm} = -\frac{\dot{h}}{2}. \tag{9.8}$$

The evolution of the linear perturbations of the DR integrated phase-space distribution multipoles is governed by the following hierarchy of equations [410, 375, 381]:

$$\dot{F}_{\rm dr,0} = -kF_{\rm dr,1} - \frac{2}{3}r_{\rm dr}\dot{h} + \dot{r}_{\rm dr}\delta_{\rm dcdm}, \tag{9.9}$$

$$\dot{F}_{\rm dr,1} = \frac{k}{3}F_{\rm dr,0} - \frac{2k}{3}F_{\rm dr,2}, \tag{9.10}$$

$$\dot{F}_{\rm dr,2} = \frac{2k}{5}F_{\rm dr,1} - \frac{3k}{5}F_{\rm dr,3} + \frac{4}{15}r_{\rm dr}(\dot{h} + 6\dot{\eta}), \tag{9.11}$$

$$\dot{F}_{\rm dr,\ell} = \frac{k}{(2\ell+1)}\left[\ell F_{\rm dr,\ell-1} - (\ell+1)F_{\rm dr,\ell+1}\right] \qquad (\ell \geq 3). \tag{9.12}$$

In the previous equations we have introduced $r_{\rm dr} \equiv a^4\bar{\rho}_{\rm dr}(a)/\rho_{c,0}$ following Ref. [381], where $\rho_{c,0}$ is the critical density today. In the scenario under study, we have:

$$\dot{r}_{\rm dr} = a\Gamma(\bar{\rho}_{\rm dcdm}/\bar{\rho}_{\rm dr})r_{\rm dr}. \tag{9.13}$$

We also note that the first three multipoles are simply related to elements of the perturbed stress-energy tensor as $F_{\rm dr,0} = r_{\rm dr}\delta_{\rm dr}$, $F_{\rm dr,1} = (4r_{\rm dr}/3k)\theta_{\rm dr}$, and $F_{\rm dr,2} = 2\sigma_{\rm dr}r_{\rm dr}$. In order to truncate the hierarchy of Eqs. (9.9)-(9.12) at some $\ell_{\rm max} = 17$, we adopt the scheme proposed in Ref. [41] for massless neutrinos (and extended in `CLASS` to include nonzero curvature [411]) in order to limit the propagation of the error from $\ell_{\rm max}$ to ℓ. We extrapolate the behavior of $F_{\rm dr,\ell_{max}+1}$ thanks to the recursion relation:

$$F_{\rm dr,\ell_{max}+1} \approx \frac{2\ell_{\rm max}+1}{k\tau}F_{\rm dr,\ell_{max}} - F_{\rm dr,\ell_{max}-1}. \tag{9.14}$$

These equations have been implemented in the Boltzmann code `CLASS`, and the impact of DCDM $\to$ DR decay on the (linear) CMB and matter power spectrum has been studied in detail in the literature [410, 375, 381]. In App. F.1 we present a comparison of the EFTofLSS calculation with N-body simulations performed in Ref. [412]. The results obtained from these two methods agree up to subpercent difference for $k \lesssim 0.2\,h{\rm Mpc}^{-1}$ and $z = 0$, justifying that one can safely analyze the (mildly) nonlinear galaxy power spectrum with the EFTofLSS.

The nonlinear power spectrum

Thanks to the PyBird code, we plot in Fig. 9.1 the residuals of the nonlinear matter power spectra of the DCDM $\to$ DR model with respect to that of the ΛCDM model at $z = 0$. We also represent the associated linear matter power spectra obtained from the CLASS code. In addition, we plot in Fig. 9.2 the residuals of the monopole and quadrupole of the galaxy power spectra of this model. In these figures, we set the ΛCDM parameters [1] to their best-fit values from the analysis of *Planck* + Pantheon + EFTofBOSS + Ext-BAO (as described in Sec. 9.2). Finally, we simply vary the two parameters $f_{\rm dcdm}$ and τ to isolate their cosmological effects : in the left panels, we fix $f_{\rm dcdm} = 1$ and vary $\tau \in [0.1, 1000]$ Gyr, while in the right panel we fix $\tau = 1$ Gyr and vary $f_{\rm dcdm} \in [0.1, 1]$.

From Figs. 9.1 and 9.2, one can see that the monopole of the galaxy power spectrum shows a behavior very similar to that of the linear matter spectrum. For a realistic choice of EFT parameters, it shows an almost scale-independent power suppression due to two main reasons [410, 381]. First, the decay of DCDM decreases the duration of the matter dominated era (and at fix h, a smaller Ω_m/larger Ω_Λ), implying a shift of the power spectrum towards large scales, *i.e.*, towards small wavenumbers. Second, DCDM models involve a larger ratio of $\omega_{\rm b}/\omega_{\rm cdm}$ compared to the ΛCDM model due to the decay. Both effects manifest as a strong suppression of the small-scale power spectrum, and the latter effect leads to an additional modulation of the BAO amplitude visible as wiggles in Figs. 9.1 and 9.2. Moreover, we note that the nonlinear matter power spectrum shows a stronger scale-dependent suppression compared to the linear power spectrum at $k \gtrsim 0.1\ h{\rm Mpc}^{-1}$. There is an intuitive explanation as to why the nonlinear power spectrum is further suppressed, very similarly to what happens for standard neutrinos or warm dark matter, as reviewed *e.g.* in [166]. In general, nonlinear growth is faster than the linear growth, and the impact of nonlinearities is typically to enhance the power spectrum (this is famously the case in ΛCDM). In the DCDM case, modes that are suppressed will enter the nonlinear regime later, and therefore start experiencing their enhanced growth due to nonlinearities later. This delay leads to a further suppression of the power spectrum compared to ΛCDM when nonlinear effects are included. We checked that the amplitude of the deviation from scale-independent suppression at $k \gtrsim 0.1\ h{\rm Mpc}^{-1}$ is tied to the value of the effective dark matter sound speed c_s, and can vary a few % for $c_s \in [1, 5]\ k_{\rm nl}^2 \cdot ({\rm Mpc}/h)^2$, where $k_{\rm nl}$ corresponds to the nonlinear scale and determines the cutoff scale of the theory. On the other hand, the power suppression gets less strong with larger k in the monopole of the galaxy power spectrum, an effect indicating an additional degeneracy with other EFT parameters. Finally, and as expected, deviations with respect to ΛCDM increases as τ decreases and/or $f_{\rm dcdm}$ increases for the monopole as well as for the quadrupole.

Preliminary study

To gauge the impact of using the EFTofBOSS data in our analyses of the DCDM $\to$ DR model, we first perform a preliminary study in which we consider a set of DCDM parameters

[1] For completeness, note that the shape of the residuals of the galaxy and matter power spectra depend on the values of the EFT nuisance parameters, especially at large k. According to the notation of Ref. [59], for the numerical evaluation we set the effective dark matter sound speed $c_s = 1$ for the matter power spectra, and $b_1 = 2$, $b_2 = 1$, $b_3 = 0.5$, $b_4 = 0$, $c_{ct} = 0.5$, $c_{r,1} = 2$ and $c_{r,2} = c_{\varepsilon,0} = c_{\varepsilon,1} = c_{\varepsilon,2} = 0$ for the galaxy power spectra. In practice, these parameters are optimized when quoting best-fits, to ensure that they take realistic values.

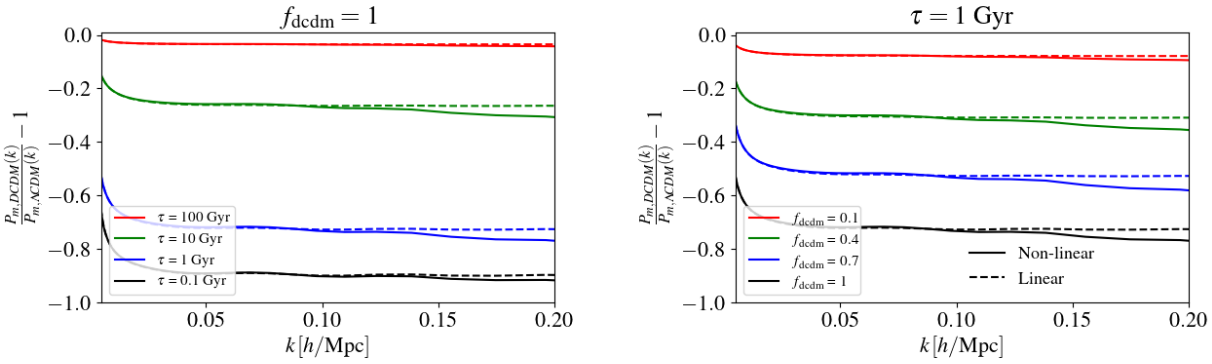

Figure 9.1: *Left* - Residuals of the linear (dashed lines) and nonlinear matter power spectrum (solid lines) for $f_{\rm dcdm}$ set to 1 and $\tau = 0.1$, 1, 10, 100 Gyr. Residuals are taken with respect to the ΛCDM model at $z = 0$. *Right* - The same, but this time τ is set to 1 Gyr and $f_{\rm dcdm} = 0.1$, 0.4, 0.7, 1.

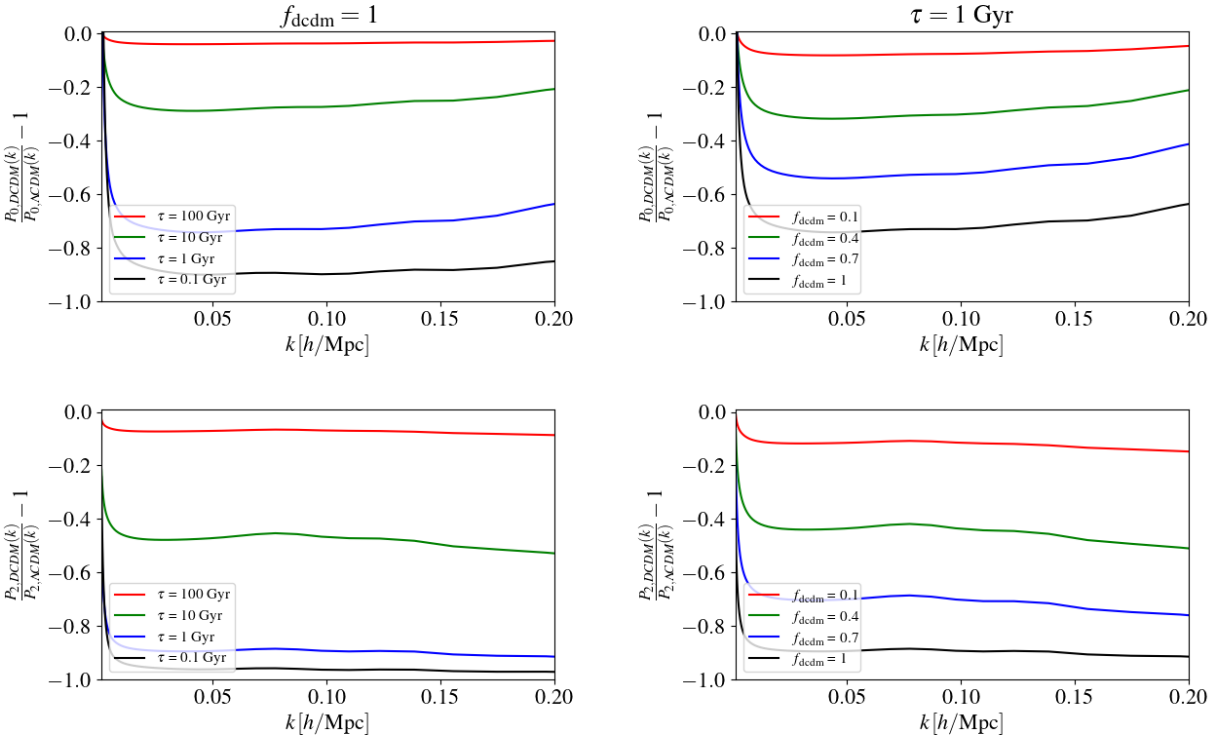

Figure 9.2: *Left* - Residuals of the monopole and the quadrupole of the galaxy power spectrum for $f_{\rm dcdm}$ set to 1 and $\tau = 0.1$, 1, 10, 100 Gyr. Residuals are taken with respect to the ΛCDM model at $z = 0$. *Right* - The same, but this time τ is set to 1 Gyr and $f_{\rm dcdm} = 0.1$, 0.4, 0.7, 1.

Parameter	$f_{\rm dcdm} = 0.0203$ & $\tau = 0.1$ Gyr	$f_{\rm dcdm} = 1$ & $\tau = 248.4$ Gyr
$\chi^2_{\rm CMASS\ NGC}$	41.3	40.7
$\chi^2_{\rm CMASS\ SGC}$	43.9	44.0
$\chi^2_{\rm LOWZ\ NGC}$	33.4	33.6
$\chi^2_{\rm EFTofBOSS}$	118.6	118.3
$\chi^2_{\rm min}({\rm DCDM}) - \chi^2_{\rm min}(\Lambda{\rm CDM})$	+0.8	+0.5

Table 9.1: χ^2 of each sky cut of the EFTofBOSS dataset for our DCDM $\rightarrow$ DR preliminary study. We also indicated the $\Delta\chi^2$ with respect to the analogous ΛCDM best-fit model (EFTofBOSS analysis in Tab. 9.7).

laying at the 95% C.L. [2] derived from *Planck* data, and compute the χ^2 of the EFTofBOSS data after optimizing the EFT nuisance parameters. The goal is to check the extent to which EFT nuisance parameters can lead to effects degenerate with those of the DCDM with a quick analysis. We set all ΛCDM parameters to their best-fit values from the analysis of *Planck* + Pantheon + EFTofBOSS + Ext-BAO (see Sec. 9.2). We perform two analyses: (i) we set $\tau = 0.1$ Gyr and take the upper bound on $f_{\rm dcdm}$ from our *Planck* + Pantheon + Ext-BAO (no Ly-α), *i.e.* $f_{\rm dcdm} = 0.0203$ (see Tab. 9.5), and (ii) we set $f_{\rm dcdm} = 1$ (*i.e.*, all the dark matter decays), while we take the lower bound of τ from our *Planck* + Pantheon + Ext-BAO (no Ly-α) analysis, *i.e.*, $\tau = 248.4$ Gyr (see Tab. 9.5). We show in Tab. 9.1 the χ^2 associated to the EFTofBOSS data, and we plot in Fig 9.3, using the `PyBird` code, the residuals (with respect to ΛCDM from the *Planck* + Pantheon + EFTofBOSS + Ext-BAO analysis) of these studies. To gauge the impact of EFT nuisance parameters, in this latter figure, we show residuals with and without the optimization procedure (in the latter case, we simply set the EFT nuisance parameters to those of ΛCDM). This preliminary study allows us to highlight two important points. First, the optimization procedure has washed out the suppression due to decay, which implies that the effect of the EFT nuisance parameters are (at least partly) degenerate with that of the decay. Second (and consequently), for these two analyses where we have chosen DCDM parameters that are excluded at 95% C.L., we obtain a χ^2 very close to that of the ΛCDM best-fit model of the full analysis, suggesting that EFTofBOSS data may not provide strong additional constraints to this model. Naturally, it does not prevent the model to potentially yield an improved fit over ΛCDM once all (cosmological and nuisance) parameters are optimized against the data, and we will check our naive results against a full analysis in Sec. 9.2.

9.1.2 Warm dark matter decay products (DCDM $\rightarrow$ WDM+DR model)

Presentation of the model

We now turn to a DCDM model where the entirety of the DM sector is considered unstable (*i.e.*, $f_{\rm dcdm} = 1$ in the language of the first model), decaying into dark radiation and a massive particle, which will act as WDM. As before, we assume the decay products do not interact with the standard model particles. The DCDM sector is now described by the DCDM lifetime τ, and the fraction ε of rest-mass energy carried away by the massless particle given by [413]

$$\varepsilon = \frac{1}{2}\left(1 - \frac{m^2_{\rm wdm}}{m^2_{\rm dcdm}}\right), \tag{9.15}$$

[2] From here on, we quote one-sided bounds at 2σ (95 % C.L.) and two-sided bounds at 1σ (68% C.L.).

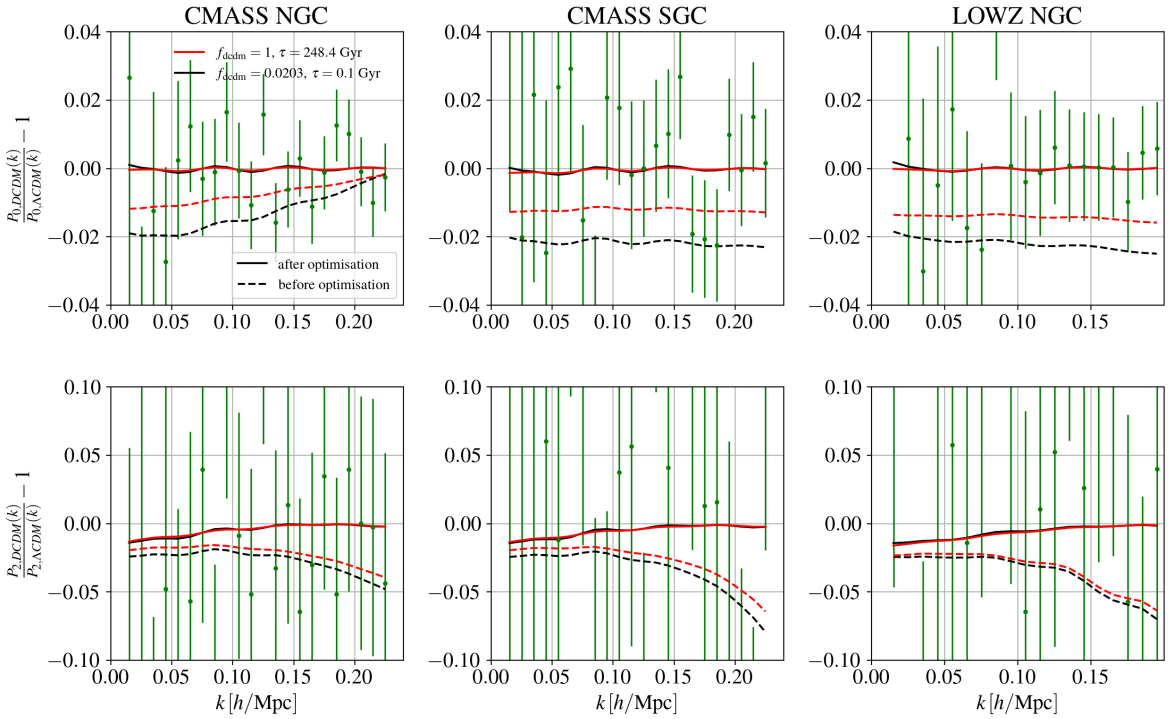

Figure 9.3: Residuals of the monopole and the quadrupole of our DCDM → DR preliminary study with respect to the ΛCDM model (EFTofBOSS analysis in Tab. 9.3) for the three sky cuts of the EFTofBOSS data. For the solid lines we optimized the EFT nuisance parameters, while for the dotted lines we set the EFT nuisance parameters to those of the ΛCDM (EFTofBOSS analysis in Tab. 9.3).

where $m_{\rm dcdm}$ and $m_{\rm wdm}$ are the mother and daughter particle masses respectively. The accurate computation of the cosmological impact of the DCDM sector requires to follow the evolution of the phase space distribution of the warm particle produced during the decay. The full set of equations is described in Refs. [414, 168]. We summarize here the sets of equations describing the evolution of the background energy densities of the dark components, as well as the linear perturbations in a fluid approximation, valid well within the horizon.

The background energy densities evolve as follows [414]:

$$\dot{\bar{\rho}}_{\rm dcdm} + 3\mathscr{H}\bar{\rho}_{\rm dcdm} = -a\Gamma\bar{\rho}_{\rm dcdm}, \tag{9.16}$$

$$\dot{\bar{\rho}}_{\rm wdm} + 3(1+w)\mathscr{H}\bar{\rho}_{\rm wdm} = (1-\varepsilon)a\Gamma\bar{\rho}_{\rm dcdm}, \tag{9.17}$$

$$\dot{\bar{\rho}}_{\rm dr} + 4\mathscr{H}\bar{\rho}_{\rm dr} = \varepsilon\Gamma a\bar{\rho}_{\rm dcdm} \tag{9.18}$$

where $w = \bar{P}_{\rm wdm}/\bar{\rho}_{\rm wdm}$ is the equation of state of the massive daughter particle. In the limit of large τ or small ε, one recovers the ΛCDM model, while setting $\varepsilon = 1/2$ leads to a decay solely into massless particles.

In the synchronous gauge comoving with the DCDM fluid, the linear perturbation equations for the parent particle and DR daughter is still given by Eq. (9.8) and Eqs. (9.9)-(9.12), respectively. However, the quantity $r_{\rm dr}$ now satisfies

$$\dot{r}_{\rm dr} = a\varepsilon\Gamma(\bar{\rho}_{\rm dcdm}/\bar{\rho}_{\rm dr})r_{\rm dr}, \tag{9.19}$$

where the parameter ε now affects the amount of energy transferred to the DR. Regarding the WDM linear perturbations, it is unfortunately not possible to integrate out the dependency on momenta as it is done for the DR species. In general one has to follow the evolution of the full phase-space distribution, which becomes very computationally demanding (see Ref. [168] for the expression of the full Boltzmann hierarchy). Nevertheless, it was shown in Ref. [168] that, well within the horizon, the dynamics of the WDM perturbations can be well approximated by the following set of fluid equations:

$$\begin{aligned}\dot{\delta}_{\rm wdm} &= -3\mathscr{H}(c_s^2-\omega)\delta_{\rm wdm} - (1+\omega)\left(\theta_{\rm wdm}+\frac{\dot{h}}{2}\right)\\ &\quad + (1-\varepsilon)a\Gamma\frac{\bar{\rho}_{\rm dcdm}}{\bar{\rho}_{\rm wdm}}(\delta_{\rm dcdm}-\delta_{\rm wdm}),\end{aligned} \tag{9.20}$$

$$\begin{aligned}\dot{\theta}_{\rm wdm} &= -\mathscr{H}(1-3c_g^2)\theta_{\rm wdm} + \frac{c_s^2}{1+\omega}k^2\delta_{\rm wdm} - k^2\sigma_{\rm wdm}\\ &\quad - (1-\varepsilon)a\Gamma\frac{1+c_g^2}{1+\omega}\frac{\bar{\rho}_{\rm dcdm}}{\bar{\rho}_{\rm wdm}}\theta_{\rm wdm},\end{aligned} \tag{9.21}$$

where c_s is the WDM sound speed in the synchronous gauge, *i.e.*, $c_s^2 = \delta P_{\rm wdm}/\delta\rho_{\rm wdm}$, and c_g is the WDM adiabatic sound speed, *i.e.*, $c_g^2 = \dot{\bar{P}}_{\rm wdm}/\dot{\bar{\rho}}_{\rm wdm}$, which one can write in the following form:

$$\begin{aligned}c_g^2 &= w\left(5 - \frac{\mathfrak{p}_{\rm wdm}}{\bar{P}_{\rm wdm}} - \frac{\bar{\rho}_{\rm dcdm}}{\bar{\rho}_{\rm wdm}}\frac{a\Gamma}{3w\mathscr{H}}\frac{\varepsilon^2}{1-\varepsilon}\right)\\ &\quad\times\left[3(1+w) - \frac{\bar{\rho}_{\rm dcdm}}{\bar{\rho}_{\rm wdm}}\frac{a\Gamma}{\mathscr{H}}(1-\varepsilon)\right]^{-1}.\end{aligned} \tag{9.22}$$

In this latter equation, $\mathfrak{p}_{\rm wdm}$ is the pseudo-pressure (introduced in the context of the fluid equations for massive neutrinos [415]), which corresponds to a higher momenta integral of the WDM homogeneous phase space distribution, reducing to the standard pressure in the relativistic limit. Solving the fluid equations requires specifying the sound speed c_s, which was found to be well described by the following formula:

$$c_s^2(k,\tau) = c_g^2[1+0.2\times(1-2\varepsilon)\sqrt{k/k_{\rm fs}}] \tag{9.23}$$

where the free-streaming scale $k_{\rm fs}$ of the WDM is computed as:

$$k_{\rm fs}(\tau) = \sqrt{\frac{3}{2}}\frac{\mathscr{H}(\tau)}{c_g(\tau)}. \tag{9.24}$$

The free-streaming scale corresponds to the scale at which pressure (coming from the "velocity kick" received during the decay process) suppresses perturbations of the WDM compared to those of the DCDM. In other words, on scales $k < k_{\rm fs}$, one has $\delta_{\rm wdm} = \delta_{\rm dcdm}$, while on scale $k > k_{\rm fs}$ the WDM perturbations are suppressed and exhibit oscillations over time.

To obtain the linear CMB and matter power spectrum, we make use of an extension of the `CLASS` code [3] described in Ref. [168], and we determine the nonlinear galaxy power spectrum

[3] https://github.com/PoulinV/class_decays

using the PyBird code. We have argued in previous section and in App. F.1, through direct comparison with N-body simulations, that PyBird can safely be used to describe DM decays with massless decay products. Unfortunately, we do not have access to such N-body simulations in the case of massive decay products. *A priori*, the problem is not the decay *per se* (as we have seen for the massless decay products). Rather, contrarily to the case of massless daugther, the massive daughter may develop perturbations whose contribution to the total matter power spectrum can be highly nontrivial. In App. F.2, following Refs [416, 417], which treated the similar case of massive neutrinos, we argue that the corrections to the EFTofLSS necessary to fully capture the model-specific effects can be neglected for most of the parameter space of interest, as the fractional contribution of the WDM to the DM density is small (in particular for the best-fit model that we derive), or the free-streaming scale exceeds the scale cut considered in the analysis.

The nonlinear power spectrum

We plot in Fig. 9.4 the residuals of the nonlinear matter power spectra of the DCDM $\to$ WDM+DR model with respect to that of the ΛCDM model at $z = 0$. We also represent the associated linear matter power spectra obtained from the CLASS code, exactly as in Fig. 4 of Ref. [168]. In addition, we plot in Fig. 9.5 the residuals of the monopole and quadrupole of the galaxy power spectra of this model. In these figures, the cosmological parameters are taken from the DCDM $\to$ WDM+DR best-fit model of Ref. [167], while the nuisance parameters are set as in Figs. 9.1 and 9.2. In the left panels, we fix $\varepsilon = 0.1$ and vary $\tau \in [10, 300]$ Gyr, while in the right panel we fix $\tau = 30$ Gyr and vary $\varepsilon \in [0.001, 0.5]$.

As for the case of the DCDM $\to$ DR model, we obtain a very similar behavior between the linear matter power spectrum and the monopole of the galaxy power spectrum, except for a mild monotonic reduction of the power suppression at larger k's in the monopole of the galaxy power spectrum (due to the choice of EFT parameters, this reduction of the suppression may change for different values). The presence of a warm dark matter component which does not cluster on small scales suppresses the matter power spectrum as well as the galaxy power spectrum, and τ– which sets the abundance of the WDM species today– controls the amplitude of the power suppression, while ε controls the cutoff scale. One can see in Fig. 9.5 that the suppression of the galaxy spectrum increases as τ decreases (left panel), while the suppression starts to occur on larger scales as ε increases (right panel). Once $\varepsilon = 0.5$, the free-streaming scale $k_{\rm fs}$ becomes equivalent to the Hubble horizon, and the effects become identical to that of the DCDM $\to$ DR model presented before. Note that because of the effect of the WDM, the $\varepsilon = 0.1$ case has a stronger suppression than the $\varepsilon = 0.5$ (pure dark radiation) case. Moreover, we find (see Fig. 9.4) that the nonlinear correction slightly modulates the slope of the power suppression compared to the linear matter power spectrum. It always leads to a stronger suppression than the linear one at large enough k (for $\varepsilon \gtrsim 0.1$, the modulation occurs at $k \gtrsim 0.1\, h\,\mathrm{Mpc}^{-1}$). However, for smaller ε (see the $\varepsilon = 0.01$ case for example), the modulation can appear as a milder power suppression compared to the linear one in the range of validity of the EFT at one loop order.

Preliminary study

Similarly to the case of the DCDM $\to$ DR model, we perform a preliminary study to test whether the EFTofBOSS data can further constrain the DCDM $\to$ WDM+DR model that re-

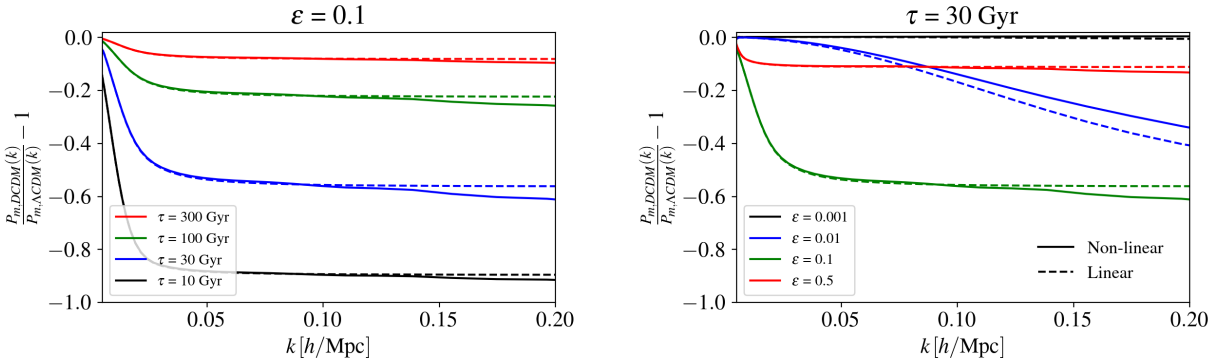

Figure 9.4: *Left* - Residuals of the linear (dashed lines) and nonlinear matter power spectrum (solid lines) for ε set to 0.1 and $\tau = 10, 30, 100, 300$ Gyr. Residuals are taken with respect to the ΛCDM model at $z = 0$. *Right* - The same, but this time τ is set to 30 Gyr and $\varepsilon = 0.001, 0.01, 0.1, 0.5$.

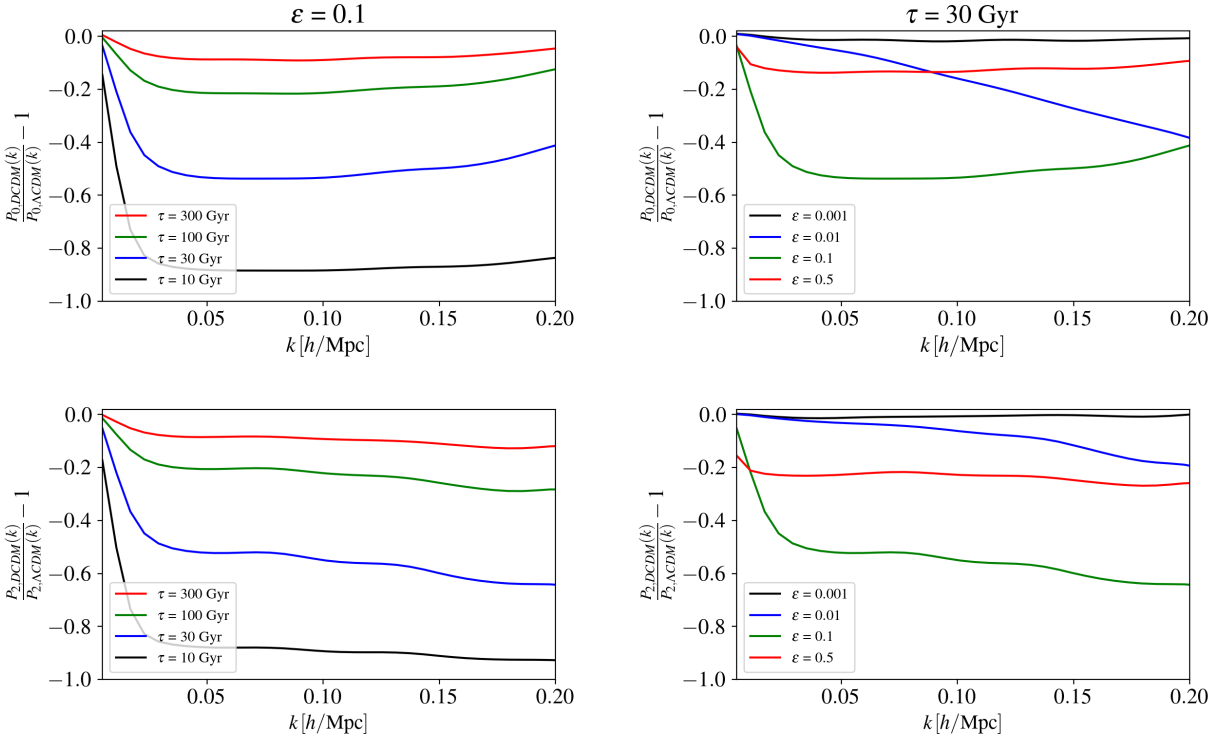

Figure 9.5: *Left* - Residuals of the monopole and the quadrupole of the galaxy power spectrum for ε set to 0.1 and $\tau = 10, 30, 100, 300$ Gyr. Residuals are taken with respect to the ΛCDM model at $z = 0$. *Right* - The same, but this time τ is set to 30 Gyr and $\varepsilon = 0.001, 0.01, 0.1, 0.5$.

Parameter	Best-fit
$\chi^2_{\text{CMASS NGC}}$	41.2
$\chi^2_{\text{CMASS SGC}}$	44.5
$\chi^2_{\text{LOWZ NGC}}$	34.4
$\chi^2_{\text{EFTofBOSS}}$	120.1
$\chi^2_{\text{min}}(\text{DCDM}) - \chi^2_{\text{min}}(\Lambda\text{CDM})$	+3.1

Table 9.2: χ^2 of each sky cut of the EFTofBOSS dataset for our DCDM $\to$ WDM+DR preliminary study. We also indicated the $\Delta\chi^2$ with respect to the analogous ΛCDM best-fit model (EFTofBOSS + S_8 analysis in Tab. 9.7).

solves the S_8 tension. We fix cosmological parameters [4] to those obtained from the joint analysis of *Planck* data, Pantheon SN1a data, a compilation of BAO data and the S_8 measurements by KiDS-1000 [80]. We optimize the EFT nuisance parameters of the galaxy power spectrum to check the extent to which they can lead to effects degenerate with those of the DCDM. We show in Tab. 9.2 the χ^2 associated to the EFTofBOSS data, while in Fig. 9.6, using the `PyBird` code, we plot the residuals with respect to the best-fit ΛCDM model from the analysis of *Planck* + Pantheon + EFTofBOSS + Ext-BAO (see Sec. 9.2). In this figure, we represent residuals with and without the EFT optimization procedure (in the latter case, we simply set the EFT nuisance parameters to those of ΛCDM). As before, one can see that the effects of the DCDM are strongly reduced once EFT nuisance parameters are optimized, suggesting a strong degeneracy between the DCDM and the EFT parameters. Nevertheless, for this preliminary study, the χ^2 is degraded by $+3.1$ compared to the best-fit χ^2 obtained in the ΛCDM model for the full analysis. Contrary to the preliminary study of the DCDM $\to$ DR model for which we obtained a χ^2 close to that of the ΛCDM model, we anticipate that the EFTofBOSS data can provide additional constraining power to this model.

9.2 A comprehensive MCMC analysis of the DCDM models

9.2.1 Data and method

We now perform a Monte Carlo Markov chain (MCMC) analyses, confronting these two DCDM models with recent cosmological observations. To do so, we make use of the `MontePython-v3` code [136, 137] interfaced with our modified `CLASS` version. We perform various analyses from a combination of the following datasets:

- **Planck**: The low-l CMB TT, EE, and the high-l TT, TE, EE data, as well as the gravitational lensing potential reconstruction from *Planck* 2018 [11, 179].
- **Pantheon**: The Pantheon SNIa catalog, spanning redshifts $0.01 < z < 2.3$ [133].
- **Ext-BAO**: The BAO measurements from 6dFGS at $z = 0.106$, SDSS DR7 at $z = 0.15$ [127, 128, 418], and the joint constraints from eBOSS DR14 Ly-α absorption autocorrelation at $z = 2.34$ and cross-correlation with quasars at $z = 2.35$ [130, 131].

[4] The analysis performed in Refs. [167, 168] made use of a S_8 prior that includes information from BOSS [177]. For consistency and to avoid double counting information, we reperformed the analysis (see Sec. 9.2) with a prior derived from KiDS-1000 data alone.

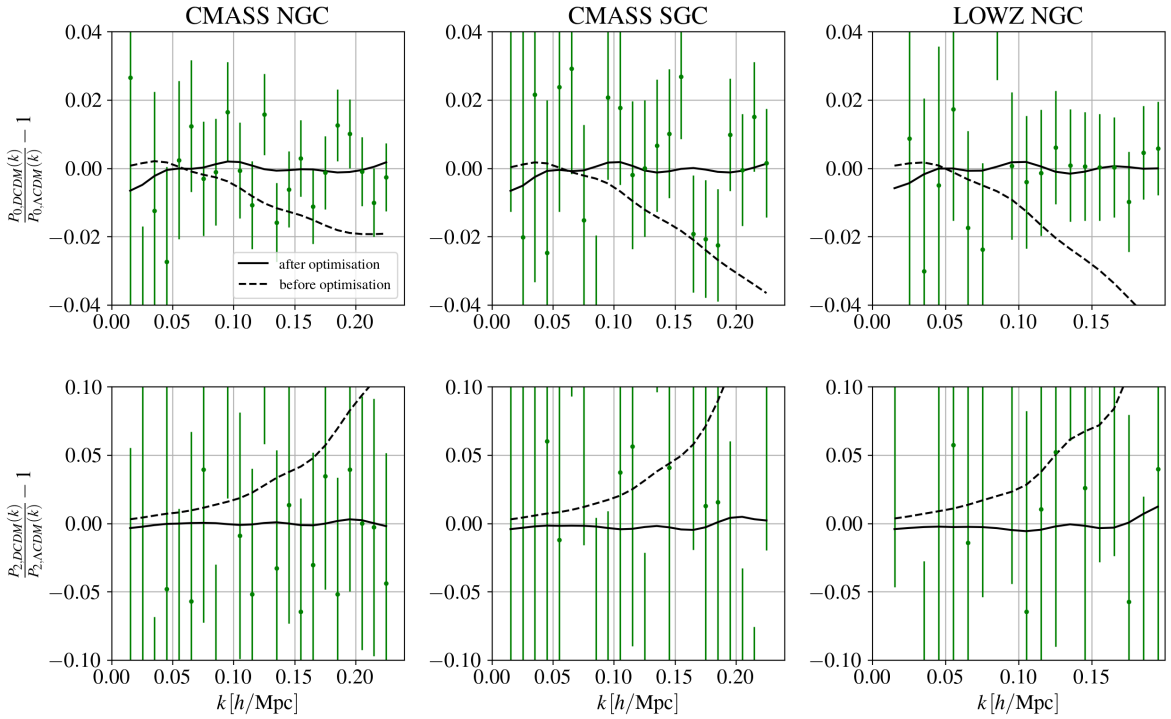

Figure 9.6: Residuals of the monopole and the quadrupole of our DCDM $\to$ WDM+DR preliminary study with respect to ΛCDM model (EFTofBOSS analysis in Tab. 9.3) for the three sky cuts of the EFTofBOSS data. For the solid lines we optimized the EFT nuisance parameters, while for the dotted lines we set the EFT nuisance parameters to those of the ΛCDM (EFTofBOSS analysis in Tab. 9.3).

- **BOSS BAO/$f\sigma_8$**: The measurements of the BAO and the redshift space distortion $f\sigma_8(z)$ from the CMASS and LOWZ galaxy samples of BOSS DR12 at $z = 0.38$, 0.51, and 0.61 [418].

- S_8: The KIDS-1000 cosmic shear measurement of $S_8 = 0.759^{+0.024}_{-0.021}$, modeled as a a split-normal likelihood [80].

- **EFTofBOSS**: The EFTofLSS analysis of BOSS DR12 LRG, cross-correlated with the reconstructed BAO parameters [126]. The SDSS-III BOSS DR12 galaxy sample data and covariances are described in [81, 125]. The measurements, obtained in [69], are from BOSS catalogs DR12 (v5) combined CMASS-LOWZ [124], and are divided in redshift bins LOWZ, $0.2 < z < 0.43$ ($z_{\rm eff} = 0.32$), and CMASS, $0.43 < z < 0.7$ ($z_{\rm eff} = 0.57$), with north and south galactic skies for each, respectively denoted NGC and SGC. From these data we use the monopole and quadrupole moments of the galaxy power spectrum. The theory prediction and likelihood for the full-modeling information are made available through `PyBird` [59].

Our analyses always includes *Planck*, Pantheon and Ext-BAO data. However, we quantify the impact of EFTofBOSS data and the S_8 prior by performing analyses with and without these data. When *not* including the EFTofBOSS data, we make use of the conventional BOSS BAO/$f\sigma_8$ data. We use *Planck* conventions for the treatment of neutrinos and include two massless and one massive species with $m_\nu = 0.06$ eV [11]. We impose a large flat prior on the

ΛCDM		
Parameter	w/ EFTofBOSS	w/ EFTofBOSS + S_8
$100\ \omega_{\rm b}$	$2.242(2.245)^{+0.014}_{-0.015}$	$2.247(2.248)\pm0.014$
$\omega_{\rm cdm}$	$0.1191(0.1191)\pm0.00095$	$0.1184(0.1184)\pm+0.00089$
$H_0/[{\rm km/s/Mpc}]$	$67.76(67.80)^{+0.42}_{-0.44}$	$68.05(68.07)\pm0.41$
$\ln(10^{10}A_s)$	$3.048(3.049)^{+0.015}_{-0.016}$	$3.043(3.043)^{+0.015}_{-0.016}$
n_s	$0.9666(0.9676)\pm0.0039$	$0.9680(0.9687)\pm0.0039$
$\tau_{\rm reio}$	$0.0571(0.0574)^{+0.0075}_{-0.0085}$	$0.0555(0.0549)^{+0.0077}_{-0.0078}$
$\Omega_{\rm m}$	$0.3098(0.3093)^{+0.0057}_{-0.0058}$	$0.3057(0.3055)\pm0.0053$
σ_8	$0.8097(0.8102)^{+0.0063}_{-0.0065}$	$0.8056(0.8055)\pm0.0062$
S_8	$0.82(0.82)\pm0.01$	$0.813(0.813)^{+0.0094}_{-0.0096}$
$\chi^2_{\rm min}$	3927.0	3933.0
$Q_{\rm DMAP}\equiv\sqrt{\chi^2_{\rm min}({\rm w/}\ S_8)-\chi^2_{\rm min}({\rm w/o}\ S_8)}$	2.4σ	

Table 9.3: The mean (best-fit) $\pm1\sigma$ errors of the cosmological parameters from our *Planck* + Pantheon + EFTofBOSS + Ext-BAO and *Planck* + Pantheon + EFTofBOSS + Ext-BAO + S_8 analyses for the ΛCDM model. For each dataset we also report its best-fit χ^2.

dimensionless baryon energy density ω_b, the Hubble parameter today H_0, the logarithm of the variance of curvature perturbations centered around the pivot scale $k_p = 0.05$ Mpc^{-1} (according to the *Planck* convention), $\ln\left(10^{10}\mathscr{A}_s\right)$, the scalar spectral index n_s, and the reionization optical depth $\tau_{\rm reio}$. We assume our MCMC chains to be converged when the Gelman-Rubin criterion $R-1<0.05$ [419]. Finally, we extract the best-fit parameters from the procedure highlighted in appendix of Ref. [183].

9.2.2 Dark radiation decay products

Let us recall that in the case of the DCDM → DR model we have two additional parameters: $\Gamma=\tau^{-1}$, the decay rate of DCDM, and $f_{\rm dcdm}$, the fraction of DCDM with respect to the total DM. In the MCMC analyses, we impose flat priors on Γ and f:

$$0\leq\Gamma/{\rm Gyr}^{-1}\leq10,$$
$$0\leq f_{\rm dcdm}\leq1.$$

Our results for the analyses with and without S_8 prior are presented in Tab. 9.4, while the results of the analyses of ΛCDM against the same datasets are given in Tab. 9.3. The χ^2 of the EFTofBOSS data are reported in Tab. 9.7. In Fig. 9.7, we display the 1D and 2D posteriors of $\left\{\Gamma/{\rm Gyr}^{-1},f_{\rm dcdm},H_0,S_8,\Omega_m\right\}$ for the DCDM → DR model with and without the EFTofBOSS dataset. In App. F.3, we represent the same figure, but this time with and without the S_8 prior (and with the EFTofBOSS dataset for both). Without the S_8 prior, the $\Delta\chi^2$ with respect to ΛCDM is compatible with zero [5] (see Tab. 9.4), implying that the data does not favor the DCDM → DR model. From Fig. 9.7, one can see that the inclusion of the EFTofBOSS data does not improve the constraint on this model, which is consistent with the "naive" analysis presented in Sec. 9.1.1. Moreover, we show that when adding the S_8 prior, the $\Delta\chi^2$ with respect to ΛCDM is still compatible with zero (and the model does not provide a good fit to the S_8 prior) while the constraints on Γ and $f_{\rm dcdm}$ are largely unaffected. We conclude (as in past studies) that this model does not resolve the S_8 tension.

[5] The improvement is below the precision of $\mathscr{O}(0.1)$ that we estimated on the minimization, and we therefore simply quote $\Delta\chi^2=0.0$. Hereafter, we follow the same approach when reporting other $\Delta\chi^2$.

DCDM→DR		
Parameter	w/ EFTofBOSS	w/ EFTofBOSS + S_8
$\Gamma/[\mathrm{Gyr}^{-1}]$	unconstrained (4.8)	unconstrained (5.8)
$f_{\rm dcdm}$	$< 0.0216 (1.62 \cdot 10^{-4})$	$< 0.0242 (1.67 \cdot 10^{-4})$
$100\ \omega_{\rm b}$	$2.236 (2.244) \pm 0.015$	$2.241 (2.248)^{+0.016}_{-0.015}$
$\omega_{\rm cdm}$	$0.1187 (0.1191) \pm 0.0010$	$0.1180 (0.1184)^{+0.001}_{-0.00093}$
$H_0/[\mathrm{km/s/Mpc}]$	$67.98 (67.77)^{+0.46}_{-0.48}$	$68.30 (68.10)^{+0.44}_{-0.47}$
$\ln(10^{10} A_s)$	$3.051 (3.049)^{+0.015}_{-0.016}$	$3.047 (3.045)^{+0.015}_{-0.016}$
n_s	$0.9650 (0.9671)^{+0.0042}_{-0.004}$	$0.9660 (0.9687)^{+0.0044}_{-0.0043}$
$\tau_{\rm reio}$	$0.0577 (0.0572)^{+0.0073}_{-0.0079}$	$0.0562 (0.0557)^{+0.0074}_{-0.0077}$
$\Omega_{\rm m}$	$0.3069 (0.3097) \pm 0.0061$	$0.3026 (0.3050)^{+0.0059}_{-0.0057}$
σ_8	$0.8110 (0.8101)^{+0.0063}_{-0.0066}$	$0.8071 (0.8061)^{+0.0062}_{-0.0063}$
S_8	$0.82 (0.82) \pm 0.01$	$0.811 (0.813)^{+0.0097}_{-0.0095}$
$\chi^2_{\rm min}$	3927.0	3933.0
$\chi^2_{\rm min}(\mathrm{DCDM}) - \chi^2_{\rm min}(\Lambda\mathrm{CDM})$	0.0	0.0
$Q_{\rm DMAP} \equiv \sqrt{\chi^2_{\rm min}(\mathrm{w/}\ S_8) - \chi^2_{\rm min}(\mathrm{w/o}\ S_8)}$	2.4σ	

Table 9.4: The mean (best-fit) $\pm 1\sigma$ errors of the cosmological parameters from our *Planck* + Pantheon + EFTofBOSS + Ext-BAO and *Planck* + Pantheon + EFTofBOSS + Ext-BAO + S_8 analyses for the DCDM $\rightarrow$ DR model. For each dataset we also report its best-fit χ^2, and the $\Delta\chi^2$ with respect to the analogous ΛCDM best-fit model.

DCDM → DR		
Datasets	$f_{\rm dcdm}$	τ (for $f_{\rm dcdm} = 1$)
Planck	< 0.0205	> 246.3 Gyr
Planck + Pantheon + Ext-BAO (no Ly-α)	< 0.0203	> 248.4 Gyr
Planck + Pantheon + BOSS BAO/$f\sigma_8$ + Ext-BAO (no Ly-α)	< 0.0190	> 260.4 Gyr
Planck + Pantheon + BOSS BAO/$f\sigma_8$ + Ext-BAO	< 0.0219	> 250.0 Gyr
Planck + Pantheon + EFTofBOSS + Ext-BAO	< 0.0216	> 249.6 Gyr

Table 9.5: The 95% C.L. limit on $f_{\rm dcdm}$ for the standard DCDM $\rightarrow$ DR analysis, and the 95% C.L. limit on τ for the DCDM $\rightarrow$ DR analysis where $f_{\rm dcdm}$ is fixed to the unit. Let us recall that "Ext-BAO" refers to the BAO measurements from 6dFGS, SDSS DR7, and the joint constraints from eBOSS DR14 Ly-α autocorrelation and cross-correlation. For some datasets we removed the Ly-α constraints ('no Ly-α') to explicitly show its impact.

To summarize our results, and present the most up-to-date constraints on DCDM with massless decay products, in Tab. 9.5 we compare the 95% C.L. limits obtained for $f_{\rm dcdm}$ and τ when successively adding datasets. To obtain the bounds on $f_{\rm dcdm}$ (in the "short-lived" regime), we marginalize over the parameter Γ in the range described above. On the other hand, to obtain the τ limits (in the "very long-lived" regime), we fix $f_{\rm dcdm} = 1$ in our MCMC analyses, *i.e.*, we assume that all DM decays. Note that, for $f_{\rm dcdm} \rightarrow 1$, one can interpret our constraints as a limit on the ratio $\tau/f_{\rm dcdm}$, as discussed in Ref. [381]. From Tab. 9.5, one can deduce the following:

- The strongest constraints are obtained when considering *Planck* + Pantheon + BOSS BAO/$f\sigma_8$ + Ext-BAO (no Ly-α). In that case, we find $f_{\rm dcdm} < 0.0190$ (in the short-lived regime), and $\tau/f_{\rm dcdm} > 260.4$ Gyr (for $f_{\rm dcdm} \rightarrow 1$).

- On the other hand, the inclusion of Ly-α BAO data slightly reduces the constraints. This is consistent with the fact that these data are compatible with ΛCDM only at the 1.7σ level [130, 131], favoring lower energy density at high-z [420]. Additionally, we find

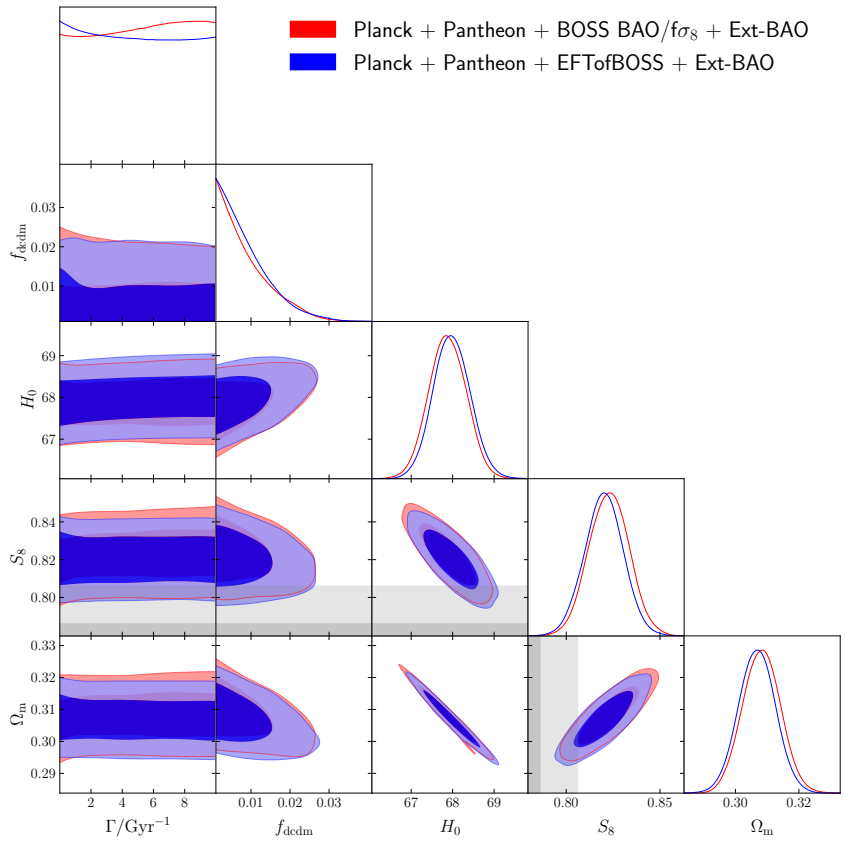

Figure 9.7: 2D posterior distributions of the DCDM $\rightarrow$ DR model with and without the EFTofBOSS dataset. The gray shaded bands refer to the joint S_8 measurement from KiDS-1000 + BOSS + 2dFLens [177].

that constraints with the EFTofBOSS data are the same as those with the standard redshift space distortion $f\sigma_8$ information. Our fiducial constraints, including all data, are therefore $f_{\rm dcdm} < 0.0216$, and $\tau/f > 249.6$ Gyr.

- Our constraints are somewhat different than those derived in Ref. [384], which considering *Planck* 2018 + BAO data (see Tab. 2 of this reference) found $f_{\rm dcdm} < 0.0262$ at 95 % C.L. and $\tau/f_{\rm dcdm} > 268.8$ Gyr. Our constraints are stronger on $f_{\rm dcdm}$, compatible with the fact that we include more data, but weaker on τ, which may be explained by the fact that their posteriors never quite reach $f_{\rm dcdm} \sim 1$, as necessary to derive constraints in the "very long-lived" regime.

9.2.3 Warm dark matter decay products

We now turn to the case of the DCDM $\rightarrow$ WDM+DR model, described by the parameters $\Gamma = \tau^{-1}$, the decay rate of DCDM, and ε, the fraction of DCDM rest mass energy converted into DR. Note that in this section, we trade the density of DM today, $\omega_{\rm cdm}$, for the initial density of DM (before decays occur) at $a \rightarrow 0$, $\omega^{\rm ini}_{\rm dcdm}$. For a stable particle, we simply have $\omega^{\rm ini}_{\rm dcdm} \equiv \omega_{\rm cdm}$ as defined previously. In the MCMC analyses, we imposed logarithmic priors [6]

[6] For discussions about the impact of prior choices, see the appendix of Ref. [168]

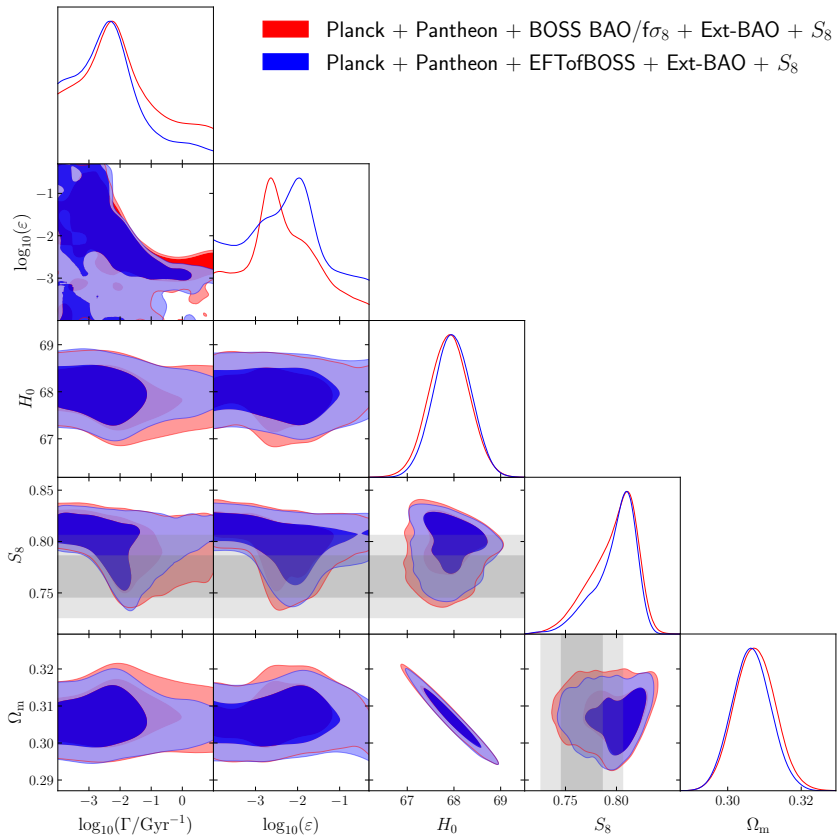

Figure 9.8: 2D posterior distributions of the DCDM → WDM+DR model with and without the EFTofBOSS dataset. We took into account the S_8 prior from KIDS-1000 for these two MCMC analyses. The gray shaded bands refer to the joint S_8 measurement from KiDS-1000 + BOSS + 2dFLens.

on ε and Γ, and a flat prior on $\omega_{\rm dcdm}^{\rm ini}$:

$$\begin{aligned} -4 \leq \log_{10}(\Gamma/[\mathrm{Gyr}^{-1}]) \leq 1, \\ -4 \leq \log_{10}(\varepsilon) \leq \log_{10}(0.5), \\ 0 \leq \omega_{\rm dcdm}^{\rm ini} \leq 1. \end{aligned}$$

We present our results for the analyses with and without S_8 prior in Tab. 9.6, while the χ^2 of the EFTofBOSS data of these analysis are reported in Tab. 9.7. All relevant χ^2 per experiment are given in App. F.4. In Fig. 9.8, we display the 1D and 2D posteriors of $\{\log_{10}(\Gamma/[\mathrm{Gyr}^{-1}]), \log_{10}(\varepsilon), H_0, S_8, \Omega_m\}$ for the DCDM → WDM+DR model with and without the EFTofBOSS dataset, always including the S_8 prior. Posteriors without the S_8 prior are shown in App. F.3.

Estimating the tension with the S_8 measurement

Without the S_8 prior, the total χ^2 does not show any improvement (see Tab. 9.6) and the data do not favor the DCDM → WDM+DR model. In fact, in the absence of the S_8 prior, it seems that one could derive apparently strong constraints on these models. [7] Yet, once the S_8

[7] In Ref. [168], it was shown through a mock data analysis that *Planck* data alone could not detect the best-fit model required to explain the S_8 tension, artificially leading to strong constraints on the DCDM model.

DCDM→WDM+DR		
Parameter	w/ EFTofBOSS	w/ EFTofBOSS + S_8
$\log_{10}(\Gamma/[\mathrm{Gyr}^{-1}])$	unconstrained (-2.98)	$2.21(-2.08)^{+1.5}_{-0.6}$
$\log_{10}(\varepsilon)$	unconstrained (-3.84)	$-2.30(-1.92)^{+0.84}_{-1.10}$
$100\ \omega_b$	$2.242(2.245)^{+0.014}_{-0.014}$	$2.245(2.242)^{+0.014}_{-0.015}$
$\omega^{\rm ini}_{\rm dcdm}$	$0.1192(0.1190)^{+0.00089}_{-0.0009}$	$0.1188(0.1192)^{+0.00084}_{-0.00099}$
$H_0/[\mathrm{km/s/Mpc}]$	$67.78(67.82)^{+0.41}_{-0.42}$	$67.97(67.73)^{+0.44}_{-0.42}$
$\ln(10^{10}A_s)$	$3.049(3.051)^{+0.015}_{-0.016}$	$3.046(3.052)^{+0.015}_{-0.016}$
n_s	$0.9668(0.9679)\pm0.0039$	$0.9676(0.9670)\pm0.0039$
$\tau_{\rm reio}$	$0.0571(0.0584)^{+0.0071}_{-0.0080}$	$0.0564(0.0584)^{+0.0074}_{-0.0077}$
$\Omega_{\rm m}$	$0.3090(0.3089)^{+0.0055}_{-0.0057}$	$0.3064(0.3094)^{+0.0055}_{-0.0058}$
σ_8	$0.806(0.811)^{+0.012}_{-0.014}$	$0.790(0.763)^{+0.027}_{-0.010}$
S_8	$0.818(0.823)^{+0.016}_{-0.012}$	$0.798(0.775)^{+0.025}_{-0.012}$
$\chi^2_{\rm min}$	3927.0	3929.3
$\chi^2_{\rm min}(\mathrm{DCDM})-\chi^2_{\rm min}(\Lambda\mathrm{CDM})$	0.0	−3.8
$Q_{\rm DMAP}\equiv\sqrt{\chi^2_{\rm min}(\mathrm{w/}\ S_8)-\chi^2_{\rm min}(\mathrm{w/o}\ S_8)}$	1.5σ	

Table 9.6: The mean (best-fit) $\pm1\sigma$ errors of the cosmological parameters from our *Planck* + Pantheon + EFTofBOSS + Ext-BAO and *Planck* + Pantheon + EFTofBOSS + Ext-BAO + S_8 analyses for the DCDM → WDM+DR model. For each dataset we also report its best-fit χ^2, and the $\Delta\chi^2$ with respect to the analogous ΛCDM best-fit model.

	ΛCDM		DCDM → DR		DCDM → WDM+DR	
	w/ EFTofBOSS	w/ EFTofBOSS + S_8	w/ EFTofBOSS	w/ EFTofBOSS + S_8	w/ EFTofBOSS	w/ EFTofBOSS + S_8
$\chi^2_{\rm CMASS\ NGC}$	40.3	39.2	40.4	39.2	40.2	40.8
$\chi^2_{\rm CMASS\ SGC}$	44.0	44.3	44.0	44.3	44.1	43.8
$\chi^2_{\rm LOWZ\ NGC}$	33.5	33.5	33.5	33.5	33.5	33.7
$\chi^2_{\rm EFTofBOSS}$	117.8	117.0	117.9	117.0	117.8	118.3
p-value	0.54	0.56	0.49	0.51	0.49	0.47

Table 9.7: χ^2 of each sky cut of the EFTofBOSS dataset for our *Planck* + Pantheon + EFTofBOSS + Ext-BAO and *Planck* + Pantheon + EFTofBOSS + Ext-BAO + S_8 analyses for ΛCDM, DCDM → DR and DCDM → WDM+DR models.

likelihood is included, we find $\Delta\chi^2=-3.8$ (for 2 extra degrees of freedom) at virtually no cost in χ^2 for other likelihoods (see App. F.4): the inclusion of the S_8 prior helps in opening up the degeneracy with the DCDM parameters, without degrading the fit to the host of cosmological data, as stressed in Refs. [167, 168].

Nevertheless, the DCDM model is not statistically favored over ΛCDM, as the preference over ΛCDM is currently solely driven by the low S_8 prior, for which we have used a value only in mild $\sim 2.4\sigma$ tension with the ΛCDM prediction. [8] We can estimate the residual tension between datasets within the various models by computing the "difference in maximum a posterior" ($Q_{\rm DMAP}$ statistics [352]) between the χ^2 obtained with and without the S_8 prior. The

[8] Different S_8 priors would lead to different preferences. The preference could also be made stronger at fixed ε (see Ref. [168]).

tension estimator [9] at their MAP point gives $Q_{\rm DMAP} = 1.5\sigma$ in the DCDM→WDM+DR model, as compared to 2.4σ in the ΛCDM and DCDM→DR models.

Impact of EFTofBOSS data

Comparing to results without the EFTofBOSS data, for which we get [10] $\Delta\chi^2 = -4.4$, we find that the $\Delta\chi^2$ is only mildly degraded by the inclusion of EFTofBOSS data. More precisely, the χ^2 of the total EFTofBOSS data for the DCDM → WDM+DR model, given in Tab. 9.7, is only slightly larger than that for ΛCDM ($\Delta\chi^2 = 1.3$) despite a much lower $S_8 \simeq 0.775$ (at the best-fit) which yields a very good fit of the KiDS-1000 prior. Comparing to the analysis with the BAO/$f\sigma_8$ measurement from BOSS-DR12 (also presented in App. F.4), we note that these "compressed" data already showed a minor degradation of χ^2 compared to ΛCDM ($\Delta\chi^2 = 1.1$). We conclude that BOSS-DR12 data are in good agreement with the DCDM → WDM+DR model, but have a non-negligible impact, as the "naive" analysis presented in Sec. 9.1.2 suggested.

More precisely, one can see in Fig. 9.8 that the main impact of EFTofBOSS data is to cut in the $\log_{10}(\Gamma/{\rm Gyr}^{-1}) - \log_{10}(\varepsilon)$ degeneracy, excluding too large values of $\log_{10}(\Gamma/{\rm Gyr}^{-1})$. In App. F.5 we show that including the EFTofBOSS data does not shift the ΛCDM parameters. Therefore, the EFTofLSS significantly improves the constraints on the $\tau = \Gamma^{-1}$ parameter at 1σ:

$$1.61 < \log_{10}(\tau/{\rm Gyr}) < 3.71 \quad ({\rm w/EFTofBOSS}),$$

to be compared with

$$1.31 < \log_{10}(\tau/{\rm Gyr}) < 3.82 \quad ({\rm w/o\ EFTofBOSS}).$$

Additionally, we observe a notable evolution of the DCDM parameters of the best-fit model compared to the analysis without EFTofBOSS (and with the BAO/$f\sigma_8$ measurement from BOSS-DR12 instead): the best-fit model, with the inclusion of the S_8 likelihood, now has $\Gamma = 0.0083$ Gyr^{-1} ($\tau = 120$ Gyr) and $\varepsilon = 0.012$, while previously $\Gamma = 0.023$ Gyr^{-1} ($\tau = 43$ Gyr) and $\varepsilon = 0.006$. This means that EFTofBOSS data favors longer lived DM models and therefore a smaller fraction of WDM today $f_{\rm wdm} \equiv \bar\rho_{\rm wdm}/(\bar\rho_{\rm dcdm} + \bar\rho_{\rm wdm}) \simeq 10\%$ compared to $f_{\rm wdm} \simeq 27\%$ previously, but a significantly larger kick velocity $v_{\rm kick}/c \simeq \varepsilon$ (and therefore a larger free-streaming scale).

It is instructive to compare these numbers with recent constraints derived from observations of Milky Way satellites by the DES collaboration [421]. These constraints exclude $\log_{10}(\Gamma/{\rm Gyr}^{-1}) \gtrsim -1.5$ for $\log_{10}(v_{\rm kick}/c) \simeq \log_{10}(\varepsilon) \gtrsim -4$. The best-fit model of our EFTofBOSS analysis, and a large fraction of the 68% C.L., lie well within the allowed region,

[9] In general, $Q_{\rm DMAP}$ is computed as the difference of effective $\chi^2 = -2{\rm Log}\mathscr{L}(\theta^{\rm MAP})$, where $\mathscr{L}(\theta^{\rm MAP})$ is the likelihood evaluated on the maximum *a posteriori* $\theta^{\rm MAP}$, between the χ^2 obtained in the combined analysis and the sum of the χ^2 obtained in the individual analyses. For Gaussian $\mathscr{L}$, it is distributed as a χ^2 distribution with $N_1 + N_2 - N_{12}$ degrees of freedom (d.o.f.), where N_i refers to the number of d.o.f. in the individual ($i = 1, 2$) and combined analysis ($i = 12$). In the case of the combination of *Planck* and a Gaussian prior on S_8, it follows a χ^2 distribution with one d.o.f., and the tension can be evaluated as $Q_{\rm DMAP} \equiv \sqrt{\chi^2_{\rm min}({\rm w/}\ S_8) - \chi^2_{\rm min}({\rm w/o}\ S_8)}$.

[10] This number is different from that quoted in Refs. [167, 168] because we recall that we make use of a different S_8 prior from KiDS-1000 alone, which does not include information from BOSS data and therefore has larger error bars.

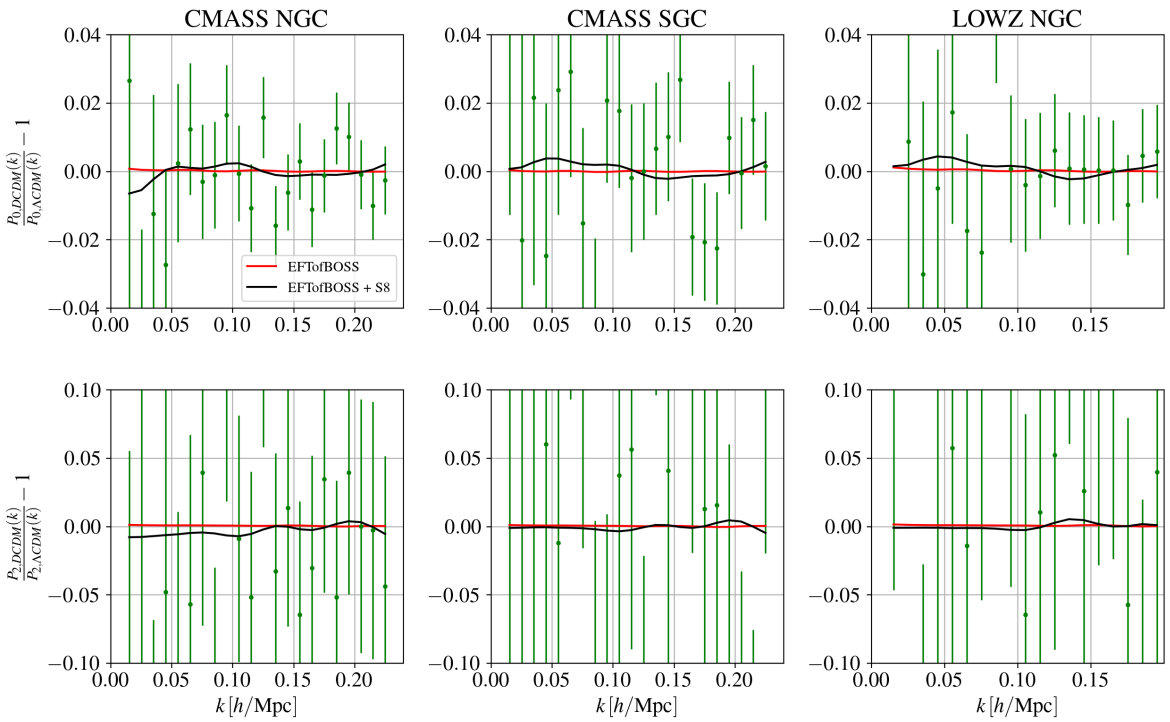

Figure 9.9: Residuals of the monopole and the quadrupole of the DCDM $\to$ WDM+DR model for EFTofBOSS data and EFTofBOSS data + S_8 prior. We normalized these residuals as well as the data with the ΛCDM best-fit (EFTofBOSS data).

but these observations certainly provide a crucial test of the DCDM cosmology, as a deficit of satellites compared to ΛCDM is expected in this model.

Towards high-accuracy measurements of the galaxy power spectrum

To gauge the importance of future surveys in constraining the DCDM $\to$ WDM+DR model, we show in Fig. 9.9 the residuals of the monopoles and quadrupoles of the galaxy power spectrum between the DCDM $\to$ WDM+DR and ΛCDM models. One can see that there are sub-percent differences between the models that gives us hope to probe the DCDM model further. Indeed, future galaxy clustering power spectrum data with higher precision and measurements at additional redshift bins such as Euclid [172], VRO [422] and DESI [171] have an expected sensitivity that should allow us to detect these mild differences. In order to estimate the impact of future observations on the preference of the DCDM $\to$ WDM+DR model with respect to the ΛCDM model, we plot in Fig. 9.10 the residuals of the nonlinear matter power spectrum [11] between the best-fit of the DCDM $\to$ WDM+DR model (for the EFTofBOSS + S_8 analysis) and ΛCDM model (for the EFTofBOSS analysis). We represent it for different redshifts, starting at the minimal redshift probed by an experiment like Euclid [172]. Note that at the level of the nonlinear matter power spectrum, the suppression with respect to the ΛCDM model at $z = 0.32$ and $z = 0.57$ corresponding to current observations is more than 1 order of magnitude stronger than what is seen in the residual of the monopole and quadrupole of the galaxy power spectrum

[11] We set here $c_s = 1$, which is an effective parameter of the one loop correction that can be interpreted as the effective sound speed of the dark matter.

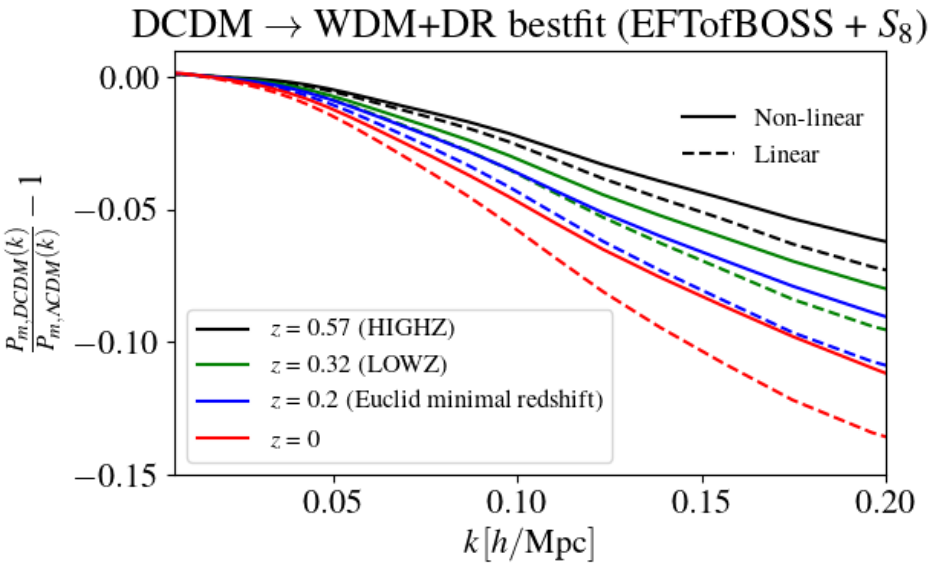

Figure 9.10: Residuals of linear (dashed lines) and nonlinear (solid line) matter power spectrum of the DCDM → WDM+DR model (EFTofBOSS data + S_8 prior) for $z = 0$, 0.2 (Euclid minimal redshift), 0.32 (effective redshift of the LOWZ sky cut) and 0.57 (effective redshift of the CMASS sky cut). We normalized these residuals with the ΛCDM best-fit (EFTofBOSS data).

(see Fig. 9.9). This is due to the impact of the degeneracy between the DCDM parameters and the EFT galaxy bias parameters, which can counteract the effect of the DCDM decay in the galaxy power spectrum. This shows that current theoretical uncertainties associated with galaxy bias parameters limit the ability to use galaxy (clustering) surveys to probe the DCDM model, and represent a potential challenge to fully exploit future surveys. Additionally, we observe that as z decreases, the deviation from ΛCDM increases significantly because of the production of WDM through the decay. We keep for future work to check through dedicated forecasts whether accumulation of low redshift data, as well as the reduction of error bars, will allow us to firmly detect or exclude the DCDM → WDM+DR model that resolves the S_8 tension.

9.3 Conclusions

In this chapter, we have confronted two models of DCDM with BOSS DR12 galaxy power spectrum data [418] as described by the EFTofLSS from Refs. [65, 60, 66, 67, 64, 94, 59]. We focused first on a model where a fraction of dark matter decays into dark radiation, the DCDM → DR model, and second on a model where all the dark matter decays into warm massive particles and dark radiation particles, the DCDM → WDM+DR model. The latter model was recently suggested as a possible resolution to the S_8 tension, the mismatch between the determination of the S_8 parameter from the *Planck* CMB power spectrum [11] and from weak lensing surveys by KiDS [177, 80], CFHTLenS [423] and DES [79]. We presented in Sec. 9.1 the first calculation of the nonlinear (matter and galaxy) power spectra in DCDM models making use of recent progresses in the EFTofLSS. We then confronted in Sec. 9.2 these two models to a compilation of *Planck* TTTEEE and lensing power spectra, BAO data from

BOSS and eBOSS (including Ly-α data), uncalibrated luminosity distance to SN1a from the Pantheon catalog [133], as well as measurements of the monopole and quadrupole of the galaxy power spectrum for three different sky cuts of BOSS-DR12 (see Ref. [69]), namely LOWZ NGC, CMASS NGC and CMASS SGC [418]. We compared the use of either the BAO/$f\sigma_8$ from that same release, or the full shape of the galaxy power spectrum. Additionally, we tested the ability of these models to resolve the S_8 tension by performing analyses with and without prior on S_8 as measured by KiDS [80]. Our results can be summarized as follows:

- We have derived the most up-to-date bound on the fraction of decaying dark matter $f_{\rm dcdm}$, which is now $f_{\rm dcdm} < 0.0216$ for short-lived DCDM. We have also updated constraints on the lifetime of dark matter for the case where $f_{\rm dcdm} \to 1$, namely $\tau/f_{\rm dcdm} > 249.6$ Gyr. However, we have found that the EFTofLSS does not provide significantly better constraints to the cosmological parameters for the DCDM $\to$ DR model, compared to the use of the standard BAO/$f\sigma_8$ data. In agreement with past studies, we have found that these models do not help neither for the S_8 nor for the H_0 tension, and the inclusion of EFTofBOSS data does not alter that conclusion.

- The DCDM $\to$ WDM+DR model can explain the low S_8 value measured by KiDS-1000 while preserving the goodness of fit to other dataset, including EFTofBOSS data. The residual tension is 1.5σ compared to 2.4σ in the ΛCDM model. Nevertheless, the model is not statistically favored over ΛCDM ($\Delta\chi^2 = -3.8$ for 2 degrees of freedom, roughly corresponding to 1.5σ). The inclusion of EFTofBOSS data only marginally affects the preference.

- EFTofBOSS data however do significantly improve the 1-σ constraint on the DCDM lifetime for the DCDM $\to$ WDM+DR model, and when combined with the S_8 prior, we now obtain $\log_{10}(\tau/{\rm Gyr}) = 2.21^{+1.5}_{-0.6}$ compared to $\log_{10}(\tau/{\rm Gyr}) = 1.92^{+1.9}_{-0.61}$ without the EFTofBOSS. The constraints on $\log_{10}(\varepsilon)$ are however slightly weaker than with BAO/$f\sigma_8$ measurements.

- The EFTofBOSS data also affects the best-fit model which, with the inclusion of the S_8 likelihood, corresponds to a longer lived DM with $\tau = 120$ Gyr (compared to $\tau = 43$ Gyr previously) and a larger kick velocity $v_{\rm kick}/c \simeq \varepsilon = 1.2\%$ (compared to $v_{\rm kick}/c \simeq 0.6\%$ previously).

Looking forward, we expect future galaxy clustering power spectrum data, with higher precision and measurements at additional redshift bins such as Euclid [172], VRO [422] and DESI [171], to provide us with exquisite sensitivity to DM decays into an invisible sector whether massive or massless. Moreover, as the error bars decrease, it will likely be necessary to identify and account for the corrections to be made to the EFTofLSS in order to capture all the specific effects of the DCDM $\to$ WDM+DR model. Following Ref. [416] for the case of massive neutrinos, it will be important to determine the one loop terms and associated counterterms of the mildly nonlinear galaxy power spectrum caused by the WDM contribution to the linear matter power spectrum (which we have argued in App. F.2 to likely be small compared to current error bars). We keep for future work to test whether these surveys will be able to firmly detect or exclude the DCDM $\to$ WDM+DR model that resolves the S_8 tension.

X

Conclusion

This thesis focuses on two different but complementary axes of research. In the first axe, we concentrated on the effective field theory of large-scale structures (EFTofLSS), and in particular the study of its constraints when applied to the BOSS and eBOSS data and the study of its self-consistency through prior effects. In the second axe, we were interested in the application of this theory (always with BOSS and sometimes eBOSS data) to non-trivial extensions of the ΛCDM model, particularly relevant to the resolution of cosmological tensions. These two axes of research are distinct in that they address different questions: *how to obtain the most robust and optimised constraints from large-scale structure data?* for the first one, and *what is the impact of large-scale structure data on the constraints of models beyond ΛCDM?* for the second one. In addition, these two axes are complementary insofar as they take place within a common framework, namely EFTofLSS. The first part of this thesis is fundamental to the second part in that it establishes the theoretical and analysis framework – and in particular its advantages and limitations – which is used in the second part. The second part, in turn, is an extension of the analysis carried out in the first part, and gives an idea of the very wide range of applications that can be covered by the EFTofLSS. In the following, we summarise the main results of each of the chapters of this thesis.

In chapters 1, 2 and 3 we respectively presented the paradigm of the modern cosmology for the smooth universe, the linearly perturbed universe (with the CMB physics) and the non-linearly perturbed universe (with the LSS physics). In particular, this last chapter sets out the conceptual and theoretical foundations on which this thesis is based.

In chapter 4, we have performed the first EFT analysis of the eBOSS QSO full-shape data. We have combined this analysis with other LSS data in order to obtain independent constraints from *Planck*. As our results are in good agreement with *Planck*, we have combined LSS and CMB probes in order to break the degeneracies present in the CMB. In addition, the EFT analysis of eBOSS QSOs provides independent measurements of the ΛCDM parameters in a different redshift range ($z \sim 1.5$) than previous EFT analyses, and from yet another tracer. Interestingly, we find good consistency between the EFT analysis of eBOSS QSO data, the EFT analysis of BOSS LRG data, and the *Planck* data. This consistency is a non-trivial check of the ΛCDM model and the many associated assumptions, as we considered very different data both in terms of redshift and in terms of the objects being probed. In addition to further testing the ΛCDM model, we have assessed that eBOSS data help improving constraints on

extended cosmological models in which the late-time background dynamics departs from flat-ΛCDM. When we combined our LSS analysis with the *Planck* data, we obtained very strong constraints on the canonical extensions to the ΛCDM model, for example on the sum of the neutrino masses. Finally, we have shown (i) the importance of going beyond conventional BAO/$f\sigma_8$ analysis with the EFTofLSS in order to constrain simple extensions to ΛCDM with LSS data only, and (ii) that the clustering data analysed with an EFT analysis are compatible with the flat-ΛCDM model, with and without the combination with the *Planck* data.

In chapter 5, we have looked at two BOSS EFT full-shape analyses, the so-called "West-coast" (WC) and "East-coast" (EC) analyses, that have been implemented in the `PyBird` and `CLASSPT` pipeline, respectively. These analyses lead to differences in the reconstructed cosmological parameters of up to 1σ. Given that they all come from the same BOSS data, this may be consider surprising and unsatisfactory. In order to explore the origin of these differences, we performed a series of analyses of the BOSS full-shape data, varying one-by-one (in order of importance) the prior choices, the BOSS measurements used (full-shape and post-reconstructed BAO parameters), the scale cuts and the number of multipoles included. Importantly, we found that cosmological constraints are sensitive to the choice of prior on the EFT parameter space, and that the two different choices of prior used in the `PyBird` and `CLASS-PT` analyses drive most of the differences in the results. On the other hand, the different BOSS full-shape measurements leads to at most 0.6σ difference among all cosmological parameters, while the different post-reconstructed BAO measurements can affect constraints by up to 0.9σ. Yet, when the choices of prior and data are the same, we show that the two pipelines agree at better than 0.2σ, which consists in an important validation check of the two public likelihoods available. Our analysis thus shows that the difference is mainly driven by prior effects emanating from the Bayesian analysis, and not from the theory, the data or the code implementations.

In chapter 6, we complement the results of the standard Bayesian analysis, as performed in chapters 4 and 5, with a profile likelihood analysis. The profile likelihood is a frequentist method based only on the maximum likelihood estimate (MLE) and, therefore, inherently reparametrization invariant and prior independent. Our goal was to understand the impact of priors on the EFT parameters on the inferred cosmological parameters and how this will change with more constraining data. We found that the WC and EC parametrizations applied to the BOSS data yield the same confidence interval for σ_8, confirming that the two parametrizations are mathematically equivalent. However, we found that the profile likelihood gives constraints on σ_8 that are factors of > 2 wider than the constraints based on the MCMC posterior. Our results clearly show the advantages and disadvantages of frequentist and Bayesian parameter inference. Since the frequentist inference does not include priors that confine the EFT parameters to the regime intended by the theory, we observe that the data prefers several EFT parameters to take on extreme values, possibly breaking the perturbativeness of the theory. The lack of prior further leads to significantly wider confidence intervals. This loss of constraining power reflects the purely data driven frequentist approach, which is completely agnostic about which model parameters are deemed more likely *a priori*. On the other hand, the priors in the Bayesian inference are informative and have an impact on the inferred cosmological parameters. This is important since it is not straightforward to define well motivated priors on the EFT parameters, which is reflected in the fact that the WC and EC parametrizations use different standard configurations for the EFT priors. As a way forward, we explored the

impact that data from future surveys like DESI will have by considering BOSS data with a data covariance matrix rescaled by 16. We find that the constraints from Bayesian and frequentist approaches converge to the same interval for σ_8 as the likelihood dominates over the prior information, suggesting that the issues discussed above will subside with more data.

In chapter 7, we reassessed the constraints on early dark energy (EDE) from the full shape of the most recent measurements of the power spectrum (or correlation function) of BOSS in light of a correction to the normalization of BOSS window functions. It has been argued that the full-shape analysis of the galaxy power spectrum of BOSS disfavors the EDE model as an efficient resolution of the H_0 tension, and we have shown that this is no longer the case with the new BOSS data. To do so, we have performed a thorough investigation of the constraints on EDE in light of the correctly normalized BOSS data and estimated the shifts introduced on the reconstructed cosmological parameters and their errors between various EFT analysis strategies. Regardless of the BOSS data or the EFT likelihood we consider, the BOSS full-shape (analyzed on their own with a BBN prior) leads to reconstructed values of H_0 that are compatible with what is obtained by the SH0ES Collaboration. In addition, we considered the combination of *Planck*TTTEEE + Lens + BAO + Pan18 + EFTBOSS which leads to $f_{\rm EDE}(z_c) < 0.083$, which is a $\sim 10\%$ improvement over the constraints without BOSS data and a $\sim 5\%$ improvement over the constraints with conventional BAO/$f\sigma_8$ data. Yet, this is much weaker than the constraints reported with the incorrect normalization, namely, $f_{\rm EDE} < 0.054$. We quantify that the Hubble tension is reduced to the 2.1σ level in the EDE cosmology (1.9σ without EFTBOSS) compared to 4.8σ in the ΛCDM model. Then, we have studied the impact of the BOSS data on the recent hints of EDE observed within ACT DR4 data. The combination of *Planck*TT650TEEE + Lens + BAO + Pan18 + ACT + EFTBOSS leads to a mild constraints on $f_{\rm EDE}(z_c) < 0.172$ with $\Delta\chi^2({\rm EDE}-\Lambda{\rm CDM}) = -11.1$, to be compared with $f_{\rm EDE}(z_c) = 0.128^{+0.064}_{-0.039}$ without EFTBOSS + Lens, with $\Delta\chi^2({\rm EDE}-\Lambda{\rm CDM}) = -14.6$. Finally, we concluded that the EFTofLSS analysis of the BOSS data do not exclude EDE as a resolution to the Hubble tension, where we consistently find $f_{\rm EDE}(z_c) \sim 10-12\%$ at $z_c \sim 3500-4000$, with $h \sim 0.72$, when the cepheid calibration is included in the analyses. However, the EFTofLSS analysis of the BOSS data constrains the most extreme EDE cosmologies, as shown by the analysis of ACT DR4 data.

In chapter 8, we have updated the constraints on the acoustic (early) dark energy (ADE) model by first assessing the impact of the EFT full-shape analysis applied to the BOSS and eBOSS data, and secondly the impact of the latest Pantheon+ data. We have demonstrated that the EFTofLSS analysis slightly reduces the ability of this model to resolve the Hubble tension compared to the BAO/$f\sigma_8$ analysis, with a residual tension of 2.6σ. Importantly, when we replace the Pantheon data with the Pantheons+ data, the ADE model no longer resolves the Hubble tension at a suitable level, leading to a 3.6σ residual tension (compared to 2.5σ for the EDE model and 6.3σ for the ΛCDM model). Whereas with the EFTofLSS analysis we had only a slight preference for EDE over ADE, with the new data from Pantheon+ and SH0ES, the preference for this model becomes clearly apparent, due to the fact that axion-like EDE manages to compensate a higher $\Omega_{\rm cdm}h^2$ in *Planck* data thanks to the scale-dependence of the sound speed. More generally, in this work, we have shown that the new data from Pantheon+ and SH0ES, and to a lesser extent the EFTofLSS applied to the BOSS and eBOSS data, can have a decisive impact on models which aim to resolve the Hubble tension.

In chapter 9, we have confronted two models of decaying cold dark matter (DCDM) with the full-shape analysis of the BOSS data, combined with *Planck* TTTEEE and lensing power spectra, BAO data from BOSS and eBOSS (including Ly-α data), and the uncalibrated luminosity distance to SNIa from the Pantheon18 catalog. We focused first on a model where a fraction of dark matter decays into dark radiation, the DCDM $\rightarrow$ DR model, and second on a model where all the dark matter decays into warm massive particles and dark radiation particles, the DCDM $\rightarrow$ WDM+DR model. The latter model was recently suggested as a possible resolution to the S_8 tension. For the DCDM $\rightarrow$ DR model, we have derived the most up-to-date bound on the fraction of decaying dark matter $f_{\rm dcdm}$, which is now $f_{\rm dcdm} < 0.0216$ for short-lived DCDM. We have also updated constraints on the lifetime of dark matter for the case where $f_{\rm dcdm} \rightarrow 1$, namely $\tau/f_{\rm dcdm} > 249.6$ Gyr. However, we have found that the EFTofLSS does not provide significantly better constraints to the cosmological parameters for the DCDM $\rightarrow$ DR model, compared to the use of the standard BAO/$f\sigma_8$ data. In agreement with past studies, we have found that this model does not help neither for the S_8 nor for the H_0 tension, and the inclusion of the EFTofLSS analysis of the BOSS data does not alter that conclusion. For the DCDM $\rightarrow$ WDM+DR model, we showed that this model can explain the low S_8 value measured by KiDS-1000 while preserving the goodness of fit to other dataset, including the EFTofLSS analysis of the BOSS data. The residual tension is 1.5σ compared to 2.4σ in the ΛCDM model. In addition, we demonstrated that the full-shape analysis of the BOSS data do significantly improve the 68% C.L. on the DCDM lifetime for the DCDM $\rightarrow$ WDM+DR model, and when combined with the S_8 prior, we now obtain $\log_{10}(\tau/{\rm Gyr}) = 2.21^{+1.5}_{-0.6}$ compared to $\log_{10}(\tau/{\rm Gyr}) = 1.92^{+1.9}_{-0.61}$ with BAO/$f\sigma_8$ measurements.

This thesis illustrates the crucial importance of large-scale structure data for accessing information in uncharted regimes, while it demonstrates the predictive power of the effective field theory of large-scale structures as well as the benefits that this theory can bring in terms of cosmological knowledge. Over the next few years, new large-scale structure data from the international DESI, EUCLID and VRO projects will provide exquisite new data to study the nature of dark matter, dark energy, and inflation, and allow to perform tests of models suggested to resolve cosmological tensions. It will therefore be necessary to pursue theoretical efforts to accurately predict the non-linear galaxy power spectrum (but also the galaxy bispectrum), and make use of the wealth of data to come.

Appendices

A

Cosmological inference from the EFTofLSS: the eBOSS QSO full-shape analysis

A.1 What happens if we vary n_s and ω_b in the LSS analyses?

In our baseline LSS analyses (*i.e.*, without combination with *Planck* data), we set $\omega_b = 0.02233$ (the central value of big-bang nucleosynthesis (BBN) experiments [134]) and $n_s = 0.965$ (the central value from *Planck* in the ΛCDM model [11]). In the following, we impose a uninformative large flat prior on n_s, while we impose the BBN Gaussian prior on ω_b, motivated from [134], namely $\omega_b = 0.02233 \pm 0.00036$, to explore the impact of the variation of n_s and ω_b in the LSS analyses presented in this work. We carried out the eBOSS + BOSS analysis either by varying one of these two parameters at a time to isolate their effects, or varying both simultaneously. In Fig. A.1, we present these results in comparison with our base-ΛCDM analysis of eBOSS + BOSS.

In this figure, one can easily gauge that the variation of ω_b within the BBN prior has a negligible impact on the cosmological results: we have a relative shift of $\lesssim 0.04\sigma$ between the mean values and $\lesssim 0.07\sigma$ between the best-fit values, while the 68% CL constraints remain the same for all parameters. However, the variation of n_s within a uninformative large flat prior leads to a relative shift $\lesssim 0.4\sigma$ between the mean values, while the best-fit values are shifted by -1.06σ, -0.50σ, 0.52σ, -1.15σ, 0.76σ, 0.13σ for Ω_m, h, σ_8, ω_{cdm}, $\ln 10^{10} A_s$ and S_8 respectively. In addition, the 68% CL constraints of the n_s-free analysis are degraded $\lesssim 10\%$ on all cosmological parameters, except for Ω_m and ω_{cdm} where the degradation reaches 57% and 79% respectively. Not surprisingly, we find that the analysis that combines the variation of these two parameters gives results very similar to the n_s-free analysis.

It is common to set the value of n_s in LSS analyses (see Refs. [97, 103, 114] for examples) to that of *Planck*. Several tests have been carried out, often imposing a Gaussian prior inspired by the *Planck* preferred value in order to evaluate the impact of the variation of n_s around this value. This is for instance the case in the ShapeFit analysis [114], where a Gaussian prior $n_s = 0.965 \pm 0.02$ is imposed. In this analysis, which also combines eBOSS and BOSS data,

best-fit $\mu^{+\sigma_u}_{-\sigma_l}$	$[n_s + \omega_b]$ (w/ eBOSS + BOSS)
Ω_m	0.288 $0.295^{+0.011}_{-0.013}$
h	0.677 $0.682^{+0.010}_{-0.010}$
σ_8	0.858 $0.797^{+0.041}_{-0.042}$
ω_{cdm}	0.1091 $0.1142^{+0.0063}_{-0.0081}$
$\ln(10^{10}A_s)$	3.24 $3.06^{+0.13}_{-0.13}$
S_8	0.842 $0.790^{+0.039}_{-0.041}$
n_s	1.015 $0.981^{+0.048}_{-0.044}$
χ^2_{min}	216.7
N_{data}	262
p-value	0.47

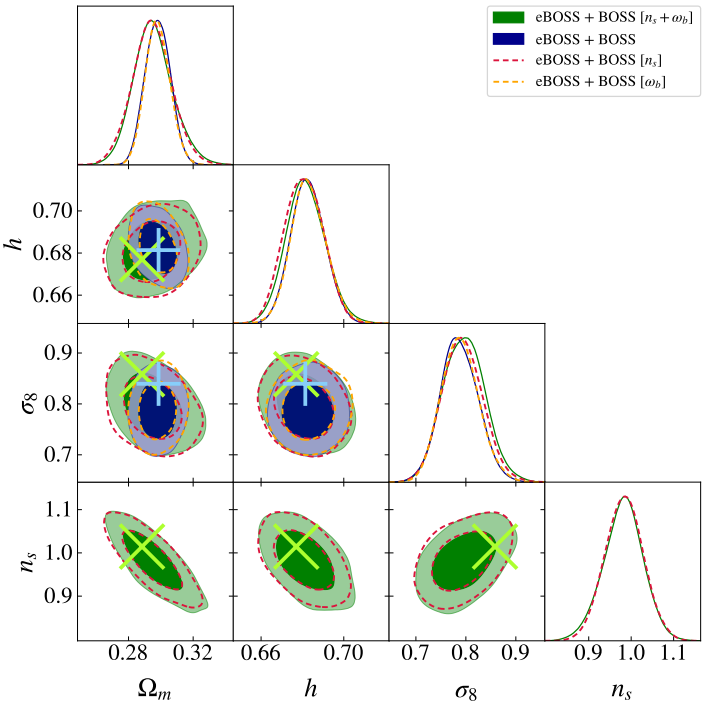

Figure A.1: *Left* - Cosmological results (best-fit, posterior mean, and 68% CL) of eBOSS + BOSS for the ΛCDM model. Here we let n_s vary freely and restrict ω_b to a BBN prior, calling such analysis "$[n_s + \omega_b]$", in contrast to the corresponding analyses in the main text where those are fixed. We also report the best-fit χ^2, the number of data points $N_{\rm data}$ and the associated p-values. *Right* - Triangles plots (1D and 2D posterior distributions) of the cosmological parameters reconstructed from the eBOSS + BOSS base-ΛCDM analysis and the eBOSS + BOSS $[n_s + \omega_b]$ analysis. We also show, in dotted lines, the eBOSS + BOSS results with only the n_s variation, denoted "eBOSS + BOSS $[n_s]$", or only the ω_b variation, denoted "eBOSS + BOSS $[\omega_b]$".

it was reported that the variation of n_s within this prior does not impact h and σ_8 posteriors, while it slightly degrades the constraints on Ω_m. This is somewhat consistent with what we observe here. However, it is essential to note that this degradation is exacerbated in our n_s-free analysis since we impose a large uninformative flat prior.

Although these differences do not alter the conclusions of this analysis, one may argue that to obtain LSS constraints that are truly independent of *Planck*, one should not include any prior on n_s. Therefore, we have redone, for all cosmological model considered in this work, the analysis of eBOSS + BOSS + ext-BAO + Pantheon, letting n_s vary freely as well as restricting ω_b to the BBN prior. Those cosmological results are presented in Tab. A.1. From the first column of this table, we can compare the n_s-free analysis with the base-ΛCDM analysis of the last column of Tab. 4.2 for the full combination of LSS datasets. We observe that the relative shifts between the mean values, the relative shifts between the best-fit values, and the degradation of the constraints are substantially similar to those observed in the above comparison on eBOSS + BOSS. In addition, we list here the impact of varying n_s (and ω_b) on the constraints of the extension parameters to flat ΛCDM from the analysis of eBOSS + BOSS + ext-BAO + Pantheon:

- For Ω_k, the relative shift between the mean values is 0.74σ, the relative shift between the best-fit values is 0.40σ, while the constraint is degraded by $\sim 30\%$.

eBOSS + BOSS + ext-BAO + Pantheon (LSS) [$n_s + \omega_b$]					
best-fit $\mu^{+\sigma_u}_{-\sigma_l}$	ΛCDM	$\Omega_k\Lambda$CDM	w_0CDM	$\nu\Lambda$CDM	$N_{\rm eff}\Lambda$CDM
$\Omega_{\rm m}$	0.2905 $0.2957^{+0.0097}_{-0.0098}$	0.291 $0.299^{+0.010}_{-0.012}$	0.2903 $0.2957^{+0.0096}_{-0.0110}$	0.290 $0.299^{+0.010}_{-0.011}$	0.292 $0.291^{+0.014}_{-0.012}$
h	0.6749 $0.6786^{+0.0085}_{-0.0088}$	0.681 $0.697^{+0.013}_{-0.015}$	0.670 $0.682^{+0.012}_{-0.013}$	0.6753 $0.6765^{+0.0085}_{-0.0094}$	0.671 $0.697^{+0.017}_{-0.038}$
σ_8	0.858 $0.794^{+0.037}_{-0.041}$	0.840 $0.755^{+0.043}_{-0.047}$	0.866 $0.789^{+0.042}_{-0.045}$	0.856 $0.811^{+0.042}_{-0.046}$	0.859 $0.793^{+0.037}_{-0.040}$
$\omega_{\rm cdm}$	0.1093 $0.1132^{+0.0056}_{-0.0062}$	0.1120 $0.1222^{+0.0076}_{-0.0096}$	0.1095 $0.1146^{+0.0060}_{-0.0079}$	0.1096 $0.1115^{+0.0055}_{-0.0070}$	0.108 $0.119^{+0.007}_{-0.012}$
$\ln(10^{10}A_s)$	3.24 $3.06^{+0.12}_{-0.12}$	3.14 $2.76^{+0.22}_{-0.21}$	3.29 $3.03^{+0.15}_{-0.15}$	3.22 $3.20^{+0.15}_{-0.21}$	3.24 $3.05^{+0.12}_{-0.12}$
S_8	0.844 $0.788^{+0.039}_{-0.039}$	0.828 $0.754^{+0.040}_{-0.045}$	0.852 $0.783^{+0.040}_{-0.044}$	0.842 $0.809^{+0.041}_{-0.047}$	0.847 $0.780^{+0.037}_{-0.043}$
n_s	1.012 $0.985^{+0.038}_{-0.038}$	0.994 $0.930^{+0.053}_{-0.048}$	1.025 $0.976^{+0.046}_{-0.043}$	1.007 $1.038^{+0.050}_{-0.087}$	1.010 $0.985^{+0.041}_{-0.039}$
Ω_k	–	-0.021 $-0.063^{+0.036}_{-0.037}$	–	–	–
w_0	–	–	-0.975 $-1.018^{+0.047}_{-0.043}$	–	–
$\sum m_\nu$ [eV]	–	–	–	0.025 < 0.777	–
$\Delta N_{\rm eff}$	–	–	–	–	-0.11 $0.48^{+0.47}_{-0.86}$
$\chi^2_{\rm min}$	1249.8	1249.6	1249.4	1249.7	1249.8
$\Delta\chi^2_{\rm min}$	–	-0.2	-0.4	-0.1	0

Table A.1: Cosmological results (best-fit, posterior mean, and 68% CL) from eBOSS + BOSS + ext-BAO + Pantheon for the ΛCDM model as well as several model extensions. In contrast to the previous analyses, we vary n_s and ω_b. Note that we quote 95% CL bound for $\sum m_\nu$. For each dataset we also report its best-fit χ^2, and the $\Delta\chi^2$ with respect to the analogous ΛCDM best-fit model.

- For w_0, the relative shift between the mean values is 0.46σ, the relative shift between the best-fit values is 0.64σ, while the constraint is degraded by $\sim 10\%$.
- For $\sum m_\nu$, there is no relative shift between the best-fit values, while the 95% CL bound becomes 2.8 times weaker.
- For $\Delta N_{\rm eff}$, the relative shift between the mean values is 0.12σ, the relative shift between the best-fit values is 0.36σ, but the constraint is not degraded.

Finally, we perform a BOSS + ext-BAO + Pantheon analysis without eBOSS (*i.e.*, the first column of Tab. A.1 without eBOSS) to assess the impact of eBOSS on the determination of n_s. In this case, we reconstruct $n_s = 0.943 \pm 0.043$ at 68% CL (with a best-fit value at 0.957). This shows that the inclusion of the eBOSS data allows us an improvement of 13% on the 68% CL error bar of n_s.

B

Consistency of EFTofLSS analyses of the BOSS data

B.1 Impact of scale cut and multipoles

In this appendix, we look at the differences when we change the scale cut and the number of multipoles analyzed. BOSS analyses using the `PyBird` likelihood usually include two multipoles, $\ell = 0,2$, with scale cut $k_{\rm max} = 0.25(0.20)h\,{\rm Mpc}^{-1}$ for z_3 (z_1). The `CLASS-PT` likelihood include three multipoles, $\ell = 0,2,4$, with scale cut $k_{\rm max} = 0.20h\,{\rm Mpc}^{-1}$ for both z_1 and z_3. In Fig. B.1 we present a comparison between the WC and the EC prior, for the exact same data and configuration (same $k_{\rm max}$ and same number of multipoles), now considering three galaxy power-spectrum multipoles. This figure can be compared with Fig. 5.1, where the same analysis was performed when considering two multipoles. One can see that, similar to Fig. 5.1, the results of the `PyBird` and `CLASS-PT` likelihoods are in good agreement when using the same prior, also when the hexadecapole is included in the analysis.

Let us now look at how the results change when going from one choice of scale cut or multipoles to another one, for each prior choice. The results can be read from Fig. B.2, going from top to bottom, either looking in the upper panel or the lower panel. We find that:

- with the WC prior, when either lowering the $k_{\rm max}$ from $0.25h\,{\rm Mpc}^{-1}$ to $0.20h\,{\rm Mpc}^{-1}$ in z_3, adding the hexadecapole, or changing both, we find at most a shift of $\lesssim 0.5\sigma$ on the cosmological 1D posteriors.

- with EC prior, we find shifts up to about 0.3σ, 0.9σ, and 0.5σ, respectively, when increasing the $k_{\rm max}$ from $0.20h\,{\rm Mpc}^{-1}$ to $0.25h\,{\rm Mpc}^{-1}$ in z_3, going from three to two multipoles, or changing both.

We stress that one does not expect the results between those various analysis settings to be the same, given that data are included (or removed). However, given that the signal-to-noise ratio of the hexadecapole is very low compared to the monopole and quadrupole, and that the data added between $k \in [0.20, 0.25]h\,{\rm Mpc}^{-1}$ are only a few bins, we expect to see only relatively small shifts in the posteriors. While this seems to be the case for the WC prior, the shifts are slightly larger for the EC prior when going from two to three multipoles. As explained in

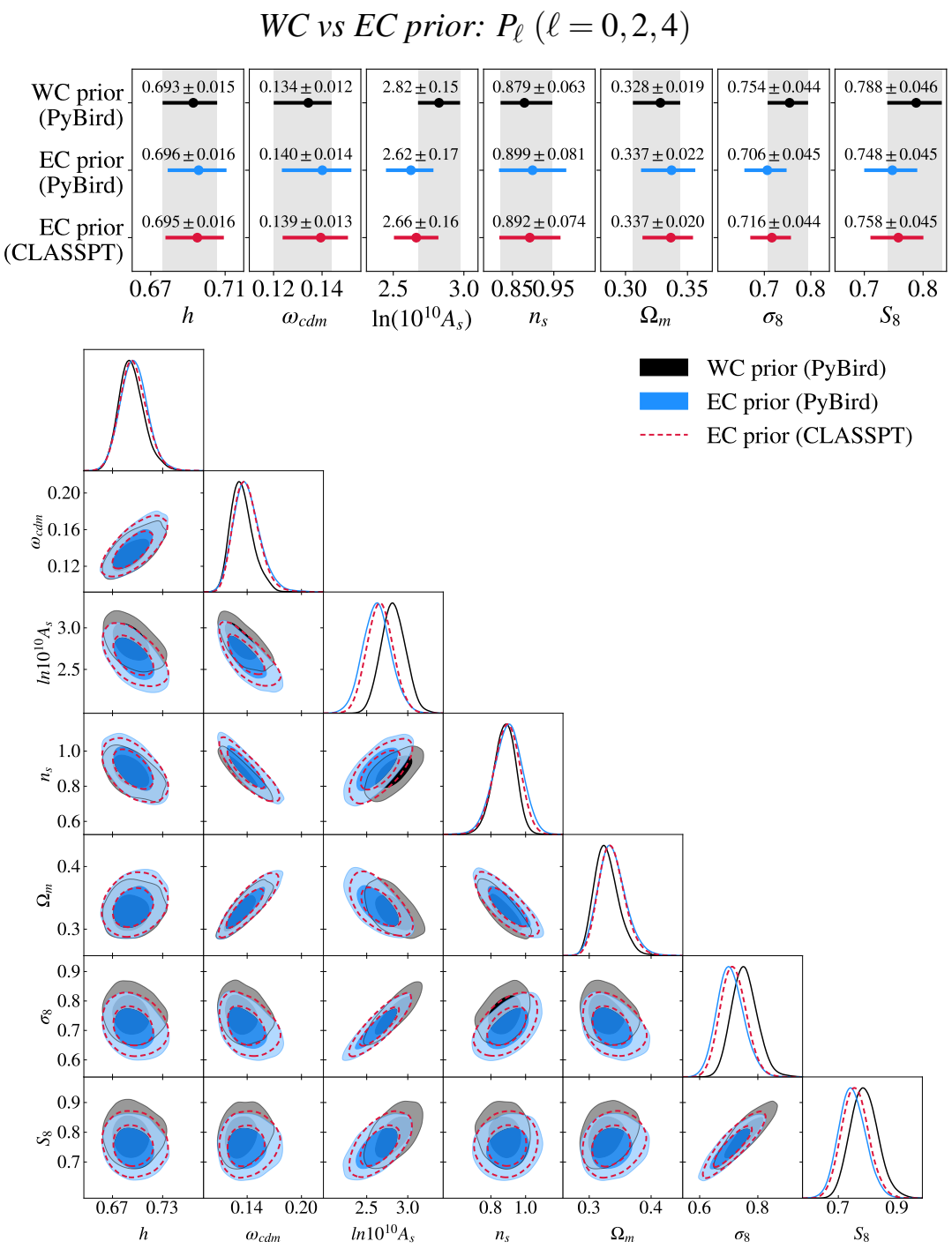

Figure B.1: Comparison of ΛCDM results (1D and 2D credible intervals) from the full-shape analyses of BOSS power spectrum using the `PyBird` likelihood or the `CLASS-PT` likelihood. Here we use the same data measurements, $P^{z_1/z_3}_{\rm QUAD}$ as specified in Tab. 5.4, and same analysis configuration: we fit three multipoles, $\ell = 0,2,4$, and use $k_{\rm max} = 0.20/0.25h\,{\rm Mpc}^{-1}$ for the z_1/z_3 redshift bins. Given the same prior choice, the EC prior, we reproduce from the `PyBird` likelihood the results from the `CLASS-PT` likelihood to very good agreement (see blue and red posteriors): we obtain shifts $\lesssim 0.2\sigma$ on the means and the errors bars similar at $\lesssim 10\%$. Given that the two pipelines have been developed independently, this comparison provides a validation check of their implementation. In contrast, the WC and the EC prior choices lead to substantial differences on the 1D marginalized posteriors (see black and blue posteriors). The gray bands on the 1D posteriors are centered on the results obtained with the WC priors.

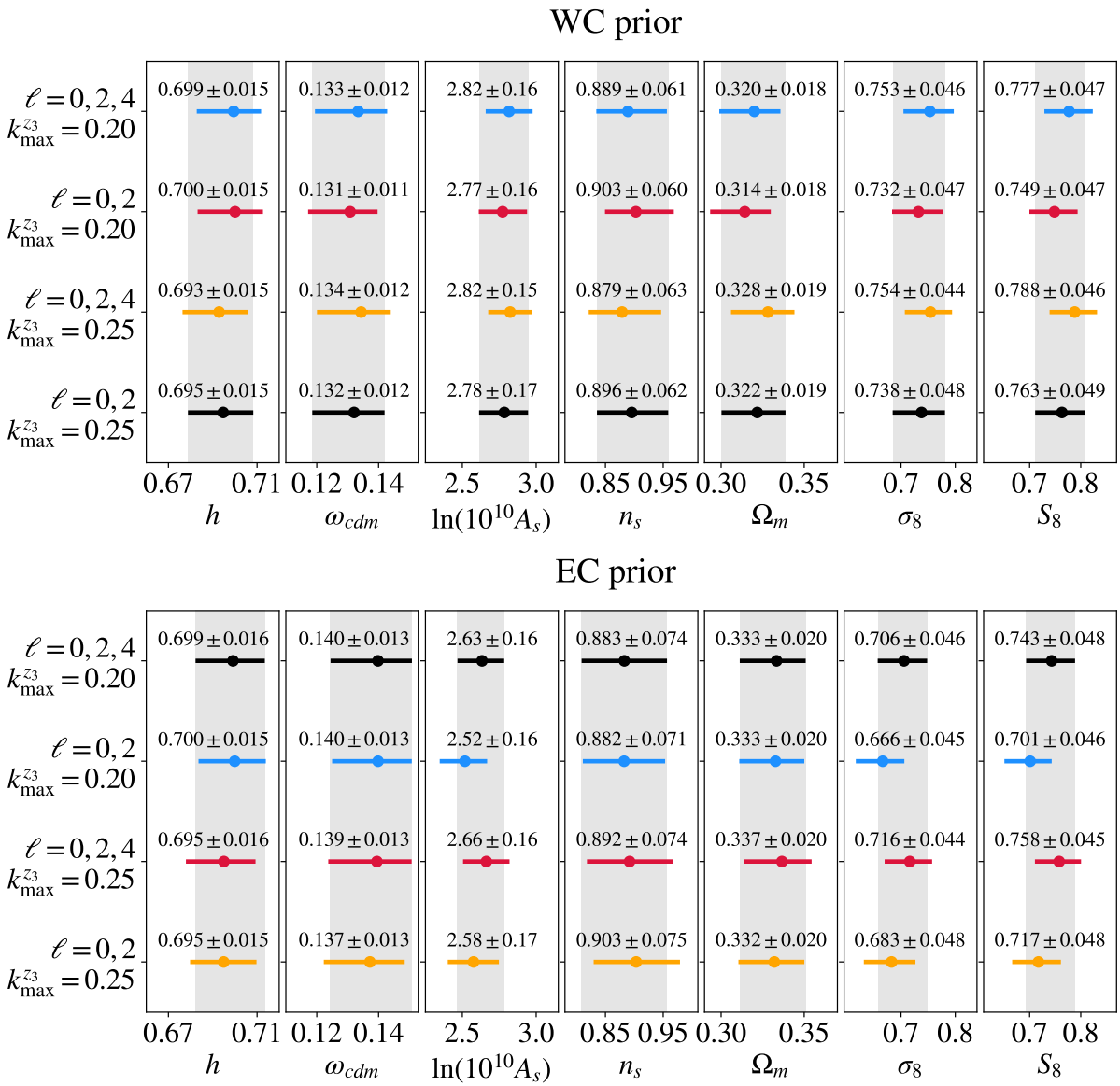

Figure B.2: Comparison of ΛCDM results from BOSS full-shape analyses using the `PyBird` likelihood (WC prior) or the `CLASS-PT` likelihood (EC prior), for various analysis settings: number of multipoles analyzed ($\ell = 0,2$ or $\ell = 0,2,4$), and $k_{\rm max}$ of z_3 ($k_{\rm max}^{z_3} = 0.20$ or $k_{\rm max}^{z_3} = 0.25$). $k_{\rm max}^{z_1} = 0.20$ for all analyses here, while all $k_{\rm max}$'s are given in $h\,{\rm Mpc}^{-1}$. Here we use the same data measurements, $P_{\rm QUAD}^{z_1/z_3}$, as specified in Tab. 5.4. The native baseline configurations used in previous BOSS full-shape analyses, highlighted by the gray bands, are $\ell = 0,2$, $k_{\rm max}^{z_3} = 0.25$ for the `PyBird` likelihood, and $\ell = 0,2,4$, $k_{\rm max}^{z_3} = 0.20$ for the `CLASS-PT` likelihood.

previous section, the EC prior leads to larger prior volume projection effects, which can explain why we see larger differences in the current comparison.

B.2 PyBird vs CLASS-PT: direct comparison

For completeness, we provide now a comparison keeping all the analysis choices different in both likelihoods: the pre- and post-reconstructed measurements, scale cut,

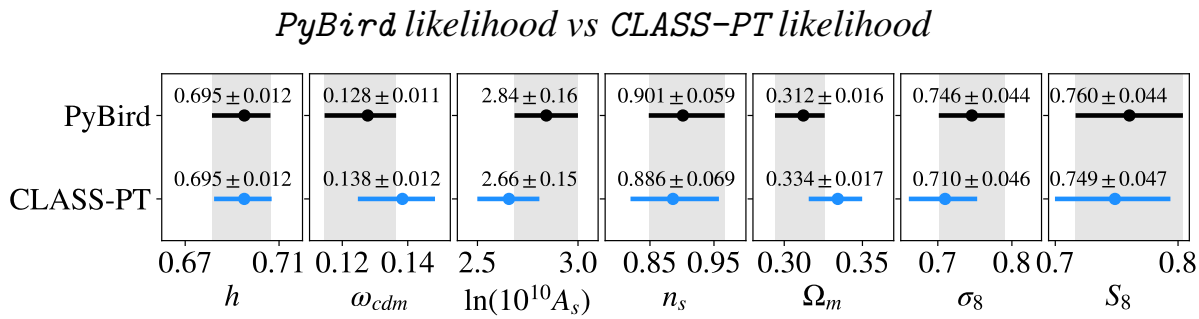

Figure B.3: Comparison of ΛCDM results (1D credible intervals) from $P_{\rm FKP}^{\rm LZ/CM} + \alpha_{rec}^{\rm LZ/CM}$ analyzed using the `PyBird` likelihood (*i.e.*, the native data and configuration of `PyBird`), and $P_{\rm QUAD}^{z_1/z_3} + \beta_{rec}^{z_1/z_3}$ analyzed using the `CLASS-PT` likelihood (*i.e.*, the native data and configuration of `CLASS-PT`). Contrary to the analysis of Ref. [69] based on the `PyBird` likelihood, we fix the total neutrino mass to minimal, and, we do not use Q_0 or B_0 as Ref. [62] in the `CLASS-PT` likelihood. The gray bands are centered on the results from `PyBird`.

number of multipoles, and prior choices. This leads to the differences on the 1D posteriors that we see in Fig. B.3. The differences between $P_{\rm FKP}^{\rm LZ/CM} + \alpha_{rec}^{\rm LZ/CM}$ analyzed using the `PyBird` likelihood, with $P_{\rm QUAD}^{z_1/z_3} + \beta_{rec}^{z_1/z_3}$ analyzed using the `CLASS-PT` likelihood, are about 0σ, 0.9σ, 1.2σ, 0.2σ, 1.3σ, 0.8σ and 0.3σ on h, ω_{cdm}, $\ln(10^{10}A_s)$, n_s, Ω_m, σ_8, and S_8, respectively. As discussed in the main text, we have found that those differences are due to different prior choices, differences in the measurements used, and the full-shape analysis settings ($k_{\rm max}$ and number of multipoles). Therefore, if the shifts between the two base analyses do not seem to be that large in the end, $\lesssim 1.3\sigma$, we understand that there are cancellations arising from the different analysis choices.

As an intermediate result, we can compare these two likelihoods with the same dataset, i.e, by changing only the prior choices and the analysis settings ($k_{\rm max}$ and the number of multipoles). We find that the largest deviations between the `PyBird` likelihood and the `CLASS-PT` likelihood for $P_{\rm QUAD}^{z_1/z_3}$ are on $\omega_{\rm cdm}$, $\ln(10^{10}A_s)$, Ω_m, and σ_8, as seen in Fig. 5.7. Without reconstructed BAO, they are about 0.6σ, 0.9σ, 0.6σ and 0.7σ, respectively. With reconstructed BAO, the deviations tend to increase, since they become equal to 0.9σ, 1.1σ, 0.9σ and 0.6σ, respectively.

To close this study, we mention a few other BOSS full-shape analyses using yet a different likelihood or measurements. First, Ref. [103], that uses another prior choice (note in particular that they fix ω_b and n_s, other reconstructed measurements from configuration space [424], and another methodology to analyze the reconstructed signal), finds $\Omega_m = 0.303 \pm 0.008$, $h = 0.6923 \pm 0.0077$, $\ln(10^{10}A_s) = 2.81 \pm 0.12$, which overall is closer to $P_{\rm FKP}^{\rm LZ/CM} + \alpha_{rec}^{\rm LZ/CM}$ than $P_{\rm FKP}^{z_1/z_3} + \alpha_{rec}^{z_1/z_3}$, especially on h. It is actually also interesting to compare to their results without reconstructed signal, for which they obtain $\Omega_m = 0.305 \pm 0.010$, $h = 0.685 \pm 0.011$, $\ln(10^{10}A_s) = 2.84 \pm 0.13$. Here again, their results are closer to $P_{\rm FKP}^{\rm LZ/CM}$ analyzed with WC prior, than, *e.g.*, $P_{\rm QUAD}^{z_1/z_3}$, analyzed either with the WC or EC prior. Second, Ref. [114] put forward another approach, dubbed ShapeFit, that extends the traditional analysis BAO and redshift-space distortion measurements with one additional compressed parameter. They obtain on BOSS data (fixing ω_b and n_s): $\Omega_m = 0.300 \pm 0.006, h = 0.6816 \pm 0.0067, \ln(10^{10}A_s) = 3.19 \pm 0.08$. Those results are also in better agreement with $P_{\rm FKP}^{\rm LZ/CM}$ analyzed with the WC

prior, than $P_{\rm QUAD}^{z_1/z_3}$ analyzed either with the WC or EC prior. We warn that it is not straightforward to interpret those comparisons given that there are many differences in the analysis setup. In particular, we have checked that fixing ω_b instead of using a BBN prior, or fixing n_s, can shift the posteriors of the other cosmological parameters up to about 1σ.

C

Frequentist investigation of EFTofLSS analyses of the BOSS and eBOSS data

C.1 Impact of priors on EFT parameters

The naturalness of the EFTofLSS framework predicts the EFT nuisance parameters to be of order unity, and too large values of these parameters would break the perturbativeness of the theory [139]. Thus, the standard WC parametrization described in Sec. 6.2.1 assigns Gaussian priors on a subset of the nuisance parameters in order to prohibit the non-perturbative regime from influencing the inference. In principle, such priors could be informed by N-body simulations and thereby promoted to likelihoods and interpreted as additional data in the frequentist approach. However, since this is not the case for the above priors, it is statistically not justified to include them in a profile likelihood analysis. In the main text, we have illustrated the impact induced by including the priors as likelihoods in the analysis. Here, we repeat this analysis varying the width of the priors.

Flat priors can be modelled as Gaussian priors in the limit that the standard deviations, or *widths*, of the Gaussian priors tend to infinity. Thus, by gradually increasing the width of the standard Gaussian priors, one uncovers the effects of the priors. Fig. C.1 shows σ_8 profiles with BOSS+BAO data with the Gaussian priors widths increased by the factor specified in the legend. The red line corresponds to the standard prior configuration of the `PyBird` likelihood (with $c_4 = c_\varepsilon^{\rm mono} = 0$). We observe that the profiles converge to the same shape at large factors, indicating that the Gaussian priors are flat, for all practical purposes, when their widths are increased by factors above ~ 40. Accordingly, for convenience purposes in the `PyBird` code, we model the flat priors on the EFT parameters which have Gaussian priors in the standard configuration by their usual Gaussian priors but with widths multiplied by 100. The 68% confidence intervals obtained from the 1x and 100x widths in the figure are

$$\begin{aligned} \sigma_8 &= 0.802 \pm 0.045 \qquad \text{(w. prior)} \\ \sigma_8 &= 0.771 \pm 0.075 \qquad \text{(no prior)}, \end{aligned}$$

amounting to a 0.35σ shift. A similar shift in σ_8 was found in chapter 5 from an MCMC analysis when increasing the Gaussian priors widths by a factor of 2. We conclude that the likelihoods imposed on the EFT parameters may influence the constraints when using

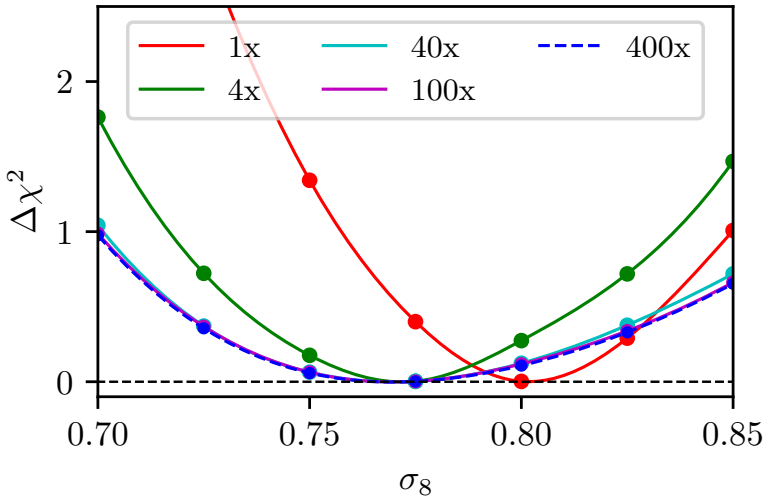

Figure C.1: Profile likelihood of σ_8 under BOSS+BAO data using Gaussian data likelihoods on the EFT parameters, which correspond to the standard WC priors multiplied by different factors indicated by the legend. There is a clear shift in σ_8 as the prior is widened. In particular, the profiles with widths multiplied by factors of 40, 100, and 400 coincide, indicating that the Gaussian priors reach the limiting case of a flat prior with these large widths. Thus, in our analysis, we model the flat priors on all EFT parameters as the usual priors, but with the widths of the Gaussian priors multiplied by 100.

BOSS data (note, however, that the influence will increase for less constraining datasets and vice-versa).

The disadvantage of not imposing these likelihoods is that one loses control over whether the EFT parameters become too large for the effective field theory description to be appropriate. Thus, the only correct frequentist approach is to let them vary freely and then check explicitly by inspection that they remain of order unity at each point in the profile likelihood. Fig. C.2 shows the values of the EFT nuisance parameters found by optimization at each point in the σ_8 profile with BOSS+BAO data, both with (red) and without (black) the explicit likelihoods on the EFT parameters. For comparison, the shaded blue region indicates the 1σ region of the Gaussian prior of the parameters, which have a prior in the standard analysis. We observe that in the case without Gaussian likelihoods mimicking priors, the EFT parameters are *not* of order unity as desired, which can break the perturbative nature of the theory. This result illustrates the conundrum of the priors: either one adopts subjective priors (in a Bayesian framework), which are informative and influence the inferred cosmological parameters, or one works without priors (in a frequentist framework), which leads to extreme values of the nuisance parameters.

C.2 Full profile and MCMC results

Fig. C.3 shows the profile likelihoods (black) and one-dimensional marginalized posterior distributions (red) for the BOSS+BAO, BOSS (without BAO post-reconstruction measurements) and eBOSS datasets, derived in this work. The profile likelihoods are normalized to their MLE. The bottom panels show the 68% and 95% confidence intervals and credible intervals.

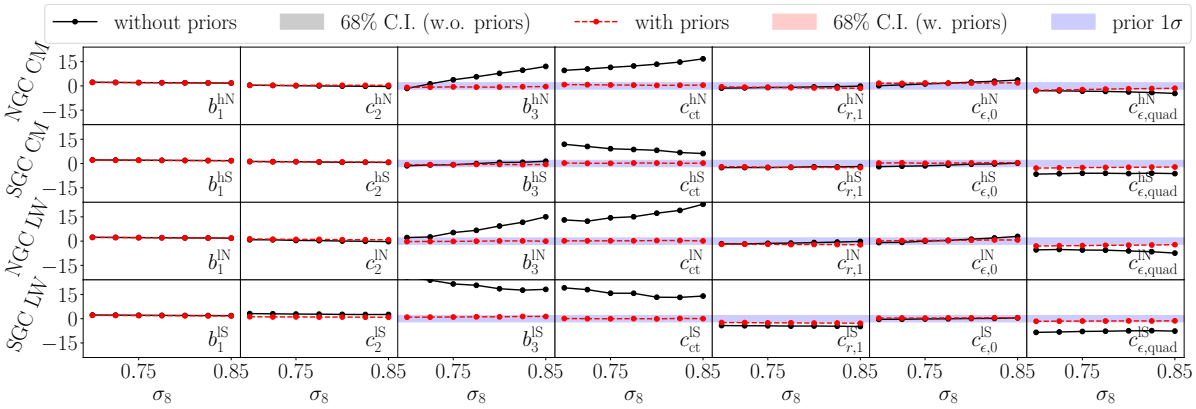

Figure C.2: Values of the EFT parameters found from optimization at each point in the σ_8 profile with BOSS+BAO data, with (red) and without (black) the standard WC priors of the `PyBird` likelihood, described in Sec. 6.2.1. The horizontal blue bands illustrate the 1σ regions of the Gaussian priors. For the parameters without such a band, a flat prior is used ($[0,4]$ for b_1 and $[-4,4]$ for c_2). The labels CM and LW denote the CMASS and LOWZ galaxy samples, respectively.

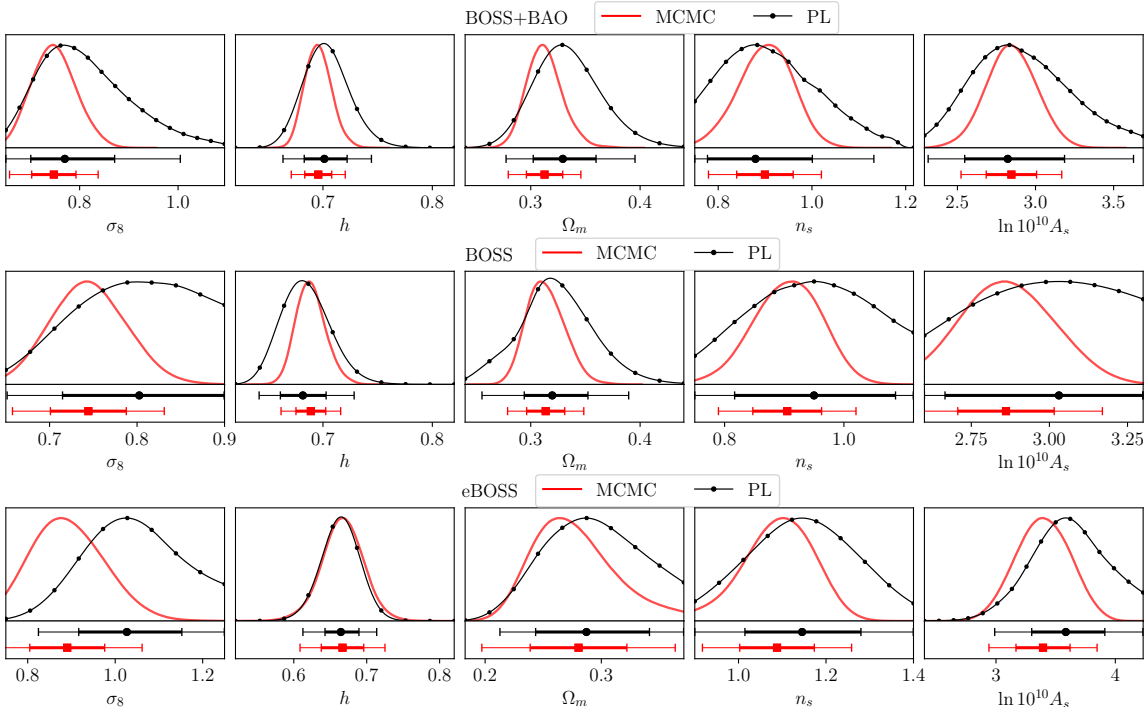

Figure C.3: Profile likelihoods (black) and one-dimensional marginalized posteriors (red) of the parameters σ_8, h, Ω_m, n_s and $\ln(10^{10}A_s)$ for the datasets BOSS+BAO, BOSS (without BAO post-reconstruction) and eBOSS. The bottom panels show the 68% and 95% confidence intervals and credible intervals, respectively.

C.3 Best-fit parameters

For the sake of reproducibility, Table C.1 shows the values of the cosmological parameters at the global best-fits found in this work. We note that the best-fits here are simply taken as the point in the profile likelihood with the maximum likelihood; due to the finite sampling of the profile, the best-fit values of these parameters may therefore be slightly inaccurate.

	BOSS+BAO	BOSS	eBOSS	*Planck*
$10^2\omega_b$	2.2686	2.2682	2.2674	2.2399
$\omega_{\rm cdm}$	0.1391	0.1259	0.1034	0.1198
h	0.7022	0.6838	0.6646	0.6750
n_s	0.8728	0.9270	1.1468	0.9663
$\ln 10^{10} A_s$	2.7925	2.9558	3.5889	3.0442
Ω_m	0.3293	0.3191	0.2869	0.3121
σ_8	0.7699	0.8025	1.0267	0.8100
$\chi^2_{\rm min}$	138.54	128.33	47.98	1387.07

Table C.1: Values of cosmological parameters at the global best-fit of the ΛCDM model under the BOSS+BAO, BOSS, eBOSS and *Planck* datasets, as specified in Sec. 6.1.2. We stress that, excepting the $\chi^2_{\rm min}$, the best-fit values here are only approximate due to the finite sampling of the profile likelihoods; a more fair comparison of the constraints is in table 6.3.

D

EFTofLSS' take on the Hubble tension and the early dark energy

D.1 Window function normalization

As discussed in Refs. [196, 175, 122] (see also [425]), the window function measurements, which are required to make an accurate theoretical calculation, have to be consistently normalized with the power spectrum measurements. The estimator for the power spectrum we are concerned with is the FKP estimator [426], later generalized to redshift space in Refs. [427, 428]. For fast estimation using FFTs [429, 430], the line of sight for a given galaxy pair is chosen to be in the direction of one of galaxy in the pair, r_1. For clarity in the discussion we are going to have next, let us first gather here pieces of derivations that can be found partially in Refs. [74, 58]. It is easy to see that the expectation value of the power spectrum FKP estimator reads (see, *e.g.*, [75])

$$\left\langle \hat{P}_\ell(k) \middle| \hat{P}_\ell(k) \right\rangle = \frac{2\ell+1}{N_P} \int \frac{d\Omega_k}{4\pi} d^3r_1 d^3s\, e^{-i\boldsymbol{k}\cdot\boldsymbol{s}} \Theta(r_1)\Theta(r_1+s)\bar{n}_w(r_1)\bar{n}_w(r_1+s)\xi(s,r_1)\mathscr{L}_\ell(\hat{k}\cdot\hat{r}_1)\,, \tag{D.1}$$

where $\mathscr{L}_\ell$ is the Legendre polynomial of order ℓ. Here $\bar{n}_w(r) \equiv w(r)\bar{n}(r)$ is the weighted mean galaxy density, with weight $w(r)$ being the FKP weights times some correction weights (usually to account for veto and instrumental/observational systematics), $\Theta(r)$ is one if the galaxy at position r falls inside the survey, zero otherwise, and $\xi(s,r_1)$ is the correlation function, with s the separation between two galaxies. Importantly, N_P is a normalization factor that is *chosen by the user*, as we will precise below. Using the following identity:

$$\int \frac{d\Omega_k}{4\pi} e^{-i\boldsymbol{k}\cdot\boldsymbol{s}} \mathscr{L}_\ell(\hat{k}\cdot\hat{r}_1) = (-i)^\ell j_\ell(ks)\mathscr{L}_\ell(\hat{s}\cdot\hat{r}_1)\,, \tag{D.2}$$

where j_ℓ is the spherical-Bessel function of order ℓ, we obtain

$$\begin{aligned}\left\langle \hat{P}_\ell(k) \middle| \hat{P}_\ell(k) \right\rangle =& \frac{(2\ell+1)}{N_P}(-i)^\ell \int ds\, s^2 j_\ell(ks) \int d\Omega_s \\ & \int d^3r_1 \Theta(r_1)\Theta(r_1+s)\bar{n}_w(r_1)\bar{n}_w(r_1+s)\xi(s,r_1)\mathscr{L}_\ell(\mu)\,,\end{aligned} \tag{D.3}$$

where we have introduced the notation $\mu \equiv \hat{s}\cdot\hat{r}_1$. We now make the following approximation. We assume that the redshift evolution of the correlation function can be neglected within the observational bin such that $\xi(s,r_1) \equiv \xi(s,\mu,r_1(z)) \simeq \xi(s,\mu,z_{\rm eff}) \equiv \xi(s,\mu)$, where the latter is evaluated at the effective redshift $z_{\rm eff}$ of the survey. [1] As such, we can pull out $\xi(s,\mu)$ from the integral over d^3r_1. We can further expand in multipoles $\xi(s,\mu) = \sum_{\ell'}\xi_{\ell'}(s)\mathscr{L}_{\ell'}(\mu)$ to pull out $\xi_{\ell'}(s)$ from the angular integrals. Then, using the identity

$$\mathscr{L}_\ell(\mu)\mathscr{L}_{\ell'}(\mu) = \sum_L \begin{pmatrix} \ell & L & \ell' \\ 0 & 0 & 0 \end{pmatrix}^2 (2L+1)\mathscr{L}_L(\mu)\,, \tag{D.4}$$

where $\begin{pmatrix} \ell & L & \ell' \\ 0 & 0 & 0 \end{pmatrix}$ are the Wigner 3-j symbols, we get

$$\left\langle \hat{P}_\ell(k)\middle|\hat{P}_\ell(k)\right\rangle = 4\pi(2\ell+1)(-i)^\ell \sum_{\ell',L}\begin{pmatrix} \ell & L & \ell' \\ 0 & 0 & 0 \end{pmatrix}^2 \int ds\, s^2 j_\ell(ks)\xi_{\ell'}(s)Q_L(s)\,, \tag{D.5}$$

where we have defined the window functions

$$Q_L(s) \equiv \frac{(2L+1)}{N_P}\int\frac{d\Omega_s}{4\pi}\int d^3r_1\Theta(r_1)\Theta(r_1+s)\bar{n}_w(r_1)\bar{n}_w(r_1+s)\mathscr{L}_L(\mu)\,. \tag{D.6}$$

Inserting the relation between the multipoles of the correlation function and those of the power spectrum,

$$\xi_{\ell'}(s) = i^{\ell'}\int\frac{dk'}{2\pi^2}k'^2 P_{\ell'}(k')j_{\ell'}(k's)\,, \tag{D.7}$$

we finally obtain

$$\left\langle \hat{P}_\ell(k)\middle|\hat{P}_\ell(k)\right\rangle = \int dk'\, k'^2 \sum_{\ell'} W_{\ell\ell'}(k,k')P_{\ell'}(k')\,, \tag{D.8}$$

where we have defined

$$W_{\ell,\ell'}(k,k') = \frac{2}{\pi}(2\ell+1)(-i)^\ell i^{\ell'}\int ds\, s^2 j_\ell(ks)j_{\ell'}(k's)\sum_L \begin{pmatrix} \ell & L & \ell' \\ 0 & 0 & 0 \end{pmatrix}^2 Q_L(s)\,. \tag{D.9}$$

Notice that, for clarity, we have neglected the integral constraints [196], as well as wide-angle contributions [74]. [2] Our master formula is Eq. (D.8): to predict the observed power spectrum $\left\langle \hat{P}_\ell(k)\middle|\hat{P}_\ell(k)\right\rangle$, we simply need to convolve our predictions $P_{\ell'}(k')$ with $W_{\ell,\ell'}(k,k')$ given by Eq. (D.9). $W_{\ell,\ell'}(k,k')$ can be precomputed, and the only input we need is $Q_L(s)$.

The window function $Q_L(s)$, Eq. (D.6), can be obtained in the following way [74]. Using Eq. (D.7) and the identity

$$\int dk\frac{(ks)^2}{2\pi^2}j_L(ks)j_L(ks') = \frac{1}{4\pi}\delta_D(s-s')\,, \tag{D.10}$$

[1] See Ref. [75] for a BOSS analysis that does not rely on this approximation.

[2] We have checked that neglecting the integral constraints in the BOSS full-shape analysis leads to small shifts in the posteriors of $\lesssim 1/4\cdot\sigma$.

where δ_D is the Dirac delta distribution, we see that

$$Q_L(s) = i^L \int \frac{dk}{2\pi^2} k^2 \mathscr{Q}_L(k) j_L(ks) \,, \tag{D.11}$$

where $\mathscr{Q}_L(k)$ is the expectation value of a power spectrum as defined in Eq. (D.3) given $\xi(s, r_1) \equiv 1$. Therefore, $\mathscr{Q}_L(k)$ can be measured as the power spectrum $P_L^r(k)$ of random objects (whose distribution is approaching Poisson) within the same geometry survey that we are dealing with,

$$\mathscr{Q}_L(k) \equiv \alpha \left\langle \hat{P}_L^r(k) \middle| \hat{P}_L^r(k) \right\rangle \,, \tag{D.12}$$

where $\alpha = N_g/N_r$ is the ratio of the number of data "galaxy" objects to the number of random objects. Such catalog of random objects is already available to us, as it is also required for the estimation of the power spectrum.

The key point is the following: $\mathscr{Q}_L(k)$ is normalized by the same normalization factor as $P_\ell(k)$, namely, N_P. As such, in the limit of vanishing separation $s \to 0$, the window function monopole does not go to unity, $Q_0(s) \neq 1$, but instead

$$Q_0(s \to 0) \to \frac{1}{N_P} \int d^3 r_1 \bar{n}_w^2(\boldsymbol{r}) \,. \tag{D.13}$$

Given that one does not know the value of the numerator in the equation above prior to making the measurement, N_P can only be estimated *approximately* in order to have $Q_0(s)$ approaching 1 at vanishing separation $s \to 0$. It is in this sense that N_P is chosen by the user. However, the normalization choice is not important as long as the window function measurements are consistently normalized with the power spectrum measurements. Given the measurement protocol sketched above, this is automatic if one is able to evaluate (D.11) accurately. [3]

In past BOSS full-shape analyses, *e.g.* [58, 97, 101, 328, 327], the window function normalizations were instead inconsistently enforced to $Q_0^{\rm wrong}(0) \equiv 1$, while in reality $Q_0(0) \sim 0.9$ given the choice of N_P. Such inconsistency of ~ 0.9 led to a shift in A_s of around -1σ depending on the normalization choice. Let us list two choices for the normalization factor N_P:

- *Choice 1*: $N_P = \alpha \sum_{\{i \in \text{randoms}\}} \bar{n}(r_i) w_{\rm FKP}^2(r_i)$. [4] This was the choice in Ref. [431], which measurements were used in, *e.g.*, Refs. [97, 328].

[3] At `https://github.com/pierrexyz/fkpwin`, we provide a code written to perform the window function measurements, based on `nbodykit`. Let us note that we find that it is not straightforward to get a precise measurements of $\hat{\mathscr{Q}}_L(k)$, namely, the power spectrum of the random objects over the *whole* range of k for which $\hat{\mathscr{Q}}_L(k)$ contributes significantly to the integral in Eq. (D.11). Furthermore, the estimator in Eq. (D.12) might have a non-negligible variance, given that only one catalog is used. We nevertheless have checked that, letting the normalization of the window functions to be different from the one of the power spectrum by a few percents leads to tolerable shifts in the posteriors ($\lesssim 1\sigma/5$) inferred fitting BOSS data. For future large-volume datasets, it would be, however, desirable to have a better numerical control over the measurements of $Q_L(s)$ such that the normalization consistency with $P_\ell(k)$ is achieved to sufficient accuracy given increasing precision of the data.

[4] Naively one might think that the sum over enough objects is a good approximation to the volume integral; Actually, *Choice 1* poorly estimates the integral in Eq. (D.13) because in the FKP estimator, $\bar{n}$ is measured from the grid for FFT with finite cell resolution, while in *Choice 1*, we are counting the objects instead.

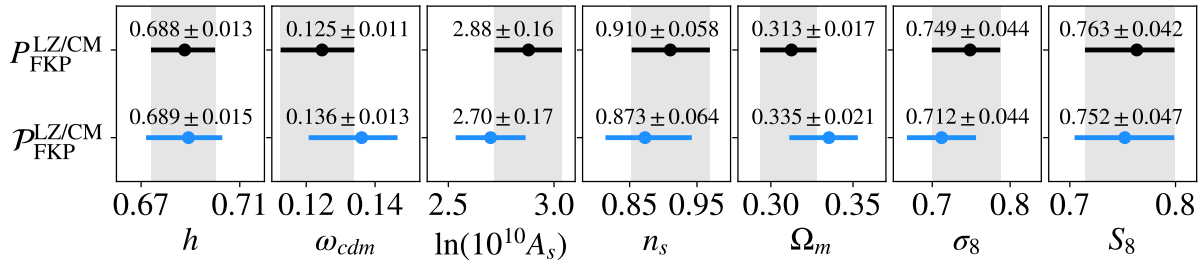

Figure D.1: Comparison of ΛCDM results from BOSS full-shape analysis of the power spectrum measurements $\mathscr{P}_{\rm FKP}^{\rm LZ/CM}$ and $P_{\rm FKP}^{\rm LZ/CM}$, analyzed with window functions inconsistently and consistently normalized, respectively (see Tab. 5.4 of chapter 5). The gray bands are centered on the results from the $P_{\rm FKP}^{\rm LZ/CM}$ data.

- *Choice 2*: $N_P = \mathscr{A} * \int dr \bar{n}_w^2(r)$, where $\bar{n}_w(r)$ is inferred from counting galaxies and binning them in shells and $\mathscr{A}$ is an associated estimated area. [5] This was the choice in Ref. [191], which measurements $\mathscr{P}_{\rm FKP}^{\rm LZ/CM}$ were used in, *e.g.*, Refs. [58, 101, 327]. $\mathscr{P}_{\rm FKP}^{\rm LZ/CM}$, as defined in Tab. 5.4 of chapter 5, is assigned window functions that are inconsistently normalized.

We stress again that those choices are not important as long as the same N_P is used to normalize the window functions and the power spectrum measurements. As already mentioned in the main text, except for $\mathscr{P}_{\rm FKP}^{\rm LZ/CM}$ that is used in this work for illustration purposes, all power spectrum measurements obtained with the FKP estimator, namely, $P_{\rm FKP}^{\rm LZ/CM}$ and $P_{\rm FKP}^{z_1/z_3}$, are instead consistently normalized with their window functions (see Tab. 5.4 of chapter 5 for more details on the measurements). We finish this section by noting that, in analyses using measurements obtained from the FKP estimator, but also from the other estimators, the posteriors may depend on the effective-redshift approximation used above. This suggests that, for each estimator, more work is needed to understand the accuracy of this approximation, along the line of, *e.g.*, [75] for the correlation function.

In Fig. D.1, we show a comparison of the 1D posteriors from the full-shape analysis of the BOSS power spectrum measured with the FKP estimator, using window functions with consistent or inconsistent normalization. The inconsistency leads to a lower amplitude A_s, or equivalently σ_8, as well as higher $\Omega_m \sim f$, where f is the logarithmic growth rate, through anticorrelation. We find notable shifts on $\omega_{\rm cdm}$, $\ln(10^{10}A_s)$, Ω_m and σ_8 of 0.9σ, 1.1σ, 1.1σ, and 0.8σ, respectively.

D.2 Additional comparison between the PyBird and CLASS-PT likelihood in EDE

In Figs. D.2, D.3, and D.4, we show the 2D posterior distributions reconstructed from BaseEFTBOSS, BaseTTTEEE+Lens+EFTBOSS, and BaseTT650TEEE+ACT+Lens+EFTBOSS, respectively, comparing the results from the `PyBird` and the `CLASS-PT` likelihoods. [6] In

[5] We thank Hector Gil-Marín for private correspondence on this point.

[6] For this comparison, LOWZ SGC is not included in the `PyBird` likelihood. As expected, we have checked that the addition of this sky cut does not change the posteriors for the corresponding analyses.

ΛCDM						
Planck high$-\ell$ TTTEEE	2342.2	2345.0	2342.2	2344.6	2342.2	2345.2
Planck low$-\ell$ TT	23.4	22.9	23.5	23.0	23.4	22.8
Planck low$-\ell$ EE	396.3	397.2	396.1	397.2	396.3	397.2
Planck lensing	8.9	9.4	9.0	9.4	9.0	9.4
BOSS BAO low$-z$	1.2	1.9	1.2	1.8	1.2	1.9
BOSS BAO DR12	4.3	3.4	–	–	–	–
BOSS BAO/$f\sigma_8$ DR12	–	–	6.7	5.9	–	–
EFTBOSS CMASS	–	–	–	–	84.6	83.1
EFTBOSS LOWZ	–	–	–	–	33.5	33.7
Pantheon	1027.2	1026.9	1027.2	1026.9	1027.2	1026.9
SH0ES	–	19.9	–	20.4	–	19.8
total $\chi^2_{\rm min}$	3803.6	3826.6	3805.7	3829.1	3917.4	3940.0
$Q_{\rm DMAP}$	4.8σ		4.8σ		4.8σ	

Table D.1: Best-fit χ^2 per experiment (and total) for ΛCDM when fit to different data combinations: BaseTTTEEE+Lens, BaseTTTEEE+Lens+$f\sigma_8$, BaseTTTEEE+Lens+EFTBOSS, with and without SH0ES. We also report the tension metric $Q_{\rm DMAP} \equiv \sqrt{\chi^2(\text{w/ SH0ES}) - \chi^2(\text{w/o SH0ES})}$.

addition, we recall that EFTBOSS corresponds to $P_{\rm FKP}^{\rm LZ/CM} + \alpha_{\rm rec}^{z_1/z_3}$ in the framework of the `PyBird` likelihood and to $P_{\rm QUAD}^{z_1/z_3} + \beta_{\rm rec}^{z_1/z_3}$ in the framework of the `CLASS-PT` likelihood (see Tab. 5.4 of chapter 5). The most striking differences occur in the BaseEFTBOSS alone case, for which `CLASS-PT` leads to much weaker constraints on $f_{\rm EDE}(z_c)$ and much larger error bars on h and $\omega_{\rm cdm}$. The origin of these differences can be traced back to the discussion presented in chapter 5, namely, to the choice of the power spectrum estimators, the BOSS post-reconstructed measurements used, the scale cut, the number of multipoles, and more importantly, the choice of EFT parameter priors. Once *Planck*TTTEEE or *Planck*TT650TEEE+ACT data are included in the analysis, we find that the reconstructed posteriors are very similar between the two EFTBOSS implementations and mostly driven by CMB data. We conclude that the main results of this work, drawn from the combination of CMB and LSS data, are unaffected by the choice of EFT implementation. However, parameter reconstruction based on EFTBOSS data alone may vary at the 1σ level.

D.3 χ^2 per experiment

In this appendix, we report the best-fit χ^2 per experiment for both ΛCDM and EDE models. In Tabs. D.1 and D.2 are presented the runs including *Planck* data, in Tab. D.3 the runs including ACT data, and in Tab. D.4 the combination of the full *Planck* data and ACT data. Finally, Tab. D.5 present runs including the PanPlus data.

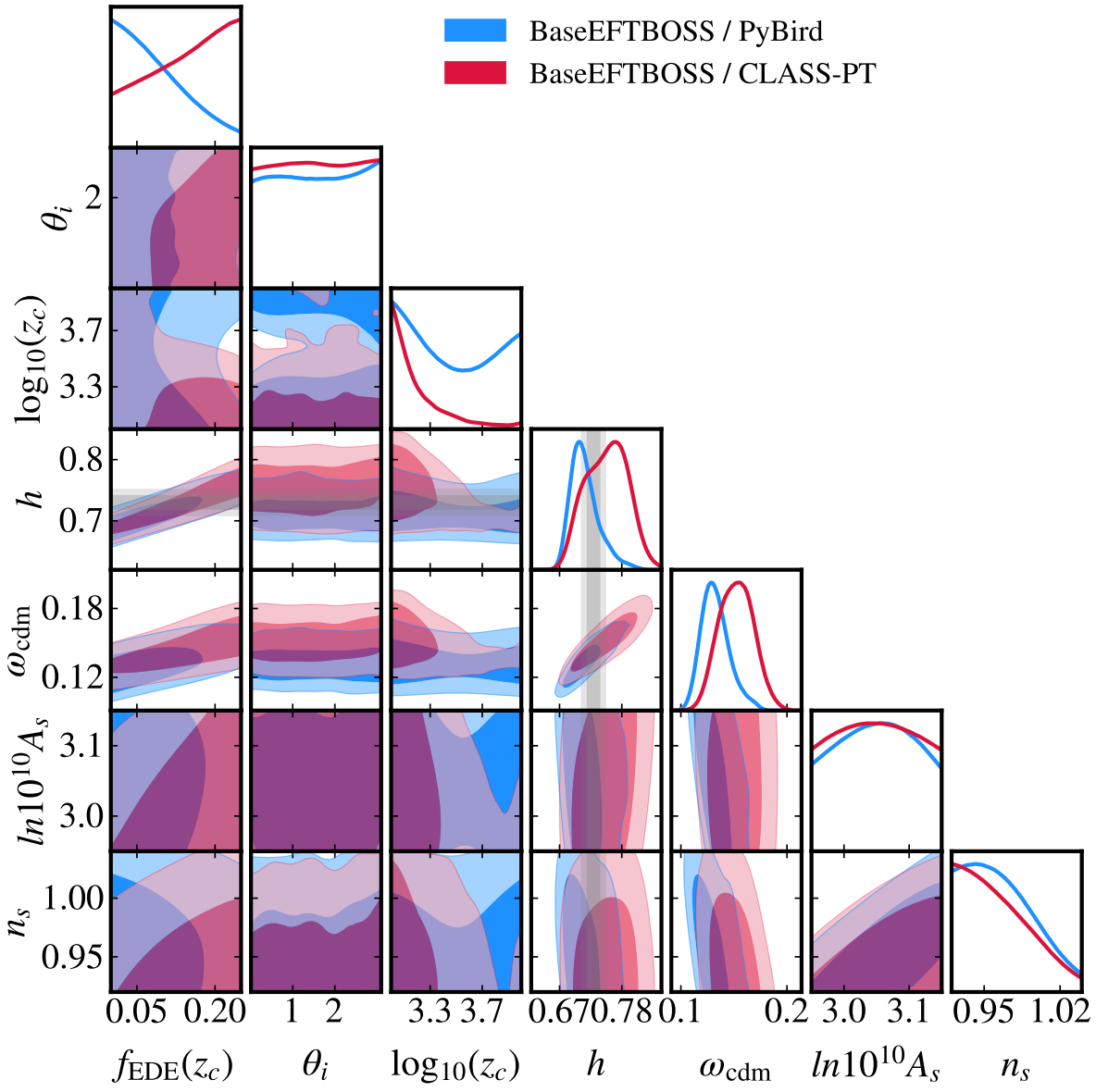

Figure D.2: Comparison between the 2D posterior distributions of a subset of parameters in the EDE model reconstructed from the `PyBird` or `CLASS-PT` likelihood, in combination with BBN+Lens+BAO+Pan18 (*i.e.*, BaseEFTBOSS).

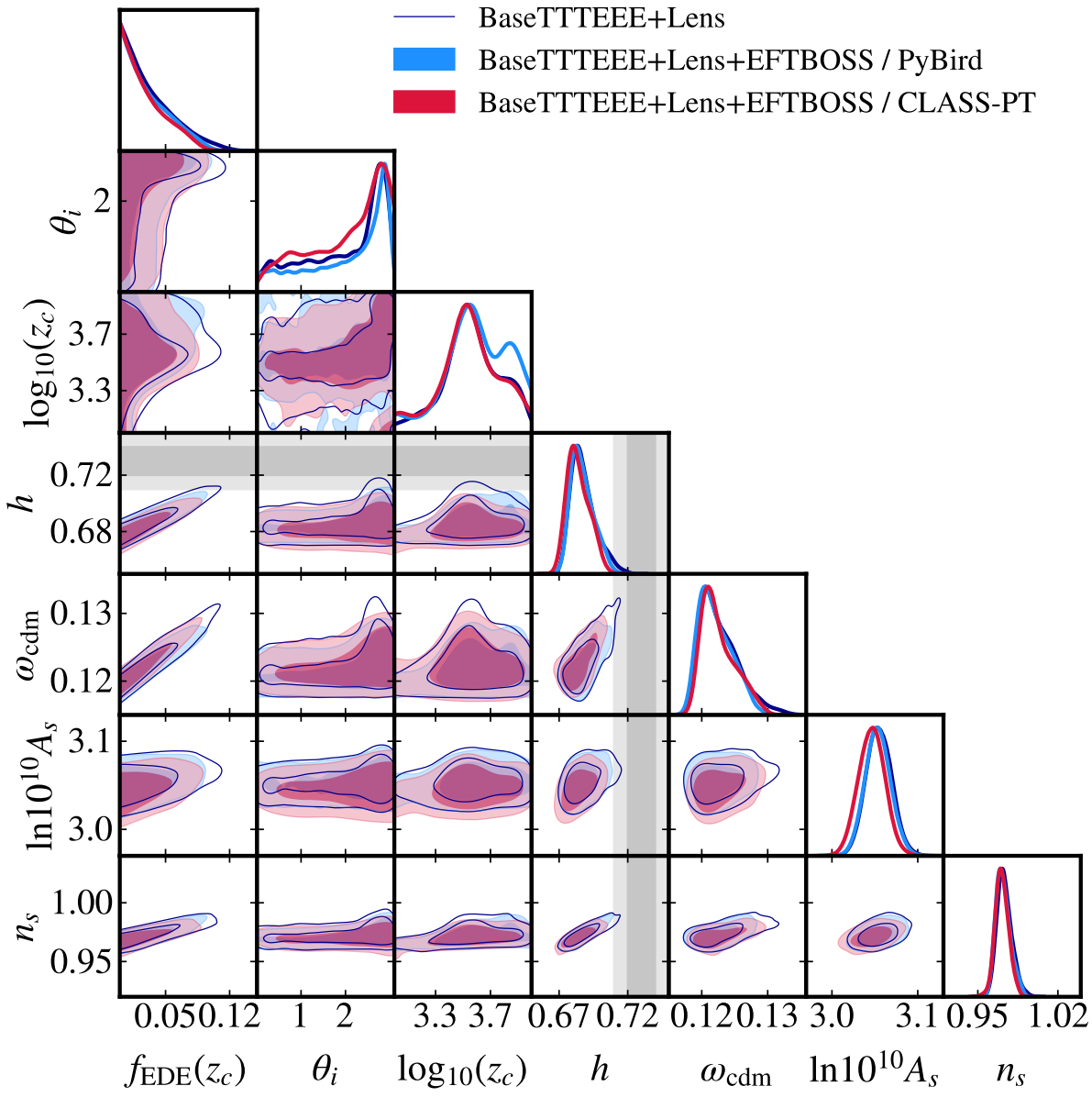

Figure D.3: Comparison between the 2D posterior distributions of a subset of parameters in the EDE model reconstructed from the `PyBird` or `CLASS-PT` likelihood, in combination with BaseTTTEEE+Lens.

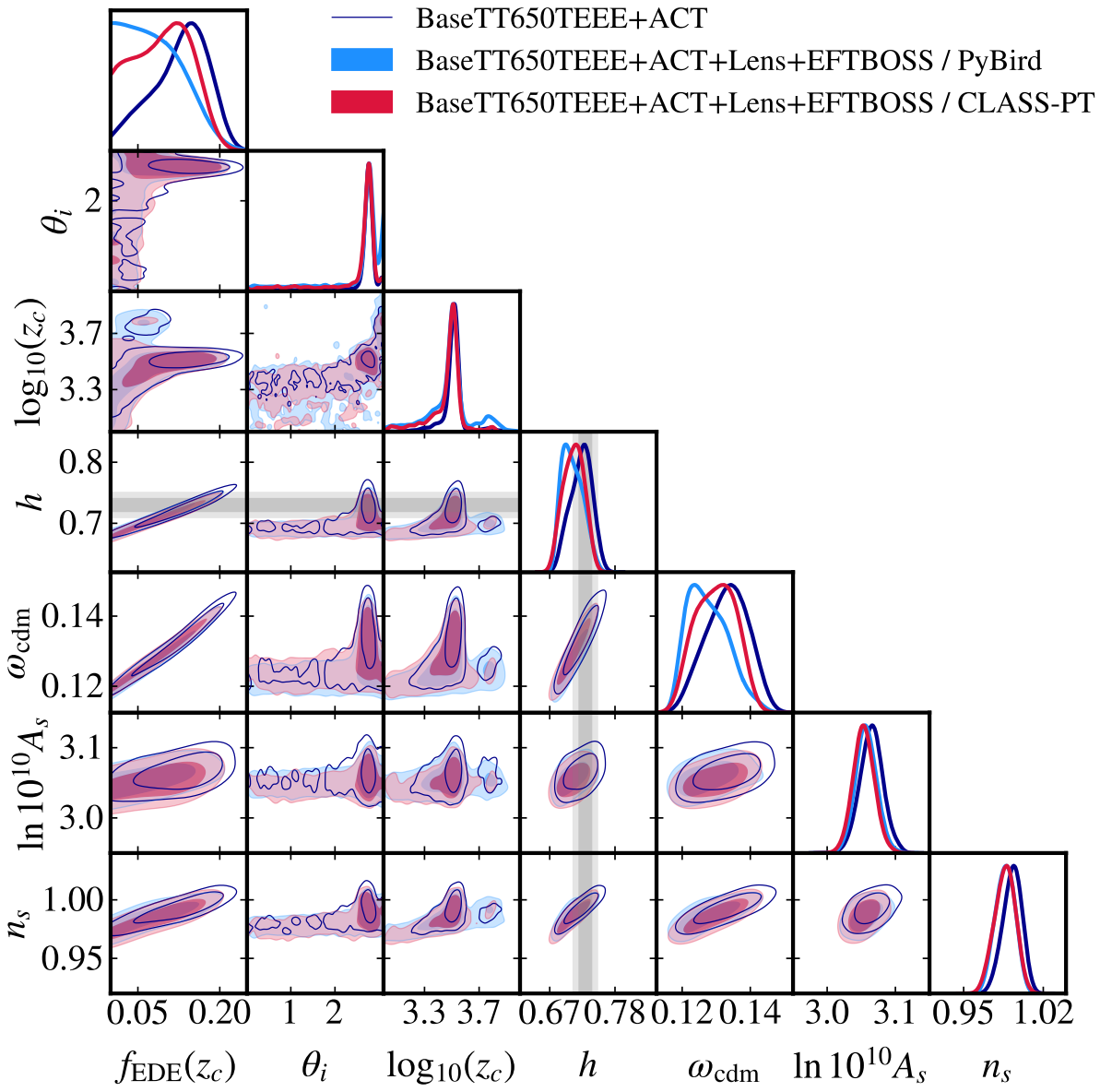

Figure D.4: Comparison between the 2D posterior distributions of a subset of parameters in the EDE model reconstructed from the `PyBird` or `CLASS-PT` likelihood, in combination with BaseTT650TEEE+ACT+Lens.

EDE						
Planck high$-\ell$ TTTEEE	2339.4	2341.5	2339.1	2340.9	2339.3	2341.1
Planck low$-\ell$ TT	21.8	20.4	22.0	20.6	21.1	20.5
Planck low$-\ell$ EE	396.4	396.8	396.1	396.4	396.1	396.9
Planck lensing	9.5	10.0	9.3	9.9	9.6	9.9
BOSS BAO low$-z$	1.6	1.8	1.4	1.7	1.4	1.9
BOSS BAO DR12	3.7	3.5	–	–	–	–
BOSS BAO/$f\sigma_8$ DR12	–	–	6.5	7.0	–	–
EFTBOSS CMASS	–	–	–	–	84.1	83.3
EFTBOSS LOWZ	–	–	–	–	34.0	34.4
Pantheon	1027.0	1026.9	1027.0	1026.9	1027.0	1026.9
SH0ES	–	2.0	–	3.2	–	2.3
total $\chi^2_{\rm min}$	3799.2	3802.9	3801.8	3806.1	3912.7	3917.3
$\Delta\chi^2_{\rm min}$(EDE $-$ ΛCDM)	-3.8	-23.7	-3.9	-23.0	-4.7	-22.7
Preference over ΛCDM	1σ	4.2σ	1.1σ	4.1σ	1.3σ	4.1σ
$Q_{\rm DMAP}$	1.9σ		2.0σ		2.1σ	

Table D.2: Best-fit χ^2 per experiment (and total) for EDE when fit to different data combinations: BaseTTTEEE+Lens, BaseTTTEEE+Lens+$f\sigma_8$, BaseTTTEEE+Lens+EFTBOSS, with and without SH0ES. We also report the $\Delta\chi^2_{\rm min} \equiv \chi^2_{\rm min}({\rm EDE}) - \chi^2_{\rm min}(\Lambda{\rm CDM})$ and the tension metric $Q_{\rm DMAP} \equiv \sqrt{\chi^2({\rm w/\ SH0ES}) - \chi^2({\rm w/o\ SH0ES})}$.

	ΛCDM					EDE				
Planck high$-\ell$ TT650TEEE	1843.5	1842.6	1842.9	1842.8	1842.6	1837.5	1838.0	1836.9	1836.8	1837.7
Planck low$-\ell$ TT	21.5	21.7	21.5	21.7	21.8	20.7	20.9	20.8	20.9	21.2
Planck low$-\ell$ EE	395.7	395.7	395.8	395.9	–	395.8	395.8	395.8	395.8	395.8
Planck lensing	–	–	–	9.0	9.0	–	–	–	10.2	9.9
ACT DR4	293.8	294.5	294.4	294.2	294.3	285.4	285.0	285.9	286.4	286.9
BOSS BAO low$-z$	1.5	1.4	1.6	1.5	1.4	2.1	2.0	2.4	2.3	1.9
BOSS BAO DR12	3.7	–	–	–	–	3.5	–	–	–	–
BOSS BAO/$f\sigma_8$ DR12	–	6.1	–	–	–	–	7.2	–	–	–
EFTBOSS CMASS	–	–	83.4	83.6	84.9	–	–	84.5	84.3	84.3
EFTBOSS LOWZ	–	–	33.7	33.7	33.7	–	–	35.1	34.7	34.4
Pantheon	1026.8	1027.0	1027.0	1027.0	–	1026.9	1026.9	1026.9	1026.9	–
Pantheon+	–	–	–	–	1411.8	–	–	–	–	1413.0
total $\chi^2_{\rm min}$	3586.5	3589.1	3700.3	3709.5	4094.3	3571.9	3575.8	3688.3	3698.4	4085.1
$\Delta\chi^2_{\rm min}$(EDE $-$ ΛCDM)	–	–	–	–	–	-14.6	-13.3	-12.0	-11.1	-9.2
Preference over ΛCDM	–	–	–	–	–	3.1σ	2.9σ	2.7σ	2.5σ	2.2σ

Table D.3: Best-fit χ^2 per experiment (and total) for ΛCDM and EDE when fit to different data combinations: BaseTT650TEEE+ACT, BaseTT650TEEE+ACT+$f\sigma_8$, BaseTT650TEEE+ACT+EFTBOSS, BaseTT650TEEE+ACT+Lens+EFTBOSS, and BaseTT650TEEE+ACT+Lens+EFTBOSS+PanPlus. We also report the $\Delta\chi^2_{\rm min} \equiv \chi^2_{\rm min}({\rm EDE}) - \chi^2_{\rm min}(\Lambda{\rm CDM})$ and the corresponding preference over ΛCDM, computed assuming the $\Delta\chi^2$ follows a χ^2 distribution with three degrees of freedom.

	ΛCDM		EDE	
Planck high$-\ell$ TTTEEE	2349.8	2352.0	2346.2	2347.2
Planck low$-\ell$ TT	22.4	22.0	21.9	21.2
Planck low$-\ell$ EE	396.2	396.8	396.1	396.4
Planck lensing	8.9	8.9	9.6	9.8
ACT DR4	240.6	241.0	236.8	236.2
BOSS BAO low$-z$	1.4	2.0	1.7	2.2
EFTBOSS CMASS	84.1	82.9	84.2	84.2
EFTBOSS LOWZ	33.6	33.8	34.2	34.6
Pantheon	1027.1	1026.9	1026.9	1026.9
SH0ES	–	19.5	–	1.10
total $\chi^2_{\rm min}$	4164.0	4185.9	4157.6	4159.8
$\Delta\chi^2_{\rm min}$(EDE $-$ ΛCDM)	–	–	-6.4	-26.1
Preference over ΛCDM	–	–	1.7σ	4.4σ
$Q_{\rm DMAP}$	4.7σ		1.5σ	

Table D.4: Best-fit χ^2 per experiment (and total) for ΛCDM and EDE when fit to BaseTTTEEE+ACT+Lens+EFTBOSS, with and without SH0ES. We also report the $\Delta\chi^2_{\rm min} \equiv \chi^2_{\rm min}({\rm EDE}) - \chi^2_{\rm min}(\Lambda{\rm CDM})$ and the tension metric $Q_{\rm DMAP} \equiv \sqrt{\chi^2({\rm w/\ SH0ES}) - \chi^2({\rm w/o\ SH0ES})}$.

	ΛCDM		EDE	
Planck high$-\ell$ TTTEEE	2346.18	2349.5	2344.0	2346.9
Planck low$-\ell$ TT	23.0	22.4	22.3	21.0
Planck low$-\ell$ EE	396.1	397.7	396.3	396.3
Planck lensing	8.8	9.1	9.0	9.6
BOSS BAO low$-z$	1.1	2.1	1.3	1.8
EFTBOSS CMASS	85.2	82.9	85.0	85.1
EFTBOSS LOWZ	33.6	33.8	33.8	34.6
Pantheon+	1411.1	–	1411.6	–
Pantheon+SH0ES	–	1321.9	–	1291.6
total $\chi^2_{\rm min}$	4305.1	4219.3	4303.2	4187.0
$\Delta\chi^2_{\rm min}$(EDE $-$ ΛCDM)	–	–	-1.9	-32.3
Preference over ΛCDM	–	–	0.5σ	5σ

Table D.5: Best-fit χ^2 per experiment (and total) for ΛCDM and EDE when fit to BaseTTTEEE+Lens+EFTBOSS+PanPlus, with and without SH0ES. We also report the $\Delta\chi^2_{\rm min} \equiv \chi^2_{\rm min}({\rm EDE}) - \chi^2_{\rm min}(\Lambda{\rm CDM})$ and the corresponding preference over ΛCDM, computed assuming the $\Delta\chi^2$ follows a χ^2 distribution with three degrees of freedom.

E

EFTofLSS' take on the Hubble tension and the acoustic dark energy

E.1 M_b prior

In this appendix, we show explicitly, thanks to Fig E.1, that the addition of the M_b prior [153] on top of the Pantheon+ likelihood is equivalent to the use of the full Pantheon+/SH_0ES likelihood as provided in Ref. [153]. Since the constraints are similar, we have chosen to show in this work the results with the M_b prior, for the sake of convenience, in order to determine the $Q_{\rm DMAP}$ values easily.

E.2 χ^2 table

In this appendix, we report the best-fit χ^2 per experiment for the ΛCDM model, the ADE model, as well as the axion-like EDE model for several combinations of data.

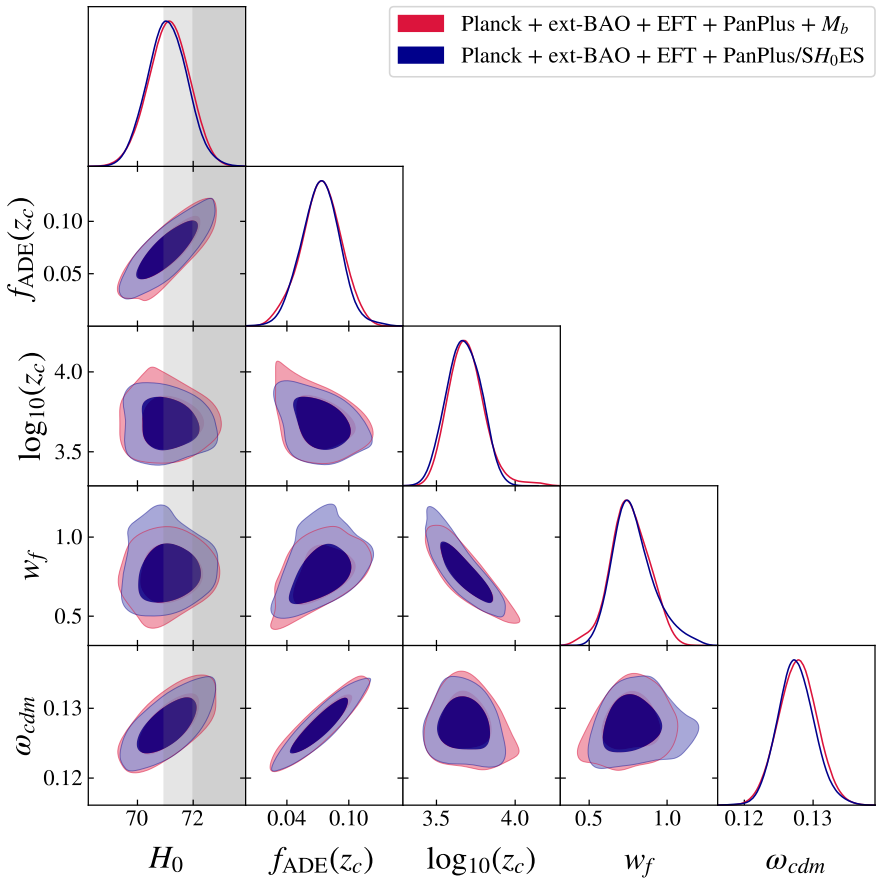

Figure E.1: 2D posterior distributions reconstructed from *Planck* + ext-BAO + EFT, either with the M_b prior on top of the Pantheon+ likelihood, or with the cross-correlation between the Pantheon+ data and the SH_0ES data (namely the Pantheon+/SH_0ES likelihood) as provided in Ref. [153]. The gray band corresponds to the H_0 constraint associated with the M_b prior, $H_0 = (73.04 \pm 1.04)$ km/s/Mpc [153].

Data	Model	χ^2 tot	P18TTTEE	P18lens	ext-BAO	BOSS	eBOSS	Pan	M_b	PanPlus/SH_0ES
BAO/$f\sigma_8$+Pan	ΛCDM	3816.39	2763.03	8.87	1.38	6.15	9.88	1027.07	–	–
	ADE	3812.50	2759.48	9.14	1.30	6.55	8.92	1027.10	–	–
	EDE	3809.87	2757.41	9.70	1.64	6.30	7.89	1026.93	–	–
BAO/$f\sigma_8$+Pan+M_b	ΛCDM	3847.33	2765.48	9.12	1.84	5.91	9.14	1026.89	28.94	–
	ADE	3819.06	2763.73	10.09	1.77	6.95	6.32	1026.89	3.32	–
	EDE	3812.26	2759.10	9.89	1.91	6.97	6.21	1026.87	1.31	–
EFT+Pan	ΛCDM	4020.07	2762.14	8.87	1.25	160.20	60.44	1027.17	–	–
	ADE	4018.67	2761.21	8.99	1.40	159.63	60.39	1027.06	–	–
	EDE	4017.09	2759.20	9.29	1.60	159.54	60.51	1026.95	–	–
EFT+Pan+M_b	ΛCDM	4051.76	2764.81	9.13	1.78	158.30	61.16	1026.90	29.61	–
	ADE	4026.87	2763.76	9.62	2.11	159.94	60.26	1026.86	4.33	–
	EDE	4022.83	2758.51	9.60	1.99	160.36	61.64	1026.87	3.86	–
EFT+PanPlus	ΛCDM	4404.28	2762.12	8.78	1.20	160.44	60.43	1411.31	–	–
	cADE	4404.07	2761.57	8.86	1.20	160.68	60.46	1411.31	–	–
	ADE	4402.96	2760.49	8.89	1.21	160.78	60.23	1411.36	–	–
	c_s^2ADE	4402.93	2760.47	8.90	1.21	160.76	60.23	1411.37	–	–
	EDE	4402.54	2758.74	9.02	1.38	160.38	61.21	1411.82	–	–
EFT+PanPlus+M_b	ΛCDM	4443.78	2766.95	9.69	1.95	158.36	60.63	1413.17	33.02	–
	cADE	4419.67	2766.20	9.67	1.92	160.68	61.17	1413.27	6.76	–
	ADE	4415.94	2763.42	9.82	1.81	160.52	60.95	1412.99	6.42	–
	c_s^2ADE	4415.89	2763.16	9.82	1.77	160.58	60.96	1412.91	6.70	–
	EDE	4408.67	2759.71	10.05	1.96	159.64	60.24	1413.35	3.72	–
EFT+PanPlus/SH_0ES	ΛCDM	4318.12	2767.42	9.24	2.20	158.01	60.39	–	–	1320.85
	ADE	4292.12	2763.74	9.77	1.94	160.31	60.20	–	–	1296.17

Table E.1: Table of best-fit χ^2 of the different models considered in this work for various combinations of likelihood. All datasets include *Planck* + ext-BAO data. Note that the columns "BOSS" and "eBOSS" refer either to the BAO/$f\sigma_8$ analysis or to the EFT full-shape analysis. Similarly, the column "Pan" refers to either Pantheon data or Pantheon+ data. Finally, "PanPlus/SH_0ES" corresponds to the full Pantheon+/SH_0ES likelihood as provided in Ref. [153].

F

EFTofLSS' take on the S_8 tension and the decaying dark matter

F.1 Comparison between the EFTofLSS and N-body methods for the DCDM $\to$ DR model

In this appendix, we compare the nonlinear matter power spectrum obtained through the EFTofLSS method with the results of dedicated N-body simulations performed in Ref. [412]. The authors of Ref. [412] have determined a fitting formula which describes the correction to the nonlinear matter power spectrum due to the DM decay compared to the ΛCDM model, as a function of τ, $f_{\rm dcdm}$, and the redshift z. In Fig. F.1, we compare this fitting formula, where we set $\tau = 32$ Gyr and $z = 0$ and vary $f_{\rm dcdm} \in [0,1]$, with the linear matter power spectrum of the `CLASS` code (left panel), and with the nonlinear matter power spectra from both the `CLASS-PT` and `PyBird` codes (right panel). Here, we set the ΛCDM parameters to the values used in Ref. [412]. The left panel of this figure is intended as a reproduction of Fig. 1 of this reference for direct comparison, while the right panel presents the comparison of interest. Indeed, from the right panel of Fig. F.1, one can clearly see that (i) the `CLASS-PT` and `PyBird` codes give very similar power spectra for the DCDM $\to$ DR model, [1] (ii) the deviation from ΛCDM predicted in these two EFTofLSS codes is very close to that obtained through N-body simulation. In order to determine more precisely the deviations between the EFTofLSS and the N-body methods, we plot, in Fig. F.2, the ratio between the residuals obtained with the N-Body simulation and those obtained with the `CLASS-PT` and `PyBird` codes. One can see that the difference is below the $\sim 1\%$ level until $k \sim 0.2\ h{\rm Mpc}^{-1}$ (the maximum k at which the EFTofLSS is valid at one loop order for a small z). Let us note that the difference between the N-body simulation and the EFTofLSS power spectrum for $k \lesssim 0.02\ h{\rm Mpc}^{-1}$ is not relevant; it is merely due to the fact that the N-body fitting formula does not encode this behavior for low k (see [412]), but this k range is well within the linear regime and does not necessitate a correction. Let us also remark that the lower $f_{\rm dcdm}$ (or the longer τ), the smaller the difference between the residuals from the N-body and those from the EFTofLSS method. Since current constraints only allow small values of $f_{\rm dcdm} \lesssim 2.5\%$ or large lifetime $\tau \gtrsim 240$ Gyr, it is safe to

[1] We set, in the `PyBird` and `CLASS-PT` codes, $c_s = 1$, which is an effective parameter of the one loop correction that can be interpreted as the effective sound speed of the dark matter.

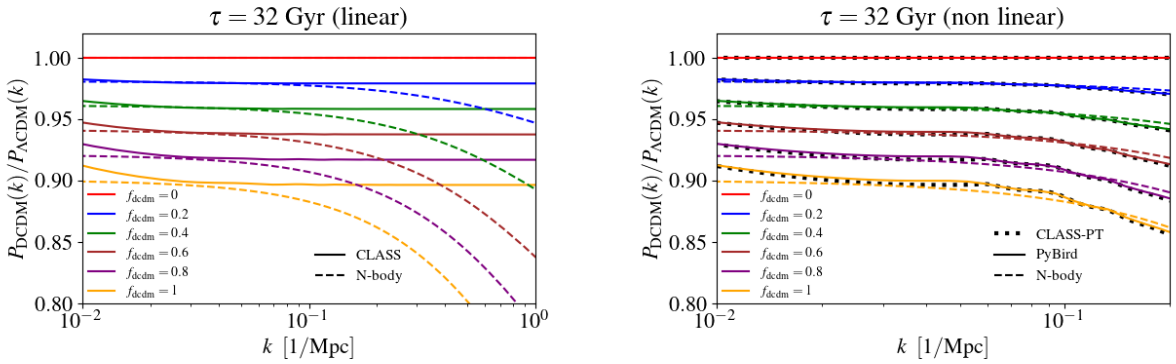

Figure F.1: Comparison between the residuals of the nonlinear matter power spectra predicted by the N-body simulation and the residuals of the linear matter power spectra predicted by the `CLASS` code on the one hand (left panel), and the residuals of the nonlinear matter power spectra predicted by the `CLASS-PT` and `PyBird` codes on the other hand (right panel). We compute these power spectra for $z = 0$ and for $\tau = 32$ Gyr, while we varied $f_{\rm dcdm}$ from 0 to 1 with a step of 0.2.

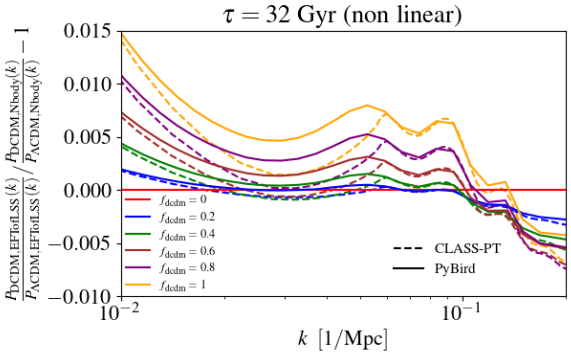

Figure F.2: Ratio between residuals of the nonlinear matter power spectra obtained from the N-body simulation and those obtained from the `CLASS-PT` and the `PyBird` codes for $z = 0$, $\tau = 32$ Gyr and $f_{\rm dcdm}$ varying from 0 to 1 with a step of 0.2.

use the `PyBird` (or `CLASS-PT`) code in their current form to describe the DCDM→DR model. This good agreement between the EFT approach and the N-body simulation, despite having made no change to the EFT modeling, may appear surprising at first sight. However, there is a fairly intuitive argument as to why the DM equations (and therefore the EFT formalism) should receive only minor corrections from the presence of a nonzero decay term. This is because, in the synchronous gauge at linear order, the DCDM equations are strictly identical to that of CDM: the effect of the decay is happening exactly at the same rate everywhere in space, and therefore cancels out the perturbed continuity and Euler equations which drive the DCDM perturbed dynamics. Although strictly speaking, the contribution of the decay term may appear at higher order, as we treat the mildly nonlinear regime, it will be subdominant. This explains why we find such a good agreement between N-body simulations and the EFT computation despite not modifying the master equations, the expansion nor the counterterms. Note that this argument is valid irrespective of the mass of the daughter particles as far as the mother particle is concerned. Similarly, corrections to the massless daughter equations may appear, but will likely have only a small impact on the observables given that the massless

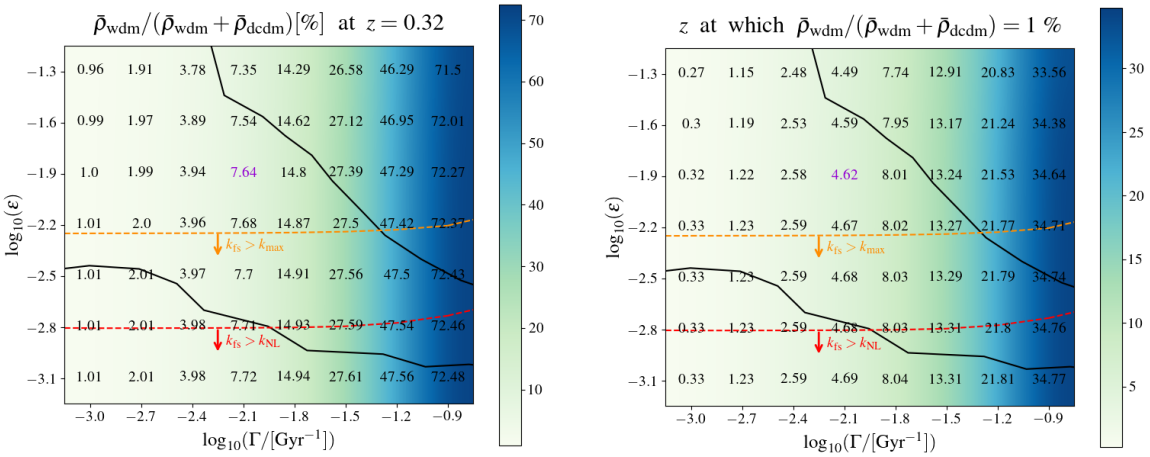

Figure F.3: Values of the WDM fraction at $z = 0.32$ (left panel) and the redshift at which the WDM fraction becomes 1% (right panel), in a region of the $\log_{10}(\varepsilon)$-$\log_{10}(\Gamma/{\rm Gyr}^{-1})$ plane. The ΛCDM parameters are fixed to the best-fit from the *Planck* + Pantheon + EFTofBOSS + Ext-BAO + S_8 analysis. The black lines indicate the 1σ limits of this analysis, while the point highlighted in purple indicates the best-fit. All the points below the yellow and red lines correspond to models having a WDM free-streaming wavenumber $k_{\rm fs}$ larger than $k_{\rm max} = 0.2\,h\,{\rm Mpc}^{-1}$ and $k_{\rm nl} = 0.7\,h\,{\rm Mpc}^{-1}$, respectively.

daughter quickly redshift away compared to other species for decays happening at late times (at times relevant for galaxy surveys).

F.2 Assessing the validity of the EFTofLSS in the DCDM → WDM+DR model

In this appendix, we discuss the validity of the EFTofLSS in the DCDM → WDM+DR model. In Ref. [416], the EFTofLSS was extended to describe massive neutrinos, an extension to ΛCDM with properties similar to that of the DCDM→WDM+DR model. Indeed, the main issue with employing the EFTofLSS to describe the DCDM→WDM+DR model does not lie in the effect of the decay itself (the effect of the decay on the perturbed equations of the DCDM is identical to that of the DCDM → DR model, which is captured by our formalism as discussed in App. F.1), but rather in the production of a warm massive species which may contribute in a nontrivial way to the power spectrum of galaxies. At the linear level, it was found the massive decay products behave similarly to CDM at wavenumbers smaller than the free-streaming scale $k_{\rm fs}$ [with $k_{\rm fs}$ approximately given by Eq. 9.24], but is strongly suppressed due to pressure terms at larger wavenumbers similarly to WDM and hot DM such as neutrinos. In Ref. [416], the contribution of neutrinos to the total one loop power spectrum was computed, and it was found that the dominant effect is a correction to the dark matter power spectrum that scales like $16 f_\nu$, where $f_\nu \equiv \bar{\rho}_\nu/(\bar{\rho}_\nu + \bar{\rho}_{\rm cdm}) \sim 1\%$, at $k > k_{\rm fs}$ and roughly half of that at $k < k_{\rm fs}$. The naive $\mathcal{O}(f_\nu)$ contribution is enhanced by twice the logarithm of the redshift of matter-radiation equality, as neutrinos are present from early times. The log-enhanced contribution represents about 70% of the contribution to the total one loop power spectrum. Additionally, at leading order, counterterms can be captured by simply rescaling the effective DM sound speed c_s^2 and do not necessitate adding new parameters to the dark-matter-only calculation. In the

case of the DCDM model, the WDM is produced at much later times. We plot in Fig. F.3 (right panel) the redshift $z_{1\%}$ at which the WDM contribution $f_{\rm wdm} \equiv \bar{\rho}_{\rm wdm}/(\bar{\rho}_{\rm wdm}+\bar{\rho}_{\rm dcdm})$ reaches $\sim 1\%$. We also represent the limit at 68% C.L. derived in our work. For the best-fit model (shown in purple in the figure), $z_{1\%} \sim 5$. The log-enhancement from the ratio of scale factor between $z \sim 5$ and $z_{eff,\rm LOWZ} = 0.32$ is $\log[(1+z_{1\%})/(1+z_0)] \approx 1-2$ compared to the $\log[(1+z_{\rm eq})/(1+z_0)] \approx 8$ in the neutrino study in Ref. [416] that gives the $16 f_\nu$ factor. We therefore expect the WDM correction to be comparable to the massive neutrino case even if the energy density (today) ratio is ≈ 10 times larger than neutrinos.

We plot in Fig. F.3 (left panel), the fractional contribution of WDM at $z = 0.32$ (the effective redshift of the low-z surveys) as a function of Γ and ε. We also represent the limit at 68% C.L. derived in this work. One can see that it is under $\sim 15\%$ as long as $\log_{10}(\Gamma/[{\rm Gyr}^{-1}]) \lesssim -1.8$. Additionally, we show the value of $\varepsilon - \Gamma$ for which the free-streaming scale $k_{\rm fs}$ is equal to the maximum k mode relevant for our analysis of BOSS data ($k_{\rm max} = 0.2\ h{\rm Mpc}^{-1}$) and the maximum scale considered in the EFT computation ($k_{\rm nl} = 0.7\ h{\rm Mpc}^{-1}$). In a large part of the parameter space favored by our analysis for which $f_{\rm wdm}$ is not small, $k_{\rm fs}$ exceeds $k_{\rm max}$ and therefore corrections should also be minor. An improved EFT treatment including the effect of the massive decay product would be necessary however to describe the power spectrum up to $k_{\rm nl}$. Given current precision of the data and the large theoretical uncertainty already present, the corrections to our calculation should be negligible, but more work needs to be done to accurately describe the part of the parameter space with large Γ (and leading to large $f_{\rm wdm}$), in particular for future surveys which can reach subpercent precision at larger wave-numbers.

F.3 The role of the S_8 prior

In this appendix, we present 2D posterior distributions obtained with and without the S_8 prior (but with the EFTofBOSS data) in both DCDM cosmologies. In the case of the DCDM $\to$ DR model, represented in Fig. F.4, the impact of the S_8 prior is minor. However, in the case of the DCDM $\to$ WDM+DR model, represented in Fig. F.5, it opens up a degeneracy with $\{\Gamma, \varepsilon\}$ which can lead to low S_8 while preserving the fit to other datasets. Without the S_8 prior, the DCDM model is not favored by *Planck* data. As discussed in the main text, when the S_8 prior is included, the fit to *Planck* data is not affected, while the DCDM model can accommodate the lower S_8 value, contrarily to the ΛCDM model. From the $Q_{\rm DMAP}$ statistics [352], we can estimate the residual tension as $Q_{\rm DMAP} \equiv \sqrt{\chi^2_{\rm min}({\rm w/}\ S_8) - \chi^2_{\rm min}({\rm w/o}\ S_8)} = 1.5\sigma$ in the DCDM$\to$WDM+DR model, as compared to 2.4σ in the ΛCDM model and DCDM$\to$DR model.

[t]

F.4 Supplementary tables of $\chi^2_{\rm min}$ values per experiment

In this appendix, we report the best-fit χ^2 per experiment for both ΛCDM (Tab. F.1) and DCDM $\to$ WDM+DR (Tab. F.2) models for our analyses with the BAO/$f\sigma_8$ + S_8, EFTofBOSS and EFTofBOSS + S_8 data. To help the reader gauge the goodness of fit, the number of d.o.f. is estimated to be 2287 for *Planck* high-l TTTEEE, 25 for *Planck* low-l EE, and 25 for *Planck* low-l TT [11]. Other experiments do not report the number of degrees of freedom, but it can be

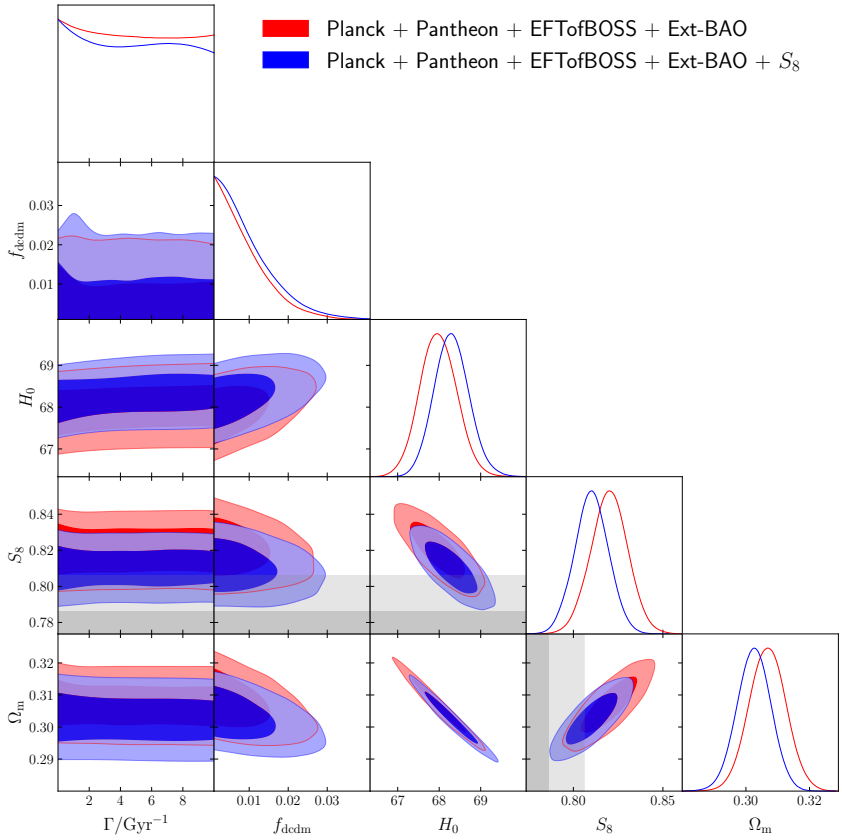

Figure F.4: 2D posterior distributions of the DCDM → DR model reconstructed from an analysis of *Planck*, Pantheon, Ext-BAO and EFTofBOSS data, with (blue) and without (red) the S_8 prior from KiDS-1000. The gray shaded bands refer to the joint S_8 measurement from KiDS-1000 + BOSS + 2dFLens.

estimated from the number of data points $N_{\rm data}$, assuming uncorrelated data points for simplicity, and the number of free parameters $N_{\rm param} = N_{\rm param,model} + N_{\rm param,nuisance}$, as $N_{\rm dof} = N_{\rm data} - N_{\rm param}$. In practice, we have $N_{\rm data} = 1048$ and $N_{\rm param,nuisance} = 1$ for Pantheon [133], $N_{\rm data} = 132$ and $N_{\rm param,nuisance} = 6$ for the sum of the three sky cuts of the EFTofBOSS data including BAO, and $N_{\rm data} = 13$ for the BOSS BAO/$f\sigma_8$ and Ext-BAO (the full BAO dataset). Finally, we have for each model $N_{\rm param,\Lambda CDM} = 6$ and $N_{\rm param,\Lambda DCDM} = 8$.

F.5 ΛCDM parameters of the DCDM → WDM+DR model

In this appendix, we compare in Fig. F.6 the ΛCDM parameters of the DCDM → WDM+DR model obtained from the analyses with (blue) and without (red) the EFTofBOSS data, while in Fig. F.7 we represent the ΛCDM parameters reconstructed from an analysis of *Planck*, Pantheon, Ext-BAO and EFTofBOSS data, with (blue) and without (red) the S_8 prior. We also show in this second figure the standard ΛCDM posteriors as a reference (green). One can see that the ΛCDM parameters are left largely unchanged in the DCDM → WDM+DR model. The decay into warm products only affects the growth of structure at late times with little impact on parameters that could affect early time physics. This is essentially why cosmological data other than those measuring S_8 (and potentially the growth of structure at late-times) are unaffected by the DCDM, despite a lower S_8 value.

ΛCDM			
Dataset	w/ BAO/$f\sigma_8$ + S_8	w/ EFTofBOSS	w/ EFTofBOSS + S_8
Planck high-l TTTEEE	2349.0	2347.4	2349.3
Planck low-l EE	396.1	396.7	396.1
Planck low-l TT	22.8	23.0	22.7
Planck lensing	9.6	8.9	9.6
Pantheon	1027.0	1027.1	1027.0
Ext-BAO	6.3	6.2	6.3
BOSS BAO/$f\sigma_8$	6.0	–	–
EFTofBOSS	–	117.8	117.0
S_8	5.3	–	5.0
total $\chi^2_{\rm min}$	3821.9	3927.0	3933.0

Table F.1: χ^2 of each dataset for our *Planck* + Pantheon + BOSS BAO/$f\sigma_8$ + Ext-BAO + S_8, *Planck* + Pantheon + EFTofBOSS + Ext-BAO and *Planck* + Pantheon + EFTofBOSS + Ext-BAO + S_8 analyses for the ΛCDM model. Since we rounded the χ^2 of each experiment, the total χ^2 is only equal to the sum of each χ^2 at $\mathcal{O}(0.1)$ precision.

DCDM→WDM+DR			
Dataset	w/ BAO/$f\sigma_8$ + S_8	w/ EFTofBOSS	w/ EFTofBOSS + S_8
Planck high-l TTTEEE	2347.7	2347.3	2348.0
Planck low-l EE	397.2	396.9	397.0
Planck low-l TT	23.1	23.0	23.2
Planck lensing	8.9	8.9	9.1
Pantheon	1027.2	1027.1	1027.2
Ext-BAO	6.1	6.2	6.2
BOSS BAO/$f\sigma_8$	7.1	–	–
EFTofBOSS	–	117.8	118.3
S_8	0.2	–	0.4
total $\chi^2_{\rm min}$	3817.5	3927.0	3929.2

Table F.2: χ^2 of each dataset for our *Planck* + Pantheon + BOSS BAO/$f\sigma_8$ + Ext-BAO + S_8, *Planck* + Pantheon + EFTofBOSS + Ext-BAO and *Planck* + Pantheon + EFTofBOSS + Ext-BAO + S_8 analyses for the DCDM → WDM+DR model. Since we rounded the χ^2 of each experiment, the total χ^2 is only equal to the sum of each χ^2 at $\mathcal{O}(0.1)$ precision.

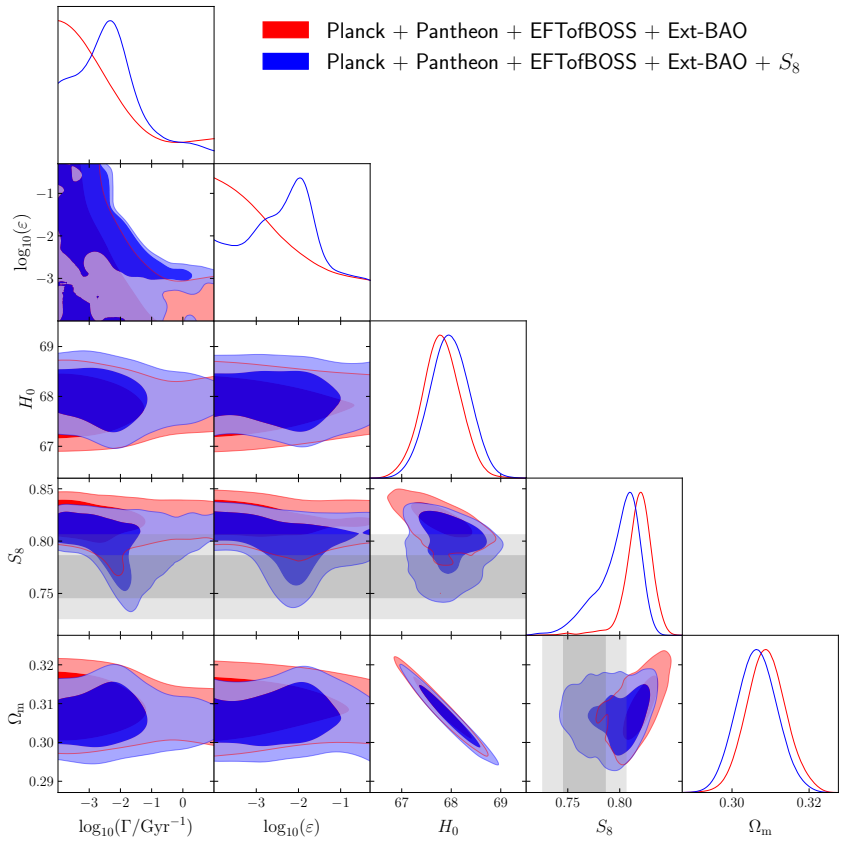

Figure F.5: 2D posterior distributions of the DCDM → WDM+DR model reconstructed from an analysis of *Planck*, Pantheon, Ext-BAO and EFTofBOSS data, with (blue) and without (red) the S_8 prior from KiDS-1000. The gray shaded bands refer to the joint S_8 measurement from KiDS-1000 + BOSS + 2dFLens.

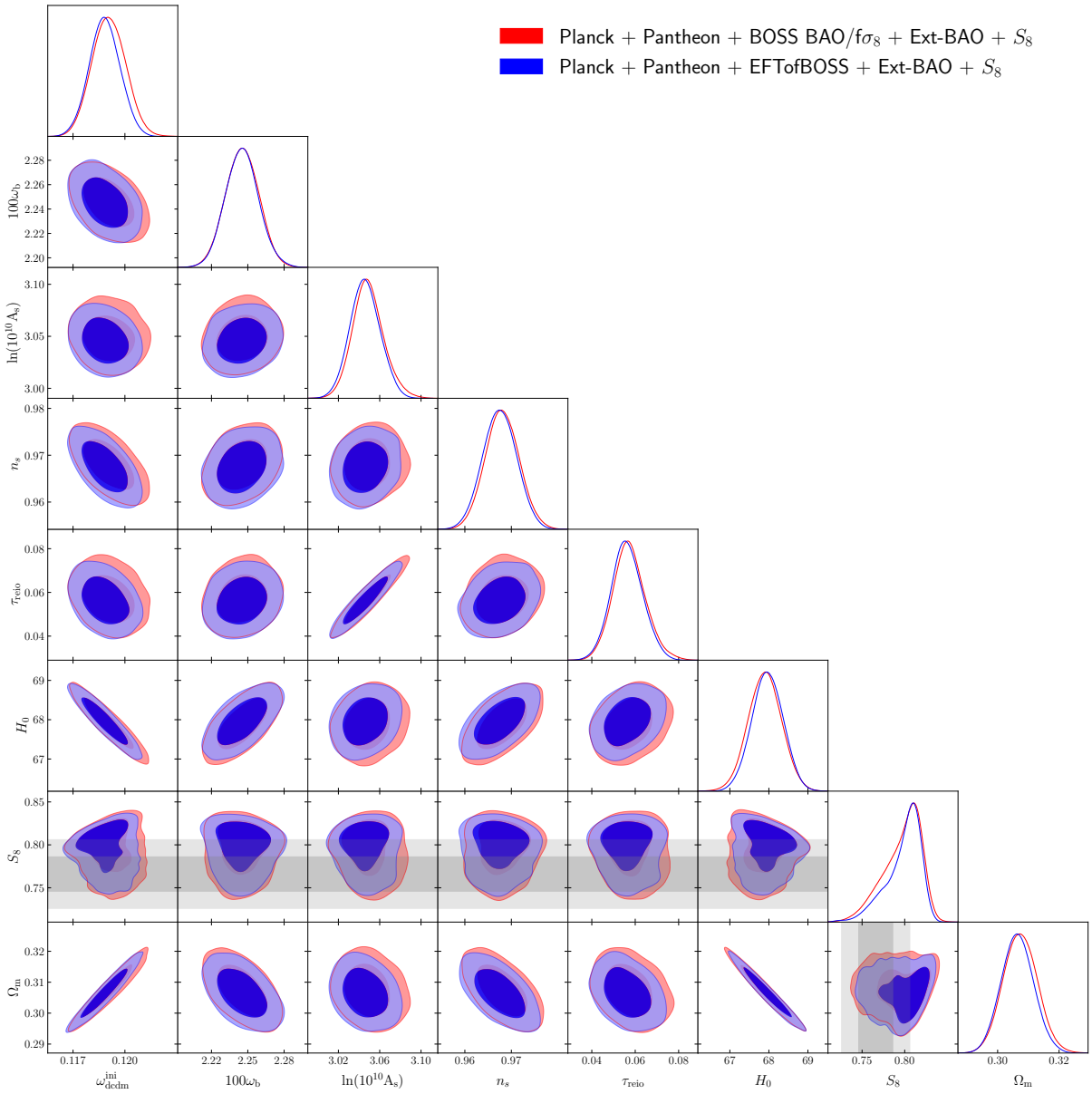

Figure F.6: 2D posterior distributions of the DCDM $\rightarrow$ WDM+DR model with and without the EFTofBOSS dataset for the ΛCDM parameters. We took into account the S_8 prior from KIDS-1000 for these two MCMC analyses. The gray shaded bands refer to the joint S_8 measurement from KIDS-1000 + BOSS + 2dFLens.

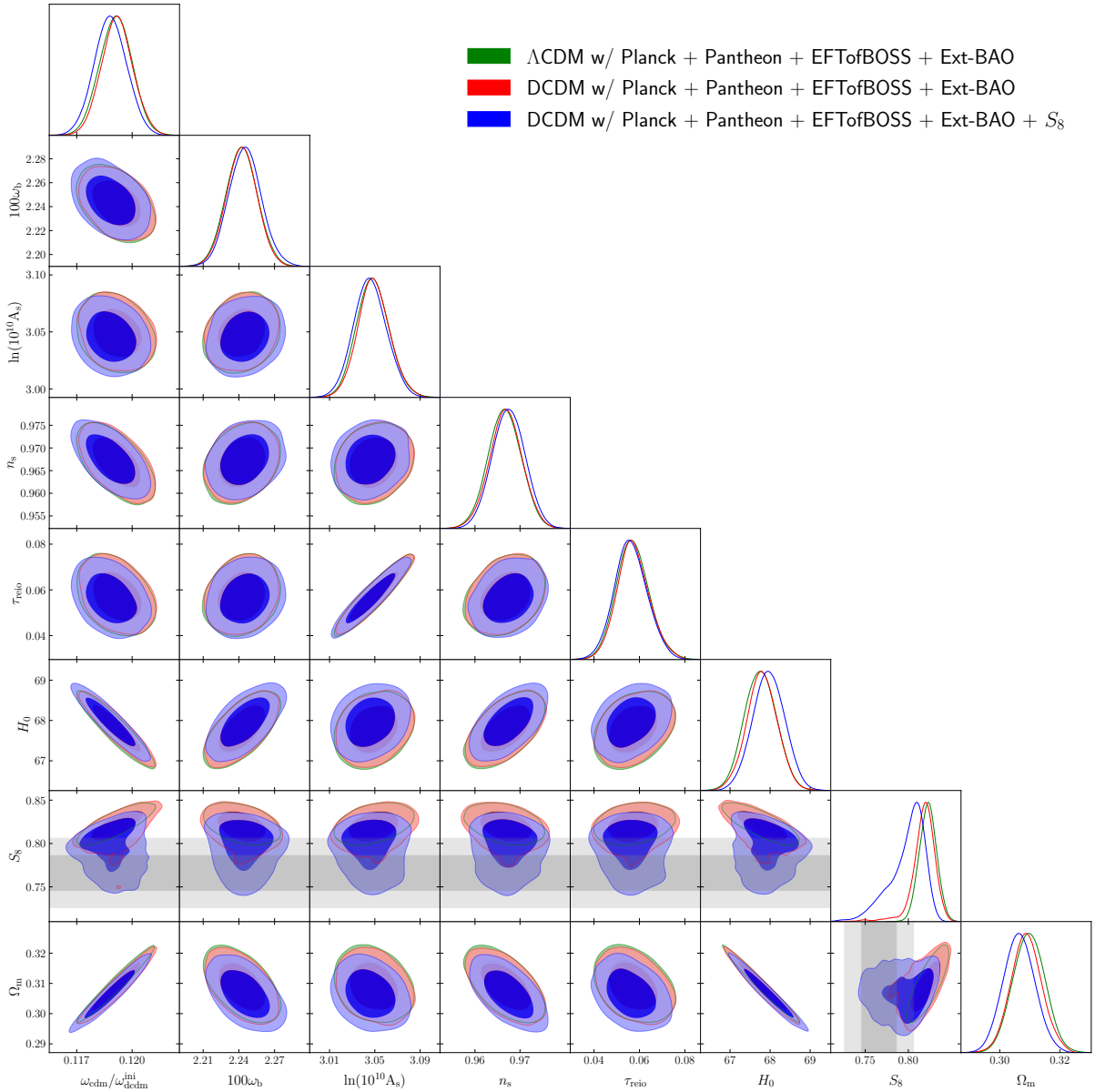

Figure F.7: 2D posterior distributions of the DCDM → WDM+DR model with and without the S_8 prior from KiDS-1000. We also plot the 2D posterior distribution for the ΛCDM model without this S_8 prior. We took into account the EFTofBOSS data for these three MCMC analyses. The gray shaded bands refer to the joint S_8 measurement from KiDS-1000 + BOSS + 2dFLens.

G

Résumé en français

Cette thèse se focalise sur deux axes de recherche à la fois différents et complémentaires. Dans le premier axe, nous nous concentrons sur la théorie effective des champs des structures à grandes échelles (EFTofLSS), et en particulier (i) sur l'étude de ses contraintes lorsqu'elle est appliquée aux données de BOSS et de eBOSS et (ii) sur l'étude de son auto-consistance à travers les conséquences sur les résultats cosmologiques des hypothèses préalables des smulations Monte-Carlo par chaînes de Markov (MCMC). Dans le second axe, nous nous sommes intéressés à l'application de cette théorie (toujours avec les données de BOSS et parfois de eBOSS) à des extensions non triviales du modèle ΛCDM, particulièrement pertinentes pour la résolution des tensions cosmologiques. Ces deux axes de recherche sont distincts dans la mesure où ils abordent des questions différentes : *comment obtenir les contraintes les plus robustes et optimisées possibles à partir des données provenant des structures à grandes échelles?* pour le premier, et *quelle est l'influence des données provenant des structures à grandes échelles sur les contraintes des modèles au-delà de ΛCDM?* pour le second. De plus, ces deux axes sont complémentaires dans la mesure où ils s'inscrivent dans un cadre commun, à savoir l'EFTofLSS. La première partie de cette thèse est fondamentale pour la deuxième partie en ce qu'elle établit le cadre théorique et d'analyse – et en particulier ses avantages et ses limites – qui est utilisé dans la deuxième partie. La deuxième partie, à son tour, est une extension de l'analyse effectuée dans la première partie, et donne une idée de la très large gamme d'applications qui peut être couverte par l'EFTofLSS. Dans ce qui suit, nous résumons les principaux résultats de chacun des chapitres de cette thèse.

Dans les chapitres 1, 2 et 3 nous avons respectivement présenté le paradigme de la cosmologie moderne dans le cadre de l'univers homogène et isotrope, de l'univers linéairement perturbé (avec la physique du fond diffus cosmologique) et de l'univers perturbé de façon non linéaire (avec la physique des structures à grandes échelles). En particulier, ce dernier chapitre expose les fondements conceptuels et théoriques sur lesquels reposent cette thèse.

Dans le chapitre 4, nous avons effectué la première analyse EFTofLSS de la forme complète des données de eBOSS QSO. Nous avons combiné cette analyse avec d'autres données provenant des structures à grandes échelles afin d'obtenir des contraintes indépendantes de *Planck*. Comme nos résultats sont en bon accord avec les données de *Planck*, nous avons combiné les sondes provenant des structures à grandes échelles et celles provenant du fond

diffus cosmologique (FDS) afin de briser les dégénérescences présentes dans le FDS. De plus, l'analyse EFTofLSS des quasars de eBOSS fournit des mesures indépendantes des paramètres ΛCDM dans un intervalle de redshift différent ($z \sim 1.5$) par rapport aux analyses EFTofLSS précédentes, et à partir d'un autre traceur. Il est intéressant de noter que nous trouvons un très bon accord entre l'analyse EFTofLSS des données QSO de eBOSS (c'est-à-dire provenant des quasars), l'analyse EFTofLSS des données LRG de BOSS (c'est-à-dire provenant des galaxies), et les données de *Planck* (c'est-à-dire provenant du FDS). Cette cohérence est une vérification non triviale du modèle ΛCDM et des nombreuses hypothèses associées, car nous avons considéré des données très différentes à la fois en termes de redshift et en termes d'objets sondés. Par ailleurs, nous avons mis en évidence que les données de eBOSS aident à améliorer les contraintes sur les modèles cosmologiques construits à partir d'une extension triviale du modèle ΛCDM pour lesquels la dynamique tardive de l'univers homogène s'écarte du modèle ΛCDM. En combinant notre analyse des structures à grandes échelles avec les données du FDS de *Planck*, nous avons obtenu des contraintes très fortes sur les extensions canoniques du modèle ΛCDM, par exemple sur la somme des masses des neutrinos. Enfin, nous avons montré (i) l'importance d'aller au-delà de l'analyse BAO/$f\sigma_8$ conventionnelle grâce à l'EFTofLSS afin de contraindre les extensions simples du modèle ΛCDM avec les données provenant des structures à grandes échelles uniquement, et (ii) que les données provenant des structures à grandes échelles analysées avec une analyse EFTofLSS sont compatibles avec le modèle ΛCDM plat, que nous considérons ou non l'analyse combinée avec les données de *Planck*.

Dans le chapitre 5, nous avons examiné deux analyses de forme complète de BOSS avec l'EFTofLSS, à savoir les analyses dites "côte ouest" (WC) et "côte est" (EC), qui sont implémentés dans les codes `PyBird` et `CLASSPT`, respectivement. Ces analyses conduisent à des différences dans les paramètres cosmologiques reconstruits allant jusqu'à 1σ. Etant donné qu'elles proviennent toutes des mêmes données de BOSS, il s'agit d'un écart surprenant et insatisfaisant. Afin d'explorer l'origine de ces différences, nous avons effectué une série d'analyses des données de la forme complète, en variant un par un (par ordre d'importance) les hypothèses préalables des MCMC, les mesures BOSS utilisées (que ce soit celles de la forme complète de BOSS ou des paramètres BAO post-reconstruits), l'échelle minimale considérée dans l'analyse et le nombre de multipôles inclus. Il est important de noter que les contraintes cosmologiques sont sensibles au choix des hypothèses préalables des MCMC sur l'espace des paramètres de l'EFTofLSS, et que les deux différents choix sur les hypothèses préalables utilisées dans les analyses `PyBird` et `CLASS-PT` sont à l'origine de la plupart des variations dans les résultats. D'autre part, les différentes mesures de la forme complète de BOSS conduisent à une différence maximale de $0,6\sigma$ parmi tous les paramètres cosmologiques, tandis que les différentes mesures des BAO post-reconstruites peuvent affecter les contraintes jusqu'à $0,9\sigma$. Par ailleurs, lorsque les choix des données et des hypothèses préalables sont les mêmes, nous montrons que les deux analyses (WC et EC) s'accordent à moins de $0,2\sigma$, ce qui constitue une validation importante des deux codes publiques disponibles. Notre analyse montre donc que la différence est principalement due aux effets des hypothèses préalables émanant de l'analyse bayésienne, et non à la théorie, aux données ou à l'implémentation des codes.

Dans le chapitre 6, nous complétons les résultats de l'analyse bayésienne standard, telle qu'elle est réalisée dans les chapitres 4 et 5, par une analyse fréquentiste. L'analyse *profile likelihood* est une méthode fréquentiste basée uniquement sur l'estimation du maximum de vraisemblance et, par conséquent, est à la fois intrinsèquement invariante par rapport

à la reparamétrisation et à la fois indépendante des hypothèses préalables. Notre objectif est de comprendre l'influence des hypothèses préalables des paramètres de l'EFTofLSS sur les paramètres cosmologiques déduits et comment cela changera avec des données plus contraignantes. Nous avons constaté que les paramétrisations WC et EC appliquées aux données de BOSS produisent le même intervalle de confiance pour σ_8, confirmant que les deux paramétrisations sont mathématiquement équivalentes. Cependant, nous avons constaté que l'analyse fréquentiste donne des contraintes sur σ_8 qui sont à un facteur > 2 plus larges que les contraintes basées sur les postérieurs MCMC. Nos résultats montrent clairement les avantages et les inconvénients de l'inférence fréquentiste et bayésienne. Étant donné que l'inférence fréquentiste n'inclut pas d'hypothèses préalables qui confinent les paramètres de l'EFTofLSS dans le régime prévu par la théorie, nous observons que les données préfèrent des valeurs extrêmes de certains de ces paramètres, ce qui pourrait violer le caractère perturbatif de l'EFTofLSS. L'absence d'hypothèses préalables conduit en outre à des intervalles de confiance beaucoup plus larges. Cette perte de pouvoir contraignant découle naturellement du fait que l'approche fréquentiste est totalement agnostique quant aux valeurs des paramètres du modèle jugés les plus probables *a priori*. D'autre part, les hypothèses préalables dans l'inférence bayésienne sont informatives et ont un impact sur les paramètres cosmologiques déduits. Ceci est important car il n'est pas simple de définir des hypothèses préalables bien motivées pour les paramètres de l'EFTofLSS, ce qui se reflète dans le fait que les paramétrisations WC et EC utilisent des configurations différentes pour ces hypothèses préalables. Pour aller de l'avant, nous avons exploré l'impact qu'auront les données des futures expériences comme DESI ou EUCLID en considérant les données de BOSS avec une matrice de covariance rééchelonnée par un facteur 16 (dans le sens où nous divisons tous les éléments de cette dernière par ce facteur). Nous constatons que les contraintes des approches bayésienne et fréquentiste convergent vers le même intervalle pour σ_8 lorsque la vraisemblance domine les informations préalables, ce qui suggère que les problèmes évoqués ci-dessus s'atténueront avec davantage de données.

Dans le chapitre 7, nous avons réévalué les contraintes sur l'énergie sombre précoce (EDE) à partir de la forme complète des mesures les plus récentes du spectre de puissance (ou fonctions de corrélation) de BOSS à la lumière de la correction de la normalisation des fonctions de fenêtre de BOSS. Il a été avancé que l'analyse de la forme complète du spectre de puissance des galaxies de BOSS défavorise le modèle EDE en tant que résolution efficace de la tension de Hubble, et nous avons montré que ce n'est plus le cas avec les nouvelles données de BOSS. Pour ce faire, nous avons effectué une étude approfondie des contraintes sur l'EDE à la lumière des données de BOSS correctement normalisées et nous avons estimé les variations introduites sur les paramètres cosmologiques reconstruits et leurs erreurs entre les différentes stratégies d'analyse de l'EFTofLSS. Indépendamment des données BOSS ou de l'analyse de l'EFTofLSS que nous considérons, la forme complète de BOSS (analysée seule avec les données de la nucléosynthèse primordiale) conduit à des valeurs reconstruites de H_0 qui sont compatibles avec ce qui est obtenu par la collaboration SH0ES. Par ailleurs, nous avons considéré la combinaison de l'analyse de la forme complète des données de BOSS avec les données de *Planck*TTTEEE + Lens + BAO + Pan18 + EFTBOSS qui conduit à $f_{\rm EDE}(z_c) < 0.083$, ce qui représente une amélioration de $\sim 10\%$ par rapport aux contraintes sans les données de BOSS et une amélioration de $\sim 5\%$ par rapport aux contraintes avec les données BAO/$f\sigma_8$ conventionnelles. Cependant, cette amélioration est beaucoup plus faible que les contraintes rapportées avec la normalisation incorrecte, à savoir $f_{\rm EDE} < 0.054$. Nous déterminons que la tension de Hubble est réduite à 2.1σ dans le cadre de la cosmologie EDE

(1.9σ sans l'analyse EFTofLSS de BOSS), comparé à 4.8σ dans le modèle ΛCDM. Ensuite, nous avons étudié l'influence des données de BOSS sur les récents indices de la détection du modèle EDE avec les données de ACT DR4. La combinaison de *Planck*TT650TEEE + Lens + BAO + Pan18 + ACT + EFTBOSS conduit à une contrainte plutôt faible sur $f_{\rm EDE}(z_c) < 0.172$ avec $\Delta\chi^2({\rm EDE}-\Lambda{\rm CDM}) = -11.1$, à comparer avec $f_{\rm EDE}(z_c) = 0.128^{+0.064}_{-0.039}$ et $\Delta\chi^2({\rm EDE}-\Lambda{\rm CDM}) = -14.6$ sans les données EFTBOSS + Lens. Enfin, nous avons conclu que l'analyse de l'EFTofLSS des données de BOSS n'exclut pas le modèle EDE comme une résolution de la tension de Hubble, où nous trouvons systématiquement $f_{\rm EDE}(z_c) \sim 10-12\%$ à $z_c \sim 3500-4000$, avec $h \sim 0.72$, lorsque la calibration des céphéides est incluse dans les analyses. Cependant, l'analyse EFTofLSS des données de BOSS contraint les cosmologies EDE les plus extrêmes, comme le montre l'analyse des données ACT DR4.

Dans le chapitre 8, nous avons mis à jour les contraintes du modèle acoustique de l'énergie sombre précoce, simplement appelé "ADE", en évaluant d'abord les conséquences de l'analyse EFTofLSS appliquée aux données de BOSS et de eBOSS, et ensuite les conséquences des dernières données de Pantheon+. Nous avons démontré que l'analyse EFTofLSS réduit légèrement la capacité de ce modèle à résoudre la tension de Hubble par rapport à l'analyse BAO/$f\sigma_8$, où nous obtenons une tension résiduelle de $2,6\sigma$. Il est important de noter que lorsque nous remplaçons les données de Pantheon par les données de Pantheon+, le modèle ADE ne résout plus la tension de Hubble à un niveau convenable, ce qui conduit à une tension résiduelle de $3,6\sigma$ (contre $2,5\sigma$ pour le modèle EDE et $6,3\sigma$ pour le modèle ΛCDM). Alors qu'avec l'analyse EFTofLSS nous n'avions qu'une légère préférence pour le modèle EDE par rapport au modèle ADE, avec les nouvelles données de Pantheon+ et de SH0ES, la préférence pour ce modèle devient clairement évidente, en raison du fait que le modèle EDE de type axion parvient à compenser un $\Omega_{\rm cdm}h^2$ plus élevé dans les données de *Planck* grâce à la dépendance d'échelle de la vitesse du son. Plus généralement, dans ce travail, nous avons montré que les nouvelles données de Pantheon+ et de SH0ES, et dans une moindre mesure l'EFTofLSS appliqué aux données de BOSS et de eBOSS, peuvent avoir des conséquences décisives sur les modèles qui visent à résoudre la tension de Hubble.

Dans le chapitre 9, nous avons confronté deux modèles de matière noire froide qui se désintègre (DCDM) à l'analyse de la forme complète des données de BOSS, combinée avec les données de *Planck* TTTEEE et le spectre de puissance des lentilles gravitationelles, les données de la BAO de BOSS et eBOSS (incluant les données provenant de la Ly-α), et les données de la distance de luminosité non calibrée des SN1a provenant du catalogue Pantheon18. Nous nous sommes d'abord concentrés sur un modèle où une fraction de la matière noire se désintègre en rayonnement sombre, le modèle DCDM $\to$ DR, et ensuite sur un modèle où toute la matière noire se désintègre en particules massives chaudes et en particules radiatives sombres, le modèle DCDM $\to$ WDM+DR. Ce dernier modèle a récemment été suggéré comme une solution possible à la tension de S_8. Pour le modèle DCDM $\to$ DR, nous avons dérivé la limite la plus à jour sur la fraction de matière noire qui se désintégre $f_{\rm dcdm}$, à savoir $f_{\rm dcdm} < 0.0216$ si nous nous limitons au régime où la DCDM possède une durée de vie inférieure à l'âge de l'Univers. Nous avons également mis à jour les contraintes sur la durée de vie de la matière noire pour le cas où $f_{\rm dcdm} \to 1$, à savoir $\tau/f_{\rm dcdm} > 249.6$ Gyr. Cependant, nous avons constaté que l'EFTofLSS ne fournit pas de contraintes significativement meilleures pour les paramètres cosmologiques du modèle DCDM $\to$ DR, par rapport à l'utilisation des données standard BAO/$f\sigma_8$. En accord avec les études antérieures, nous avons trouvé que ce

modèle n'aide ni pour la tension de S_8 ni pour la tension de H_0, et que l'inclusion de l'analyse EFTofLSS des données BOSS ne modifie pas cette conclusion. Pour le modèle DCDM $\rightarrow$ WDM+DR, nous avons montré que ce modèle peut expliquer la faible valeur de S_8 mesurée par l'expérience KiDS-1000, tout en préservant la qualité de l'ajustement des autres donnés, y compris de l'analyse EFTofLSS des données BOSS. La tension résiduelle est de $1,5\sigma$ contre $2,4\sigma$ dans le cadre du modèle ΛCDM. En outre, nous avons démontré que l'analyse de la forme complète des données de BOSS améliore de manière significative les contraintes sur la durée de vie de DCDM pour le modèle DCDM $\rightarrow$ WDM+DR, et lorsqu'elle est combinée avec les données S_8 de KiDS-1000, nous obtenons désormais $\log_{10}(\tau/\mathrm{Gyr}) = 2.21^{+1.5}_{-0.6}$ contre $\log_{10}(\tau/\mathrm{Gyr}) = 1.92^{+1.9}_{-0.61}$ avec les mesures de BAO/$f\sigma_8$.

Cette thèse illustre l'importance cruciale des données provenant des structures à grandes échelles pour obtenir des informations cosmologiques dans des régimes inexplorés, tout en démontrant le pouvoir prédictif de la théorie effective des champs des structures à grandes échelles ainsi que les avantages que cette théorie peut apporter en termes de connaissances cosmologiques. Au cours des prochaines années, les nouvelles données provenant des structures à grandes échelles issues des projets internationaux DESI, EUCLID et VRO fourniront de nouvelles données très précises pour étudier la nature de la matière noire, de l'énergie noire et de l'inflation, et permettront de tester les modèles suggérés pour résoudre les tensions cosmologiques. Il sera donc nécessaire de poursuivre les efforts théoriques pour prédire avec précision le spectre de puissance non linéaire des galaxies (mais aussi le bispectre des galaxies), et ainsi utiliser la richesse des données à venir.

Bibliography

[1] G. F. R. Ellis. "Issues in the philosophy of cosmology". *Philosophy of physics*. Ed. by J. Butterfield and J. Earman. 2006, pp. 1183–1285. DOI: 10.1016/B978-044451560-5/50014-2. arXiv: astro-ph/0602280 [p. 6].

[2] J. Ehlers, P. Geren, and R. K. Sachs. "Isotropic solutions of the Einstein-Liouville equations." *Journal of Mathematical Physics* 9 (Jan. 1968), pp. 1344–1349. DOI: 10.1063/1.1664720 [p. 7].

[3] W. R. Stoeger, R. Maartens, and G. F. R. Ellis. "Proving Almost-Homogeneity of the Universe: an Almost Ehlers-Geren-Sachs Theorem". *Astrophysical Journal* 443 (Apr. 1995), p. 1. DOI: 10.1086/175496 [p. 7].

[4] J. Wainwright, A. A. Coley, G. F. R. Ellis, and M. Hancock. "On the isotropy of the Universe: do Bianchi ? cosmologies isotropize?" *Classical and Quantum Gravity* 15.2 (Feb. 1998), pp. 331–350. DOI: 10.1088/0264-9381/15/2/008 [p. 7].

[5] M. Kamionkowski and A. Loeb. "Getting around cosmic variance". *Phys. Rev. D* 56 (1997), pp. 4511–4513. DOI: 10.1103/PhysRevD.56.4511. arXiv: astro-ph/9703118 [p. 7].

[6] J. Goodman. "Geocentrism reexamined". *Phys. Rev. D* 52 (1995), pp. 1821–1827. DOI: 10.1103/PhysRevD.52.1821. arXiv: astro-ph/9506068 [p. 7].

[7] G. F. R. Ellis and J. E. Baldwin. "On the expected anisotropy of radio source counts". *Mon. Not. Roy. Astron. Soc.* 206 (Jan. 1984), pp. 377–381. DOI: 10.1093/mnras/206.2.377 [p. 7].

[8] N. J. Secrest, S. von Hausegger, M. Rameez, R. Mohayaee, S. Sarkar, and J. Colin. "A Test of the Cosmological Principle with Quasars". *Astrophys. J. Lett.* 908.2 (2021), p. L51. DOI: 10.3847/2041-8213/abdd40. arXiv: 2009.14826 [astro-ph.CO] [p. 7].

[9] S. Dodelson. *Modern Cosmology*. Amsterdam: Academic Press, 2003. ISBN: 978-0-12-219141-1 [pp. 10, 11, 18, 19, 22, 25, 32, 33, 40, 47, 51, 52, 55, 58–60, 64, 68, 69, 72–74, 76, 79–81, 88, 91–93, 95, 97, 98].

[10] D. J. Fixsen, E. S. Cheng, J. M. Gales, J. C. Mather, R. A. Shafer, and E. L. Wright. "The Cosmic Microwave Background Spectrum from the Full COBE FIRAS Data Set". *Astrophysical Journal* 473 (Dec. 1996), p. 576. DOI: 10.1086/178173. arXiv: astro-ph/9605054 [astro-ph] [p. 11].

[11] N. Aghanim et al. "Planck 2018 results. VI. Cosmological parameters". *Astron. Astrophys.* 641 (2020), A6. DOI: 10.1051/0004-6361/201833910. arXiv: 1807.06209 [astro-ph.CO] [pp. 12–14, 51, 53, 60, 63, 86, 89–91, 121, 125, 126, 144–148, 160, 162, 164, 174, 182, 199–202, 210, 211, 234, 256, 257, 265, 275, 306].

[12] R. J. Cooke, M. Pettini, and C. C. Steidel. "One Percent Determination of the Primordial Deuterium Abundance". *Astrophys. J.* 855.2 (2018), p. 102. DOI: 10.3847/1538-4357/aaab53. arXiv: 1710.11129 [astro-ph.CO] [pp. 12, 153, 182, 210].

[13] Y. Fukuda et al. "Evidence for oscillation of atmospheric neutrinos". *Phys. Rev. Lett.* 81 (1998), pp. 1562–1567. DOI: 10.1103/PhysRevLett.81.1562. arXiv: hep-ex/9807003 [p. 13].

[14] M. Aker et al. "Direct neutrino-mass measurement with sub-electronvolt sensitivity". *Nature Phys.* 18.2 (2022), pp. 160–166. DOI: 10.1038/s41567-021-01463-1. arXiv: 2105.08533 [hep-ex] [p. 13].

[15] I. Esteban, M. C. Gonzalez-Garcia, A. Hernandez-Cabezudo, M. Maltoni, and T. Schwetz. "Global analysis of three-flavour neutrino oscillations: synergies and tensions in the determination of θ_{23}, δ_{CP}, and the mass ordering". *JHEP* 01 (2019), p. 106. DOI: 10.1007/JHEP01(2019)106. arXiv: 1811.05487 [hep-ph] [pp. 13, 146].

[16] F. Zwicky. “Die Rotverschiebung von extragalaktischen Nebeln”. *Helvetica Physica Acta* 6 (Jan. 1933), pp. 110–127 [p. 13].

[17] V. C. Rubin, J. Ford W. K., and N. Thonnard. “Rotational properties of 21 SC galaxies with a large range of luminosities and radii, from NGC 4605 (R=4kpc) to UGC 2885 (R=122kpc).” *Astrophysical Journal* 238 (June 1980), pp. 471–487. DOI: 10.1086/158003 [p. 13].

[18] A. G. Riess et al. “Observational evidence from supernovae for an accelerating universe and a cosmological constant”. *Astron. J.* 116 (1998), pp. 1009–1038. DOI: 10.1086/300499. arXiv: astro-ph/9805201 [p. 14].

[19] S. Perlmutter et al. “Measurements of Ω and Λ from 42 high redshift supernovae”. *Astrophys. J.* 517 (1999), pp. 565–586. DOI: 10.1086/307221. arXiv: astro-ph/9812133 [p. 14].

[20] A. H. Guth. “The Inflationary Universe: A Possible Solution to the Horizon and Flatness Problems”. *Phys. Rev. D* 23 (1981). Ed. by L.-Z. Fang and R. Ruffini, pp. 347–356. DOI: 10.1103/PhysRevD.23.347 [p. 14].

[21] D. Baumann. *Cosmology*. Cambridge University Press, July 2022. ISBN: 978-1-108-93709-2, 978-1-108-83807-8. DOI: 10.1017/9781108937092 [pp. 24, 47, 50, 51].

[22] G. Franco Abellán. “Searching for new physics with CMB precision cosmology”. PhD thesis. Laboratoire Univers et Particules de Montpellier, France, Montpellier U., 2022 [pp. 27, 57].

[23] R. H. Cyburt, B. D. Fields, K. A. Olive, and T.-H. Yeh. “Big Bang Nucleosynthesis: 2015”. *Rev. Mod. Phys.* 88 (2016), p. 015004. DOI: 10.1103/RevModPhys.88.015004. arXiv: 1505.01076 [astro-ph.CO] [p. 27].

[24] K. Umetsu. “Cluster–galaxy weak lensing”. *Astron. Astrophys. Rev.* 28.1 (2020), p. 7. DOI: 10.1007/s00159-020-00129-w. arXiv: 2007.00506 [astro-ph.CO] [p. 27].

[25] R. Mandelbaum. “Weak lensing for precision cosmology”. *Ann. Rev. Astron. Astrophys.* 56 (2018), pp. 393–433. DOI: 10.1146/annurev-astro-081817-051928. arXiv: 1710.03235 [astro-ph.CO] [p. 27].

[26] G. Arcadi, M. Dutra, P. Ghosh, M. Lindner, Y. Mambrini, M. Pierre, S. Profumo, and F. S. Queiroz. “The waning of the WIMP? A review of models, searches, and constraints”. *Eur. Phys. J. C* 78.3 (2018), p. 203. DOI: 10.1140/epjc/s10052-018-5662-y. arXiv: 1703.07364 [hep-ph] [p. 28].

[27] B. Carr and F. Kuhnel. “Primordial black holes as dark matter candidates”. *SciPost Phys. Lect. Notes* 48 (2022), p. 1. DOI: 10.21468/SciPostPhysLectNotes.48. arXiv: 2110.02821 [astro-ph.CO] [p. 28].

[28] S. Weinberg. “A New Light Boson?” *Phys. Rev. Lett.* 40 (1978), pp. 223–226. DOI: 10.1103/PhysRevLett.40.223 [p. 28].

[29] F. Wilczek. “Problem of Strong *P* and *T* Invariance in the Presence of Instantons”. *Phys. Rev. Lett.* 40 (1978), pp. 279–282. DOI: 10.1103/PhysRevLett.40.279 [p. 28].

[30] R. D. Peccei and H. R. Quinn. “CP Conservation in the Presence of Instantons”. *Phys. Rev. Lett.* 38 (1977), pp. 1440–1443. DOI: 10.1103/PhysRevLett.38.1440 [p. 28].

[31] F. Chadha-Day, J. Ellis, and D. J. E. Marsh. “Axion dark matter: What is it and why now?” *Sci. Adv.* 8.8 (2022), abj3618. DOI: 10.1126/sciadv.abj3618. arXiv: 2105.01406 [hep-ph] [p. 28].

[32] D. J. E. Marsh. “Axion Cosmology”. *Phys. Rept.* 643 (2016), pp. 1–79. DOI: 10.1016/j.physrep.2016.06.005. arXiv: 1510.07633 [astro-ph.CO] [p. 28].

[33] A. Boyarsky, M. Drewes, T. Lasserre, S. Mertens, and O. Ruchayskiy. “Sterile neutrino Dark Matter”. *Prog. Part. Nucl. Phys.* 104 (2019), pp. 1–45. DOI: 10.1016/j.ppnp.2018.07.004. arXiv: 1807.07938 [hep-ph] [p. 28].

[34] B. Ratra and P. J. E. Peebles. “Cosmological consequences of a rolling homogeneous scalar field”. *Phys. Rev. D* 37.12 (June 1988), pp. 3406–3427. DOI: 10.1103/PhysRevD.37.3406 [p. 29].

[35] G. W. Horndeski. “Second-order scalar-tensor field equations in a four-dimensional space”. *Int. J. Theor. Phys.* 10 (1974), pp. 363–384. DOI: 10.1007/BF01807638 [p. 29].

[36] G. Efstathiou and S. Gratton. "A Detailed Description of the CamSpec Likelihood Pipeline and a Reanalysis of the Planck High Frequency Maps" (Oct. 2019). DOI: 10.21105/astro.1910.00483. arXiv: 1910.00483 [astro-ph.CO] [p. 30].

[37] S. Q. Hou, J. J. He, A. Parikh, D. Kahl, C. A. Bertulani, T. Kajino, G. J. Mathews, and G. Zhao. "Non-extensive Statistics to the Cosmological Lithium Problem". *Astrophys. J.* 834.2 (2017), p. 165. DOI: 10.3847/1538-4357/834/2/165. arXiv: 1701.04149 [astro-ph.CO] [p. 30].

[38] J. S. Bullock and M. Boylan-Kolchin. "Small-Scale Challenges to the ΛCDM Paradigm". *Ann. Rev. Astron. Astrophys.* 55 (2017), pp. 343–387. DOI: 10.1146/annurev-astro-091916-055313. arXiv: 1707.04256 [astro-ph.CO] [p. 30].

[39] C. Dalang and C. Bonvin. "On the kinematic cosmic dipole tension". *Mon. Not. Roy. Astron. Soc.* 512.3 (2022), pp. 3895–3905. DOI: 10.1093/mnras/stac726. arXiv: 2111.03616 [astro-ph.CO] [p. 30].

[40] E. Abdalla et al. "Cosmology intertwined: A review of the particle physics, astrophysics, and cosmology associated with the cosmological tensions and anomalies". *JHEAp* 34 (2022), pp. 49–211. DOI: 10.1016/j.jheap.2022.04.002. arXiv: 2203.06142 [astro-ph.CO] [pp. 30, 152, 200, 244].

[41] C.-P. Ma and E. Bertschinger. "Cosmological perturbation theory in the synchronous and conformal Newtonian gauges". *Astrophys. J.* 455 (1995), pp. 7–25. DOI: 10.1086/176550. arXiv: astro-ph/9506072 [pp. 33, 34, 37, 44, 209, 232, 247, 248].

[42] V. Poulin. "Gravitational and electromagnetic signatures of massive relics in Cosmology". PhD thesis. U. Grenoble Alpes, 2017 [p. 46].

[43] D. Blas, J. Lesgourgues, and T. Tram. "The Cosmic Linear Anisotropy Solving System (CLASS). Part II: Approximation schemes". *Journal of Cosmology and Astroparticle Physics* 2011.07 (July 2011), pp. 034–034. DOI: 10.1088/1475-7516/2011/07/034 [pp. 46, 113, 126].

[44] A. Lewis, A. Challinor, and A. Lasenby. "Efficient computation of CMB anisotropies in closed FRW models". *Astrophys. J.* 538 (2000), pp. 473–476. DOI: 10.1086/309179. arXiv: astro-ph/9911177 [astro-ph] [pp. 46, 100, 113].

[45] A. Lewis and A. Challinor. "Weak gravitational lensing of the CMB". *Phys. Rept.* 429 (2006), pp. 1–65. DOI: 10.1016/j.physrep.2006.03.002. arXiv: astro-ph/0601594 [p. 65].

[46] T. Matsubara. "Resumming Cosmological Perturbations via the Lagrangian Picture: One-loop Results in Real Space and in Redshift Space". *Phys. Rev. D* 77 (2008), p. 063530. DOI: 10.1103/PhysRevD.77.063530. arXiv: 0711.2521 [astro-ph] [p. 82].

[47] T. Matsubara. "Nonlinear perturbation theory with halo bias and redshift-space distortions via the Lagrangian picture". *Phys. Rev. D* 78 (2008). [Erratum: Phys.Rev.D 78, 109901 (2008)], p. 083519. DOI: 10.1103/PhysRevD.78.109901. arXiv: 0807.1733 [astro-ph] [p. 82].

[48] L. Senatore and M. Zaldarriaga. "Redshift Space Distortions in the Effective Field Theory of Large Scale Structures" (2014). arXiv: 1409.1225 [astro-ph.CO] [pp. 82, 109–111, 113, 116, 121, 155].

[49] Z. Vlah and M. White. "Exploring redshift-space distortions in large-scale structure". *JCAP* 03 (2019), p. 007. DOI: 10.1088/1475-7516/2019/03/007. arXiv: 1812.02775 [astro-ph.CO] [p. 82].

[50] N. Kaiser. "Clustering in real space and in redshift space". *Mon. Not. Roy. Astron. Soc.* 227 (1987), pp. 1–27 [pp. 84, 121].

[51] F. Beutler et al. "The clustering of galaxies in the completed SDSS-III Baryon Oscillation Spectroscopic Survey: baryon acoustic oscillations in the Fourier space". *Mon. Not. Roy. Astron. Soc.* 464.3 (2017), pp. 3409–3430. DOI: 10.1093/mnras/stw2373. arXiv: 1607.03149 [astro-ph.CO] [pp. 88, 165, 166, 172].

[52] M. H. Goroff, B. Grinstein, S. J. Rey, and M. B. Wise. "Coupling of Modes of Cosmological Mass Density Fluctuations". *Astrophys. J.* 311 (1986), pp. 6–14. DOI: 10.1086/164749 [p. 96].

[53] F. Bernardeau, S. Colombi, E. Gaztanaga, and R. Scoccimarro. "Large scale structure of the universe and cosmological perturbation theory". *Phys. Rept.* 367 (2002), pp. 1–248. DOI: 10.1016/S0370-1573(02)00135-7. arXiv: astro-ph/0112551 [astro-ph] [pp. 96, 114].

[54] J. J. M. Carrasco, M. P. Hertzberg, and L. Senatore. "The Effective Field Theory of Cosmological Large Scale Structures". *JHEP* 09 (2012), p. 082. DOI: 10.1007/JHEP09(2012)082. arXiv: 1206.2926 [astro-ph.CO] [pp. 100, 103–105, 108, 121, 127, 155].

[55] D. Baumann, A. Nicolis, L. Senatore, and M. Zaldarriaga. "Cosmological Non-Linearities as an Effective Fluid". *JCAP* 1207 (2012), p. 051. DOI: 10.1088/1475-7516/2012/07/051. arXiv: 1004.2488 [astro-ph.CO] [pp. 101, 104, 121, 127].

[56] M. M. Ivanov. "Effective Field Theory for Large-Scale Structure". 2023. DOI: 10.1007/978-981-19-3079-9_5-1. arXiv: 2212.08488 [astro-ph.CO] [pp. 106–109].

[57] T. Baldauf, L. Mercolli, M. Mirbabayi, and E. Pajer. "The Bispectrum in the Effective Field Theory of Large Scale Structure". *JCAP* 1505.05 (2015), p. 007. DOI: 10.1088/1475-7516/2015/05/007. arXiv: 1406.4135 [astro-ph.CO] [pp. 106, 107].

[58] G. D'Amico, J. Gleyzes, N. Kokron, D. Markovic, L. Senatore, P. Zhang, F. Beutler, and H. Gil-Marín. "The Cosmological Analysis of the SDSS/BOSS data from the Effective Field Theory of Large-Scale Structure". *JCAP* 05 (2020), p. 005. DOI: 10.1088/1475-7516/2020/05/005. arXiv: 1909.05271 [astro-ph.CO] [pp. 111, 116, 122, 125, 126, 128, 131, 155, 166, 183, 185, 190, 210, 225, 230, 289, 291, 292].

[59] G. D'Amico, L. Senatore, and P. Zhang. "Limits on *w*CDM from the EFTofLSS with the PyBird code". *JCAP* 01 (2021), p. 006. DOI: 10.1088/1475-7516/2021/01/006. arXiv: 2003.07956 [astro-ph.CO] [pp. 111, 116, 125–127, 145, 147, 152, 157, 158, 165, 166, 180–182, 185, 194, 202, 211, 212, 225, 233, 249, 257, 265].

[60] M. Mirbabayi, F. Schmidt, and M. Zaldarriaga. "Biased Tracers and Time Evolution". *JCAP* 1507.07 (2015), p. 030. DOI: 10.1088/1475-7516/2015/07/030. arXiv: 1412.5169 [astro-ph.CO] [pp. 111, 112, 121, 156, 183, 265].

[61] A. Chudaykin, M. M. Ivanov, O. H. E. Philcox, and M. Simonović. "Nonlinear perturbation theory extension of the Boltzmann code CLASS". *Phys. Rev. D* 102.6 (2020), p. 063533. DOI: 10.1103/PhysRevD.102.063533. arXiv: 2004.10607 [astro-ph.CO] [pp. 111, 150, 152, 157, 182, 183, 194, 212].

[62] O. H. E. Philcox and M. M. Ivanov. "BOSS DR12 full-shape cosmology: ΛCDM constraints from the large-scale galaxy power spectrum and bispectrum monopole". *Phys. Rev. D* 105.4 (2022), p. 043517. DOI: 10.1103/PhysRevD.105.043517. arXiv: 2112.04515 [astro-ph.CO] [pp. 111, 122, 152, 156, 165, 173, 175, 182, 212, 223, 225, 226, 282].

[63] T. Fujita and Z. Vlah. "Perturbative description of biased tracers using consistency relations of LSS". *JCAP* 10 (2020), p. 059. DOI: 10.1088/1475-7516/2020/10/059. arXiv: 2003.10114 [astro-ph.CO] [pp. 112, 156, 183].

[64] A. Perko, L. Senatore, E. Jennings, and R. H. Wechsler. "Biased Tracers in Redshift Space in the EFT of Large-Scale Structure" (2016). arXiv: 1610.09321 [astro-ph.CO] [pp. 112–114, 121, 122, 155, 265].

[65] L. Senatore. "Bias in the Effective Field Theory of Large Scale Structures". *JCAP* 1511.11 (2015), p. 007. DOI: 10.1088/1475-7516/2015/11/007. arXiv: 1406.7843 [astro-ph.CO] [pp. 113, 114, 121, 127, 155, 265].

[66] R. Angulo, M. Fasiello, L. Senatore, and Z. Vlah. "On the Statistics of Biased Tracers in the Effective Field Theory of Large Scale Structures". *JCAP* 1509 (2015), p. 029. DOI: 10.1088/1475-7516/2015/09/029,10.1088/1475-7516/2015/9/029. arXiv: 1503.08826 [astro-ph.CO] [pp. 114, 121, 155, 265].

[67] T. Fujita, V. Mauerhofer, L. Senatore, Z. Vlah, and R. Angulo. "Very Massive Tracers and Higher Derivative Biases". *JCAP* 01 (2020), p. 009. DOI: 10.1088/1475-7516/2020/01/009. arXiv: 1609.00717 [astro-ph.CO] [pp. 114, 121, 155, 265].

[68] M. Simonovic, T. Baldauf, M. Zaldarriaga, J. J. Carrasco, and J. A. Kollmeier. "Cosmological perturbation theory using the FFTLog: formalism and connection to QFT loop integrals". *JCAP* 1804.04 (2018), p. 030. DOI: 10.1088/1475-7516/2018/04/030. arXiv: 1708.08130 [astro-ph.CO] [p. 115].

[69] P. Zhang, G. D'Amico, L. Senatore, C. Zhao, and Y. Cai. "BOSS Correlation Function analysis from the Effective Field Theory of Large-Scale Structure". *JCAP* 02.02 (2022), p. 036. DOI: 10.1088/1475-7516/2022/02/036. arXiv: 2110.07539 [astro-ph.CO] [pp. 116, 122, 125, 128, 131, 152, 165, 166, 168, 181, 211, 216, 225, 233, 257, 266, 282].

[70] M. Lewandowski and L. Senatore. "An analytic implementation of the IR-resummation for the BAO peak". *JCAP* 03 (2020), p. 018. DOI: 10.1088/1475-7516/2020/03/018. arXiv: 1810.11855 [astro-ph.CO] [pp. 116, 121, 157, 212].

[71] L. Senatore and M. Zaldarriaga. "The IR-resummed Effective Field Theory of Large Scale Structures". *JCAP* 1502.02 (2015), p. 013. DOI: 10.1088/1475-7516/2015/02/013. arXiv: 1404.5954 [astro-ph.CO] [pp. 116, 121, 157, 174, 212].

[72] M. Lewandowski, L. Senatore, F. Prada, C. Zhao, and C.-H. Chuang. "EFT of large scale structures in redshift space". *Phys. Rev.* D97.6 (2018), p. 063526. DOI: 10.1103/PhysRevD.97.063526. arXiv: 1512.06831 [astro-ph.CO] [pp. 116, 128, 157, 212].

[73] C. Alcock and B. Paczynski. "An evolution free test for non-zero cosmological constant". *Nature* 281 (1979), pp. 358–359. DOI: 10.1038/281358a0 [pp. 116, 121].

[74] F. Beutler, E. Castorina, and P. Zhang. "Interpreting measurements of the anisotropic galaxy power spectrum". *JCAP* 03 (2019), p. 040. DOI: 10.1088/1475-7516/2019/03/040. arXiv: 1810.05051 [astro-ph.CO] [pp. 116, 131, 132, 289, 290].

[75] P. Zhang and Y. Cai. "BOSS full-shape analysis from the EFTofLSS with exact time dependence". *JCAP* 01.01 (2022), p. 031. DOI: 10.1088/1475-7516/2022/01/031. arXiv: 2111.05739 [astro-ph.CO] [pp. 117, 289, 290, 292].

[76] S. Aiola et al. "The Atacama Cosmology Telescope: DR4 Maps and Cosmological Parameters". *JCAP* 12 (2020), p. 047. DOI: 10.1088/1475-7516/2020/12/047. arXiv: 2007.07288 [astro-ph.CO] [pp. 121, 201, 202].

[77] K. Aylor et al. "A Comparison of Cosmological Parameters Determined from CMB Temperature Power Spectra from the South Pole Telescope and the Planck Satellite". *Astrophys. J.* 850.1 (2017), p. 101. DOI: 10.3847/1538-4357/aa947b. arXiv: 1706.10286 [astro-ph.CO] [p. 121].

[78] F. Bianchini et al. "Constraints on Cosmological Parameters from the 500 deg^2 SPTpol Lensing Power Spectrum". *Astrophys. J.* 888 (2020), p. 119. DOI: 10.3847/1538-4357/ab6082. arXiv: 1910.07157 [astro-ph.CO] [p. 121].

[79] T. M. C. Abbott et al. "Dark Energy Survey Year 3 results: Cosmological constraints from galaxy clustering and weak lensing". *Phys. Rev. D* 105.2 (2022), p. 023520. DOI: 10.1103/PhysRevD.105.023520. arXiv: 2105.13549 [astro-ph.CO] [pp. 121, 152, 174, 201, 227, 244, 265].

[80] M. Asgari et al. "KiDS-1000 Cosmology: Cosmic shear constraints and comparison between two point statistics". *Astron. Astrophys.* 645 (2021), A104. DOI: 10.1051/0004-6361/202039070. arXiv: 2007.15633 [astro-ph.CO] [pp. 121, 140, 201, 256, 257, 265, 266].

[81] S. Alam et al. "The clustering of galaxies in the completed SDSS-III Baryon Oscillation Spectroscopic Survey: cosmological analysis of the DR12 galaxy sample". *Mon. Not. Roy. Astron. Soc.* 470.3 (2017), pp. 2617–2652. DOI: 10.1093/mnras/stx721. arXiv: 1607.03155 [astro-ph.CO] [pp. 121, 125, 126, 165, 181, 211, 230, 233, 257].

[82] S. Alam et al. "Completed SDSS-IV extended Baryon Oscillation Spectroscopic Survey: Cosmological implications from two decades of spectroscopic surveys at the Apache Point Observatory". *Phys. Rev. D* 103.8 (2021), p. 083533. DOI: 10.1103/PhysRevD.103.083533. arXiv: 2007.08991 [astro-ph.CO] [pp. 121, 124, 137, 175, 181, 230, 233].

[83] A. Kehagias and A. Riotto. "Symmetries and Consistency Relations in the Large Scale Structure of the Universe". *Nucl. Phys. B* 873 (2013), pp. 514–529. DOI: 10.1016/j.nuclphysb.2013.05.009. arXiv: 1302.0130 [astro-ph.CO] [p. 121].

[84] M. Peloso and M. Pietroni. "Galilean invariance and the consistency relation for the nonlinear squeezed bispectrum of large scale structure". *JCAP* 05 (2013), p. 031. DOI: 10.1088/1475-7516/2013/05/031. arXiv: 1302.0223 [astro-ph.CO] [p. 121].

[85] P. Creminelli, J. Noreña, M. Simonović, and F. Vernizzi. "Single-Field Consistency Relations of Large Scale Structure". *JCAP* 12 (2013), p. 025. DOI: 10.1088/1475-7516/2013/12/025. arXiv: 1309.3557 [astro-ph.CO] [p. 121].

[86] R. A. Porto, L. Senatore, and M. Zaldarriaga. "The Lagrangian-space Effective Field Theory of Large Scale Structures". *JCAP* 1405 (2014), p. 022. DOI: 10.1088/1475-7516/2014/05/022. arXiv: 1311.2168 [astro-ph.CO] [p. 121].

[87] E. Pajer and M. Zaldarriaga. "On the Renormalization of the Effective Field Theory of Large Scale Structures". *JCAP* 1308 (2013), p. 037. DOI: 10.1088/1475-7516/2013/08/037. arXiv: 1301.7182 [astro-ph.CO] [p. 121].

[88] A. A. Abolhasani, M. Mirbabayi, and E. Pajer. "Systematic Renormalization of the Effective Theory of Large Scale Structure". *JCAP* 1605.05 (2016), p. 063. DOI: 10.1088/1475-7516/2016/05/063. arXiv: 1509.07886 [hep-th] [p. 121].

[89] T. Baldauf, M. Mirbabayi, M. Simonovic, and M. Zaldarriaga. "Equivalence Principle and the Baryon Acoustic Peak". *Phys. Rev.* D92.4 (2015), p. 043514. DOI: 10.1103/PhysRevD.92.043514. arXiv: 1504.04366 [astro-ph.CO] [p. 121].

[90] L. Senatore and G. Trevisan. "On the IR-Resummation in the EFTofLSS". *JCAP* 1805.05 (2018), p. 019. DOI: 10.1088/1475-7516/2018/05/019. arXiv: 1710.02178 [astro-ph.CO] [pp. 121, 157].

[91] D. Blas, M. Garny, M. M. Ivanov, and S. Sibiryakov. "Time-Sliced Perturbation Theory II: Baryon Acoustic Oscillations and Infrared Resummation". *JCAP* 1607.07 (2016), p. 028. DOI: 10.1088/1475-7516/2016/07/028. arXiv: 1605.02149 [astro-ph.CO] [pp. 121, 157, 212].

[92] J. J. M. Carrasco, S. Foreman, D. Green, and L. Senatore. "The 2-loop matter power spectrum and the IR-safe integrand". *JCAP* 1407 (2014), p. 056. DOI: 10.1088/1475-7516/2014/07/056. arXiv: 1304.4946 [astro-ph.CO] [p. 121].

[93] J. J. M. Carrasco, S. Foreman, D. Green, and L. Senatore. "The Effective Field Theory of Large Scale Structures at Two Loops". *JCAP* 1407 (2014), p. 057. DOI: 10.1088/1475-7516/2014/07/057. arXiv: 1310.0464 [astro-ph.CO] [p. 121].

[94] E. O. Nadler, A. Perko, and L. Senatore. "On the Bispectra of Very Massive Tracers in the Effective Field Theory of Large-Scale Structure". *JCAP* 1802.02 (2018), p. 058. DOI: 10.1088/1475-7516/2018/02/058. arXiv: 1710.10308 [astro-ph.CO] [pp. 121, 265].

[95] G. D'Amico, Y. Donath, M. Lewandowski, L. Senatore, and P. Zhang. "The BOSS bispectrum analysis at one loop from the Effective Field Theory of Large-Scale Structure" (June 2022). arXiv: 2206.08327 [astro-ph.CO] [pp. 121, 122, 158, 162, 171, 173–175, 227].

[96] V. Desjacques, D. Jeong, and F. Schmidt. "The Galaxy Power Spectrum and Bispectrum in Redshift Space". *JCAP* 12 (2018), p. 035. DOI: 10.1088/1475-7516/2018/12/035. arXiv: 1806.04015 [astro-ph.CO] [p. 122].

[97] M. M. Ivanov, M. Simonović, and M. Zaldarriaga. "Cosmological Parameters from the BOSS Galaxy Power Spectrum". *JCAP* 05 (2020), p. 042. DOI: 10.1088/1475-7516/2020/05/042. arXiv: 1909.05277 [astro-ph.CO] [pp. 122, 225, 275, 291].

[98] T. Nishimichi, G. D'Amico, M. M. Ivanov, L. Senatore, M. Simonović, M. Takada, M. Zaldarriaga, and P. Zhang. "Blinded challenge for precision cosmology with large-scale structure: results from effective field theory for the redshift-space galaxy power spectrum". *Phys. Rev. D* 102.12 (2020), p. 123541. DOI: 10.1103/PhysRevD.102.123541. arXiv: 2003.08277 [astro-ph.CO] [pp. 122, 155, 162, 166, 182].

[99] J. N. Grieb et al. "The clustering of galaxies in the completed SDSS-III Baryon Oscillation Spectroscopic Survey: Cosmological implications of the Fourier space wedges of the final sample". *Mon. Not. Roy. Astron. Soc.* 467.2 (2017), pp. 2085–2112. DOI: 10.1093/mnras/stw3384. arXiv: 1607.03143 [astro-ph.CO] [p. 122].

[100] A. G. Sanchez et al. "The clustering of galaxies in the completed SDSS-III Baryon Oscillation Spectroscopic Survey: cosmological implications of the configuration-space clustering wedges". *Mon. Not. Roy. Astron. Soc.* 464.2 (2017), pp. 1640–1658. DOI: 10.1093/mnras/stw2443. arXiv: 1607.03147 [astro-ph.CO] [p. 122].

[101] T. Colas, G. D'amico, L. Senatore, P. Zhang, and F. Beutler. "Efficient Cosmological Analysis of the SDSS/BOSS data from the Effective Field Theory of Large-Scale Structure". *JCAP* 06 (2020), p. 001. DOI: 10.1088/1475-7516/2020/06/001. arXiv: 1909.07951 [astro-ph.CO] [pp. 122, 127, 166, 202, 210, 211, 225, 291, 292].

[102] O. H. E. Philcox, M. M. Ivanov, M. Simonović, and M. Zaldarriaga. "Combining Full-Shape and BAO Analyses of Galaxy Power Spectra: A 1.6\% CMB-independent constraint on H_0". *JCAP* 05 (2020), p. 032. DOI: 10.1088/1475-7516/2020/05/032. arXiv: 2002.04035 [astro-ph.CO] [pp. 122, 165, 172].

[103] S.-F. Chen, Z. Vlah, and M. White. "A new analysis of the BOSS survey, including full-shape information and post-reconstruction BAO" (Oct. 2021). arXiv: 2110.05530 [astro-ph.CO] [pp. 122, 171, 174, 178, 182, 188, 225, 275, 282].

[104] S.-F. Chen, M. White, J. DeRose, and N. Kokron. "Cosmological analysis of three-dimensional BOSS galaxy clustering and Planck CMB lensing cross correlations via Lagrangian perturbation theory". *JCAP* 07.07 (2022), p. 041. DOI: 10.1088/1475-7516/2022/07/041. arXiv: 2204.10392 [astro-ph.CO] [p. 122].

[105] T. Simon, P. Zhang, V. Poulin, and T. L. Smith. "Consistency of effective field theory analyses of the BOSS power spectrum". *Phys. Rev. D* 107.12 (2023), p. 123530. DOI: 10.1103/PhysRevD.107.123530. arXiv: 2208.05929 [astro-ph.CO] [pp. 122, 140, 194].

[106] O. H. E. Philcox, M. M. Ivanov, G. Cabass, M. Simonović, M. Zaldarriaga, and T. Nishimichi. "Cosmology with the redshift-space galaxy bispectrum monopole at one-loop order". *Phys. Rev. D* 106.4 (2022), p. 043530. DOI: 10.1103/PhysRevD.106.043530. arXiv: 2206.02800 [astro-ph.CO] [p. 122].

[107] G. Cabass, M. M. Ivanov, O. H. E. Philcox, M. Simonović, and M. Zaldarriaga. "Constraints on Single-Field Inflation from the BOSS Galaxy Survey". *Phys. Rev. Lett.* 129.2 (2022), p. 021301. DOI: 10.1103/PhysRevLett.129.021301. arXiv: 2201.07238 [astro-ph.CO] [p. 122].

[108] G. D'Amico, M. Lewandowski, L. Senatore, and P. Zhang. "Limits on primordial non-Gaussianities from BOSS galaxy-clustering data" (Jan. 2022). arXiv: 2201.11518 [astro-ph.CO] [pp. 122, 227].

[109] G. Cabass, M. M. Ivanov, O. H. E. Philcox, M. Simonović, and M. Zaldarriaga. "Constraints on multifield inflation from the BOSS galaxy survey". *Phys. Rev. D* 106.4 (2022), p. 043506. DOI: 10.1103/PhysRevD.106.043506. arXiv: 2204.01781 [astro-ph.CO] [p. 122].

[110] T. Tröster et al. "Cosmology from large-scale structure: Constraining ΛCDM with BOSS". *Astron. Astrophys.* 633 (2020), p. L10. DOI: 10.1051/0004-6361/201936772. arXiv: 1909.11006 [astro-ph.CO] [p. 122].

[111] Y. Kobayashi, T. Nishimichi, M. Takada, and H. Miyatake. "Full-shape cosmology analysis of the SDSS-III BOSS galaxy power spectrum using an emulator-based halo model: A 5% determination of $\sigma 8$". *Phys. Rev. D* 105.8 (2022), p. 083517. DOI: 10.1103/PhysRevD.105.083517. arXiv: 2110.06969 [astro-ph.CO] [p. 122].

[112] A. Semenaite et al. "Cosmological implications of the full shape of anisotropic clustering measurements in BOSS and eBOSS". *Mon. Not. Roy. Astron. Soc.* 512.4 (2022), pp. 5657–5670. DOI: 10.1093/mnras/stac829. arXiv: 2111.03156 [astro-ph.CO] [pp. 122, 137, 185].

[113] R. Neveux et al. "Combined full shape analysis of BOSS galaxies and eBOSS quasars using an iterative emulator". *Mon. Not. Roy. Astron. Soc.* 516.2 (2022), pp. 1910–1922. DOI: 10.1093/mnras/stac2114. arXiv: 2201.04679 [astro-ph.CO] [pp. 122, 137, 139].

[114] S. Brieden, H. Gil-Marín, and L. Verde. "Model-agnostic interpretation of 10 billion years of cosmic evolution traced by BOSS and eBOSS data". *JCAP* 08.08 (2022), p. 024. DOI: 10.1088/1475-7516/2022/08/024. arXiv: 2204.11868 [astro-ph.CO] [pp. 122, 137, 139, 140, 144, 145, 147, 148, 275, 282].

[115] A. Semenaite, A. G. Sánchez, A. Pezzotta, J. Hou, A. Eggemeier, M. Crocce, C. Zhao, J. R. Brownstein, G. Rossi, and D. P. Schneider. "Beyond ΛCDM constraints from the full shape clustering measurements from BOSS and eBOSS" (Oct. 2022). arXiv: 2210.07304 [astro-ph.CO] [pp. 122, 185].

[116] A. Amon et al. "Consistent lensing and clustering in a low-S_8 Universe with BOSS, DES Year 3, HSC Year 1 and KiDS-1000" (Feb. 2022). arXiv: 2202.07440 [astro-ph.CO] [pp. 122, 152, 201, 202, 227].

[117] T. Simon, P. Zhang, and V. Poulin. "Cosmological inference from the EFTofLSS: the eBOSS QSO full-shape analysis". *JCAP* 07 (2023), p. 041. DOI: 10.1088/1475-7516/2023/07/041. arXiv: 2210.14931 [astro-ph.CO] [pp. 122, 230].

[118] E. B. Holm, L. Herold, T. Simon, E. G. M. Ferreira, S. Hannestad, V. Poulin, and T. Tram. "Bayesian and frequentist investigation of prior effects in EFT of LSS analyses of full-shape BOSS and eBOSS data". *Phys. Rev. D* 108.12 (2023), p. 123514. DOI: 10.1103/PhysRevD.108.123514. arXiv: 2309.04468 [astro-ph.CO] [p. 122].

[119] M. M. Ivanov. "Cosmological constraints from the power spectrum of eBOSS emission line galaxies". *Phys. Rev. D* 104.10 (2021), p. 103514. DOI: 10.1103/PhysRevD.104.103514. arXiv: 2106.12580 [astro-ph.CO] [pp. 124, 150].

[120] A. J. Ross et al. "The Completed SDSS-IV extended Baryon Oscillation Spectroscopic Survey: Large-scale structure catalogues for cosmological analysis". *Mon. Not. Roy. Astron. Soc.* 498.2 (2020), pp. 2354–2371. DOI: 10.1093/mnras/staa2416. arXiv: 2007.09000 [astro-ph.CO] [pp. 124, 181, 233].

[121] C.-H. Chuang, F.-S. Kitaura, F. Prada, C. Zhao, and G. Yepes. "EZmocks: extending the Zel'dovich approximation to generate mock galaxy catalogues with accurate clustering statistics". *Mon. Not. Roy. Astron. Soc.* 446 (2015), pp. 2621–2628. DOI: 10.1093/mnras/stu2301. arXiv: 1409.1124 [astro-ph.CO] [pp. 124, 181, 233].

[122] F. Beutler and P. McDonald. "Unified galaxy power spectrum measurements from 6dFGS, BOSS, and eBOSS". *JCAP* 11 (2021), p. 031. DOI: 10.1088/1475-7516/2021/11/031. arXiv: 2106.06324 [astro-ph.CO] [pp. 125, 165, 166, 168, 182, 233, 289].

[123] J. Hou et al. "The Completed SDSS-IV extended Baryon Oscillation Spectroscopic Survey: BAO and RSD measurements from anisotropic clustering analysis of the Quasar Sample in configuration space between redshift 0.8 and 2.2". *Mon. Not. Roy. Astron. Soc.* 500.1 (2020), pp. 1201–1221. DOI: 10.1093/mnras/staa3234. arXiv: 2007.08998 [astro-ph.CO] [pp. 125, 233].

[124] B. Reid et al. "SDSS-III Baryon Oscillation Spectroscopic Survey Data Release 12: galaxy target selection and large scale structure catalogues". *Mon. Not. Roy. Astron. Soc.* 455.2 (2016), pp. 1553–1573. DOI: 10.1093/mnras/stv2382. arXiv: 1509.06529 [astro-ph.CO] [pp. 125, 165, 181, 211, 233, 257].

[125] F.-S. Kitaura et al. "The clustering of galaxies in the SDSS-III Baryon Oscillation Spectroscopic Survey: mock galaxy catalogues for the BOSS Final Data Release". *Mon. Not. Roy. Astron. Soc.* 456.4 (2016), pp. 4156–4173. DOI: 10.1093/mnras/stv2826. arXiv: 1509.06400 [astro-ph.CO] [pp. 125, 165, 181, 211, 233, 257].

[126] H. Gil-Marín et al. "The clustering of galaxies in the SDSS-III Baryon Oscillation Spectroscopic Survey: BAO measurement from the LOS-dependent power spectrum of DR12 BOSS galaxies". *Mon. Not. Roy. Astron. Soc.* 460.4 (2016), pp. 4210–4219. DOI: 10.1093/mnras/stw1264. arXiv: 1509.06373 [astro-ph.CO] [pp. 125, 165, 166, 181, 211, 233, 257].

[127] F. Beutler, C. Blake, M. Colless, D. H. Jones, L. Staveley-Smith, L. Campbell, Q. Parker, W. Saunders, and F. Watson. "The 6dF Galaxy Survey: Baryon Acoustic Oscillations and the Local Hubble Constant". *Mon. Not. Roy. Astron. Soc.* 416 (2011), pp. 3017–3032. DOI: 10.1111/j.1365-2966.2011.19250.x. arXiv: 1106.3366 [astro-ph.CO] [pp. 125, 211, 233, 256].

[128] A. J. Ross, L. Samushia, C. Howlett, W. J. Percival, A. Burden, and M. Manera. "The clustering of the SDSS DR7 main Galaxy sample – I. A 4 per cent distance measure at $z = 0.15$". *Mon. Not. Roy. Astron. Soc.* 449.1 (2015), pp. 835–847. DOI: 10.1093/mnras/stv154. arXiv: 1409.3242 [astro-ph.CO] [pp. 125, 211, 233, 256].

[129] A. Cuceu, A. Font-Ribera, S. Nadathur, B. Joachimi, and P. Martini. "New constraints on the expansion rate at redshift 2.3 from the Lyman-α forest" (Sept. 2022). arXiv: 2209.13942 [astro-ph.CO] [p. 125].

[130] V. de Sainte Agathe et al. "Baryon acoustic oscillations at z = 2.34 from the correlations of Lyα absorption in eBOSS DR14". *Astron. Astrophys.* 629 (2019), A85. DOI: 10.1051/0004-6361/201935638. arXiv: 1904.03400 [astro-ph.CO] [pp. 125, 256, 259].

[131] M. Blomqvist et al. "Baryon acoustic oscillations from the cross-correlation of Lyα absorption and quasars in eBOSS DR14". *Astron. Astrophys.* 629 (2019), A86. DOI: 10.1051/0004-6361/201935641. arXiv: 1904.03430 [astro-ph.CO] [pp. 125, 256, 259].

[132] D. Brout et al. "The Pantheon+ Analysis: Cosmological Constraints" (Feb. 2022). arXiv: 2202.04077 [astro-ph.CO] [pp. 125, 207, 211, 222, 230, 233, 238, 243].

[133] D. M. Scolnic et al. "The Complete Light-curve Sample of Spectroscopically Confirmed SNe Ia from Pan-STARRS1 and Cosmological Constraints from the Combined Pantheon Sample". *Astrophys. J.* 859.2 (2018), p. 101. DOI: 10.3847/1538-4357/aab9bb. arXiv: 1710.00845 [astro-ph.CO] [pp. 125, 211, 233, 243, 256, 266, 307].

[134] V. Mossa et al. "The baryon density of the Universe from an improved rate of deuterium burning". *Nature* 587.7833 (2020), pp. 210–213. DOI: 10.1038/s41586-020-2878-4 [pp. 126, 275].

[135] B. W. Lyke et al. "The Sloan Digital Sky Survey Quasar Catalog: Sixteenth Data Release". *Astrophys. J. Suppl.* 250.1 (2020), p. 8. DOI: 10.3847/1538-4365/aba623. arXiv: 2007.09001 [astro-ph.GA] [p. 126].

[136] T. Brinckmann and J. Lesgourgues. "MontePython 3: boosted MCMC sampler and other features" (2018). arXiv: 1804.07261 [astro-ph.CO] [pp. 126, 153, 180, 210, 233, 256].

[137] B. Audren, J. Lesgourgues, K. Benabed, and S. Prunet. "Conservative Constraints on Early Cosmology: an illustration of the Monte Python cosmological parameter inference code". *JCAP* 1302 (2013), p. 001. DOI: 10.1088/1475-7516/2013/02/001. arXiv: 1210.7183 [astro-ph.CO] [pp. 126, 180, 210, 233, 256].

[138] P. A. R. Ade et al. "Planck intermediate results. XVI. Profile likelihoods for cosmological parameters". *Astron. Astrophys.* 566 (2014), A54. DOI: 10.1051/0004-6361/201323003. arXiv: 1311.1657 [astro-ph.CO] [pp. 127, 140, 146, 165, 180, 191, 194].

[139] G. D'Amico, L. Senatore, P. Zhang, and T. Nishimichi. "Taming redshift-space distortion effects in the EFTofLSS and its application to data" (Sept. 2021). arXiv: 2110.00016 [astro-ph.CO] [pp. 128, 129, 155, 162, 183, 187, 285].

[140] S. Alam, N. P. Ross, S. Eftekharzadeh, J. A. Peacock, J. Comparat, A. D. Myers, and A. J. Ross. "Quasars at intermediate redshift are not special; but they are often satellites". 504.1 (June 2021), pp. 857–870. DOI: 10.1093/mnras/stab898. arXiv: 2007.02612 [astro-ph.GA] [pp. 128, 149].

[141] M. M. Ivanov, O. H. E. Philcox, M. Simonović, M. Zaldarriaga, T. Nischimichi, and M. Takada. "Cosmological constraints without nonlinear redshift-space distortions". *Phys. Rev. D* 105.4 (2022), p. 043531. DOI: 10.1103/PhysRevD.105.043531. arXiv: 2110.00006 [astro-ph.CO] [p. 129].

[142] E. Castorina and M. White. "Beyond the plane-parallel approximation for redshift surveys". *Mon. Not. Roy. Astron. Soc.* 476.4 (2018), pp. 4403–4417. DOI: 10.1093/mnras/sty410. arXiv: 1709.09730 [astro-ph.CO] [p. 131].

[143] E. Castorina and E. di Dio. "The observed galaxy power spectrum in General Relativity". *JCAP* 01.01 (2022), p. 061. DOI: 10.1088/1475-7516/2022/01/061. arXiv: 2106.08857 [astro-ph.CO] [p. 131].

[144] M. Noorikuhani and R. Scoccimarro. "Wide-angle and Relativistic effects in Fourier-Space Clustering statistics" (July 2022). arXiv: 2207.12383 [astro-ph.CO] [p. 131].

[145] K. Zwetsloot and N. E. Chisari. "Impact of intrinsic alignments on clustering constraints of the growth rate". *Mon. Not. Roy. Astron. Soc.* 516.1 (2022), pp. 787–793. DOI: 10.1093/mnras/stac2283. arXiv: 2208.07062 [astro-ph.CO] [p. 131].

[146] C. M. Hirata. "Tidal alignments as a contaminant of redshift space distortions". *Mon. Not. Roy. Astron. Soc.* 399 (2009), p. 1074. DOI: 10.1111/j.1365-2966.2009.15353.x. arXiv: 0903.4929 [astro-ph.CO] [p. 131].

[147] N. Agarwal, V. Desjacques, D. Jeong, and F. Schmidt. "Information content in the redshift-space galaxy power spectrum and bispectrum". *JCAP* 03 (2021), p. 021. DOI: 10.1088/1475-7516/2021/03/021. arXiv: 2007.04340 [astro-ph.CO] [p. 131].

[148] C. Hahn, R. Scoccimarro, M. R. Blanton, J. L. Tinker, and S. A. Rodríguez-Torres. "The effect of fibre collisions on the galaxy power spectrum multipoles". *Mon. Not. Roy. Astron. Soc.* 467.2 (2017), pp. 1940–1956. DOI: 10.1093/mnras/stx185. arXiv: 1609.01714 [astro-ph.CO] [p. 131].

[149] K. S. Dawson et al. "The SDSS-IV extended Baryon Oscillation Spectroscopic Survey: Overview and Early Data". *Astron. J.* 151 (2016), p. 44. DOI: 10.3847/0004-6256/151/2/44. arXiv: 1508.04473 [astro-ph.CO] [p. 131].

[150] F. Beutler and E. Di Dio. "Modeling relativistic contributions to the halo power spectrum dipole". *JCAP* 07.07 (2020), p. 048. DOI: 10.1088/1475-7516/2020/07/048. arXiv: 2004.08014 [astro-ph.CO] [p. 132].

[151] P. Zarrouk et al. "The clustering of the SDSS-IV extended Baryon Oscillation Spectroscopic Survey DR14 quasar sample: measurement of the growth rate of structure from the anisotropic correlation function between redshift 0.8 and 2.2". *Mon. Not. Roy. Astron. Soc.* 477.2 (2018), pp. 1639–1663. DOI: 10.1093/mnras/sty506. arXiv: 1801.03062 [astro-ph.CO] [p. 133].

[152] R. Neveux et al. "The completed SDSS-IV extended Baryon Oscillation Spectroscopic Survey: BAO and RSD measurements from the anisotropic power spectrum of the quasar sample between redshift 0.8 and 2.2". *Mon. Not. Roy. Astron. Soc.* 499.1 (2020), pp. 210–229. DOI: 10.1093/mnras/staa2780. arXiv: 2007.08999 [astro-ph.CO] [p. 134].

[153] A. G. Riess et al. "A Comprehensive Measurement of the Local Value of the Hubble Constant with 1 km/s/Mpc Uncertainty from the Hubble Space Telescope and the SH0ES Team" (Dec. 2021). arXiv: 2112.04510 [astro-ph.CO] [pp. 140, 199, 200, 223, 234, 237, 239, 242, 243, 299–301].

[154] N. Schöneberg, L. Verde, H. Gil-Marín, and S. Brieden. "BAO+BBN revisited – Growing the Hubble tension with a 0.7km/s/Mpc constraint" (Sept. 2022). arXiv: 2209.14330 [astro-ph.CO] [p. 140].

[155] O. H. E. Philcox, B. D. Sherwin, G. S. Farren, and E. J. Baxter. "Determining the Hubble Constant without the Sound Horizon: Measurements from Galaxy Surveys". *Phys. Rev. D* 103.2 (2021), p. 023538. DOI: 10.1103/PhysRevD.103.023538. arXiv: 2008.08084 [astro-ph.CO] [pp. 140, 202].

[156] G. S. Farren, O. H. E. Philcox, and B. D. Sherwin. "Determining the Hubble constant without the sound horizon: Perspectives with future galaxy surveys". *Phys. Rev. D* 105.6 (2022), p. 063503. DOI: 10.1103/PhysRevD.105.063503. arXiv: 2112.10749 [astro-ph.CO] [pp. 140, 202].

[157] O. H. E. Philcox, G. S. Farren, B. D. Sherwin, E. J. Baxter, and D. J. Brout. "Determining the Hubble constant without the sound horizon: A 3.6% constraint on H0 from galaxy surveys, CMB lensing, and supernovae". *Phys. Rev. D* 106.6 (2022), p. 063530. DOI: 10.1103/PhysRevD.106.063530. arXiv: 2204.02984 [astro-ph.CO] [pp. 140, 202, 206, 223, 226].

[158] T. L. Smith, V. Poulin, and T. Simon. "Assessing the robustness of sound horizon-free determinations of the Hubble constant". *Phys. Rev. D* 108.10 (2023), p. 103525. DOI: 10.1103/PhysRevD.108.103525. arXiv: 2208.12992 [astro-ph.CO] [pp. 140, 144, 202].

[159] J. Bel, J. Larena, R. Maartens, C. Marinoni, and L. Perenon. "Constraining spatial curvature with large-scale structure". *JCAP* 09 (2022), p. 076. DOI: 10.1088/1475-7516/2022/09/076. arXiv: 2206.03059 [astro-ph.CO] [p. 144].

[160] G. D'Amico, Y. Donath, L. Senatore, and P. Zhang. "Limits on Clustering and Smooth Quintessence from the EFTofLSS" (Dec. 2020). arXiv: 2012.07554 [astro-ph.CO] [pp. 145, 155, 202, 225].

[161] N. Palanque-Delabrouille, C. Yèche, N. Schöneberg, J. Lesgourgues, M. Walther, S. Chabanier, and E. Armengaud. "Hints, neutrino bounds and WDM constraints from SDSS DR14 Lyman-α and Planck full-survey data". *JCAP* 04 (2020), p. 038. DOI: 10.1088/1475-7516/2020/04/038. arXiv: 1911.09073 [astro-ph.CO] [pp. 147, 149].

[162] M. M. Ivanov, M. Simonović, and M. Zaldarriaga. "Cosmological Parameters and Neutrino Masses from the Final Planck and Full-Shape BOSS Data". *Phys. Rev. D* 101.8 (2020), p. 083504. DOI: 10.1103/PhysRevD.101.083504. arXiv: 1912.08208 [astro-ph.CO] [pp. 147, 202].

[163] R. Jimenez, C. Pena-Garay, K. Short, F. Simpson, and L. Verde. "Neutrino masses and mass hierarchy: evidence for the normal hierarchy". *JCAP* 09 (2022), p. 006. DOI: 10.1088/1475-7516/2022/09/006. arXiv: 2203.14247 [hep-ph] [p. 147].

[164] S. Gariazzo et al. "Neutrino mass and mass ordering: no conclusive evidence for normal ordering". *JCAP* 10 (2022), p. 010. DOI: 10.1088/1475-7516/2022/10/010. arXiv: 2205.02195 [hep-ph] [p. 147].

[165] J. J. Bennett, G. Buldgen, P. F. De Salas, M. Drewes, S. Gariazzo, S. Pastor, and Y. Y. Y. Wong. "Towards a precision calculation of $N_{\rm eff}$ in the Standard Model II: Neutrino decoupling in the presence of flavour oscillations and finite-temperature QED". *JCAP* 04 (2021), p. 073. DOI: 10.1088/1475-7516/2021/04/073. arXiv: 2012.02726 [hep-ph] [p. 147].

[166] J. Lesgourgues, G. Mangano, G. Miele, and S. Pastor. *Neutrino Cosmology*. Cambridge University Press, Feb. 2013. ISBN: 978-1-108-70501-1, 978-1-139-60341-6 [pp. 148, 249].

[167] G. Franco Abellán, R. Murgia, V. Poulin, and J. Lavalle. "Implications of the S_8 tension for decaying dark matter with warm decay products". *Phys. Rev. D* 105.6 (2022), p. 063525. DOI: 10.1103/PhysRevD.105.063525. arXiv: 2008.09615 [astro-ph.CO] [pp. 149, 202, 246, 254, 256, 262, 263].

[168] G. Franco Abellán, R. Murgia, and V. Poulin. "Linear cosmological constraints on two-body decaying dark matter scenarios and the S8 tension". *Phys. Rev. D* 104.12 (2021), p. 123533. DOI: 10.1103/PhysRevD.104.123533. arXiv: 2102.12498 [astro-ph.CO] [pp. 149, 246, 252–254, 256, 260–263].

[169] T. Simon, G. Franco Abellán, P. Du, V. Poulin, and Y. Tsai. "Constraining decaying dark matter with BOSS data and the effective field theory of large-scale structures". *Phys. Rev. D* 106.2 (2022), p. 023516. DOI: 10.1103/PhysRevD.106.023516. arXiv: 2203.07440 [astro-ph.CO] [pp. 149, 202, 203].

[170] V. Poulin, J. L. Bernal, E. Kovetz, and M. Kamionkowski. "The Sigma-8 Tension is a Drag" (Sept. 2022). arXiv: 2209.06217 [astro-ph.CO] [p. 149].

[171] Aghamousa, Amir and others. "The DESI Experiment Part I: Science,Targeting, and Survey Design" (10 2016). eprint: {1611.00036} [pp. 150, 162, 189, 264, 266].

[172] L. Amendola et al. "Cosmology and Fundamental Physics with the Euclid Satellite" (2016). arXiv: 1606.00180 [astro-ph.CO] [pp. 150, 162, 189, 264, 266].

[173] H. Gil-Marin et al. "The Completed SDSS-IV extended Baryon Oscillation Spectroscopic Survey: measurement of the BAO and growth rate of structure of the luminous red galaxy sample from the anisotropic power spectrum between redshifts 0.6 and 1.0". *Mon. Not. Roy. Astron. Soc.* 498.2 (2020), pp. 2492–2531. DOI: 10.1093/mnras/staa2455. arXiv: 2007.08994 [astro-ph.CO] [p. 150].

[174] J. E. Bautista et al. "The Completed SDSS-IV extended Baryon Oscillation Spectroscopic Survey: measurement of the BAO and growth rate of structure of the luminous red galaxy sample from the anisotropic correlation function between redshifts 0.6 and 1". *Mon. Not. Roy. Astron. Soc.* 500.1 (2020), pp. 736–762. DOI: 10.1093/mnras/staa2800. arXiv: 2007.08993 [astro-ph.CO] [p. 150].

[175] A. de Mattia et al. "The Completed SDSS-IV extended Baryon Oscillation Spectroscopic Survey: measurement of the BAO and growth rate of structure of the emission line galaxy sample from the anisotropic power spectrum between redshift 0.6 and 1.1". *Mon. Not. Roy. Astron. Soc.* 501.4 (2021), pp. 5616–5645. DOI: 10.1093/mnras/staa3891. arXiv: 2007.09008 [astro-ph.CO] [pp. 150, 289].

[176] A. Chudaykin and M. M. Ivanov. "Cosmological constraints from the power spectrum of eBOSS quasars". *Phys. Rev. D* 107.4 (2023), p. 043518. DOI: 10.1103/PhysRevD.107.043518. arXiv: 2210.17044 [astro-ph.CO] [p. 150].

[177] C. Heymans et al. "KiDS-1000 Cosmology: Multi-probe weak gravitational lensing and spectroscopic galaxy clustering constraints". *Astron. Astrophys.* 646 (2021), A140. DOI: 10.1051/0004-6361/202039063. arXiv: 2007.15632 [astro-ph.CO] [pp. 152, 174, 201, 202, 227, 244, 256, 260, 265].

[178] J. U. Lange, A. Leauthaud, S. Singh, H. Guo, R. Zhou, T. L. Smith, and F.-Y. Cyr-Racine. "On the halo-mass and radial scale dependence of the lensing is low effect". *Mon. Not. Roy. Astron. Soc.* 502.2 (2021), pp. 2074–2086. DOI: 10.1093/mnras/stab189. arXiv: 2011.02377 [astro-ph.CO] [pp. 152, 175, 201].

[179] N. Aghanim et al. "Planck 2018 results. VIII. Gravitational lensing". *Astron. Astrophys.* 641 (2020), A8. DOI: 10.1051/0004-6361/201833886. arXiv: 1807.06210 [astro-ph.CO] [pp. 153, 210, 233, 256].

[180] N. Schöneberg, J. Lesgourgues, and D. C. Hooper. "The BAO+BBN take on the Hubble tension". *JCAP* 10 (2019), p. 029. DOI: 10.1088/1475-7516/2019/10/029. arXiv: 1907.11594 [astro-ph.CO] [pp. 153, 182, 210].

[181] R. Consiglio, P. F. de Salas, G. Mangano, G. Miele, S. Pastor, and O. Pisanti. "PArthENoPE reloaded". *Comput. Phys. Commun.* 233 (2018), pp. 237–242. DOI: 10.1016/j.cpc.2018.06.022. arXiv: 1712.04378 [astro-ph.CO] [pp. 153, 182, 210].

[182] E. Aver, K. A. Olive, and E. D. Skillman. "The effects of He I λ10830 on helium abundance determinations". *JCAP* 07 (2015), p. 011. DOI: 10.1088/1475-7516/2015/07/011. arXiv: 1503.08146 [astro-ph.CO] [pp. 153, 182, 210].

[183] N. Schöneberg, G. Franco Abellán, A. Pérez Sánchez, S. J. Witte, V. Poulin, and J. Lesgourgues. "The H0 Olympics: A fair ranking of proposed models". *Phys. Rept.* 984 (2022), pp. 1–55. DOI: 10.1016/j.physrep.2022.07.001. arXiv: 2107.10291 [astro-ph.CO] [pp. 153, 181, 200, 206, 211, 212, 218, 219, 225, 234–236, 238, 239, 258].

[184] A. Lewis. "GetDist: a Python package for analysing Monte Carlo samples" (Oct. 2019). arXiv: 1910.13970 [astro-ph.IM] [pp. 153, 212, 234].

[185] M. M. Ivanov, O. H. E. Philcox, T. Nishimichi, M. Simonović, M. Takada, and M. Zaldarriaga. "Precision analysis of the redshift-space galaxy bispectrum". *Phys. Rev. D* 105.6 (2022), p. 063512. DOI: 10.1103/PhysRevD.105.063512. arXiv: 2110.10161 [astro-ph.CO] [pp. 156, 185].

[186] M. M. Ivanov and S. Sibiryakov. "Infrared Resummation for Biased Tracers in Redshift Space". *JCAP* 1807.07 (2018), p. 053. DOI: 10.1088/1475-7516/2018/07/053. arXiv: 1804.05080 [astro-ph.CO] [pp. 157, 212].

[187] P. Carrilho, C. Moretti, and A. Pourtsidou. "Cosmology with the EFTofLSS and BOSS: dark energy constraints and a note on priors" (July 2022). arXiv: 2207.14784 [astro-ph.CO] [pp. 160, 178, 185, 194, 202].

[188] L. Herold, E. G. M. Ferreira, and E. Komatsu. "New constraint on Early Dark Energy from Planck and BOSS data using the profile likelihood" (Dec. 2021). arXiv: 2112.12140 [astro-ph.CO] [pp. 165, 179, 206, 218, 219, 226].

[189] A. Reeves, L. Herold, S. Vagnozzi, B. D. Sherwin, and E. G. M. Ferreira. "Restoring cosmological concordance with early dark energy and massive neutrinos?" (July 2022). arXiv: 2207.01501 [astro-ph.CO] [pp. 165, 179, 206, 219, 226].

[190] A. Gómez-Valent. "A fast test to assess the impact of marginalization in Monte Carlo analyses, and its application to cosmology" (Mar. 2022). arXiv: 2203.16285 [astro-ph.CO] [pp. 165, 179, 206].

[191] H. Gil-Marín et al. "The clustering of galaxies in the SDSS-III Baryon Oscillation Spectroscopic Survey: RSD measurement from the LOS-dependent power spectrum of DR12 BOSS galaxies". *Mon. Not. Roy. Astron. Soc.* 460.4 (2016), pp. 4188–4209. DOI: 10.1093/mnras/stw1096. arXiv: 1509.06386 [astro-ph.CO] [pp. 165, 292].

[192] C. Zhao et al. "The completed SDSS-IV extended Baryon Oscillation Spectroscopic Survey: 1000 multi-tracer mock catalogues with redshift evolution and systematics for galaxies and quasars of the final data release". *Mon. Not. Roy. Astron. Soc.* 503.1 (2021), pp. 1149–1173. DOI: 10.1093/mnras/stab510. arXiv: 2007.08997 [astro-ph.CO] [p. 165].

[193] N. Hand, Y. Feng, F. Beutler, Y. Li, C. Modi, U. Seljak, and Z. Slepian. "nbodykit: an open-source, massively parallel toolkit for large-scale structure". *Astron. J.* 156.4 (2018), p. 160. DOI: 10.3847/1538-3881/aadae0. arXiv: 1712.05834 [astro-ph.IM] [p. 165].

[194] C. Zhao. "Fast Correlation Function Calculator – A high-performance pair counting toolkit" (Jan. 2023). arXiv: 2301.12557 [astro-ph.IM] [p. 165].

[195] O. H. E. Philcox. "Cosmology without window functions: Quadratic estimators for the galaxy power spectrum". *Phys. Rev. D* 103.10 (2021), p. 103504. DOI: 10.1103/PhysRevD.103.103504. arXiv: 2012.09389 [astro-ph.CO] [pp. 165, 166, 168, 223, 226].

[196] A. de Mattia and V. Ruhlmann-Kleider. "Integral constraints in spectroscopic surveys". *JCAP* 08 (2019), p. 036. DOI: 10.1088/1475-7516/2019/08/036. arXiv: 1904.08851 [astro-ph.CO] [pp. 166, 168, 289, 290].

[197] S.-F. Chen, Z. Vlah, and M. White. "Consistent Modeling of Velocity Statistics and Redshift-Space Distortions in One-Loop Perturbation Theory". *JCAP* 07 (2020), p. 062. DOI: 10.1088/1475-7516/2020/07/062. arXiv: 2005.00523 [astro-ph.CO] [pp. 174, 178, 182, 188].

[198] S.-F. Chen, Z. Vlah, E. Castorina, and M. White. "Redshift-Space Distortions in Lagrangian Perturbation Theory". *JCAP* 03 (2021), p. 100. DOI: 10.1088/1475-7516/2021/03/100. arXiv: 2012.04636 [astro-ph.CO] [pp. 174, 178, 182, 188].

[199] M. Maus, S.-F. Chen, and M. White. "A comparison of template vs. direct model fitting for redshift-space distortions in BOSS" (Feb. 2023). arXiv: 2302.07430 [astro-ph.CO] [pp. 174, 178, 188].

[200] A. Amon and G. Efstathiou. "A non-linear solution to the S_8 tension?" (June 2022). arXiv: 2206.11794 [astro-ph.CO] [pp. 174, 175, 202, 227].

[201] C. Heymans et al. "CFHTLenS: The Canada-France-Hawaii Telescope Lensing Survey". *Mon. Not. Roy. Astron. Soc.* 427 (2012), p. 146. DOI: 10.1111/j.1365-2966.2012.21952.x. arXiv: 1210.0032 [pp. 174, 201].

[202] T. M. C. Abbott et al. "Joint analysis of DES Year 3 data and CMB lensing from SPT and Planck III: Combined cosmological constraints" (June 2022). arXiv: 2206.10824 [astro-ph.CO] [p. 175].

[203] C. Moretti, M. Tsedrik, P. Carrilho, and A. Pourtsidou. "Modified gravity and massive neutrinos: constraints from the full shape analysis of BOSS galaxies and forecasts for Stage IV surveys" (June 2023). arXiv: 2306.09275 [astro-ph.CO] [pp. 178, 194, 202].

[204] J. Donald-McCann, R. Gsponer, R. Zhao, K. Koyama, and F. Beutler. "Analysis of Unified Galaxy Power Spectrum Multipole Measurements" (July 2023). arXiv: 2307.07475 [astro-ph.CO] [pp. 178, 188, 192, 194].

[205] R. Zhao et al. "A Multi-tracer Analysis for the eBOSS galaxy sample based on the Effective Field Theory of Large-scale Structure" (Aug. 2023). arXiv: 2308.06206 [astro-ph.CO] [p. 178].

[206] Y. Pawitan. *In All Likelihood. Statistical Modelling and Inference Using Likelihood*. Oxford University Press, 2013 [pp. 179, 180, 189].

[207] P. Campeti, O. Özsoy, I. Obata, and M. Shiraishi. "New constraints on axion-gauge field dynamics during inflation from Planck and BICEP/Keck data sets". *JCAP* 07.07 (2022), p. 039. DOI: 10.1088/1475-7516/2022/07/039. arXiv: 2203.03401 [astro-ph.CO] [p. 179].

[208] P. Campeti and E. Komatsu. "New Constraint on the Tensor-to-scalar Ratio from the Planck and BICEP/Keck Array Data Using the Profile Likelihood". *Astrophys. J.* 941.2 (2022), p. 110. DOI: 10.3847/1538-4357/ac9ea3. arXiv: 2205.05617 [astro-ph.CO] [p. 179].

[209] L. Herold and E. G. M. Ferreira. "Resolving the Hubble tension with early dark energy". *Phys. Rev. D* 108.4 (2023), p. 043513. DOI: 10.1103/PhysRevD.108.043513. arXiv: 2210.16296 [astro-ph.CO] [p. 179].

[210] E. B. Holm, L. Herold, S. Hannestad, A. Nygaard, and T. Tram. "Decaying dark matter with profile likelihoods". *Phys. Rev. D* 107.2 (2023), p. L021303. DOI: 10.1103/PhysRevD.107.L021303. arXiv: 2211.01935 [astro-ph.CO] [pp. 179, 180].

[211] J. S. Cruz, S. Hannestad, E. B. Holm, F. Niedermann, M. S. Sloth, and T. Tram. "Profiling cold new early dark energy". *Phys. Rev. D* 108.2 (2023), p. 023518. DOI: 10.1103/PhysRevD.108.023518. arXiv: 2302.07934 [astro-ph.CO] [pp. 179, 180].

[212] B. Hadzhiyska, K. Wolz, S. Azzoni, D. Alonso, C. García-García, J. Ruiz-Zapatero, and A. Slosar. "Cosmology with 6 parameters in the Stage-IV era: efficient marginalisation over nuisance parameters" (Jan. 2023). DOI: 10.21105/astro.2301.11895. arXiv: 2301.11895 [astro-ph.CO] [p. 179].

[213] J. Neyman. "Outline of a Theory of Statistical Estimation Based on the Classical Theory of Probability". *Philosophical Transactions of the Royal Society of London A* 236.767 (1937), pp. 333–380. DOI: 10.1098/rsta.1937.0005 [p. 179].

[214] S. S. Wilks. "The Large-Sample Distribution of the Likelihood Ratio for Testing Composite Hypotheses". *Annals Math. Statist.* 9.1 (1938), pp. 60–62. DOI: 10.1214/aoms/1177732360 [p. 180].

[215] N. Aghanim et al. "Planck 2018 results. V. CMB power spectra and likelihoods". *Astron. Astrophys.* 641 (2020), A5. DOI: 10.1051/0004-6361/201936386. arXiv: 1907.12875 [astro-ph.CO] [pp. 180, 233, 240].

[216] G. J. Feldman and R. D. Cousins. "A Unified approach to the classical statistical analysis of small signals". *Phys. Rev. D* 57 (1998), pp. 3873–3889. DOI: 10.1103/PhysRevD.57.3873. arXiv: physics/9711021 [p. 180].

[217] S. Kirkpatrick, C. D. Gelatt, and M. P. Vecchi. "Optimization by Simulated Annealing". *Science* 220 (1983), pp. 671–680. DOI: 10.1126/science.220.4598.671 [p. 180].

[218] A. Nygaard, E. B. Holm, S. Hannestad, and T. Tram. "Fast and effortless computation of profile likelihoods using CONNECT" (Aug. 2023). arXiv: 2308.06379 [astro-ph.CO] [p. 180].

[219] S. Henrot-Versillé, O. Perdereau, S. Plaszczynski, B. R. d'Orfeuil, M. Spinelli, and M. Tristram. "Agnostic cosmology in the CAMEL framework" (July 2016). arXiv: 1607.02964 [astro-ph.CO] [p. 180].

[220] S. Hannestad. "Stochastic optimization methods for extracting cosmological parameters from cosmic microwave background radiation power spectra". *Phys. Rev. D* 61 (2000), p. 023002. DOI: 10.1103/PhysRevD.61.023002. arXiv: astro-ph/9911330 [p. 180].

[221] D. Blas, J. Lesgourgues, and T. Tram. "The Cosmic Linear Anisotropy Solving System (CLASS) II: Approximation schemes". *JCAP* 1107 (2011), p. 034. DOI: 10.1088/1475-7516/2011/07/034. arXiv: 1104.2933 [astro-ph.CO] [pp. 180, 210, 233].

[222] M. Schmittfull, M. Simonović, M. M. Ivanov, O. H. E. Philcox, and M. Zaldarriaga. "Modeling Galaxies in Redshift Space at the Field Level". *JCAP* 05 (2021), p. 059. DOI: 10.1088/1475-7516/2021/05/059. arXiv: 2012.03334 [astro-ph.CO] [p. 183].

[223] H. Rubira and F. Schmidt. "Galaxy bias renormalization group" (July 2023). arXiv: 2307.15031 [astro-ph.CO] [p. 185].

[224] A. G. Sanchez. "Arguments against using h^{-1}Mpc units in observational cosmology". *Phys. Rev. D* 102.12 (2020), p. 123511. DOI: 10.1103/PhysRevD.102.123511. arXiv: 2002.07829 [astro-ph.CO] [p. 185].

[225] S. Brieden, H. Gil-Marín, and L. Verde. "ShapeFit: extracting the power spectrum shape information in galaxy surveys beyond BAO and RSD". *JCAP* 12.12 (2021), p. 054. DOI: 10.1088/1475-7516/2021/12/054. arXiv: 2106.07641 [astro-ph.CO] [p. 185].

[226] A. Aghamousa et al. "The DESI Experiment Part I: Science,Targeting, and Survey Design" (Oct. 2016). arXiv: 1611.00036 [astro-ph.IM] [p. 194].

[227] A. G. Riess, L. Breuval, W. Yuan, S. Casertano, L. M. ~Macri, D. Scolnic, T. Cantat-Gaudin, R. I. Anderson, and M. C. Reyes. "Cluster Cepheids with High Precision Gaia Parallaxes, Low Zeropoint Uncertainties, and Hubble Space Telescope Photometry" (Aug. 2022). arXiv: 2208.01045 [astro-ph.CO] [p. 199].

[228] L. Verde, T. Treu, and A. G. Riess. "Tensions between the Early and the Late Universe". *Nature Astronomy 2019*. 2019. DOI: 10.1038/s41550-019-0902-0. arXiv: 1907.10625 [astro-ph.CO] [p. 199].

[229] M. G. Dainotti, B. De Simone, T. Schiavone, G. Montani, E. Rinaldi, and G. Lambiase. "On the Hubble constant tension in the SNe Ia Pantheon sample". *Astrophys. J.* 912.2 (2021), p. 150. DOI: 10.3847/1538-4357/abeb73. arXiv: 2103.02117 [astro-ph.CO] [p. 200].

[230] M. G. Dainotti, B. De Simone, T. Schiavone, G. Montani, E. Rinaldi, G. Lambiase, M. Bogdan, and S. Ugale. "On the Evolution of the Hubble Constant with the SNe Ia Pantheon Sample and Baryon Acoustic Oscillations: A Feasibility Study for GRB-Cosmology in 2030". *Galaxies* 10.1 (2022), p. 24. DOI: 10.3390/galaxies10010024. arXiv: 2201.09848 [astro-ph.CO] [p. 200].

[231] E. Mortsell, A. Goobar, J. Johansson, and S. Dhawan. "Sensitivity of the Hubble Constant Determination to Cepheid Calibration" (May 2021). arXiv: 2105.11461 [astro-ph.CO] [p. 200].

[232] E. Mortsell, A. Goobar, J. Johansson, and S. Dhawan. "The Hubble Tension Revisited: Additional Local Distance Ladder Uncertainties" (June 2021). arXiv: 2106.09400 [astro-ph.CO] [p. 200].

[233] B. Follin and L. Knox. "Insensitivity of the distance ladder Hubble constant determination to Cepheid calibration modelling choices". *Mon. Not. Roy. Astron. Soc.* 477.4 (2018), pp. 4534–4542. DOI: 10.1093/mnras/sty720. arXiv: 1707.01175 [astro-ph.CO] [p. 200].

[234] M. Rigault et al. "Confirmation of a Star Formation Bias in Type Ia Supernova Distances and its Effect on Measurement of the Hubble Constant". *Astrophys. J.* 802.1 (2015), p. 20. DOI: 10.1088/0004-637X/802/1/20. arXiv: 1412.6501 [astro-ph.CO] [p. 200].

[235] M. Rigault et al. "Strong Dependence of Type Ia Supernova Standardization on the Local Specific Star Formation Rate". *Astron. Astrophys.* 644 (2020), A176. DOI: 10.1051/0004-6361/201730404. arXiv: 1806.03849 [astro-ph.CO] [p. 200].

[236] D. O. Jones et al. "Should Type Ia Supernova Distances be Corrected for their Local Environments?" *Astrophys. J.* 867.2 (2018), p. 108. DOI: 10.3847/1538-4357/aae2b9. arXiv: 1805.05911 [astro-ph.CO] [p. 200].

[237] D. Brout and D. Scolnic. "It's Dust: Solving the Mysteries of the Intrinsic Scatter and Host-galaxy Dependence of Standardized Type Ia Supernova Brightnesses". *Astrophys. J.* 909.1 (2021), p. 26. DOI: 10.3847/1538-4357/abd69b. arXiv: 2004.10206 [astro-ph.CO] [p. 200].

[238] G. E. Addison, Y. Huang, D. J. Watts, C. L. Bennett, M. Halpern, G. Hinshaw, and J. L. Weiland. "Quantifying discordance in the 2015 Planck CMB spectrum". *Astrophys. J.* 818.2 (2016), p. 132. DOI: 10.3847/0004-637X/818/2/132. arXiv: 1511.00055 [p. 200].

[239] N. Aghanim et al. "Planck intermediate results. LI. Features in the cosmic microwave background temperature power spectrum and shifts in cosmological parameters". *Astron. Astrophys.* 607 (2017), A95. DOI: 10.1051/0004-6361/201629504. arXiv: 1608.02487 [astro-ph.CO] [p. 200].

[240] E. Di Valentino, A. Melchiorri, and J. Silk. "Planck evidence for a closed Universe and a possible crisis for cosmology". *Nature Astron.* 4.2 (2019), pp. 196–203. DOI: 10.1038/s41550-019-0906-9. arXiv: 1911.02087 [astro-ph.CO] [p. 200].

[241] W. Handley. "Curvature tension: evidence for a closed universe". *Phys. Rev. D* 103.4 (2021), p. L041301. DOI: 10.1103/PhysRevD.103.L041301. arXiv: 1908.09139 [astro-ph.CO] [p. 200].

[242] B. Li and P. R. Shapiro. "Precision cosmology and the stiff-amplified gravitational-wave background from inflation: NANOGrav, Advanced LIGO-Virgo and the Hubble tension". *JCAP* 10 (2021), p. 024. DOI: 10.1088/1475-7516/2021/10/024. arXiv: 2107.12229 [astro-ph.CO] [p. 200].

[243] G. E. Addison, D. J. Watts, C. L. Bennett, M. Halpern, G. Hinshaw, and J. L. Weiland. "Elucidating ΛCDM: Impact of Baryon Acoustic Oscillation Measurements on the Hubble Constant Discrepancy". *Astrophys. J.* 853.2 (2018), p. 119. DOI: 10.3847/1538-4357/aaa1ed. arXiv: 1707.06547 [astro-ph.CO] [p. 200].

[244] W. L. Freedman et al. "The Carnegie-Chicago Hubble Program. VIII. An Independent Determination of the Hubble Constant Based on the Tip of the Red Giant Branch". *Astrophysical Journal* 882.1, 34 (July 2019), p. 34. DOI: 10.3847/1538-4357/ab2f73. arXiv: 1907.05922 [astro-ph.CO] [p. 200].

[245] W. L. Freedman. "Measurements of the Hubble Constant: Tensions in Perspective" (June 2021). arXiv: 2106.15656 [astro-ph.CO] [p. 200].

[246] G. S. Anand, R. B. Tully, L. Rizzi, A. G. Riess, and W. Yuan. "Comparing Tip of the Red Giant Branch Distance Scales: An Independent Reduction of the Carnegie-Chicago Hubble Program and the Value of the Hubble Constant". *Astrophys. J.* 932.1 (2022), p. 15. DOI: 10.3847/1538-4357/ac68df. arXiv: 2108.00007 [astro-ph.CO] [p. 200].

[247] W. Yuan, A. G. Riess, L. M. Macri, S. Casertano, and D. Scolnic. "Consistent Calibration of the Tip of the Red Giant Branch in the Large Magellanic Cloud on the Hubble Space Telescope Photometric System and Implications for the Determination of the Hubble Constant" (2019). arXiv: 1908.00993 [astro-ph.GA] [p. 200].

[248] J. Soltis, S. Casertano, and A. G. Riess. "The Parallax of ω Centauri Measured from Gaia EDR3 and a Direct, Geometric Calibration of the Tip of the Red Giant Branch and the Hubble Constant". *Astrophys. J. Lett.* 908.1 (2021), p. L5. DOI: 10.3847/2041-8213/abdbad. arXiv: 2012.09196 [astro-ph.GA] [p. 200].

[249] N. Khetan et al. "A new measurement of the Hubble constant using Type Ia supernovae calibrated with surface brightness fluctuations". *Astron. Astrophys.* 647 (2021), A72. DOI: 10.1051/0004-6361/202039196. arXiv: 2008.07754 [astro-ph.CO] [p. 200].

[250] C. D. Huang, A. G. Riess, W. Yuan, L. M. Macri, N. L. Zakamska, S. Casertano, P. A. Whitelock, S. L. Hoffmann, A. V. Filippenko, and D. Scolnic. "Hubble Space Telescope Observations of Mira Variables in the Type Ia Supernova Host NGC 1559: An Alternative Candle to Measure the Hubble Constant" (2019). DOI: 10.3847/1538-4357/ab5dbd. arXiv: 1908.10883 [astro-ph.CO] [p. 200].

[251] J. Schombert, S. McGaugh, and F. Lelli. "Using the Baryonic Tully-Fisher Relation to Measure H_o". *Astrophysical Journal* 160.2, 71 (Aug. 2020), p. 71. DOI: 10.3847/1538-3881/ab9d88. arXiv: 2006.08615 [astro-ph.CO] [p. 200].

[252] K. C. Wong et al. "H0LiCOW XIII. A 2.4% measurement of H_0 from lensed quasars: 5.3σ tension between early and late-Universe probes" (2019). arXiv: 1907.04869 [astro-ph.CO] [p. 200].

[253] S. Birrer et al. "TDCOSMO - IV. Hierarchical time-delay cosmography – joint inference of the Hubble constant and galaxy density profiles". *Astron. Astrophys.* 643 (2020), A165. DOI: 10.1051/0004-6361/202038861. arXiv: 2007.02941 [astro-ph.CO] [p. 200].

[254] D. W. Pesce et al. "The Megamaser Cosmology Project. XIII. Combined Hubble constant constraints" (2020). arXiv: 2001.09213 [astro-ph.CO] [p. 200].

[255] B. P. Abbott et al. "A Gravitational-wave Measurement of the Hubble Constant Following the Second Observing Run of Advanced LIGO and Virgo". *Astrophys. J.* 909.2 (2021), p. 218. DOI: 10.3847/1538-4357/abdcb7. arXiv: 1908.06060 [astro-ph.CO] [p. 200].

[256] E. Di Valentino, O. Mena, S. Pan, L. Visinelli, W. Yang, A. Melchiorri, D. F. Mota, A. G. Riess, and J. Silk. "In the realm of the Hubble tension—a review of solutions". *Class. Quant. Grav.* 38.15 (2021), p. 153001. DOI: 10.1088/1361-6382/ac086d. arXiv: 2103.01183 [astro-ph.CO] [p. 200].

[257] J. L. Bernal, L. Verde, and A. G. Riess. "The trouble with H_0". *JCAP* 1610.10 (2016), p. 019. DOI: 10.1088/1475-7516/2016/10/019. arXiv: 1607.05617 [p. 200].

[258] K. Aylor, M. Joy, L. Knox, M. Millea, S. Raghunathan, and W. L. K. Wu. "Sounds Discordant: Classical Distance Ladder & ΛCDM -based Determinations of the Cosmological Sound Horizon" (2018). arXiv: 1811.00537 [p. 200].

[259] L. Knox and M. Millea. "Hubble constant hunter's guide". *Phys. Rev. D* 101.4 (2020), p. 043533. DOI: 10.1103/PhysRevD.101.043533. arXiv: 1908.03663 [astro-ph.CO] [p. 200].

[260] D. Camarena and V. Marra. "On the use of the local prior on the absolute magnitude of Type Ia supernovae in cosmological inference". *mnras* 504.4 (July 2021), pp. 5164–5171. DOI: 10.1093/mnras/stab1200. arXiv: 2101.08641 [astro-ph.CO] [pp. 200, 211].

[261] G. Efstathiou. "To H0 or not to H0?" *arXiv e-prints* (Mar. 2021). arXiv: 2103.08723 [astro-ph.CO] [pp. 200, 211].

[262] C. D. Kreisch, F.-Y. Cyr-Racine, and O. Doré. "Neutrino puzzle: Anomalies, interactions, and cosmological tensions". *Phys. Rev. D* 101.12 (2020), p. 123505. DOI: 10.1103/PhysRevD.101.123505. arXiv: 1902.00534 [astro-ph.CO] [p. 200].

[263] M. Berbig, S. Jana, and A. Trautner. "The Hubble tension and a renormalizable model of gauged neutrino self-interactions". *Phys. Rev. D* 102.11 (2020), p. 115008. DOI: 10.1103/PhysRevD.102.115008. arXiv: 2004.13039 [hep-ph] [p. 200].

[264] S. Ghosh, R. Khatri, and T. S. Roy. "Can dark neutrino interactions phase out the Hubble tension?" *Phys. Rev. D* 102.12 (2020), p. 123544. DOI: 10.1103/PhysRevD.102.123544. arXiv: 1908.09843 [hep-ph] [p. 200].

[265] F. Forastieri, M. Lattanzi, and P. Natoli. "Cosmological constraints on neutrino self-interactions with a light mediator". *Phys. Rev. D* 100.10 (2019), p. 103526. DOI: 10.1103/PhysRevD.100.103526. arXiv: 1904.07810 [astro-ph.CO] [p. 200].

[266] M. Escudero and S. J. Witte. "A CMB search for the neutrino mass mechanism and its relation to the Hubble tension". *Eur. Phys. J. C* 80.4 (2020), p. 294. DOI: 10.1140/epjc/s10052-020-7854-5. arXiv: 1909.04044 [astro-ph.CO] [p. 200].

[267] M. Escudero and S. J. Witte. "The hubble tension as a hint of leptogenesis and neutrino mass generation". *Eur. Phys. J. C* 81.6 (2021), p. 515. DOI: 10.1140/epjc/s10052-021-09276-5. arXiv: 2103.03249 [hep-ph] [p. 200].

[268] N. Blinov and G. Marques-Tavares. "Interacting radiation after Planck and its implications for the Hubble Tension". *JCAP* 09 (2020), p. 029. DOI: 10.1088/1475-7516/2020/09/029. arXiv: 2003.08387 [astro-ph.CO] [p. 200].

[269] S. Ghosh, S. Kumar, and Y. Tsai. "Free-streaming and Coupled Dark Radiation Isocurvature Perturbations: Constraints and Application to the Hubble Tension" (July 2021). arXiv: 2107.09076 [astro-ph.CO] [p. 200].

[270] M. Archidiacono and S. Gariazzo. "Two sides of the same coin: sterile neutrinos and dark radiation. Status and perspectives" (Jan. 2022). arXiv: 2201.10319 [hep-ph] [p. 200].

[271] D. Aloni, A. Berlin, M. Joseph, M. Schmaltz, and N. Weiner. "A Step in understanding the Hubble tension". *Phys. Rev. D* 105.12 (2022), p. 123516. DOI: 10.1103/PhysRevD.105.123516. arXiv: 2111.00014 [astro-ph.CO] [p. 200].

[272] N. Schöneberg and G. Franco Abellán. "A step in the right direction? Analyzing the Wess Zumino Dark Radiation solution to the Hubble tension" (June 2022). arXiv: 2206.11276 [astro-ph.CO] [p. 200].

[273] N. Schöneberg, G. Franco Abellán, T. Simon, A. Bartlett, Y. Patel, and T. L. Smith. "Comparative analysis of interacting stepped dark radiation". *Phys. Rev. D* 108.12 (2023), p. 123513. DOI: 10.1103/PhysRevD.108.123513. arXiv: 2306.12469 [astro-ph.CO] [pp. 200, 202].

[274] T. Karwal and M. Kamionkowski. "Dark energy at early times, the Hubble parameter, and the string axiverse". *Phys. Rev.* D94.10 (2016), p. 103523. DOI: 10.1103/PhysRevD.94.103523. arXiv: 1608.01309 [astro-ph.CO] [pp. 200, 206, 232].

[275] V. Poulin, T. L. Smith, T. Karwal, and M. Kamionkowski. "Early Dark Energy Can Resolve The Hubble Tension". *Phys. Rev. Lett.* 122.22 (2019), p. 221301. DOI: 10.1103/PhysRevLett.122.221301. arXiv: 1811.04083 [astro-ph.CO] [pp. 200, 206, 209, 210, 213, 225, 232, 244].

[276] T. L. Smith, V. Poulin, and M. A. Amin. "Oscillating scalar fields and the Hubble tension: a resolution with novel signatures". *Phys. Rev. D* 101.6 (2020), p. 063523. DOI: 10.1103/PhysRevD.101.063523. arXiv: 1908.06995 [astro-ph.CO] [pp. 200, 206, 208, 209, 232].

[277] F. Niedermann and M. S. Sloth. "New early dark energy". *Phys. Rev. D* 103.4 (2021), p. L041303. DOI: 10.1103/PhysRevD.103.L041303. arXiv: 1910.10739 [astro-ph.CO] [pp. 200, 206, 213, 244].

[278] F. Niedermann and M. S. Sloth. "Resolving the Hubble Tension with New Early Dark Energy" (June 2020). arXiv: 2006.06686 [astro-ph.CO] [pp. 200, 244].

[279] G. Ye and Y.-S. Piao. "Is the Hubble tension a hint of AdS phase around recombination?" *Phys. Rev. D* 101.8 (2020), p. 083507. DOI: 10.1103/PhysRevD.101.083507. arXiv: 2001.02451 [astro-ph.CO] [pp. 200, 206].

[280] V. Poulin, T. L. Smith, and T. Karwal. "The Ups and Downs of Early Dark Energy solutions to the Hubble tension: a review of models, hints and constraints circa 2023" (Feb. 2023). arXiv: 2302.09032 [astro-ph.CO] [pp. 200, 230].

[281] J. Renk, M. Zumalacárregui, F. Montanari, and A. Barreira. "Galileon gravity in light of ISW, CMB, BAO and H_0 data". *JCAP* 1710.10 (2017), p. 020. DOI: 10.1088/1475-7516/2017/10/020. arXiv: 1707.02263 [p. 200].

[282] C. Umiltà, M. Ballardini, F. Finelli, and D. Paoletti. "CMB and BAO constraints for an induced gravity dark energy model with a quartic potential". *JCAP* 1508 (2015), p. 017. DOI: 10.1088/1475-7516/2015/08/017. arXiv: 1507.00718 [p. 200].

[283] M. Ballardini, F. Finelli, C. Umiltà, and D. Paoletti. "Cosmological constraints on induced gravity dark energy models". *JCAP* 1605.05 (2016), p. 067. DOI: 10.1088/1475-7516/2016/05/067. arXiv: 1601.03387 [p. 200].

[284] M. Rossi, M. Ballardini, M. Braglia, F. Finelli, D. Paoletti, A. A. Starobinsky, and C. Umiltà. "Cosmological constraints on post-Newtonian parameters in effectively massless scalar-tensor theories of gravity". *Phys. Rev. D* 100.10 (2019), p. 103524. DOI: 10.1103/PhysRevD.100.103524. arXiv: 1906.10218 [astro-ph.CO] [p. 200].

[285] M. Braglia, M. Ballardini, W. T. Emond, F. Finelli, A. E. Gumrukcuoglu, K. Koyama, and D. Paoletti. "Larger value for H_0 by an evolving gravitational constant". *Phys. Rev. D* 102.2 (2020), p. 023529. DOI: 10.1103/PhysRevD.102.023529. arXiv: 2004.11161 [astro-ph.CO] [p. 200].

[286] M. Zumalacarregui. "Gravity in the Era of Equality: Towards solutions to the Hubble problem without fine-tuned initial conditions". *Phys. Rev. D* 102.2 (2020), p. 023523. DOI: 10.1103/PhysRevD.102.023523. arXiv: 2003.06396 [astro-ph.CO] [p. 200].

[287] T. Abadi and E. D. Kovetz. "Can conformally coupled modified gravity solve the Hubble tension?" *Phys. Rev. D* 103.2 (2021), p. 023530. DOI: 10.1103/PhysRevD.103.023530. arXiv: 2011.13853 [astro-ph.CO] [p. 200].

[288] M. Ballardini, M. Braglia, F. Finelli, D. Paoletti, A. A. Starobinsky, and C. Umiltà. "Scalar-tensor theories of gravity, neutrino physics, and the H_0 tension". *JCAP* 10 (2020), p. 044. DOI: 10.1088/1475-7516/2020/10/044. arXiv: 2004.14349 [astro-ph.CO] [p. 200].

[289] M. Braglia, W. T. Emond, F. Finelli, A. E. Gumrukcuoglu, and K. Koyama. "Unified framework for early dark energy from α-attractors". *Phys. Rev. D* 102.8 (2020), p. 083513. DOI: 10.1103/PhysRevD.102.083513. arXiv: 2005.14053 [astro-ph.CO] [p. 200].

[290] E. Di Valentino, A. Melchiorri, and J. Silk. "Cosmological hints of modified gravity?" *Phys. Rev. D* 93.2 (2016), p. 023513. DOI: 10.1103/PhysRevD.93.023513. arXiv: 1509.07501 [astro-ph.CO] [p. 200].

[291] S. Bahamonde, K. F. Dialektopoulos, C. Escamilla-Rivera, G. Farrugia, V. Gakis, M. Hendry, M. Hohmann, J. L. Said, J. Mifsud, and E. Di Valentino. "Teleparallel Gravity: From Theory to Cosmology" (June 2021). arXiv: 2106.13793 [gr-qc] [p. 200].

[292] M. Raveri. "Reconstructing Gravity on Cosmological Scales". *Phys. Rev. D* 101.8 (2020), p. 083524. DOI: 10.1103/PhysRevD.101.083524. arXiv: 1902.01366 [astro-ph.CO] [p. 200].

[293] S.-F. Yan, P. Zhang, J.-W. Chen, X.-Z. Zhang, Y.-F. Cai, and E. N. Saridakis. "Interpreting cosmological tensions from the effective field theory of torsional gravity". *Phys. Rev. D* 101.12 (2020), p. 121301. DOI: 10.1103/PhysRevD.101.121301. arXiv: 1909.06388 [astro-ph.CO] [p. 200].

[294] N. Frusciante, S. Peirone, L. Atayde, and A. De Felice. "Phenomenology of the generalized cubic covariant Galileon model and cosmological bounds". *Phys. Rev. D* 101.6 (2020), p. 064001. DOI: 10.1103/PhysRevD.101.064001. arXiv: 1912.07586 [astro-ph.CO] [p. 200].

[295] J. Solà Peracaula, A. Gomez-Valent, J. de Cruz Pérez, and C. Moreno-Pulido. "Brans–Dicke Gravity with a Cosmological Constant Smoothes Out ΛCDM Tensions". *Astrophys. J. Lett.* 886.1 (2019), p. L6. DOI: 10.3847/2041-8213/ab53e9. arXiv: 1909.02554 [astro-ph.CO] [p. 200].

[296] J. Solà Peracaula, A. Gómez-Valent, J. de Cruz Pérez, and C. Moreno-Pulido. "Brans–Dicke cosmology with a Λ-term: a possible solution to ΛCDM tensions". *Class. Quant. Grav.* 37.24 (2020), p. 245003. DOI: 10.1088/1361-6382/abbc43. arXiv: 2006.04273 [astro-ph.CO] [p. 200].

[297] G. Ballesteros, A. Notari, and F. Rompineve. "The H_0 tension: ΔG_N vs. $\Delta N_{\rm eff}$". *JCAP* 11 (2020), p. 024. DOI: 10.1088/1475-7516/2020/11/024. arXiv: 2004.05049 [astro-ph.CO] [p. 200].

[298] M. Braglia, M. Ballardini, F. Finelli, and K. Koyama. "Early modified gravity in light of the H_0 tension and LSS data". *Phys. Rev. D* 103.4 (2021), p. 043528. DOI: 10.1103/PhysRevD.103.043528. arXiv: 2011.12934 [astro-ph.CO] [pp. 200, 202, 244].

[299] H. Desmond, B. Jain, and J. Sakstein. "Local resolution of the Hubble tension: The impact of screened fifth forces on the cosmic distance ladder". *Phys. Rev. D* 100.4 (2019). [Erratum: Phys.Rev.D 101, 069904 (2020), Erratum: Phys.Rev.D 101, 129901 (2020)], p. 043537. DOI: 10.1103/PhysRevD.100.043537. arXiv: 1907.03778 [astro-ph.CO] [p. 200].

[300] M.-X. Lin, M. Raveri, and W. Hu. "Phenomenology of Modified Gravity at Recombination". *Phys. Rev. D* 99.4 (2019), p. 043514. DOI: 10.1103/PhysRevD.99.043514. arXiv: 1810.02333 [astro-ph.CO] [p. 200].

[301] C.-T. Chiang and A. Slosar. "Inferences of H_0 in presence of a non-standard recombination" (Nov. 2018). arXiv: 1811.03624 [astro-ph.CO] [p. 200].

[302] L. Hart and J. Chluba. "Updated fundamental constant constraints from Planck 2018 data and possible relations to the Hubble tension". *Mon. Not. Roy. Astron. Soc.* 493.3 (2020), pp. 3255–3263. DOI: 10.1093/mnras/staa412. arXiv: 1912.03986 [astro-ph.CO] [p. 200].

[303] T. Sekiguchi and T. Takahashi. "Early recombination as a solution to the H_0 tension". *Phys. Rev. D* 103.8 (2021), p. 083507. DOI: 10.1103/PhysRevD.103.083507. arXiv: 2007.03381 [astro-ph.CO] [p. 200].

[304] K. Jedamzik and L. Pogosian. "Relieving the Hubble tension with primordial magnetic fields" (Apr. 2020). arXiv: 2004.09487 [astro-ph.CO] [pp. 200, 206].

[305] F.-Y. Cyr-Racine, F. Ge, and L. Knox. "A Symmetry of Cosmological Observables, and a High Hubble Constant as an Indicator of a Mirror World Dark Sector" (July 2021). arXiv: 2107.13000 [astro-ph.CO] [pp. 200, 202].

[306] A. Leauthaud et al. "Lensing is Low: Cosmology, Galaxy Formation, or New Physics?" *Mon. Not. Roy. Astron. Soc.* 467.3 (2017), pp. 3024–3047. DOI: 10.1093/mnras/stx258. arXiv: 1611.08606 [astro-ph.CO] [p. 201].

[307] C. Hikage et al. "Cosmology from cosmic shear power spectra with Subaru Hyper Suprime-Cam first-year data". *Publ. Astron. Soc. Jap.* 71.2 (2019), p. 43. DOI: 10.1093/pasj/psz010. arXiv: 1809.09148 [astro-ph.CO] [p. 201].

[308] P. A. R. Ade et al. "Planck 2015 results. XXIV. Cosmology from Sunyaev-Zeldovich cluster counts". *Astron. Astrophys.* 594 (2016), A24. DOI: 10.1051/0004-6361/201525833. arXiv: 1502.01597 [astro-ph.CO] [p. 201].

[309] S. Bocquet et al. "Cluster Cosmology Constraints from the 2500 deg^2 SPT-SZ Survey: Inclusion of Weak Gravitational Lensing Data from Magellan and the Hubble Space Telescope". *Astrophys. J.* 878.1 (2019), p. 55. DOI: 10.3847/1538-4357/ab1f10. arXiv: 1812.01679 [astro-ph.CO] [p. 202].

[310] S. Bridle and L. King. "Dark energy constraints from cosmic shear power spectra: impact of intrinsic alignments on photometric redshift requirements". *New J. Phys.* 9 (2007), p. 444. DOI: 10.1088/1367-2630/9/12/444. arXiv: 0705.0166 [astro-ph] [p. 202].

[311] A. Mead, S. Brieden, T. Tröster, and C. Heymans. "HMcode-2020: Improved modelling of non-linear cosmological power spectra with baryonic feedback" (Sept. 2020). DOI: 10.1093/mnras/stab082. arXiv: 2009.01858 [astro-ph.CO] [pp. 202, 234].

[312] T. M. C. Abbott et al. "DES Y3 + KiDS-1000: Consistent cosmology combining cosmic shear surveys". *Open J. Astrophys.* 6 (2023), p. 2305.17173. DOI: 10.21105/astro.2305.17173. arXiv: 2305.17173 [astro-ph.CO] [p. 202].

[313] J. Lesgourgues, G. Marques-Tavares, and M. Schmaltz. "Evidence for dark matter interactions in cosmological precision data?" *JCAP* 02 (2016), p. 037. DOI: 10.1088/1475-7516/2016/02/037. arXiv: 1507.04351 [astro-ph.CO] [p. 202].

[314] M. A. Buen-Abad, G. Marques-Tavares, and M. Schmaltz. "Non-Abelian dark matter and dark radiation". *Phys. Rev. D* 92.2 (2015), p. 023531. DOI: 10.1103/PhysRevD.92.023531. arXiv: 1505.03542 [hep-ph] [p. 202].

[315] Z. Chacko, Y. Cui, S. Hong, T. Okui, and Y. Tsai. "Partially Acoustic Dark Matter, Interacting Dark Radiation, and Large Scale Structure". *JHEP* 12 (2016), p. 108. DOI: 10.1007/JHEP12(2016)108. arXiv: 1609.03569 [astro-ph.CO] [p. 202].

[316] M. A. Buen-Abad, M. Schmaltz, J. Lesgourgues, and T. Brinckmann. "Interacting Dark Sector and Precision Cosmology". *JCAP* 01 (2018), p. 008. DOI: 10.1088/1475-7516/2018/01/008. arXiv: 1708.09406 [astro-ph.CO] [p. 202].

[317] S. Heimersheim, N. Schöneberg, D. C. Hooper, and J. Lesgourgues. "Cannibalism hinders growth: Cannibal Dark Matter and the S_8 tension". *JCAP* 12 (2020), p. 016. DOI: 10.1088/1475-7516/2020/12/016. arXiv: 2008.08486 [astro-ph.CO] [p. 202].

[318] A. Gómez-Valent, V. Pettorino, and L. Amendola. "Update on coupled dark energy and the H_0 tension". *Phys. Rev. D* 101.12 (2020), p. 123513. DOI: 10.1103/PhysRevD.101.123513. arXiv: 2004.00610 [astro-ph.CO] [p. 202].

[319] E. Di Valentino, A. Melchiorri, O. Mena, and S. Vagnozzi. "Interacting dark energy in the early 2020s: A promising solution to the H_0 and cosmic shear tensions". *Phys. Dark Univ.* 30 (2020), p. 100666. DOI: 10.1016/j.dark.2020.100666. arXiv: 1908.04281 [astro-ph.CO] [p. 202].

[320] M. Lucca. "Dark energy–dark matter interactions as a solution to the S8 tension". *Phys. Dark Univ.* 34 (2021), p. 100899. DOI: 10.1016/j.dark.2021.100899. arXiv: 2105.09249 [astro-ph.CO] [p. 202].

[321] E. Di Valentino et al. "Cosmology Intertwined III: $f\sigma_8$ and S_8". *Astropart. Phys.* 131 (2021), p. 102604. DOI: 10.1016/j.astropartphys.2021.102604. arXiv: 2008.11285 [astro-ph.CO] [p. 202].

[322] S. Bansal, J. H. Kim, C. Kolda, M. Low, and Y. Tsai. "Mirror twin Higgs cosmology: constraints and a possible resolution to the H_0 and S_8 tensions". *JHEP* 05 (2022), p. 050. DOI: 10.1007/JHEP05(2022)050. arXiv: 2110.04317 [hep-ph] [p. 202].

[323] S. Kumar, R. C. Nunes, and P. Yadav. "Updating non-standard neutrinos properties with Planck-CMB data and full-shape analysis of BOSS and eBOSS galaxies". *JCAP* 09 (2022), p. 060. DOI: 10.1088/1475-7516/2022/09/060. arXiv: 2205.04292 [astro-ph.CO] [p. 202].

[324] I. J. Allali, F. Rompineve, and M. P. Hertzberg. "Dark Sectors with Mass Thresholds Face Cosmological Datasets" (May 2023). arXiv: 2305.14166 [astro-ph.CO] [p. 202].

[325] A. Chudaykin, K. Dolgikh, and M. M. Ivanov. "Constraints on the curvature of the Universe and dynamical dark energy from the Full-shape and BAO data". *Phys. Rev. D* 103.2 (2021), p. 023507. DOI: 10.1103/PhysRevD.103.023507. arXiv: 2009.10106 [astro-ph.CO] [p. 202].

[326] A. Glanville, C. Howlett, and T. M. Davis. "Full-Shape Galaxy Power Spectra and the Curvature Tension" (May 2022). arXiv: 2205.05892 [astro-ph.CO] [p. 202].

[327] G. D'Amico, L. Senatore, P. Zhang, and H. Zheng. "The Hubble Tension in Light of the Full-Shape Analysis of Large-Scale Structure Data". *JCAP* 05 (2021), p. 072. DOI: 10.1088/1475-7516/2021/05/072. arXiv: 2006.12420 [astro-ph.CO] [pp. 202, 206, 207, 214, 215, 225, 230, 291, 292].

[328] M. M. Ivanov, E. McDonough, J. C. Hill, M. Simonović, M. W. Toomey, S. Alexander, and M. Zaldarriaga. "Constraining Early Dark Energy with Large-Scale Structure". *Phys. Rev. D* 102.10 (2020), p. 103502. DOI: 10.1103/PhysRevD.102.103502. arXiv: 2006.11235 [astro-ph.CO] [pp. 202, 206, 207, 214, 215, 225, 230, 291].

[329] F. Niedermann and M. S. Sloth. "New Early Dark Energy is compatible with current LSS data". *Phys. Rev. D* 103.10 (2021), p. 103537. DOI: 10.1103/PhysRevD.103.103537. arXiv: 2009.00006 [astro-ph.CO] [pp. 202, 206].

[330] T. Simon, P. Zhang, V. Poulin, and T. L. Smith. "Updated constraints from the effective field theory analysis of the BOSS power spectrum on early dark energy". *Phys. Rev. D* 107.6 (2023), p. 063505. DOI: 10.1103/PhysRevD.107.063505. arXiv: 2208.05930 [astro-ph.CO] [pp. 202, 203].

[331] H. Rubira, A. Mazoun, and M. Garny. "Full-shape BOSS constraints on dark matter interacting with dark radiation and lifting the S_8 tension" (Sept. 2022). arXiv: 2209.03974 [astro-ph.CO] [p. 202].

[332] R. C. Nunes, S. Vagnozzi, S. Kumar, E. Di Valentino, and O. Mena. "New tests of dark sector interactions from the full-shape galaxy power spectrum". *Phys. Rev. D* 105.12 (2022), p. 123506. DOI: 10.1103/PhysRevD.105.123506. arXiv: 2203.08093 [astro-ph.CO] [p. 202].

[333] M. Gonzalez, M. P. Hertzberg, and F. Rompineve. "Ultralight Scalar Decay and the Hubble Tension". *JCAP* 10 (2020), p. 028. DOI: 10.1088/1475-7516/2020/10/028. arXiv: 2006.13959 [astro-ph.CO] [p. 202].

[334] A. Laguë, J. R. Bond, R. Hložek, K. K. Rogers, D. J. E. Marsh, and D. Grin. "Constraining ultralight axions with galaxy surveys". *JCAP* 01.01 (2022), p. 049. DOI: 10.1088/1475-7516/2022/01/049. arXiv: 2104.07802 [astro-ph.CO] [p. 202].

[335] I. J. Allali, M. P. Hertzberg, and F. Rompineve. "Dark sector to restore cosmological concordance". *Phys. Rev. D* 104.8 (2021), p. L081303. DOI: 10.1103/PhysRevD.104.L081303. arXiv: 2104.12798 [astro-ph.CO] [pp. 202, 227].

[336] T. Simon. "Can acoustic early dark energy still resolve the Hubble tension?" (Oct. 2023). arXiv: 2310.16800 [astro-ph.CO] [p. 203].

[337] M.-X. Lin, G. Benevento, W. Hu, and M. Raveri. "Acoustic Dark Energy: Potential Conversion of the Hubble Tension". *Phys. Rev.* D100.6 (2019), p. 063542. DOI: 10.1103/PhysRevD.100.063542. arXiv: 1905.12618 [astro-ph.CO] [pp. 206, 230–232, 240, 241, 243, 244].

[338] K. V. Berghaus and T. Karwal. "Thermal Friction as a Solution to the Hubble Tension". *Phys. Rev. D* 101.8 (2020), p. 083537. DOI: 10.1103/PhysRevD.101.083537. arXiv: 1911.06281 [astro-ph.CO] [p. 206].

[339] T. Karwal, M. Raveri, B. Jain, J. Khoury, and M. Trodden. "Chameleon Early Dark Energy and the Hubble Tension". *arXiv e-prints*, arXiv:2106.13290 (June 2021), arXiv:2106.13290. arXiv: 2106.13290 [p. 206].

[340] J. C. Hill et al. "The Atacama Cosmology Telescope: Constraints on Pre-Recombination Early Dark Energy" (Sept. 2021). arXiv: 2109.04451 [astro-ph.CO] [pp. 206, 213, 214, 220].

[341] V. Poulin, T. L. Smith, and A. Bartlett. "Dark Energy at early times and ACT: a larger Hubble constant without late-time priors" (Sept. 2021). arXiv: 2109.06229 [astro-ph.CO] [pp. 206, 213, 214, 220].

[342] A. La Posta, T. Louis, X. Garrido, and J. C. Hill. "Constraints on Pre-Recombination Early Dark Energy from SPT-3G Public Data" (Dec. 2021). arXiv: 2112.10754 [astro-ph.CO] [pp. 206, 213, 214, 220].

[343] T. L. Smith, M. Lucca, V. Poulin, G. F. Abellan, L. Balkenhol, K. Benabed, S. Galli, and R. Murgia. "Hints of Early Dark Energy in Planck, SPT, and ACT data: new physics or systematics?" (Feb. 2022). arXiv: 2202.09379 [astro-ph.CO] [pp. 206, 213, 214, 220].

[344] J. C. Hill, E. McDonough, M. W. Toomey, and S. Alexander. "Early dark energy does not restore cosmological concordance". *Phys. Rev. D* 102.4 (2020), p. 043507. DOI: 10.1103/PhysRevD.102.043507. arXiv: 2003.07355 [astro-ph.CO] [pp. 206, 244].

[345] S. Vagnozzi. "Consistency tests of ΛCDM from the early ISW effect: implications for early-time new physics and the Hubble tension". *arXiv e-prints*, arXiv:2105.10425 (May 2021), arXiv:2105.10425. arXiv: 2105.10425 [pp. 206, 210, 244].

[346] T. L. Smith, V. Poulin, J. L. Bernal, K. K. Boddy, M. Kamionkowski, and R. Murgia. "Early dark energy is not excluded by current large-scale structure data". *Phys. Rev. D* 103.12 (2021), p. 123542. DOI: 10.1103/PhysRevD.103.123542. arXiv: 2009.10740 [astro-ph.CO] [pp. 206, 218, 225, 230, 235].

[347] R. Murgia, G. F. Abellán, and V. Poulin. "Early dark energy resolution to the Hubble tension in light of weak lensing surveys and lensing anomalies". *Phys. Rev. D* 103.6 (2021), p. 063502. DOI: 10.1103/PhysRevD.103.063502. arXiv: 2009.10733 [astro-ph.CO] [pp. 206, 218].

[348] M. S. Turner. "Coherent Scalar Field Oscillations in an Expanding Universe". *Phys. Rev. D* 28 (1983), p. 1243. DOI: 10.1103/PhysRevD.28.1243 [p. 208].

[349] V. Poulin, T. L. Smith, D. Grin, T. Karwal, and M. Kamionkowski. "Cosmological implications of ultralight axionlike fields". *Phys. Rev.* D98.8 (2018), p. 083525. DOI: 10.1103/PhysRevD.98.083525. arXiv: 1806.10608 [pp. 208, 230, 232].

[350] K. Jedamzik, L. Pogosian, and G.-B. Zhao. "Why reducing the cosmic sound horizon alone can not fully resolve the Hubble tension". *Commun. in Phys.* 4 (2021), p. 123. DOI: 10.1038/s42005-021-00628-x. arXiv: 2010.04158 [astro-ph.CO] [p. 210].

[351] S. K. Choi et al. "The Atacama Cosmology Telescope: a measurement of the Cosmic Microwave Background power spectra at 98 and 150 GHz". *JCAP* 12 (2020), p. 045. DOI: 10.1088/1475-7516/2020/12/045. arXiv: 2007.07289 [astro-ph.CO] [p. 210].

[352] M. Raveri and W. Hu. "Concordance and Discordance in Cosmology" (2018). arXiv: 1806.04649 [pp. 219, 235, 262, 306].

[353] E. McDonough, M.-X. Lin, J. C. Hill, W. Hu, and S. Zhou. "The Early Dark Sector, the Hubble Tension, and the Swampland" (Dec. 2021). arXiv: 2112.09128 [astro-ph.CO] [p. 227].

[354] V. I. Sabla and R. R. Caldwell. "The Microphysics of Early Dark Energy" (Feb. 2022). arXiv: 2202.08291 [astro-ph.CO] [p. 227].

[355] S. J. Clark, K. Vattis, J. Fan, and S. M. Koushiappas. "The H_0 and S_8 tensions necessitate early and late time changes to ΛCDM" (Oct. 2021). arXiv: 2110.09562 [astro-ph.CO] [p. 227].

[356] J. L. Bernal, L. Verde, R. Jimenez, M. Kamionkowski, D. Valcin, and B. D. Wandelt. "The trouble beyond H_0 and the new cosmic triangles". *Phys. Rev. D* 103.10 (2021), p. 103533. DOI: 10.1103/PhysRevD.103.103533. arXiv: 2102.05066 [astro-ph.CO] [p. 227].

[357] M. Boylan-Kolchin and D. R. Weisz. "Uncertain times: the redshift–time relation from cosmology and stars". *Mon. Not. Roy. Astron. Soc.* 505.2 (2021), pp. 2764–2783. DOI: 10.1093/mnras/stab1521. arXiv: 2103.15825 [astro-ph.CO] [p. 227].

[358] A. Klypin, V. Poulin, F. Prada, J. Primack, M. Kamionkowski, V. Avila-Reese, A. Rodriguez-Puebla, P. Behroozi, D. Hellinger, and T. L. Smith. "Clustering and Halo Abundances in Early Dark Energy Cosmological Models". *Mon. Not. Roy. Astron. Soc.* 504.1 (2021), pp. 769–781. DOI: 10.1093/mnras/stab769. arXiv: 2006.14910 [astro-ph.CO] [p. 227].

[359] M. Boylan-Kolchin. "Stress Testing ΛCDM with High-redshift Galaxy Candidates" (Aug. 2022). arXiv: 2208.01611 [astro-ph.CO] [p. 227].

[360] G. D'Amico, N. Kaloper, and A. Westphal. "General double monodromy inflation". *Phys. Rev. D* 105.10 (2022), p. 103527. DOI: 10.1103/PhysRevD.105.103527. arXiv: 2112.13861 [hep-th] [p. 227].

[361] R. Kallosh and A. Linde. "Hybrid cosmological attractors". *Phys. Rev. D* 106.2 (2022), p. 023522. DOI: 10.1103/PhysRevD.106.023522. arXiv: 2204.02425 [hep-th] [p. 227].

[362] J.-Q. Jiang and Y.-S. Piao. "Towards early dark energy and n_s=1 with Planck, ACT and SPT" (Feb. 2022). arXiv: 2202.13379 [astro-ph.CO] [p. 227].

[363] F. Takahashi and W. Yin. "Cosmological implications of $n_s \approx 1$ in light of the Hubble tension" (Dec. 2021). arXiv: 2112.06710 [astro-ph.CO] [p. 227].

[364] R. Gsponer, R. Zhao, J. Donald-McCann, D. Bacon, K. Koyama, R. Crittenden, T. Simon, and E.-M. Mueller. "Cosmological constraints on early dark energy from the full shape analysis of eBOSS DR16". *Mon. Not. Roy. Astron. Soc.* 530.3 (2024), pp. 3075–3099. DOI: 10.1093/mnras/stae992. arXiv: 2312.01977 [astro-ph.CO] [pp. 227, 238].

[365] A. Blanchard, J.-Y. Héloret, S. Ilić, B. Lamine, and I. Tutusaus. "ΛCDM is alive and well" (May 2022). arXiv: 2205.05017 [astro-ph.CO] [p. 230].

[366] C. Armendariz-Picon, V. F. Mukhanov, and P. J. Steinhardt. "Essentials of k essence". *Phys. Rev. D* 63 (2001), p. 103510. DOI: 10.1103/PhysRevD.63.103510. arXiv: astro-ph/0006373 [p. 231].

[367] C. Gordon and W. Hu. "A Low CMB quadrupole from dark energy isocurvature perturbations". *Phys. Rev. D* 70 (2004), p. 083003. DOI: 10.1103/PhysRevD.70.083003. arXiv: astro-ph/0406496 [p. 231].

[368] A. Gómez-Valent, Z. Zheng, L. Amendola, V. Pettorino, and C. Wetterich. "Early dark energy in the pre- and postrecombination epochs". *Phys. Rev. D* 104.8 (2021), p. 083536. DOI: 10.1103/PhysRevD.104.083536. arXiv: 2107.11065 [astro-ph.CO] [p. 232].

[369] M.-X. Lin, W. Hu, and M. Raveri. "Testing H_0 in Acoustic Dark Energy with Planck and ACT Polarization". *Phys. Rev. D* 102 (2020), p. 123523. DOI: 10.1103/PhysRevD.102.123523. arXiv: 2009.08974 [astro-ph.CO] [pp. 232, 235, 241, 243, 244].

[370] J. Lesgourgues. "The Cosmic Linear Anisotropy Solving System (CLASS) I: Overview" (Apr. 2011). arXiv: 1104.2932 [astro-ph.IM] [p. 233].

[371] A. G. Riess, S. Casertano, W. Yuan, L. M. Macri, and D. Scolnic. "Large Magellanic Cloud Cepheid Standards Provide a 1% Foundation for the Determination of the Hubble Constant and Stronger Evidence for Physics beyond ΛCDM". *Astrophys. J.* 876.1 (2019), p. 85. DOI: 10.3847/1538-4357/ab1422. arXiv: 1903.07603 [astro-ph.CO] [p. 235].

[372] G. Liu, J. Gao, Y. Han, Y. Mu, and L. Xu. "Mitigating Cosmological Tensions via Momentum-Coupled Dark Sector Model" (Oct. 2023). arXiv: 2310.09798 [astro-ph.CO] [p. 244].

[373] P. Agrawal, F.-Y. Cyr-Racine, D. Pinner, and L. Randall. "Rock 'n' roll solutions to the Hubble tension". *Phys. Dark Univ.* 42 (2023), p. 101347. DOI: 10.1016/j.dark.2023.101347. arXiv: 1904.01016 [astro-ph.CO] [p. 244].

[374] G. Franco Abellán, M. Braglia, M. Ballardini, F. Finelli, and V. Poulin. "Probing Early Modification of Gravity with Planck, ACT and SPT" (Aug. 2023). arXiv: 2308.12345 [astro-ph.CO] [p. 244].

[375] K. Enqvist, S. Nadathur, T. Sekiguchi, and T. Takahashi. "Decaying dark matter and the tension in σ_8". *JCAP* 09 (2015), p. 067. DOI: 10.1088/1475-7516/2015/09/067. arXiv: 1505.05511 [astro-ph.CO] [pp. 246–248].

[376] Z. Berezhiani, A. D. Dolgov, and I. I. Tkachev. "Reconciling Planck results with low redshift astronomical measurements". *Phys. Rev. D* 92.6 (2015), p. 061303. DOI: 10.1103/PhysRevD.92.061303. arXiv: 1505.03644 [astro-ph.CO] [p. 246].

[377] N. Blinov, C. Keith, and D. Hooper. "Warm Decaying Dark Matter and the Hubble Tension". *JCAP* 06 (2020), p. 005. DOI: 10.1088/1475-7516/2020/06/005. arXiv: 2004.06114 [astro-ph.CO] [p. 246].

[378] K. Vattis, S. M. Koushiappas, and A. Loeb. "Dark matter decaying in the late Universe can relieve the H0 tension". *Phys. Rev. D* 99.12 (2019), p. 121302. DOI: 10.1103/PhysRevD.99.121302. arXiv: 1903.06220 [astro-ph.CO] [p. 246].

[379] A. Chudaykin, D. Gorbunov, and I. Tkachev. "Dark matter component decaying after recombination: Lensing constraints with Planck data". *Phys. Rev. D* 94 (2016), p. 023528. DOI: 10.1103/PhysRevD.94.023528. arXiv: 1602.08121 [astro-ph.CO] [p. 246].

[380] A. Chudaykin, D. Gorbunov, and I. Tkachev. "Dark matter component decaying after recombination: Sensitivity to baryon acoustic oscillation and redshift space distortion probes". *Phys. Rev. D* 97.8 (2018), p. 083508. DOI: 10.1103/PhysRevD.97.083508. arXiv: 1711.06738 [astro-ph.CO] [p. 246].

[381] V. Poulin, P. D. Serpico, and J. Lesgourgues. "A fresh look at linear cosmological constraints on a decaying dark matter component". *JCAP* 08 (2016), p. 036. DOI: 10.1088/1475-7516/2016/08/036. arXiv: 1606.02073 [astro-ph.CO] [pp. 246–249, 259].

[382] S. J. Clark, K. Vattis, and S. M. Koushiappas. "Cosmological constraints on late-universe decaying dark matter as a solution to the H_0 tension". *Phys. Rev. D* 103.4 (2021), p. 043014. DOI: 10.1103/PhysRevD.103.043014. arXiv: 2006.03678 [astro-ph.CO] [p. 246].

[383] B. S. Haridasu and M. Viel. "Late-time decaying dark matter: constraints and implications for the H_0-tension". *Mon. Not. Roy. Astron. Soc.* 497.2 (2020), pp. 1757–1764. DOI: 10.1093/mnras/staa1991. arXiv: 2004.07709 [astro-ph.CO] [p. 246].

[384] A. Nygaard, T. Tram, and S. Hannestad. "Updated constraints on decaying cold dark matter". *JCAP* 05 (2021), p. 017. DOI: 10.1088/1475-7516/2021/05/017. arXiv: 2011.01632 [astro-ph.CO] [pp. 246, 260].

[385] S. Alvi, T. Brinckmann, M. Gerbino, M. Lattanzi, and L. Pagano. "Do you smell something decaying? Updated linear constraints on decaying dark matter scenarios". *JCAP* 11 (2022), p. 015. DOI: 10.1088/1475-7516/2022/11/015. arXiv: 2205.05636 [astro-ph.CO] [p. 246].

[386] V. Berezinsky, A. Masiero, and J. W. F. Valle. "Cosmological signatures of supersymmetry with spontaneously broken R-parity". *Phys. Lett. B* 266 (1991), pp. 382–388. DOI: 10.1016/0370-2693(91)91055-Z [p. 246].

[387] H.-B. Kim and J. E. Kim. "Late decaying axino as CDM and its lifetime bound". *Phys. Lett. B* 527 (2002), pp. 18–22. DOI: 10.1016/S0370-2693(01)01507-6. arXiv: hep-ph/0108101 [p. 246].

[388] L. Covi, J. E. Kim, and L. Roszkowski. "Axinos as cold dark matter". *Phys. Rev. Lett.* 82 (1999), pp. 4180–4183. DOI: 10.1103/PhysRevLett.82.4180. arXiv: hep-ph/9905212 [p. 246].

[389] J. L. Feng, A. Rajaraman, and F. Takayama. "Superweakly interacting massive particles". *Phys. Rev. Lett.* 91 (2003), p. 011302. DOI: 10.1103/PhysRevLett.91.011302. arXiv: hep-ph/0302215 [p. 246].

[390] J. L. Feng, A. Rajaraman, and F. Takayama. "SuperWIMP dark matter signals from the early universe". *Phys. Rev. D* 68 (2003), p. 063504. DOI: 10.1103/PhysRevD.68.063504. arXiv: hep-ph/0306024 [p. 246].

[391] R. Allahverdi, B. Dutta, F. S. Queiroz, L. E. Strigari, and M.-Y. Wang. "Dark Matter from Late Invisible Decays to/of Gravitinos". *Phys. Rev. D* 91.5 (2015), p. 055033. DOI: 10.1103/PhysRevD.91.055033. arXiv: 1412.4391 [hep-ph] [p. 246].

[392] K. N. Abazajian et al. "Light Sterile Neutrinos: A White Paper" (Apr. 2012). arXiv: 1204.5379 [hep-ph] [p. 246].

[393] M. Drewes et al. "A White Paper on keV Sterile Neutrino Dark Matter". *JCAP* 01 (2017), p. 025. DOI: 10.1088/1475-7516/2017/01/025. arXiv: 1602.04816 [hep-ph] [p. 246].

[394] C.-R. Chen, F. Takahashi, and T. T. Yanagida. "Gamma rays and positrons from a decaying hidden gauge boson". *Phys. Lett. B* 671 (2009), pp. 71–76. DOI: 10.1016/j.physletb.2008.11.048. arXiv: 0809.0792 [hep-ph] [p. 246].

[395] G. Choi, M. Suzuki, and T. T. Yanagida. "Degenerate Sub-keV Fermion Dark Matter from a Solution to the Hubble Tension". *Phys. Rev. D* 101.7 (2020), p. 075031. DOI: 10.1103/PhysRevD.101.075031. arXiv: 2002.00036 [hep-ph] [p. 246].

[396] G. Choi, M. Suzuki, and T. T. Yanagida. "Degenerate fermion dark matter from a broken $U(1)_{B-L}$ gauge symmetry". *Phys. Rev. D* 102.3 (2020), p. 035022. DOI: 10.1103/PhysRevD.102.035022. arXiv: 2004.07863 [hep-ph] [p. 246].

[397] G. Choi and T. T. Yanagida. "Gravitino cosmology helped by a right handed (s)neutrino". *Phys. Lett. B* 827 (2022), p. 136954. DOI: 10.1016/j.physletb.2022.136954. arXiv: 2104.02958 [hep-ph] [p. 246].

[398] E. B. Holm, T. Tram, and S. Hannestad. "Decaying warm dark matter revisited". *JCAP* 08.08 (2022), p. 044. DOI: 10.1088/1475-7516/2022/08/044. arXiv: 2205.13628 [astro-ph.CO] [p. 246].

[399] G. Choi, M. Suzuki, and T. T. Yanagida. "XENON1T Anomaly and its Implication for Decaying Warm Dark Matter". *Phys. Lett. B* 811 (2020), p. 135976. DOI: 10.1016/j.physletb.2020.135976. arXiv: 2006.12348 [hep-ph] [p. 246].

[400] S. Xu and S. Zheng. "Resolving XENON Excess With Decaying Cold Dark Matter". *Eur. Phys. J. C* 81.5 (2021), p. 446. DOI: 10.1140/epjc/s10052-021-09262-x. arXiv: 2012.10827 [hep-ph] [p. 246].

[401] K. Dutta, A. Ghosh, A. Kar, and B. Mukhopadhyaya. "Decaying fermionic warm dark matter and XENON1T electronic recoil excess". *Phys. Dark Univ.* 33 (2021), p. 100855. DOI: 10.1016/j.dark.2021.100855. arXiv: 2103.14664 [hep-ph] [p. 246].

[402] W. B. Lin, D. H. Huang, X. Zhang, and R. H. Brandenberger. "Nonthermal production of WIMPs and the subgalactic structure of the universe". *Phys. Rev. Lett.* 86 (2001), p. 954. DOI: 10.1103/PhysRevLett.86.954. arXiv: astro-ph/0009003 [p. 246].

[403] F. J. Sanchez-Salcedo. "Unstable cold dark matter and the cuspy halo problem in dwarf galaxies". *Astrophys. J. Lett.* 591 (2003), pp. L107–L110. DOI: 10.1086/377092. arXiv: astro-ph/0305496 [p. 246].

[404] J. A. R. Cembranos, J. L. Feng, A. Rajaraman, and F. Takayama. "SuperWIMP solutions to small scale structure problems". *Phys. Rev. Lett.* 95 (2005), p. 181301. DOI: 10.1103/PhysRevLett.95.181301. arXiv: hep-ph/0507150 [p. 246].

[405] M. Kaplinghat. "Dark matter from early decays". *Phys. Rev. D* 72 (2005), p. 063510. DOI: 10.1103/PhysRevD.72.063510. arXiv: astro-ph/0507300 [p. 246].

[406] L. E. Strigari, M. Kaplinghat, and J. S. Bullock. "Dark Matter Halos with Cores from Hierarchical Structure Formation". *Phys. Rev. D* 75 (2007), p. 061303. DOI: 10.1103/PhysRevD.75.061303. arXiv: astro-ph/0606281 [p. 246].

[407] F. Borzumati, T. Bringmann, and P. Ullio. "Dark matter from late decays and the small-scale structure problems". *Phys. Rev. D* 77 (2008), p. 063514. DOI: 10.1103/PhysRevD.77.063514. arXiv: hep-ph/0701007 [p. 246].

[408] A. H. G. Peter, C. E. Moody, and M. Kamionkowski. "Dark-Matter Decays and Self-Gravitating Halos". *Phys. Rev. D* 81 (2010), p. 103501. DOI: 10.1103/PhysRevD.81.103501. arXiv: 1003.0419 [astro-ph.CO] [p. 246].

[409] A. H. G. Peter and A. J. Benson. "Dark-matter decays and Milky Way satellite galaxies". *Phys. Rev. D* 82 (2010), p. 123521. DOI: 10.1103/PhysRevD.82.123521. arXiv: 1009.1912 [astro-ph.GA] [p. 246].

[410] B. Audren, J. Lesgourgues, G. Mangano, P. D. Serpico, and T. Tram. "Strongest model-independent bound on the lifetime of Dark Matter". *JCAP* 12 (2014), p. 028. DOI: 10.1088/1475-7516/2014/12/028. arXiv: 1407.2418 [astro-ph.CO] [pp. 247–249].

[411] J. Lesgourgues and T. Tram. "Fast and accurate CMB computations in non-flat FLRW universes". *JCAP* 09 (2014), p. 032. DOI: 10.1088/1475-7516/2014/09/032. arXiv: 1312.2697 [astro-ph.CO] [p. 248].

[412] J. Hubert, A. Schneider, D. Potter, J. Stadel, and S. K. Giri. "Decaying dark matter: simulations and weak-lensing forecast". *JCAP* 10 (2021), p. 040. DOI: 10.1088/1475-7516/2021/10/040. arXiv: 2104.07675 [astro-ph.CO] [pp. 248, 303].

[413] G. Blackadder and S. M. Koushiappas. "Dark matter with two- and many-body decays and supernovae type Ia". *Phys. Rev. D* 90.10 (2014), p. 103527. DOI: 10.1103/PhysRevD.90.103527. arXiv: 1410.0683 [astro-ph.CO] [p. 251].

[414] S. Aoyama, T. Sekiguchi, K. Ichiki, and N. Sugiyama. "Evolution of perturbations and cosmological constraints in decaying dark matter models with arbitrary decay mass products". *JCAP* 07 (2014), p. 021. DOI: 10.1088/1475-7516/2014/07/021. arXiv: 1402.2972 [astro-ph.CO] [p. 252].

[415] J. Lesgourgues and T. Tram. "The Cosmic Linear Anisotropy Solving System (CLASS) IV: efficient implementation of non-cold relics". *JCAP* 09 (2011), p. 032. DOI: 10.1088/1475-7516/2011/09/032. arXiv: 1104.2935 [astro-ph.CO] [p. 253].

[416] L. Senatore and M. Zaldarriaga. "The Effective Field Theory of Large-Scale Structure in the presence of Massive Neutrinos" (2017). arXiv: 1707.04698 [astro-ph.CO] [pp. 254, 266, 305, 306].

[417] R. de Belsunce and L. Senatore. "Tree-Level Bispectrum in the Effective Field Theory of Large-Scale Structure extended to Massive Neutrinos" (2018). arXiv: 1804.06849 [astro-ph.CO] [p. 254].

[418] S. Alam et al. "The clustering of galaxies in the completed SDSS-III Baryon Oscillation Spectroscopic Survey: cosmological analysis of the DR12 galaxy sample". *Mon. Not. Roy. Astron. Soc.* 470.3 (2017), pp. 2617–2652. DOI: 10.1093/mnras/stx721. eprint: 1607.03155 [pp. 256, 257, 265, 266].

[419] A. Gelman and D. B. Rubin. "Inference from Iterative Simulation Using Multiple Sequences". *Statist. Sci.* 7 (1992), pp. 457–472. DOI: 10.1214/ss/1177011136 [p. 258].

[420] V. Poulin, K. K. Boddy, S. Bird, and M. Kamionkowski. "Implications of an extended dark energy cosmology with massive neutrinos for cosmological tensions". *Phys. Rev. D* 97.12 (2018), p. 123504. DOI: 10.1103/PhysRevD.97.123504. arXiv: 1803.02474 [astro-ph.CO] [p. 259].

[421] S. Mau et al. "Milky Way Satellite Census. IV. Constraints on Decaying Dark Matter from Observations of Milky Way Satellite Galaxies" (Jan. 2022). arXiv: 2201.11740 [astro-ph.CO] [p. 263].

[422] D. Alonso et al. "The LSST Dark Energy Science Collaboration (DESC) Science Requirements Document" (Sept. 2018). eprint: 1809.01669 [pp. 264, 266].

[423] C. Heymans et al. "CFHTLenS tomographic weak lensing cosmological parameter constraints: Mitigating the impact of intrinsic galaxy alignments". *Mon. Not. Roy. Astron. Soc.* 432 (2013), p. 2433. DOI: 10.1093/mnras/stt601. eprint: 1303.1808 [p. 265].

[424] M. Vargas-Magaña et al. "The clustering of galaxies in the completed SDSS-III Baryon Oscillation Spectroscopic Survey: theoretical systematics and Baryon Acoustic Oscillations in the galaxy correlation function". *Mon. Not. Roy. Astron. Soc.* 477.1 (2018), pp. 1153–1188. DOI: 10.1093/mnras/sty571. arXiv: 1610.03506 [astro-ph.CO] [p. 282].

[425] N. S. Sugiyama, S. Saito, F. Beutler, and H.-J. Seo. "A complete FFT-based decomposition formalism for the redshift-space bispectrum". *Mon. Not. Roy. Astron. Soc.* 484.1 (2019), pp. 364–384. DOI: 10.1093/mnras/sty3249. arXiv: 1803.02132 [astro-ph.CO] [p. 289].

[426] H. A. Feldman, N. Kaiser, and J. A. Peacock. "Power spectrum analysis of three-dimensional redshift surveys". *Astrophys. J.* 426 (1994), pp. 23–37. DOI: 10.1086/174036. arXiv: astro-ph/9304022 [p. 289].

[427] K. Yamamoto. "Optimal weighting scheme in redshift space power spectrum analysis and a prospect for measuring the cosmic equation of state". *Astrophys. J.* 595 (2003), pp. 577–588. DOI: 10.1086/377488. arXiv: astro-ph/0208139 [p. 289].

[428] K. Yamamoto, M. Nakamichi, A. Kamino, B. A. Bassett, and H. Nishioka. "A Measurement of the quadrupole power spectrum in the clustering of the 2dF QSO Survey". *Publ. Astron. Soc. Jap.* 58 (2006), pp. 93–102. DOI: 10.1093/pasj/58.1.93. arXiv: astro-ph/0505115 [p. 289].

[429] D. Bianchi, H. Gil-Marín, R. Ruggeri, and W. J. Percival. "Measuring line-of-sight dependent Fourier-space clustering using FFTs". *Mon. Not. Roy. Astron. Soc.* 453.1 (2015), pp. L11–L15. DOI: 10.1093/mnrasl/slv090. arXiv: 1505.05341 [astro-ph.CO] [p. 289].

[430] R. Scoccimarro. "Fast Estimators for Redshift-Space Clustering". *Phys. Rev. D* 92.8 (2015), p. 083532. DOI: 10.1103/PhysRevD.92.083532. arXiv: 1506.02729 [astro-ph.CO] [p. 289].

[431] F. Beutler et al. “The clustering of galaxies in the completed SDSS-III Baryon Oscillation Spectroscopic Survey: Anisotropic galaxy clustering in Fourier-space”. *Mon. Not. Roy. Astron. Soc.* 466.2 (2017), pp. 2242–2260. DOI: 10.1093/mnras/stw3298. arXiv: 1607.03150 [astro-ph.CO] [p. 291].

Abstract

Over the last two decades, the standard cosmological model "Λ cold dark matter" (ΛCDM) has been firmly established by a variety of observations. Nevertheless, the nature of the dominant components of the Universe – namely dark matter and dark energy – and the process of creation of its initial conditions – namely inflation – are not yet known. Furthermore, as the precision of the data has increased, intriguing anomalies have appeared within the standard cosmological model. These anomalies arise from a discrepancy between the value of some cosmological parameters predicted from their calibration in the distant Universe, for example with the cosmic microwave background (CMB), and the measurement of these parameters from the local Universe. The two most significant tensions in modern cosmology concern the parameter that determines the expansion rate of the Universe, *i.e.*, the Hubble parameter H_0, and the parameter that quantifies the amplitude of local matter fluctuations, *i.e.*, the parameter S_8. A number of surveys dedicated to measuring large-scale structures (LSS) of the Universe (BOSS and eBOSS in particular, and the forthcoming DESI and EUCLID) can be used to weigh in on these cosmological tensions. The first axis of this thesis is based on a semi-analytical method, known as *effective field theory of large-scale structures* (EFTofLSS), which provides an accurate description of the galaxy power spectrum, and aims at improving cosmological constraints from LSS surveys, a major challenge in the context of the forthcoming data from DESI and Euclid. In particular, we apply an EFTofLSS analysis to describe the BOSS and eBOSS data, and demonstrate that these surveys can be used to obtain constraints that are competitive with those coming from CMB data. We also establish the self-consistency of this theory within the ΛCDM model, as it appears at first sight that the different EFTofLSS parametrizations proposed in the literature seem to provide different constraints on cosmological parameters. We thus identify these discrepancies as originating from subtleties of the commonly used Bayesian framework. In addition, we develop a systematic method for applying the EFTofLSS to different LSS data and obtain robust results contrasting the Bayesian framework with the frequentist approach, for an in depth cosmological inference. The second aspect of my work aims to establish the possible theoretical implications of cosmological tensions for our understanding of the dark sector of the Universe. In particular, we confront various models that can resolve these tensions with the BOSS and eBOSS data analysed under the EFTofLSS. We conclude that current clustering data are not in tension with ΛCDM, and can be used to set important constraints on model suggested to resolve cosmological tensions.

Résumé

Au cours des deux dernières décennies, le modèle cosmologique standard "Λ matière noire froide" (ΛCDM) a été fermement établi par une variété d'observations. Néanmoins, la nature des composants dominants de l'Univers – à savoir la matière noire et l'énergie noire – et le processus de création de ses conditions initiales – à savoir l'inflation – ne sont pas encore connus. En outre, à mesure que la précision des données s'est accrue, des anomalies intrigantes sont apparues au sein du modèle cosmologique standard. Ces anomalies résultent d'une divergence entre la valeur de certains paramètres cosmologiques prédite à partir de leur étalonnage dans l'Univers lointain, par exemple avec le fond diffus cosmologique (CMB), et la mesure de ces paramètres dans l'Univers local. Les deux tensions les plus importantes en cosmologie moderne concernent le paramètre qui détermine le taux d'expansion de l'Univers, à savoir le paramètre de Hubble H_0, et le paramètre qui quantifie l'amplitude des fluctuations locales de la matière, à savoir le paramètre S_8. Un certain nombre de relevés dédiés à la mesure des structures à grande échelle de l'Univers (BOSS et eBOSS en particulier, et prochainement DESI et EUCLID) peut être utilisé pour arbitrer ces tensions cosmologiques. Le premier axe de cette thèse est basé sur une méthode semi-analytique, connue sous le nom de *théorie effective des champs des structures à grandes échelles* (EFTofLSS), qui fournit une description précise du spectre de puissance des galaxies, et vise à améliorer les contraintes cosmologiques provenant des structures à grandes échelles, un défi majeur dans le contexte des prochaines données de DESI et EUCLID. En particulier, nous appliquons une analyse EFTofLSS pour décrire les données de BOSS et eBOSS, et nous démontrons que ces relevés peuvent être utilisés pour obtenir des contraintes qui sont compétitives avec celles provenant des données CMB. Nous établissons également l'auto-consistance de cette théorie au sein du modèle ΛCDM, car il semble à première vue que les différentes paramétrisations de l'EFTofLSS proposées dans la littérature fournissent des contraintes différentes sur les paramètres cosmologiques. Nous avons ainsi mis en évidence que ces divergences proviennent de certaines subtilités du cadre bayésien couramment utilisé. Par ailleurs, nous développons une méthode systématique pour appliquer l'EFTofLSS à différentes données provenant des structures à grandes échelles et obtenons des résultats robustes, tout en contrastant le cadre bayésien avec l'approche fréquentiste. Le second axe de mon travail vise à établir les implications théoriques éventuelles des tensions cosmologiques sur notre compréhension du secteur sombre de l'Univers. En particulier, nous confrontons différents modèles qui peuvent résoudre ces tensions à la lumière des données de BOSS et eBOSS analysées dans le cadre de l'EFTofLSS. Nous concluons que les données actuelles provenant des structures à grandes échelles ne sont pas en tension avec ΛCDM, et peuvent être utilisées pour établir des contraintes importantes sur les modèles suggérés pour résoudre les tensions cosmologiques.